

Synthesis of Sequence-Controlled Copolymers via Ring-Opening Metathesis Polymerization of Norbornene Derivatives

Zur Erlangung des akademischen Grades eines

DOKTORS DER NATURWISSENSCHAFTEN

(Dr. rer. nat.)

von der KIT-Fakultät für Chemie und Biowissenschaften

des Karlsruher Instituts für Technologie (KIT)

genehmigte

DISSERTATION

von

M. Sc. Dennis Barther

aus

Sinsheim

Dekan: Prof. Dr. Hans-Achim Wagenknecht

1. Referent: Prof. Dr. Michael A. R. Meier

2. Referent: Prof. Dr. Patrick Théato

Tag der mündlichen Prüfung: 26.04.2022



Dieses Werk ist lizenziert unter einer Creative Commons Namensnennung -
Weitergabe unter gleichen Bedingungen 4.0 International Lizenz (CC BY-SA 4.0):
<https://creativecommons.org/licenses/by-sa/4.0/deed.de>

„Im Walde zwei Wege boten sich mir dar und ich ging den,
der weniger betreten war — und das veränderte mein Leben.“

Walt Whitman

Danksagung

An dieser Stelle möchte ich mich zuerst bei allen Personen bedanken, die mich während der Promotion, aber auch während meines Studiums begleitet und unterstützt haben, und ohne die das Verfassen dieser Arbeit nicht möglich gewesen wäre. Außerdem möchte ich mich bei allen bedanken, die abseits der Universität für mich da waren und mir in den letzten Jahren so vielen schöne Momente beschert haben.

Zunächst geht mein Dank an Mike, dafür, dass er mich vor einigen Jahren in seinen Arbeitskreis aufgenommen und es mir ermöglicht hat dort sowohl die Vertieferarbeit als auch die Masterarbeit und anschließend die Promotion durchzuführen. Danke auch für deine Unterstützung während der gesamten Promotionszeit und dein Vertrauen in mich und meine Arbeit. Wie alle im AK Meier, weiß auch ich die freundschaftliche und familiäre Atmosphäre im Arbeitskreis, wie auch deine offene Tür sehr zu schätzen. Du hast immer ein offenes Ohr für neue Ideen und alte Probleme. Trotz aller Herausforderungen, deren ich mich während meiner Promotionszeit stellen musste, habe ich nie daran gezweifelt, dass die Promotion in deinem Arbeitskreis die richtige Entscheidung war. Nochmals vielen Dank dafür!

Another huge THANKS goes to Dafni, my almighty co supervisor. Thank you for the opportunity to work on this topic, since your research proposal was the starting point of this thesis. I also want to thank you for the confidence and patience that you had with me and my “shoulders”. You were always available for all kinds of questions and ideas, remembering our “short” meetings, both, in person and virtual. Even though we were not able to meet in person for a long time, you always gave me the feeling that I can handle this beast of a topic. Nonetheless, this work would have been definitely not possible without you. Thank you also for the nonscientific conversations, the English lessons for free, and the great time we had together. ...and as I end every meeting, greetings to Bodo and Finn.

A big thank you to the whole AK Meier group, since you were a big part for my life in the last years. Thanks to the new, but also the old members of the group for the great time we had during the everyday lab work, but also during barbecues, group trips, or several other activities. As we all know, the life of a PhD student is not always easy but being part of AK Meier and working with you is something I do not want to miss.

Herzlichen Dank auch an alle Korrekturleser: Luca, Pete, Clara, Federico und Jonas. Vielen Dank für eure Hilfe, nur so konnte die Arbeit auch zu dem werden was sie ist. Again, a huge thanks to Dafni, for investing so much work and time into the corrections, making this thesis something special.

Außerdem gilt mein Dank allen jetzigen und ehemaligen Mitgliedern des IOC Teams des AK Meier. Die arbeitsreichen Tage sind mit euch wie im Flug vergangen. Ich danke allen für die großartige Zusammenarbeit und eine unvergessliche Zeit. Roman, danke für die konstruktiven Gespräche, aber auch für deine freundliche Art und deine Hilfsbereitschaft. Ich wünsche dir viel Erfolg bei allen Dingen, die das Leben für dich bereithält. Another special thanks goes to you Federico for being a great companion since you started your Master thesis at AK Meier. I am thankful for the time we shared together and wish you all the best. Grazie.

Danke auch an alle, die mich in der langen Zeit im Arbeitskreis begleitet haben: Ben, Gregor, Katharina, Pia, Rebecca, Eren, Yasmin, Juli, Kevin, Maxi, Dani, Bohni, Michi, Anja und Caitlyn. Vielen Dank an Marius und Martin, die ihre Bachelor- bzw. Vertieferarbeit unter meiner Betreuung angefertigt haben, sowie an Heidi und Benny, die mich bei der Laborarbeit unterstützt haben.

Meinem Namenvetter Herrn Dr. Harijan danke ich für die schönen Spaziergänge und die viele Gespräche, die wir während unserer gemeinsamen Promotionszeit genießen konnten. Ich bin sehr dankbar dich damals im OCF Praktikum kennengelernt zu haben.

Nicht zuletzt gilt mein Dank auch den Angestellten und ehemaligen Angestellten des IOC, sowie unseren Sekretärinnen, Pinar und Ann Kathrin, die mich während meiner Promotionszeit unterstützt haben und daher auch einen Beitrag zu dieser Arbeit geleistet haben.

Ich danke außerdem Prof. Manfred Wilhelm, der mir ermöglicht hat die Bachelorarbeit in seinem Arbeitskreis durchzuführen. Danke auch an meine ehemaligen Betreuer Lukas Arens und Stefan Oelmann.

Dem Ministerium für Wissenschaft, Forschung und Kunst Baden-Württemberg (MWK) danke ich für die Finanzierung meiner Doktorarbeit im Rahmen des Research Seed Capital (RiSC) Förderprogramms. Sowie dem Karlsruher Institut für Technologie (KIT), das mein Studium und die anschließende Promotion erst ermöglicht hat.

Meinen herzlichen Dank möchte ich auch allen meinen Freunden aussprechen: Bea, Yasmin, Benno, Tamara und Lisa. Im Besonderen an Patrick, für die beste Sandkastenfreundschaft, die man sich nur wünschen kann. Marvin, für die vielen gemeinsamen Stunden am Lagerfeuer und auf Reisen. Lukas und Nils, für die wunderbare Abiturzeit und darüber hinaus.

Der größte Dank gilt meiner Familie, ganz besonders meinen Eltern, meiner Schwester und meiner Oma. Ihr habt mich immer unterstützt, gefördert und letztendlich aus mir den Menschen gemacht, der ich heute bin. Danke auch, dass ihr immer ein großer Rückhalt wart, auf den ich mich verlassen konnte. Ohne euch wäre das alles nicht möglich gewesen. Wo ihr seid, da ist zuhause. Zuletzt gilt mein Dank meiner Frieda, die immer für mich da war und mit der ich solch eine wunderschöne Zeit erleben darf. Ich danke dir von ganzem Herzen für deine unablässige Liebe und Unterstützung! Ich freue mich schon auf die Zukunft mit dir und bin gespannt, was das Leben für uns bereithält.

Declaration of authorship

Die vorliegende Arbeit wurde von November 2018 bis März 2022 unter Anleitung von Herrn Prof. Dr. Michael A. R. Meier und Frau Dr. Dafni Moatsou am Institut für Organische Chemie (IOC) des Karlsruher Instituts für Technologie (KIT) angefertigt.

Hiermit versichere ich, dass ich die Arbeit selbstständig angefertigt, nur die angegebenen Quellen und Hilfsmittel benutzt und mich keiner unzulässigen Hilfe Dritter bedient habe. Insbesondere habe ich wörtlich oder sinngemäß aus anderen Werken übernommene Inhalte als solche kenntlich gemacht. Die Satzung des Karlsruher Instituts für Technologie (KIT) zur Sicherung wissenschaftlicher Praxis habe ich beachtet. Des Weiteren erkläre ich, dass ich mich derzeit in keinem laufenden Promotionsverfahren befinde, und auch keine vorausgegangenen Promotionsversuche unternommen habe. Die elektronische Version der Arbeit stimmt mit der schriftlichen Version überein und die Primärdaten sind gemäß Abs. A (6) der Regeln zur Sicherung guter wissenschaftlicher Praxis des KIT beim Institut abgegeben und archiviert. Zudem versichere ich, dass die eingereichte Fassung mit der vom Promotionsausschuss gemäß Abs. 2 genehmigten Fassung der Dissertation inhaltlich übereinstimmt.

Karlsruhe, den 12. Mai 2022

Dennis Barther

Abstract

Since the polymer sciences were established in the beginning of the 20th century, the need for functionalized polymers is undeniable, potentially gaining even more importance in the future. Inspired by nature, the ability to control the monomer sequence in such materials offers great opportunities in the manipulation of intramolecular interactions, influencing the polymeric microstructure and thus resulting in interesting macroscopic properties. The development of controlled polymerization techniques has laid a robust foundation in order to achieve these goals. As such, ring-opening metathesis polymerization (ROMP) offers a versatile platform to synthesize functionalized and sequence-controlled polymers.

In the first part of this thesis, a robust method to synthesize a variety of functionalized polymers is described. Here, carboxylic acid-functional norbornene derivatives are reacted with different aldehydes and isocyanides in the Passerini three-component reaction (P-3CR), generating a variety of bifunctional monomers capable of undergoing ROMP. Furthermore, the influence of the monomer structure on their polymerizability and their respective polymerization kinetics are determined. The thermal properties of the obtained functional polymers are evaluated by differential scanning calorimetry (DSC) and thermogravimetric analysis (TGA).

In the second part of this thesis, different ROMP-based synthesis procedures are investigated to obtain graft polymers. Therefore, norbornene-based macromonomers are synthesized *via* atom transfer radical polymerization (ATRP) and examined regarding their homo- and copolymerizability. The influence of the macromonomer structure on the ROMP kinetics and the polymerization control are investigated using standard analytical methods. Additionally, the synthesis of sequence-controlled graft copolymers by reacting different macromonomers in an iterative manner is examined and further discussed, as well as the introduction of a novel strategy to synthesize graft copolymers from bifunctional macromonomers derived from the P-3CR.

In the third part of this thesis, the synthesis of sequence-controlled graft copolymers is investigated, whereby norbornene-based macromonomers are added consecutively into an ongoing ROMP. The delayed addition of fast-propagating *exo* norbornene-based macromonomers to a relatively slow polymerization of an *endo* norbornene monomer leads

to the targeted insertion of macroblocks along the polymeric backbone. By applying this kinetic approach, the effect of the macromonomer structure on the ROMP kinetics and the polymerization control is investigated using standard analytical methods. Here, sequence-controlled graft copolymers are successfully synthesized in a controlled fashion, whereby diblock- and triblock-like architectures with variable molar fractions are obtained by using different macromonomers.

Overall, the applied methodologies were found successful, albeit the widely reported sequential addition of (macro)monomers onto a “living” polymer was found the least efficient and the most limited by the structural characteristics of the employed monomer. Nonetheless, the use of a largely overlooked catalyst for the same purpose and by taking advantage of the kinetic quirk that norbornene isomers present, a versatile method to prepare sequence-controlled polymers was identified. Moreover, the use of a multicomponent reaction was successful in introducing bifunctional monomers into a sequence-controlled polymer.

Kurzzusammenfassung

Seit dem Aufkommen der Polymerchemie, zu Beginn des zwanzigsten Jahrhunderts, steigt die Nachfrage nach funktionalisierten Polymeren kontinuierlich an. Des Weiteren werden hoch spezialisierte Polymere zukünftig vermutlich weiter an Bedeutung gewinnen. Die Natur dient in vielen Forschungsbereichen als Vorbild, so auch in der Polymerchemie. Die Kontrolle über die Monomersequenz in synthetischen Materialien, inspiriert von der definierten Abfolge von Nukleinbasen in der Desoxyribonukleinsäure (DNA), ermöglicht die Beeinflussung von intramolekularen Wechselwirkungen und damit der polymeren Mikrostruktur. Diese Struktur hat weiterhin einen Einfluss auf potenziell interessante makroskopische Eigenschaften des Polymers. Die Entwicklung von kontrollierten Polymerisationstechniken hat eine stabile Grundlage geschaffen, um sequenzkontrollierte Makromoleküle zu synthetisieren und entsprechende Forschungsziele zu erreichen. Als solche stellt die Ringöffnungsmetathese Polymerisation (ROMP) eine vielseitige Plattform dar, um funktionalisierte und sequenzkontrollierte Polymere zu synthetisieren.

Im ersten Abschnitt dieser Dissertation wird eine Vielzahl an funktionalisierten Polymeren synthetisiert, wobei sich die verwendete Methode durch ihre Robustheit und Vielseitigkeit auszeichnet. Dabei werden Norbornen-funktionalisierte Carbonsäurederivate mit unterschiedlichen Aldehyden und Isocyaniden in einer Passerini-Dreikomponentenreaktion (P-3KR) umgesetzt. Die resultierenden bifunktionellen Monomere werden anschließend in einer ROMP zu den entsprechenden Polymeren umgesetzt. Des Weiteren wird der Einfluss der Monomerstruktur auf deren Polymerisierbarkeit und die Polymerisationskinetik untersucht. Die thermischen Eigenschaften der synthetisierten Polymere werden anschließend mit Hilfe dynamischer Differenzkalorimetrie (DDK) und thermogravimetrischer Analyse (TGA) ermittelt.

Im zweiten Abschnitt der Dissertation werden verschiedene ROMP-basierte Synthesemethoden untersucht, um Pfropfcopolymere zu erzeugen. Hierfür werden zunächst Norbornen-funktionalisierte Makromonomere durch radikalische Polymerisation unter Atomtransfer (ATRP) synthetisiert und anschließend deren Homo- und Copolymerisierbarkeit mittels ROMP untersucht. Der Einfluss der Makromonomerstruktur auf die Polymerisationskinetik und die Polymerisationskontrolle wird mit Hilfe grundlegender Analysemethoden erforscht. Außerdem wird die iterative Synthese von

sequenzkontrollierten Pfropfcopolymeren durch die Copolymerisation von unterschiedlichen Makromonomeren mittels ROMP untersucht und diskutiert. Zuletzt wird eine neue Strategie zur Synthese von bifunktionellen Makromonomeren mittels P-3KR vorgestellt, die einen einfachen Zugang zu ROMP-basierten Pfropfcopolymeren bietet.

Im dritten Abschnitt dieser Dissertation wird die Synthese von sequenzkontrollierten Pfropfcopolymeren erforscht, wobei Norbornen-funktionalisierte Makromonomere nacheinander zu einer kontinuierlich fortschreitenden ROMP gegeben werden. Die verzögerte Zugabe von *exo* Norbornen-funktionellen Makromonomeren, die hohe Polymerisationsgeschwindigkeiten aufweisen, zu der relativ langsamen Polymerisation eines *endo* Norbornenderivates führt zu dem gezielten Einbau eines makromolekularen Blocks in das polymere Rückgrat. Hierbei wird der Einfluss der Makromonomerstruktur auf die Polymerisationskinetik und die Polymerisationskontrolle erforscht. Mit Hilfe dieses kinetischen Ansatzes können sequenzkontrollierte Pfropfcopolymere synthetisiert werden. Die Verwendung von verschiedenen Makromonomeren führt zu diblock-, sowie triblockartigen Architekturen und ermöglicht die Variation der entsprechenden Molfraktionen auf kontrollierte Weise.

Insgesamt wurden die angewendeten Methoden erfolgreich durchgeführt, obgleich der vielfach berichtete sequenzielle Einbau von (Makro)monomeren in ein „lebendes“ Polymer als die ineffizienteste und am stärksten limitierte Methode identifiziert wurde. Ein weitaus vielversprechenderer Ansatz wurde mit Hilfe eines (in diesem Bereich) größtenteils übersehenen Katalysators erarbeitet. Dieser Ansatz nutzt die speziellen kinetischen Eigenschaften von Norbornen-Isomeren aus und stellt ein vielseitiges Verfahren zur Synthese von sequenzkontrollierten Pfropfcopolymeren dar. Außerdem wurden Multikomponentenreaktionen erfolgreich zur Synthese von bifunktionellen Monomeren verwendet, die anschließend in sequenzkontrollierte Polymere umgewandelt wurden.

Table of Contents

Danksagung.....	I
Declaration of authorship	V
Abstract.....	VII
Kurzzusammenfassung.....	IX
1 Introduction	1
2 Theoretical background	3
2.1 Sequence-control: from natural to synthetic macromolecules	3
2.2 Tools in organic chemistry.....	6
2.2.1 Multicomponent reactions (MCRs)	6
2.2.2 Isocyanide chemistry.....	8
2.2.3 Isocyanide-based multicomponent reactions (IMCRs).....	10
2.2.4 Azide chemistry	15
2.3 Polymerization techniques.....	18
2.3.1 Basic techniques.....	18
2.3.2 Atom transfer radical polymerization (ATRP).....	23
2.3.3 Ring-opening metathesis polymerization (ROMP)	28
3 Aim	37
4 Functional poly(norbornene)s <i>via</i> a combination of ROMP and P-3CR	39
4.1 Abstract.....	39
4.2 Introduction	39
4.3 Results and discussion.....	41
4.3.1 Synthesis of functionalized norbornenes <i>via</i> the P-3CR.....	41

4.3.2	ROMP of functional norbornenes	44
4.3.3	Kinetic studies	51
4.4	Conclusion	59
5	Sequence-controlled graft copolymers <i>via</i> ROMP of macromonomers	61
5.1	Abstract	61
5.2	Introduction	61
5.3	Results and discussion.....	63
5.3.1	Synthesis of norbornene dicarboximide–based macromonomers	63
5.3.2	Synthesis of graft polymers using the G1 catalyst.....	75
5.3.3	Synthesis of graft polymers using the G3 catalyst.....	86
5.3.4	Sequence-controlled graft copolymers	95
5.3.5	Janus copolymers	113
5.4	Conclusion	128
6	Sequence-controlled graft copolymers by delayed macromonomer addition	129
6.1	Abstract	129
6.2	Introduction	129
6.3	Results and discussion.....	131
6.3.1	Introduction of monoblocks <i>via</i> ROMP	131
6.3.2	Synthesis of norbornene ester–based macromonomers.....	144
6.3.3	Introduction of multiblocks <i>via</i> ROMP	148
6.4	Conclusion	158
7	Conclusion and outlook.....	159
8	Experimental Section	161
8.1	Materials	161
8.2	Analytical instruments and methods	162
8.3	Synthesis procedures and analytical data	164

8.3.1 Materials synthesized in chapter 4	164
8.3.2 Materials synthesized in chapter 5	211
8.3.3 Materials synthesized in chapter 6	268
9 Appendix	317
9.1 List of abbreviations	317
9.2 List of publications	320
10 List of figures, schemes, and tables.....	321
10.1 List of figures	321
10.2 List of supporting figures.....	327
10.3 List of schemes	344
10.4 List of tables	347
11 Bibliography	349

1 Introduction

Since centuries, nature has inspired generations of scientists by its complexity, versatility, and adaptivity. Within the last 300 years, modern chemistry has gained more and more importance by exposing the secrets of nature.¹⁻⁴ In the early 20th century, H. Staudinger established the field of macromolecular chemistry, which has had a major impact to the present day.⁵⁻⁷ Furthermore, discoveries such as the double-helical structure of deoxyribonucleic acid (DNA) and the investigation of other biopolymers, such as proteins, have emphasized the importance of structure-property relationships and thus revealed the hidden potential of well-defined macromolecules.⁸⁻¹²

In recent years, the development of controlled polymerization techniques has enabled the synthesis of copolymers comprising controlled monomer sequences.¹³⁻¹⁶ In relevance to this work, ring-opening metathesis polymerization (ROMP) has been established as a powerful tool for the preparation of such materials due to its kinetically controlled character,¹⁷ high tolerance toward functional groups and high polymerization rates.¹⁸⁻²⁰ Especially the ROMP of norbornene derivatives provides a straightforward method to synthesize a variety of polymers in a “living” fashion.²¹⁻²³ Norbornene monomers possess many advantages, including a high reactivity and stability in ROMP,²⁴ and an easy preparation *via* Diels-Alder reactions.^{25,26} Furthermore, the functionalization of such monomers is achievable by various methods,²⁷⁻²⁹ including multicomponent reactions (MCRs) which provide a high degree of versatility by introducing a wide range of functional groups.³⁰ Recently, MCRs have been used to synthesize a range of monomers with peptide-like side groups, whereby subsequent ROMP yielded the corresponding polymers in a controlled fashion.³¹ Since the Passerini three-component reaction (P-3CR) is well-established in the polymer sciences, for instance for the preparation of sequence-defined oligomers,³²⁻³⁴ it provides a versatile and robust platform to generate highly functionalized monomers without the necessity of post-polymerization functionalization. Subsequent ROMP enables the straightforward synthesis of peptoid-functional polymers with the potential to hydrogen bond, an interesting feature, e.g., in the field of drug delivery.³⁵

In order to increase the structural complexity in polymeric materials, graft copolymers are prepared from macromonomers *via* “living” polymerization techniques.^{36,37} As such, macromonomers comprise a polymerizable moiety and a polymeric chain and are synthesized e.g. *via* anionic polymerization.³⁸ Atom transfer radical polymerization (ATRP) has been shown to be a suitable method due to the ability to synthesize low dispersity polymers with precisely controlled molecular weights and diverse functionalities.^{39,40} Additionally, the synthesis of graft copolymers enables the generation of well-defined structures which exhibit gradient,⁴¹ block,⁴² hyper-branched,⁴³ and dendritic topologies.⁴⁴ Recently, the synthesis of graft copolymers from norbornene-based macromonomers *via* ROMP has gained attention, obtaining sequence-controlled polymers that exhibit interesting micro- and macroscopic properties, including the ability to self-assemble into periodic structures.^{45,46} Hereby, Grubbs-type catalysts are extensively employed.⁴⁷⁻⁴⁹ These systems provide a high degree of control and yield multiblock copolymers *via* sequential addition of macromonomers.⁵⁰ While the story of sequence-controlled polymers has just begun, future achievements in mimicking and replicating nature are supposed to have a large influence and bring significant advantages on several areas of life.⁵¹⁻⁵³

2 Theoretical background

Parts of this chapter are adapted from my master thesis:⁵⁴

D. Barther, *Master thesis, KIT 2018*.

2.1 Sequence-control: from natural to synthetic macromolecules

Inspired from the precise synthesis of peptides in the middle of the 20th century,^{12,55} and the decoding of the first human gene in 1977,⁵⁶ intensive efforts have been made in understanding and controlling the monomer sequence in synthetic polymers.⁵⁷⁻⁵⁹ With the emergence of controlled polymerization techniques and the development of designed catalysts,⁶⁰⁻⁶⁴ research in this field of science intensified in recent years, revealing the potential of sequence-control in synthetic polymers (**Figure 2.1**).

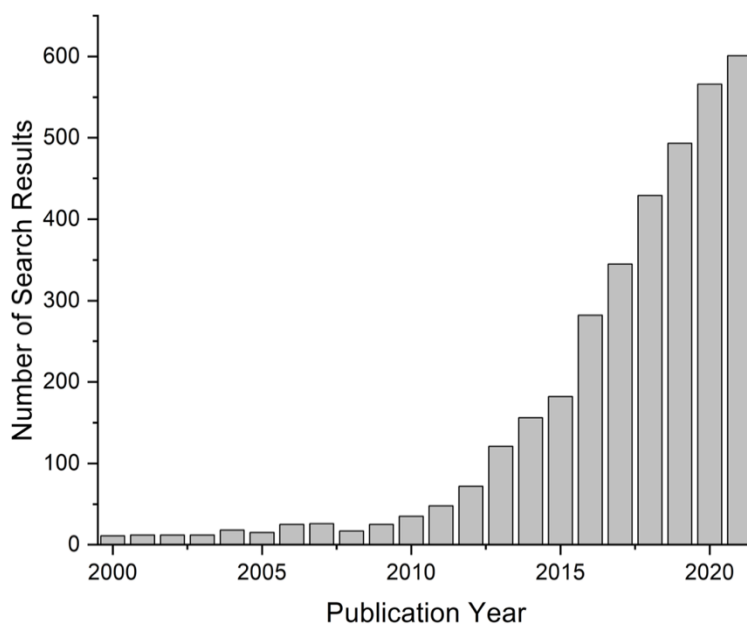


Figure 2.1. Number of search results per year associated with the term “sequence-controlled polymers” (2000 - 2021) available *via* Google Scholar (date of excess: 06.03.2022).

In a review article published in 2013, Lutz, Ouchi, Liu, and Sawamoto proposed the following definition:

“Sequence-controlled polymers are macromolecules in which monomer units of different chemical nature are arranged in an ordered fashion.”⁶⁵

Although this definition appears to be generic, since it includes precisely ordered biopolymers such as DNA,^{8,66,67} and less defined polymers like periodic and aperiodic copolymers,^{68,69} it has proven to be an important first step in the evaluation of controlled polymeric systems (Figure 2.2).

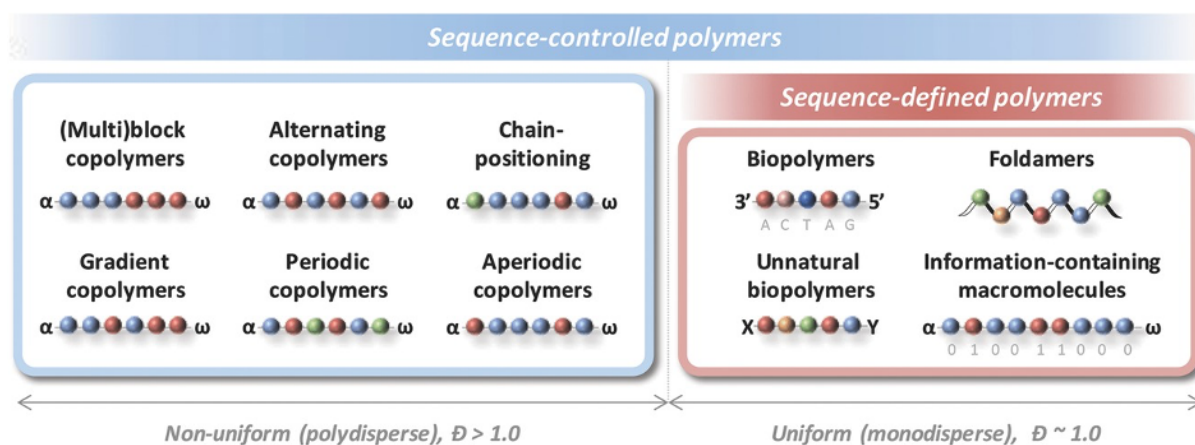


Figure 2.2. Schematic representation of the terms “sequence-controlled polymers” and “sequence-defined polymers”. Reprinted with permission (<https://onlinelibrary.wiley.com/doi/full/10.1002/marc.201700582>).⁷⁰

In order to emphasize the differences in the structural ordering, the terms “disperse” and “uniform” were introduced,^{71,72} whereby polymeric compounds are categorized by their dispersity (\mathcal{D}) as sequence-controlled or sequence-defined polymers. Macromolecules with a disperse chain-length distribution ($\mathcal{D} > 1$) are termed non-uniform or polydisperse, whereas macromolecules which are strictly defined in size and composition ($\mathcal{D} = 1$) are termed uniform or monodisperse (Figure 2.2).⁷³

In recent years, the accessibility to uniform macromolecules or polymers has been enabled by iterative synthesis procedures,⁷⁴ and the replication of biochemical processes.⁷⁵⁻⁷⁸ The application of uniform biopolymers in the pharmaceutical industry is crucial,⁷⁹ and potentially becomes even more important in the future e.g. in the production of ribonucleic acid (RNA)-based therapeutics.⁸⁰ However, the commercial application of synthetically generated uniform macromolecules is limited to date, while offering unique opportunities in understanding structure-property relationships and thus being potentially important in the production of highly specialized materials.⁸¹⁻⁸³

The accessibility of sequence-controlled polymers has been achieved by copolymerizing monomers which show different kinetic behaviors, such as in the case of monomers unable to undergo homopolymerization but readily copolymerize (**Figure 2.3**).⁸⁴⁻⁸⁶

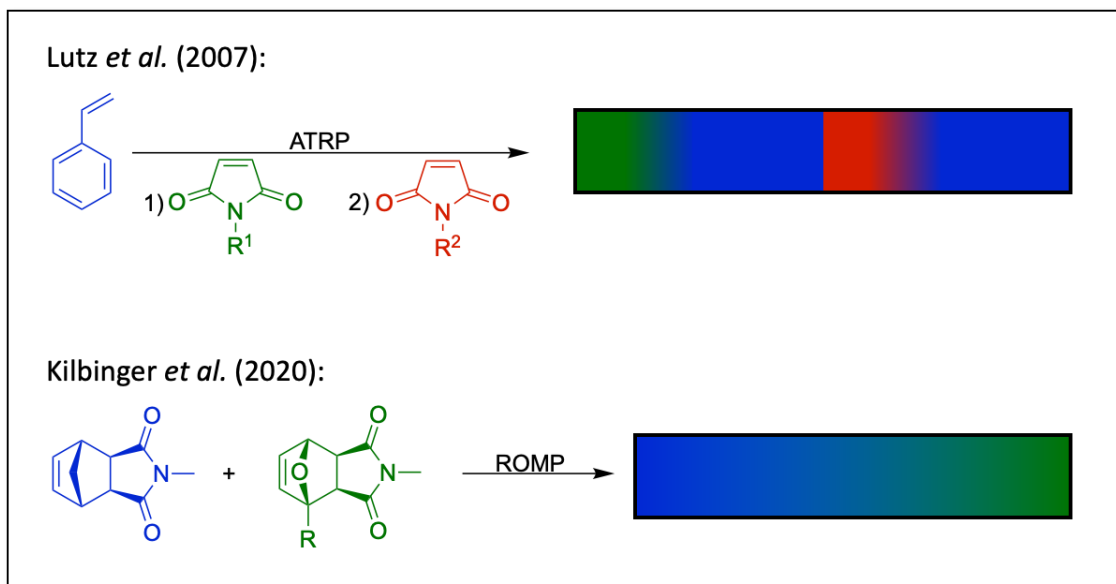


Figure 2.3. Representative examples for the kinetic approach in the synthesis of sequence-controlled polymers, using ATRP (top) and ROMP (bottom).^{87,88}

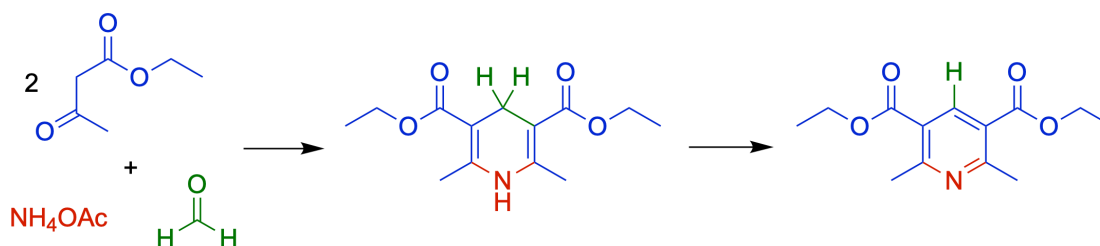
In 2007, Lutz *et al.* used this kinetic approach to control the monomer sequence distribution in a reversible-deactivation radical polymerization (RDRP) using styrene and different *N*-substituted maleimides as monomers (**Figure 2.3**, top).⁸⁷ It has been further shown that the chemical structure of the maleimide comonomers influences the reactivity ratios, and thus the microstructure of the generated polymers.^{89,90} Similarly, monomers with different kinetic profiles have been employed in other types of polymerizations, such as anionic polymerization,^{91,92} or ROMP (**Figure 2.3**, bottom),⁹³⁻⁹⁶ to prepare sequence-controlled polymers. The synthesis of the latter has also been shown using e.g. iterative processes in chain-growth polymerizations,⁹⁷⁻⁹⁹ as well as in step-growth polymerizations.¹⁰⁰⁻¹⁰² The ability of polymeric materials with spatially periodic structures to organize into complex morphologies enables, for instance, the manipulation of light propagation and is thus potentially interesting in the preparation of photonic materials.¹⁰³⁻¹⁰⁵ Potential biomedical applications include targeted drug delivery,¹⁰⁶ phototherapy,¹⁰⁷ or biosensing.¹⁰⁸

2.2 Tools in organic chemistry

2.2.1 Multicomponent reactions (MCRs)

In classic synthesis approaches, most reactions require two reactants which will be converted to the desired product.¹⁰⁹⁻¹¹¹ To synthesize more complex molecules, it is often necessary to perform a stepwise synthesis.¹¹² In contrast, multicomponent reactions (MCRs) facilitate the formation of a single product by combination of three or more components and thus enable the generation of highly diverse products.¹¹³ Furthermore, most examples entail simple synthesis procedures and generate products with excellent yields.¹¹⁴ In the following section, an overview about typical MCRs is given, whereas isocyanide-based multicomponent reactions (IMCRs) are discussed in more detail in **chapter 2.2.3**.

The Hantzsch synthesis of 1,4-dihydropyridines represents a famous example and was reported for the first time in 1881 by A. R. Hantzsch.¹¹⁵ Here, an aldehyde component, a nitrogen donor and two equivalents of a β -keto ester form a 1,4-dihydropyridine (1,4-DHP) which is then oxidized to the respective pyridine derivative (**Scheme 2.1**).¹¹⁶

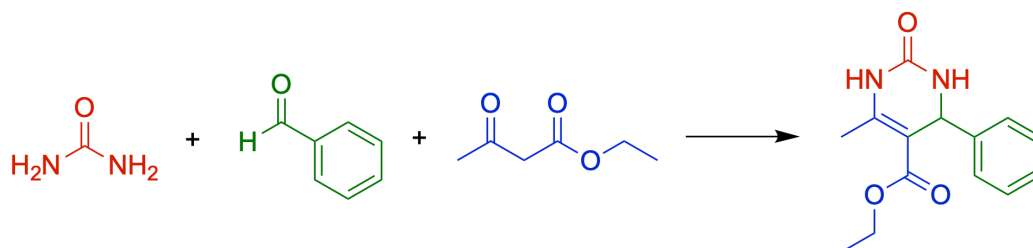


Scheme 2.1. Representative Hantzsch synthesis of 1,4-dihydropyridines (1,4-DHPs) and subsequent oxidation yielding 1,4-disubstituted pyridines.^{115,116}

The reaction exhibits a high robustness and was performed e.g. in a one-pot fashion in refluxing water using iron(III) chloride and potassium permanganate as oxidizing agents.¹¹⁷ In order to avoid harsh reaction conditions and long reaction times, 1,4-DHPs are e.g. synthesized under acidic catalysis in aqueous micelles under ultrasonication.¹¹⁸ The Hantzsch synthesis is important in the development of drugs, since the obtained 1,4-DHPs were found to be bioactive, exhibiting a high affinity for binding calcium channels.¹¹⁹ 1,4-DHPs are further used e.g. as anticonvulsants and in the treatment of vasodilation.^{120,121} Current research includes the enantioselective and asymmetric Hantzsch synthesis,^{122,123} as well as more

sustainable approaches to obtain bioactive 1,4-DHP derivatives and modified three-component Hantzsch protocols.^{124,125}

Another MCR capable of generating heterocyclic compounds was developed in 1891 by the Italian chemist P. Biginelli.¹²⁶ This hitherto referred to as Biginelli reaction was first performed utilizing urea, benzaldehyde, and ethyl acetoacetate. The acid-catalyzed reaction results in the formation of 3,4-dihydropyrimidine-2(1H)-one (DHPM, **Scheme 2.2**).¹²⁷

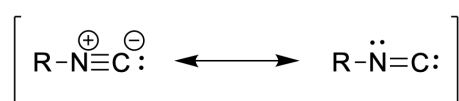


Scheme 2.2. Synthesis of 3,4-dihydropyrimidine-2(1H)-one from urea, benzaldehyde, and ethyl acetoacetate *via* the Biginelli reaction.^{126,127}

However, the Biginelli reaction is not limited to the above-mentioned components. Instead of urea it is also possible to use substituted urea and thiourea derivatives.¹²⁸ Furthermore, the aldehyde component is adjustable and the ethyl acetoacetate is exchangeable with a variety of other β -keto esters.¹²⁹ The variation of these three components leads to a large number of possible pyrimidine derivatives. Comparable to 1,4-DHPs, DHPMs act as calcium antagonists, lowering the intake of calcium ions by muscle cells.¹³⁰ Hence, DHPM-containing drugs are used in the therapy of hypertension, cardiac arrhythmias, and other diseases of the coronary vessels.¹³¹ Current research examines the antitumor bioactivity of DHPMs,¹³² whereby Biginelli-based polymers were synthesized and found to efficiently inhibit the growth of cancer cells.¹³³ Beside pharmaceutical applications, the Biginelli reaction is commonly used in polymer sciences, e.g. in the synthesis of polycondensates with tunable thermal properties and in the synthesis of UV-protective polymers from biobased resources.^{134,135}

2.2.2 Isocyanide chemistry

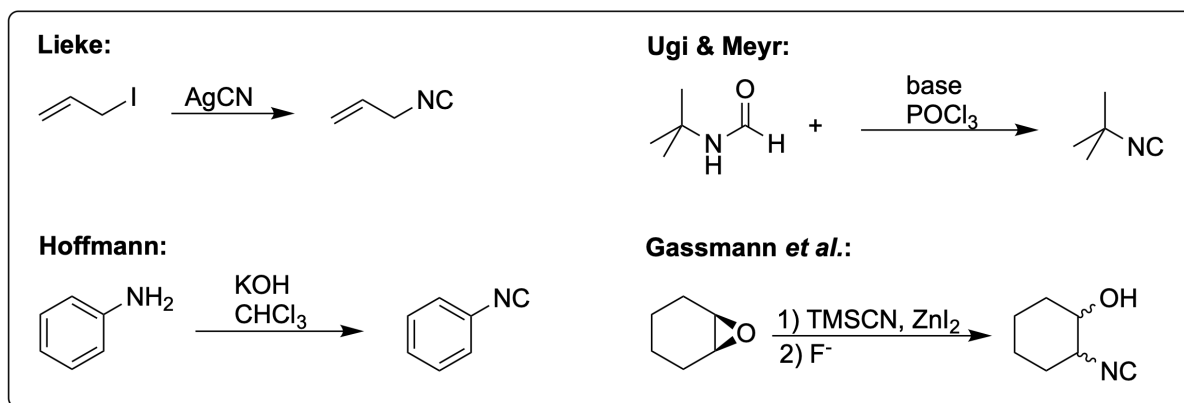
In the following section, the synthesis, properties, and applications of isocyanides are described, since they are essential reactants in IMCRs, which are described in **chapter 2.2.3**. Isocyanides are a nitrogen-containing class of organic compounds with the chemical formula R-NC and were first reported by W. Lieke in 1859.¹³⁶ In contrast to nitriles, the organic moiety in isocyanides is attached to the nitrogen atom. The chemical structure of isocyanides is best described by two resonance structures, a zwitterionic and a carbenoid structure (**Scheme 2.3**).¹³⁷



Scheme 2.3. Resonance structures of isocyanides: zwitterionic (left) and carbenoid (right).¹³⁷

Although isocyanides are known to have a “penetrating and extremely unpleasant odour”,¹³⁶ they have been extensively used as electrophiles and nucleophiles in organic chemistry and polymer sciences,^{138,139} as shown by several examples later within this section.

Since the first report of isocyanides, different synthesis procedures have been developed e.g. starting from amines,^{140,141} formamides,¹⁴²⁻¹⁴⁴ epoxides,¹⁴⁵ or organic halides (**Scheme 2.4**).¹³⁶

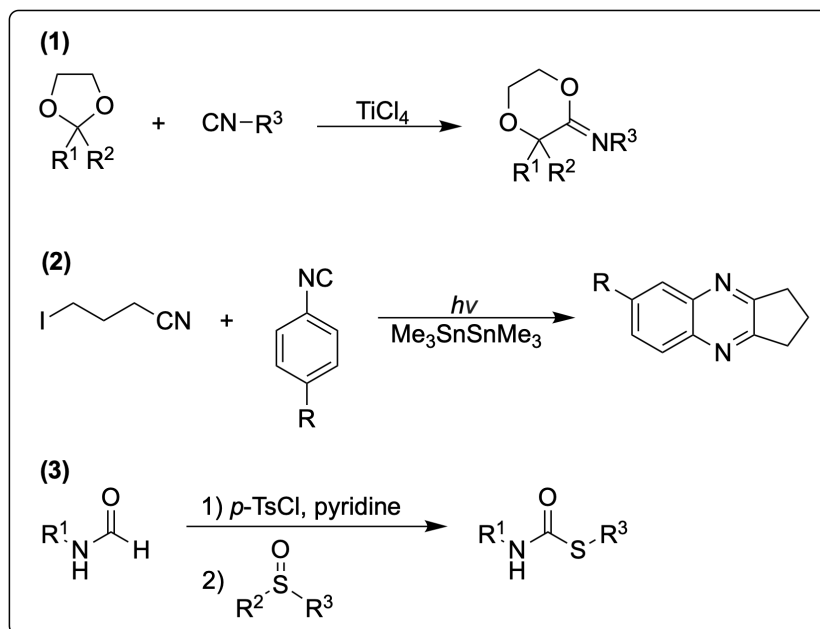


Scheme 2.4. Representative isocyanide synthesis strategies.^{136,141,142,145}

The dehydration of formamides using different dehydrating agents, such as phosphoryl trichloride (POCl_3),¹⁴² phosgene,¹⁴⁶ or a mixture of triphenylphosphine (PPh_3) and iodine,¹⁴⁴ is nowadays commonly used to synthesize isocyanides (**Scheme 2.4**). Recently, Meier *et al.* reported a variation of the Ugi strategy by exchanging highly reactive and corrosive POCl_3 with

p-toluenesulfonyl chloride (*p*-TsCl) and further improved the reaction in terms of sustainability.¹⁴³

As mentioned earlier in this section, isocyanides act as both electrophiles and nucleophiles,^{138,139} and thus are extensively used in organic syntheses (**Scheme 2.5**).



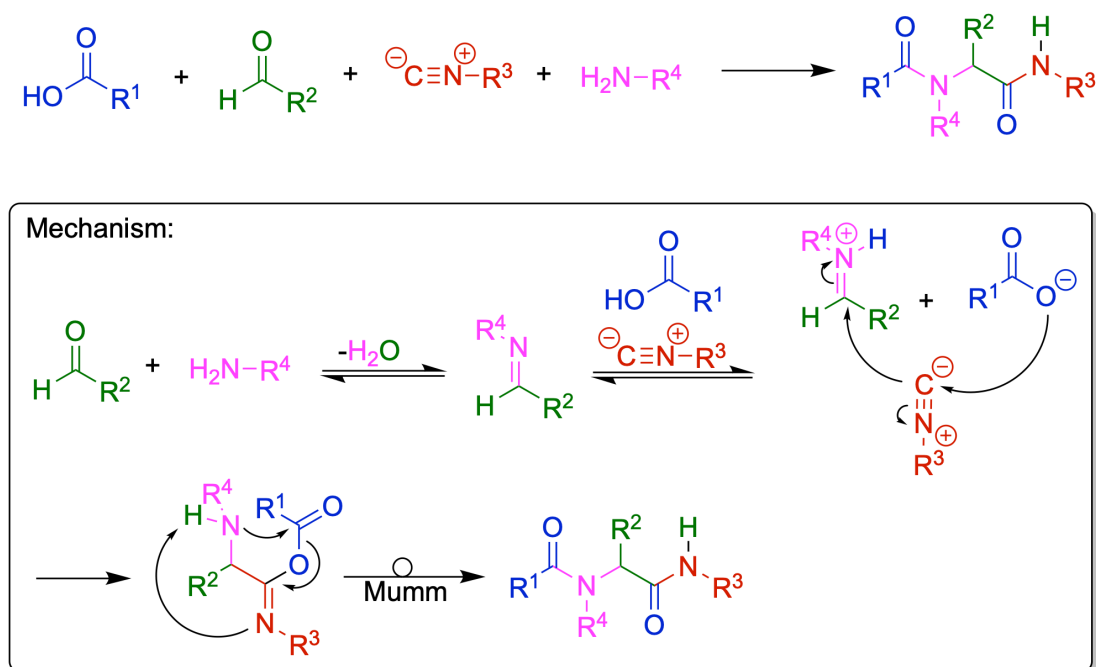
Scheme 2.5. Representative applications of isocyanides in organic syntheses.¹⁴⁷⁻¹⁴⁹

Due to their electrophilicity, isocyanides are well-known to undergo Lewis and Brønsted acid-catalyzed insertion into C-O (**Scheme 2.6**),¹⁴⁷ C-S,¹⁵⁰ C-Si,¹⁵¹ and B-Si¹⁵² bonds. Furthermore, several transition metal-catalyzed insertions are known, including insertion into S-H and N-H bonds by using copper complexes,^{153,154} and insertion into Si-Si and S-S bonds by using palladium catalysis.^{155,156} Recently, the synthesis of thiocarbamates has been performed in a one-pot fashion starting from the formamide, where the isocyanide is formed *in situ* and subsequently converted to the respective thiocarbamate.¹⁴⁹ Isocyanides are further used in IMCRs, which are discussed in **chapter 2.2.3**. In polymer chemistry, isocyanides have been used since half a century,^{157,158} whereby a recent example represents the catalyst-free multicomponent polymerization of diisocyanides, diamines, and sulfur, yielding poly(thiourea)s.¹⁵⁹

2.2.3 Isocyanide-based multicomponent reactions (IMCRs)

In contrast to the Hantzsch synthesis and the Biginelli reaction, IMCRs usually yield linear peptoid-like products with a high degree of structural diversity.¹⁶⁰ The Ugi four-component reaction (U-4CR) and the P-3CR are the most famous representatives of this reaction type and are discussed in more detail within this section.

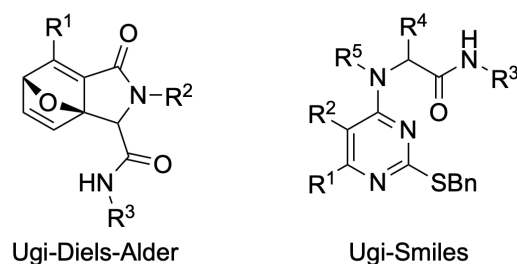
The U-4CR was first reported by I. Ugi in 1959.¹⁶¹ The four components involved in this reaction are a carboxylic acid, a primary amine, an oxo-component such as a ketone or an aldehyde, and an isocyanide. These four components react in a condensation reaction to form an α -amino acylamide (**Scheme 2.6**).¹⁶¹



Scheme 2.6. U-4CR and commonly accepted mechanism involving a carboxylic acid, a primary amine, an aldehyde, and an isocyanide.¹⁶⁰⁻¹⁶²

The commonly accepted reaction mechanism involves the formation of a Schiff base by condensation of the amine and the aldehyde as an initiation step. Subsequent protonation of the Schiff base by the carboxylic acid forms an iminium ion. In the next step, the isocyanide simultaneously acts as a nucleophile toward the electrophilic center of the iminium and as an electrophile toward the carboxylate (α -addition).¹⁶⁰ This reaction step likely proceeds in a concerted fashion. Subsequently, an intramolecular Mumm rearrangement forms the α -amino acylamide (**Scheme 2.6**).¹⁶³

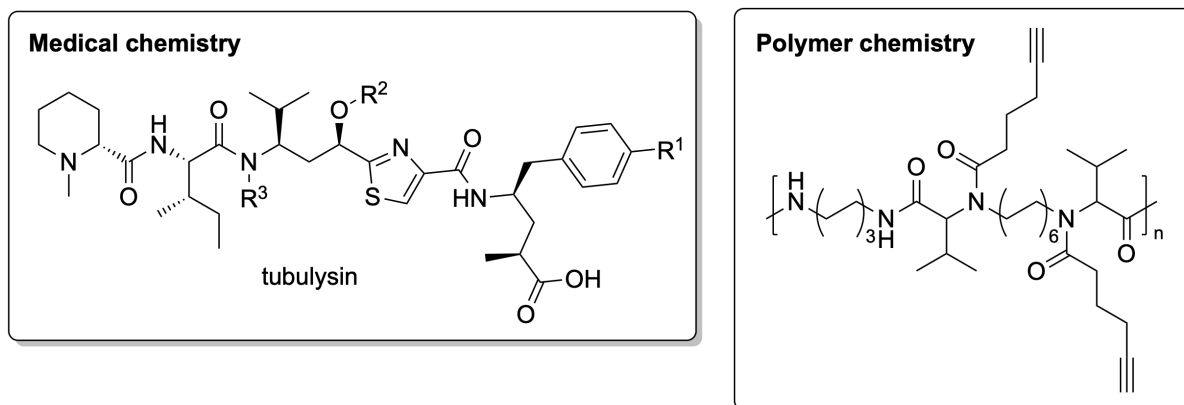
The U-4CR offers a versatile platform for the combination of bifunctional reaction components, leading to structurally interesting products (**Scheme 2.7**).



Scheme 2.7. Representative U-4CR variations: Ugi-Diels-Alder and Ugi-Smiles.^{164,165}

In the recent literature, Ugi-Diels-Alder reactions were performed by the synthesis of U-4CR products capable of undergoing intramolecular Diels-Alder reactions, yielding highly substituted tricyclic lactams.¹⁶⁴ Another famous example is represented by the Ugi-Smiles reaction, where the carboxylic acid component is replaced by an electron poor phenol derivative and the Smiles rearrangement represents the final reaction step.^{165,166}

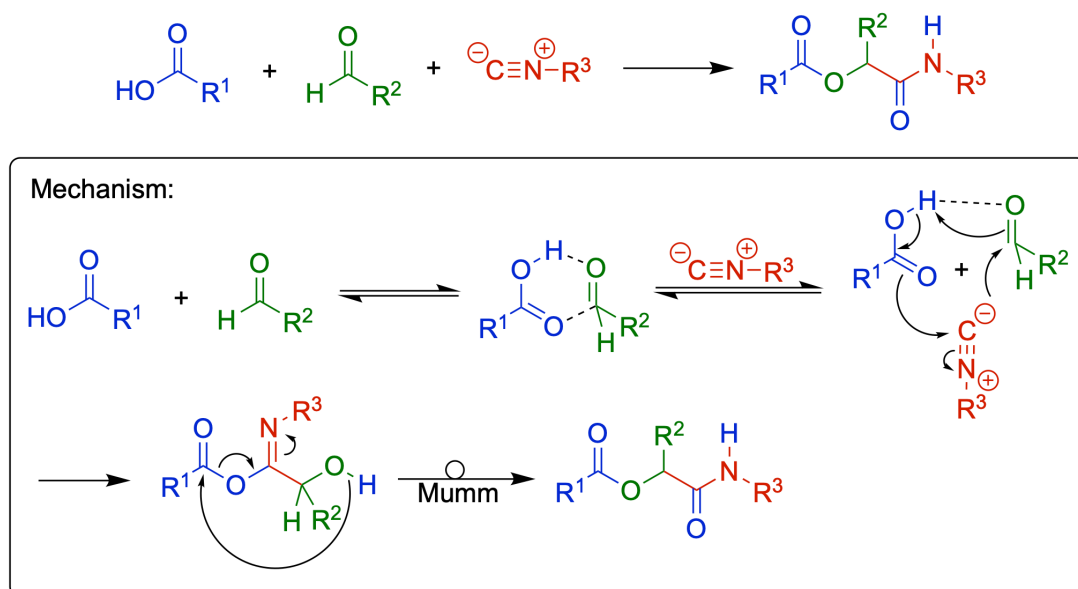
Due to the straightforward synthesis procedure in a one-pot fashion and the structural variety of the peptoid-like products, the U-4CR is extensively used to establish chemical libraries.^{167,168} Therefore, the involved components and their composition are varied, based on the principles of combinatorial chemistry. This method is widely used in the field of pharmaceutical research, whereby new biologically active substances are synthesized, examined, and optimized in a relatively small amount of time.¹⁶⁹ Hereby, the peptoid-like structure of the products obtained by the U-4CR enables their application e.g. in the synthesis of tubulysins, which exhibit potent anti-proliferative activities against human cancer cells (**Scheme 2.8**).¹⁷⁰



Scheme 2.8. Possible application areas of the U-4CR: medical and polymer chemistry.^{170,171}

Furthermore, the U-4CR is extensively used in polymer chemistry, generating polypeptoidic structures and in the formation of sequence-defined oligomers with potential application in data storage or cryptography (**Scheme 2.8**).¹⁷¹⁻¹⁷³ Since classical U-4CRs generate racemic product mixtures, current research includes the introduction of enantioselectivity by using e.g. conformationally restricted chiral phosphoric acids as organocatalysts.^{174,175} Furthermore, the U-4CR is currently used in the synthesis of catalytic systems capable of performing CO₂ fixation reactions, yielding cyclic carbonates.¹⁷⁶

The P-3CR was reported for the first time by M. Passerini in 1921.¹⁷⁷ As the U-4CR, the P-3CR is an isocyanide-based multicomponent reaction, which involves a carboxylic acid, an oxo-component, such as a ketone or an aldehyde, and an isocyanide. These three components react to form an α -acyloxy amide (**Scheme 2.9**).¹⁷⁸



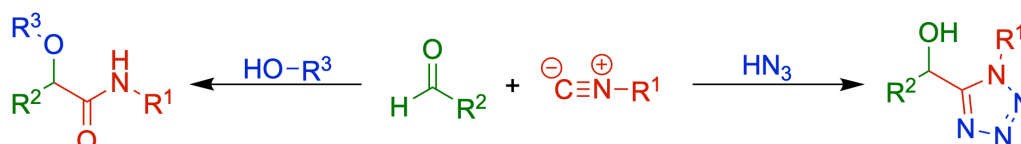
Scheme 2.9. P-3CR involving a carboxylic acid, an aldehyde, and an isocyanide, and non-ionic reaction mechanism in aprotic solvents postulated by I. Ugi.^{162,177,178}

First kinetic studies conducted by Baker and Stanonis indicated a trimolecular reaction process between the carboxylic acid, the oxo-component, and the isocyanide. The postulated reaction mechanism involves two separate steps, which both follow first order kinetics. In the first step, the isocyanide and the oxo-component are assumed to form a reversible transition state which reacts with the carboxylic acid in an irreversible second step to the desired α -acyloxy amide.¹⁷⁹ The reaction mechanism of the P-3CR was described for the first time by I. Ugi. It has been shown that the reaction rate increases in aprotic solvents, such as

tetrahydrofuran (THF). It was also observed that high concentrations of the reagents and performing the reaction at room temperature dramatically increase the yield.¹⁸⁰

As a result of his work and the previous kinetic investigations done by Baker and Stanonis, Ugi postulated a non-ionic reaction mechanism (**Scheme 2.9**).¹⁶² Initially, the carboxylic acid and the aldehyde form a six-membered ring transition state. At this point, the formation of hydrogen bonds is essential. Within the six-membered ring transition state, the carbonyl group of the aldehyde is more polar and is consequently more prone to be attacked by a nucleophile. In the next step, the free electron pair of the isocyanide attacks the carbonyl group of the aldehyde, while the acid component simultaneously attacks the isocyanide in a nucleophilic manner (α -addition). A seven-membered ring transition state is formed and finally in an irreversible step, an intramolecular Mumm rearrangement forms the α -acyloxy amide.¹⁶²

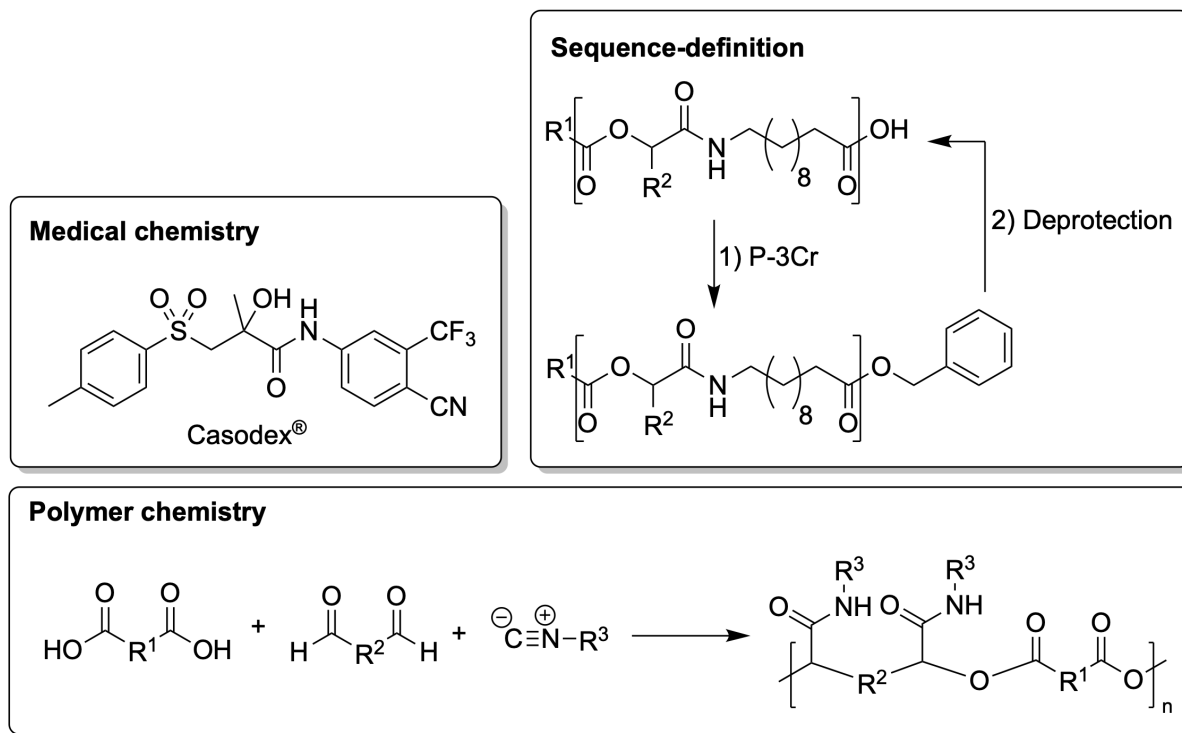
Since the products of the P-3CR are structurally highly versatile due to the variation of the used components, replacement of the carboxylic acid component further increases the versatility of the P-3CR. As an example, alcohols and hydrazoic acid are used to generate α -alkoxy amide derivatives and 5-(1-hydroxyalkyl)tetrazoles, respectively (**Scheme 2.10**).^{181,182}



Scheme 2.10. Representative P-3CR variations: replacement of the carboxylic acid by an alcohol to obtain α -alkoxy amides and by hydrazoic acid to obtain 5-(1-hydroxyalkyl)tetrazoles.^{181,182}

A straightforward synthesis procedure in a one-pot fashion as well as the possibility to obtain peptoid-like compounds in a highly diverse and enantioselective fashion offers a wide application range in the area of medical chemistry,^{170,183} including the buildup of chemical libraries using combinatorial methods.¹⁶⁸ As an example, the P-3CR is applied in the synthesis of pharmaceutical products such as Casodex® (**Scheme 2.11**), a leading drug in the treatment of prostate cancer.¹⁷⁰

Furthermore, linear and star-shaped amphiphilic copolymers obtained by the P-3CR are potentially interesting in the field of drug delivery,^{184,185} whereby the release of the encapsulated drug is influenced by physiological conditions, such as temperature and pH.¹⁸⁶



Scheme 2.11. Possible application areas of the P-3CR: medical and polymer chemistry and the synthesis of sequence-defined macromolecules.^{170,187,188}

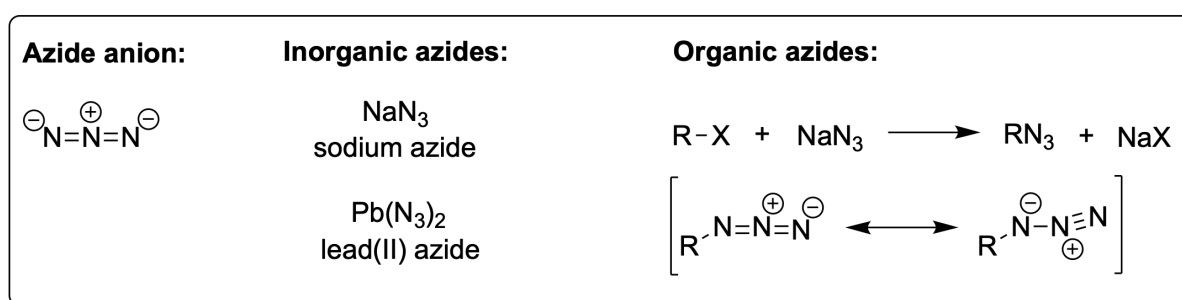
Similar to the U-4CR, the P-3CR is used in the synthesis of sequence-defined macromolecules using iterative synthesis procedures, i.e. the reaction of isocyanides which bear a benzyl ester-protected carboxylic acid moiety with different aldehydes and an initial carboxylic acid (**Scheme 2.11**).¹⁸⁷ Using different iterative procedures, the synthesis of highly branched sequence-defined macromolecules, such as dendrimers and star-shaped amphiphilic block copolymers, has been recently performed by combining the P-3CR with olefin metathesis and copper(I)-mediated azide-alkyne cycloaddition (CuAAC),^{189,190} respectively, and further demonstrates the versatility and robustness of the P-3CR.

The application of the P-3CR in polymer chemistry is well-known in the literature, generating macromolecules with polypeptidic structures.¹⁹¹ Therefore, different synthesis approaches are used, ranging from simple monomer synthesis and subsequent polymerization e.g. using acyclic diene metathesis (ADMET),¹⁹² toward the step-growth polymerization of bifunctional monomers *via* the P-3CR (**Scheme 2.11**),^{188,193,194} and post-polymerization modification.¹⁹⁵

The P-3CR is currently applied in a variety of different research areas, including one-pot cascade polycondensations for the synthesis of functional polyesters,¹⁹⁶ the functionalization of cellulose,¹⁹⁷ and the examination of the Passerini four-component reaction (P-4CR), which enables direct use of CO₂ in MCRs.^{198,199}

2.2.4 Azide chemistry

The azide anion has the chemical formula N₃⁻ and represents the conjugated base of hydrazoic acid (HN₃, **Scheme 2.12**).²⁰⁰

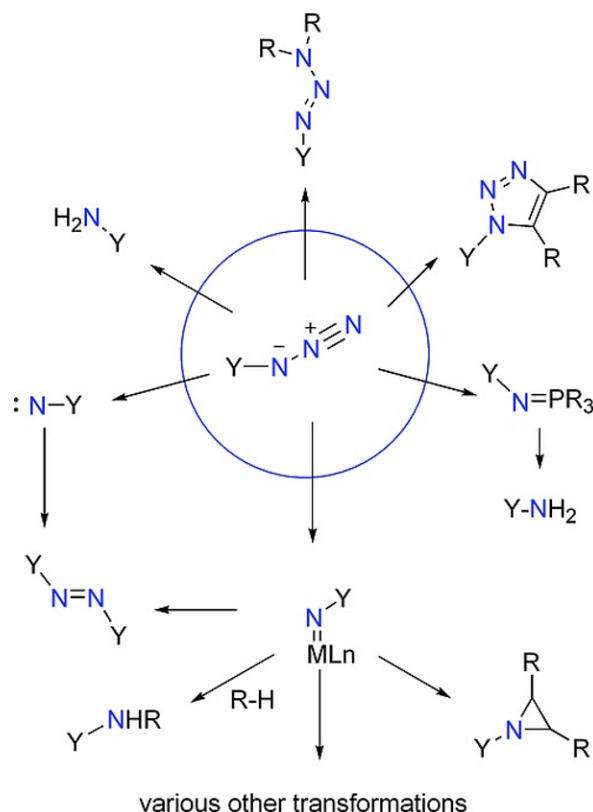


Scheme 2.12. Chemical structure of the azide anion (left),²⁰¹ representative inorganic azide compounds (middle),²⁰² and representative azidation of organic compounds by nucleophilic substitution using sodium azide and the resonance structure of the obtained organic azide (right).²⁰³

Inorganic azides have a broad scope of applications, sodium azide (NaN₃) for instance is used for airbag inflation and lead(II) azide is used as a shock-sensitive detonator (**Scheme 2.12**).²⁰⁴ Most inorganic azides are toxic and nearly all of them are explosive.²⁰³

Beside a variety of inorganic azides,^{205,206} organic azides have been synthesized *via* nucleophilic substitution, e.g. using NaN₃ and an organohalide (**Scheme 2.12**).²⁰³ Since azides are excellent nucleophiles, even compounds bearing weak leaving groups easily undergo nucleophilic substitution. Other methods include the nucleophilic aromatic substitution of electron-poor aromatic systems,²⁰⁷ the reaction of nitrosoarenes with hydrazoic acid,²⁰⁸ the diazotization of hydrazines,²⁰⁹ 1,4-addition reactions of α,β-unsaturated carbonyl compounds,²¹⁰ and the radical azidation of C-H bonds.²¹¹ The resulting organic azides exhibit a broad field of applications, serving as photoaffinity labels,²¹² cross-linkers in photoresistors,²¹³ reactants in the total synthesis of natural products,²¹⁴ and as efficient protecting groups for amine and alcohol functionalities.²¹⁵

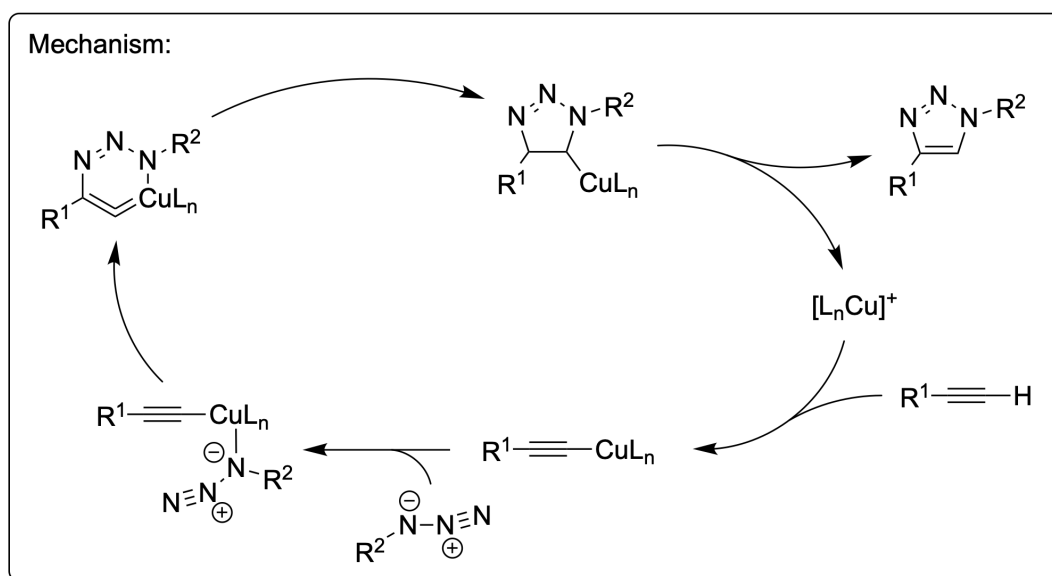
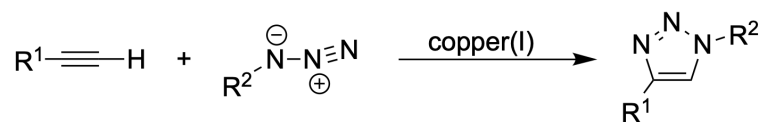
In recent years, a large number of reactions involving organic azides were developed, including the synthesis of heterocycles by intramolecular cycloaddition of nitrenes to olefins,²¹⁶ the insertion into C-H bonds,²¹⁷ and the formation of tri- and tetrazoles (**Scheme 2.13**).^{218,219}



Scheme 2.13. Different reactions of organic azides. Reprinted with permission (<https://chemistry-europe.onlinelibrary.wiley.com/doi/full/10.1002/ejoc.201601390>).²²⁰

An important application of organic azides is represented by the Huisgen 1,3-dipolar cycloaddition (**Scheme 2.13**), named by R. Huisgen who intensively studied this type of cycloaddition in the middle of the 20th century.²²¹ In principle, the latter describes the reaction between a 1,3-dipole and a dipolarophile, with 1,3-dipolar compounds exhibiting delocalized electrons distributed over three atoms, and electrophilic dipolarophiles usually comprising double or triple bonds.²²² The term “Huisgen 1,3-dipolar cycloaddition” is often used equally to describe the reaction between organic azides and terminal alkynes yielding 1,2,3-triazoles. Since the reaction was found to be relatively slow and had to be performed under harsh conditions,²²³ its application was limited e.g. with respect to biological systems. These issues were tackled by Sharpless *et al.* and Meldal *et al.* in 2002, who independently developed a copper(I)-mediated version of the Huisgen 1,3-dipolar cycloaddition (**Scheme 2.14**).^{224,225}

Different catalysis strategies have been reported, including the *in situ* reduction of copper(II) salts with sodium ascorbate under aqueous conditions or the direct use of copper(I) salts with amine bases or *N*-heterocyclic carbenes (NHCs) as ligands in organic solvents.^{224,226,227}



Scheme 2.14. Representative copper(I)-mediated azide-alkyne cycloaddition (CuAAC) yielding 1,4-disubstituted 1,2,3-triazoles, and mononuclear mechanism proposed by Sharpless *et al.*²²⁸

Further research has been focused on the mechanism of the copper(I)-mediated azide-alkyne cycloaddition (CuAAC), whereby Sharpless *et al.* proposed a reaction mechanism in 2002 (**Scheme 2.14**).²²⁸ According to the proposed mechanism, the reaction starts with the formation of a stabilized copper-acetylide, followed by coordination of the azide. Subsequent ring-closing leads to a metallacycle whose rearrangement generates a copper-coordinated 1,2,3-triazole. Cleavage of the catalytic complex finally yields the 1,4-disubstituted product. In recent years, the mechanism of CuAAC has been extensively examined.²²⁹⁻²³¹

The CuAAC has been used in a wide range of applications e.g. in the labelling of DNA and RNA,²³² the synthesis of antimicrobial peptides,²³³ the development of radiopharmaceuticals,²³⁴ the synthesis of polymeric networks,²³⁵ and in the synthesis of end-on-end linearly assembled fibers.²³⁶

2.3 Polymerization techniques

2.3.1 Basic techniques

Polymerization reactions are divided into two main groups, step-growth and chain-growth polymerizations. The former is characterized by the absence of an initiator, a non-linear relationship between the molecular weight of the forming polymeric chains and the monomer conversion, and the random growth within the reaction mixture.²³⁷ Hereby, multifunctional monomers, e.g. equimolar amounts of two different bifunctional monomers (AA/BB-type) or one bifunctional monomer with two different functionalities (AB-type), react to form small oligomers. Due to the step-like process, the monomers are rapidly consumed merely yielding low molecular weights. Further reaction between oligomers leads to the formation of higher DP oligomers, eventually generating macromolecules at high monomer conversion. In order to obtain high molecular weights, it is essential to reach nearly quantitative monomer conversion. This behavior is described by the Carothers equation, which was proposed to evaluate the degree of polymerization (X_n) attainable in a step-growth polymerization for a given fractional monomer conversion (p).²³⁸ Considering a linear step-growth polymerization using AB-type monomers, it is represented by:

$$X_n = \frac{1}{1-p} \quad (2.1)$$

with the monomer conversion being calculated from the number of monomers initially present (N_0) and the number of monomers present after a defined time (N) according to:

$$p = \frac{N_0 - N}{N_0} \quad (2.2)$$

As an example, a monomer conversion of 95% ($p = 0.95$) is required to obtain polymers with an X_n of 20, whereas a monomer conversion of 99.5% ($p = 0.995$) is required to obtain polymers with an X_n of 200 (**Figure 2.4**).

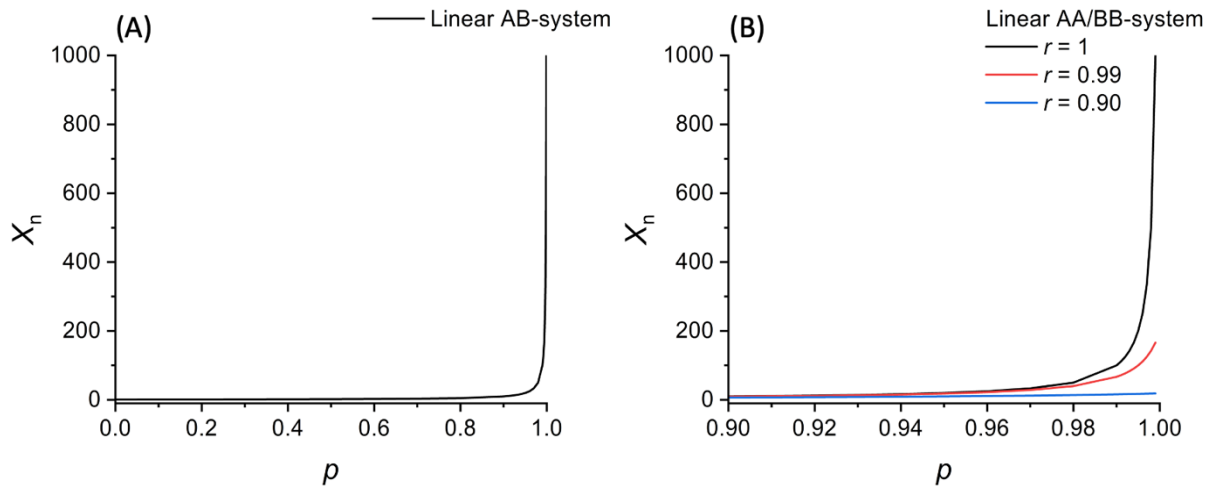


Figure 2.4. Graphical representation of the Carothers equation for (A) linear AB-systems and (B) linear AA/BB-systems.²³⁸

When applying a mixture of monomers in a step-growth polymerization, e.g. using AA/BB-type monomers, one monomer can be present in excess and the Carothers equation becomes:

$$X_n = \frac{1 + r}{1 + r - 2rp} \quad (2.3)$$

with r being the stoichiometric ratio of the reactants. If equimolar amounts of monomers are used, then $r = 1$ and the equation reduces to the AB-type equation above (**Equation 2.1, Figure 2.4**).²³⁹

In non-linear AB-systems, e.g. in the synthesis of branched polymers, the Carothers equation is modified, leading to:

$$X_n = \frac{2}{2 - pf_{av}} \quad (2.4)$$

with p being calculated from:

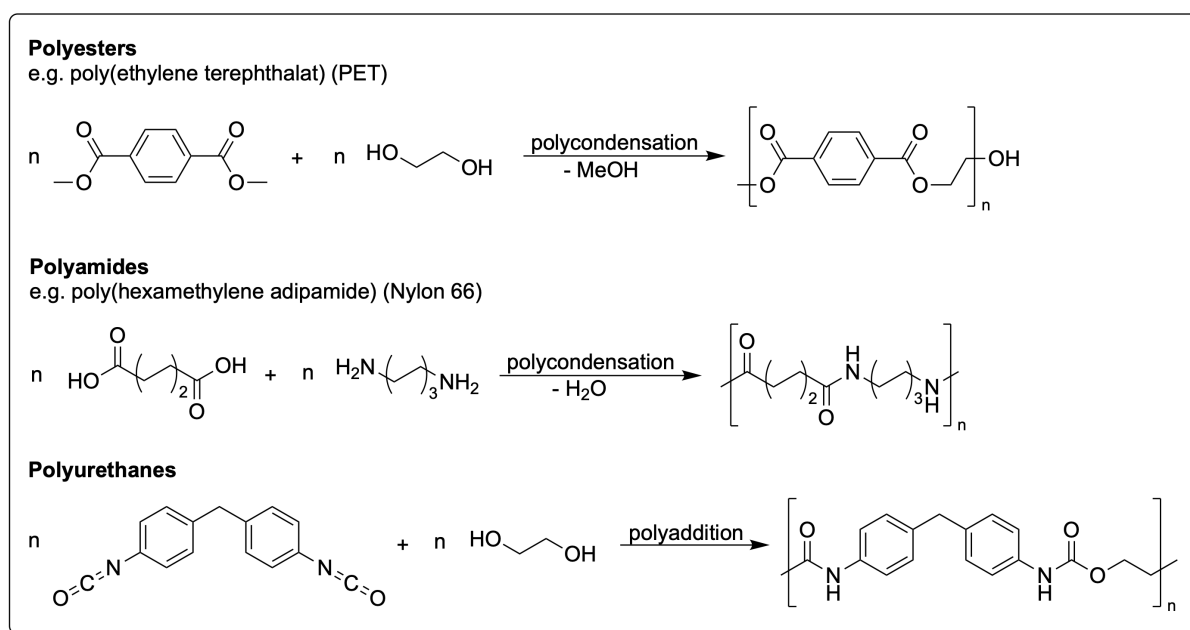
$$p = \frac{2(N_0 - N)}{f_{av}N_0} \quad (2.5)$$

with f_{av} being the average functionality per monomer unit, f_i being the number of functionalities of monomer i , and N_i being the amount of monomer i .²⁴⁰

$$f_{av} = \frac{\sum N_i f_i}{\sum N_i} \quad (2.6)$$

In step-growth polymerizations, one type of reaction is responsible for polymer formation, while no termination is required and thus the chain ends remain active. Depending on the used monomers, linear, branched, or crosslinked polymers are attainable *via* step-growth polymerization techniques.²³⁷

Step-growth polymerizations are further divided into polycondensation and polyaddition reactions,²⁴¹ both usually acid or base catalyzed,²⁴²⁻²⁴⁴ where the former is characterized by the release of a small molecule such as water as by-product.²³⁷ In order to increase the monomer conversion and thus reach high molecular weights in polycondensation reactions, the chemical equilibrium is shifted toward the product side by continuous removal of the by-product. Therefore, polycondensation reactions are often carried out at high temperature.²³⁷ Polycondensation reactions are of great importance in the chemical industry, e.g. in the production of polyesters, polyamides, polysiloxanes, and others (**Scheme 2.15**).²⁴⁵

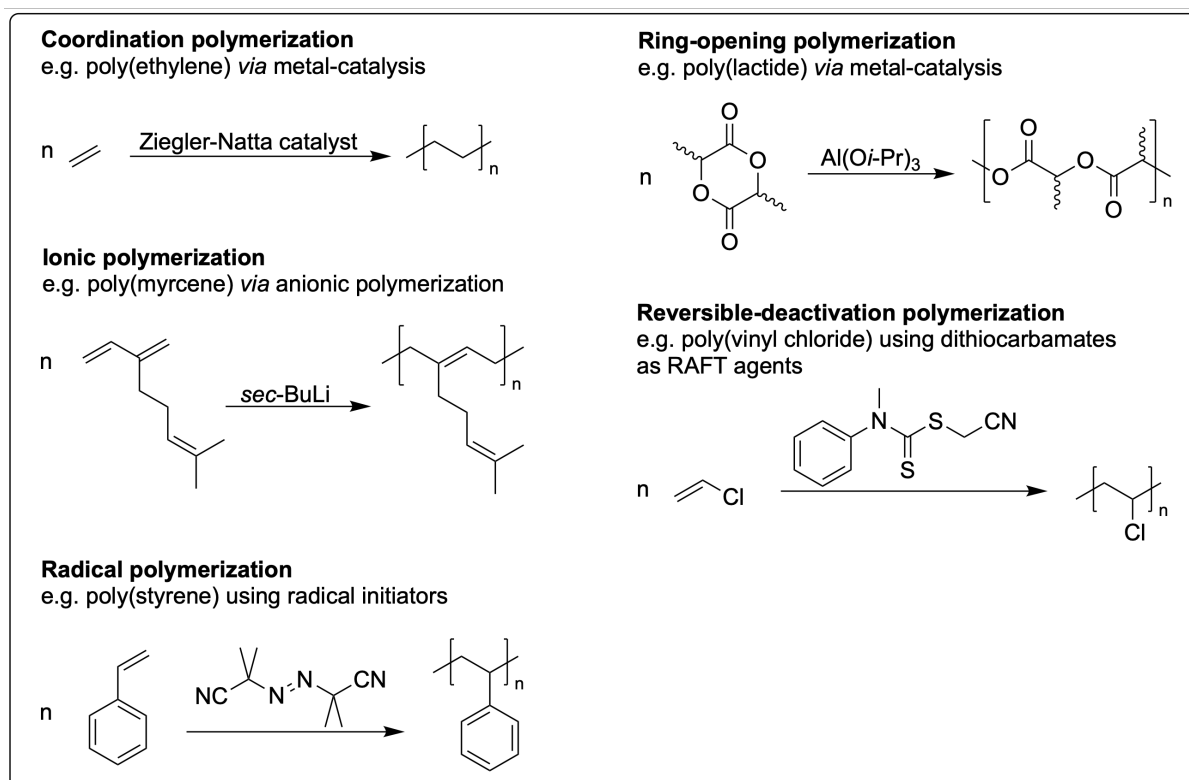


Scheme 2.15. Representative step-growth polymerizations.²⁴⁶⁻²⁴⁸

Since the synthesis of polyurethanes (PUs) *via* the polyaddition of diisocyanates and diols was first reported by O. Bayer in 1937 (**Scheme 2.15**),²⁴⁸ extensive research has been conducted on this topic.²⁴⁹ Due to the environmentally and sanitarly harmful industrial synthesis of isocyanates using phosgene and their toxic potential in the production of PUs,²⁵⁰⁻²⁵² recent research focuses on the synthesis of non-isocyanate PUs (NIPUs),²⁵³ e.g. by replacing isocyanates with cyclic carbonates.²⁵⁴⁻²⁵⁶

In contrast to step-growth polymerizations, chain-growth polymerizations are characterized by the presence of an initiator and thus a limited number of active sites, the polymer growth by monomer addition at one end or both ends of the chain, and the presence of different reaction steps during the polymerization process.²⁵⁷ The first reaction step is called chain initiation, in which an active site is formed e.g. by an initiator molecule, by radiation, or by thermal initiation. In the next step, chain propagation occurs by recurring reactions of the active site with the monomers to form longer molecules with new active sites. Deactivation of the active sites leads to chain termination. During chain transfer, the active site of a polymer is exchanged with the atom of another molecule, potentially leading to a new growing polymer chain.²⁵⁷ Additionally, intramolecular chain transfer can occur, so-called backbiting.²⁵⁸ An exemplary reaction mechanism of a controlled chain-growth polymerization, namely ATRP, is depicted in **chapter 2.3.2 (Scheme 2.17)**.

Chain-growth polymerizations are divided into different classes which are defined by the involved chain carrier.²⁵⁸ This includes coordination polymerization, as well as ionic, radical, reversible-deactivation, and ring-opening polymerization (ROP, **Scheme 2.16**).



Scheme 2.16. Representative chain-growth polymerization techniques.²⁵⁹⁻²⁶³

In the following section, a brief overview and the basic description on commonly used chain-growth polymerizations is given, however, there are smooth transitions between the different approaches. Extensive research was conducted for all herein presented polymerization techniques.²⁶⁴⁻²⁶⁹

Coordination polymerization is catalyzed by transition metal salts and their complexes,²⁷⁰⁻²⁷² with the monomer preliminarily coordinating to the transition metal center, followed by the formation of a four-membered ring transition state, and subsequent insertion of the monomer into the transition metal-carbon bond.²⁷³ Typical monomers include vinyl compounds or epoxides.^{273,274} An important example represents the polymerization of 1-alkenes using Ziegler-Natta catalysts, such as triethylaluminium (**Scheme 2.16**).^{263,275}

Ionic polymerizations are divided into cationic and anionic polymerizations, whereby the active site bears a positive or a negative charge, respectively.²⁵⁷ For both, a variety of initiation strategies have been developed in recent years, including initiation with Lewis acids,²⁷⁶ carbenium ion salts,²⁷⁷ and ionizing radiation in cationic polymerizations,²⁷⁸ and initiation by electron transfer and reactive anions in anionic polymerizations (**Scheme 2.16**).^{279,280} Typical monomers include e.g. vinylic compounds for cationic polymerization and heterocycles for anionic polymerization.²⁸¹⁻²⁸⁴

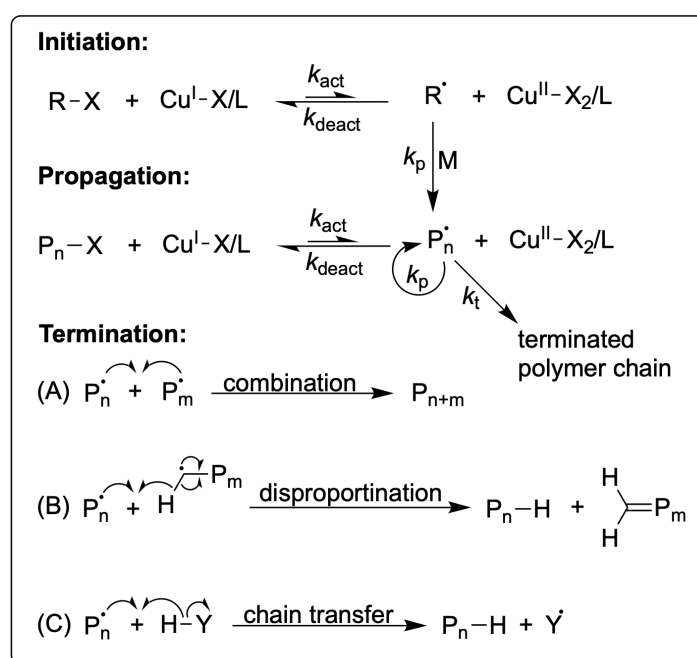
In radical polymerization, the active site comprises a radical which is generated using different strategies, e.g. by the thermal decomposition or photolysis of chemical initiators (**Scheme 2.16**).²⁸⁵⁻²⁸⁸ Typical monomers in radical polymerizations include acrylates,²⁸⁹ methacrylates,²⁹⁰ styrene,²⁶⁰ and vinylic olefins.²⁹¹ Radical polymerization processes are used for a wide range of application in industry, e.g. in the production of superabsorbent polymeric networks in diapers or in the production of electrically conductive polymer glasses.^{292,293}

In ring-opening polymerization, the chain propagation is associated with the ring-opening of cyclic monomers, such as lactides or lactams (**Scheme 2.16**).^{261,294} Here, the active site is either radical,²⁹⁵ anionic,²⁹⁴ cationic,²⁹⁶ or neutral.²⁹⁷ Since cyclic monomers are used in this approach, the polymerization is usually driven by the relief of the ring-strain, generating a negative change in enthalpy and thus favors ring-opening.²⁹⁸ An important type of ring-opening polymerization is represented by ROMP, whereby unsaturated polymers are obtained from cyclic olefins.²⁶⁸ The basic principles of ROMP are discussed in more detail within **chapter 2.3.3**.

Reversible-deactivation polymerizations are characterized by an equilibrium between an active and a dormant species, leading to a controlled polymerization process. The most important variation is the RDRP, including polymerizations such as ATRP,²⁹⁹ the reversible addition-fragmentation chain transfer (RAFT) polymerization,³⁰⁰ and the nitroxide-mediated radical polymerization (NMP).³⁰¹

2.3.2 Atom transfer radical polymerization (ATRP)

As mentioned in **chapter 2.3.1**, ATRP is a chain-growth polymerization and is further assigned to the class of RDRPs involving a radical as chain carrier.²⁵⁸ ATRP was independently reported by Sawamoto *et al.* and Matyjaszewski *et al.* in 1995,^{302,303} while research on this topic was strongly influenced by the latter. ATRP is described as a kinetically controlled radical polymerization and exhibits an equilibrium between the propagating radicals and the dormant species (**Scheme 2.17**).³⁰² It is noted that the following section focuses on copper-mediated ATRP.



Scheme 2.17. Reaction mechanism of copper-mediated ATRP with termination *via* (A) combination, (B) disproportionation, and (C) chain transfer.³⁰²

An ATRP is typically mediated by a copper(I) complex (Cu^I-X/L), namely the activator. The latter reacts reversibly with an initiating alkyl halide species ($R-X$) which is the dormant species. During this reaction, characterized by the rate constant of activation (k_{act}), the

copper(I) salt is oxidized to its copper(II) species ($\text{Cu}^{\text{II}}\text{-X}_2/\text{L}$), namely the deactivator, among transfer of the alkyl-bonded halide, forming an alkyl radical (R^*) which is the propagating species. During the chain propagation, the alkyl radical irreversibly reacts with a monomer (M) to form a growing radical (P_n^*), whereby the reaction is characterized by the rate constant of propagation (k_p). The reverse reaction between the deactivator and the propagating radicals re-forms the dormant species ($\text{P}_n\text{-X}$) and the activator and is characterized by the rate constant of deactivation (k_{deact}). The equilibrium between the activation and the deactivation process is described by the equilibrium constant ($K_{\text{ATRP}} = k_{\text{act}}/k_{\text{deact}}$), which determines the concentration of radicals. In order to perform a controlled polymerization, large k_{act} and k_{deact} are required to ensure a reasonable polymerization rate, while $k_{\text{act}} \ll k_{\text{deact}}$. The equilibrium between the propagating radicals and the dormant species is maintained until irreversible chain termination occurs, characterized by the rate constant of termination (k_t).^{304,305}

Different termination mechanisms have been reported, including combination, radical disproportionation, and chain transfer.³⁰⁶ During combination (**Scheme 2.14A**), the two propagating radicals (P_n^* and P_m^*) react to form one deactivated species (P_{n+m}).³⁰⁷ Interactions of the propagating radicals with e.g. oxygen or other impurities potentially trigger termination by combination.^{308,309} During radical disproportionation (**Scheme 2.14B**), a hydrogen atom is abstracted from the chain end of another propagating species, leading to the formation of two deactivated polymer chains with one having a saturated and the other an unsaturated chain end.³¹⁰ Both termination processes are characterized by the loss of the propagating radicals. As a third possibility, termination by chain transfer describes the reaction of a propagating radical with a molecule by abstracting a hydrogen or another atom and thus transferring the radical character (**Scheme 2.14C**).³¹¹ Chain transfer potentially involves solvent molecules,³¹² polymer chains,³⁰⁶ or monomers.³¹³ In contrast to combination and disproportionation, chain transfer retains the total number of radicals.

Even though copper complexes are most often used in ATRP,³¹⁴⁻³¹⁶ other transition metals, such as Ru,³⁰³ Fe,³¹⁷ Mo,³¹⁸ and Os,³¹⁹ have been studied. The selection of a certain transition metal has an influence on K_{ATRP} . Here, different equilibria are involved such as the oxidation of the metal complex, describing the ability to perform an electron transfer, the reduction of a halogen to a halide ion which is determined by its electron affinity, and the association of the halide ion to the higher oxidation state metal complex.³²⁰ Research on this topic indicated

twice the reducing potential for Cu compared to Ru and Os, whereas the halide affinity of Ru and Os was suggested to be seven to nine orders of magnitude higher than Cu.³²⁰

Furthermore, K_{ATRP} is influenced by the relative homolytic bond strengths of the metal-halide bond, which decreases in the order $\text{F} > \text{Cl} > \text{Br} > \text{I}$, whereas the catalytic reactivity increases in this order.³²¹

Another important contribution to K_{ATRP} is described by the nature of the used ligand. Typically, multidentate nitrogen ligands are used to complex the copper ion (**Figure 2.5**),³²²⁻³²⁴ since phosphorus, oxygen, and sulfur ligands are less effective due to e.g. unfavorable binding constants.^{325,326}

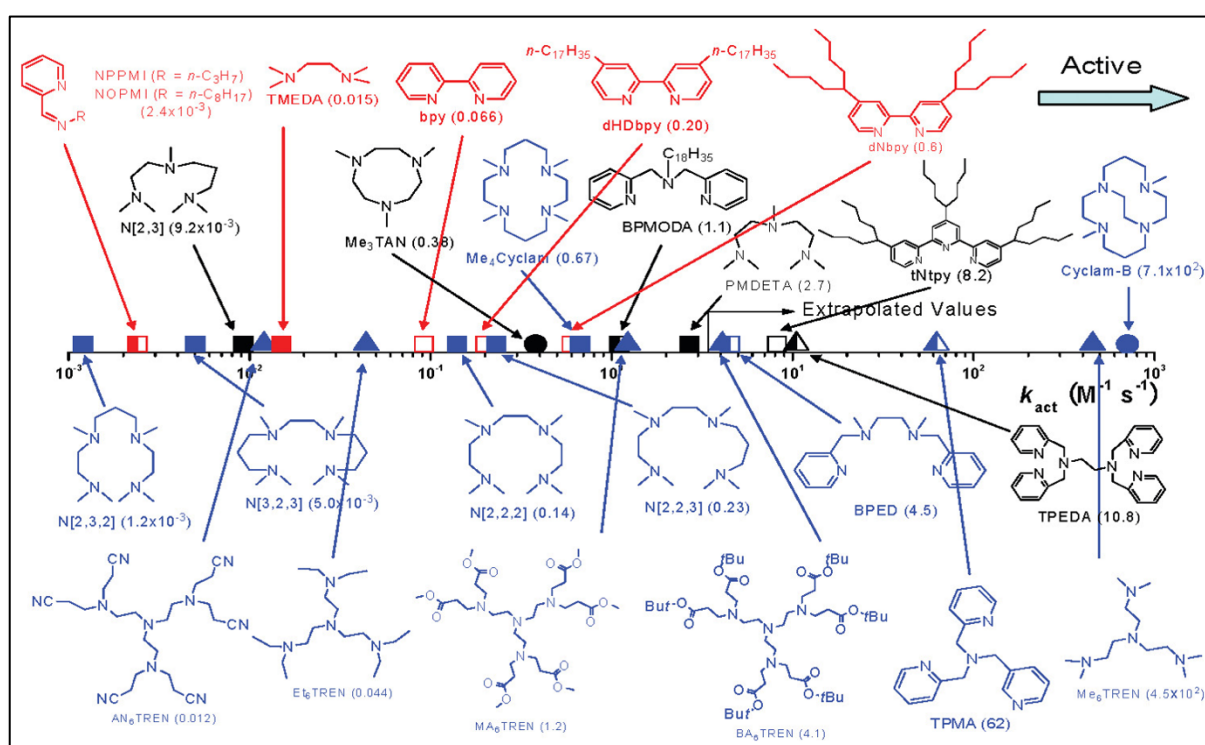


Figure 2.5. ATRP activation rate constants (k_{act}) for different bidentate (red), tridentate (black), and tetradentate (blue) ligands with ethyl α -bromoisobutyrate in the presence of copper(I) bromide in acetonitrile at 35 °C. Reprinted with permission (<https://pubs.acs.org/doi/full/10.1021/ma0609634>).³²⁶ Copyright 2006 American Chemical Society.

Several copper complexes with nitrogen-based ligands were compared, whereby the k_{act} s were determined applying standardized reaction conditions. It was found that the activity of the catalyst increases with an increasing stability of the copper(II) state provided by the complexing ligand.³²⁷

Hence, k_{act} decreases in the following order: tetradentate (cyclic-bridged) > tetradentate (branched) > tetradentate (cyclic) > tridentate > tetradentate (linear) > bidentate ligands.³²⁶ Furthermore, the chemical environment of the nitrogen atoms influences the activity of the respective copper complex, thus k_{act} decreases in the following order: pyridine \geq aliphatic amine > imine.³²⁶

In another study, the effect of the used ATRP initiator was examined, applying standardized reaction conditions, ensuring comparability of the determined k_{act} s (**Figure 2.6**).

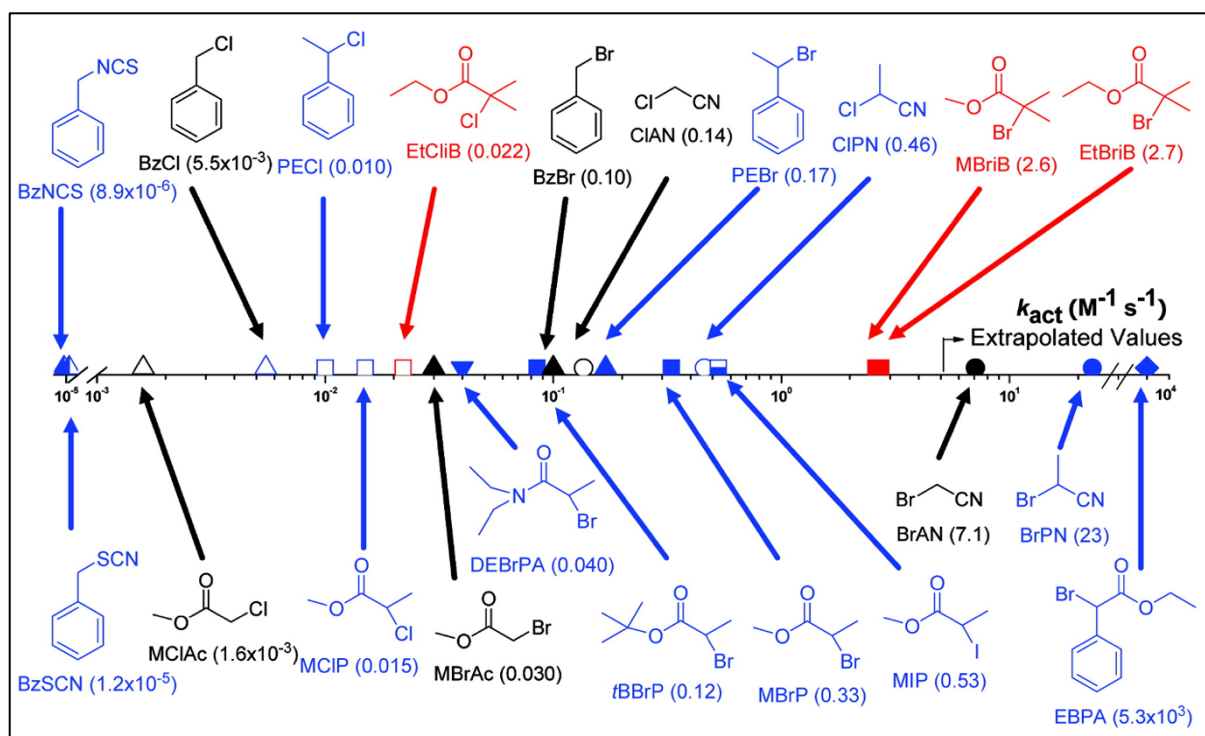


Figure 2.6. ATRP activation rate constants (k_{act}) for different tertiary (red), secondary (blue), and primary (black) alkyl initiators with $\text{Cu}^{\text{I}}\text{-X}/\text{PMDETA}$ ($\text{X} = \text{Cl}$ or Br) in acetonitrile at $35\text{ }^\circ\text{C}$. Reprinted with permission (<https://pubs.acs.org/doi/full/10.1021/ma062897b>).³²⁸ Copyright 2007 American Chemical Society.

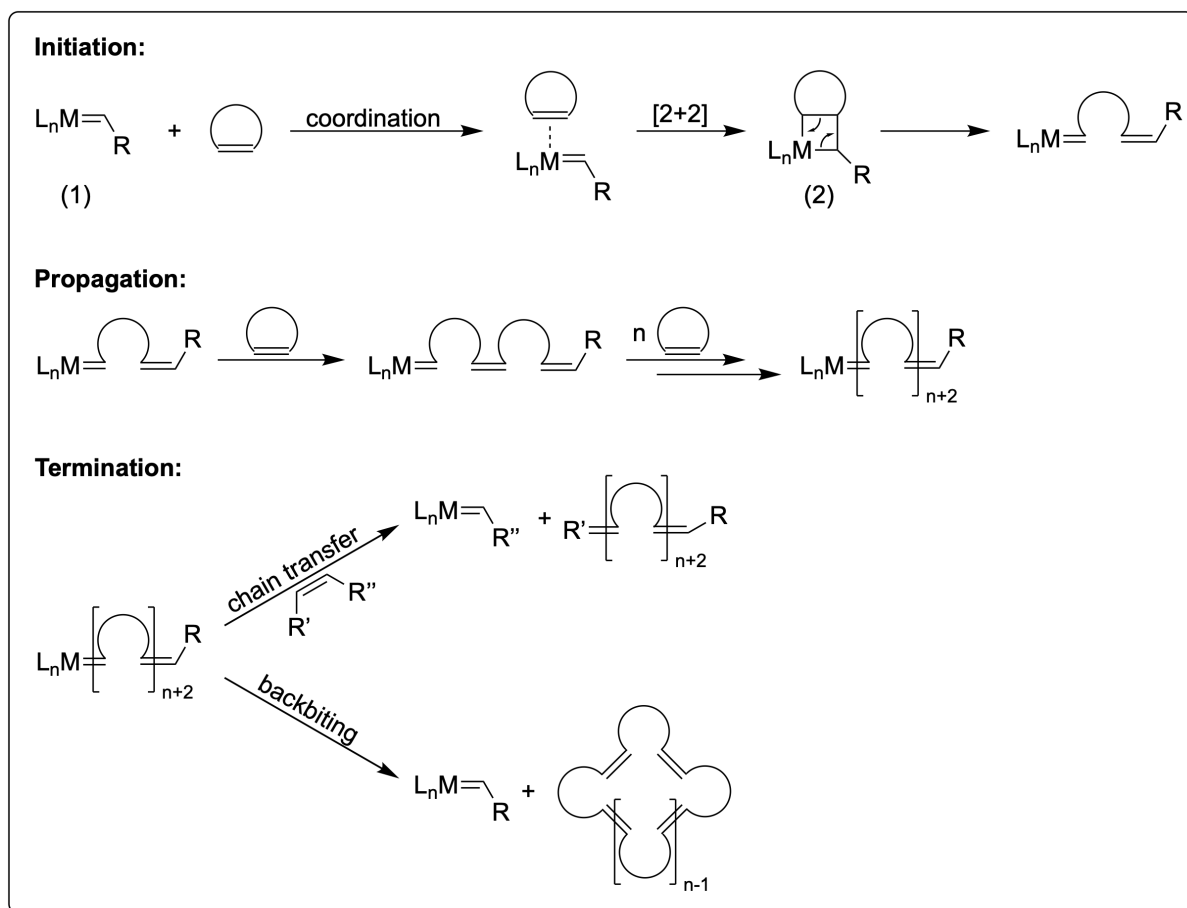
Here, several alkyl (pseudo)halides were examined, and it was found that the activity of the alkyl group is defined by its ability to stabilize a formed radical by electronic effects. Thus, the activity decreases in the following order: tertiary > secondary > primary alkyl, and phenyl ester > cyanide > ester > benzyl > amide.³²⁸ Furthermore, the (pseudo)halide affects the activity of the ATRP initiator, depending on its ability to act as a leaving group and the stability of the formed species. Thus, the activity decreases in the following order: $\text{I} \geq \text{Br} > \text{Cl} \gg \text{SCN} \approx \text{NCS}$.³²⁸ The activity trends for the herein presented nitrogen ligands and ATRP initiators were further

confirmed by the determination of the respective K_{ATRP} , considering the contribution of k_{deact} on the catalytic activity.³²⁹

In recent years, extensive research has been conducted on ATRP variations which tackle disadvantages assigned to the classic copper(I)-mediated ATRP, such as the catalyst poisoning by oxygen and the relatively high catalyst concentration needed.³³⁰ In order to minimize the required copper concentration in ATRP, so-called activator regeneration methods have been developed, which provide sufficient activity with low amounts of copper and enable polymerization in protic and aqueous media. Prominent examples are ARGET (activators regenerated by electron transfer) ATRP,³³¹⁻³³³ ICAR (initiators for continuous activator regeneration) ATRP,³³⁴⁻³³⁶ and SARA (supplemental activator and reducing agent) ATRP.³³⁷⁻³³⁹ Other ATRP variations are based on the photo-induced reduction of the transition metal complex or the generation of the copper(I) activator by electrochemical processes.^{340,341} Current research on ATRP includes the development of organocatalysts for metal-free ATRP,³⁴² the surface-initiated ATRP of bio-based monomers,^{343,344} the compatibility between different controlled radical polymerization techniques in the synthesis of polymeric networks,³⁴⁵ and the preparation of biomolecule-polymer conjugates.³⁴⁶

2.3.3 Ring-opening metathesis polymerization (ROMP)

ROMP is a variation of the olefin metathesis reaction and was first reported in a patent by Du Pont,³⁴⁷ describing the metal-mediated polymerization of norbornene. The mechanism of ROMP was explained based on the olefin metathesis mechanism proposed by Chauvin in 1971 (Scheme 2.18).³⁴⁸



Scheme 2.18. ROMP mechanism based on the related olefin metathesis mechanism proposed by Chauvin,^{17,348} with metal alkylidene (1) and metallacyclobutane intermediate (2).

In the first step, the metal alkylidene (1) coordinates to the cyclic olefin and reacts in a [2+2] cycloaddition, leading to the formation of the metallacyclobutane intermediate (2). The following cycloreversion is usually driven by the relief of the ring strain of the intermediate and results in the generation of the metathesis product and a new metal alkylidene, which exhibits a comparable reactivity toward the coordination and metallacyclobutane formation. The presence of an excess of cyclic olefin and typically the release of ring strain of the latter leads to propagation and thus to the generation of a polymeric chain. It is important to note

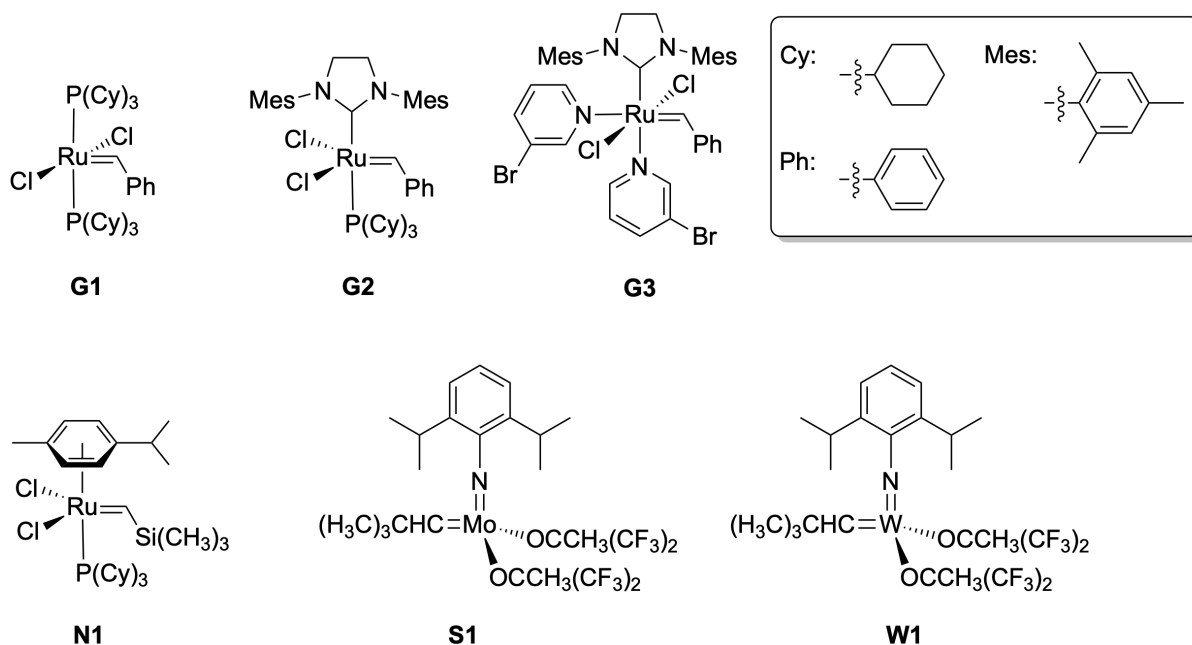
that the propagating metal center attached to the growing polymer chain is either found in the metal alkylidene or the metallacyclobutane form.¹⁷ Termination is usually initiated by an olefinic compound capable of undergoing a cross metathesis reaction with the propagating chain end. This process is called chain transfer and results in the formation of a terminated polymer chain and a deactivated metal complex. A propagating polymer chain may undergo an intramolecular chain transfer reaction, resulting in the formation of a cyclic polymer and the regeneration of the initial metal alkylidene. This process is called backbiting and strongly depends on the used monomer.⁶²

Since ROMP is a variation of olefin metathesis which is characterized by reversibility, there were discussions about whether to denote ROMP as a “living” polymerization technique. The term “living” was defined by M. Szwarc in 1956,³⁴⁹ and describes a polymerization which is characterized by the absence of chain termination and irreversible chain transfer, as well as by the rate of initiation being fast compared to the rate of propagation.²⁵⁸ In addition to this definition, a ROMP reaction is described as “living and controlled” if there is (1) fast and complete initiation, (2) a linear relationship between the degree of polymerization (DP) and the monomer consumption, and (3) dispersity values lower than 1.5 for the obtained polymers.^{350,351} Hence, the “living” nature and the efficiency of ROMP is ultimately defined by the choice of monomer and catalyst.

Potential monomers for ROMP usually exhibit a ring strain higher than 5 kcal/mol as for example norbornene, cyclobutene, cyclopentene, and cyclooctene.³⁵² Six-membered rings are not likely to undergo ring-opening due to their low ring strain energies, e.g. -0.84 kcal/mol for cyclohexene.³⁵² Since the success of a reaction is not only influenced by enthalpic factors, but depends on the Gibbs free energy, the activation energy for ROMP can also be generated by a negative entropy term.³⁵³ This variation is called entropy-driven ROMP (ED-ROMP) and is discussed later within this section.

As shown in the reaction mechanism (**Scheme 2.18**), ROMP is usually a metal-mediated polymerization technique. Initially, heterogeneous catalysts were prepared by mixing Ti, W, or Mo halides with Lewis acidic Al co-catalysts.¹⁷ However, the ROMP of cyclic olefins gained commercial importance after Calderon *et al.* reported the preparation of a homogeneous catalyst by *in situ* activation of WCl_6 using $EtAlCl_2$ in ethanol.³⁵⁴ In the following years, the development of new olefin metathesis catalysts was intensified, utilizing a wide range of

transition metals.³⁵⁵⁻³⁵⁷ Schrock *et al.* focused on Mo- and W-based imido alkylidenes,^{358,359} whereas Grubbs *et al.* established Ru-based vinylidene and benzylidene complexes (Scheme 2.19).^{360,361}

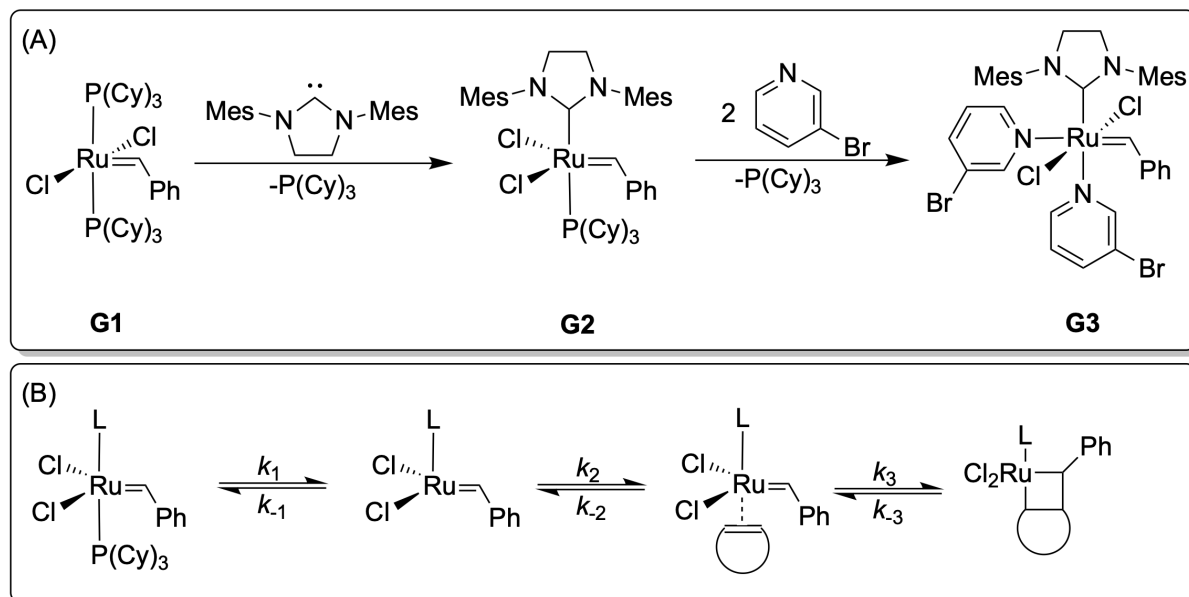


Scheme 2.19. Commonly used Ru-, Mo-, and W-based ROMP catalysts.³⁶²

It is important to mention that the activity, stability, and functional group tolerance depends on the used transition metal and on the attached ligands. Thus, both factors are of great importance to conduct a successful ROMP. As an example, Schrock-type W-based imido alkylidenes (W1, Scheme 2.19) show high activity in ROMP, leading to polymers with a narrow molecular weight distribution.³⁶³ The functional group tolerance of the catalyst and its stability toward moisture, water, and air was further improved by exchanging the W with Mo.³⁶⁴ These Mo-based alkylidenes (S1, Scheme 2.19) enable the controlled polymerization of cyclic olefins with demanding functional groups, such as imines,³⁶⁵ cyanides,³⁶⁶ or halides.³⁶⁷

Comparable to the Schrock-type catalysts, Ru-based vinylidene complexes show a high tolerance toward functional groups and are capable of polymerizing norbornene and cyclobutene derivatives.³⁶⁰ These complexes were found to be highly stable in the solid state, as well as in degassed and dry organic solvents.³⁶⁰ Further optimization led to the introduction of tricyclohexyl phosphine ligands and a benzylidene functionality, resulting in the so-called

Grubbs first generation catalyst (G1, **Scheme 2.19**).^{368,369} In recent years, different Grubbs-like catalysts such as the Noels catalyst (N1, **Scheme 2.19**),³⁷⁰ and the Grubbs second and third generation catalysts (G2 and G3, **Scheme 2.19**) were developed.^{371,372} The latter comprise NHC ligands introduced through a phosphine exchange-type reaction (**Scheme 2.20A**).³⁷³



Scheme 2.20. (A) Relationship between the commonly used Grubbs catalysts and (B) initiation phase using the G1 or the G2 catalyst with kinetic constants k_1 , k_{-1} , k_2 , k_{-2} , k_3 and k_{-3} .^{17,374}

As mentioned earlier within this section, the attached ligands have a strong influence on the reactivity of the respective catalyst in ROMP. Concerning the phosphine-containing catalysts, the reaction which forms the activated species is governed by the rate of phosphine dissociation (k_1 , **Scheme 2.20B**).³⁷⁴ Comparing the G1 and the G2 catalyst, they differ structurally on account of one ligand, with the PCy_3 ligand of the G1 catalyst exhibiting better dissociation ability, compared to that of the NHC-stabilized G2 catalyst [$k_1(\text{G1}) > k_1(\text{G2})$].³⁷⁵ The catalytic activity is quantified as the ratio of the rate of olefin coordination (k_2) and the rate of phosphine association (k_{-1}). The NHC ligand shows the ability of being an σ -donor without being a π -acceptor, resulting in a higher affinity of the catalyst regarding the coordination of olefinic substrates [$k_2(\text{G1}) < k_2(\text{G2})$]. As a result, the combination of a sterically demanding and basic ligand (NHC) with a labile ligand (e.g. PCy_3) shows the best properties regarding a high catalytic activity in olefin metathesis and thus in ROMP.^{374,375}

However, relatively slow initiation rates and the presence of competing secondary metathesis reactions in the G2-mediated ROMP usually leads to uncontrolled polymerizations and broad

molecular weight distributions. In order to increase the initiation rates of ROMP, labile pyridine ligands have been introduced through a phosphine exchange–type reaction (**Scheme 2.20A**).³⁷⁶ Different pyridine derivatives were used, with the 3-bromopyridine ligated catalyst (G3) exhibiting the highest initiation rates.³⁷⁷ In the solid state, the G3 catalyst appears as the di-pyridine complex, which is denoted as the precatalyst. In solution, one pyridine ligand is fully dissociated while forming the catalytically active mono-pyridine species. Furthermore, G3-mediated ROMP was found to exhibit an apparent zero-order rate dependence of the catalyst.³⁷⁷

Since ROMP is considered a “living” polymerization, termination must be induced by the addition of a potent chain transfer agent (CTA). In order to ensure an efficient termination process, a high affinity of the added compound toward the cross-metathesis reaction with the propagating chain end is required. Here, an excess of CTA is usually added to ensure sufficient termination. The termination *via* chain transfer further leads to the ω -chain end functionalization of the polymer.³⁷⁸ Vinyl ethers have shown to be suitable to serve as CTAs,³⁷⁹ ethyl vinyl ether (EVE) being commonly used to quench Ru-based ROMP reactions. As a result, an olefin-terminated polymer and a catalytic inactive Fischer carbene are obtained.³⁸⁰ A variety of different CTAs have been used to specifically functionalize the ω -chain end of polymers synthesized *via* ROMP, including acrylates,³⁸¹ alcohols,³⁸² aldehydes,³⁸³ RAFT agents,³⁸⁴ and many others.^{385,386}

In the following, the applications of the Grubbs-type catalysts in polymer chemistry are discussed, whereby different monomers and monomer combinations have been used to synthesize a variety of homo- and copolymers. Furthermore, a brief overview concerning ROMP variations, such as the metal-free ROMP (MF-ROMP) and the ED-ROMP, is given.

As mentioned earlier in this section, ROMP is a highly versatile and robust polymerization technique, which shows a “living” nature under optimized reaction conditions. Among others, the synthesis of dendronized polymers has been performed in a “living” fashion using Ru-based catalysts.³⁸⁷ As an example, azobenzene-based dendrons capable of photoinduced bending motion show potential use in controllable wireless actuators and light-switchable logic devices.³⁸⁸ Furthermore, challenging ROMP in aqueous media has been successfully performed by the addition of chloride sources, such as HCl, NaCl and tetrabutylammonium chloride (TBACl), preventing the formation of unstable and metathesis-inactive $\text{Ru}(\text{OH})_n$

complexes.³⁸⁹ DNA-polymer conjugates were further synthesized under aqueous conditions by copolymerizing DNA- and poly(ethylene glycol) (PEG)-based macromonomers,³⁹⁰ whereas protein-like polymers were synthesized in various solvents *via* grafting-to and grafting-through approaches.³⁹¹ Another interesting field of research represents the synthesis of mechanoactive polymers comprising bicyclic cyclopentene derivatives, which undergo chemical transformations induced by mechanical stress, e.g. during sonification or stirring of the polymer solution, and grinding of the polymer solid.^{392,393} Furthermore, noticeable research is currently conducted in the synthesis of more sustainable polymers *via* ROMP. This includes the polymerization of bio-based monomers such as lactones and pinenes,^{394,395} the synthesis of bio-derived self-healing polymers,³⁹⁶ or the synthesis of photodegradable copolymers.^{397,398}

Since the synthesis of sequence-controlled polymers has been denoted as the next “holy grail” of polymer chemistry,³⁹⁹ various approaches have been investigated to precisely introduce monomers and monomeric sequences *via* ROMP.^{94,400-402} An interesting concept was reported by O’Reilly *et al.* in 2014 (**Figure 2.7**).⁹³

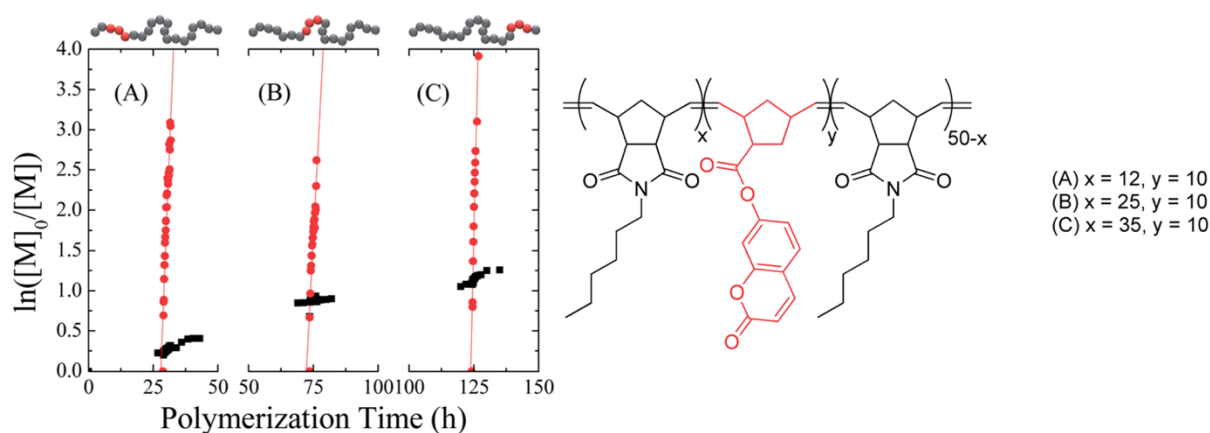


Figure 2.7. The G1-mediated ROMP of kinetically different norbornene-based monomers, generating copolymers with relatively controlled monomer sequences. Reprinted with permission (<https://pubs.rsc.org/en/content/articlelanding/2014/sc/c4sc00752b>).⁹³

In this approach, norbornene-based monomers with different kinetic behavior were copolymerized using the G1 catalyst. Here, a slow homopolymerization was performed using an *endo* norbornene, followed by the addition of rapidly polymerizing *exo* monomers after defined reaction times (**Figure 2.7**). This technique was found to be compatible with the

“living” nature of ROMP and further generated copolymers containing up to four different functionalities at controllable positions along the polymeric backbone.⁹³

Beside the polymerization of relatively small monomers, the ROMP of macromonomers has been performed for nearly two decades,⁴⁰³ whereupon the development of the fast-initiating G3 catalyst revealed the opportunities of this strategy in order to obtain narrow dispersity graft polymers.^{404,405} Since then, macromonomers have been synthesized using various controlled polymerization techniques, e.g. *via* anionic polymerization,⁴⁰⁶ ATRP,⁴⁰⁷ RAFT,⁴⁰⁸ ROP,⁴⁰⁹ and others.^{390,410}

As an example, Matson *et al.* synthesized norbornene-functional macromonomers with molecular weights up to 10,000 g/mol *via* the ATRP of styrene (**Figure 2.8**).⁴¹¹

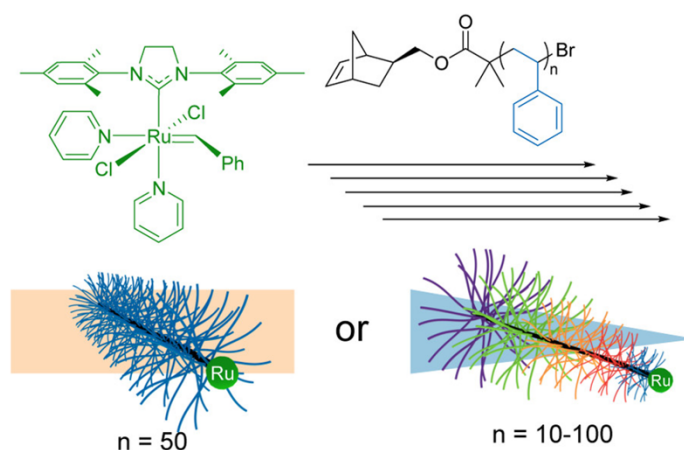


Figure 2.8. G3-mediated synthesis of symmetric and unsymmetric bottlebrush polymers using a sequential addition of macromonomers strategy. Reprinted with permission (<https://pubs.acs.org/doi/full/10.1021/acsmacrolett.7b00724>).⁴¹¹ Further permissions related to the material excerpted must be directed to the ACS.

Subsequent G3-mediated ROMP resulted in symmetric and unsymmetric bottlebrush polymers. The latter was synthesized using a sequential addition of macromonomer strategy. It was further possible to visualize the obtained polymers *via* atomic force microscopy (AFM), where the cone-shaped polymer showed an end-to-end gradient in height of *ca.* 0.2 nm.⁴¹¹ Since the G3-mediated ROMP of macromonomers represents a feasible method to synthesize graft polymers in a controlled fashion, iterative copolymerization of different macromonomers has been performed to obtain sequence-controlled block-like graft copolymers with the ability to self-assemble into well-defined structures.^{50,412,413} These materials are further interesting for the use in photonics.⁴¹⁴ Current research includes the

ROMP-induced self-assembly (ROMPISA), leading to the *in situ* preparation of nano-objects, such as spherical or worm-like micelles.⁴¹⁵

Although metal-mediated ROMP has proven to be highly versatile and robust, the used transition metal initiators remain a problem in certain applications, such as in the field of biomedicine,⁴¹⁶ as removal of the metal is rather challenging.⁴¹⁷ Therefore, investigations toward MF-ROMP have been conducted. As an example, the photoredox-mediated cyclobutane formation using visible light is a promising alternative to avoid transition metal catalysts.^{418,419} The use of pyrylium and thiopyrylium photo-oxidants further enabled the successful ROMP of norbornene.⁴²⁰ MF-ROMP is a relatively new field of research and thus has the potential of gaining importance in the future.

Another ROMP variation that is recently studied is the ED-ROMP. As mentioned earlier within this section, a classic ROMP is driven by the relief of the ring strain of cyclic olefins, resulting in a decreasing enthalpy upon ring-opening.¹⁷ Although macrocycles with more than 14 ring atoms exhibit negligible ring strain and thus ring-opening is enthalpically not favored,⁴²¹ the latter is achieved by an increasing entropic factor. This factor is influenced by the entropy of mixing and by an increasing conformational entropy due to the ring-opening of the macrocycle, assuming its linear form.^{422,423} ED-ROMP is typically initiated by classic metathesis catalysts, such as the G2 catalyst.⁴²⁴ Since these catalysts usually exhibit only low selectivity toward the olefin moieties present,⁴²⁵ different metathesis reactions are competing: ring-opening, ring-closing, and cross metathesis. In order to favor ring-opening, the reactions have to be optimized carefully, e.g. by choosing high monomer and low catalyst concentrations or by increased polymerization temperatures.⁴²⁴ ED-ROMP was recently used in the synthesis of cleavable multiblock copolymers,⁴²⁶ shape memory polymers,⁴²⁷ and metalated poly(pseudorotaxane)s.⁴²⁸

3 Aim

The aim of this thesis is to investigate the ROMP behavior of functionalized norbornenes using Grubbs-type catalysts and reveal the macro- and microscopic properties of the corresponding functional polymers. The resulting polymers are further interesting regarding their highly versatile structure and their wide range of possible applications, e.g. in photonics.⁴²⁹

The thesis is divided into three main topics: in the first chapter of the results and discussion part (**Chapter 4**), the synthesis and polymerizability of bifunctional norbornene-based monomers is investigated focusing on the ROMP kinetics and the thermal properties of the resulting polymers. For the monomer synthesis, *exo* and *endo* norbornenes are functionalized using the well-established P-3CR. The attached functional groups are varied according to the used components in a straightforward fashion, influencing the macroscopic characteristics of the functional polymers obtained *via* subsequent ROMP. Furthermore, the effects of the monomer structure on the polymerization and copolymerization kinetics are examined.

In the second results and discussion chapter (**Chapter 5**), the synthesis of *exo* norbornene-based macromonomers *via* ATRP is investigated, resulting in different polymers carrying a norbornene-moiety and thus capable of undergoing ROMP. The polymerization conditions are optimized to enable controlled ROMP while the resulting architectures are graft polymers. Additionally, the iterative polymerization of macromonomers is investigated through the influence of the catalytic system and focusing on the chain-extension process. Furthermore, the synthesis of bifunctional macromonomers by combining P-3CR, ATRP and CuAAC to connect two different polymer chains to a polymerizable *exo* norbornene moiety is shown. Subsequent ROMP results in Janus graft copolymers obtained in a controlled fashion.

In the third chapter of the results and discussion part (**Chapter 6**), the synthesis of sequence-controlled graft copolymers by the delayed addition of macromonomers during a ROMP process is investigated. The differences of *exo* and *endo* norbornenes in the ROMP kinetics are examined and enable the precise introduction of graft-like repeat units into a growing poly(norbornene) (PNB) chain. Here, the effect of the applied polymerization conditions and the macromonomer structure on the ROMP kinetics, as well as the grafting density (σ) and the architecture of the resulting graft copolymers are examined.

In summary, this thesis stives for the sequence-controlled polymerization of norbornene-based monomers *via* ROMP using Grubbs-type catalysts, resulting in block-like architectures and highly versatile polymeric materials.

4 Functional poly(norbornene)s *via* a combination of ROMP and P-3CR

Parts of this chapter contain results that have already been published:

D. Barther, D. Moatsou, *Macromol. Rapid Commun.* **2021**, *42*, 2100027.

4.1 Abstract

A robust method to synthesize a variety of functionalized polymers is described in this chapter. Furthermore, the influence of the monomer structure on their polymerizability and their respective polymerization kinetics are determined. The monomer structures are varied with special interest on sterically demanding groups, their distance to the polymerizable unit and the used isomers. *Exo* and *endo* norbornene derivatives are used as precursors and further functionalized *via* the Passerini three-component reaction (P-3CR). Therefore, the norbornenes are introduced as carboxylic acid components, whereby aldehyde and isocyanide components are varied utilizing sterically demanding pyrene and adamantane groups or aliphatic propane and pentane side groups. The polymerizations are performed *via* ring-opening metathesis polymerization (ROMP) using the Grubbs first generation (G1) catalyst and monitored by on-line ^1H nuclear magnetic resonance (NMR) spectroscopy to determine kinetic parameters, describing the polymerization processes. Furthermore, the molecular weight distributions of the obtained polymers are determined by size exclusion chromatography (SEC) and the thermal properties are evaluated by differential scanning calorimetry (DSC) and thermogravimetric analysis (TGA).

4.2 Introduction

The synthesis of functional polymers exhibiting precise macro- and microscopic properties is a major task in polymer science, often accomplished either by post-polymerization modification methods or by directly polymerizing the respective functionalized monomer.⁴³⁰⁻⁴³² Depending on the functional groups used, steric effects as well as electronic effects or unfavorable interactions between catalyst and monomer has been shown to hamper controlled polymerization processes.^{433,434} Therefore, robust, versatile, and straightforward synthesis procedures need to be developed. ROMP is used in the polymerization of cyclic molecules exhibiting high ring strain using organometallic complexes as catalysts, e.g.

ruthenium-based Grubbs-type complexes and molybdenum-based Schrock-type complexes.¹⁷ ROMP is widely used due to its well-controlled kinetics and its high tolerance toward functional groups.⁴³⁵ In **chapter 2.3.3** of the theoretical background, more detailed information and mechanistic insights regarding ROMP are given. The synthesis of functional materials *via* ROMP is limited by the used monomers precursor, whereas functionalization of e.g. norbornene derivatives often results in monofunctionalized monomers.⁴³⁶ The synthesis of bifunctional monomers is typically accomplished by complex, multistep synthesis procedures.⁴¹⁰ The resulting multifunctional polymers are interesting, e.g. serving as potent electrolytes in batteries.⁴³⁷

The combination of controlled ROMP and monomer preparation *via* multicomponent reactions (MCRs) has emerged as an alternative method to introduce multiple functionalities along the polymeric backbone, leading to a variety of functional materials. Recently, the U-4CR was used to modify a carboxylic acid–functionalized norbornene, using a variety of different aldehydes. The obtained monomers exhibited dipeptide-like functional groups and were successfully polymerized by ROMP, obtaining, among others, chiral polymeric materials.³¹ Partials derived from chiral polymers are well-known in the recent literature, exhibiting a wide range of applications, e.g. in asymmetric catalysis.⁴³⁸ Another versatile MCR is the P-3CR where an oxo component, such as an aldehyde or a ketone, reacts with a carboxylic acid and an isocyanide forming an α -acyloxy amide,^{177,178} thus bifunctional monomers are accessible in a straightforward one-step process. More detailed information regarding MCRs and the P-3CR are given in **chapters 2.2.2** and **2.2.3** of the theoretical background. The resulting polymers have the ability to form hydrogen bonds, both inter- and intramolecular, making them interesting, e.g. in the field of drug delivery.⁴³⁹

Hence, in this chapter, the synthesis of bifunctional norbornene-based monomers *via* the P-3CR is introduced, as well as their subsequent polymerization using ruthenium-catalyzed ROMP. The polymerization was further monitored by on-line ¹H nuclear magnetic resonance (NMR) spectroscopy, investigating the influence of the monomer structure on the polymerization process. It is noted that the term “on-line ¹H NMR spectroscopy” further implies that the ¹H NMR spectra were measured during the reaction process at predetermined time points. Furthermore, copolymerization processes, applying two different

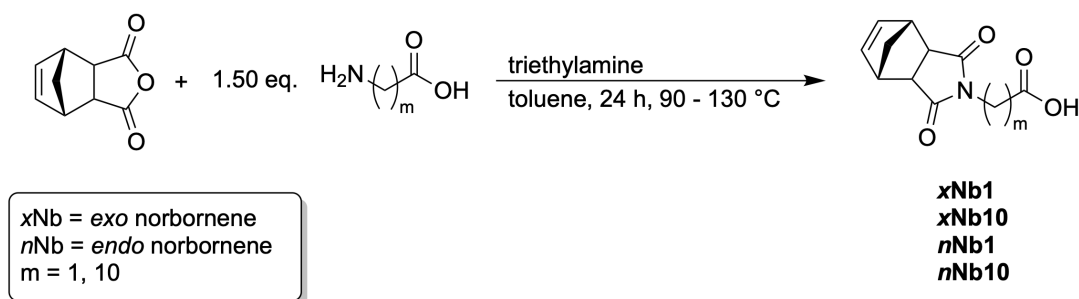
monomers, were examined, resulting in the synthesis of multifunctional copolymers with a statistical or block-like architecture.

4.3 Results and discussion

4.3.1 Synthesis of functionalized norbornenes *via* the P-3CR

In the following section, the synthesis of bifunctional *exo* and *endo* norbornenes is described using the P-3CR. The versatility of the applied method further enables the straightforward exchange of side groups by variation of the used components, particularly aldehydes and isocyanides.

First, the reactants used in the P-3CR were evaluated, aiming at controlled polymerizability and high variability of the attached functional groups. Norbornene derivatives were used as carboxylic acid components, with enantiomerically pure *exo* and *endo* norbornene anhydride (*cis*-5-norbornene-2,3-dicarboxylic anhydride) used as the precursors (**Scheme 4.1**). ROMP kinetics are well-known to be influenced by the stereoisomerism of the norbornene monomer leading to differences in reactivity of more than three orders of magnitude.⁹³

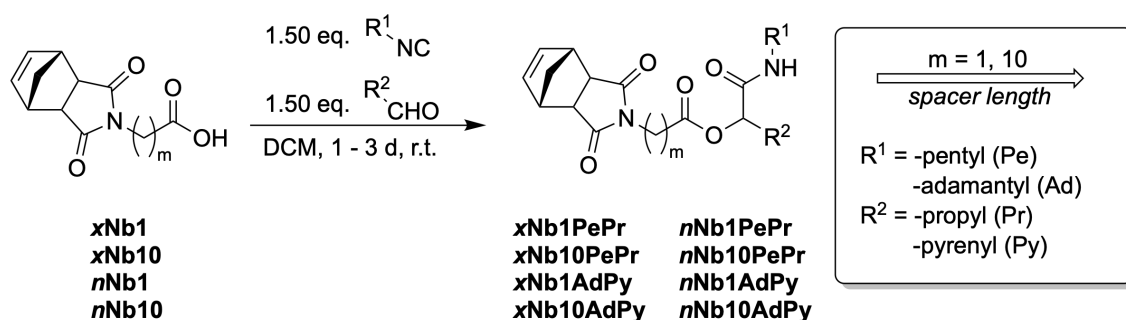


Scheme 4.1. Synthesis of norbornene-functional carboxylic acids **xNb1**, **xNb10**, **nNb1** and **nNb10** *via* condensation of *exo* and *endo* norbornene anhydride with glycine and 11-aminoundecanoic acid.

The respective anhydrides were reacted with an equimolar amount of selected amino acids at elevated temperatures with concomitant release of water, forming the norbornene-functional carboxylic acid components **xNb1**, **xNb10**, **nNb1** and **nNb10**. Here, glycine and 11-aminoundecanoic acid were used to obtain molecules with a short (methylene) and a long alkane linker (decylene) between the polymerizable norbornene and the carboxylic acid group. Reactions involving the *endo* derivative were carried out at 90 °C to reduce

thermal isomerization to the *exo* species,⁴⁴⁰ whereas the *exo* derivative was reacted at 130 °C, leading to higher yields. After purification, the products were obtained as white solids exhibiting yields ranging from 44% to 91%.

As mentioned in the introduction (**Chapter 4.2**), the P-3CR additionally involves an isocyanide and an aldehyde to form the desired α -acyloxy amide, which is further termed as the Passerini unit. In order to evaluate structural effects of the used monomer on the subsequent ROMP, pentyl isocyanide and propionaldehyde were used to obtain sterically less demanding Passerini units, whereas reactions using adamantyl isocyanide and pyrenyl aldehyde led to bulky Passerini units. In all cases, both the *exo* and the *endo* derivatives were prepared to assess the significance of the alkane linker between the polymerizable norbornene and the Passerini units, potentially affecting the ROMP process. The reactions were conducted in dichloromethane (DCM) using literature-known procedures,¹⁸⁰ while applying an excess of isocyanide and aldehyde to compensate for possible decomposition of both (**Scheme 4.2**). The obtained monomers are termed as follows: the *exo* and *endo* norbornene moieties are abbreviated as *xNb* and *nNb*, respectively, the length of the alkane linker between norbornene and Passerini unit is described by the number of carbon atoms (1 for methylene, 10 for decylene), and the attached side groups are indicated as Pe for pentyl, Ad for adamantyl, Pr for propyl, and Py for pyrenyl.

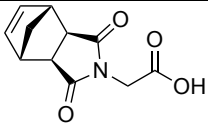
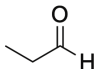
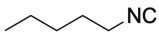
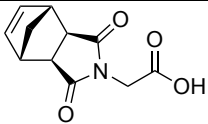
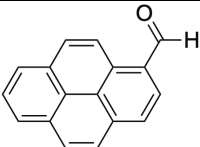
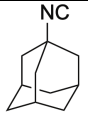
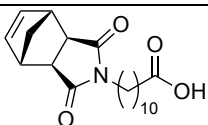
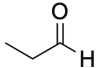
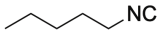
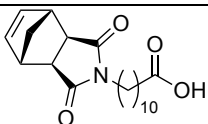
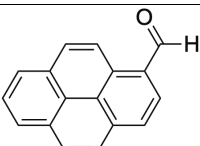
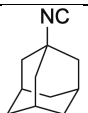
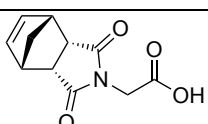
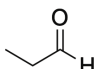
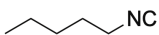
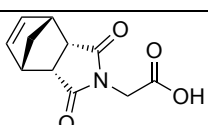
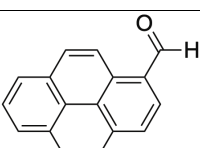
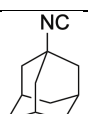
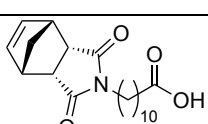
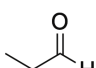
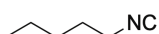
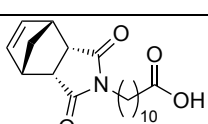
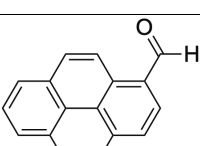
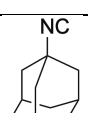


Scheme 4.2. P-3CRs using norbornene-functional carboxylic acids **xNb1**, **xNb10**, **nNb1**, and **nNb10**, pentyl- and adamantyl isocyanide, and propyl- and pyrenyl aldehyde, forming the *exo* norbornene bifunctional monomers **xNb1PePr**, **xNb10PePr**, **xNb1AdPy**, and **xNb10AdPy**, and their *endo* counterparts **nNb1PePr**, **nNb10PePr**, **nNb1AdPy**, and **nNb10AdPy** (**Table 4.1**).

After purification, the products were obtained as white solids and colorless viscous liquids in satisfying yields ranging from 55% to 94%, with the higher yields corresponding to the aliphatic *exo* norbornene monomers (**Table 4.1**).

It is noted that the compounds **xNb10PePr**, **nNb10PePr** and **nNb10AdPy** were synthesized by A. Seliwjorstow under my supervision.

Table 4.1. Bifunctional norbornene-based monomers obtained *via* the P-3CR.

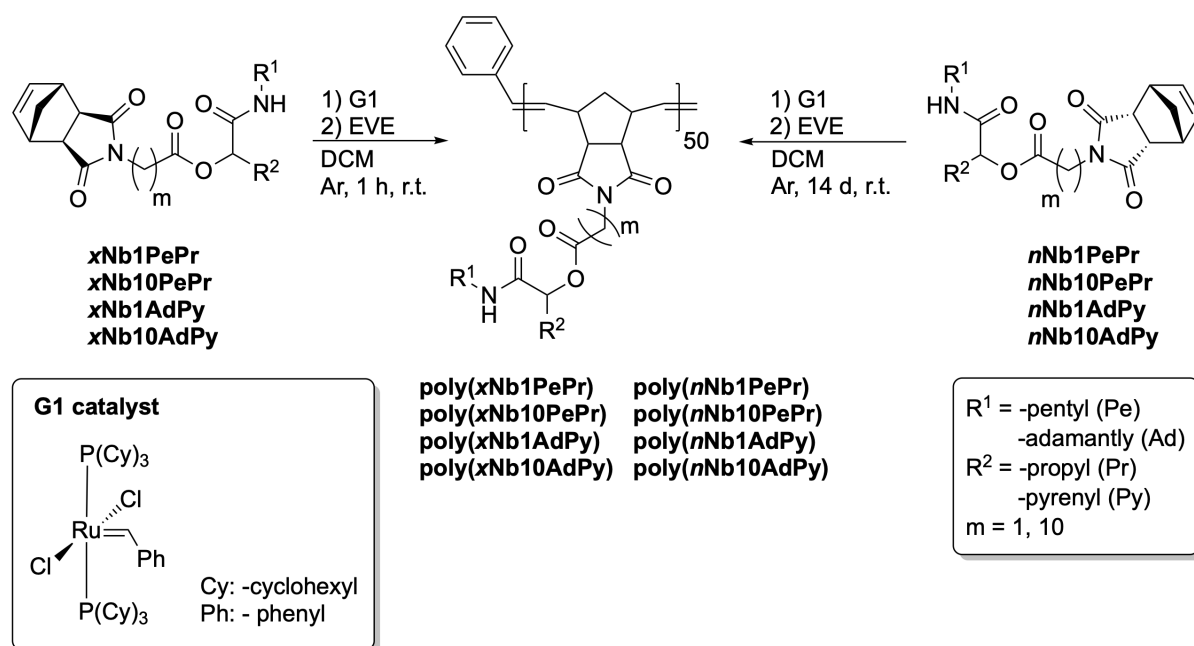
Monomer ^a	Acid	Aldehyde	Isocyanide	Yield [%] ^b
xNb1PePr				94
xNb1AdPy				63
xNb10PePr				92
xNb10AdPy				82
nNb1PePr				91
nNb1AdPy				55
nNb10PePr				71
nNb10AdPy				76

^aReaction conditions: 1.00 eq. acid, 1.50 eq. aldehyde and 1.50 eq. isocyanide in DCM (1 mol/L) were stirred for 48 h at ambient temperature. ^bYield refers to isolated yield after column chromatography.

4.3.2 ROMP of functional norbornenes

In the following section, the ROMP of the bifunctional monomers synthesized in **chapter 4.3.1** is described. The obtained polymers are further examined regarding their thermal properties, such as glass transition temperature (T_g) and decomposition temperature (T_d).

The obtained monomers were polymerized *via* ROMP using the G1 catalyst (**Scheme 4.3**). If not mentioned otherwise, all ROMPs conducted in **chapter 4.3** were performed in argon-flushed ampoules equipped with J Young taps using degassed DCM as solvent and at ambient temperature to minimize catalyst poisoning or side reactions.⁴⁴¹ It is noted that the term “argon-flushed” further implies that the used reaction vessel was thrice dried with a heat gun under high vacuum and flushed with argon while hot. After reaching the desired monomer conversion, the polymerizations were quenched by adding an excess of EVE, forming a metathesis-inactive catalyst derivative and the respective alkene terminated PNB chain.⁴⁴²



Scheme 4.3. ROMP of the *exo* norbornenes **xNb1PePr**, **xNb10PePr**, **xNb1AdPy** and **xNb10AdPy** (left) and the *endo* norbornenes **nNb1PePr**, **nNb10PePr**, **nNb1AdPy** and **nNb10AdPy** (right) using the G1 catalyst (**Table 4.2**).

Here, the monomer to catalyst (M:I) ratio was 50:1. The polymerizations of the *exo* monomers exhibited complete conversion after one hour (**Figure 4.1**), whereas their *endo* counterparts were quenched before reaching complete conversion after 14 days. The *endo*-derived

polymers were additionally purified by precipitation to remove unreacted monomer. Further, it is noted that removal of ruthenium traces by the addition of potassium 2-isocyanoacetate, as described in the recent literature,⁴⁴³ was not carried out as it led to cleavage of the side groups (**Figure S4.38**).

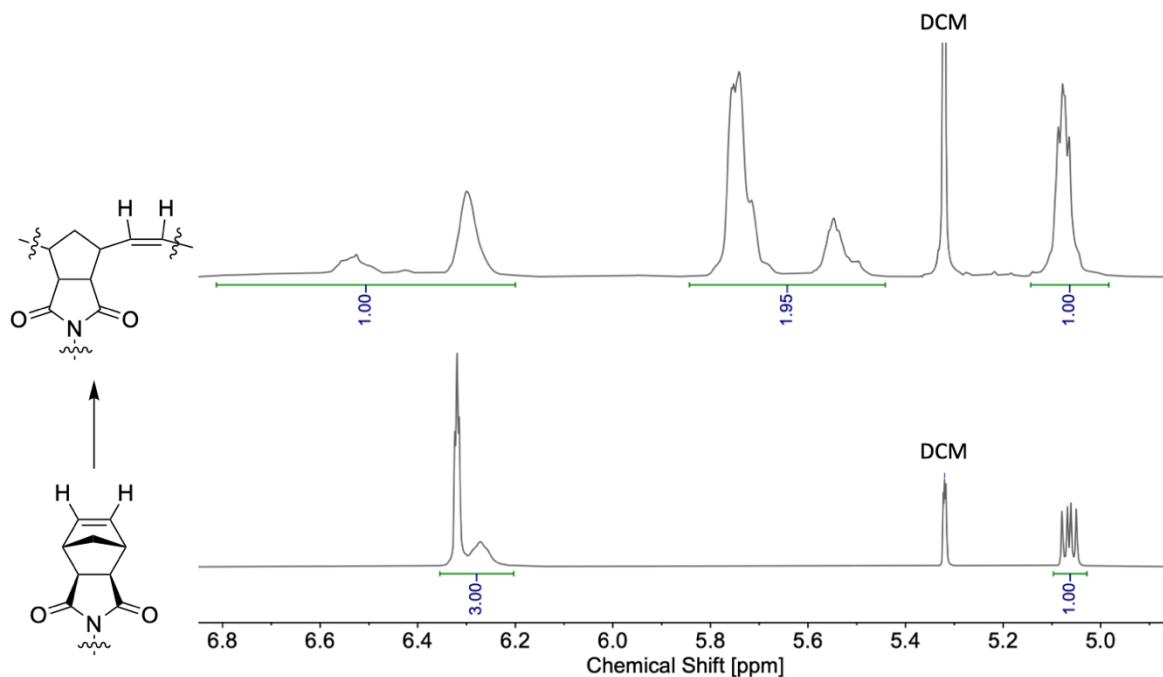


Figure 4.1. Stacked ^1H NMR spectra (section: 6.85 – 4.85 ppm) of the representative ROMP of *exo* monomer **xNb1PePr** (bottom) and the obtained polymer **poly(xNb1PePr)** (top), highlighting the vanishing of the olefinic norbornene signal at 6.32 ppm and the appearing of a broad signal assigned to the protons at the polymeric backbone at 5.8 – 5.4 ppm, with the respective functional groups (left). The tertiary carbon proton of the Passerini unit served as a reference. Measured in DCM-d_2 .

The polymers were obtained as off-white solids and were further analyzed *via* ^1H NMR spectroscopy, observing the vanishing of the olefinic *exo* norbornene signal at 6.32 ppm and appearing of a broad signal at 5.8 – 5.4 ppm assigned to the olefinic protons at the polymeric backbone. This behavior was observed for all *exo* monomers, hence, the representative ROMP of **xNb1PePr** is further described. The signal at 6.28 ppm, overlapping with the olefinic signal of the norbornene, was assigned to the amide proton of the Passerini unit. The respective signal in the ^1H NMR spectrum of the obtained polymer was found as a broad signal at 6.8 – 6.2 ppm. The tertiary carbon proton of the Passerini unit at 5.17 ppm served as a reference.

The ^1H NMR spectra of the *endo* monomers and the obtained polymers were similar compared to their *exo* counterparts (**Figure 4.2**).

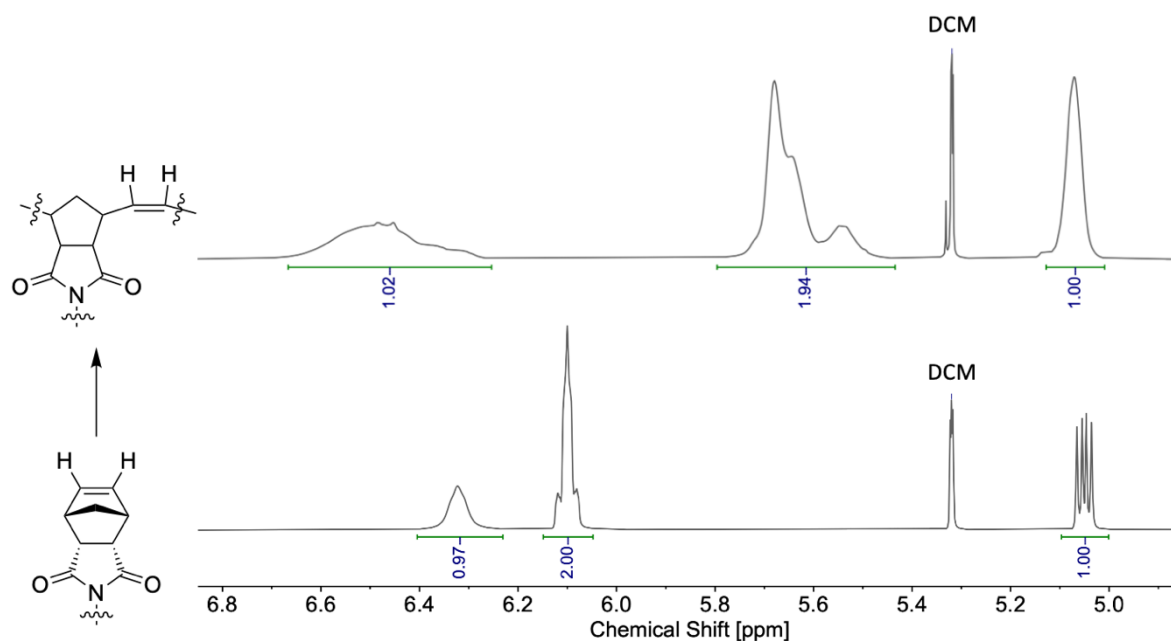


Figure 4.2. Stacked ^1H NMR spectra (section: 6.85 – 4.85 ppm) of the representative ROMP of *endo* monomer ***nNb1PePr*** (bottom) and the obtained polymer **poly(*nNb1PePr*)** (top), highlighting the vanishing of the olefinic norbornene signal at 6.1 ppm and the appearing of a broad signal assigned to the protons at the polymeric backbone at 5.8 – 5.4 ppm, with the respective functional groups (left). The tertiary carbon proton of the Passerini unit served as a reference. Measured in deuterated DCM- d_2 .

Here, vanishing of the olefinic *endo* norbornene signal at 6.1 ppm and appearing of a broad signal at 5.8 – 5.4 ppm assigned to the protons at the polymeric backbone was determined. This behavior was observed for all *endo* monomers, hence, the representative ROMP of ***nNb1PePr*** is further described. The signal at 6.31 ppm was assigned to the amide proton of the Passerini unit, whereas the respective signal in the ^1H NMR spectrum of the obtained polymer was found as a broad signal at 6.66 – 6.25 ppm. The tertiary carbon proton of the Passerini unit at 5.05 ppm served as a reference.

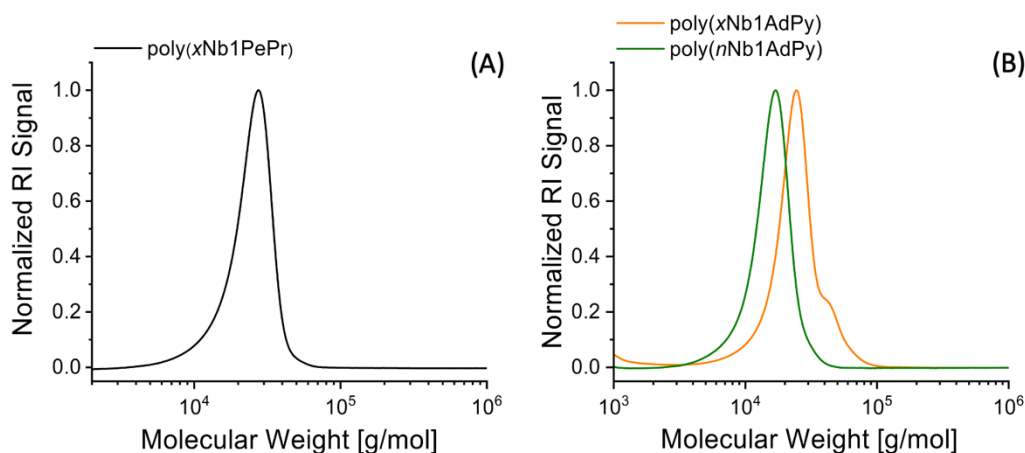
The obtained polymers were further characterized by size exclusion chromatography (SEC) to determine their molecular weight characteristics while their thermal properties were assessed by differential scanning calorimetry (DSC) and thermogravimetric analysis (TGA) (**Table 4.2**).

Table 4.2. Homopolymers synthesized *via* the G1-mediated ROMP of bifunctional *exo* and *endo* norbornene-based monomers.

Polymer ^a	Conversion [%] ^b	$M_{n,calc}$ [g/mol] ^c	M_n [g/mol] ^d	\mathcal{D}_M^d	T_g [°C] ^e	T_d [°C] ^f
poly(<i>x</i> Nb1PePr)	≥99	18,900	23,000	1.10	83	319
poly(<i>x</i> Nb1AdPy)	≥99	30,700	22,400	1.17	-	310
poly(<i>x</i> Nb10PePr)	≥99	25,200	32,000	1.07	-2	347
poly(<i>x</i> Nb10AdPy)	≥99	37,000	28,800	1.09	92	305
poly(<i>n</i> Nb1PePr)	74	13,900	18,700	1.06	99	328
poly(<i>n</i> Nb1AdPy)	67	20,500	15,400	1.11	-	323
poly(<i>n</i> Nb10PePr)	63	15,800	22,100	1.06	1	349
poly(<i>n</i> Nb10AdPy)	64	23,600	20,300	1.08	114	306

^aReaction conditions: Monomer (0.1 mol/L) and G1 catalyst (M:I ratio = 50:1) in degassed DCM for 1 h (*exo*) or 14 d (*endo*) at ambient temperature. ^bDetermined by ¹H NMR spectroscopy. ^cCalculated by conversion. ^dDetermined by SEC. ^eOnset, determined by DSC. ^fTemperature at 10% weight loss, determined by TGA.

The SEC traces exhibited narrow molecular weight distributions with relatively low dispersity values ($\mathcal{D}_M = M_w/M_n = \leq 1.17$), whereas M_w describes the mass-average molecular weight and M_n the number-average molecular weight of the corresponding polymer.²³⁸ Hence, indicating good polymerization control using this procedure (**Figure 4.3A**).

**Figure 4.3.** Representative SEC traces of (A) **poly(*x*Nb1PePr)** and (B) **poly(*x*Nb1AdPy)** and its *endo*-derived analogue **poly(*n*Nb1AdPy)**.

However, the SEC trace of **poly(xNb1AdPy)** exhibited a high molecular weight shoulder, not being present in the corresponding *endo* norbornene-derived polymer **poly(nNb1AdPy)** (Figure 4.3B). It was hypothesized that the bimodal molecular weight distribution of **poly(xNb1AdPy)** was caused by the increased steric hindrance at the propagating chain end at high monomer conversion. However, **poly(nNb1AdPy)** was quenched after reaching 67% conversion and exhibited an M_n of 15,400 g/mol with a relatively narrow molecular weight distribution, whereas its *exo* norbornene-derived counterpart exhibited an M_n of 22,400 g/mol after reaching complete conversion (Figure 4.3B). Furthermore, **poly(xNb10AdPy)**, comprising a longer alkane linker unit, exhibited a monomodal distribution even at a high monomer conversion, supporting the previous hypothesis and indicating a significant reduction of the steric hindrance at the propagating chain end and thus being beneficial regarding polymerization control. Nonetheless, as the overall dispersity of **poly(xNb1AdPy)** was rather low ($\mathcal{D}_M = 1.17$), no further investigation to improve the ROMP was conducted. The molecular weights determined by SEC differed from the expected (Table 4.2), which was attributed to the SEC calibration standards used, namely poly(methyl methacrylate)s (PMMA)s, and their different hydrodynamic radii (R_h) compared to the herein synthesized polymers. It is noted that consistently higher M_n s were obtained for the alkyl-functional polymers **poly(xNb1PePr)**, **poly(xNb10PePr)**, **poly(nNb1PePr)** and **poly(nNb10PePr)**, in contrast to the consistently lower M_n s obtained for the polymers with bulky side groups **poly(xNb1AdPy)**, **poly(xNb10AdPy)**, **poly(nNb1AdPy)** and **poly(nNb10AdPy)** (Table 4.2).

The thermal properties of the obtained polymers were determined by DSC and TGA, respectively (Figure 4.4). The T_g s were determined by the onset temperature regarding the change in thermal capacity attributed to the transition from glassy to viscous liquid and were found, as expected, to vary according to the functional groups attached to the polymeric backbone.⁴⁴⁴ It is noted that all herein measured T_g values were determined by the onset temperature of the thermal transition in the second heating cycle, applying a heating rate of 20 °C/min.

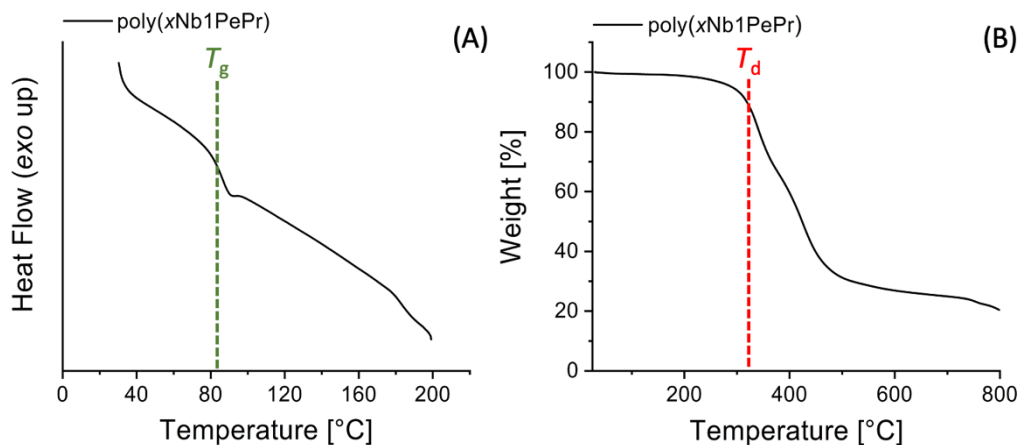


Figure 4.4. Representative thermal analysis of **poly(xNb1PePr)**, (A) DSC trace (green dotted line represents the T_g) and (B) TGA trace (red dotted line represents the T_d).

Poly(xNb1PePr) and **poly(xNb10PePr)**, bearing aliphatic side groups, exhibited lower T_g s compared to the pyrenyl- and adamantyl-functional polymers **poly(xNb1AdPy)** and **poly(xNb10AdPy)** by at least 94 °C. This observation is consistent with observations in recent literature, where adamantyl moieties lead to an increase in the T_g of the corresponding polymer.⁴⁴⁵ Furthermore, differences in the T_g s depending on the length of the alkane linker were observed. **Poly(xNb10PePr)** and **poly(xNb10AdPy)**, comprising the long alkane linker units, exhibited lower T_g s compared to **poly(xNb1PePr)** and **poly(xNb1AdPy)**, comprising the short linker units. The same trends were observed in the *endo*-derived polymers, whereby the T_g s were found to be up to 22 °C higher than their *exo*-derived analogues. It is further noted that for **poly(xNb1AdPy)** and **poly(nNb1AdPy)**, comprising the short alkane linker units and the bulky side groups, no T_g s were observed in the examined temperature range.

In order to showcase the versatility in thermal properties by simple combination of different monomers, the statistical copolymer **poly(xNb10PePr-*stat*-xNb10AdPy)** was prepared by reacting equimolar amounts of **xNb10PePr** and **xNb10AdPy** in a ROMP using the G1 catalyst (**Figure 4.5**).

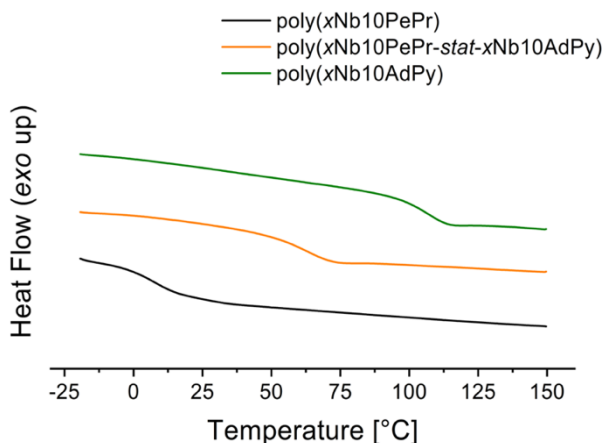


Figure 4.5. Stacked DSC traces of the homopolymers **poly(xNb10PePr)** and **poly(xNb10AdPy)**, and the statistical copolymer **poly(xNb10PePr-stat-xNb10AdPy)**.

Indeed, the resulting T_g was found to be at 55 °C between those of the corresponding homopolymers **poly(xNb10PePr)** ($T_g = -1$ °C) and **poly(xNb10AdPy)** ($T_g = 99$ °C). The Fox equation provides a model to predict T_{gs} of miscible polymer blends and statistical copolymers by using **equation 5.1**, whereby w_1 and w_2 are the weight fractions of the components and $T_{g,1}$ and $T_{g,2}$ the glass transition temperatures of the pure components.⁴⁴⁶

$$\frac{1}{T_g} = \frac{w_1}{T_{g,1}} + \frac{w_2}{T_{g,2}} \quad (4.1)$$

Here, the $T_{g,1}$ and $T_{g,2}$ values were obtained from the DSC of the corresponding homopolymers (**Table 4.2**) while w_1 and w_2 were calculated as $w_i = M_i * n_i$ with M_i corresponding to the molecular weight of the repeat unit i (namely **xNb10PePr** and **xNb10AdPy**) and the number of repeat units, n_i , derived from the ^1H NMR measurements. Using this prediction, the T_g of **poly(xNb10PePr-stat-xNb10AdPy)** was expected at *ca.* 52 °C which was found to be relatively consistent with the measured value determined by DSC.

The T_d s were determined at 10% weight loss of the material (**Figure 4.4B**). In all cases, the T_d was above 300 °C with the decomposition occurring in multiple steps attributed to the different thermal stability of the PNB backbone and the attached Passerini units (**Table 4.2**).^{447,448} It is noted that the data obtained from the thermal analysis is presented in the experimental section in **chapter 8.3.1**.

4.3.3 Kinetic studies

Since the polymerizability of the bifunctional norbornene-based monomers was evaluated in **chapter 4.3.2**, the following section exhibits more detailed insights into their ROMP behavior, assessing and comparing the obtained kinetic data of the bifunctional monomers.

The kinetic measurements were conducted using on-line ^1H NMR spectroscopy. It is noted that the herein presented kinetic measurements were conducted in degassed deuterated DCM (DCM- d_2) and in argon-flushed NMR tubes equipped with J Young taps, applying the same conditions as described in **chapter 4.3.1**. The conversion at different time intervals was used to calculate apparent propagation rate constants (k_{app}) and monomer half-lives ($t_{1/2}$), where $t_{1/2}$ is further defined as the time until the monomer reaches a conversion of 50%.⁴⁴⁹ The k_{app} s were determined from the slope of the best linear fit of the $\ln([M]_0/[M])$ versus time data, where $[M]_0$ represents the initial monomer concentration and $[M]$ represents the monomer concentration after a specific time interval (**Table 4.3**).

Table 4.3. Summary of kinetic analyses of the homopolymerizations and the copolymerizations of the bifunctional monomers.

Entry ^a	Monomer	Conversion [%] ^b	Reaction Time [h]	k_{app} [s ⁻¹] ^c	$t_{1/2}$ [h] ^d
4.1	<i>x</i> Nb1PePr	≥99	0.37	3.94×10^{-3}	0.049
4.2	<i>x</i> Nb1AdPy	≥99	0.38	3.46×10^{-3}	0.056
4.3	<i>x</i> Nb10PePr	≥99	0.28	4.56×10^{-3}	0.042
4.4	<i>x</i> Nb10AdPy	≥99	0.27	5.42×10^{-3}	0.036
4.5	<i>n</i> Nb1PePr	83	335	1.45×10^{-6}	133
4.6	<i>n</i> Nb1AdPy	75	335	1.05×10^{-6}	183
4.7	<i>n</i> Nb10PePr	78	340	1.23×10^{-6}	156
4.8	<i>n</i> Nb10AdPy	74	340	1.05×10^{-6}	183
4.9 ^e	<i>x</i> Nb10PePr	≥99	0.37	4.39×10^{-3}	0.044
4.10	<i>x</i> Nb10PePr <i>x</i> Nb10AdPy	≥99	0.27	5.57×10^{-3}	0.034
4.11	<i>n</i> Nb1PePr <i>n</i> Nb1AdPy	83 79	334	1.47×10^{-6} 1.19×10^{-6}	131 162
4.12	<i>x</i> Nb1PePr <i>n</i> Nb10AdPy	≥99 74	336	- -	- -
4.13 ^f	<i>n</i> Nb10PePr <i>x</i> Nb10AdPy	84 ≥99	330	2.32×10^{-6} -	83 -

^aReaction conditions: Monomer (0.1 mol/L) and G1 catalyst (M:I = 50:1) in DCM-*d*₂ at ambient temperature under argon atmosphere. ^bDetermined by ¹H NMR spectroscopy before quenching with EVE. ^cCalculated from conversion using first order kinetics. ^dCalculated from the linear regression fits using $t_{1/2} = \ln(2)/k_{app}$. ^eThe monomer to G1 ratio was 200:1. ^f k_{app} and $t_{1/2}$ values were determined before addition of the *exo* monomer.

Both norbornene isomers, *exo* and *endo*, exhibited pseudo first order kinetic behavior, hence first order kinetics were applied for analyses (**Figure 4.6**).³⁷⁷

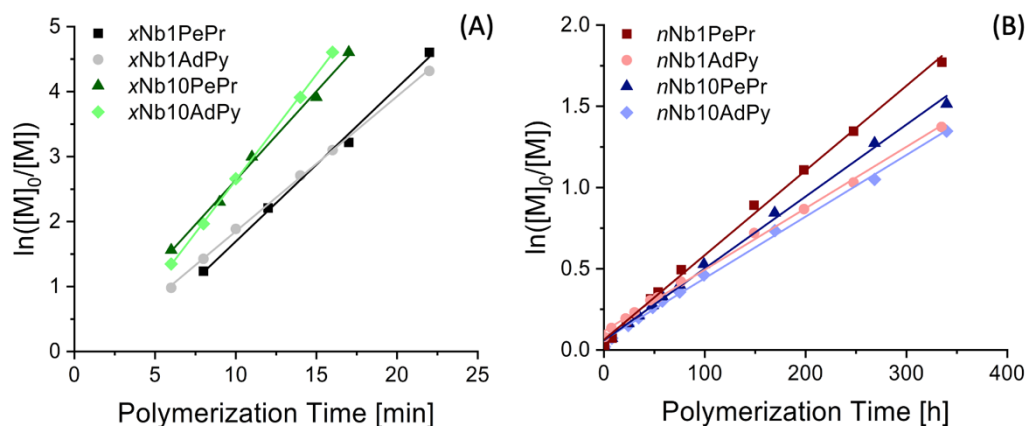


Figure 4.6. Kinetic plots of the (A) homopolymerizations of the *exo* monomers **xNb1PePr**, **xNb10PePr**, **xNb1AdPy** and **xNb10AdPy**, and (B) homopolymerizations of the *endo* monomers **nNb1PePr**, **nNb10PePr**, **nNb1AdPy** and **nNb10AdPy**, based on ^1H NMR spectroscopy data (Figures S4.55 and S4.62, Table 4.3). Lines represent linear fits.

Minor trends regarding the effect of the steric hindrance of the side group and spacer length were observed: the k_{app} s of the *exo* monomers showed an increase with an increasing spacer length, while the size of the functional groups was not found to affect the kinetics. In contrast, when *endo* monomers were employed, higher k_{app} s were obtained for **nNb1PePr** attributed to the less bulky alkyl functional groups, and for **nNb10PePr** attributed to the longer spacer. In order to determine potential high molecular weight limitations, a ROMP was performed applying a 200-fold excess of the *exo* monomer **xNb1PePr**, with respect to the G1 catalyst (Figure 4.7).

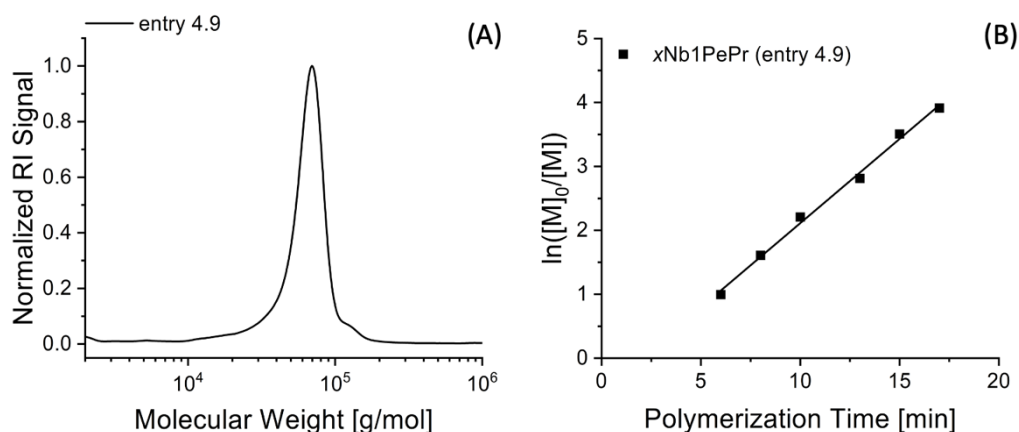


Figure 4.7. (A) SEC trace of the homopolymer obtained from entry 4.9 (Table 4.3) and (B) corresponding kinetic plot, based on ^1H NMR spectroscopy data (Figure S4.63). Line represents linear fit.

Characterization by SEC indicated a relatively narrow molecular weight distribution ($M_n = 55,600$ g/mol; $D_M = 1.16$; **Figure 4.7A**), whereas a small high molecular weight shoulder was observed. Furthermore, pseudo first order kinetic behavior was detected and the calculated k_{app} was found to be $4.36 \times 10^{-3} \text{ s}^{-1}$ (**Figure 4.7B**), comparable to that of **poly(xNb1PePr)**, and thus indicating that higher molecular weights are attainable with comparable polymerization kinetics (**Table 4.3**).

In order to evaluate the influence of the structural characteristics of the monomer on their copolymerizability, kinetic measurements employing two different monomers were conducted using on-line ^1H NMR spectroscopy. The comonomer ratio was 1:1 with a targeted total DP of 50 (**Figure 4.8**). The copolymers obtained from entries 4.11 – 4.13 (**Table 4.3**) were additionally purified by precipitation to remove unreacted *endo* monomer. The copolymers were obtained as brown and off-white solids.

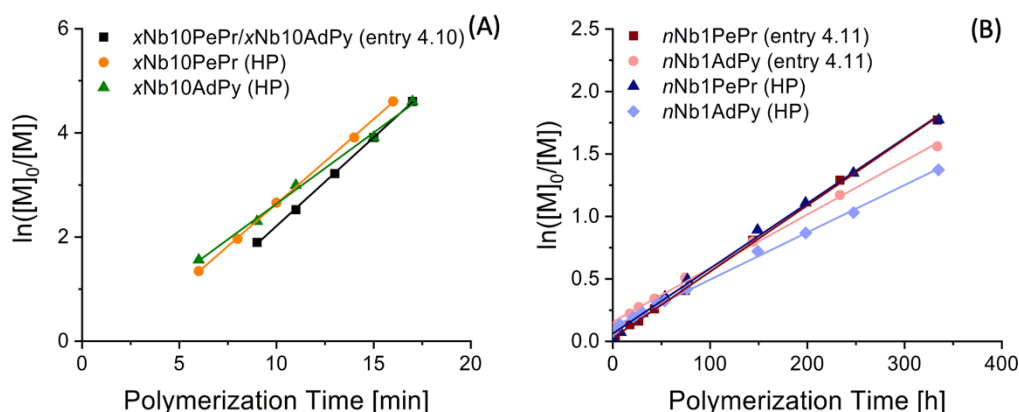


Figure 4.8. (A) Kinetic plots of the copolymerization (entry 4.10, **Table 4.3**) of **xNb10PePr** and **xNb10AdPy** and homopolymerizations (HP) of the respective monomers, and the (B) copolymerization (entry 4.11, **Table 4.3**) of **nNb1PePr** and **nNb1AdPy** and homopolymerizations of the respective monomers, based on ^1H NMR spectroscopy data (**Figures S4.64 and S4.67**). Lines represent linear fits.

The copolymerization (entry 4.10, **Table 4.3**) of the *exo* monomers **xNb10PePr** and **xNb10AdPy** resulted in a similar overall k_{app} compared to the corresponding homopolymerizations (**Figure 4.8A**), indicating that the bulky side groups of **xNb10AdPy** had no decelerating effect on the copolymerization process. Furthermore, the copolymerization (entry 4.11, **Table 4.3**) of the *endo* monomers **nNb1PePr** and **nNb1AdPy** resulted in an increase of the k_{app} s of **nNb1AdPy** compared to its corresponding homopolymerization, whereas the kinetics of **nNb1PePr** remained unchanged (**Figure 4.8B**). In both cases, the

copolymerization of monomers with the same stereoisomerism proceeded with kinetics comparable to the respective homopolymerizations, regardless of the linker length or the bulkiness of the functional groups.

Subsequently, the copolymerization (entry 4.12, **Table 4.3**) of *endo* and *exo* norbornenes was investigated (**Figure 4.9**).

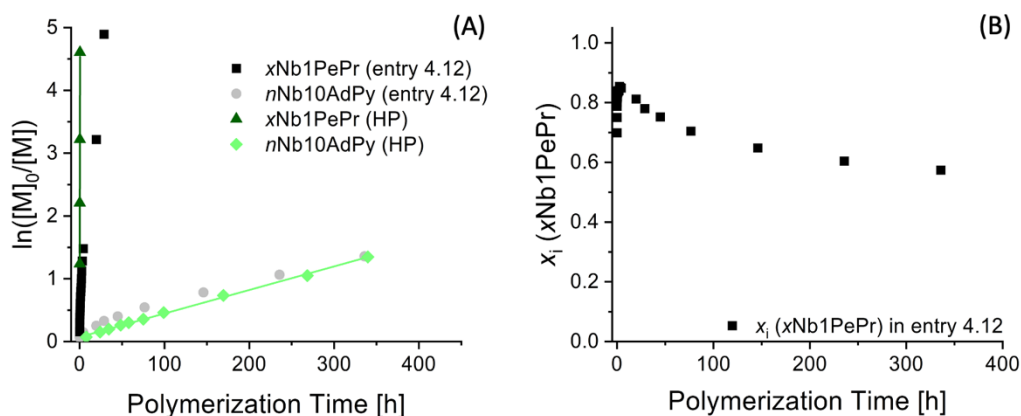


Figure 4.9. (A) Kinetic plot of the copolymerization (entry 4.12, **Table 4.3**) of $xNb1PePr$ and $nNb10AdPy$ and homopolymerizations (HP) of the respective monomers, and (B) molar fraction (x_i) of $xNb1PePr$ in the respective copolymer as a function of polymerization time, based on 1H NMR spectroscopy data (**Figure S4.70**). Lines represent linear fits.

The copolymer (entry 4.12, **Table 4.3**) was synthesized using an equimolar mixture of the alkyl-functional *exo* monomer $xNb1PePr$ and the pyrenyl-adamantyl-functional *endo* monomer $nNb10AdPy$. As previously observed,⁹³ such a combination slows down the polymerization of the fast monomer and accelerates that of the slow monomer. Therefore, the pseudo first order kinetics are skewed (**Figure 4.9A**). With $xNb1PePr$ still present in the reaction mixture, the consumption of $nNb10AdPy$ was accelerated compared to its homopolymerization by its sixfold. As an example, the former reached 14% monomer conversion after *ca.* four hours, wherefore the latter required a reaction time of 24 hours. Since the kinetics of both monomers are defined by the current *exo:endo* ratio which decreases during the copolymerization process, the consumption of $nNb10AdPy$ decelerated with increasing *exo* monomer conversion while reaching a minimum after complete conversion of $xNb1PePr$. Owing to the fast consumption of the *exo* monomer compared to the polymerization of the *endo* monomer, a diblock-like copolymer was obtained.⁸⁸ It is noted that both blocks are diluted by the building block of the other block, as evidenced by

determining the copolymer composition at different time points through the conversions (**Figure 4.9B**). The first data point (at *ca.* six min) showed that 6% of the *endo* monomer and 14% of the *exo* monomer had polymerized, corresponding to a copolymer with a relative composition of 0.7 for **xNb1PePr**. Over the subsequent two hours, this value gradually increased as the *exo* monomer was rapidly consumed and reached a maximum value of 0.85. At this point, **xNb1PePr** had not been fully consumed (conversion 72%) and **nNb10AdPy** had reached a conversion of 13%, thus confirming the **nNb10AdPy** “diluted” **xNb1PePr** block composition. Over the next days, both monomers were slowly consumed with the *exo* monomer reaching $\geq 99\%$ conversion after 45 hours and the *endo* monomer reaching 74% conversion after 336 hours. Therefore, the second block was deemed to be a **nNb10AdPy** block “diluted” by **xNb1PePr**.

In order to obtain a triblock-like polymer architecture, the fast-propagating *exo* monomer **xNb10PePr** was added to a homopolymerization of the slow *endo* monomer **nNb10AdPy** after reaching a predetermined *endo* monomer conversion. According to recent literature, the large differences in k_{app} values lead to the incorporation of a distinct *exo*-block after addition, whereas the *endo* polymerization continues after complete consumption of the *exo* monomer.^{88,93} The initial homopolymerization of **nNb10AdPy** was performed in an argon-flushed ampoule equipped with a J Young tap with a targeted M:I ratio of 25:1, using degassed DCM- d_2 as solvent and the G1 catalyst. Subsequently, **xNb10PePr** was added to an argon-flushed NMR tube equipped with a J Young tap and pre-dissolved in a small amount of solvent to ensure homogeneous mixing after addition of the homopolymerization solution. The targeted comonomer ratio was 1:1. The copolymerization was initiated after reaching an *endo* monomer conversion of 63% and adding the homopolymerization mixture to the NMR tube (**Figure 4.10**).

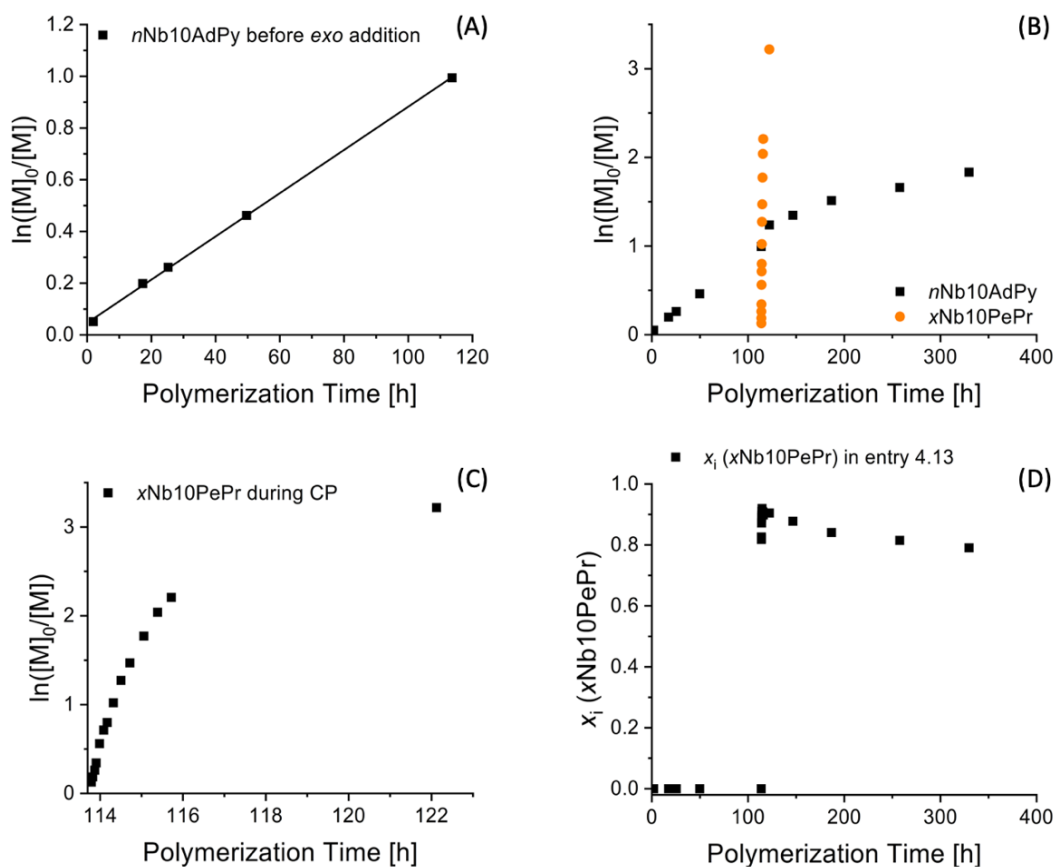


Figure 4.10. (A) Kinetic plots of the polymerization of *nNb10AdPy* before addition of *xNb10PePr*, (B) copolymerization (entry 4.13, Table 4.3) of *nNb10AdPy* and *xNb10PePr*, (C) copolymerization kinetics of *xNb10PePr*, and (D) molar fraction (x_i) of *xNb10PePr* in the respective copolymer as a function of polymerization time, based on ^1H NMR spectroscopy data (Figure S4.73). Line represents linear fit.

The polymerization kinetics of the *endo* monomer exhibited a pseudo first order kinetic behavior before the addition of the fast-propagating *exo* monomer (Figure 4.10A). The addition led to a temporarily acceleration of *nNb10AdPy*, whereas its conversion increased by 8% during a copolymerization time of less than nine hours. Furthermore, during the copolymerization process the kinetics of each monomer was skewed, not following pseudo first order kinetic behavior (Figure 4.10B, similar to entry 4.12, Table 4.3), whereby *xNb10PePr* was completely consumed in *ca.* eight hours (Figure 4.10C). As expected, the copolymerization process had a decelerating effect on the *exo* monomer compared to the corresponding homopolymerization (Table 4.3). The first data point (at *ca.* seven min) corresponded to an *exo* monomer conversion of 12%, whereas during the same period the *endo* monomer showed 3% conversion, leading to a relative composition of 0.82 for *xNb10PePr* within the *exo*-block. Over the subsequent nine hours, this value increased as the

exo monomer was rapidly consumed and reached a maximum value of 0.92 (**Figure 4.10D**). At this point, *xNb10PePr* had not been fully consumed (conversion 72%) and *nNb10AdPy* had reached a conversion of 68%, thus confirming the successful incorporation of a distinct *exo*-block. After complete conversion of the *exo* monomer, the *endo* monomer continued polymerizing until the polymerization was quenched after *ca.* 330 hours (84% conversion of *nNb10AdPy*). Hence, the copolymer was obtained with a triblock-like architecture, exhibiting “diluted” blocks to a certain extent.

SEC measurements were further conducted, to assess the influence of the different copolymerization processes (entries 4.10 – 4.13, **Table 4.3**) on the polymerization (**Figure 4.11**).

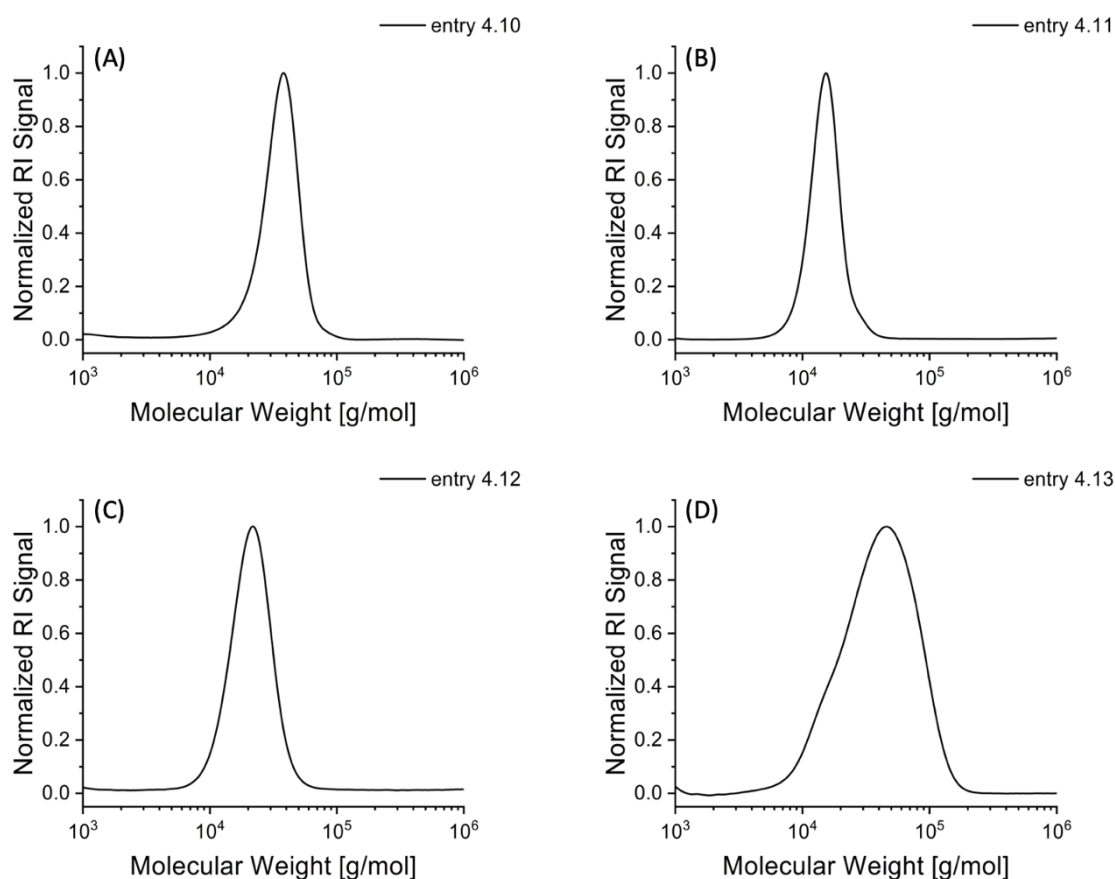


Figure 4.11. SEC traces of (A) *exo/exo*-derived copolymer of entry 4.10, (B) *endo/endo*-derived copolymer of entry 4.11, (C) *exo/endo*-derived diblock-like copolymer of entry 4.12, and (D) *endo/exo*-derived triblock-like copolymer of entry 4.13 (**Table 4.3**).

Narrow molecular weight distributions were found for both statistical copolymers (entry 4.10: $M_n = 28,300$ g/mol; $D_M = 1.08$ and entry 4.11: $M_n = 14,300$ g/mol; $D_M = 1.09$), as well as for the diblock-like copolymer (entry 4.12: $M_n = 19,400$ g/mol; $D_M = 1.14$). In contrast, the

triblock-like copolymer (entry 4.13: $M_n = 31,500$ g/mol; $D_M = 1.45$) exhibited a broader molecular weight distribution and a low molecular weight shoulder. It was hypothesized that the poor control was caused by the steric limitations at the propagating chain end during the initiation of the copolymerization process leading to an irregular incorporation of the added *exo* monomer and possible catalyst poisoning. However, this hypothesis is further discussed and examined in **chapter 5.3.4**.

As a result, the homopolymerization kinetics were found to be well-controlled, exhibiting pseudo first order kinetics, and resulting in polymers with narrow molecular weight distributions. The copolymerizability of the synthesized monomers exhibited a similar behavior as the corresponding homopolymerizations when the same norbornene isomers were polymerized in a statistical fashion. Furthermore, copolymer with block-like structures were synthesized by mixing equal amounts of *exo* and *endo* monomers.

4.4 Conclusion

In this chapter it was shown that the P-3CR was successfully used to synthesize a variety of norbornene-based bifunctional monomers capable of polymerizing *via* ROMP using the G1 catalyst. The structure of the respective monomers was varied in a straightforward fashion by targeted selection of the used components, namely carboxylic acid, aldehyde, and isocyanide. Here, four *exo* and four *endo* norbornene-based bifunctional monomers were obtained in satisfying yields ranging from 55% to 94% in a straightforward fashion. Furthermore, functional PNBs were obtained and analyzed with special interest on their thermal properties. A wide range of T_g s was determined, whereby the values were influenced by the incorporated alkane linkers and the attached side groups. The polymers exhibited similar T_g s regardless of the respective monomer structure. Deeper investigation of the polymerization kinetics found that the polymerization process was well-controlled, exhibiting pseudo first order kinetics, and resulting in homopolymers with narrow molecular weight distributions. The copolymerizability of the synthesized monomers was further examined by synthesizing two statistical copolymers, using either two *exo* or two *endo* monomers, exhibiting similar behavior as the corresponding homopolymerizations. Furthermore, two copolymers exhibiting diblock- and triblock-like structures were synthesized by mixing equal amounts of *exo* and *endo* monomers. The pseudo first order kinetics were found to be skewed

in both experiments due to the copolymerization process, leading to block-like *exo* monomer-derived segments with a gradient substructure. However, the herein presented method exhibits a straightforward procedure to synthesize highly diverse and multifunctional polymers in a sequence-controlled fashion.

Future work on this topic will focus on the mimicking of proteins or enzymes by copolymerizing P-3CR-derived monomers and macromonomers in a sequence-controlled fashion, in order to fulfill functions in cellular environments or catalyze the conversion of biomolecules.⁴⁵⁰

5 Sequence-controlled graft copolymers *via* ROMP of macromonomers

5.1 Abstract

In this chapter, different ring-opening metathesis polymerization (ROMP)-based synthesis procedures are investigated to obtain graft polymers. Especially norbornene-based macromonomers, herein synthesized *via* atom transfer radical polymerization (ATRP), are examined in terms of homo- and copolymerizability using ruthenium-catalyzed ROMP. Here, poly(benzyl methacrylate) (PBnMA), poly(methyl methacrylate) (PMMA) and poly(styrene) (PS) are mainly used as macromonomers. Furthermore, the influence of the macromonomer structure on the subsequent ROMP is examined focusing on the used norbornene precursor, the length of the alkane linker between the polymerizable norbornene unit and the polymer chain, the molecular weight, and the applied synthesis procedure. Therefore, homo- and copolymerization kinetics are determined by on-line ^1H nuclear magnetic resonance (NMR) spectroscopy, whereas size exclusion chromatography (SEC) measurements are conducted to determine beneficial and unfavorable influences of the applied ROMP procedure on the polymerization control and the molecular weight distribution. Additionally, the synthesis of sequence-controlled graft copolymers by adding different macromonomers in an iterative manner is examined and further discussed, as well as the introduction of a novel strategy to synthesize graft copolymers from bifunctional macromonomers derived from the Passerini three-component reaction (P-3CR).

5.2 Introduction

Controlling the monomer sequence in synthetic polymers and thus moving one step toward functional and highly complex structures,⁴⁵¹ as observed in various compounds found in nature,^{452,453} is identified to be a major task in polymer sciences. As such, polymers consisting of different monomer species that are arranged in a predetermined order are denoted as sequence-controlled polymers and are typically characterized by good polymerization control, resulting in low dispersity values (<1.50). In contrast, sequence-defined polymers are uniform and exhibit dispersity values of 1.00.⁴⁵⁴ Providing a wide range of possible applications, sequence-controlled polymers are, for example, used as drug formulation additives or photonic materials.^{455,456} A variety of established polymerization techniques is

used to synthesize sequence-controlled polymers, e.g. reversible-deactivation radical polymerization methods or ROMP.^{457,458} In **chapter 2.3** of the theoretical background, more detailed information and mechanistic insights regarding different polymerization techniques are given. As mentioned in the introduction of **chapter 4**, ROMP is a versatile polymerization technique, exhibiting a “living” character and a high tolerance toward functional groups.⁴³⁵ Furthermore, extensive research on the synthesis of macromonomers capable of undergoing ROMP has been conducted.⁴⁵⁹ Norbornene derivatives are well-known as polymerizable initiators used in RAFT polymerization,⁴⁶⁰⁻⁴⁶² ring-opening polymerization (ROP),⁴⁶³⁻⁴⁶⁵ and ATRP,^{460,465-467} due to their commercial availability and stability during ROMP. Furthermore, bifunctional macromonomers have been developed e.g. by combining ROP and ATRP to generate graft copolymers in a single step.^{410,465,468} However, the preparation of macromonomers is not limited to norbornene as a polymerizable unit. As an example, cyclobutene- and cyclopentene-based macromonomers were synthesized in an analog fashion, followed by controlled polymerization *via* ROMP.^{407,469-471} Even though the literature offers various examples,^{93,464,472} the precise synthesis of sequence-controlled polymers *via* ROMP and the targeted incorporation of monomers into a growing polymeric chain remains challenging, due to a variety of possible deactivation processes.⁴¹¹ Compared to small monomers, successful polymerization of macromonomers not only depends on the polymerizable moiety and the functional groups attached, it further depends on its molecular weight, beneficial or unfavorable interactions with the solvent during ROMP and the applied synthesis procedure.^{386,473}

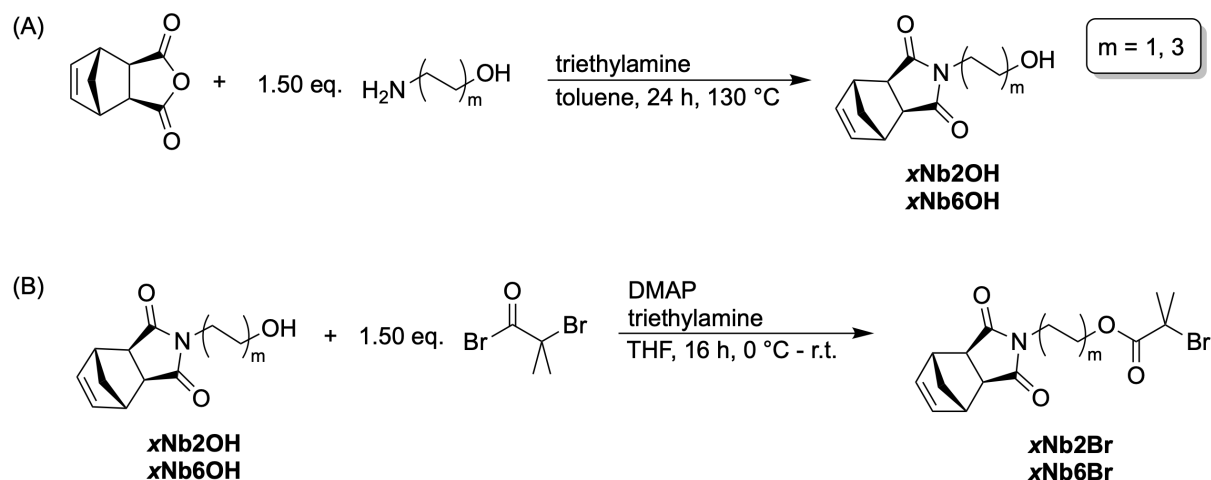
In this chapter, the ROMP behavior of different macromonomers synthesized *via* ATRP is investigated with special interest on the applied conditions, like solvent, temperature, and the used catalyst. The influence of the ROMP procedure on the polymerization kinetics is evaluated by on-line ¹H NMR spectroscopy. Furthermore, sequence-controlled graft copolymers are synthesized by the iterative addition of macromonomers to the polymerization, whereas bifunctional macromonomers comprising two different polymer chains are also used to synthesize graft copolymers in a straightforward fashion.

5.3 Results and discussion

5.3.1 Synthesis of norbornene dicarboximide-based macromonomers

In the following section, the synthesis of *exo* norbornene dicarboximide-based macromonomers *via* ATRP is described, whereby two different ATRP initiators are used, while methyl and benzyl methacrylate, and styrene serve as monomers. The obtained macromonomers are further examined regarding their molecular structure and their thermal properties.

In order to perform an ATRP and use the obtained polymer as a macromonomer for ROMP, norbornene-functional ATRP initiators were synthesized, as suitable synthesis procedures are well-known in the literature.⁴⁷⁴ In all cases, *exo* norbornene dicarboxylic anhydride was used as the starting molecule. The initiator was attached to it through an alkane linker unit which was varied between ethyl and hexyl (**Scheme 5.1**), examining its influence on the ROMP of the subsequent macromonomers, with special interest on the polymerization kinetics and control.



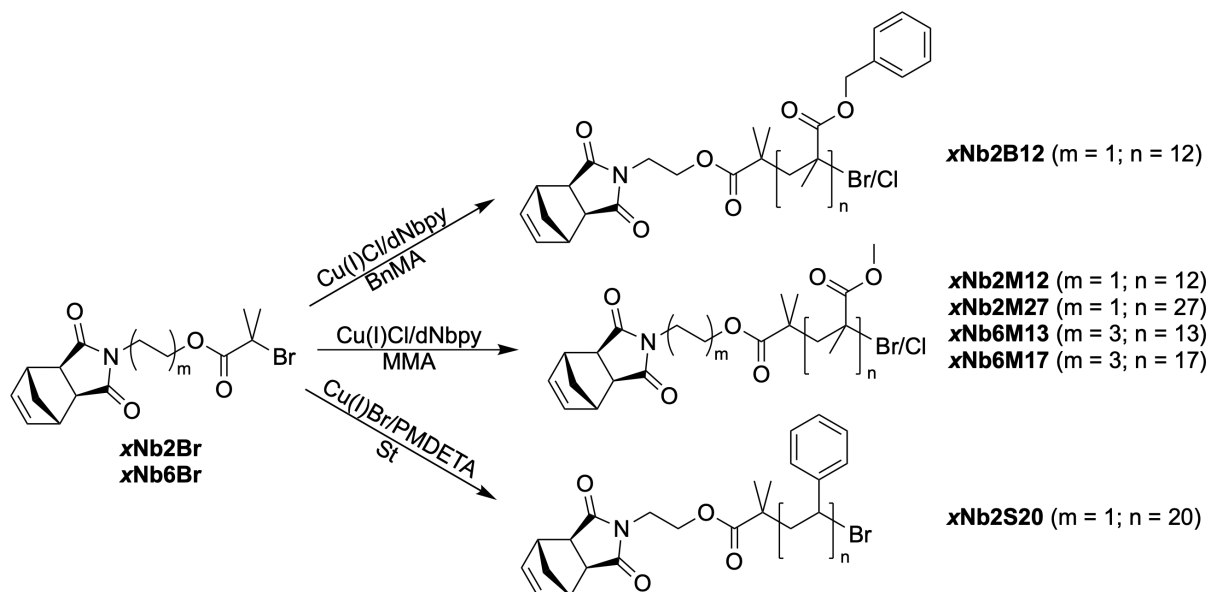
Scheme 5.1. Synthesis of (A) hydroxylated *exo* norbornenes **xNb2OH** and **xNb6OH** *via* condensation of *exo* norbornene anhydride with 2-aminoethanol and 6-aminohexanol, and (B) subsequent esterification using α -bromoisobutyryl bromide, obtaining **xNb2Br** and **xNb6Br**.

Exo norbornene anhydride (*cis*-5-norbornene-*exo*-2,3-dicarboxylic anhydride) was used as precursor due to its commercial availability and straightforward functionalization using primary amines. Thus, 2-aminoethanol and 6-aminohexanol were used in a condensation reaction (**Scheme 5.1A**), yielding the hydroxylated *exo* norbornenes **xNb2OH** and **xNb6OH**.

The former was obtained as a white waxy solid in a yield of 85% (**Figure S5.1**), whereas the latter appeared as a colorless liquid and was obtained in a yield of 98% (**Figure S5.3**).

Subsequently, **xNb2OH** and **xNb6OH** were esterified using α -bromoisobutyryl bromide and a mixture of triethylamine and 4-dimethylaminopyridine (DMAP) in THF, obtaining the *exo* norbornene–functional ATRP initiators **xNb2Br** and **xNb6Br** (**Scheme 5.1B**). The tertiary alkyl bromide was used due to its high activation rate constant ($k_{\text{act}} = 2.7 \text{ M}^{-1}\text{s}^{-1}$ for ethyl α -bromoisobutyrate) compared to secondary or primary alkyl bromides and alkyl chlorides.³²⁸ The products were obtained as a white solid in a yield of 96% and a colorless liquid in a yield of 88%, respectively (**Figures S5.5 and S5.7**). It is noted that the compounds **xNb6OH** and **xNb6Br** were synthesized by P. Conen under my supervision during his advanced organic practical course.

In order to examine the homo- and copolymerizability of *exo* norbornene–functional macromonomers in ROMP, highlighting the macromonomer structure and size, different polymers were synthesized *via* ATRP using **xNb2Br** and **xNb6Br** as initiators (**Scheme 5.2**). It is noted that the term “argon-flushed” further implies that the used reaction vessel was thrice dried with a heat gun under high vacuum and flushed with argon while hot.



Scheme 5.2. Synthesis of *exo* norbornene–functional macromonomers *via* ATRP using **xNb2Br** and **xNb6Br** as ATRP initiators and benzyl methacrylate (BnMA, top), methyl methacrylate (MMA, middle) and styrene (St, bottom) as monomers.

The ATRPs of the methacrylates, i.e. benzyl methacrylate (BnMA) and methyl methacrylate (MMA), were mediated by Cu(I)Cl and 4,4'-dinonyl-2,2'-bipyridine (dNbpy) as ligand (L) under

an argon atmosphere. The polymerizations were carried out in argon-flushed Schlenk flasks at 90 °C for 2.5 hours and reaching nearly complete conversions. As such, PBnMA- and PMMA-based *exo* norbornene–functional macromonomers were obtained. Additionally, a PS-based *exo* norbornene–functional macromonomer was synthesized mediated by Cu(I)Br and *N,N,N',N'',N''*-pentamethyl diethylenetriamine (PMDETA) as ligand under an argon atmosphere. The polymerization was carried out in argon-flushed Schlenk flasks at 80 °C for 70 minutes. The catalyst was changed for the polymerization of styrene to reduce the polymerization rate and the possibility to trigger side reactions at high monomer conversion,⁴⁷⁵ since polymers that comprise a hydrogen atom at the α -position tend to undergo combination during radical polymerization processes.³⁰⁶ This behavior potentially leads to the radical-radical coupling of two polymer chains, resulting in the formation of an telechelic dinorbornene species which would act as a crosslinking agent in the subsequent ROMP.⁴⁶⁰ In contrast, polymethacrylates exhibit this behavior to a lesser extent, whereby termination occurs predominantly *via* disproportionation.³⁰⁶ The macromonomers were purified by precipitation from cold *n*-hexane (polymethacrylates) and from cold methanol (PS, (Table 5.1).

Table 5.1. Synthesized *exo* norbornene dicarboximide–based macromonomers *via* ATRP.

Polymer ^a	DP	Monomer	ATRP Initiator	$M_{n,NMR}$ [g/mol] ^b	$M_{n,SEC}$ [g/mol] ^c	\bar{D}_M ^c
xNb2M12	12	MMA	xNb2Br	1,600	1,700	1.16
xNb2M27	27	MMA	xNb2Br	3,100	3,200	1.13
xNb6M13	13	MMA	xNb6Br	1,700	1,700	1.13
xNb6M17	17	MMA	xNb6Br	2,100	2,500	1.16
xNb2B12	12	BnMA	xNb2Br	2,500	2,600	1.18
xNb2S20 ^d	20	St	xNb2Br	2,400	2,100	1.17

^aReaction conditions: Monomer, initiator (0.05 mol/L), Cu(I)Cl and dNbpy in toluene for 2.5 h at 90 °C under argon atmosphere (M:I:Cu:L ratio – 12/30/12/12/10:1:1:2). ^bDetermined by ¹H NMR spectroscopy. ^cDetermined by SEC. ^dReaction conditions: Monomer, initiator (0.04 mol/L), Cu(I)Br and PMDETA in toluene for 70 min at 80 °C under argon atmosphere (M:I:Cu:L ratio – 120:1:1:1).

The obtained macromonomers are termed as follows: the *exo* norbornene moiety is abbreviated as xNb, the length of the alkane linker between norbornene and polymer chain is described by the number of carbon atoms (2 for ethyl; 6 for hexyl), and the attached polymer chain is abbreviated by M for PMMA, B for PBnMA and S for PS, while the following number describes the average DP of the respective polymer chain determined by ^1H NMR spectroscopy. Molecular weights of 1,600 – 3,100 g/mol were thus obtained (**Table 5.1**). The obtained macromonomers were also characterized by SEC to evaluate the applied ATRP procedures (**Figure 5.1**). It is noted that the macromonomer **xNb6M17** was synthesized by B. Felker under my co-supervision.

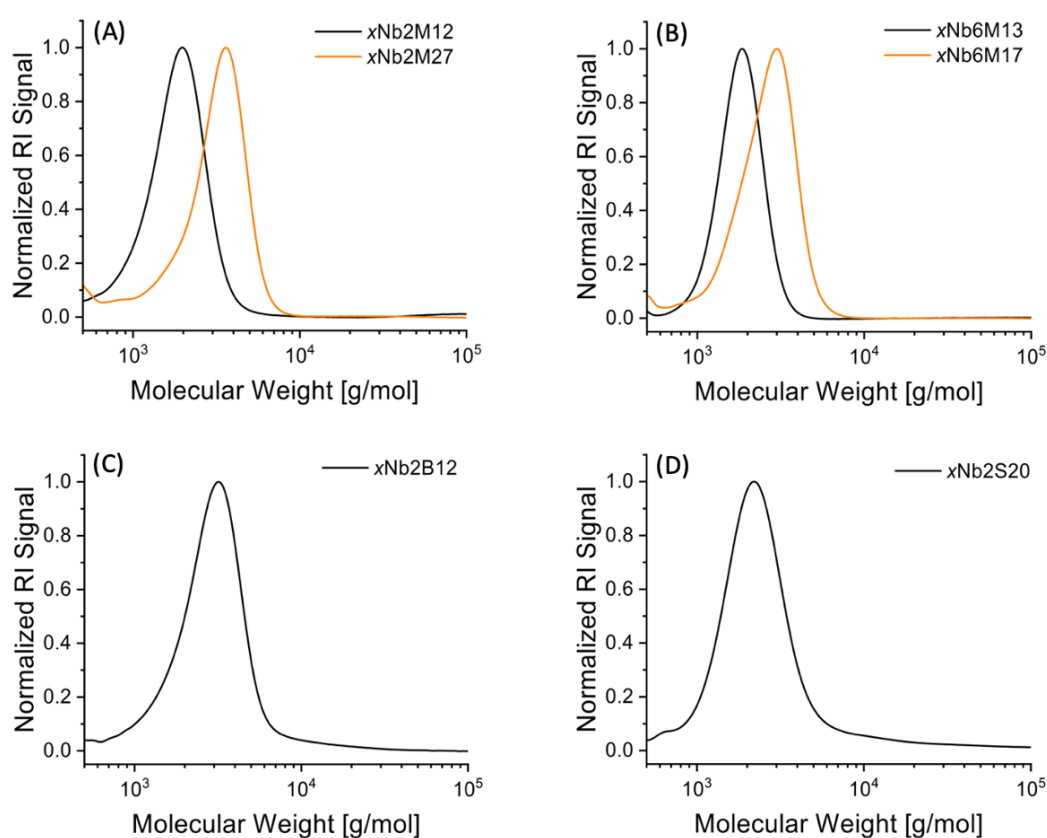


Figure 5.1. SEC traces of (A) the PMMA-based macromonomers comprising an ethyl linker, (B) the PMMA-based macromonomers comprising a hexyl linker, (C) the PBnMA-based macromonomer, and (D) the PS-based macromonomer.

Narrow molecular weight distributions (≤ 1.18) were observed for all macromonomers indicating well-controlled polymerization processes. The average M_n s determined *via* SEC and ^1H NMR spectroscopy were found to be consistent with a small variation for **xNb2S20** which was attributed to the different R_h s of PS and the PMMA calibration standards.⁴⁷⁶ The macromonomers were further analyzed using matrix-assisted laser desorption/ionization

mass spectrometry equipped with a time-of-flight detector (MALDI-TOF MS). In all cases, the obtained signals were identified to confirm the presence of the norbornene moiety within the macromonomers and thus to ensure polymerizability in subsequent ROMPs. Additionally, the attached end groups at the ω -positions were determined, further evaluating the applied ATRP procedures. The MALDI-TOF results of **xNb2M12** are discussed as an example for the PMMA-based macromonomers (**Figure 5.2**). MALDI-TOF MS data of **xNb2M27**, **xNb6M13** and **xNb6M17** are presented in the experimental section in **chapter 8.3.2**. It is noted that all herein presented MALDI-TOF data are unprocessed.

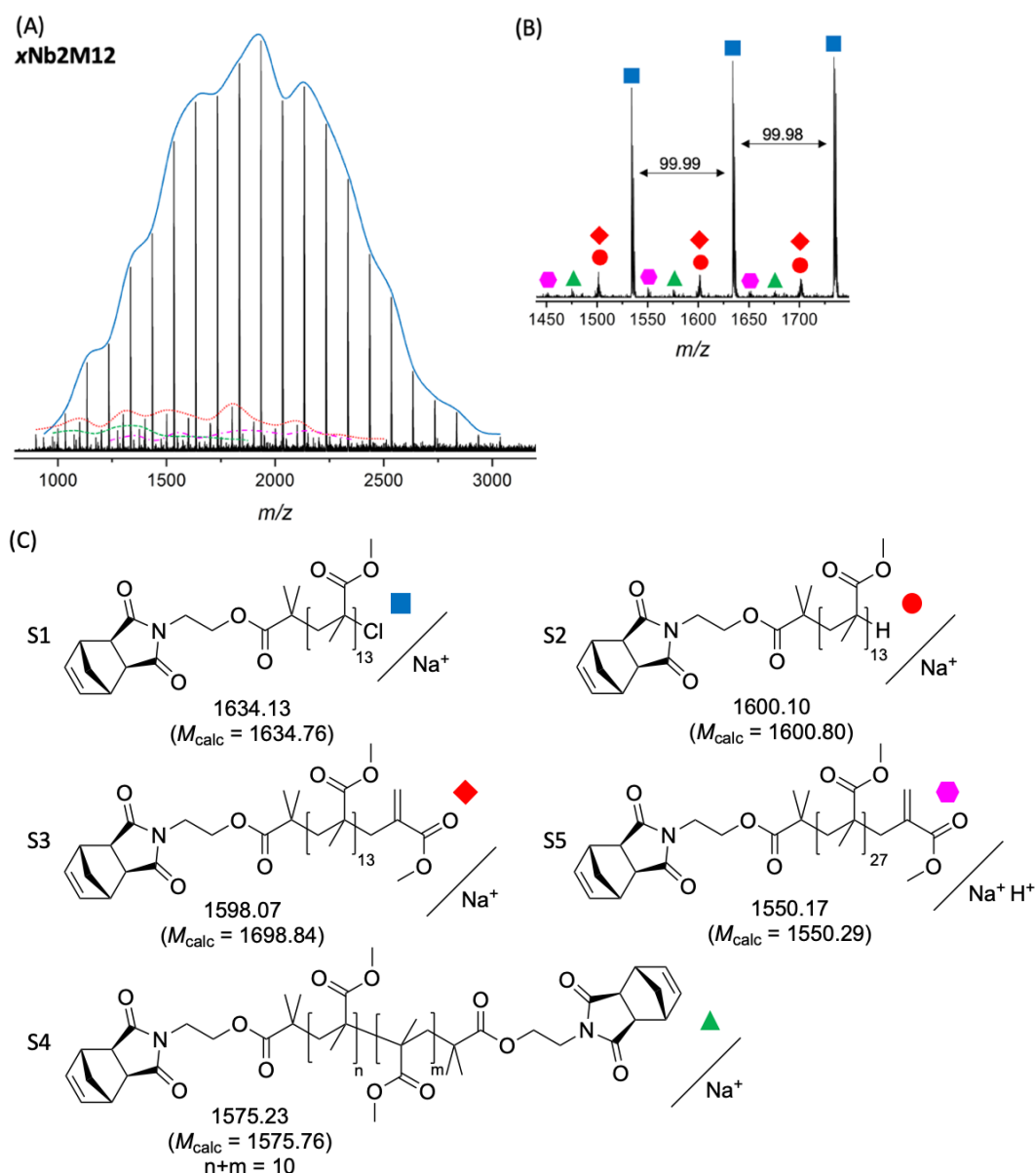


Figure 5.2. (A) MALDI-TOF spectrum (DCTB, NaTFA) of **xNb2M12** with highlighted mass distributions in color to guide the eye, (B) selected region of the spectrum (1455 – 1745 m/z) with peaks color coded as per the identified species, and (C) structures of **xNb2M12** species (S1 – S5) and their calculated and measured monoisotopic masses.

The MALDI-TOF mass distribution of **xNb2M12** was found to comprise five distinct distributions (**Figure 5.2A**). In all cases, the distance between two consecutive signals was found to correspond to the mass of one methyl methacrylate repeat unit (expected: 100.05 m/z , **Figure 5.2B**). It is noted that the signals were determined as the sodium adducts, unless otherwise stated. Furthermore, the distributions were assigned to the determined species (S1 – S5) by comparing the observed isotopic patterns with the calculated (**chapter 8.3.2, Figure S5.11**). The highest intensity distribution was assigned to the chloride-terminated species (S1, **Figure 5.2C**). The positions of the four remaining distributions are further described related to the position of the main distribution. However, at $\Delta(m/z) = -34.03$ and -36.06 , two overlapping distributions were detected ascribed to the hydrogen- and the vinylidene-terminated species, respectively (S2 and S3, **Figure 5.2C**). Both structures are obtained as disproportionation products, whereby a hydrogen of the methyl group at the chain end is transferred to another polymer chain, forming a saturated and an unsaturated end group functionality. The latter can additionally arise from halogen abstraction processes.⁴⁷⁷ The distribution at $\Delta(m/z) = -58.90$ was ascribed to the recombination product, resulting in the radical coupling of two PMMA chain ends and the formation of an α,ω -dinorbornene species (S4, **Figure 5.2C**).⁴⁶⁰ The last detectable distribution at $\Delta(m/z) = -83.96$ was ascribed to the double charged hydrogen-terminated species ionized by one sodium and one proton (S5, **Figure 5.2C**). It is not determined whether the detected species were obtained during the ATRP process since end group degradation during MALDI-TOF is well-known in the literature.⁴⁷⁸ A potentially present non-norbornene containing PMMA chain comprising a chloride at the ω -position and a carboxylic acid functionality at the α -position would be expected at $\Delta(m/z) = -188.45$. However, the low intensity in this region of the spectrum is indicative of its absence. In contrast, the presence of the norbornene moiety in **xNb2M12** was confirmed within all detected species. It is noted that the bromide-terminated species was not detected either due to insufficient ionization or its low abundance in the sample, the latter caused by the weaker C-Br bond compared to the C-Cl bond,³²⁸ and the stronger affinity of bromides to copper.⁴⁷⁹ It is noted for all MALDI-TOF spectra that the relative intensities shown do not necessarily reflect the concentration of the determined species in the corresponding sample. However, the findings were in agreement with the data obtained by SEC and ¹H NMR spectroscopy. The latter indicated an end group

fidelity of 86% for **xNb2M12**, 77% for **xNb6M13**, and 76% for **xNb6M17** when comparing the signals at 2.60 – 2.25 ppm, assigned to the methylene groups of the last MMA repeat units, to the characteristic olefinic signals of the norbornene moieties at 6.35 – 6.24 ppm. It is noted that the determination of the end group fidelity by ¹H NMR spectroscopy was not possible for **xNb2M27** due to overlapping signals at 2.60 – 2.25 ppm.

In order to evaluate the obtained PBnMA-based macromonomer **xNb2B12**, MALDI-TOF data are further discussed (**Figure 5.3**)

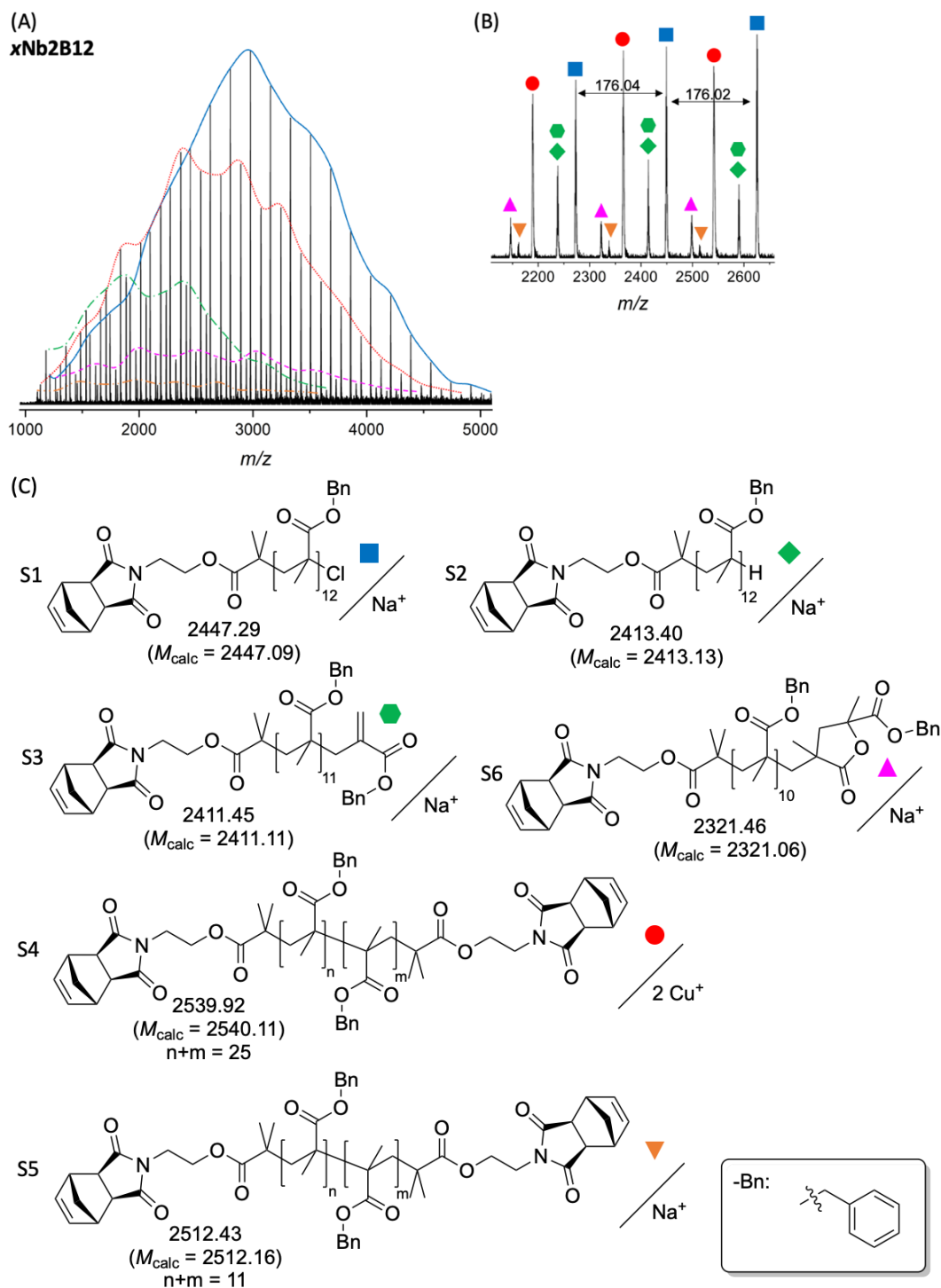


Figure 5.3. (A) MALDI-TOF spectrum (DCTB, NaTFA) of **xNb2B12** with highlighted mass distributions in color to guide the eye, (B) selected region of the spectrum (2110 – 2660 m/z) with peaks color coded as per the identified species, and (C) structures of **xNb2B12** species (S1 – S6) and their calculated and measured monoisotopic masses.

The MALDI-TOF spectrum of **xNb2B12** exhibited six distinct distributions (**Figure 5.3A**). In all cases, the distance between two consecutive signals was found to correspond to the mass of one benzyl methacrylate repeat unit (expected: 176.08 m/z , **Figure 5.3B**). The highest intensity distribution was ascribed to the chloride-terminated species (S1, **Figure 5.3C**). Similar to the MALDI-TOF data of **xNb2M12**, the distributions at $\Delta(m/z) = -33.98$ and -35.84 were ascribed to the hydrogen- and the vinylidene-terminated species, respectively (S2 and S3, **Figure 5.3C**). Another high intensity distribution was located at $\Delta(m/z) = -83.69$, which was ascribed to the double charged α,ω -dinorbornene species ionized by two copper(I) ions (S4, **Figure 5.3C**). The ability of copper to act as an ionizing agent in MALDI-TOF MS is well-known in the literature, whereby the photochemical reduction of copper(II) to copper(I) was found to appear during the laser ionization process.^{480,481} Since the workup procedure and the MALDI-TOF sample preparation of **xNb2B12** and **xNb2M12** were identical, it is assumed that in contrast to the methyl side groups, the interaction between the benzyl side groups and the copper favored sufficient ionization. Additionally, an α,ω -dinorbornene species was detected at $\Delta(m/z) = -111.08$ (S5, **Figure 5.3C**). The distribution at $\Delta(m/z) = -155.83$ was ascribed to the lactone-terminated species (S6, **Figure 5.3C**). The MALDI-TOF-induced intramolecular ring-closing reaction at the chain end of polymethacrylate-based polymers and thus formation of terminal lactone units is well-known in the literature.^{482,483} As discussed in the MALDI-TOF analysis of **xNb2M12**, the relative abundances of the detected species do not display the absolute concentrations of the respective species in the sample, it is not determined whether these species were obtained during the ATRP or during the ionization process.⁴⁷⁸ The assignments of the distributions were additionally verified by comparing the obtained isotopic patterns with the calculated (**chapter 8.3.2, Figure S5.26**). The findings were in agreement with the data obtained by SEC and ¹H NMR spectroscopy. Since the latter indicated a nearly quantitative end group fidelity for **xNb2B12** when comparing the signal at 2.60 – 2.25 ppm, assigned to the methylene group of the last BnMA repeat unit, and the characteristic olefinic signal of the norbornene moiety at 6.35 – 6.24 ppm.

Finally, the PS-based macromonomer **xNb2S20** was also examined by MALDI-TOF MS, using dithranol as matrix (**Figure 5.4**).

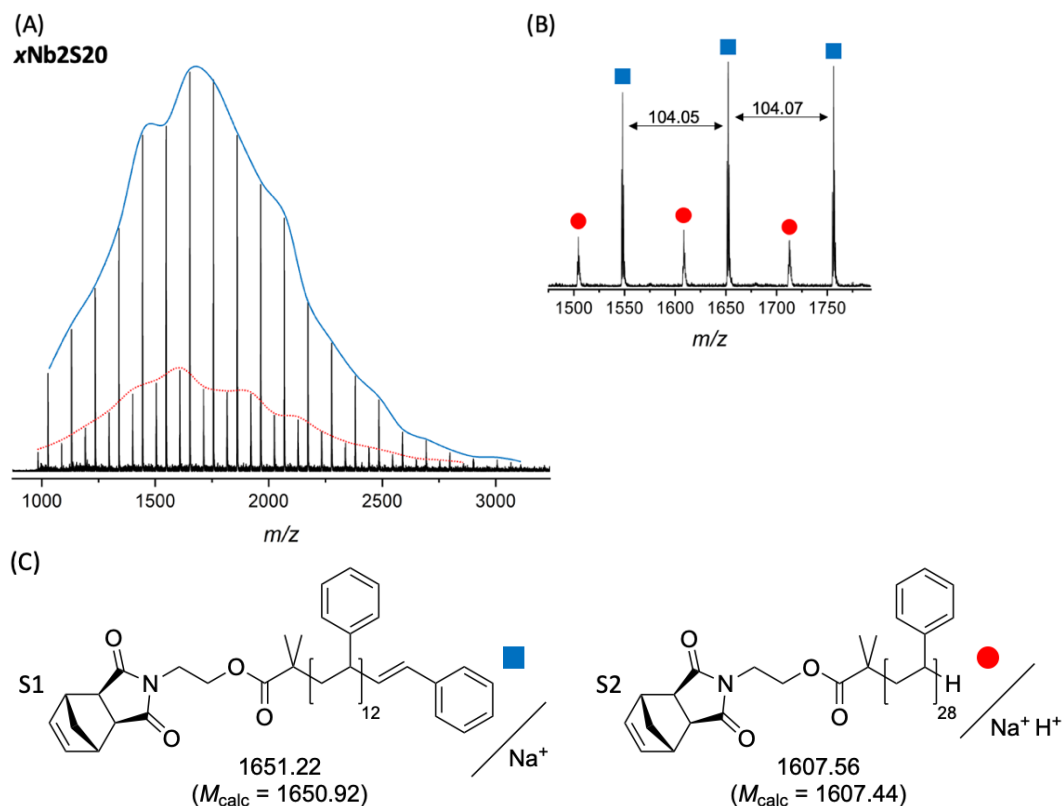


Figure 5.4. (A) MALDI-TOF spectrum (dithranol, NaTFA) of **xNb2S20** with highlighted mass distributions in color to guide the eye, (B) selected region of the spectrum (1475 – 1775 m/z) with peaks color coded as per the identified species, and (C) structures of **xNb2S20** species (S1 – S2) and their calculated and measured monoisotopic masses.

The MALDI-TOF spectrum of **xNb2S20** exhibited two distinct distributions (**Figure 5.4A**). In both cases, the distance between two consecutive signals corresponded to the mass of one styrene repeat unit (expected: 104.06 m/z , **Figure 5.4B**). The highest intensity distribution was ascribed to the species comprising an unsaturated end group (S1, **Figure 5.4C**), obtained from the dehydrohalogenation of the chain terminal group during the MALDI-TOF measurement.⁴⁷⁸ The second distribution at $\Delta(m/z) = -43.66$ was ascribed to the double charged hydrogen-terminated species ionized by one sodium and one proton (S2, **Figure 5.4C**). The respective comparison between measured and calculated isotopic patterns is presented in the experimental section in **chapter 8.3.2 (Figure S5.29)**. The findings were in agreement with the data obtained by SEC and ^1H NMR spectroscopy. However, the determination of the end group fidelity by ^1H NMR spectroscopy was not possible for **xNb2M20** due to overlapping signals at 2.60 – 2.25 ppm.

MMA, BnMA, and styrene were chosen as monomers in ATRP since the resulting macromonomers exhibit literature-known differences in T_g s.⁴⁸⁴ Furthermore, the homopolymers of each of these monomers are known to be immiscible with each other.⁴⁸⁵ Immiscibility further leads to phase separation which is evident by distinct T_g s, each corresponding to the respective homopolymer. In contrast, miscibility results in a T_g that is between the respective homopolymer T_g s.⁴⁸⁶ This phenomenon has been shown in **chapter 4.3.2**, whereby the Fox equation (**Equation 4.1**) is used to estimate the thermal behavior of a polymer blend.⁴⁴⁶ The combination of immiscible polymers, e.g. in block copolymers, results in short range phase separation and potentially self-assembling.⁴⁸⁷ In order to examine the thermal behavior of the different macromonomers and thus estimate the potential of an obtained block copolymer to self-assemble into ordered structures, DSC measurements were conducted and the T_g s of the pure macromonomers as well as their blends (at mass ratios of 1:1) were determined (**Figure 5.5**).

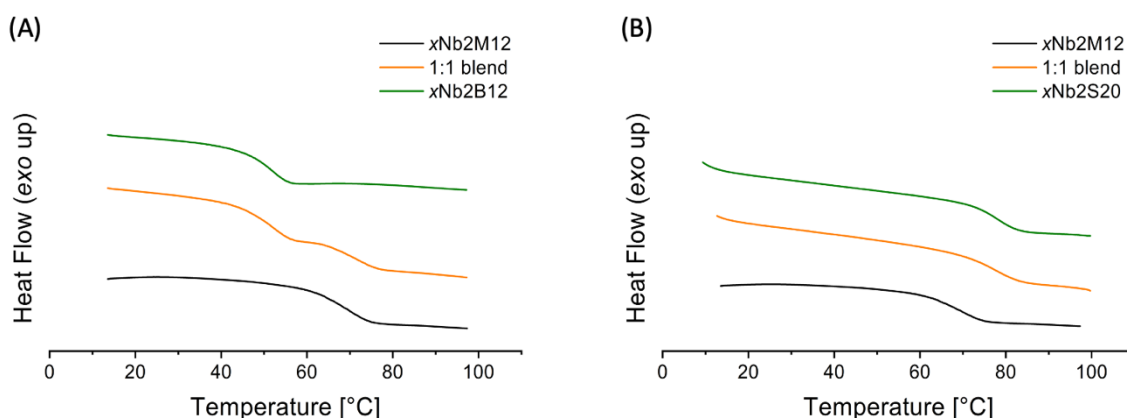


Figure 5.5. DSC traces of (A) $xNb2M12$, $xNb2B12$, and the respective 1:1 blend, and of (B) $xNb2M12$, $xNb2S20$, and the respective 1:1 blend.

According to the literature, PMMA and PBnMA are expected to exhibit T_g s at 105 °C and 54 °C, respectively, whereas PS is expected to exhibit a T_g at 100 °C.⁴⁸⁴ However, the PMMA-based macromonomer $xNb2M12$ exhibited a T_g at 63 °C, whereas the PBnMA-based macromonomer $xNb2B12$ exhibited a T_g at 46 °C. Furthermore, the PS-based macromonomer $xNb2S20$ exhibited a T_g at 73 °C. The observed reduction of the determined T_g s is explained by its molecular weight dependency, whereby the T_g s decrease with decreasing molecular weight of the corresponding polymer.^{488,489} Blending of the methacrylate-based

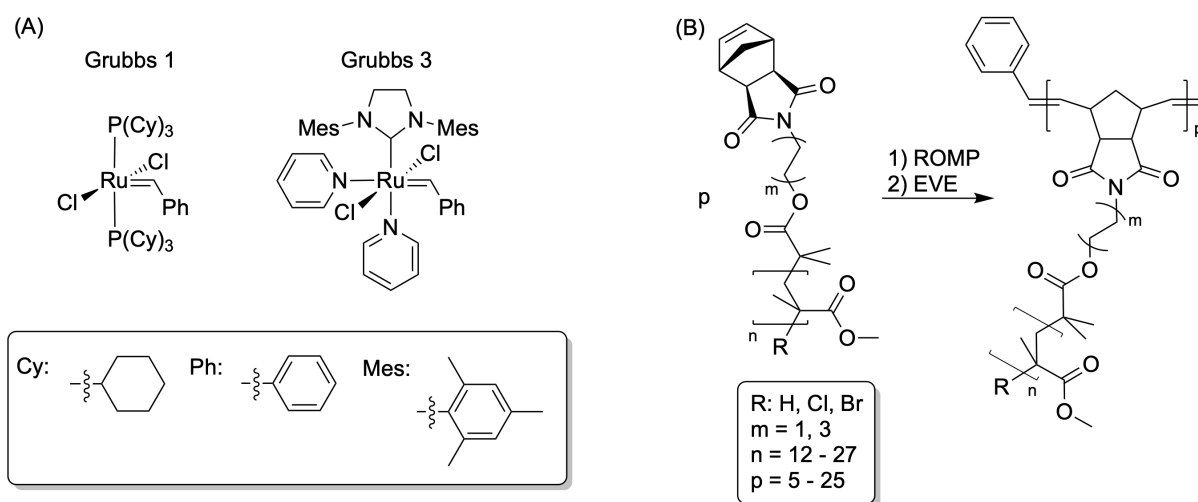
macromonomers at a 1:1 mass ratio resulted in the presence of two T_g s at 65 °C, ascribed to the PMMA component, and at 47 °C for the PBnMA one (**Figure 5.5A**). In contrast, blending of **xNb2S20** with **xNb2M12** led to a T_g at 72 °C (**Figure 5.5B**), which was relatively consistent with the estimated T_g calculated by **equation 4.1** (*ca.* 69 °C). However, according to the literature, PS and PMMA are immiscible.⁴⁹⁰ The herein made observation was explained by partial miscibility due to the low molecular weight of the used macromonomers.⁴⁹¹ It is noted that all herein measured T_g values were determined by the onset temperature of the thermal transition in the second heating cycle, applying a heating rate of 20 °C/min.

As a result, three different *exo* norbornene–functional macromonomers were successfully synthesized *via* the ATRP of MMA, BnMA, and styrene, whereby the obtained methacrylate-based polymers show immiscibility in a 1:1 blend and thus are interesting in potentially self-assembling when combined in a copolymer.

5.3.2 Synthesis of graft polymers using the G1 catalyst

In the following section, the synthesis of graft polymers using the G1 catalyst is investigated. Here, the effects of the macromonomer structure and size, as well as the effects of the used solvent and concentration on their polymerization *via* ROMP are examined.

In order to perform a successful ROMP of macromonomers, suitable polymerization conditions had to be evaluated regarding catalyst, solvent, macromonomer (MM), and concentration. Different Grubbs-type catalysts were thus used in all ROMPs, due to their tolerance toward functional groups, relatively high stability, and commercial availability (**Scheme 5.3**).⁴⁹²



Scheme 5.3. (A) Grubbs-type catalysts used in the ROMP of macromonomers and (B) schematic ROMP of PMMA-based macromonomers.

The G1-mediated ROMP of PMMA-based macromonomers was used to examine advantageous and unfavorable influences on the polymerization process, e.g. on polymerization kinetics and control (**Scheme 5.3B**). However, the ROMP of macromonomers using Grubbs third generation (G3) catalyst is presented in **chapter 5.3.3**. It is noted that all herein performed ROMPs were quenched by adding an excess of EVE, however, further removal of the catalyst and purification by precipitation was not carried out, unless otherwise stated, due to time limitations and given that preliminary experiments showed such purification was not necessary when assessing kinetics.

In order to determine the influence of the macromonomer size on the ROMP using the G1 catalyst, **xNb2M12** (1,600 g/mol, **Table 5.1**) and **xNb2M27** (3,100 g/mol, **Table 5.1**) were used to synthesize graft polymers with different DPs (**Table 5.2**).

Table 5.2. ROMPs using PMMA-based macromonomers with different molecular weights.

Entry ^a	MM	M:I ratio	Conversion [%] ^b	$M_{n,calc}$ [g/mol] ^c	M_n [g/mol] ^d	\mathcal{D}_M ^d
5.1	xNb2M12	5:1	≥99	8,000	11,400	1.11
5.2	xNb2M12	10:1	≥99	16,000	15,500	1.17
5.3	xNb2M12	15:1	93	22,300	43,900	1.58
5.4	xNb2M12	20:1	54	17,300	66,200	18.8
5.5	xNb2M12	25:1	0	-	-	-
5.6	xNb2M27	5:1	≥99	15,500	17,700	1.11
5.7	xNb2M27	10:1	≥99	31,000	25,900	1.13
5.8	xNb2M27	15:1	≥99	46,500	43,300	1.15
5.9	xNb2M27	20:1	≥99	62,000	52,300	1.19
5.10	xNb2M27	25:1	≥99	77,500	60,100	1.19

^aReaction conditions: MM and G1 catalyst (2 mmol/L) in DCM at ambient temperature overnight. ^bDetermined by ¹H NMR spectroscopy. ^cCalculated by conversion. ^dDetermined by SEC.

The reactions (entries 5.1 – 5.10, **Table 5.2**) were performed in DCM at ambient temperature overnight, keeping the catalyst concentration constant in all polymerizations. The resulting polymers were analyzed *via* ¹H NMR spectroscopy to determine the conversions, using the vanishing of the signals assigned to the olefinic norbornene moieties of the *exo* macromonomers (6.32 ppm) and the appearing of the olefinic backbone signals of the resulting polymers (5.86 – 5.60 ppm), as described in **chapter 4.3.2 (Figure 4.1)**. Furthermore, SEC measurements were conducted to determine molecular weight and dispersity (**Table 5.2**). Interestingly, the conversion of **xNb2M12** decreased with increasing the targeted DP. Entries 5.1 and 5.2 exhibited complete conversions, whereas entries 5.3 and 5.4 reached conversions of 93% and 54% after overnight reactions, respectively (**Figure S5.30, Table 5.2**).

No macromonomer conversion was detected in entry 5.5 (Figure S5.30, Table 5.2). Nonetheless, the ROMPs using the larger **xNb2M27** (entries 5.6 – 5.10, Table 5.2) were performed applying similar conditions. The conversions were found to be quantitative for all ROMPs (Figure S5.31, Table 5.2). In order to further examine the polymerization processes, SEC measurements of the obtained graft polymers were conducted (Figure 5.6).

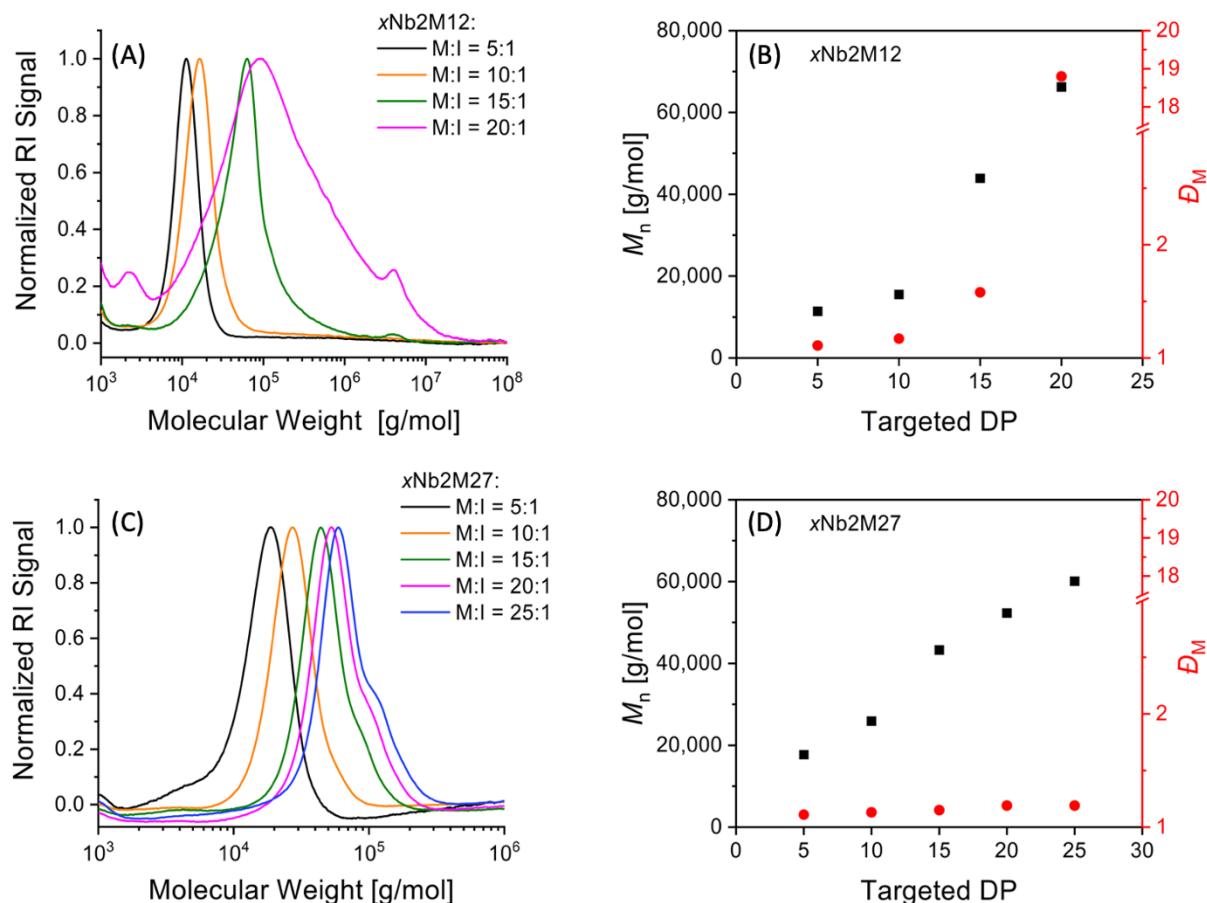


Figure 5.6. SEC traces and plots of the molecular weight and dispersity versus targeted DP, determined by SEC, in the G1-mediated ROMP of (A,B) **xNb2M12** and (C,D) **xNb2M27**, respectively.

Entries 5.1 and 5.2 (Table 5.2) exhibited narrow molecular weight distributions suggesting good polymerization control. However, the distributions obtained from entries 5.3 and 5.4 (Table 5.2) were found to be broad, indicating loss of polymerization control for entry 5.4 (Figure 5.6A). It is noted that entry 5.4 (Table 5.2) reached the exclusion limit of the SEC instrument, corresponding to molecular weights higher than 1,000,000 g/mol. Here, the molecular weight and the dispersity of the obtained graft polymers were found to increase

monotonically albeit in a non-linear fashion with increasing targeted DP (**Figure 5.6B**). In contrast, the SEC measurements obtained from the larger macromonomer (entries 5.6 – 5.10, **Table 5.2**) exhibited relatively narrow molecular weight distributions independent from the targeted DP. However, an increasing high molecular weight shoulder was found to appear in the higher DP samples, namely for entries 5.8 – 5.10 (**Figure 5.6C**, **Table 5.2**). The graft polymers derived from **xNb2M27** exhibited a linear relationship between targeted DP and molecular weight, and a minimal increase in dispersity with increasing DP (**Figure 5.6D**). Furthermore, the M_n s determined by SEC differed from the expected M_n s calculated by conversion (**Table 5.2**). The low DP polymers of entries 5.1 and 5.6 showed slightly higher M_n s than expected (**Table 5.2**). In contrast, the M_n s of the relatively narrow dispersity polymers of entries 5.2, 5.7 – 5.10 showed lower M_n s than expected (**Table 5.2**). It is noted that the difference of the determined to the expected M_n s of entries 5.3 and 5.4 increased with increasing dispersity, which was mainly attributed to the broad molecular weight distributions (**Figure 5.6**). These observations were further attributed to the different morphologies of the SEC calibration standards (linear PMMAs) and the measured polymers (grafts), resulting in different R_h s and thus in different retention times and molecular weights, respectively. It is noted that the repetition of entries 5.4 and 5.5 resulted in similar results, suggesting a systemic error generated by either the applied ROMP conditions, the used macromonomer, or unfavorable steric interactions between the PMMA chain and the propagating PNB chain end.

In order to determine the influence of the macromonomer concentration on the polymerization process, the reaction conditions of entry 5.2 (**Table 5.2**) were adapted by decreasing the catalyst concentration and thus reaching a higher DP of the resulting graft polymer (**Table 5.3**).

Table 5.3. ROMPs with different catalyst concentrations using **xNb2M12** as macromonomer.

Entry ^a	M:I ratio	c(G1) [mmol/L]	Conversion [%] ^b	M_n [g/mol] ^c	D_M^c
5.11	15:1	1.33	37	25,700	1.47
5.12	20:1	1.00	0	-	-

^aReaction conditions: **xNb2M12** (20 mmol/L) and G1 catalyst in DCM at ambient temperature overnight. ^bDetermined by ¹H NMR spectroscopy. ^cDetermined by SEC.

The concentration of **xNb2M12** was retained at 20 mmol/L, whereas the catalyst concentration was lowered to 1.33 mmol/L for entry 5.11 and 1.00 mmol/L for entry 5.12 (**Table 5.3**), hence, the targeted DPs were 15 and 20, respectively. Analysis by ¹H NMR spectroscopy indicated low macromonomer conversion of 37% for entry 5.11 and no detectable conversion for entry 5.12 (**Figure S5.32**, **Table 5.3**). The molecular weight distribution of entry 5.11 was further examined by SEC (**Figure 5.7**).

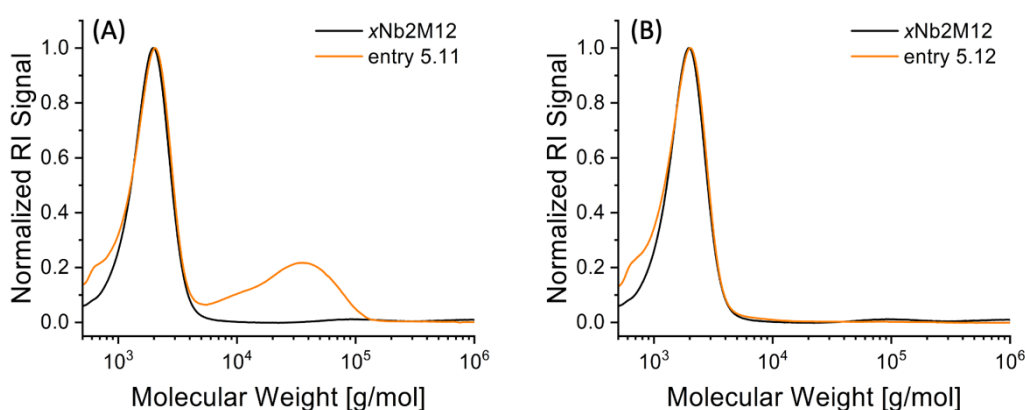


Figure 5.7. SEC traces of (A) entry 5.11 and the used macromonomer, and (B) entry 5.12 and the used macromonomer (**Table 5.2** and **Table 5.3**).

As expected, a distinct distribution was detected at low molecular weights, assigned to remaining **xNb2M12** (**Figure 5.7**). The broad distribution at high molecular weights was

ascribed to the graft polymer, whereby the high dispersity and the relatively low conversion indicated poor polymerization control (**Figure 5.7A**). Confirming the ^1H NMR data, the SEC trace of entry 5.12 (**Table 5.3**) exhibited no detectable macromonomer conversion (**Figure 5.7B**). These observations showed that an increase in DP, be it from increasing the macromonomer concentration or reduction of the G1 concentration, reduces monotonically the resulting polymer molecular weight. This is surprising since “living” chain-growth polymerizations such as ROMP are well-known to show a linear relationship between monomer conversion and molecular weight,¹⁷ therefore it has been hypothesized that the used solvent plays a role in the process.

In order to determine the influence of the solvent on the ROMP of **xNb2M12**, the reaction conditions of entry 5.5 (**Table 5.2**) were adapted by varying the solvent (**Table 5.4**).

Table 5.4. ROMPs of **xNb2M12** as macromonomer using different solvents.

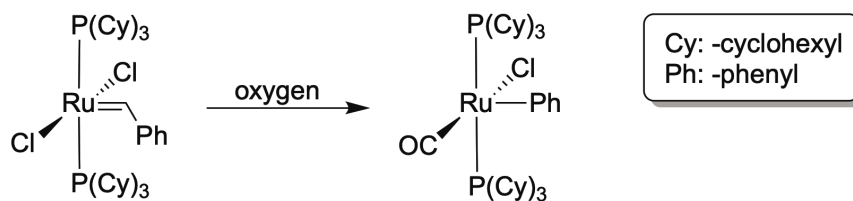
Entry ^a	Solvent	Conversion [%] ^b	M_n [g/mol] ^c	\mathcal{D}_M^c
5.13	Chloroform	0	-	-
5.14	Dimethyl carbonate	≥99	59,100	2.23
5.15	Tetrahydrofuran	0	-	-
5.16	Toluene	0	-	-

^aReaction conditions: **xNb2M12** (50 mmol/L) and G1 catalyst (2 mmol/L) in the respective solvent at ambient temperature overnight. ^bDetermined by ^1H NMR spectroscopy. ^cDetermined by SEC.

Chloroform was considered as a promising candidate, since recent literature describes the successful ROMP of norbornene-based monomers using the G1 catalyst.⁹³ Surprisingly, no macromonomer conversion was detected (entry 5.13, **Figure S5.33**, **Table 5.4**). Dimethyl carbonate (DMC) was also tested as a solvent in the ROMP of **xNb2M12**, due to its related chemical structure compared the MMA (entry 5.14, **Table 5.4**). The G1 catalyst only showed moderate solubility in DMC at ambient temperature, however, complete dissolution was observed a few minutes after the monomer was added. Analysis *via* ^1H NMR spectroscopy showed quantitative conversion (**Figure S5.33**), although the SEC trace exhibited a relatively broad molecular weight distribution with a small high molecular weight shoulder (**Figure**

S5.34). The moderate solubility of the G1 catalyst in DMC was considered as the main issue, leading to an inhomogeneous reaction mixture and further to an irregular initiation process, resulting in lack of polymerization control. THF is a well-known solvent for the ROMP of small monomers using the G1 catalyst and for macromonomers using the G3 catalyst.^{406,493} Nonetheless, no macromonomer conversion was detected (entry 5.15, **Figure S5.33**, **Table 5.4**). Finally, toluene was considered as a nonpolar solvent, as recent literature describes the successful ROMP of norbornene-functional dendrimers using toluene and the Grubbs second generation (G2) catalyst at elevated temperatures.⁴⁹⁴ However, the G1 catalyst only showed moderate solubility in toluene at ambient temperature and analysis *via* ¹H NMR spectroscopy showed no detectable macromonomer conversion (entry 5.16, **Figure S5.33**, **Table 5.4**). The herein presented observations considered DCM being the most suitable solvent under the applied conditions. However, the ROMP of **xNb2M12** was potentially influenced by interactions between the PMMA chain and the PNB “living” chain end which inhibits further monomer addition. It is noted that longer polymerization times were not found to have an advantageous effect on the respective ROMPs. In contrast, the ROMP of the larger PMMA-based macromonomer **xNb2M27** was found to be successful under the applied conditions, hence, other effects are suspected and are investigated in the context of further research focused on end group steric and supramolecular effects.

Despite the ROMP of **xNb2M27** being relatively controlled, a high molecular weight shoulder appeared at higher targeted DPs (e.g. entry 5.10, **Figure 5.6C**, **Table 5.2**). This behavior is undesirable in terms of polymerization control as it leads to complications in the synthesis of sequence-controlled graft copolymers. It was hypothesized that the presence of oxygen had an unfavorable effect on the ROMP process using macromonomers and the G1 catalyst. All ROMPs presented in **chapter 5.3.2** were performed at air, applying no inert conditions. According to the literature, Grubbs-type catalysts, such as the G1 catalyst, undergo poisoning in the presence of oxygen (**Scheme 5.4**).⁴⁹⁵



Scheme 5.4. Oxygen-induced poisoning of the G1 catalyst.

The herein formed monocarbonyl species has been found to exhibit catalytic activity in isomerization side reactions, favoring secondary metathesis products.⁴⁹⁵ However, it was not verified if this type of catalyst poisoning caused the observed high molecular weight shoulders in the SEC traces of entries 5.8 – 5.10 (**Figure 5.6C**, **Table 5.2**). Other decomposition pathways, leading to side reactions between polymer chains, such as cross metathesis or bimolecular coupling,⁴⁹⁶ were not excluded.

In order to eliminate the effect of oxygen on the catalyst and thus prevent the formation of undesired high molecular weight species, the ROMP of **xNb2M27** using the G1 catalyst was performed under Schlenk conditions (entry 5.17, **Table 5.5**).

Table 5.5. ROMP of **xNb2M27** using G1 catalyst under Schlenk conditions.

Entry ^a	M:I ratio	Conversion [%] ^b	M_n [g/mol] ^c	\mathcal{D}_M ^c
5.17	25:1	≥99	26,700	1.12

^aReaction conditions: **xNb2M27** (10 mmol/L) and G1 catalyst (0.4 mmol/L) in degassed DCM-d₂ at ambient temperature overnight. ^bDetermined by ¹H NMR spectroscopy. ^cDetermined by SEC.

The polymerization was performed in an NMR tube equipped with a J Young tap using degassed DCM-d₂ under argon atmosphere. The polymerization kinetics were monitored by on-line ¹H NMR spectroscopy at ambient temperature (**Figure 5.8**). It is noted that this experiment was performed by H. Garbus under my co-supervision.

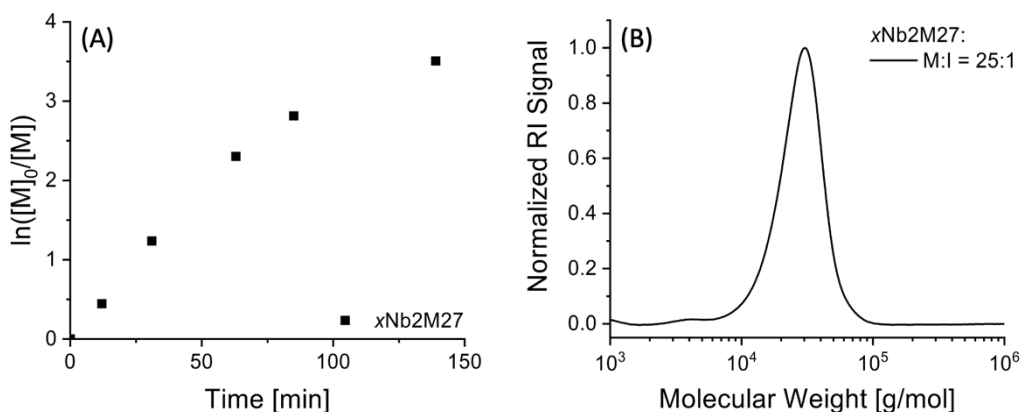


Figure 5.8. (A) Kinetic plot of the ROMP of **xNb2M27**, based on ^1H NMR spectroscopy data (**Figure S5.35**), and (B) SEC trace of the obtained graft polymer after overnight reaction.

The polymerization was performed overnight, whereby 97% macromonomer conversion was determined after 140 minutes (**Figure S5.35**). The polymerization kinetics exhibited no pseudo first order kinetic behavior and were found to be slightly skewed (**Figure 5.8A**). However, an SEC measurement exhibited a narrow molecular weight distribution ($M_n = 26,700$ g/mol; $D_M = 1.12$; **Figure 5.8B**). It is further emphasized that no high molecular weight shoulder was detectable, indicating the importance of oxygen-free conditions in ROMP. The ROMP procedure using degassed solvent and Schlenk conditions enabled high degree of polymerization control and is further used in the homo- and copolymerization of *exo* norbornene–functional macromonomers. It is noted that dry solvents were not employed, unless noted otherwise.

In order to verify the encouraging results shown above and to examine the effect of the alkane linker on the ROMP process, **xNb6M13** and **xNb2M12** were used as macromonomers and polymerized in degassed DCM under Schlenk conditions (**Table 5.6**).

Table 5.6. ROMP of macromonomers using degassed DCM and applying different M:I ratios.

Entry ^a	MM	M:I ratio	c(G1) [mmol/L]	Conversion [%] ^b	M_n [g/mol] ^c	\mathcal{D}_M^c
5.18	xNb6M13	5:1	2.00	≥99	12,100	1.13
5.19	xNb6M13	25:1	2.00	≥99	37,800	1.22
5.20	xNb2M12	25:1	0.40	66	23.900	1.44

^aReaction conditions: MM and G1 catalyst in degassed DCM at ambient temperature under argon atmosphere overnight. ^bDetermined by ¹H NMR spectroscopy. ^cDetermined by SEC.

Additional polymerization conditions, such as catalyst concentration, temperature, or reaction time, were adapted from entry 5.5 (**Table 5.6**). The obtained graft polymers were analyzed *via* SEC to determine differences in the ROMP process of **xNb6M13** compared to **xNb2M12** through the molecular weight distributions of the corresponding polymers, attributed to the longer alkane linker (**Figure 5.9A**). Therefore, the DP of the PMMA chain was similar. Furthermore, the G1 concentration in entry 5.20 was reduced compared to entries 5.5 (2 mmol/L, **Table 5.2**), 5.11 (1.33 mmol/L, **Table 5.3**), and 5.12 (1 mmol/L, **Table 5.3**) to minimize potentially unfavorable steric interactions, whereby working under Schlenk conditions was assumed to decrease catalyst poisoning in highly diluted systems.

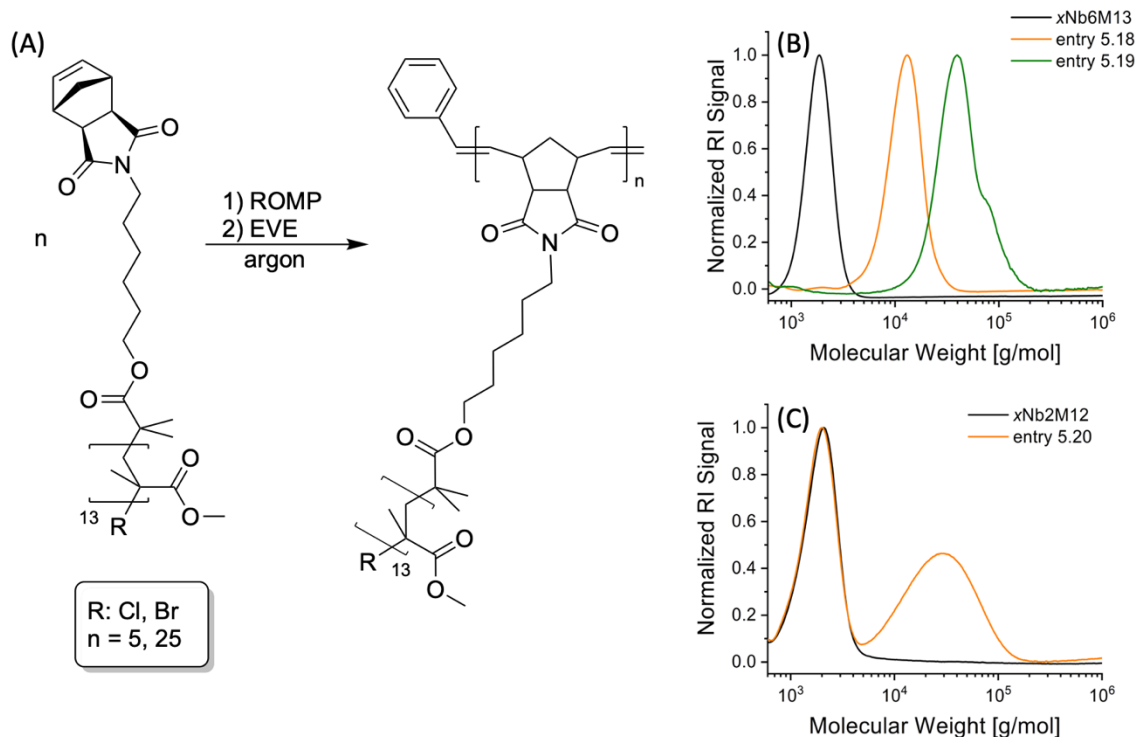


Figure 5.9. (A) Schematic ROMP of **xNb6M13** under argon atmosphere, (B) corresponding SEC traces and (C) SEC trace entry 5.20 (Table 5.6).

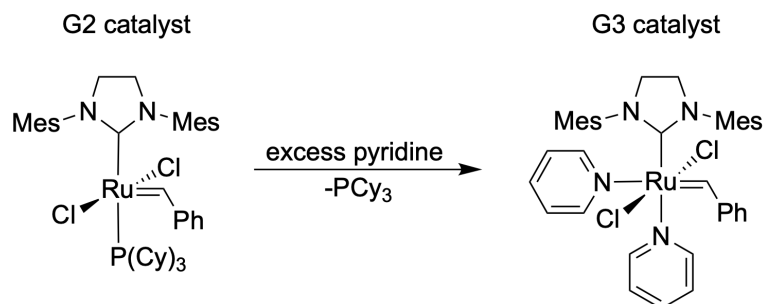
Entries 5.18 and 5.19 (Table 5.6) with M:I ratios of 5:1 and 25:1, respectively, both yielded complete macromonomer conversions (Figure S5.36), contrasting the corresponding ROMP of **xNb2M12** (entry 5.20, Figure S5.37, Table 5.6). Furthermore, the obtained graft polymers of entries 5.18 and 5.19 (Table 5.6) exhibited relatively narrow molecular weight distributions, albeit a high molecular weight shoulder was detected in entry 5.19 (Figure 5.9B). The SEC trace of entry 5.20 exhibited a broad distribution (Figure 5.9C, Table 5.6), indicating lack of polymerization control and confirming the incomplete macromonomer conversion determined by ¹H NMR spectroscopy, as the low molecular weight peak overlapped that of the macromonomer and was thus ascribed to unreacted **xNb2M12**. Overall, the polymerization process was better controlled once the distance between the polymerizable norbornene moiety and the PMMA chain was increased from ethyl to hexyl. This observation further supported the previous assumptions that the increasing loss of control in entries 5.3 – 5.5 (Table 5.2) resulted from increasing steric limitations at the propagating chain end, and catalyst poisoning induced by oxygen contamination. Since Schlenk conditions were applied, the high molecular weight shoulder detected in entry 5.19 (Table 5.6) was attributed to steric limitations, as hypothesized previously.

As a result, the structure of the macromonomer was found to influence the overall monomer conversion, as well as the molecular weight distribution of the resulting graft polymers. Here, a higher DP of the PMMA chain, and a larger distance to the polymerizable norbornene moiety had a favorable effect on the polymerization control. Furthermore, the use of degassed solvent and working under Schlenk conditions potentially decreased catalyst poisoning and thus enabled the ROMP of macromonomers at low catalyst concentrations.

5.3.3 Synthesis of graft polymers using the G3 catalyst

In the following section, the synthesis of graft polymers using the G3 catalyst is described. The polymerizability of the macromonomers synthesized in **chapter 5.3.2** is further examined *via* kinetic measurements using on-line ^1H NMR spectroscopy.

As mentioned in the previous section, steric hindrance at the propagating chain end was found to reduce the polymerization control for some macromonomers using the G1 catalyst. This behavior was hereinto considered to lead to problems during the synthesis of sequence-controlled graft copolymers, whereby higher molecular weights are desirable. The accessibility of the propagating chain end is largely defined by the used catalyst. The G1 catalyst comprises two tricyclohexyl phosphine ligands, whereas the G3 catalyst comprises an NHC ligand, as well as two pyridine ligands (**Scheme 5.3A**), exhibiting a different steric demand. It is noted that one pyridine ligand is fully dissociated in solution, leading to the highly active mono-pyridine species.³⁷⁷ Furthermore, G3 type catalysts are widely used in the ROMP of macromonomers due to their high initiation rates.^{377,406} Since the polymerization control in the ROMP of small PMMA-based macromonomers was moderate using the G1 catalyst (entries 5.3 – 5.5, **Table 5.2**, entries 5.19 and 5.20, **Table 5.6**), the G3 catalyst was rationally used to evaluate the influence of the catalyst on the accessibility of the propagating chain end. The G3 catalyst was synthesized according to the literature (**Scheme 5.5**).⁴⁹⁷



Scheme 5.5. Synthesis of the G3 catalyst by reacting the G2 catalyst with an excess of pyridine.

The G3 catalyst was synthesized from the G2 catalyst by adding an excess of pyridine (**Figure S5.38**). The following ROMPs were performed in argon-flushed ampoules using the synthesized G3 catalyst in degassed DCM at ambient temperature under argon atmosphere (**Table 5.7**), unless otherwise stated.

Table 5.7. ROMPs of **xNb2M12** using the G3 catalyst.

Entry ^a	<i>c</i> (G3) [mmol/L]	Reaction Time [h]	Conversion [%] ^b	<i>M</i> _{n,calc} [g/mol] ^c	<i>M</i> _n [g/mol] ^d	<i>D</i> _M ^d
5.21	2.00	17.6	≥99	40,000	20,500	1.18
5.22	1.00	15.6	≥99	40,000	27,400	1.21

^aReaction conditions: **xNb2M12** and G3 catalyst (M:I ratio = 25:1) in degassed DCM at ambient temperature under argon atmosphere. ^bDetermined by ¹H NMR spectroscopy. ^cCalculated by conversion. ^dDetermined by SEC.

Similar to the ROMPs mediated by the G1 catalyst, entry 5.21 (**Table 5.7**) was quenched after *ca.* 18 hours, whereby the polymerization was carried out overnight. In contrast to the corresponding ROMP of entry 5.5 (**Table 5.2**), quantitative macromonomer conversion was determined by ¹H NMR spectroscopy (**Figure S5.41**). This observation suggested that the structure of the catalyst indeed affects the accessibility of the propagating chain end during the ROMP process. SEC measurements were conducted to further examine the polymerization processes (**Figure 5.11**).

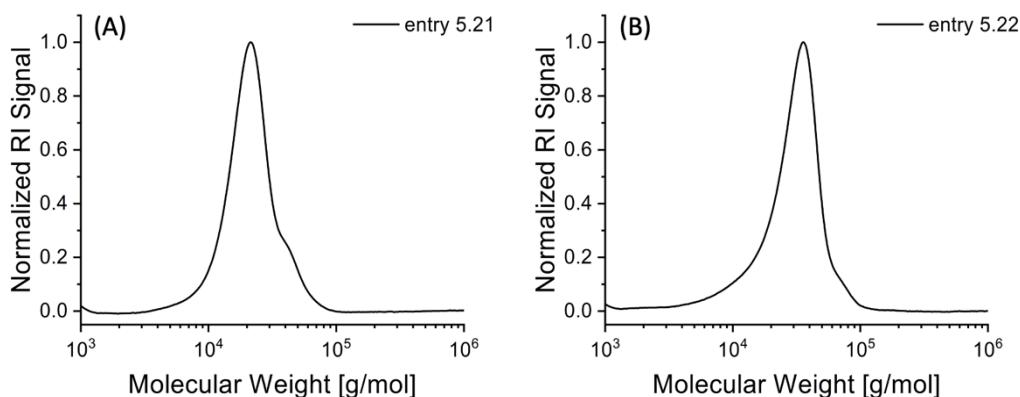


Figure 5.10. SEC traces of the graft polymers obtained by the G3-mediated ROMP of **xNb2M12**, applying catalyst concentrations of (A) 2 mmol/L (entry 5.21, **Table 5.7**) and (B) 1 mmol/L (entry 5.22, **Table 5.7**).

The SEC trace of the graft polymer exhibited a relatively narrow molecular weight distribution, although a shoulder was observed at the high molecular weight region of the distribution (**Figure 5.11A**). Nonetheless, the M_n and the dispersity of the obtained graft polymer were found to be lower compared to entry 5.20 which reached only 66% conversion and exhibited a relatively broad molecular weight distribution (**Table 5.6, Figure 5.9C**). This observation is encouraging, since the latter was synthesized at a lower catalyst concentration which is assumed to have a beneficial effect on the ROMP of macromonomers. Comparing the M_n calculated by conversion and the M_n determined by SEC (**Table 5.7**), the latter was found to be lower than expected. As mentioned in **chapter 5.3.2**, this observation was attributed to the different morphologies of the SEC calibration standards (linear PMMAs) and the measured polymer of entry 5.21 (graft, **Table 5.7**), leading to different R_h s and thus affecting the retention time and the determined molecular weight. It is assumed that the high molecular weight shoulder in entry 5.21 (**Figure 5.10A**) either resulted from unfavorable steric interactions hampering the access to the propagating chain end or from polymer-polymer coupling reactions, since the molecular weight of the highest peak ($M_p = 36,000$ g/mol) of the shoulder was found to be *ca.* twice compared to the M_p of the main distribution ($M_p = 19,700$ g/mol). However, the clear identification of the potential coupling byproduct is not possible with the applied analysis methods. In order to reduce the steric hindrance at the propagating chain end, entry 5.21 was repeated while reducing the catalyst concentration and keeping the M:I ratio the same (entry 5.22, **Table 5.7**). The polymerization was quenched after *ca.* 16 hours, whereby the ^1H NMR spectrum of entry 5.22

showed quantitative macromonomer conversion (**Figure S5.41, Table 5.7**). The corresponding SEC trace exhibited a relatively narrow molecular weight distribution and, crucially, the high molecular weight shoulder was reduced compared to that of entry 5.21 (**Figure 5.11B, Table 5.7**). The M_n of entry 5.22 was found to be higher compared to entry 5.21 which was attributed to the reduced high molecular weight shoulder, indicating a more consistent growth of the graft polymer. However, the dispersity of entry 5.22 was found to be similar to that of entry 5.21 (**Table 5.7**). This observation was explained by a low molecular weight tailing detected in the SEC trace of entry 5.22 which potentially results from catalyst poisoning during the ROMP process (**Figure 5.10B**). The large difference between the calculated and the determined M_n was further consistent with the observations made for entry 5.21 (**Table 5.7**). According to the recent literature, long polymerization times using highly active G3-type catalysts lead to undesired side reactions causing high molecular weight shoulders in the respective SEC traces.³⁹⁴ Hence, the ROMP of **xNb2M12** was subsequently monitored by on-line ^1H NMR spectroscopy to quench the polymerization immediately after complete macromonomer conversion (entry 5.23, **Table 5.8**).

Table 5.8. Kinetic measurements of G3-mediated ROMPs using different *exo* norbornene macromonomers.

Entry ^a	MM	Reaction Time [min]	Conversion [%] ^b	k_{app} [s ⁻¹] ^c	$t_{1/2}$ [min] ^d	M_n [g/mol] ^e	\mathcal{D}_M ^e
5.23	xNb2M12	28	98	2.22×10^{-3}	5.20	17,600	1.10
5.24	xNb2M27	63	97	0.83×10^{-3}	13.9	32,400	1.10
5.25	xNb2B12	32	97	2.00×10^{-3}	5.78	20,600	1.10
5.26	xNb2S20	41	98	-	-	35,300	1.15
5.27 ^f	xNb2M12	17	99	4.32×10^{-3}	2.67	26,400	1.07

^aReaction conditions: MM (10 mmol/L) and G3 catalyst (0.4 mmol/L) in degassed DCM- d_2 at ambient temperature under argon atmosphere. ^bDetermined by ^1H NMR spectroscopy. ^cCalculated from conversion using first order kinetics. ^dCalculated from the linear regression fits using $t_{1/2} = \ln(2)/k_{\text{app}}$. ^eDetermined by SEC. ^fDegassed deuterated THF as solvent.

It is noted that the following kinetic measurements were performed in argon-flushed NMR tubes equipped with a J Young tap using the G3 catalyst and degassed DCM- d_2 as solvent. The G3 catalyst concentrations were 0.40 mmol/L and the M:I ratios 25:1. The ROMP of **xNb2M12** (entry 5.23, **Table 5.8**) was started by mixing the macromonomer solution and the catalyst solution in the NMR tube, whereby the first ^1H NMR measurement was conducted after six minutes. Within these first minutes, the macromonomer conversion reached a value of 68%. The ROMP was quenched after a total reaction time of 28 minutes upon reaching a conversion of 98% (**Figure S5.42**), and thus the hypothesis that this would prevent side reactions occurring after quantitative macromonomer conversion was investigated (**Figure 5.11**). Unsurprisingly, small amounts of remaining macromonomer were detected by overlaying the SEC traces of the obtained graft polymer and the corresponding macromonomer.

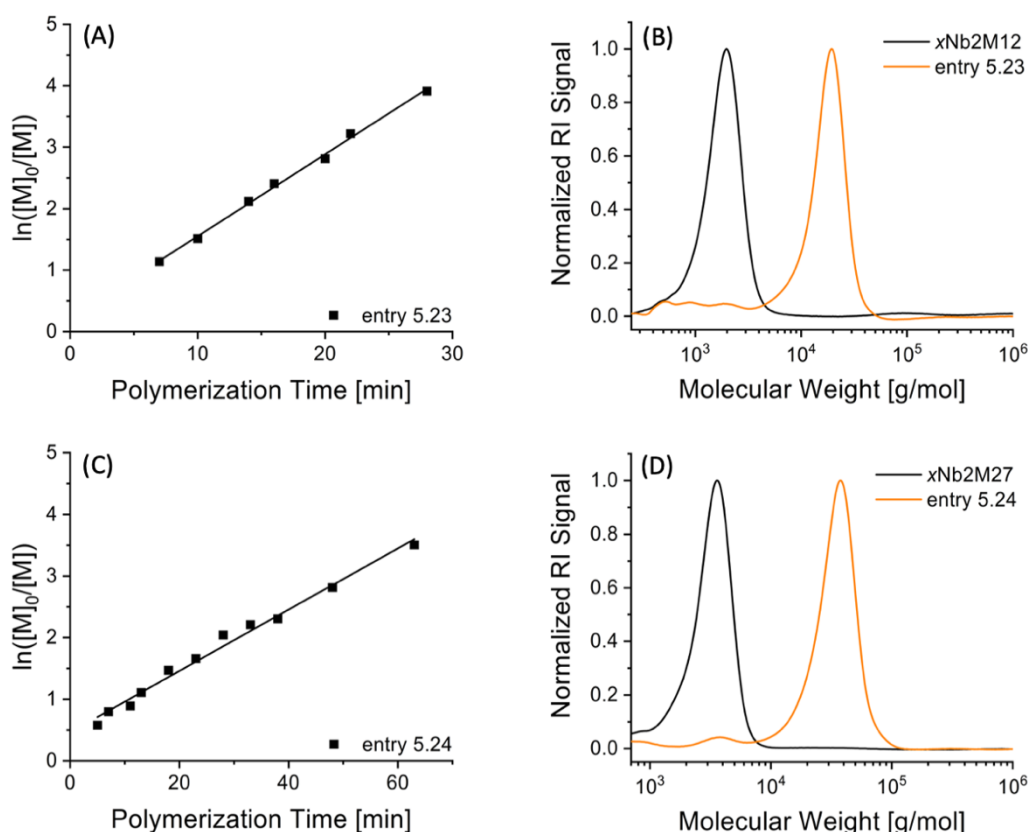


Figure 5.11. (A) Kinetic plot of the polymerization of **xNb2M12**, based on ^1H NMR spectroscopy data (**Figure S5.42**), and (B) SEC traces of **xNb2M12** and the obtained graft polymer after 30 minutes of reaction time (entry 5.23, **Table 5.8**). (C) Kinetic plot of the polymerization of **xNb2M27**, based on ^1H NMR spectroscopy data (**Figure S5.43**), and (D) SEC traces of **xNb2M27** and the obtained graft polymer after 72 minutes of reaction time (entry 5.24, **Table 5.8**). Lines represent linear fits.

The polymerization kinetics of **xNb2M12** exhibited a pseudo first order kinetic behavior (**Figure 5.11A**), whereby k_{app} was calculated from the linear regression fit as $2.22 \times 10^{-3} \text{ s}^{-1}$. The molecular weight distribution of the graft polymer obtained after 30 minutes of reaction time was narrow, neither exhibiting a detectable high molecular weight shoulder nor low molecular weight tailing, both indicating loss of polymerization control (**Figure 5.11B**). Supporting the previous hypothesis, quenching the ROMP before reaching complete macromonomer conversion ensures a controlled polymerization process and the generation of a graft polymer with a monomodal molecular weight distribution.

An identical ROMP procedure was used to polymerize **xNb2M27** (entry 5.24, **Table 5.8**), comprising the larger PMMA chain. The polymerization was quenched after 72 minutes, reaching 97% macromonomer conversion after a reaction time of 63 minutes (**Figure S5.43**). As expected, a pseudo first order kinetic behavior was observed (**Figure 5.11C**), whereby the calculated k_{app} was found to be *ca.* 2.5 times lower compared to that of **xNb2M12**. This observation was attributed to the larger PMMA attached to the *exo* norbornene moiety, since the reaction time roughly doubled while the M_n of the used macromonomer increased from 1,600 g/mol to 3,100 g/mol (**Table 5.1**). Hence, it is assumed that high molecular weight side chains slow down the ROMP. Nonetheless, the molecular weight distribution of the obtained graft polymer was narrow, indicating a high degree of polymerization control (**Figure 5.11D**). As a result, the herein performed ROMPs of the PMMA-based macromonomers **xNb2M12** and **xNb2M27** were found to be controlled, independently from the length of the PMMA chain, when quenching the ROMPs before reaching complete conversion. The M_n determined by SEC nearly doubled when the larger macromonomer was used, whereas the dispersities were identical. For both macromonomers, the M_n determined by SEC was lower than the M_n calculated by the conversion, whereby the ratio of the calculated ($M_{n,entry\ 5.23} = 39,200 \text{ g/mol}$, $M_{n,entry\ 5.24} = 75,200 \text{ g/mol}$) to the determined M_n (**Table 5.8**) was found to be similar (entry 5.23: 2.23, entry 5.24: 2.32), supporting the previously made assumption that the difference is attributed to the SEC calibration.

Due to the successfully preformed ROMPs of the PMMA-based macromonomers using the G3 catalyst, the PBnMA- and the PS-based macromonomers were similarly polymerized (entries 5.25 and 5.26, **Table 5.8**, **Figure 5.12**).

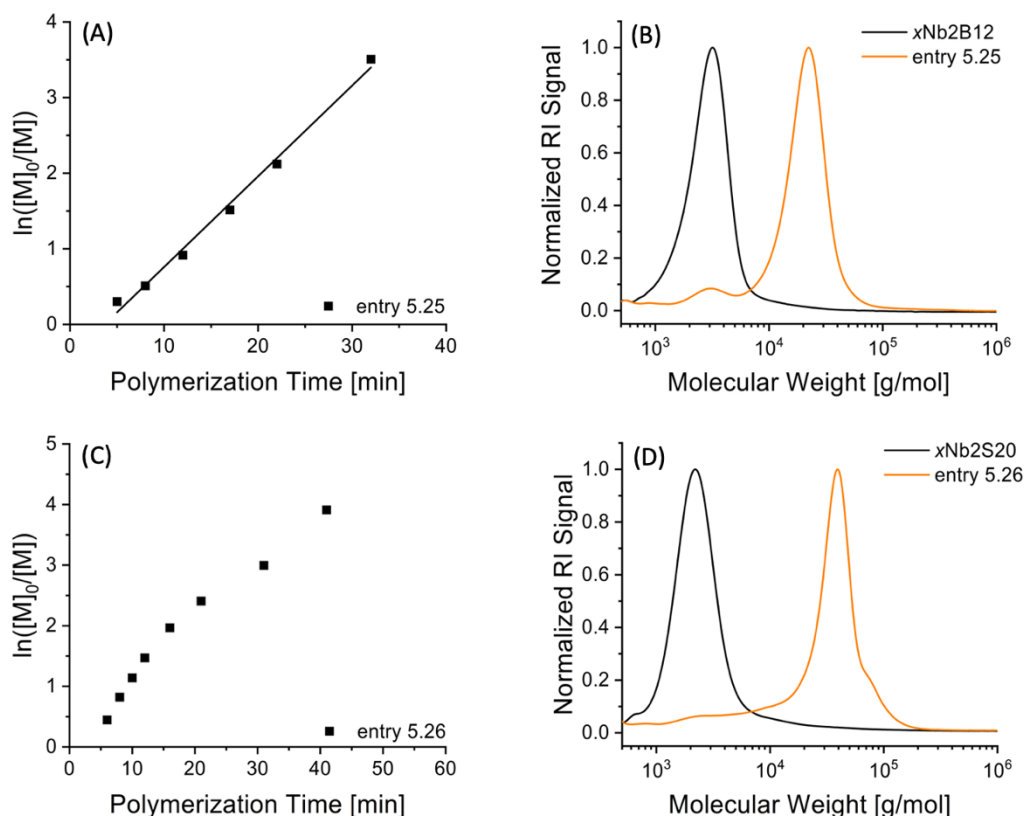


Figure 5.12. (A) Kinetic plot of the polymerization of **xNb2B12**, based on ^1H NMR spectroscopy data (Figure S5.44), and (B) SEC traces of **xNb2B12** and the obtained graft polymer after 45 minutes of reaction time (entry 5.25, Table 5.8). (C) Kinetic plot of the polymerization of **xNb2S20**, based on ^1H NMR spectroscopy data (Figure S5.45), and (D) SEC traces of **xNb2S20** and the obtained graft polymer after 49 minutes of reaction time (entry 5.26, Table 5.8). Lines represent linear fits.

Interestingly, the benzyl methacrylate-based macromonomer, **xNb2B12**, reached 97% conversion after 32 minutes (Figure 5.12A), which is comparable to the **xNb2M12** in entry 5.23 (Table 5.8), although its M_n was twice that of **xNb2M12**. The calculated k_{app} s were found to be similar. This observation suggests that methacrylate-based macromonomers show a similar behavior in the G3-mediated ROMP, whereby the polymerization rate is mainly influenced by the average DP of the polymeric side chain and not by its total molecular weight. However, this remained an assumption since no further experiments were performed to verify this observation. The obtained graft polymer exhibited a narrow molecular weight distribution after 45 minutes of reaction time (Figure 5.12B), exhibiting a similar dispersity compared to that of entries 5.23 and 5.24. The M_n determined by SEC was found to be slightly higher than that of the corresponding PMMA-based graft polymer (entry 5.23, Table 5.8),

hence, as well showing lower values compared to the M_n calculated by conversion (60,600 g/mol).

Finally, **xNb2S20** was also used as macromonomer in the G3-mediated ROMP, performing a similar kinetic measurement. ^1H NMR spectroscopy showed 98% macromonomer conversion after 41 minutes (**Figure S5.45**), however, the polymerization kinetics were found to be skewed, i.e. did not fit the previously observed pseudo first order kinetic trend (**Figure 5.12C**). Therefore, the kinetic parameters were not determined. Furthermore, the SEC trace of the graft polymer after 49 minutes reaction time was obtained. The molecular weight distribution exhibited a high molecular weight shoulder, indicating side reactions during the ROMP process (**Figure 5.12D**). As mentioned in **chapter 5.3.1**, the synthesis of PS *via* ATRP potentially leads to coupled byproducts, acting as crosslinking agents in subsequent ROMP, hence, the loss of polymerization control was attributed to the used PS-based macromonomer. Entry 5.26 was characterized by a higher M_n compared to that of the polymethacrylate-based graft polymers (entries 5.23 – 5.25, **Table 5.8**) and an increased dispersity which resulted from the bimodal distribution (**Table 5.8**, **Figure 5.12D**). Similar to the polymethacrylate-based graft polymers (entries 5.23 – 5.25, **Table 5.8**), the M_n of entry 5.26 which was determined by SEC exhibited lower values compared to the M_n calculated by conversion (51,500 g/mol). Despite the fact that the ^1H NMR spectroscopy and the MALDI-TOF data of **xNb2S20** did not indicate the presence of an α,ω -dinorbornyl species (**Figure 5.4**), PS-based macromonomers were not further used in the synthesis of sequence-controlled graft copolymers.

According to the recent literature, THF is a suitable solvent in the ROMP of macromonomers using G3-type catalysts.⁴⁰⁸ Therefore, the ability of the latter to serve as a solvent in the ROMP of **xNb2M12** was evaluated, whereby the procedure of entry 5.23 (**Table 5.8**) was adapted by using degassed deuterated THF (entry 5.27, **Figure 5.13**).

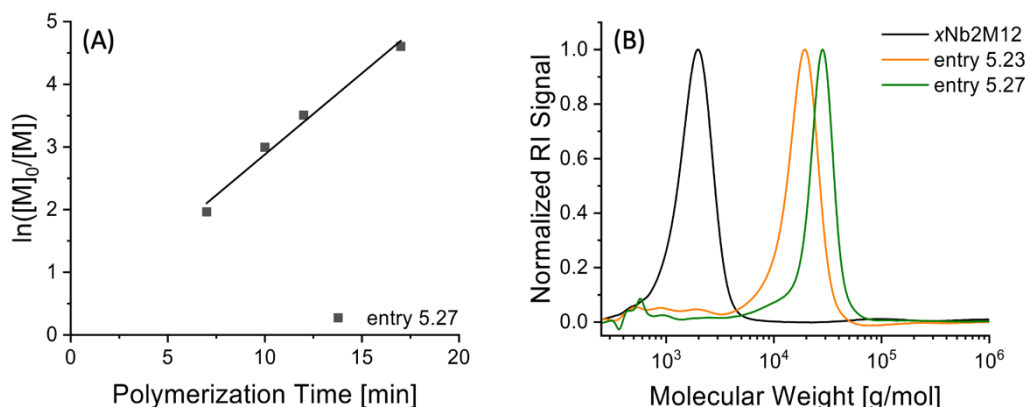


Figure 5.13. (A) Kinetic plot of the polymerization of **xNb2M12** in deuterated THF, based on ^1H NMR spectroscopy data (**Figure S5.46**), and (B) SEC traces of **xNb2M12** and comparison between the obtained graft polymers using degassed DCM-d_2 (entry 5.23, **Table 5.8**) and degassed deuterated THF (entry 5.27, **Table 5.8**) as solvent, both after 30 minutes of reaction time. Line represents linear fit.

The polymerization kinetics were monitored by on-line ^1H NMR spectroscopy, indicating 99% macromonomer conversion after 17 minutes (**Figure 5.13A**). The k_{app} was found to be double that of entry 5.23, where DCM-d_2 was used as solvent (**Table 5.8**). Due to the fast polymerization process, merely four ^1H NMR spectra were measured and thus interpretation was rather difficult. Hence, first order kinetic behavior could not be fully confirmed. A narrow molecular weight distribution was determined by SEC after 30 minutes of reaction time, whereas a small low molecular weight shoulder was detected (**Figure 5.13B**). Interestingly, the measured M_n in entry 5.27 was found to be *ca.* 10,000 g/mol higher compared to entry 5.23, both using **xNb2M12** as macromonomer and applying identical M:I ratios (**Table 5.8**). It is assumed that, during the initiation process, minimal catalyst poisoning occurred, leading to an increased M:I ratio and to a higher M_n of the resulting graft polymer. Since DCM was found to be a suitable solvent in the G3-mediated ROMP, THF was not considered further as solvent in the synthesis of sequence-controlled graft copolymers.

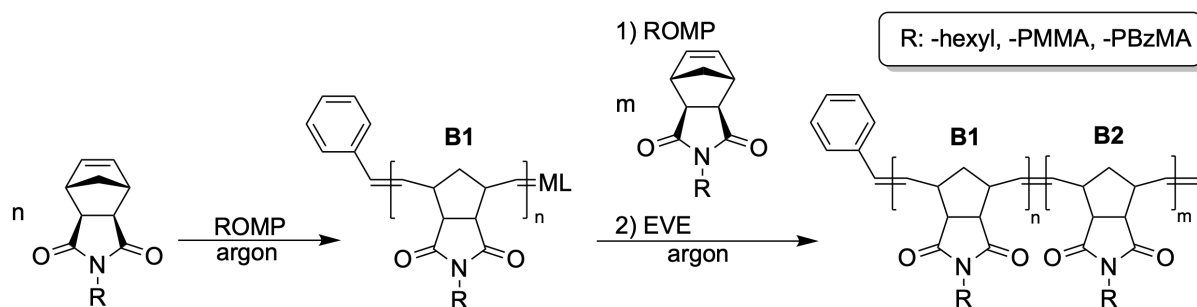
In this section, the synthesis of graft polymers *via* the G3-mediated ROMP was investigated, whereby pseudo first order kinetic behavior was determined for the ROMP of the polymethacrylate-based macromonomers. Here, narrow dispersity graft polymers were obtained which were characterized by the absence of a high molecular weight shoulder and low molecular weight tailing. Furthermore, the determined k_{app} s depended on the length of the polymer side chain, rather than on its M_n (**Table 5.8**). In contrast, the ROMP of the PS-based macromonomer did not fit the pseudo first order kinetic trend (**Figure 5.12C**),

additionally, the obtained graft polymer exhibited a bimodal molecular weight distribution, indicating the presence of side reactions (**Figure 5.12D**). Due to potential catalyst poisoning, THF was not considered further as solvent in the synthesis of sequence-controlled graft copolymers. It is noted that the G3-mediated ROMP of the PMMA- and the PBnMA-based macromonomers did not generate graft polymers with a detectable high molecular weight shoulder, indicating the absence of α,ω -dinorbornyl species.⁴⁶⁰ Hence, the respective distributions observed in the MALDI-TOF spectra of the macromonomers examined in **chapter 5.3.1** were generated during the ionization process.

5.3.4 Sequence-controlled graft copolymers

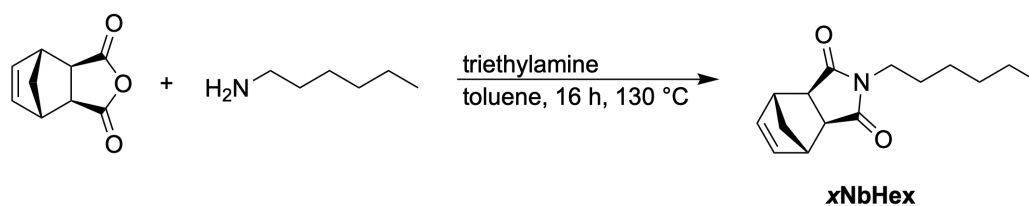
In the following section, the synthesis of sequence-controlled graft copolymers is described and optimized. An iterative copolymerization process is performed, leading to distinct monomeric sequence. Additionally, the influence of a spacer block, consisting of small monomers, on the iterative process is evaluated.

Since the G1- and the G3-mediated ROMP behavior of various macromonomers was evaluated in **chapters 5.3.2** and **5.3.3**, the synthesis of diblock graft copolymers was further examined. Therefore, an iterative procedure was applied, whereby the second monomer was added after complete consumption of the first monomer, initiating the second block (**Scheme 5.6**). ¹H NMR and SEC measurements were conducted for each block to evaluate the polymerization control and the reliability of the applied procedure. It is noted that the term “macroblock” describes the block-like sequence introduced by the addition of a macromonomer. It is further noted that the respective blocks (consisting either of small monomers or macromonomers) were abbreviated as B1 for the first block, B2 for the second block, and B3 for the third block. The structure of the resulting graft copolymer is described as di- and triblock.



Scheme 5.6. Schematic of the iterative ROMP procedure to obtain sequence-controlled graft copolymers, exhibiting a block-like structure (M: metal, L: ligand, B1: first block, B2: second block).

As shown in **chapter 5.3.2**, the homopolymerization of macromonomers using the G1 catalyst was successfully performed in degassed DCM under argon atmosphere overnight (**Figure 5.8**), whereby limitations regarding the macromonomer structures and the applied M:I ratios were observed. In order to evaluate the synthesis of a sequence-controlled diblock using an iterative procedure, a small *exo* norbornene-based monomer was synthesized according to the literature (**Scheme 5.7**).⁴⁹⁸



Scheme 5.7. Synthesis of the *exo* norbornene monomer **xNbHex** *via* condensation of *exo* norbornene anhydride with 1-aminohexane.

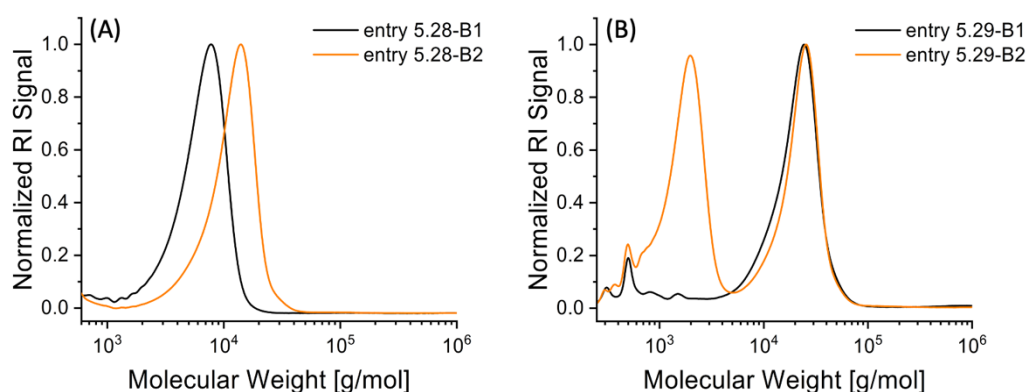
As a result, **xNbHex** was obtained as a light brown and viscous liquid in a yield of 99% (**Figure S5.47**). The following copolymerization reactions were performed using an iterative ROMP procedure, whereby the second monomers were pre-dissolved to ensure homogeneous mixing and then added to the polymerization mixture, applying an argon counterflow to prevent contamination with oxygen. In all cases, **xNbHex** and **xNb2M12** were used as the small monomer and the macromonomer, respectively (**Table 5.9**).

Table 5.9. Graft polymers synthesized using **xNbHex** and **xNb2M12** as monomers *via* an iterative ROMP procedure.

Entry ^a	Monomer	c(G1) [mmol/L]	Reaction Time [min] ^b	Conversion [%] ^c	M _n [g/mol] ^d	Đ _M ^d
5.28-B1	xNbHex	10.0	1.03	≥99	6,400	1.18
5.28-B2		5.00	2.05	≥99	11,100	1.18
5.29-B1	xNb2M12	2.00	18.2	≥99	18,500	1.23
5.29-B2		1.00	22.6	-	-	-

^aReaction conditions: Monomer and G1 catalyst (M:I ratio = 10:1 for B1 and B2) in degassed DCM at ambient temperature under argon atmosphere. ^bReaction time for each block separately. ^cDetermined by ¹H NMR spectroscopy. ^dDetermined by SEC.

In the first step and in order to examine the addition process, leading to the chain-extension of the propagating chain end, the same monomers were used for the homopolymer and the diblock, applying targeted M:I ratios of 10:1 for each block. The concentration of the repeat unit was kept constant in both blocks to prevent unfavorable steric interactions, resulting in a decreasing catalyst concentration. First, **xNbHex** was used in entry 5.28 (Table 5.9), whereby ¹H NMR spectroscopy showed complete conversion after *ca.* one hour for the homopolymer and after *ca.* two hours for the second block (Figure S5.49). SEC measurements were conducted, with special interest on the chain-extension process as visualized by the shift of the molecular weight distribution to higher values (Figure 5.14).

**Figure 5.14.** SEC traces of (A) homopolymer and diblock of entry 5.28, and (B) homopolymer and diblock of entry 5.29 (Table 5.9).

While the M_n determined by SEC increased from 6,400 g/mol to 11,100 g/mol, due to the second monomer addition, the dispersity retained a value of 1.18 (**Table 5.9**). As a result, both, the homopolymer and the diblock of entry 5.28 (**Table 5.9**) exhibited relatively narrow molecular weight distributions (**Figure 5.14A**), whereby no low molecular weight residue was detected for the diblock, therefore suggesting a successful chain-extension process. Hence, the G1-mediated iterative ROMP of **xNbHex** was found to be well-controlled. However, the M_n s determined by SEC (entry 5.28, **Table 5.9**) were higher compared to the expected M_n s calculated by conversion (entry 5.28-B1: 2,500 g/mol, entry 5.28-B1: 4,900 g/mol). In a second step, given the encouraging results from the xNbHex, entry 5.29 was performed using **xNb2M12** as macromonomer, applying a similar ROMP procedure (**Table 5.9**).

The macromonomer conversion of the homopolymer was found to be quantitative after a reaction time of *ca.* 18 hours (**Figure S5.50**), however, no conversion was detected for the second block after *ca.* 23 hours (**Table 5.9**). The SEC traces of entry 5.29 exhibited a relatively narrow molecular weight distribution for the monoblock, showing a dispersity of 1.23, and, as expected, no shift in the M_n for the attempted diblock (**Table 5.9**), while unreacted macromonomer was detected in the low molecular weight region. Since the chain-extension process was successful in the ROMP of **xNbHex** and failed in the ROMP of the macromonomer **xNb2M12**, it was assumed that the chain-extension process is influenced by steric limitations at the propagating chain end. Hence, parameters such as the structure of the repeat unit at the propagating chain end, the catalyst type, and the structure of the added second monomer were assumed to affect the chain-extension process.

In order to further examine these hypotheses, the synthesis of triblock graft copolymers was targeted, whereby **xNbHex** served as a spacer block between the two macroblocks (**Figure 5.15**), because of its smaller size and thus assuming that it facilitates the reaction of the PNB chain end and the incoming macromonomer.

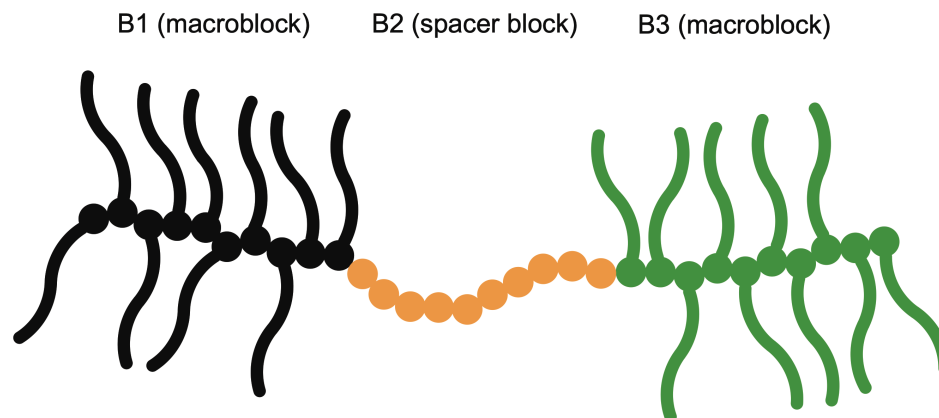


Figure 5.15. Schematic representation of a triblock graft copolymer synthesized by the iterative ROMP procedure, comprising two macroblocks (black and green) and a spacer block (orange).

The amount of **xNbHex** was varied with respect to the amount of macromonomer to determine the minimum size of the spacer block needed to ensure successful chain-extension (**Table 5.10**).

Table 5.10. Triblock graft copolymers comprising a variable spacer block synthesized applying the iterative ROMP procedure using the G1 catalyst.

Entry ^a	Monomer	M:I ratio	<i>c</i> (G1) [mmol/L]	Convers. [%] ^b	<i>M_n</i> [g/mol] ^c	<i>M_p</i> [g/mol] ^c	<i>D_M</i> ^c
5.30/31/32-B1 ^d	xNb2M12	10:1	2.00	≥99	20,600	24,200	1.15
5.30-B2	xNbHex	20:1	1.33	≥99	30,700	45,400	1.23
5.30-B3	xNb2M12	10:1	1.00	-	-	-	-
5.31-B2	xNbHex	50:1	1.33	≥99	47,300	79,800	1.33
5.31-B3	xNb2M12	10:1	1.00	-	-	-	-
5.32-B2	xNbHex	100:1	1.33	≥99	49,400	135,500	1.45
5.32-B3	xNb2M12	10:1	1.00	-	-	-	-

^aReaction conditions: Monomer and G1 catalyst in degassed DCM at ambient temperature under argon atmosphere for 14 h (B1), 3 h (B2) and 62 h (B3). ^bDetermined by ¹H NMR spectroscopy. ^cDetermined by SEC. ^dThe same homopolymer was used for all entries.

Here, **xNb2M12** was used as macromonomer in the homopolymer and the third block, applying M:I ratios of 10:1 for both blocks, whereas **xNbHex** was used as a monomer in the second block, applying M:I ratios of 20:1, 50:1, and 100:1 (entries 5.30 – 5.32, **Table 5.10**). It is noted that the homopolymer was synthesized in one big batch and was therefore the same for entries 5.30 – 5.32 (**Table 5.10**). The homopolymer reached complete macromonomer conversion after *ca.* 14 hours (**Figure S5.51**, **Table 5.10**). The latter which is the same for all three graft copolymers, exhibited a relatively narrow and symmetrical molecular weight distribution (**Figure 5.16**), exhibiting an M_n of 20,600 g/mol and a dispersity of 1.15 (**Table 5.10**). Similar to previous observations in **chapters 5.3.2** and **5.3.3**, the M_n of the graft polymer determined by SEC differed from the expected M_n calculated by conversion (16,000 g/mol).

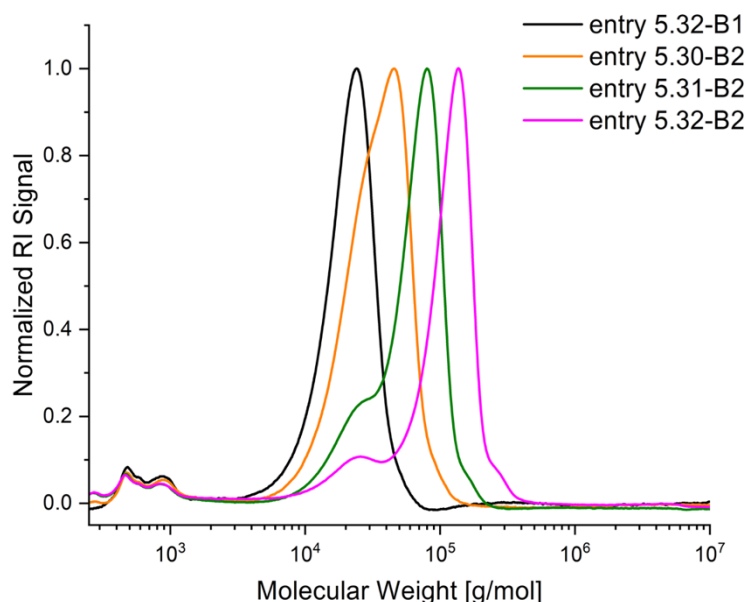


Figure 5.16. SEC traces of the homopolymer and the respective diblocks of entries 5.30 – 5.32 (**Table 5.10**).

Subsequently, the polymerization mixture was split into three and the polymer was chain-extended by adding the desired amount of pre-dissolved **xNbHex**. In all cases, ¹H NMR spectroscopy showed complete conversions after two hours. However, low molecular shoulders were detected after complete consumption of the second monomer in all cases (**Figure 5.16**), suggesting moderate chain-extension efficiency. Interestingly, the relative intensities of the low molecular weight shoulders decreased with increasing the amount of **xNbHex** added (**Figure 5.16**, **Table 5.10**). It was assumed that a higher concentration of

xNbHex increased the probability for the monomer to reach the sterically hindered propagating chain end and thus resulting in a more efficient chain-extension process. However, the interpretation of this observation was rather difficult, since the refractive indices of the graft copolymers change according to the number of **xNbHex** repeat units attached which influences the relative intensities of the not chain-extended species and chain-extended ones.⁴⁹⁹ As expected, the M_n s and the dispersities determined by SEC increased with increasing the amount of **xNbHex** added, exhibiting a maximum M_n of 49,400 g/mol and dispersity of 1.45 for entry 5.32-B2 (**Table 5.10**). Due to the increasing dispersity, M_n increases monotonically albeit in a non-linear fashion, which further demonstrates loss of polymerization control during the chain-extension process. Nonetheless, the shift of the M_p s of the diblocks ($\Delta M_p = M_{p,diblock} - M_{p,monoblock}$) was consistent with the equivalents of **xNbHex** used ($M_{n,block} = DP * M_{n,xNbHex}$), leading to ratios of 4.29 for entry 5.30, 4.50 for entry 5.31, and 4.51 for entry 5.32 (**Table 5.10**). Therefore, the second chain-extension and the generation of a third block was intended.

Finally, pre-dissolved **xNb2M12** was added to each copolymerization mixture, triggering the second chain-extension and introducing the third block. However, ¹H NMR spectroscopy indicated no detectable macromonomer conversion for entries 5.30 – 5.32 (**Figures S5.51 – S5.53, Table 5.10**). Nonetheless, SEC measurements were conducted to evaluate the, presumably, failed chain-extension process (**Figure 5.17**).

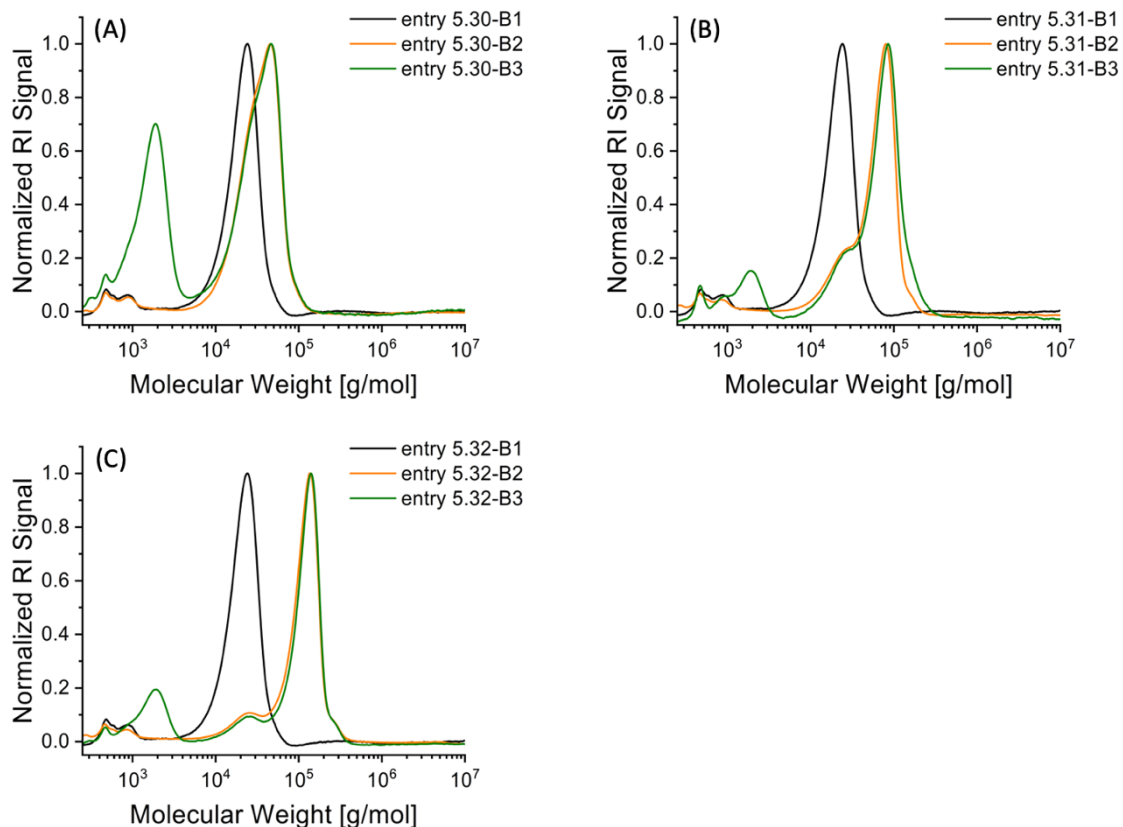


Figure 5.17. SEC traces of the graft copolymers from (A) entry 5.30, (B) entry 5.31, and (C) entry 5.32 (Table 5.10).

The SEC data further confirmed the absence of the second chain-extension, as the corresponding SEC traces comprised peaks corresponding to the unchanged diblock and unreacted $x\text{Nb}2\text{M}12$ (Figure 5.17).

The herein obtained results suggested that the controlled iterative copolymerization of macromonomers was prevented due to steric limitations at the propagating chain end, hampering the chain-extension process.

Since the G3-mediated ROMP was found to polymerize a variety of different macromonomers in a fast and controlled fashion (Chapter 5.3.3), further investigations regarding the iterative ROMP procedure using the G3 catalyst were conducted. The kinetic data of the homopolymers were used to determine the optimal addition times as to avoid potential side reactions, as previously observed in chapter 5.3.3, and successfully introduce the second blocks. Similar to the SEC traces of the kinetic measurements, signals at low molecular weights resulted from remaining macromonomer. However, such impurities are common in the relevant literature, whereby removal of the latter is rarely shown.^{406,411,460,500} The multiblock

graft copolymers were synthesized applying the optimized conditions described in **chapter 5.3.3**. Here, the small monomer **xNbHex** and the PMMA-based macromonomers **xNb2M12** and **xNb6M13** were used to examine the suitability of the G3 catalyst to mediate the iterative ROMP and obtain sequence-controlled graft copolymers (**Table 5.11**). It is noted that the ROMP procedure was performed similar to the G1-mediated approach.

Table 5.11. Multiblock graft copolymers synthesized applying the iterative ROMP procedure using the G3 catalyst.

Entry ^a	Monomer	c(G3) [mmol/L]	Reaction Time [min] ^b	Conversion [%] ^c	M_n [g/mol] ^d	\mathcal{D}_M ^d
5.33-B1	xNbHex	10.0	15	≥99	3,900	1.09
5.33-B2		6.67	15	≥99	9,400	1.07
5.34-B1	xNb2M12	1.00	36	≥99	16,300	1.09
5.34-B2	xNbHex	0.50	15	≥99	19,600	1.13
5.35-B1	xNb6M13	1.00	38	≥99	16,300	1.11
5.35-B2		0.50	61	≥99	25,000	1.23
5.36-B1	xNb6M13	1.00	52	≥99	17,000	1.12
5.36-B2 ^e	xNbHex	0.50	20	≥99	25,300	1.18
5.36-B3	xNb6M13	0.25	103	51	43,900	1.41

^aReaction conditions: Monomer and G3 catalyst (M:I ratio = 10:1 for B1, B2 and B3) in degassed DCM at ambient temperature under argon atmosphere. ^bReaction time for each block separately. ^cDetermined by ¹H NMR spectroscopy. ^dDetermined by SEC. ^eThe M:I ratio was 15:1.

The targeted M:I ratios were 10:1 for all blocks, whereas the second block (spacer block) in entry 5.36 was performed applying a targeted M:I ratio of 15:1 (**Table 5.11**). Similar to the G1-mediated iterative ROMP of **xNbHex** (entry 5.28, **Table 5.9**), the procedure using the G3 catalyst exhibited complete monomer conversion for both blocks after 15 minutes (entry 5.33, **Figure S5.54**, **Table 5.11**). The M_n s determined by SEC were slightly higher compared to the expected M_n s calculated by conversion (e.g. $\Delta M_{n, \text{entry 5.33-B1}} = 1,400$ g/mol, **Table 5.11**), however, the difference was smaller than that of entry 5.28 (e.g. $\Delta M_{n, \text{entry 5.28-B1}} = 3,900$ g/mol, **Table 5.9**). The SEC traces of the homopolymer and the diblock

exhibited narrow molecular weight distributions, while no low molecular weight shoulders were detected, suggesting successful chain-extension (**Figure 5.18A**). Furthermore, the dispersity decreased after the chain-extension, whereby the diblock exhibited an M_n of 9,400 g/mol and a dispersity of 1.07 (**Table 5.11**).

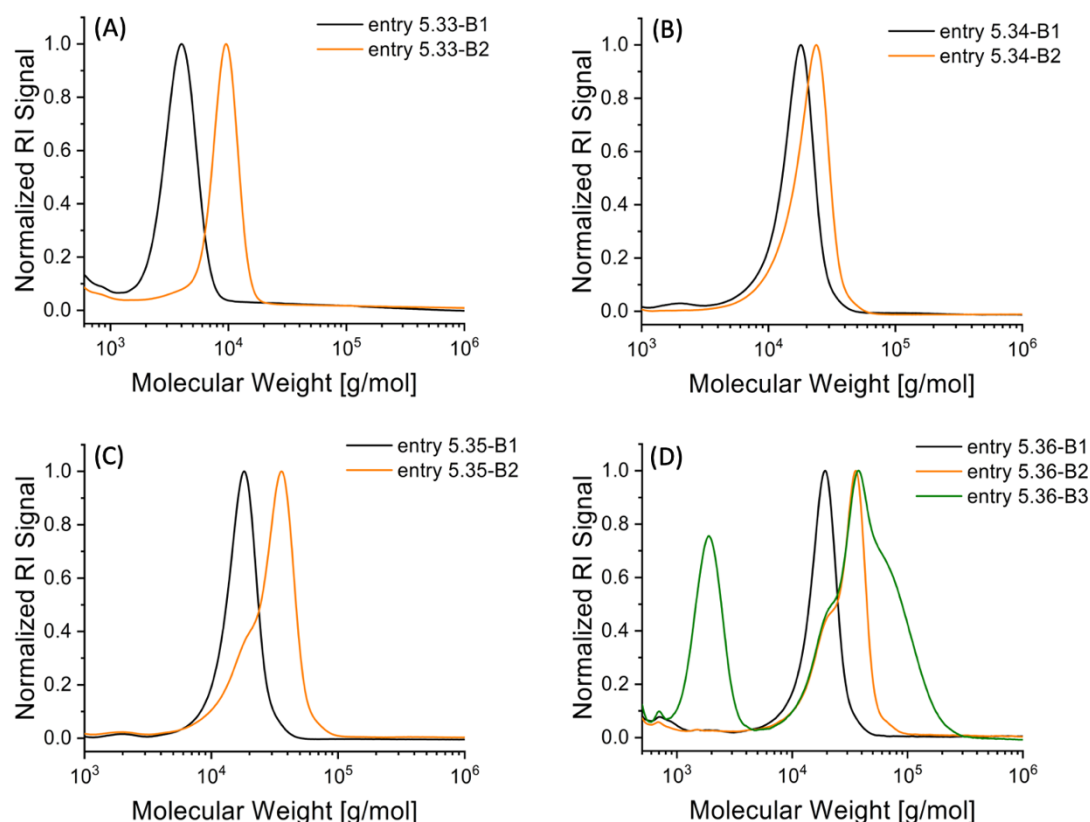


Figure 5.18. SEC traces of the homopolymers and the (A) diblock graft copolymers from entry 5.33, (B) entry 5.34, and (C) entry 5.35, and (D) of the triblock graft copolymer from entry 5.36 (**Table 5.11**).

In order to further examine the chain-extension using **xNbHex** in the G3-mediated ROMP, **xNb2M12** was used to synthesize a homopolymer which was then chain-extended using **xNbHex** (entry 5.34, **Table 5.11**). Complete conversion was determined for the macromonomer after 36 minutes and for **xNbHex** after 15 minutes (**Figure S5.55**, **Table 5.11**). Furthermore, the SEC traces exhibited narrow molecular weight distributions for the homopolymer and the diblock, while no low molecular weight shoulders were detected. However, since the dispersity slightly increased after the chain-extension (from 1.09 to 1.13), which was attributed to a more unsymmetrical distribution, and the molecular weight difference between the homopolymer and the diblock was rather small ($\Delta M_n = 3,300$ g/mol, **Table 5.11**), a solid evaluation of the chain-extension efficiency in entry 5.34 was not possible.

In order to examine the chain-extension process using macromonomers for both, the homopolymer and the diblock, **xNb6M13** (**Table 5.1**) was used in entry 5.35 due to its larger alkyl linker which was assumed to reduce the steric limitations during the chain-extension process. In contrast to the G1-mediated iterative ROMP, the latter was found to be successful using macromonomers for both blocks, reaching complete conversions after 38 minutes and 61 minutes, respectively (**Figure S5.56**, **Table 5.11**). The SEC trace of the homopolymer exhibited a narrow and symmetrical molecular weight distribution (**Figure 5.18C**), whereby the herein determined M_n (16,300 g/mol, **Table 5.11**) was found to be comparable to the expected M_n calculated by conversion (17,000 g/mol). However, the SEC trace of the diblock (entry 5.35-B2, **Figure 5.18C**), exhibited a low molecular weight shoulder that was ascribed to the unreacted homopolymer. As expected, the M_n increased after the chain-extension (**Table 5.11**), exhibiting a maximum of 25,000 g/mol which is lower than the expected M_n calculated by conversion (34,000 g/mol). Furthermore, the dispersity increased after the chain-extension (from 1.11 to 1.23), which was attributed to the bimodal distribution (**Figure 5.18C**). As a result, the larger alkyl linker had no favorable influence of the chain-extension process, either due to persistent steric limitations or potential catalyst poisoning.

In order to further examine these hypotheses, a triblock graft copolymer was synthesized using **xNb6M13** as macromonomer and **xNbHex** as small monomer, whereby the two macroblocks were separated by the spacer block (entry 5.36, **Table 5.11**). ^1H NMR spectroscopy showed complete conversion for the first two blocks after 52 minutes and 20 minutes, respectively, whereas the third block only reached 51% macromonomer conversion after 103 minutes (**Figure S5.57**, **Table 5.11**). It is noted that a longer reaction time did not lead to an increasing macromonomer conversion, thus the third block reached a maximum of 51%. Similar to the SEC trace of entry 5.35-B1 (**Figure 5.18C**), the SEC trace of the homopolymer exhibited a narrow and symmetrical molecular weight distribution (**Figure 5.18D**), whereby the M_n (17,000 g/mol, **Table 5.11**) was the same as the expected M_n calculated by conversion (17,000 g/mol). Chain-extension of the homopolymer with 15 equivalents **xNbHex** facilitated an M_n difference of 8,300 g/mol (**Table 5.11**), large enough to detect a potentially forming low molecular weight shoulder and thus indicating inefficient chain-extension. The SEC trace of the diblock was similar to that of entry 5.35-B2 (**Figure 5.18C** and **Figure 5.18D**), exhibiting a low molecular weight shoulder and thus an increasing

dispersity (from 1.12 to 1.18, **Table 5.11**). Nonetheless, a second chain-extension was induced by adding **xNb6M13** to the reaction mixture. Interestingly, the SEC trace of the third block exhibited two low molecular weight shoulders that were assigned to the homopolymer and the diblock (**Figure 5.18D**), whereby the latter represented the main distribution and thus indicated a massive loss of efficiency during the second chain-extension. Here, the M_n (43,900 g/mol, **Table 5.11**) was higher than the expected M_n calculated by conversion (29,400 g/mol). Resulting from the trimodal distribution, the dispersity increased from 1.18 to 1.41 after the second chain-extension. Additionally, the SEC trace of entry 5.36-B3 confirmed the incomplete macromonomer conversion which was previously indicated by ^1H NMR spectroscopy (**Figure S5.57, Table 5.10**) and represented by a distinct distribution in the low molecular weight region (**Figure 5.18D**).

Since persistent steric limitations were assumed to be unlikely, while applying a sterically less demanding macromonomer, such as **xNb6M13**, and an additional spacer block between the macroblocks, it is herein hypothesized that catalyst poisoning occurred during the chains-extension steps, ultimately leading to the multimodal molecular weight distributions. However, the unfavorable influence of potential steric interactions between the propagating chain end and the added macromonomer, hampering successful chain-extension, cannot be fully excluded.

In order to examine the chain-extension process in the G3-mediated iterative ROMP, the polymerization kinetics were monitored after the addition of the second macromonomer (**Table 5.12**).

Table 5.12. Multiblock graft copolymers synthesized applying the iterative ROMP procedure using the G3 catalyst.

Entry ^a	Monomer	$c(\text{G3})$ [mmol/L]	Reaction Time [min] ^b	Conversion [%] ^c	M_n [g/mol] ^d	\mathcal{D}_M^d
5.37-B1	xNb2M12	0.33	34	97	30,500	1.12
5.37-B2	xNb2B12	0.28	48	97	50,500	1.32

^aReaction conditions: MM and G3 catalyst (M:I ratio = 30:1 for B1 and B2) in degassed DCM- d_2 at ambient temperature under argon atmosphere. ^bReaction time for each block separately. ^cDetermined by ^1H NMR spectroscopy. ^dDetermined by SEC.

Here, **xNb2M12** and **xNb2B12** were used as macromonomers, whereby the ROMP of the former was performed in an argon-flushed ampoule, while the chain-extension using **xNb2B12** was performed in an argon-flushed NMR tube, both equipped with a J Young tap (entry 5.37, **Table 5.12**). The M:I ratios were 30:1 for each block, applying a catalyst concentration of 0.33 mmol/L for the homopolymer and 0.28 mmol/L for the diblock (**Figure 5.19**). It is noted that the previously determined homopolymerization kinetics of **xNb2M12** (entry 5.23, **Table 5.8**) were used to anticipate a suitable addition time for the second macromonomer, inducing the chain-extension.

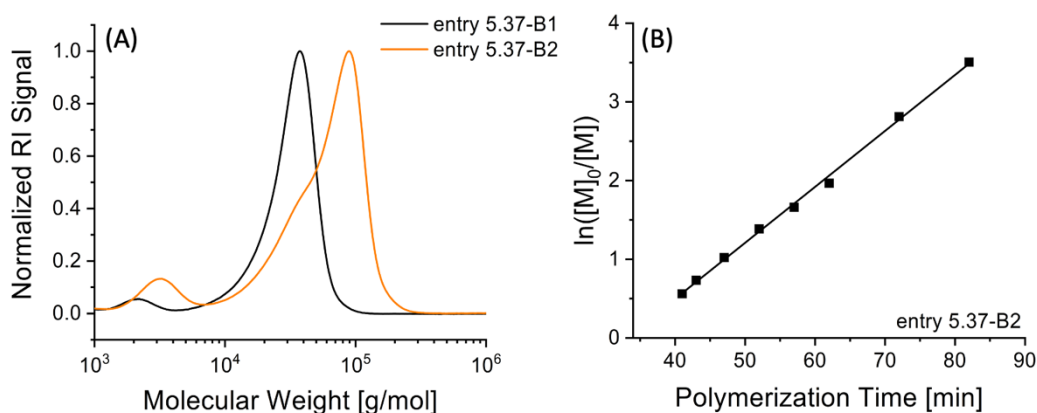


Figure 5.19. (A) SEC traces of the obtained homopolymer after 34 minutes of reaction time and the diblock after 65 minutes of reaction time and (B) kinetic plot of the copolymerization of **xNb2B12**, based on ¹H NMR spectroscopy data (**Figure S5.58**, **Table 5.12**). Line represents linear fit.

After 34 minutes of reaction time, a defined amount of the homopolymer solution was transferred to the NMR which was loaded with pre-dissolved **xNb2B12**, inducing the chain-extension process. The homopolymerization mixture was immediately quenched by adding an excess of EVE. As expected, ¹H NMR spectroscopy showed 97% conversion of **xNb2M12** (**Figure S5.58**, **Table 5.12**). The SEC trace of the homopolymer exhibited a narrow molecular weight distribution and, confirming the incomplete conversion determined by ¹H NMR spectroscopy, a small distribution in the low molecular weight region which was ascribed to unreacted **xNb2M12** (**Figure 5.19A**). As expected for **xNb2M12**-derived graft polymers, the M_n determined by SEC (30,500 g/mol, **Table 5.12**) was lower than the expected M_n calculated by conversion (46,600 g/mol). The diblock reached 97% macromonomer conversion after 41 minutes (**Figure S5.58**, **Table 5.12**), exhibiting a pseudo first order kinetic

behavior (**Figure 5.19B**). The k_{app} was calculated as $1.19 \times 10^{-3} \text{ s}^{-1}$, comparable to that of entry 5.25 ($k_{app} = 2.00 \times 10^{-3}$, **Table 5.8**), whereas the discrepancy between the latter was attributed to the lower catalyst concentration (entry 5.25: 0.40 mmol/L, **Table 5.8**, entry 5.37-B2: 0.28 mmol/L, **Table 5.12**). However, the SEC trace of the diblock exhibited a low molecular weight shoulder which was ascribed to not chain-extended homopolymer, whereas the small distribution in the low molecular weight region was ascribed to unreacted **xNb2B12** (**Figure 5.19A**). The dispersity increased from 1.18 to 1.41 after the second chain-extension (**Table 5.12**). Furthermore, the M_n determined by SEC (50,500 g/mol, **Table 5.11**) was lower than the expected M_n calculated by conversion (119,300 g/mol). As observed in the homopolymerization of **xNb2B12** (entry 5.25, **Table 5.8**), the discrepancy between the determined and the expected M_n is high when the latter is used, potentially caused by the different architecture (graft) and the different side groups (benzyl) compared to the SEC calibration standards (linear PMMAs). Interestingly, the polymerization kinetics were not affected by the incomplete chain-extension, indicating that the latter is not crucially caused by unfavorable steric interactions between the propagating chain end and the macromonomer. Moreover, the pseudo first order kinetic behavior indicated that the error had occurred before the first ^1H NMR measurement. This observation supported the previous hypothesis that catalyst poisoning occurred during the chain-extension process, leading to the presence of unreacted blocks in the corresponding SEC traces.

In the literature, the synthesis of sequence-controlled graft copolymers using G3-type catalysts, e.g. in the successful synthesis of block-like structures, is mainly performed using glovebox conditions.⁴⁰⁶ Furthermore, recent studies suggested that even low concentrations of water cause catalyst poisoning, whereby fast-initiating examples were most affected.⁵⁰¹ In order to minimize catalyst poisoning during the chain-extension process and evaluate the influence of moisture, iterative ROMPs were performed using dry solvents and low temperatures (**Table 5.13**). Here, gas-tight glass syringes and reusable metal needles were used to handle the reagents under argon atmosphere, avoiding contamination with oxygen and other potential contaminants. Prior to the ROMP, the metal needles and the used glassware were dried in a vacuum oven at elevated temperature overnight to remove moisture. Before dissolving, the catalyst and the macromonomers were added to argon-flushed ampoules and dried under high vacuum overnight.

Table 5.13. The G3-mediated iterative ROMP of PMMA- and PBnMA-based macromonomers using dry solvents and low temperatures.

Entry ^a	MM	c(G3) [mmol/L]	T [°C]	Reaction Time [h] ^b	Conver. [%] ^c	M _n [g/mol] ^d	Đ _M ^d
5.38-B1	xNb2M12	0.33	r.t.	0.42	97	40.700	1.04
5.38-B2	xNb2B12	0.17		1.00	89	74.000	1.22
5.39-B1	xNb2B12	1.00	-15	53.9	93	19,900	1.10
5.39-B2	xNb2M12	0.50		65.3	94	29,400	1.10

^aReaction conditions: MM and G3 catalyst (M:I ratio = 30:1 for B1 and B2 for entry 5.38; M:I ratio = 10:1 for B1 and B2 for entry 5.39) in degassed dry DCM under argon atmosphere.

^bReaction time for each block separately. ^cDetermined by ¹H NMR spectroscopy. ^dDetermined by SEC.

Commercially available anhydrous DCM was used in both iterative ROMPs, whereby **xNb2M12** and **xNb2B12** were used as macromonomers, applying M:I ratios of 30:1 and 10:1 (entries 5.38 and 5.39, **Table 5.13**) for the homopolymer and the diblock, respectively. The ROMP procedure for entry 5.38 (**Table 5.13**) was adapted from entry 5.37 (**Table 5.12**) to compare the influence of moisture on the chain-extension process, whereas the ROMP of entry 5.39 was additionally performed at -15 °C, using a cryostat (**Table 5.13**). Entry 5.38 exhibited 97% conversion of the first macromonomer after 25 minutes (**Figure S5.59**, **Table 5.13**). The SEC trace of the obtained homopolymer exhibited a narrow and highly symmetrical molecular weight distribution (**Figure 5.20A**). It is noted that the dispersity of 1.04 determined for the homopolymer was the lowest value achieved within this work (**Table 5.13**).

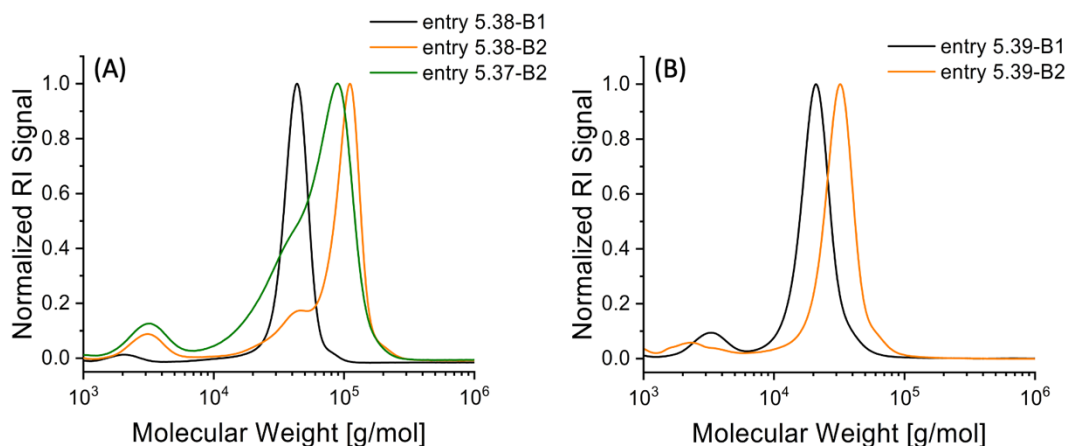


Figure 5.20. SEC traces of the homopolymers and the diblocks from (A) entry 5.38, compared with the diblock of entry 5.37, and (B) entry 5.39 (Table 5.13).

Since the ROMP was quenched before reaching complete conversion and thus preventing side reactions, a small distribution in the low molecular weight region was detected which was ascribed to unreacted **xNb2M12** (Figure 5.20A). As expected for **xNb2M12**-derived graft polymers, the M_n determined by SEC (40,700 g/mol, Table 5.13) was lower than the expected M_n calculated by conversion (46,600 g/mol). Due to the low dispersity, the molecular weight difference was considerably lower for entry 5.38-1 ($\Delta M_n = 5,300$ g/mol, Table 5.13) than for entry 5.37-B1 ($\Delta M_n = 16,100$ g/mol, Table 5.12). After the chain-extension was induced by adding **xNb2B12** as second macromonomer, 89% conversion was reached after one hour reaction time (Figure S5.59, Table 5.13). It is noted that the previously determined homopolymerization kinetics of **xNb2M12** (entry 5.23, Table 5.8) and the copolymerization kinetics of **xNb2B12** (entry 5.37-B2, Table 5.12) were used to anticipate a suitable addition time for the second macromonomer and for quenching the ROMP. The relatively low macromonomers conversion during the copolymerization was attributed to early quenching of the ROMP due to the lower catalyst concentration (entry 5.37-B2: 0.28 mmol/L, Table 5.12, entry 5.38-B2: 0.17 mmol/L, Table 5.13). Therefore, the small distribution detected in the low molecular weight region was ascribed to unreacted **xNb2B12** (Figure 5.20A). However, the latter did not interfere with the distribution of the graft copolymer or a potentially present low molecular weight shoulder and was thus not considered as an issue toward the interpretation of the SEC data. The SEC trace of the diblock exhibited a small low molecular weight shoulder (entry 5.38-B2, Figure 5.20A), indicating catalyst poisoning during the chain-extension. However, the comparison of the second blocks of entries 5.37 and 5.38

indicated a lower amount of unreacted homopolymer present in the latter (**Figure 5.20A**, **Table 5.13**), suggesting less catalyst poisoning. Additionally, the main distribution, representing the diblock graft copolymer, was found to be narrow and relatively symmetrical, exhibiting a dispersity of 1.22 (**Table 5.13**). Hence, for entry 5.38 (**Table 5.13**), a relatively controlled chain-growth and a good chain-extension efficiency was observed, contrasting the previous reaction (entry 5.37, **Table 5.12**) which was characterized by a broad distribution and a prominent low molecular weight shoulder (**Figure 5.20A**). Due to the relatively low dispersity, the molecular weight difference between the determined and the expected M_n s (entry 5.37-B2: 119,300 g/mol, entry 5.38-B2: 113,000 g/mol) was considerably lower for entry 5.38-B2 ($\Delta M_n = 39,000$ g/mol) than for entry 5.37-B2 ($\Delta M_n = 68,800$ g/mol). However, as discussed for entry 5.37-B2 (**Table 5.12**), the present discrepancy was attributed to the use of **xNb2B12** as second macromonomer. Since the preparative procedure by using basic Schlenk conditions was optimized, it was assumed that the commercially available anhydrous DCM still contained traces of water, hampering the chain-extension process.

In order to decrease the rate of catalyst poisoning, entry 5.39 was performed at -15 °C (**Table 5.13**). Therefore, the polymerization rate decreased, reaching 93% conversion of the first macromonomer after *ca.* 54 hours (**Figure S5.60**). As expected, the SEC trace of the macromonomer exhibited a narrow and symmetrical molecular weight distribution (**Figure 5.20B**), whereby unreacted **xNb2B12** was still present. As expected for **xNb2B12**-derived graft polymers, the M_n determined by SEC (19,900 g/mol, **Table 5.13**) was lower than the expected M_n calculated by conversion (23,300 g/mol). The chain-extension was induced by the addition of pre-dissolved and pre-cooled **xNb2B12** to the reaction mixture. The diblock exhibited 94% macromonomer conversion after an additional 65 hours (**Figure S5.60**). Interestingly, the SEC trace exhibited a narrow and symmetrical molecular weight distribution (**Figure 5.20B**), characterized by the absence of a low molecular weight shoulder. Furthermore, the determined dispersity retained at a value of 1.10 (**Table 5.13**). Here, the determined M_n (29,400 g/mol, **Table 5.13**) was lower compared to the expected M_n (38,300 g/mol) and is thus consistent with previous observations. The SEC data further indicated a high degree of polymerization control and a high chain-extension efficiency (**Figure 5.20B**). These observations supported the previous assumption that the bimodal distribution, appearing after chain-extension with a new macromonomer block, was caused by catalyst poisoning.

However, the correlation between the chain-extension efficiency, the temperature, and the amount of water present are not part of this work, albeit offering a possibility for future examinations toward the herein observed effects.

In the G3-mediated ROMP, the chain-extension was mainly affected by catalyst poisoning during the addition of the second macromonomer, potentially induced by traces of water within the reaction mixture. Incomplete chain-extension further led to the presence of unreacted homopolymers. Here, the use of dry solvents and performing the ROMP at a low temperature reduced this phenomenon. Additionally, no steric limitations were found when using the G3-mediated ROMP, potentially hampering a successful chain-extension process. However, unfavorable steric effect cannot be fully excluded, especially when high molecular weight polymers are used as macromonomers. In contrast, the G1-mediated synthesis of sequence-controlled graft copolymers in an iterative fashion was found to be strongly influenced by steric interactions between the propagating chain end and the macromonomers. The use of sterically less demanding monomers and the introduction of a variable spacer block located between the macroblocks led to an increasing chain-extension efficiency and thus to a higher degree of polymerization control. Furthermore, it has been found that traces of contaminants had no detectable effect on the catalyst poisoning in G1-mediated ROMP, and thus on the chain-extension process. Here, the latter was successfully demonstrated in the ROMP of a small monomer.

As a result, the synthesis of sequence-controlled graft copolymers was successfully performed applying an iterative ROMP procedure using the G3 catalyst. It was possible to synthesize a precisely grafted diblock-like copolymer from two different macromonomers, whereby the ROMP was characterized by a high degree of polymerization control, indicated by a narrow and symmetrical molecular weight distribution and by a high chain-extension efficiency.

5.3.5 Janus copolymers

Parts of this subchapter contain results that have already been published,⁵⁰² and that are currently part of a manuscript in preparation:

M. Jäger, *Bachelor thesis*, KIT **2022**.

The author conducted the planning and the final evaluation of the experiments performed by M. Jäger (Bachelor thesis under my supervision).

In the following section, the synthesis of a bifunctional macromonomer and its subsequent ROMP using the G3 catalyst is described, obtaining graft copolymers. Here, the P-3CR is used to connect a polymerizable *exo* norbornene unit with two different polymeric chains which are synthesized *via* ATRP.

Since the controlled synthesis of graft copolymers using the G3 catalyst was complicated due to its poisoning during the chain-extension process, the block-like structure was redesigned to be attained as bifunctional macromonomers. The macromonomer, thus, comprised two different polymeric chains coupled onto an *exo* norbornene moiety, capable of polymerizing *via* ROMP. Therefore, sensitive chain-extension processes were no longer required to obtain graft copolymers with characteristics that would allow nanostructuring, e.g. through self-assembling.⁴⁸⁷ The obtained bottlebrush copolymers were thus termed as “Janus” copolymers (**Figure 5.21**), named after the two-faced Roman god Janus.⁵⁰³

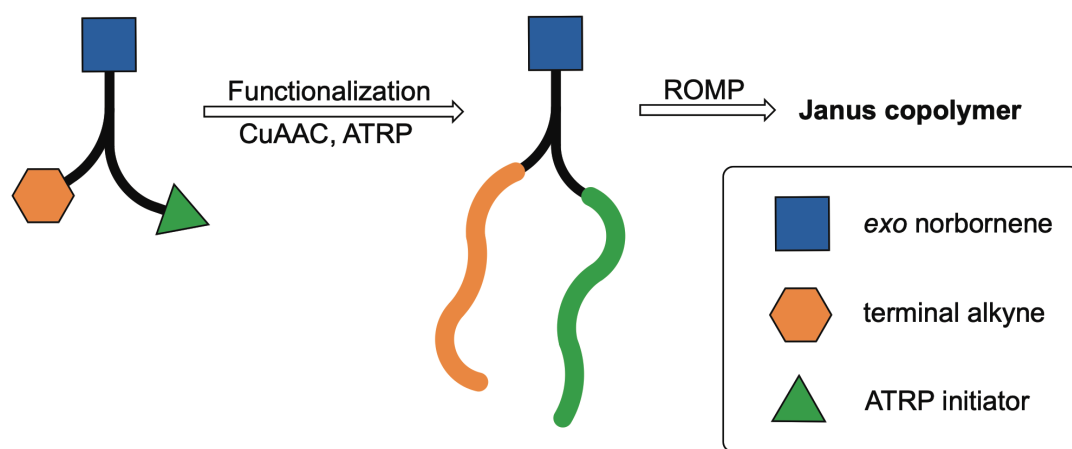
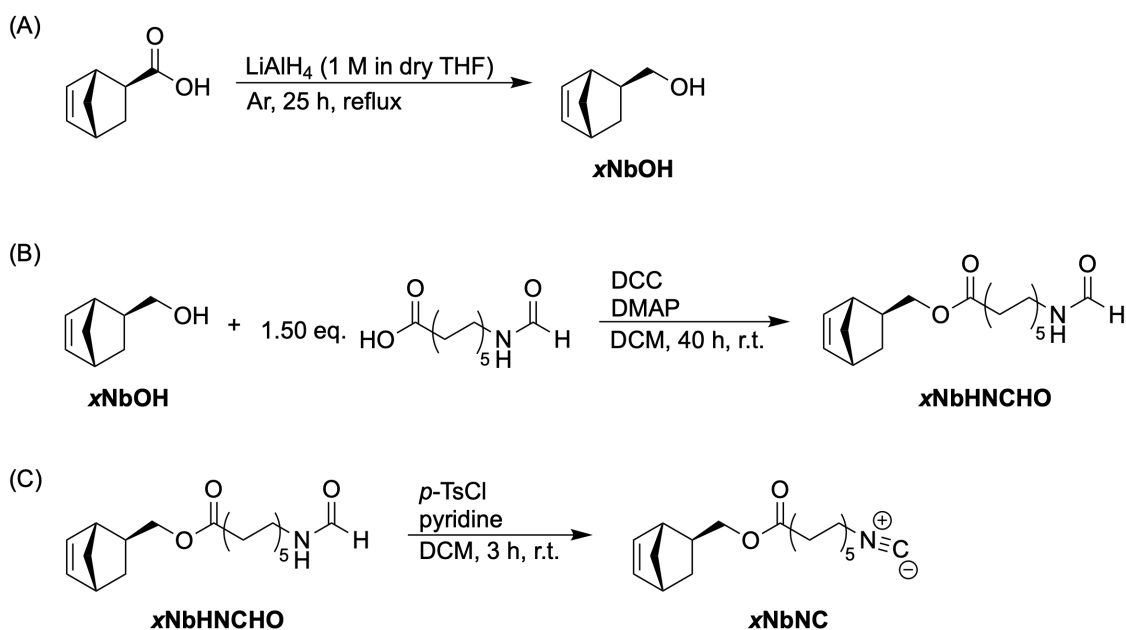


Figure 5.21. Schematic representation of the synthesis of Janus copolymers *via* the functionalization of a bifunctional precursor, using copper-catalyzed alkyne-azide cycloaddition (CuAAC) and ATRP, and subsequent ROMP.

As presented in **chapter 4.3**, the application of the P-3CR in the synthesis of bifunctional norbornene-based monomers was found to be versatile and robust. Subsequent ROMP using the G1 catalyst led to highly diverse and multifunctional polymers and copolymers. Targeted selection of the participating components was herein essential to achieve selective functionalization with a high end group fidelity. 2-Bromo-2-methylpropionic acid was used as carboxylic acid component due to its commercial availability and the introduction of a potent ATRP initiator unit. Furthermore, 4-TMS-ethynyl-benzaldehyde was used as the oxo-component, introducing a trimethylsilyl (TMS)-protected alkyne, capable of copper-catalyzed alkyne-azide cycloaddition (CuAAC) after deprotection.⁵⁰⁴ The *exo* norbornene was further used as the isocyanide component, whereby a three-step synthesis was performed (**Scheme 5.8**). It is noted that 4-TMS-ethynyl-benzaldehyde and 11-formamidoundecanoic acid were generous gifts provided by D. Hahn and K. Waibel, respectively.

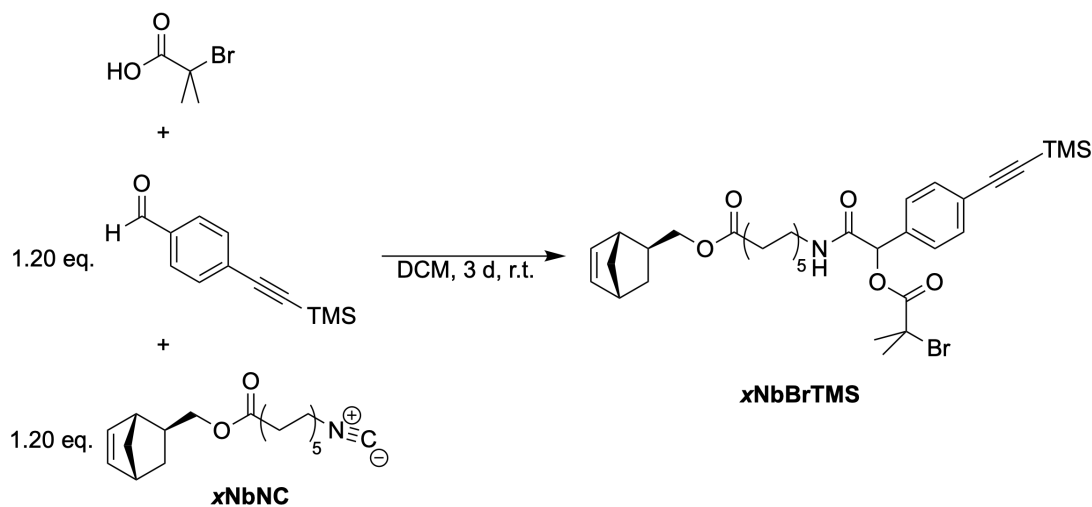


Scheme 5.8. Synthesis of (A) **xNbOH** *via* reduction of *exo* norbornene carboxylic acid using LiAlH_4 , (B) Steglich esterification using 11-formamidoundecanoic acid, obtaining **xNbHNCHO**, and (C) subsequent dehydration reaction using *p*-TsCl, obtaining the *exo* norbornene-functional isocyanide **xNbNC**.

In the synthesis of the norbornene-functional isocyanide, *exo*-5-norbornene-2-carboxylic acid was used as precursor due to its suitability in the ROMP of sterically demanding monomers when targeting high bottlebrush backbone DPs.⁵⁰⁵ In the first step, the carboxylic acid functionality was reduced with lithium aluminum hydride to obtain

exo-5-norbornene-2-methanol (**xNbOH**).⁴⁶⁴ The desired product was obtained as a colorless liquid in a yield of 86% (**Figure S5.61**). In the next step, **xNbOH** and an excess of 11-formamidoundecanoic acid were reacted *via* a Steglich esterification, using *N,N'*-dicyclohexylcarbodiimide (DCC) and DMAP (**Scheme 5.8B**). Hereby, the norbornene-functional formamide **xNbHNCHO** was obtained as a white waxy solid in a yield of 84% (**Figure S5.63**). Finally, the formamide functionality was dehydrated using *p*-toluenesulfonyl chloride (*p*-TsCl) as dehydrating agent (**Scheme 5.8C**). Phosphoryl trichloride was avoided due to its high reactivity, potentially interacting with the olefinic moiety of the norbornene.⁵⁰⁶ As a result, the norbornene-functional isocyanide **xNbNC** was obtained as a brown viscous liquid in a yield of 94% (**Figure S5.65**).

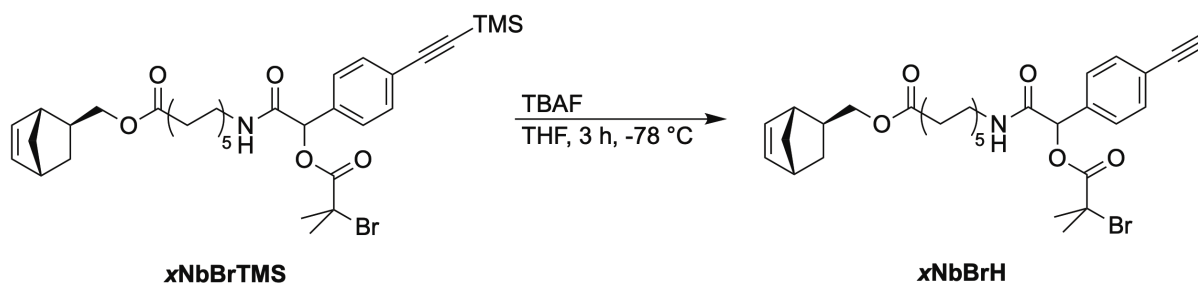
As mentioned at the beginning of the section, 2-bromo-2-methylpropionic acid, 4-TMS-ethynyl-benzaldehyde, and **xNbNC** were reacted in a P-3CR to obtain an *exo* norbornene derivative, comprising functionalities capable of undergoing CuAAC and ATRP (**Scheme 5.9**).



Scheme 5.9. Synthesis of *exo* norbornene derivative **xNbBrTMS** comprising a TMS-protected alkyne and an ATRP initiator unit *via* P-3CR.

It is noted that a small excess of the relatively sensitive aldehyde and isocyanide were added to maximize the obtained yield, since the contribution of an aromatic compound usually decrease the latter.⁵⁰⁷ After the purification process, the bifunctional macromonomer precursor **xNbBrTMS** was obtained as a brown solid in a yield of 52% (**Figure S5.67**).

In order to perform a successful CuAAC, the TMS-protected alkyne of **xNbBrTMS** was deprotected using tetrabutylammonium fluoride (TBAF) at low temperature (**Scheme 5.10**). It is noted that the deprotection *via* TBAF at higher temperatures and subsequent purification by column chromatography led to a variety of unidentified decomposition products.



Scheme 5.10. TMS-deprotection using TBAF at low temperature, obtaining the *exo* norbornene derivative **xNbBrH** comprising a terminal alkyne and an ATRP initiator unit.

Hence, the deprotection was performed in THF at $-78\text{ }^\circ\text{C}$, obtaining the deprotected alkyne **xNbBrH** (**Figure 5.22**).

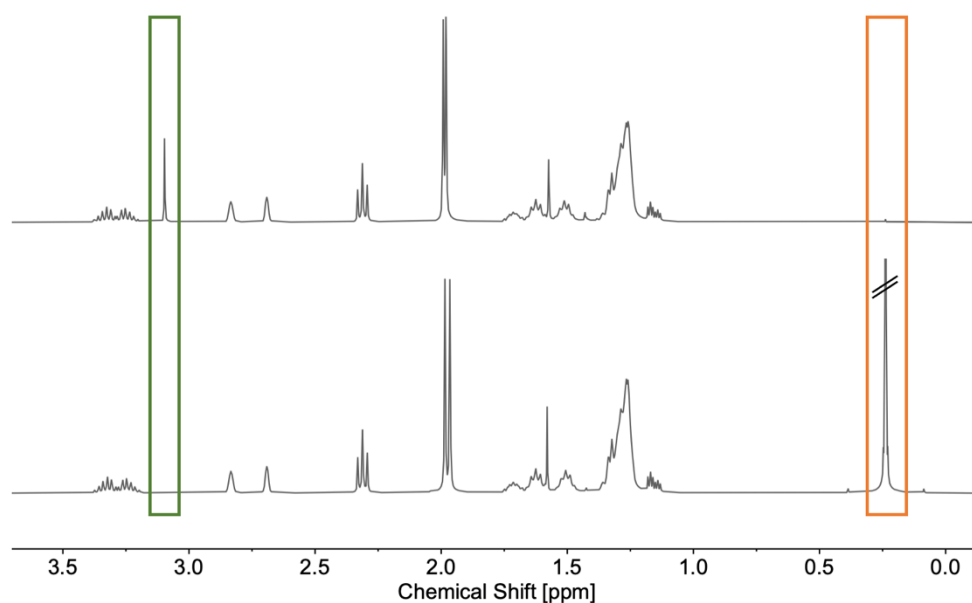
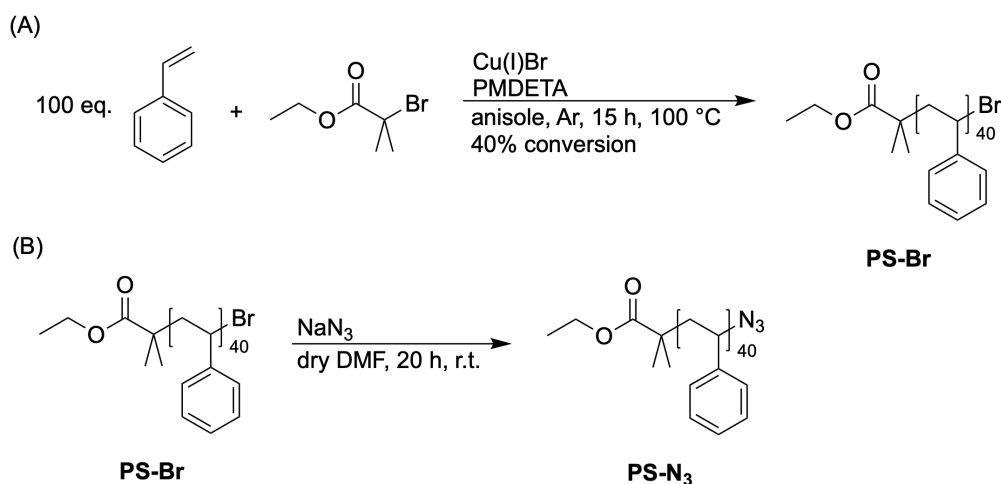


Figure 5.22. Stacked ^1H NMR spectra (section: 3.7 – 0 ppm) of **xNbBrTMS** (bottom) and **xNbBrH** (top), highlighting the vanishing of the TMS signal at 0.25 ppm (orange box) and the appearing of the proton at the terminal alkyne at 3.1 ppm (green box).

The characteristic TMS signal at 0.25 ppm vanished after three hours, whereas the signal at 3.1 ppm ascribed to the proton of the terminal alkyne appeared. It is noted that the conversion reached a plateau after *ca.* two hours, whereby a maximum conversion of 92% was calculated. The crude product was further purified by several washing steps, while

additional purification *via* column chromatography was avoided due to the low stability of the terminal alkyne observed in a previous attempt. The slightly impure macromonomer precursor **xNbBrH** was obtained as an off-white solid in a yield of 89% (**Figure S5.69**). However, the present impurity was determined to not interfere with the subsequent reaction step.

In order to perform a successful CuAAC and thus introduce the first polymeric chain onto the macromonomer precursor, styrene was polymerized *via* ATRP and subsequently azidated, adapting literature-known synthesis procedures (**Scheme 5.11**).⁴⁷²



Scheme 5.11. Synthesis of (A) **PS-Br** *via* Cu(I)-mediated ATRP of styrene, and (B) subsequent azidation using NaN_3 , obtaining **PS-N₃**.

As mentioned in **chapter 5.3.1**, radical polymerization processes undergo termination reactions, such as disproportionation or combination.³⁰⁶ In order to obtain a high end group fidelity in the subsequent azidation, cleavage of the terminal bromide was minimized by quenching the ATRP at a low monomer conversion. Here, styrene was used as monomer, ethyl α -bromoisobutyrate as initiator (M:I ratio = 100:1), and Cu(I)Br/PMDETA as catalyst (**Scheme 5.11A**). The polymerization was quenched after 15 hours, reaching 40% monomer conversion. The purification process was performed similarly to **xNb2S20** (**Chapter 5.3.1**). The product **PS-Br** was obtained as a white fluffy solid. Analysis by ^1H NMR spectroscopy exhibited a broad signal in the aromatic region (7.5 – 6.3 ppm), which was ascribed to the styrenic repeat units. Furthermore, the signal at *ca.* 4.5 ppm was ascribed to the proton next to the bromide at the last repeat unit. Comparison with a reference signal at *ca.* 3.6 ppm, which was ascribed to the methylene group of the ATRP initiator, indicated nearly quantitative end group

fidelity. Furthermore, comparison of the latter with the signal of the repeat units indicated an M_n of 4,400 g/mol (**Figure S5.71**), corresponding to an average DP of 40. The SEC trace of **PS-Br** exhibited a narrow and symmetrical molecular weight distribution (**Figure 5.23**), indicating the absence of coupled byproducts. Here, the dispersity was found to be 1.16, whereas the M_n was determined as 4,000 g/mol, being relatively consistent with the M_n determined by ^1H NMR spectroscopy and thus further supporting the good control of the ATRP.

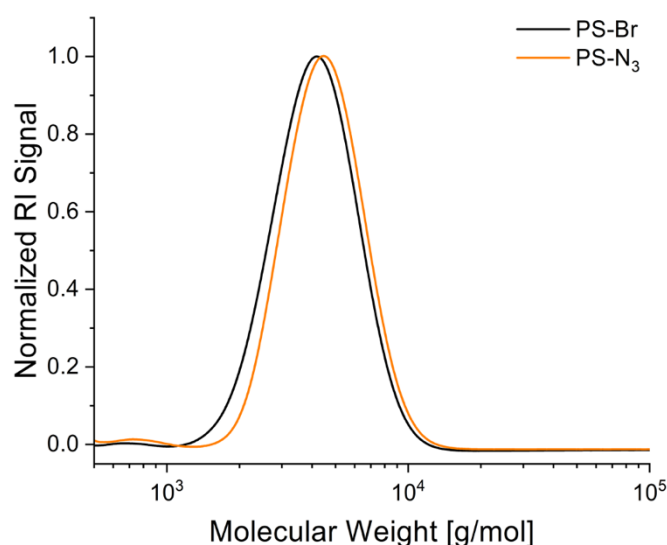


Figure 5.23. SEC traces of PS before (**PS-Br**) and after (**PS-N₃**) azidation.

The synthesis of the **PS-Br** was further examined by MALDI-TOF MS, whereby the respective figure is presented in the experimental section in **chapter 8.3.2 (Figure S5.73A)**. Crucially, the spectrum exhibited one distinct distribution assigned to the olefin-terminated species obtained due to MALDI-TOF-induced cleavage of the bromide end group,⁴⁷⁸ whereby the distance between two consecutive signals corresponded to the mass of one styrene unit (expected: 104.06 m/z , **Figure S5.73B**). The assignment was verified by comparing the determined and the calculated isotopic patterns (**Figure S5.74**). End group analysis was inconclusive as MALDI-TOF characterization showed no bromide-terminated distribution. However, as discussed in **chapter 5.3.1**, it is hypothesized that the end group was cleaved during the ionization process, forming an olefin-terminated polymer. Since ^1H NMR spectroscopy and SEC indicated the successful synthesis of **PS-Br** and a high end group fidelity, the obtained polymer was used in the subsequent azidation as a starting material.

In the next step, the bromide end groups of **PS-Br** were substituted by an azide, using sodium azide in dry dimethylformamide (DMF, **Scheme 5.11B**). The azidation was performed at ambient temperature under argon atmosphere for 20 hours, whereby a white solid precipitated, suggesting the formation of sodium bromide as byproduct. After purification, the product was obtained as a white solid in a yield of 83%. Furthermore, the product was analyzed *via* ^1H NMR spectroscopy, verifying the successful substitution (**Figure 5.24**).

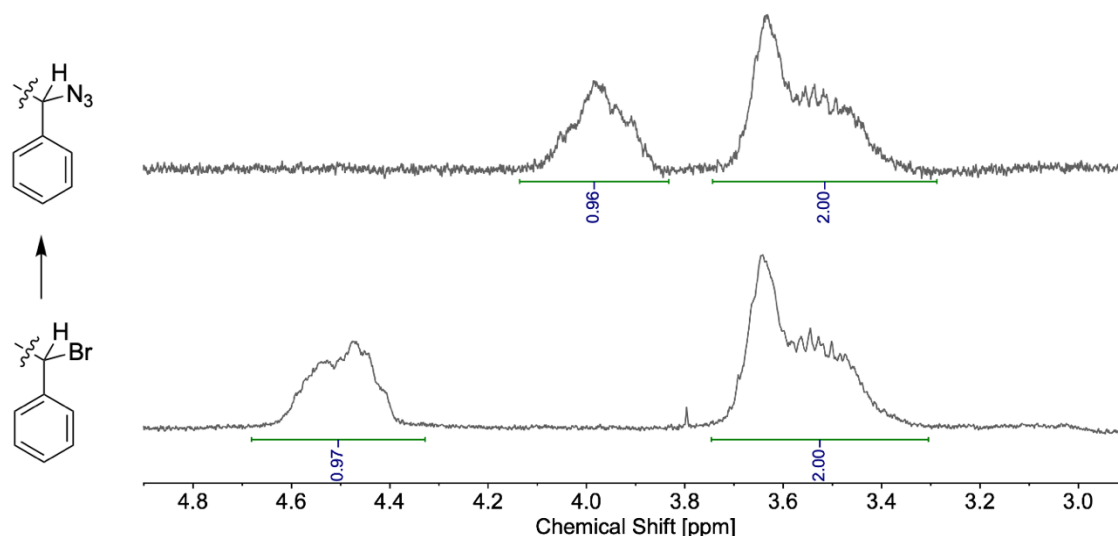
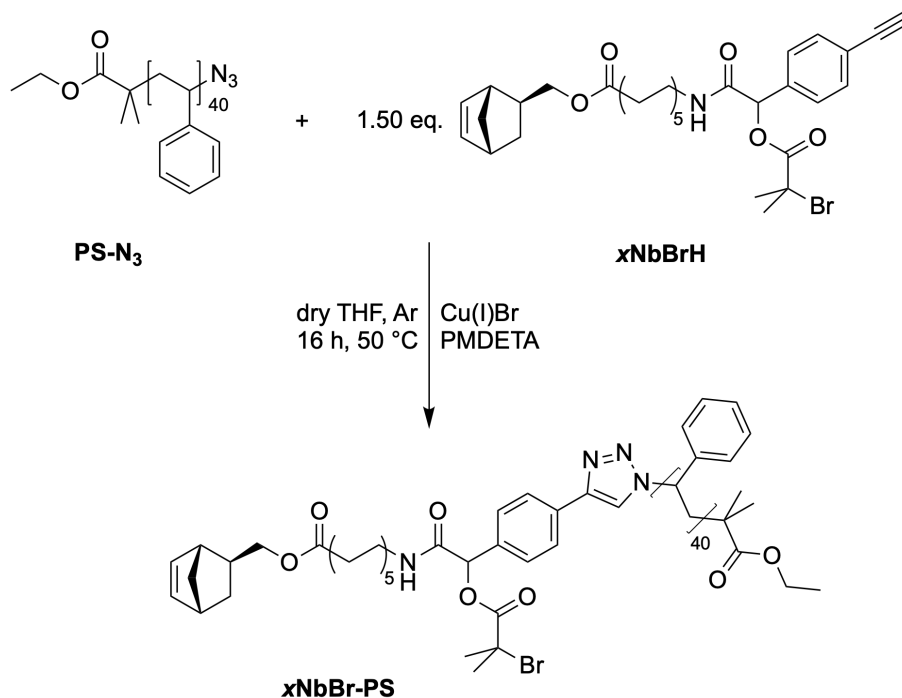


Figure 5.24. Stacked ^1H NMR spectra (section: 4.9 – 3.9 ppm) of **PS-Br** (bottom) and **PS-N₃** (top), highlighting the shift of the proton next to the bromide toward high-field after azidation (4.5 ppm \rightarrow 4.0 ppm), with the respective end groups (left). Methylene groups of the initiator units at 3.6 ppm served as a reference.

Quantitative conversion of the bromide end groups was determined, whereby the signal assigned to the proton next to the bromide at 4.5 ppm was shifted toward high-field at 4.0 ppm. In both spectra, the methylene groups of the initiator units at 3.6 ppm were used as a reference (**Figure 5.24**). Furthermore, end group analysis *via* ^1H NMR spectroscopy exhibited an M_n of 4,400 g/mol for **PS-N₃** (**Figure S5.75**), corresponding to an average DP of 40. The SEC trace of **PS-N₃** exhibited a narrow and symmetrical molecular weight distribution (**Figure 5.23**), indicating the absence of side reactions. As expected, the SEC trace of **PS-N₃** exhibited a similar molecular weight distribution compared to **PS-Br**, albeit a minimal shift toward higher molecular weights was detected ($M_n = 4,300$ g/mol; $D_M = 1.14$). This observation was attributed to the contribution of the different end groups toward the R_h s of the polymers, leading to slightly shifted distributions. Additional verification of the azidation by MALDI-TOF MS was not possible due to fragmentation involving the azide functionality

during the ionization process.⁵⁰⁸ However, the azide-terminated PS was further used in a CuAAC to obtain a monofunctional macromonomer (**Scheme 5.12**), serving as a macroinitiator in subsequent ATRP. The success of the CuAAC served as a token of the azidation being successful.



Scheme 5.12. Synthesis of **xNbBr-PS** *via* CuAAC using **PS-N₃** as azide and **xNbBrH** as alkyne.

Here, **PS-N₃** was reacted with the previously synthesized **xNbBrH**, whereby the CuAAC of the terminal alkyne and the azide formed a triazole moiety, connecting both molecules. The reaction was performed in dry THF at 50 °C under argon atmosphere, using Cu(I)Br/PMDETA as catalyst. It is noted that the alkyne component was used in excess to ensure complete conversion of the azide and to prevent remaining unreacted PS within the reaction mixture, since the latter cannot be easily removed during the purification process. Furthermore, the product was monitored *via* ¹H NMR spectroscopy (**Figure 5.25**).

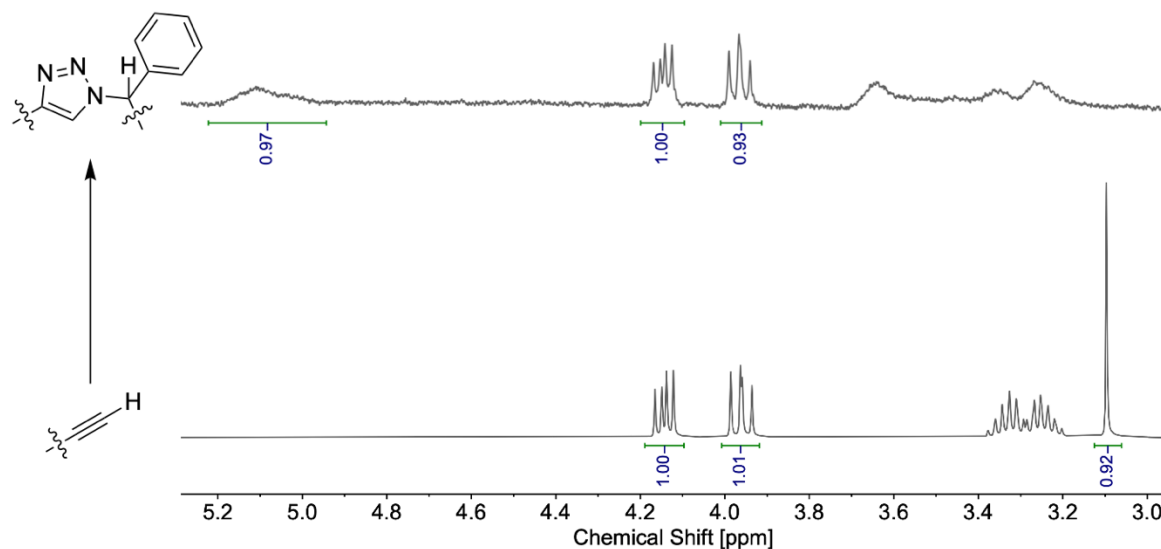


Figure 5.25. Stacked ^1H NMR spectra (section: 5.25 – 2.95 ppm) of \mathbf{xNbBrH} (bottom) and $\mathbf{xNbBr-PS}$ (top), highlighting the vanishing of the terminal alkyne signal at 3.1 ppm and the appearing of a signal assigned to the proton next to the triazole at 5.1 ppm, with the respective functional groups (left). Methylene groups ($\text{CH}_2\text{-CO}$) of the norbornene units at ca. 4.1 ppm served as a reference.

The successful CuAAC was determined after 19 hours, whereby a signal appeared at 5.1 ppm that was assigned to the proton next to the triazole. In both spectra, the methylene group ($\text{CH}_2\text{-CO}$) of the norbornene unit at 4.15 and 3.95 ppm, respectively, were used as a reference. The signal assigned to the terminal alkyne of \mathbf{xNbBrH} at 3.10 ppm vanished after the reaction, suggesting complete conversion of the alkyne (**Figure 5.25**). However, since the alkyne was used in an excess, the presence of a side reaction was suggested. The combination of CuAAC and ATRP to obtain functional polymers or macromonomers is well-known in the literature, whereby the reaction between two alkynes (Glaser coupling) was found to appear under ATRP conditions.⁵⁰⁹ It is herein hypothesized that the Glaser coupling occurred during the CuAAC, converting the remaining \mathbf{xNbBrH} to the respective bifunctional norbornene species, potentially acting as a crosslinker for the subsequent ROMP. However, since this molecule is rather small, purification by precipitation was expected to remove the impurity. The purification procedure was similar to the purification of polymers synthesized *via* ATRP (**Chapter 5.3.1**). After purification, an SEC measurement was conducted to further examine the obtained $\mathbf{xNbBr-PS}$ and compare it to the polymeric starting material (**Figure 5.26**).

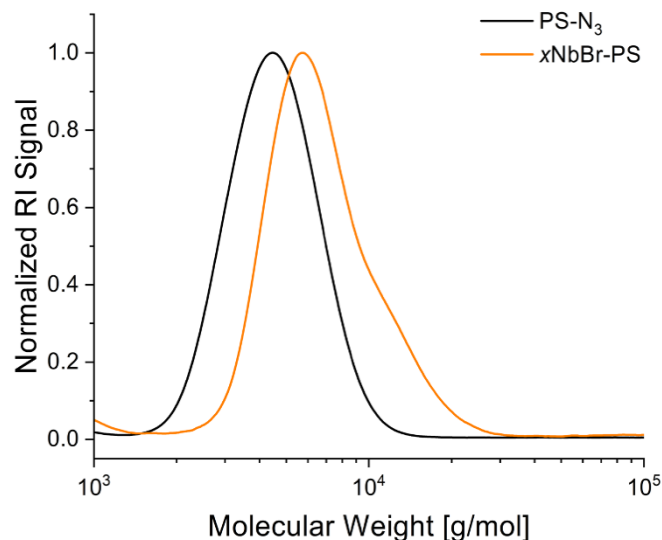


Figure 5.26. SEC traces of the polymeric starting material **PS-N₃** and the ATRP macroinitiator **xNbBr-PS**, obtained *via* CuAAC.

The obtained SEC trace exhibited a bimodal molecular weight distribution ($M_n = 6,100$ g/mol; $D_M = 1.18$), whereby a high molecular weight shoulder was detected, indicating the presence of a macromolecular impurity. Since the Glaser coupling would convert remaining **xNbBrH** to a relatively small bifunctional norbornene species, another side reaction occurred under CuAAC conditions. The literature describes the presence of radical coupling reactions between bromide end groups of ATRP initiators under the applied conditions.⁵⁰⁹ Since **xNbBr-PS** comprised a bromide end group rendering it a macroinitiator in subsequent ATRP, radical coupling was assumed to occur during or after successful CuAAC, leading to a high molecular weight species. According to this hypothesis, the undesired coupling product would comprise two PS chains and two polymerizable norbornene moieties. However, the coupling product was not detectable *via* ¹H NMR spectroscopy (**Figure S5.77**), showing the importance of additional analysis *via* SEC. The removal of the side product by precipitation was not possible due to macroscopic characteristics similar to **xNbBr-PS**. Potentially acting as a crosslinker in ROMP, the side product had to be removed before performing the synthesis of the Janus copolymers. It was hypothesized that after subsequent ATRP using MMA as monomer, the macroscopic characteristics of the coupling byproduct and the obtained bifunctional macromonomer differ and efficient purification by precipitation is possible. Hence, the impure **xNbBr-PS** was used as a macroinitiator in the ATRP of MMA (**Scheme 5.13**), whereby the coupling byproduct was expected to act as a spectator, not interfering with the

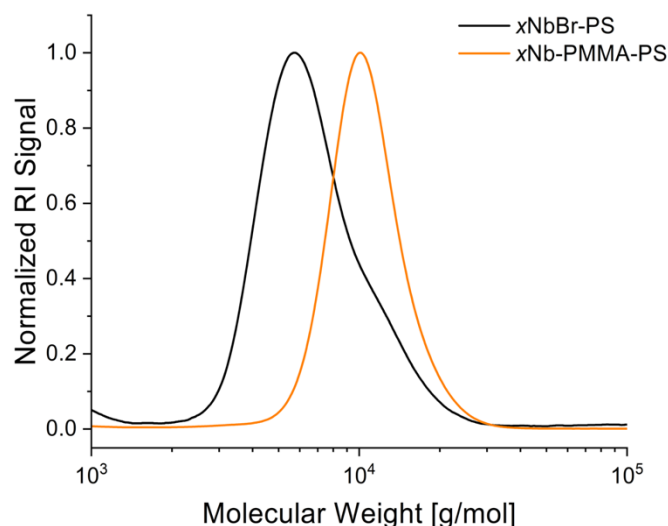


Figure 5.27. SEC traces of the macroinitiator **xNbBr-PS** and the bifunctional macromonomer **xNb-PMMA-PS**, obtained *via* ATRP of MMA.

The SEC trace of the purified macromonomer exhibited a narrow molecular weight distribution ($M_n = 10,100$ g/mol; $D_M = 1.11$), suggesting a high degree of polymerization control using the ATRP macroinitiator. It is, however, noted that the coupling byproduct impurity was not confirmed to be completely removed due to the overlapping molecular weight distributions of the latter and the obtained **xNb-PMMA-PS**. Other analytical methods to verify the successful purification were considered. End group analysis *via* ^1H NMR spectroscopy indicated an M_n of 8,000 g/mol (**Figure S5.80**), whereby the methylene group (CH-CH₂-CH) of the norbornene unit at 2.83 ppm was used as a reference. Therefore, the average DP of the PS chain was 40, whereas that of the PMMA chain was 34. Furthermore, the ^1H NMR spectra of the filtrates obtained during the purification process showed varying ratios of the different repeat units (PS: 7.5 – 6.3 ppm; PMMA: 3.7 – 3.4 ppm, **Figure S5.79**), which were decreasing in the order: 22 (filtrate 1) \gg 5 (filtrate 2) $>$ 4 (filtrate 3) $>$ 2 (product). It is noted that MALDI-TOF MS was not successfully performed, due to the high molecular weight of the sample and its copolymeric character, making sufficient ionization rather difficult.

The thermal properties of the obtained bifunctional macromonomer were determined by DSC (Figure 5.28).

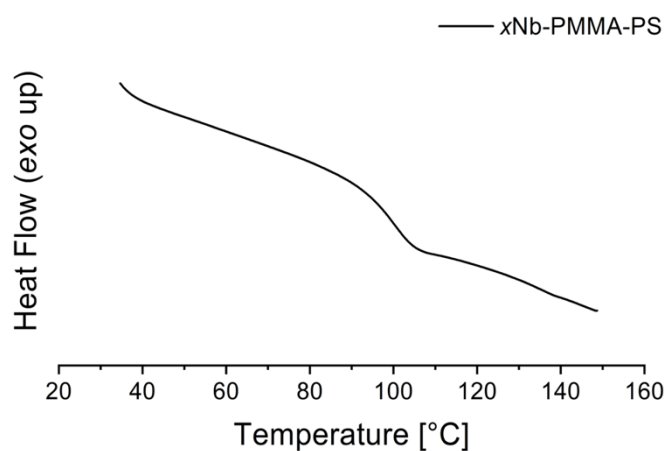
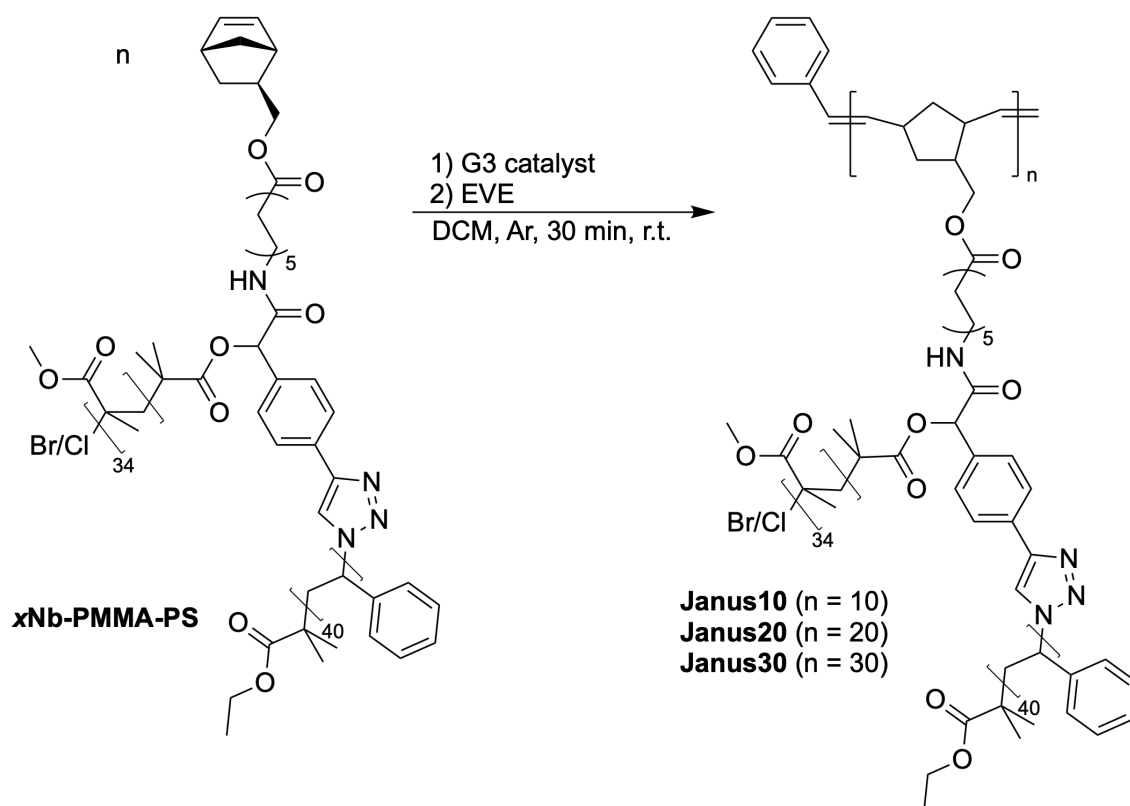


Figure 5.28. DSC trace of bifunctional macromonomer **xNb-PMMA-PS**.

The measured T_g value was determined by the onset temperature of the thermal transition in the second heating cycle, applying a heating rate of 20 °C/min. Here, the DSC trace of **xNb-PMMA-PS** exhibited one T_g at 95 °C (Figure 5.28). This behavior was expected, since it was observed and discussed in **chapter 5.3.1**, as well as in the literature.^{510,511}

Finally, **xNb-PMMA-PS** was polymerized *via* ROMP using the G3 catalyst (**Scheme 5.14**).



Scheme 5.14. Synthesis of Janus copolymers *via* the G3-mediated ROMP of **xNb-PMMA-PS**.

The polymerizations were performed in argon-flushed ampoules using degassed DCM at ambient temperature. The M:I ratios were 10:1, 20:1, and 30:1, probing the ability to reach high molecular weights (**Table 5.14**).

Table 5.14. Summary of synthesized Janus copolymers *via* the G3-mediated ROMP of **xNb-PMMA-PS**.

Polymer ^a	M:I ratio	Conversion [%] ^b	$M_{n,calc}$ [g/mol] ^c	M_n [g/mol] ^d	\mathcal{D}_M ^d
Janus10	10:1	≥99	80,000	47,500	1.07
Janus20	20:1	≥99	160,000	83,500	1.10
Janus30	30:1	≥99	240,000	110,000	1.15

^aReaction conditions: **xNb-PMMA-PS** and G3 catalyst (1 mmol/L) in degassed DCM at ambient temperature under argon atmosphere for 30 min. ^bDetermined by ¹H NMR spectroscopy. ^cCalculated by conversion. ^dDetermined by SEC.

According to ^1H NMR spectroscopy, the ROMPs exhibited complete conversion after 30 minutes and were immediately quenched (**Figure S5.83**). After purification, the products (**Janus10**, **Janus 20** and **Janus30**, **Table 5.14**) were obtained as white solids. Additionally, SEC measurements were conducted to evaluate the polymerization control during the ROMP processes (**Figure 5.29**).

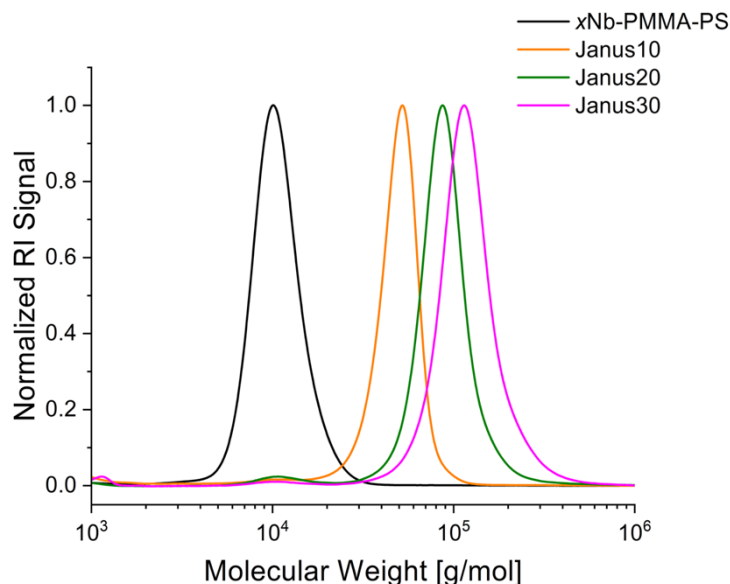


Figure 5.29. SEC traces of the bifunctional macromonomer **xNb-PMMA-PS** and of the obtained Janus copolymers **Janus10**, **Janus20** and **Janus30** (**Table 5.14**).

The SEC traces exhibited narrow and relatively symmetrical molecular weight distributions (**Figure 5.29**), suggesting a high degree of polymerization control using **xNb-PMMA-PS** as bifunctional macromonomer. However, broadening of the distributions and thus slightly increasing dispersities were observed for the higher molecular weight Janus copolymers (**Figure 5.29**, **Table 5.14**). The success of the ROMP served as a token of the fractionated precipitation being successful. The M_n s determined by SEC were lower compared to the expected M_n s calculated by conversion (**Table 5.14**). As discussed in **chapters 5.3.2 – 5.3.4**, this observation was attributed to the different morphologies of the SEC calibration standards (linear PMMAs) and the measured polymers (grafts). It is noted that despite ^1H NMR data verifying complete macromonomer conversion, the corresponding signals were detected in low intensities for **Janus20** and **Janus30** (**Figure 5.29**).

As a result, the synthesis of a bifunctional macromonomer using a combination of the P-3CR, ATRP, and CuAAC was successful, enabling subsequent polymerization *via* ROMP in a controlled fashion.

5.4 Conclusion

In this chapter, it was shown that the ROMP of norbornene-based macromonomers was successful to synthesize sequence-controlled graft copolymers. The herein used macromonomers were obtained *via* ATRP of methacrylates and styrene in a controlled fashion. The thermal properties of the macromonomers and polymer blends were further examined *via* DSC. PMMA and PBnMA were found to be immiscible, exhibiting two separate T_g s in the respective 1:1 blend and thus being interesting comonomers for the future self-assembly of their copolymers.

The polymerization behavior of the macromonomers in Ru-mediated ROMP was examined in terms of macromonomer structure, solvent, concentration, and catalyst. Polymethacrylates were found to be suitable for controlled polymerization *via* ROMP using the G1 and the G3 catalyst. Additionally, using DCM as solvent and applying low macromonomer concentrations during polymerization improved the performance of the respective ROMP. The polymerization kinetics of the G3-mediated ROMP using a variety of macromonomers were determined by on-line ^1H NMR spectroscopy, obtaining pseudo first order kinetic behaviors for most macromonomers and leading to graft polymers with narrow molecular weight distributions. An iterative ROMP procedure was further examined, whereby sequence-controlled graft copolymers were obtained, exhibiting high polymerization control when using dry solvents and low temperature.

Furthermore, it was shown that a bifunctional macromonomer, comprising a PMMA and a PS chain were successfully synthesized in a controlled fashion by combining P-3CR, CuAAC and ATRP. Subsequent G3-mediated ROMP showed a high degree of polymerization control, and well-defined Janus copolymers with molecular weights up to 110,000 g/mol were obtained. A future consideration of this project is to examine the self-assembly of the obtained graft copolymers in thin films using AFM and small-angle X-ray scattering (SAXS) and further examine the influence of polymer dispersity on the generated self-assembled structures.

6 Sequence-controlled graft copolymers by delayed macromonomer addition

Parts of this chapter contain results that are currently part of a manuscript in preparation.

6.1 Abstract

In this chapter, the synthesis of sequence-controlled graft copolymers is investigated, whereby polymethacrylate-based macromonomers are added consecutively into an ongoing ring-opening metathesis polymerization (ROMP) using the Grubbs first generation (G1) catalyst. The delayed addition of fast-propagating *exo* norbornene-based macromonomers to a relatively slow polymerization of a small *endo* norbornene monomer leads to the targeted insertion of macroblocks along the polymeric backbone. The kinetically controlled insertion process is examined regarding effects of the macromonomer structure, including the chemical structure of the used norbornene precursor, the length of the alkane linker between the polymerizable norbornene unit and the polymer chain and its molecular weight. Furthermore, the effect of the *exo:endo* ratio on parameters such as the grafting density (σ) of the macroblock and the apparent propagation rate constant (k_{app}) of the macromonomer during the copolymerization process are examined. Therefore, the copolymerization kinetics are determined by on-line ^1H nuclear magnetic resonance (NMR) spectroscopy, whereas size exclusion chromatography (SEC) measurements are conducted to determine beneficial and unfavorable influences of the applied ROMP procedure on the molecular weight distribution. Sequence-controlled graft copolymers are synthesized, exhibiting diblock- and triblock-like architectures with variable molar fractions when two different macromonomers are used.

6.2 Introduction

Inspired by biochemical systems and the decoding of the first human gene in 1977,⁵⁶ intensive efforts have been made in understanding and controlling the monomer sequence in synthetic polymers.^{57,58} As mentioned in the introduction of **chapter 5**, the synthesis of polymers consisting of different monomer species that are arranged in a predetermined order, are denoted as sequence-controlled polymers and are typically characterized by good

polymerization control, resulting in low dispersity values (<1.50).⁴⁵⁴ Nowadays, there are various approaches to synthesize sequence-controlled copolymers,⁵¹²⁻⁵¹⁴ leading to materials with a wide range of possible applications, for example, as photonic materials,⁵¹⁵ or in the field of data storage and encryption.^{81,516} The ROMP of norbornene-based monomers is a powerful tool for the preparation of such materials due to its “living” character,¹⁷ tolerance toward functional groups and high polymerization rates.^{517,518} In **chapter 2.3** of the theoretical background, more detailed information and mechanistic insights regarding different polymerization techniques are given.

As observed in **chapter 5.3.4**, the synthesis of sequence-controlled graft copolymers using the fast-initiating G3 catalyst was found to be sensitive to traces of oxygen and water, leading to inefficient chain-extension processes and thus to rarely controlled copolymers. In contrast, the G1-mediated iterative ROMP of macromonomers has been found to exhibit lower polymerization rates and unfavorable steric interactions, hampering the chain-extension process. Since the G1-type catalysts are less prone to catalyst poisoning,⁴⁹⁶ the increasing steric hindrance during the ROMP of macromonomers needs to be reduced. Hereby, the delayed addition of monomers into an ongoing ROMP represents a promising technique to introduce macroblocks along the polymeric backbone in a controlled fashion.⁹³ As observed in **chapters 5.3.2** and **5.3.3**, the polymerization behavior of *endo* and *exo* norbornenes is influenced by the used catalyst. In the G1-mediated ROMP (**Chapter 4.3.3**), the apparent propagation rate of *exo* norbornenes has been found to be more than two orders of magnitude higher compared to that of their *endo* counterparts. It is therefore apparent that the nature of different norbornene isomers is potentially useful in the synthesis of sequence-controlled copolymers, applying basic Schlenk techniques and non-dry solvents.

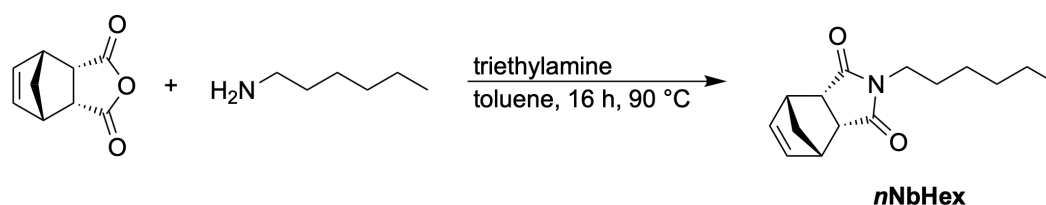
Inspired by the synthesis of sequence-controlled block copolymers *via* ROMP and the large differences in reactivity of *exo* and *endo* norbornene-based monomers, the synthesis of kinetically controlled graft block copolymers is herein reported. To achieve this, the G1-mediated homopolymerization of an *endo* norbornene monomer is initiated, achieving a slow and controlled polymerization process. After reaching a defined DP, an *exo* norbornene-based macromonomer is added, leading to its fast incorporation into the growing polymeric chain.

6.3 Results and discussion

6.3.1 Introduction of monoblocks *via* ROMP

In this section, the introduction of a macroblock into a growing polynorbornene (PNB) chain by delayed macromonomer addition using the G1-mediated ROMP is examined. Therefore, the PMMA-based macromonomers introduced in **chapter 5.3.1** are used.

In order to perform a relatively slow ROMP, enabling the addition of a fast-propagating macromonomer and thus introducing a macroblock at kinetically specified positions into the polymer, an *endo* norbornene was synthesized according to the literature (**Scheme 6.1**).⁹³



Scheme 6.1. Synthesis of the *endo* norbornene monomer **nNbHex** *via* condensation reaction of *endo* norbornene anhydride with 1-aminohexane.

Endo norbornene anhydride (*cis*-5-norbornene-*endo*-2,3-dicarboxylic anhydride) was used as a precursor to synthesize **nNbHex** in a condensation reaction at 90 °C, whereby the synthesis procedure was similar to its *exo* counterpart **xNbHex** (**Scheme 5.7, Chapter 5.3.4**). The product **nNbHex** was obtained as a light yellow and viscous liquid in a yield of 82% (**Figure S6.1**). It is noted that the ROMP of **nNbHex** was a continuous polymerization process, preventing complete monomer conversion during the copolymerization process and thus facilitating the chain-extension process. Since the *endo* monomer also reduces the grafting density of the macroblocks, **nNbHex** is further referred to as a dilutant.

In order to examine the polymerizability of **nNbHex** using the G1-mediated ROMP and evaluate the macromonomer addition after a defined reaction time, three homopolymerization reactions were performed, varying the M:I ratio and the catalyst concentration (entries 6.1 – 6.3, **Table 6.1**). It is noted that all ROMPs conducted in **chapter 6.3** were performed in argon-flushed ampoules or NMR tubes equipped with J Young taps using degassed DCM or degassed DCM- d_2 as solvent at ambient temperature. It is further noted that the term “argon-flushed” implies that the used reaction vessel was thrice dried with a heat gun under high vacuum and flushed with argon while hot. After reaching the

desired monomer conversion, the polymerizations were quenched by adding an excess of EVE, forming an inactive catalyst derivative and the corresponding alkene-terminated PNB chain.⁴⁴²

Table 6.1. Homopolymerizations using *n*NbHex with different M:I ratios and catalyst concentrations *via* the G1-mediated ROMP.

Entry ^a	M:I ratio	Conversion [%] ^b	Reaction Time [h]	k_{app} [s ⁻¹] ^c	$t_{1/2}$ [h] ^d	M_n [g/mol] ^e	\mathcal{D}_M ^e
6.1	50:1	90	306	2.11×10^{-6}	91.3	15,100	1.09
6.2	100:1	85	384	1.40×10^{-6}	138	28,400	1.14
6.3	100:1	82	628	0.77×10^{-6}	250	26,200	1.07
6.4	100:1	93	262	2.84×10^{-6}	68.8	28,400	1.13

^aReaction conditions: *n*NbHex and G1 catalyst (entries 6.1 and 6.2: 2 mmol/L, entry 6.3: 1 mmol/L, entry 6.4: 4 mmol/L) in degassed DCM-d₂ at ambient temperature under argon atmosphere. ^bDetermined by ¹H NMR spectroscopy. ^cCalculated from conversion using first order kinetics. ^dCalculated from the linear regression fits using $t_{1/2} = \ln(2)/k_{app}$. ^eDetermined by SEC.

The M:I ratios were 50:1 and 100:1 (entries 6.1 – 6.3, **Table 6.1**), whereby the latter was performed applying catalyst concentrations of 2 mmol/L and 1 mmol/L (entries 6.2 and 6.3, **Table 6.1**), respectively. The reactions were quenched after reaching *endo* norbornene conversions $\geq 82\%$ to evaluate a suitable conversion for the macromonomer addition. The polymerization kinetics were monitored by on-line ¹H NMR spectroscopy (**Figure 6.1**), whereby the vanishing of the signal assigned to the olefinic norbornene moiety of the *endo* monomer (6.07 ppm) and the appearance of the olefinic backbone signal of the obtained polymer (5.75 – 5.40 ppm) were similar to that described in **chapter 4.3.2 (Figure 4.2)**.

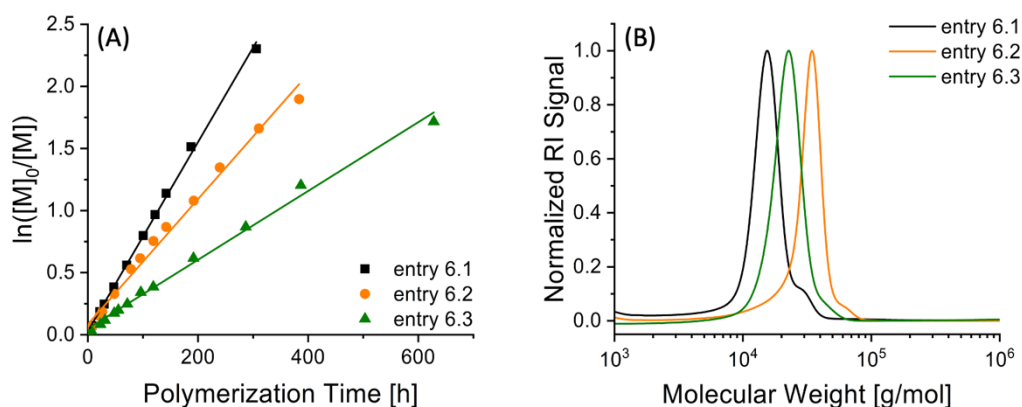


Figure 6.1. (A) Kinetic plot of the homopolymerizations of *nNbHex*, based on ^1H NMR spectroscopy data, and (B) SEC traces of the obtained polymers (entries 6.1 – 6.3, **Table 6.1**). Lines represent linear fits.

In order to monitor the polymerization process over a wide range of conversions, the ROMPs were quenched after 306 hours, 384 hours and 628 hours, corresponding to 90%, 85% and 82% monomer conversion (entries 6.1 – 6.3), respectively. In all cases, the determined M_n of the obtained polymer was higher compared to the M_n calculated by conversion. As discussed in **chapters 4** and **5**, this observation was attributed to the SEC calibration standards used and their different R_h s compared to the herein synthesized polymers. In all cases, the ratio of the determined to the calculated M_n was found to be similar (1.36 for entry 6.1, 1.35 for entry 6.2 and 1.29 for entry 6.3), supporting this assumption. The polymerization kinetics of entries 6.1 – 6.3 showed a pseudo first order kinetic behavior (**Figure 6.1A**, **Table 6.1**), whereby the kinetics of entry 6.2 were found to be slightly skewed, hence, the polymerization rate decreased with increasing reaction time (**Figure 6.1A**). It is noted that e.g. oxygen contamination during the synthesis preparation cannot fully be excluded. However, since the error of the linear fit was rather small ($R^2 = 0.98887$), the k_{app} of entry 6.2 was determined to compare all three homopolymerization reactions (**Table 6.1**). While exhibiting a k_{app} of $2.11 \times 10^{-6} \text{ s}^{-1}$, entry 6.1 was found to be the fastest herein presented ROMP of *nNbHex*. Due to the reduced catalyst concentration, entry 6.3 only exhibited a k_{app} of $0.77 \times 10^{-6} \text{ s}^{-1}$, which was 1.8 times slower compared to that of entry 6.2 and 2.7 times slower compared to that of entry 6.1 (**Table 6.1**). The determined SEC traces exhibited relatively narrow molecular weight distributions for the obtained polymers, whereby a small high molecular weight shoulder was detected for all polymers (**Figure 6.1B**). Since the shoulders showed different relative intensities (compared to the main polymer distribution) and further correlated with the

monomer conversion, it was assumed that a side reaction occurred at high conversions ($\geq 82\%$). Furthermore, the SEC trace of entry 6.2 showed a low molecular weight tailing (**Figure 6.1B**), potentially induced by catalyst poisoning, which is further assumed to lead to the skewed ROMP kinetics (**Figure 6.1A**). Interestingly, lowering the G1 concentration in entry 6.3 resulted in a decreasing dispersity and no detectable tailing within the corresponding SEC trace (**Figure 6.1B, Table 6.1**).

In order to examine this observation in more detail, the ROMP of *n*NbHex was repeated applying similar conditions compared to that of entry 6.2 (entry 6.4, **Table 6.1**). The M:I ratio was 100:1, whereby the monomer and the catalyst concentrations were increased to 0.4 mol/L and 4 mmol/L, respectively, to exclude unfavorable steric interactions causing the skewed polymerization kinetics of entry 6.2 (**Table 6.1**). During the ROMP process, samples were withdrawn and immediately quenched. The samples were then analyzed by ^1H NMR spectroscopy and SEC, determining the polymerization kinetics and the evolution of the molecular weight distribution with increasing monomer conversion (**Figure 6.2**).

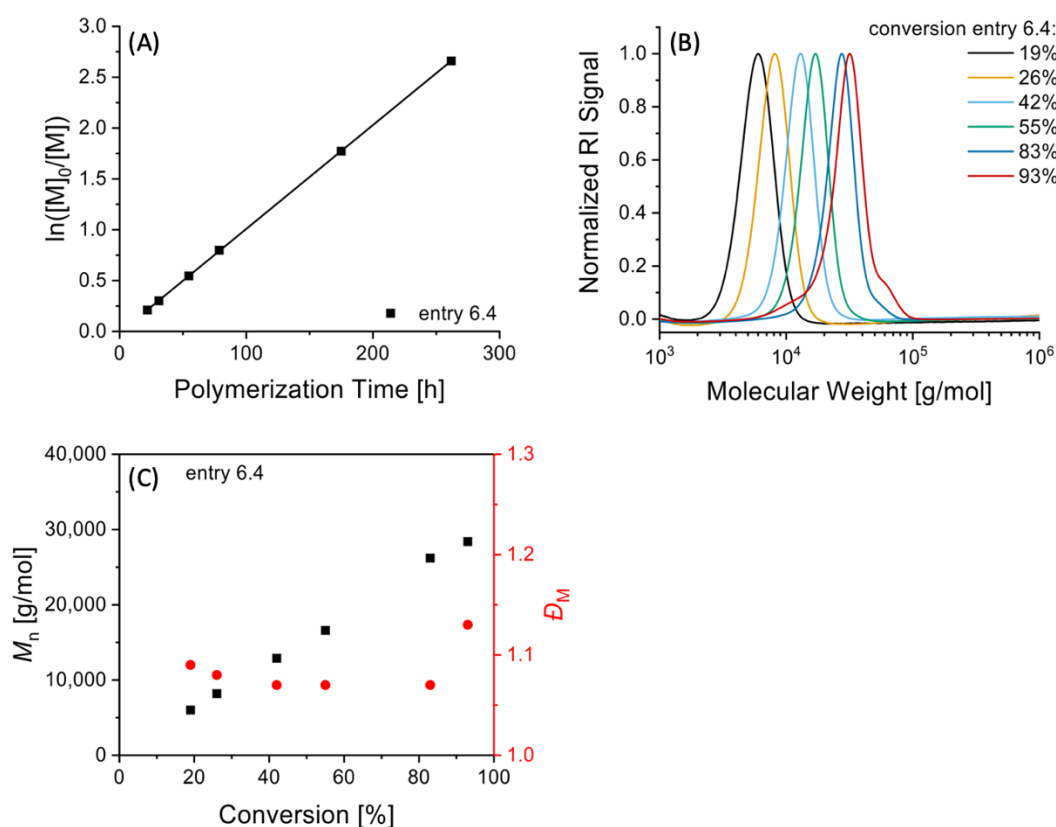


Figure 6.2. (A) Kinetic plot of the homopolymerizations of *n*NbHex, based on ^1H NMR spectroscopy data (**Figure S6.9**), (B) SEC traces of the withdrawn samples during ROMP (entry 6.4), and (C) plot of the monomer conversion versus molecular weight and dispersity, determined by SEC. Line represents linear fit.

The polymerization kinetics of entry 6.4 showed a pseudo first order kinetic behavior (**Figure 6.2A, Table 6.1**). As expected, the k_{app} of entry 6.4 ($k_{app} = 2.84 \times 10^{-6} \text{ s}^{-1}$) was found to be higher compared to that of entries 6.1 and 6.2 due to the higher catalyst concentration (**Table 6.1**). The SEC traces of the withdrawn samples exhibited narrow molecular weight distributions upon reaching a monomer conversion of 83% (**Figure 6.2B**). The penultimate sample (83% conversion) showed a small high molecular weight shoulder, not affecting the determined dispersity, whereas the last sample (93% conversion) showed a more pronounced high molecular weight shoulder and a low molecular weight tailing. However, the relationship between the monomer conversion and the corresponding molecular weight appeared to be linear, suggesting a controlled polymerization process (**Figure 6.2C**). The dispersity values slightly decreased with increasing conversion, reaching a minimum between 42% and 83% ($D_M = 1.07$). Afterwards the dispersity increased, reaching a maximum value of 1.13 after 93% monomer conversion, representing the emergence of the high molecular weight shoulder. Similar to entries 6.1 to 6.3, the M_n of the last sample, which was determined by SEC, was found to be higher compared to the M_n calculated by conversion (ratio: 1.23). It is noted that the removal of the catalyst and the purification by precipitation was not carried out for the samples withdrawn from entry 6.4 due to time limitations and given that previous experiments showed such purification was not necessary when assessing kinetics.

The ROMP conditions applied in entry 6.1 were considered as the most suitable for the continuous polymerization using *n*NbHex. Here, the pseudo first order kinetics were slow enough to ensure reproducible macromonomer additions, while maintaining a reasonable time scale (**Figure 6.1A, Table 6.1**). The obtained polymer exhibited a narrow molecular weight distribution, which was further characterized by the absence of a low molecular weight tailing (**Figure 6.1B**). Since the evolution of the molecular weight distribution was examined for entry 6.4, the SEC data showed a suitable period for macromonomer addition after reaching *ca.* 40% *endo* conversion.

The *n*NbHex polymerizations were performed in argon-flushed ampoules using a M:I ratio of 50:1, whereas the copolymerizations were conducted in argon-flushed NMR tubes by adding a defined amount of solution of the former to the dissolved macromonomer to ensure homogeneous mixing (**Figure 6.3**). The copolymerization kinetics were monitored by on-line ^1H NMR spectroscopy.

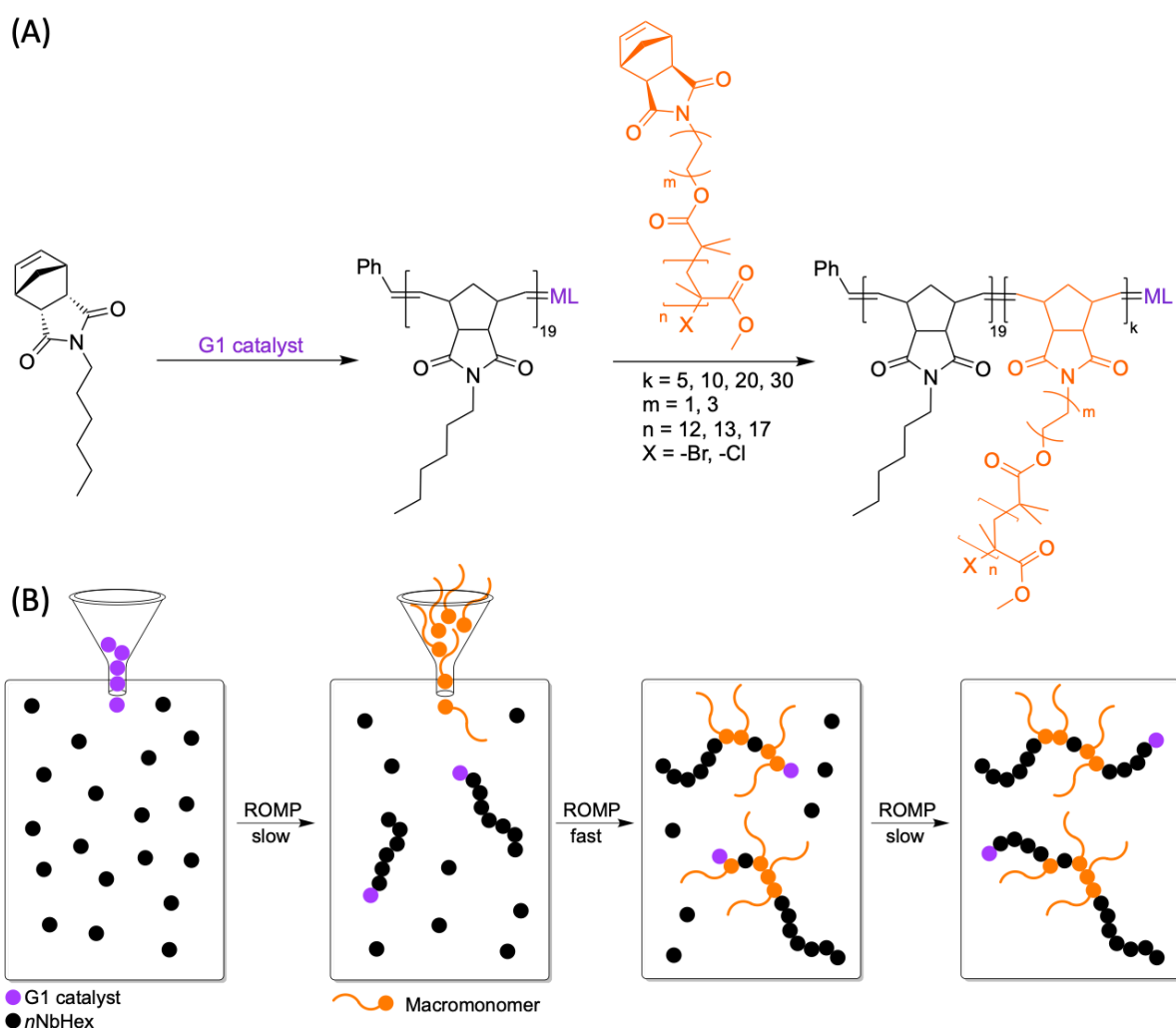


Figure 6.3. (A) Homopolymerization of *n*NbHex using the G1 catalyst and subsequent addition of macromonomer resulting in a block-like graft copolymer. (B) Schematic synthesis of graft copolymers by the delayed addition of macromonomer.

Three different PMMA-based macromonomers (*x*Nb2M12, *x*Nb6M13, and *x*Nb6M17) were used in the delayed addition procedure to evaluate the effect of the macromonomer structure on the copolymerization process. Here, comonomer ratios (M:MM) of 50:5, 50:10, 50:20 and 50:30 were applied (Table 6.2). The grafting density, which is herein defined as the number of macromonomer units per *n*NbHex unit within the macroblock, is an important measure to evaluate the molecular structure of the macroblock. A higher value indicates a lower dilution and thus a more densely grafted macroblock. It is noted that the herein performed ROMPs were divided into three sets, one per macromonomer, with four polymerizations each.

Table 6.2. Graft copolymers synthesized by ROMP of *n*NbHex and PMMA-based macromonomers.

entry ^a	M:MM ratio	MM	addition [%] ^b	$k_{app,endo}$ [s ⁻¹] ^c	$k_{app,exo}$ [s ⁻¹] ^d	σ^e	M_n [g/mol] ^f	\mathcal{D}_M^f
6.5	50:5	xNb2M12	38	2.20×10^{-6}	1.62×10^{-5}	0.40	16,300	1.11
6.6	50:10	xNb2M12	39	2.68×10^{-6}	2.08×10^{-5}	0.68	22,600	1.12
6.7	50:20	xNb2M12	38	2.71×10^{-6}	2.75×10^{-5}	1.39	32,400	1.14
6.8	50:30	xNb2M12	39	3.69×10^{-6}	3.50×10^{-5}	1.72	45,300	1.21
6.9	50:5	xNb6M13	39	2.04×10^{-6}	2.51×10^{-5}	0.36	17,500	1.13
6.10	50:10	xNb6M13	39	3.86×10^{-6}	4.25×10^{-5}	0.78	23,900	1.14
6.11	50:20	xNb6M13	39	4.09×10^{-6}	5.57×10^{-5}	1.35	35,400	1.16
6.12	50:30	xNb6M13	39	5.11×10^{-6}	7.16×10^{-5}	2.17	48,900	1.27
6.13	50:5	xNb6M17	37	1.77×10^{-6}	2.14×10^{-5}	0.41	20,300	1.13
6.14	50:10	xNb6M17	37	2.95×10^{-6}	3.30×10^{-5}	0.74	29,200	1.15
6.15	50:20	xNb6M17	37	3.92×10^{-6}	4.85×10^{-5}	1.52	44,300	1.24
6.16	50:30	xNb6M17	37	5.82×10^{-6}	6.45×10^{-5}	2.33	78,500	1.84

^aReaction conditions: *n*NbHex, G1 catalyst (2 mmol/L) and macromonomer (MM) in degassed DCM-d₂ under argon atmosphere at ambient temperature. ^bConversion of *n*NbHex before addition of the MM, determined by ¹H NMR spectroscopy. ^cCalculated from data points at low *n*NbHex conversion during copolymerization using pseudo first order kinetics. ^dCalculated from data points at low MM conversions using pseudo first order kinetics. ^eCalculated from monomer conversions during copolymerization using $\sigma = N(\text{MM})/N(\textit{nNbHex})$. ^fDetermined by SEC.

Due to the large amount of data, the kinetic evaluation is represented by entry 6.5 (**Figure 6.4, Table 6.2**). The kinetic plot, the molar fraction (x_i) of the macromonomer within the macroblock and the SEC traces before and after macromonomer addition are shown. The respective figures of the other kinetic measurements are presented in the experimental section in **chapter 8.3.3**. The vanishing of the ¹H NMR signal assigned to the olefinic norbornene moiety of the *exo* macromonomers (6.32 ppm) and the appearance of the olefinic backbone signal of the resulting polymers (5.80 – 5.40 ppm) were similar as described in **chapter 4.3.2 (Figure 4.1)**.

The first set of copolymerization reactions (entries 6.5 – 6.8, **Table 6.2**) was performed using **xNb2M12**, offering the lowest molecular weight available and a short ethyl linker unit (**Figure 6.4**).

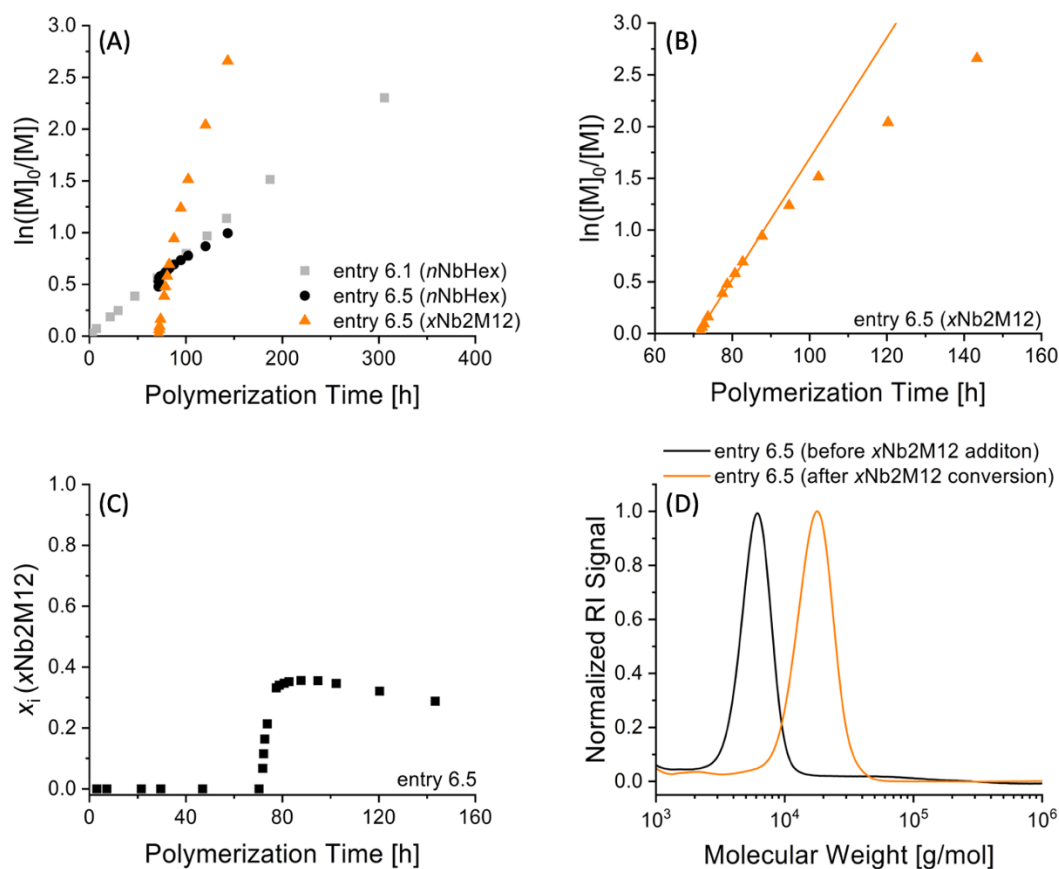


Figure 6.4. Representative (A) kinetic plots of entries 6.1 (**Table 6.1**) and 6.5 (**Table 6.2**), (B) highlighting **xNb2M12** during copolymerization, (C) molar fraction (x_i) of **xNb2M12** in entry 6.5 as a function of polymerization time, based on ^1H NMR spectroscopy data (**Figure S6.10**), and (D) SEC traces of entry 6.5 before **xNb2M12** addition and after **xNb2M12** conversion. Line represents linear fit.

In all cases, fast integration of the macromonomers into the polymeric chain was observed. Furthermore, no poisoning of the catalyst was observed during the macromonomer addition. As described in **chapter 4.3.3**, the combination of a slow *endo* norbornene and a fast *exo* norbornene leads to skewed kinetics (**Figure 6.4A**). However, the copolymerization kinetics of **xNb2M12** appeared to be linear at low macromonomer conversions ($\leq 68\%$), flattening at higher conversions. This observation was explained by the changing *exo:endo* ratio during the copolymerization process, whereby a large amount of *exo* macromonomer was assumed to neutralize the decelerating effect of the *endo* monomer. Simultaneously, the decelerating effect was assumed to increase with increasing macromonomer conversion and

thus leading to skewed kinetics at high macromonomer conversions (>68%). In order to compare the copolymerization kinetics of the macromonomers and calculate k_{appS} , the kinetics at low conversions ($\leq 68\%$) were deemed to be pseudo first order (**Figure 6.4B**). It is noted that the linear fits are extended to highlight the increasing decelerating effect of the *endo* monomer on the copolymerization kinetics with increasing macromonomer conversion. As expected, the k_{appS} of **xNb2M12** in the entries 6.5 – 6.8 increased with increasing amount of macromonomer (**Table 6.2**). This behavior was explained by the increasing *exo:endo* ratio (0.16:1 for entry 6.5 to 0.97:1 for entry 6.8), which limited the decelerating effect of **nNbHex** on the copolymerization rate. During the copolymerization process, the k_{appS} of **nNbHex** slightly increased compared to the homopolymerization. Nonetheless, the k_{appS} of the macromonomers were consistently one order of magnitude higher than that of **nNbHex**, thus leading to a block-like, yet gradient, macromonomer distribution in the copolymer (**Figure 6.4C**). The grafting density increased with increasing amount of macromonomer and increasing k_{app} , respectively. Despite the somewhat complex architecture, the resulting copolymers exhibited narrow molecular weight distributions when analyzed by SEC (**Figure 6.4D**), albeit a high molecular weight shoulder was observed for entry 6.8 (**Table 6.2**). This behavior was attributed to the increasing steric hindrance at the propagating chain end, resulting in an inconsistent macromonomer distribution. According to this hypothesis, molecular weight and solubility of the forming graft copolymer are important parameters regarding polymerization control.

The delayed addition of fast *exo* macromonomer to an ongoing polymerization of a slow *endo* norbornene monomer was successfully executed. This proof of concept demonstrates an innovative and robust method to synthesize sequence-controlled graft copolymers in a straightforward fashion. In the following, effects of macromonomer structure are examined to fully understand the herein present copolymerization process. The figures representing the entries 6.6 – 6.8 (**Table 6.2**) are presented in the experimental section in **chapter 8.3.3**.

When increasing the length of the linker between the norbornene moiety and the pendant PMMA (from ethyl to hexyl) and using **xNb6M13** in the next set of copolymerization reactions (entry 6.9 – 6.12, **Table 6.2**), an increase of the k_{app} was expected (**Figure 6.5**).

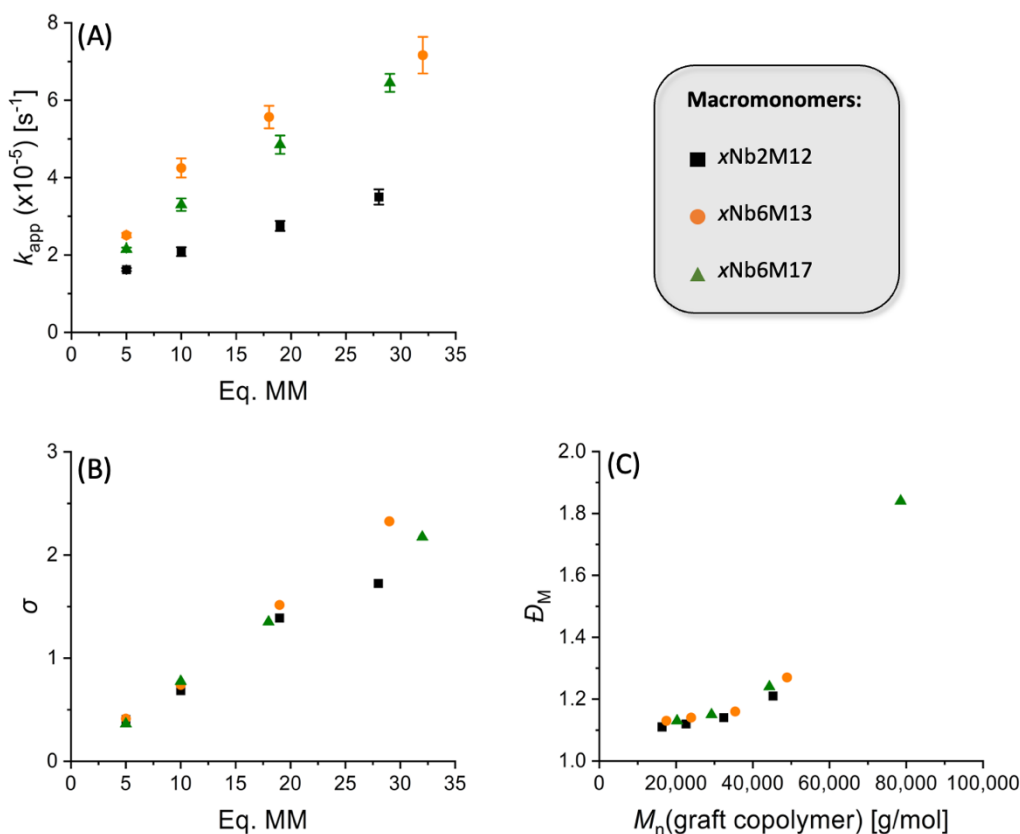


Figure 6.5. (A) Relationship between apparent copolymerization rate (k_{app}) of the macromonomer, its structure and amount, (B) evolution of macroblock grafting density (σ) with increasing macromonomer amount and (C) relationship between dispersity (D_M) of the resulting graft copolymer and its molecular weight.

The kinetic data determined by ^1H NMR spectroscopy supported this assumption. Indeed, comparing e.g. the copolymerization reactions of **xNb6M13** of entry 6.10 (Table 6.2) and **xNb2M12** of entry 6.6 (Table 6.2), **xNb6M13** bearing the hexyl linker was incorporated two times faster (Figure 6.5A). This behavior was mainly attributed to the higher mobility of the copolymer side chains, leading to a more accessible propagating chain end, and further to the sterically less hindered norbornene unit at the incoming macromonomer. Similar to the first set, the copolymerization kinetics of **xNb6M13** were found to be linear at low macromonomer conversions ($\leq 66\%$) and were skewed at high macromonomer conversions ($>66\%$) due to the changing *exo:endo* ratio. However, increasing the amount of macromonomer led to an increasing k_{app} of the respective macromonomer (Figure 6.5A). Surprisingly, although the k_{app} s were increased due to the hexyl linker, the effect on the grafting density of the macroblocks was rather small (Figure 6.5B). This phenomenon was explained by the skewed linear kinetics during the copolymerization process, whereas the

calculated k_{appS} only picture the kinetics at low macromonomer conversions. Due to decreasing *exo:endo* ratios, the differences in polymerization kinetics, a result of the hexyl linker, vanished. As a result, the total reaction times and the grafting densities of both copolymerization sets tended to equalize. Nonetheless, an increase in the k_{appS} with consistent grafting densities led to sharper transitions between the **nNbHex** parts and the macroblocks. The resulting copolymers exhibited relatively narrow molecular weight distributions (**Table 6.2**). This behavior was mainly attributed to the higher mobility of the copolymer side chains, leading to a more accessible propagating chain end, and further to the sterically less hindered norbornene unit at the incoming macromonomer. It is noted that a high molecular weight shoulder was detected in entry 6.12 (**Figure S6.38, Table 6.2**). Nonetheless, the herein synthesized blocky, yet gradient, graft copolymers exhibit a more complex architecture than comparable literature-known block copolymers e.g. synthesized using G3 catalyst.⁴¹² The latter necessarily exhibit sharp transitions after each macroblock due to the iterative synthesis procedure, leading to strong segregation between the segments and highly dense grafts. Whereas the former facilitates more possibilities in terms of structural design, e.g. by the targeted variation of macromonomers and diluents used. The figures representing the entries 6.9 – 6.12 (**Table 6.2**) are presented in the experimental section in **chapter 8.3.3**.

The basic structure of graft copolymers is mainly defined by the backbone DP, which is further defined by the (macro)monomer to catalyst ratio and by the side chain DP or the molecular weight of the macromonomer, respectively. Albeit the macromonomer size has a large effect on the properties of the resulting copolymer,⁵¹⁹ high molecular weights come along with steric hindrance at the propagating chain end and thus have a negative effect on polymerization control and becoming apparent as bimodal molecular weight distributions.⁵²⁰ Therefore, the third set of copolymerization reactions (entries 6.13 – 6.16, **Table 6.2**) was performed using **xNb6M17** to evaluate the influence of the macromonomer size on the copolymerization process. The polymerization of bulky monomers *via* ROMP is assumed to be slower compared to smaller monomers.⁵¹⁸ The same trend was observed comparing two macromonomers with an identical hexyl linker, but different molecular weights, in particular 2,100 g/mol for **xNb6M17** and 1,700 g/mol for **xNb6M13**. Furthermore, the former was incorporated 1.7 times faster in entry 6.15 (**Table 6.2**) than **xNb2M12** in entry 6.7 (**Table 6.2**), leading to the conclusion that the influence of the longer linker unit exceeded the retarding

influence of increasing macromonomer size (**Figure 6.5A**). Analogously to previous copolymerization reactions, the copolymerization kinetics were found to be skewed at high macromonomer conversions and a higher amount of macromonomer led to an increasing k_{app} of the respective macromonomer (**Figure 6.5A**). The effect of **xNb6M17** on the grafting densities of the respective macroblocks was rather small (**Figure 6.5B**), leading to the assumption that the grafting density is mainly defined by the propagation rate of the used macromonomer, whereas high molecular weights are compensable e.g. by a longer alkyl linker unit. The SEC measurements of entries 6.13 and 6.14 (**Table 6.2**) exhibited narrow molecular weight distributions, whereas entries 6.15 and 6.16 (**Table 6.2**) exhibited an increasing high molecular weight shoulder. Interestingly, the dispersity of the resulting copolymers was found to increase monotonically albeit in a non-linear fashion with increasing molecular weights (>50,000 g/mol) (**Figure 6.5C**). According to these results, it is hypothesized that the relative structures of the PMMA-based macromonomers, in particular linker length and size, do not influence the copolymerizability using this synthesis procedure. Hence, polymerization control is mainly determined by the molecular weight of the obtained product. As a result, the herein presented graft copolymer synthesis exhibits a high degree of versatility regarding macromonomer structure and sequence control. Furthermore, characteristics like propagation rate and macroblock composition can be controlled in a straightforward fashion by macromonomer design and selection of suitable diluents. The figures representing the entries 6.13 – 6.16 (**Table 6.2**) are presented in the experimental section in **chapter 8.3.3**.

Since the influences of the linker lengths and the macromonomer sizes on the copolymerization processes were examined, the variation in the grafting densities of the respective macroblocks were investigated. It is herein hypothesized that a lower grafting density within the macroblock or less steric hindrance at the propagating chain end, respectively, favor a controlled copolymerization process even at high molecular weights (>50,000 g/mol). Therefore, the amount of slow polymerizing **nNbHex** was doubled in entry 6.17 (**Table 6.3**), while the amount of **xNb6M17** and the reaction volume was not changed compared to that of entry 6.15 (**Table 6.2**).

Table 6.3. Graft copolymers synthesized by ROMP from *nNbHex* and *xNb6M17*, applying different catalyst concentrations and M:I ratios of 100:1.

entry ^a	M:MM ratio	c(G1) [mmol/L]	addition [%] ^b	$k_{app,endo}$ [s ⁻¹] ^c	$k_{app,exo}$ [s ⁻¹] ^d	σ ^e	M_n [g/mol] ^f	\mathcal{D}_M ^f
6.17	100 : 20	2.00	16	3.43×10^{-6}	2.47×10^{-5}	0.60	57,700	1.33
6.18	100 : 20	1.00	16	1.80×10^{-6}	1.42×10^{-5}	0.50	45,100	1.15

^aReaction conditions: *nNbHex*, G1 catalyst and *xNb6M17* in degassed DCM-d₂ under argon atmosphere at ambient temperature. ^bConversion of *nNbHex* before addition of the MM, determined by ¹H NMR spectroscopy. ^cCalculated from data points at low *nNbHex* conversion during copolymerization using pseudo first order kinetics. ^dCalculated from data points at low *xNb6M17* conversions using pseudo first order kinetics. ^eCalculated from monomer conversions during copolymerization using $\sigma = N(xNb6M17)/N(nNbHex)$. ^fDetermined by SEC.

The copolymerization process in entry 6.17 (**Table 6.3**) was initiated after reaching a DP of 16 (16% conversion of *nNbHex*) to obtain a comparable copolymer. As expected, the decreasing *exo:endo* ratio led to a decrease in k_{app} and to a decreasing grafting density within the macroblock. Interestingly, the decrease of the *exo:endo* ratio by the factor of two (comparing entries 6.15 and 6.17) led to a decrease of in the k_{app} and the graft density by the factors of two, respectively. However, the SEC trace of entry 6.17 showed a large high molecular weight shoulder, resulting in a larger dispersity than that of entry 6.15. It was assumed that the higher total monomer concentration during the ROMP of entry 6.17 had an unfavorable effect on the polymerization control. In order to investigate this assumption, the total monomer concentration was reduced, reducing unfavorable steric interactions and thus potentially leading to a more controlled polymerization process. Therefore, the reaction conditions were modified by reducing the amounts of the macromonomer *xNb6M17* and the G1 catalyst (entry 6.18, **Table 6.3**), while keeping the amount of *nNbHex* and the reaction volume constant. Similar to entry 6.17 (**Table 6.3**), the copolymerization process was initiated after reaching a DP of 16 (16% conversion of *nNbHex*). The decreased *exo:endo* ratio led to a decreased k_{app} of the corresponding macromonomer and a decreased grafting density within the macroblock. Although a higher molecular weight shoulder was detected, lower dispersity compared to entry 6.15 (**Table 6.2**) indicated an advantageous effect on the polymerization control. This finding supports the assumption that the molecular weight and the preorientation of the growing graft copolymer in solution have a large influence on the

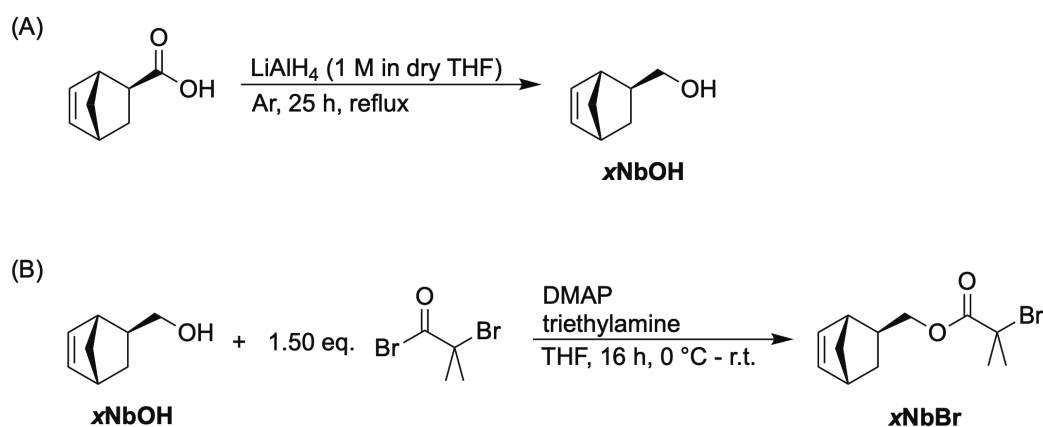
polymerization process. The figures representing entries 6.17 and 6.18 (**Table 6.3**) are presented in the experimental section in **chapter 8.3.3**.

As a result, a variety of graft copolymers was successfully synthesized by the G1-mediated ROMP, whereby the macromonomers were added at a specific *endo* monomer conversion. Although the kinetics were skewed during the copolymerization process, the herein presented strategy was characterized by the absence of low molecular weight tailing and low molecular weight shoulders, which are generated by catalyst poisoning. The rapidly incorporated macroblocks showed a gradient substructure which was affected by the applied *exo:endo* ratio. Furthermore, parameters such as the apparent propagation rate constant and the grafting density were affected by the latter, enabling the targeted design of complex architectures.

6.3.2 Synthesis of norbornene ester-based macromonomers

In this section, the synthesis of *exo* norbornene ester-functional macromonomer *via* ATRP is described. Methyl and benzyl methacrylate serve as monomers. The obtained macromonomers are further examined regarding their molecular structure and their thermal properties.

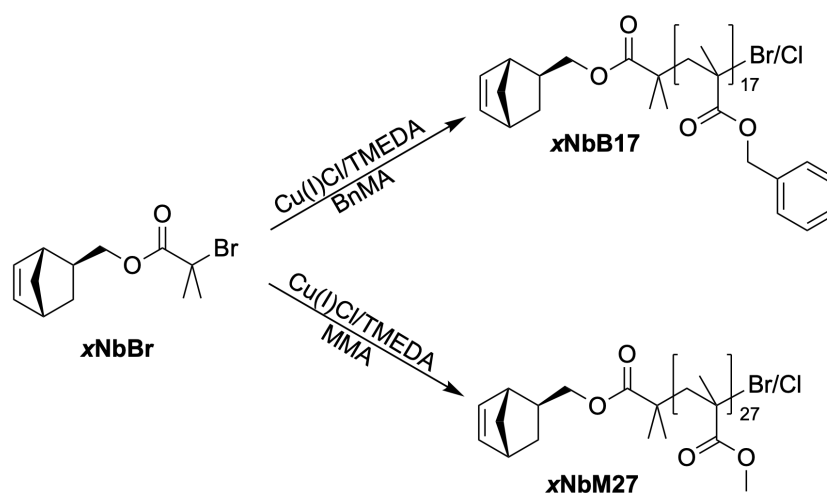
Since the steric interactions of the growing graft copolymer were assumed to affect the copolymerization process in ROMP using the delayed macromonomer addition procedure, a less sterically hindered polymerizable norbornene unit was used to synthesize a new type of ATRP initiator (**Scheme 6.2**).⁵⁰⁵



Scheme 6.2. Synthesis of (A) **xNbOH** *via* reduction of *exo* norbornene carboxylic acid using LiAlH_4 , and (B) subsequent esterification *via* using α -bromoisobutyryl bromide, obtaining **xNbBr**.

The synthesis of **xNbOH** using *exo*-5-norbornene-2-carboxylic acid as precursor was described in **chapter 5.3.5 (Scheme 6.2A)**, whereas the subsequent esterification using α -bromoisobutyryl bromide was described in **chapter 5.3.1 (Scheme 6.2B)**. Hereby, the ATRP initiator **xNbBr** was obtained as a colorless liquid in a yield of 79% (**Figure S6.66**).

In order to synthesize sequence-controlled graft copolymers in a multiblock architecture, different macromonomer types were synthesized *via* ATRP (**Scheme 6.3**). Here, a different synthesis procedure was used compared to the ATRPs described in **chapter 5.3.1 (Scheme 5.2, Table 5.1)**, obtaining a reduced polymerization rate and thus preventing high monomer conversions, which potentially lead to side reactions.



Scheme 6.3. Synthesis of *exo* norbornene ester-functional macromonomers *via* ATRP using **xNbBr** as ATRP initiator and benzyl methacrylate (BnMA, top) and methyl methacrylate (MMA, bottom) as monomers.

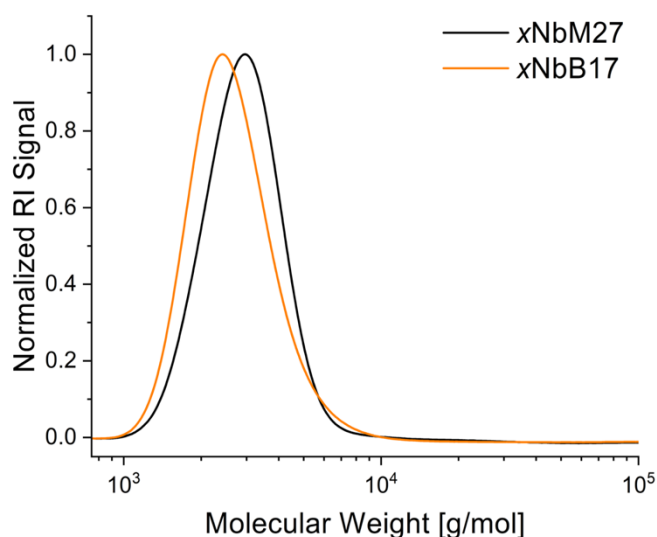
Therefore, the synthesis and the purification of the PMMA- and the PBnMA-based macromonomer were adapted from **chapter 5.3.5**. The ATRPs were quenched after *ca.* nine hours for the PMMA-based macromonomer, reaching a monomer conversion of 54%, and after 3.5 hours for the PBnMA-based macromonomer, reaching a monomer conversion of 34%, to obtain macromonomers with a comparable molecular weight (**Table 6.4**). The macromonomers were obtained as white solids.

Table 6.4. Synthesized *exo* norbornene ester–based macromonomers *via* ATRP.

Polymer ^a	Monomer	Reaction Time [h]	Conversion [%] ^b	$M_{n,NMR}$ [g/mol] ^b	$M_{n,SEC}$ [g/mol] ^c	\mathcal{D}_M^c
xNbM27	MMA	8.75	54	3,000	2,800	1.11
xNbB17	BnMA	3.50	34	3,300	2,600	1.14

^aReaction conditions: Monomer, initiator (0.045 mol/L), Cu(I)Cl and TMEDA in anisole at 70 °C under argon atmosphere (M:I:Cu:L ratio – 50:1:1:2). ^bDetermined by ¹H NMR spectroscopy. ^cDetermined by SEC.

The obtained macromonomers are termed as previously defined in **chapter 5.3.1**. Hereby, molecular weights of 3,000 g/mol and 3,300 g/mol were determined by ¹H NMR spectroscopy. The obtained macromonomers were further characterized by SEC to examine the molecular weight distribution and thus evaluate the applied ATRP procedure (**Figure 6.6**).

**Figure 6.6.** SEC traces of polymethacrylate-based macromonomers, comprising polymerizable *exo* norbornene moieties (**Table 6.4**)

For both macromonomers, narrow molecular weight distributions (≤ 1.14) were observed, indicating well-controlled polymerization processes, whereby the determined dispersity values were similar to that of the macromonomers synthesized in **chapter 5.3.1** (**Table 5.1**). The M_n s determined *via* SEC and ¹H NMR spectroscopy were found to be consistent.

The macromonomers were further analyzed using MALDI-TOF MS. The obtained data were determined to confirm the macromonomer structure, including the potential determination

of the attached end groups, and to evaluate the applied ATRP procedure. The results of **xNbM27** and **xNbB17** were found to be similar to the corresponding macromonomers described in **chapter 5.3.1** and are presented in the experimental section in **chapter 8.3.3**. The assignment of the signals was additionally verified by comparing the observed isotopic patterns with the calculated. It is noted that the positions of the lower intensity distributions are further described related to the position of the main distribution. The MALDI-TOF data of **xNbM27** exhibited two distinct distributions, whereby the distance between two consecutive signals corresponded to the mass of one methyl methacrylate unit (expected: 100.05 m/z , **Figure S6.70B**). The highest intensity distribution was assigned to the chloride-terminated species, whereas the distribution at $\Delta(m/z) = -33.00$ was assigned to the hydrogen-terminated species (**Figure S6.70C**). The MALDI-TOF data of **xNbB17** also exhibited two distinct distributions. The distance between two consecutive signals corresponded to the mass of one benzyl methacrylate unit (expected: 176.08 m/z , **Figure S6.74B**), whereby the highest intensity distribution was assigned to the chloride-terminated species. Similar to the MALDI-TOF data of **xNb2B12** discussed in **chapter 5.3.1** (**Figure 5.3**), the distribution at $\Delta(m/z) = -83.66$ was assigned to the double charged α,ω -dinorbornyl species ionized by two copper(I) ions (**Figure S6.74C**). This supported the previously made assumption that in contrast to the methyl side groups, the interaction between the benzyl side groups and the copper favored sufficient ionization of the corresponding species. The relative intensities shown in the spectra do not necessarily reflect the concentration of the determined species in the samples. However, the findings were in agreement with the data obtained by SEC and ^1H NMR spectroscopy. The latter indicated a nearly quantitative end group fidelity for both macromonomers by comparing the signals at 2.60 – 2.25 ppm, assigned to the methylene groups of the last methacrylate repeat units, and the characteristic olefinic signals of the norbornene moieties at 6.15 – 6.02 ppm. As discussed in **chapter 5.3.1**, it is assumed that the cleavage of the halide end group, and thus the formation of the hydrogen-terminated species in **xNbM27** and α,ω -dinorbornyl species in **xNbB17**, was induced by the ionization process during the measurement.⁴⁷⁸

Furthermore, the thermal behavior of the macromonomers was determined by DSC, whereby a similar behavior was observed compared to the corresponding macromonomers described in **chapter 5.3.1**. Since the molecular weight of the PMMA-based macromonomer **xNbM27** was found to be double than that of **xNb2M12**, the T_g increased by 15 °C and was detected at

87 °C (**Figure S6.76**).⁵²¹ The PBnMA-based macromonomer **xNbB17** exhibited a T_g at 46 °C (**Figure S6.76**). Analogously to the results in **chapter 5.3.1**, blending of both macromonomers resulted in the presence of two T_g s determined at 90 °C, ascribed to the PMMA component, and at 47 °C for the PBnMA one (**Figure S6.76**). It is noted that all herein measured T_g values were determined by the onset temperature of the thermal transition in the second heating cycle, applying a heating rate of 20 °C/min.

As a result, two *exo* norbornene ester-based macromonomers, namely **xNbM27** and **xNbB17**, were synthesized while the corresponding ATRPs were quenched after 54% and 34% monomer conversion, respectively. This further ensured minimal side reactions and the generation of polymers with comparable molecular weights. Similar to previous observations in **chapter 5.3.1**, the obtained methacrylate-based polymers showed immiscibility in a 1:1 blend and thus are interesting in potentially self-assembling when combined in a copolymer.

6.3.3 Introduction of multiblocks *via* ROMP

In this section, the introduction of multiblocks into a growing PNB chain by delayed macromonomer addition using the G1-mediated ROMP is examined. Here, the PMMA-based macromonomers **xNb6M17** and **xNbM27**, and the PBnMA-based macromonomer **xNbB17** are used to obtain graft copolymers with a diblock- and triblock-like architecture, varying the molar fraction of the different macromonomers.

The reliability of the applied ROMP procedure which was introduced in **chapter 6.3.1**, was examined in terms of multiple macromonomer additions and its effect on the kinetics and the controlled character of the polymerization process and thus to gain access to even more complex architectures and the preparation of sequence-controlled graft copolymers. As a proof of concept, two consecutive macromonomer additions were performed using **xNb6M17** (entry 6.19, **Table 6.5**), obtaining a copolymer with two distinct macroblocks.

Table 6.5. Diblock graft copolymer synthesized by the G1-mediated ROMP of *nNbHex* and two consecutive additions of *xNb6M17*.

entry ^a	M:MM ratio	addition [%] ^b	$k_{app,endo}$ [s ⁻¹] ^c	$k_{app,exo}$ [s ⁻¹] ^d	σ ^e	M_n [g/mol] ^f	\mathcal{D}_M ^f
6.19-B1	50:5	36	2.12×10^{-6}	2.25×10^{-5}	0.33	23,600	1.13
6.19-B2	50:5	69	1.79×10^{-6}	2.25×10^{-5}	0.96	37,400	1.15

^aReaction conditions: *nNbHex*, G1 catalyst (2 mmol/L) and *xNb6M17* in degassed DCM-d₂ under argon at ambient temperature. ^bConversion of *nNbHex* before addition of *xNb6M17*, determined by ¹H NMR spectroscopy. ^cCalculated from data points at low *nNbHex* conversion during copolymerization using pseudo first order kinetics. ^dCalculated from data points at low *xNb6M17* conversion using pseudo first order kinetics. ^eCalculated from monomer conversions during copolymerization using $\sigma = N(xNb6M17)/N(nNbHex)$. ^fDetermined by SEC.

The homopolymerization of *nNbHex* was performed applying a M:I ratio of 50:1, whereas *xNb6M17* was used as macromonomer with a targeted MM:I ratio of 5:1 for each addition. The macromonomers were added after reaching a DP of *ca.* 20 (36% conversion of *nNbHex*) and *ca.* 43 (69% conversion of *nNbHex*, $\geq 99\%$ conversion of *xNb6M17*), respectively (**Figure S6.65**). Although the additions were conducted at different conversions of the *endo* monomer, identical k_{app} s were obtained for both (**Table 6.5**, **Figure 6.7A**). As discussed in **chapter 6.3.1**, the copolymerization kinetics of the macromonomers were deemed to be pseudo first order at low macromonomer conversions.

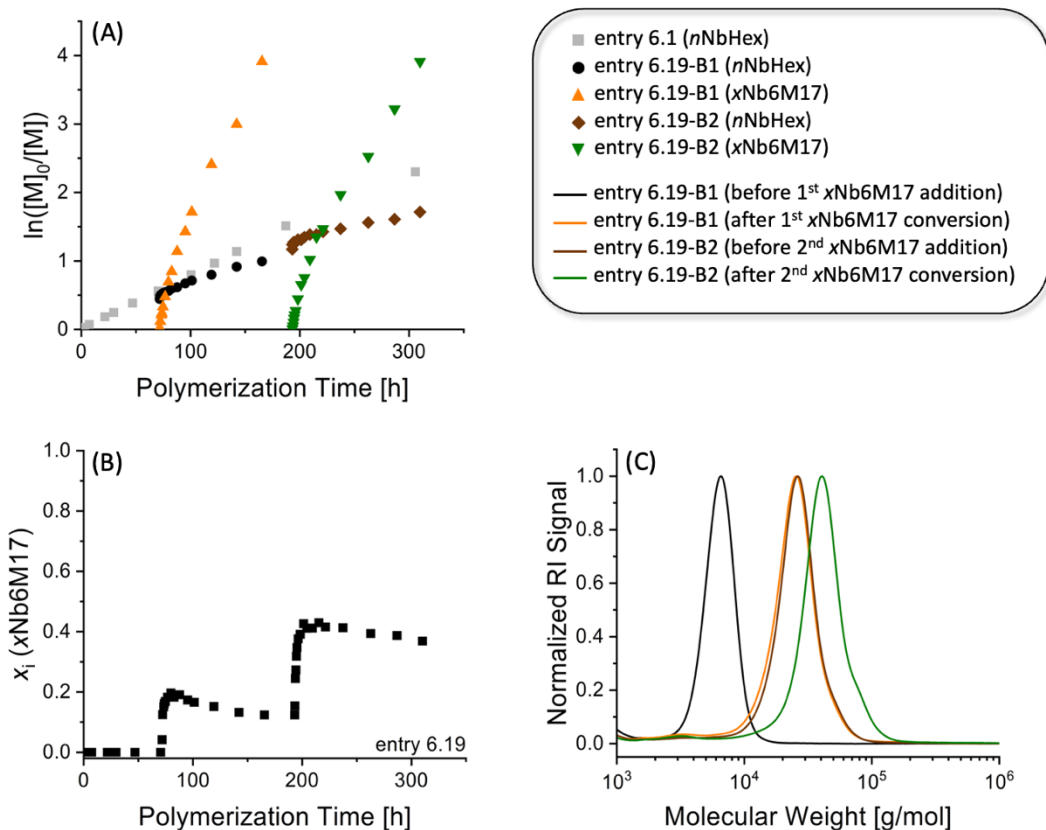


Figure 6.7. (A) Kinetic plots of entry 6.1 (Table 6.1), entry 6.19-B1 and entry 6.19-B2 (Table 6.5), (B) molar fraction (x_i) of $x\text{Nb6M17}$ in entry 6.19 as a function of polymerization time, based on ^1H NMR spectroscopy data (Figure S6.65), and (C) SEC traces of entry 6.19 before addition of first and second macroblock and after complete conversion of the first and second macroblock.

The $n\text{NbHex}$ polymerization was not affected by the incorporation of the macromonomers in a consecutive fashion (Figure 6.7A), demonstrating the high reliability of the herein presented polymerization method and confirming observations shown in recent literature for small norbornene-based monomers.⁹³ The obtained diblock graft copolymer exhibited a block-like structure that was characterized by relatively sharp transitions between the $n\text{NbHex}$ parts and the macroblocks, whereas the macroblocks were progressively diluted by $n\text{NbHex}$ during the copolymerization process, exhibiting a gradient substructure (Figure 6.7B). As expected, the grafting density of the second macroblock increased due to a larger *exo:endo* ratio than that of the first macroblock (0.16:1 for entry 6.19-B1, 0.32:1 for entry 6.19-B2). The SEC traces of entry 6.19 (Table 6.5) exhibited relatively narrow molecular weight distributions for both macroblocks (Figure 6.7C), suggesting that the position of the macroblock along the polymeric chain had no unfavorable effect on the ROMP. A small high molecular weight shoulder was detected after complete incorporation of the second macromonomer, potentially caused by

the high molecular weight of the formed diblock graft copolymer as discussed in **chapter 6.3.1**. However, the macromonomer sequences were precisely introduced into the growing PNB backbone at defined positions along the polymeric backbone, generating a diblock-like graft copolymer with a relatively low dispersity.

In order to apply the herein presented ROMP procedure in the synthesis of high molecular weight graft copolymers and retain monomodal and narrow molecular weight distributions, macromonomers with different polymerizable *exo* norbornene units were used, namely **xNbM27** and **xNbB17**. The syntheses of the latter were described in **chapter 6.3.2 (Scheme 6.3, Table 6.4)**. Similar to entry 6.19, the ROMP of **nNbHex** was used as a continuous polymerization, followed by delayed macromonomer additions to obtain a variety of sequence-controlled macroblocks (**Figure 6.8**).

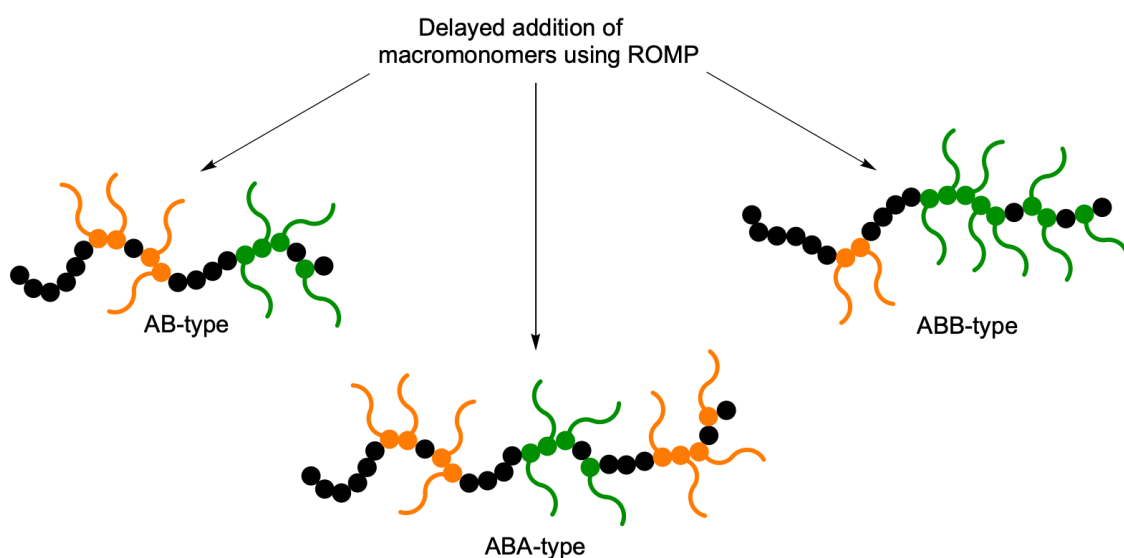


Figure 6.8. Schematic representation of different polymer architectures using ROMP with delayed addition of macromonomers, indicating the gradient substructures by progressive dilution of the macroblocks. Here, A and B only represent the different macromonomers.

The macromonomers obtained in **chapter 6.3.2** were used to synthesize three types of sequence-controlled graft copolymer: a diblock comprising equal amounts of two different macromonomers (AB-type), a diblock comprising unequal amounts of two different macromonomers (ABB-type), and a triblock comprising two different macromonomers in an alternating fashion (ABA-type, **Table 6.6**).

It is noted that A and B only represent the different macromonomers, whereas the amount and position of the diluent is not defined within this classification.

Table 6.6. Multiblock graft copolymers synthesized by the G1-mediated ROMP of *nNbHex* and delayed macromonomer addition.

entry ^a	MM	M:MM ratio	addition [%] ^b	$k_{app,exo}$ [s ⁻¹] ^c	σ ^d	M_n [g/mol] ^e	\mathcal{D}_M ^e
6.20-B1	xNbM27	50:20	30	2.55×10^{-4}	5.20	47.700	1.15
6.20-B2	xNbB17	50:20	59	2.64×10^{-4}	16.5	87.000	1.21
6.21-B1	xNbM27	50:8	35	3.77×10^{-4}	2.13	26.900	1.10
6.21-B2	xNbB17	50:32	61	2.70×10^{-4}	18.4	94.200	1.26
6.22-B1	xNbM27	50:16	33	2.07×10^{-4}	4.76	39.900	1.13
6.22-B2	xNbB17	50:8	60	1.38×10^{-4}	1.80	54.200	1.15
6.22-B3	xNbM27	50:16	72	1.36×10^{-4}	6.51	87.200	1.26

^aReaction conditions: *nNbHex*, G1 catalyst (2 mmol/L) and macromonomer (MM) in degassed DCM-d₂ under argon at ambient temperature. ^bConversion of *nNbHex* before addition of MM, determined by ¹H NMR spectroscopy. ^cCalculated from data points at low MM conversion using pseudo first order kinetics. ^dCalculated from monomer conversions during copolymerization using $\sigma = N(\text{MM})/N(\textit{nNbHex})$. ^eDetermined by SEC.

Since the *exo* norbornene dicarboximide–based macromonomers, e.g. **xNb6M17 (Scheme 5.2, Table 5.1)**, were limited toward the synthesis of high molecular weight graft polymers, the *exo* norbornene ester–based macromonomers (**Scheme 6.3, Table 6.4**) were used applying comparable conditions (**Table 6.6**). The *nNbHex* polymerization was performed applying a M:I ratio of 50:1, whereas the first macromonomer was added after reaching 30% to 35% *endo* conversion (entry 6.20 – 6.23, **Table 6.6**). The second macromonomer was added after reaching 60% to 61% *endo* conversion (entry 6.20 – 6.23, **Table 6.6**) and the third macromonomer addition (entry 6.22, **Table 6.6**) was executed after reaching 72% *endo* conversion. In all cases, the total ratio between *nNbHex* and the macromonomers was 50:40, whereby the macromonomer ratios were defined as 1:1, 1:3, and 2:1:2 (entries 6.20 – 6.22, **Table 6.6**). The AB-type diblock was performed using equimolar amounts of **xNbM27** and **xNbB17**, respectively (**Figure 6.9**).

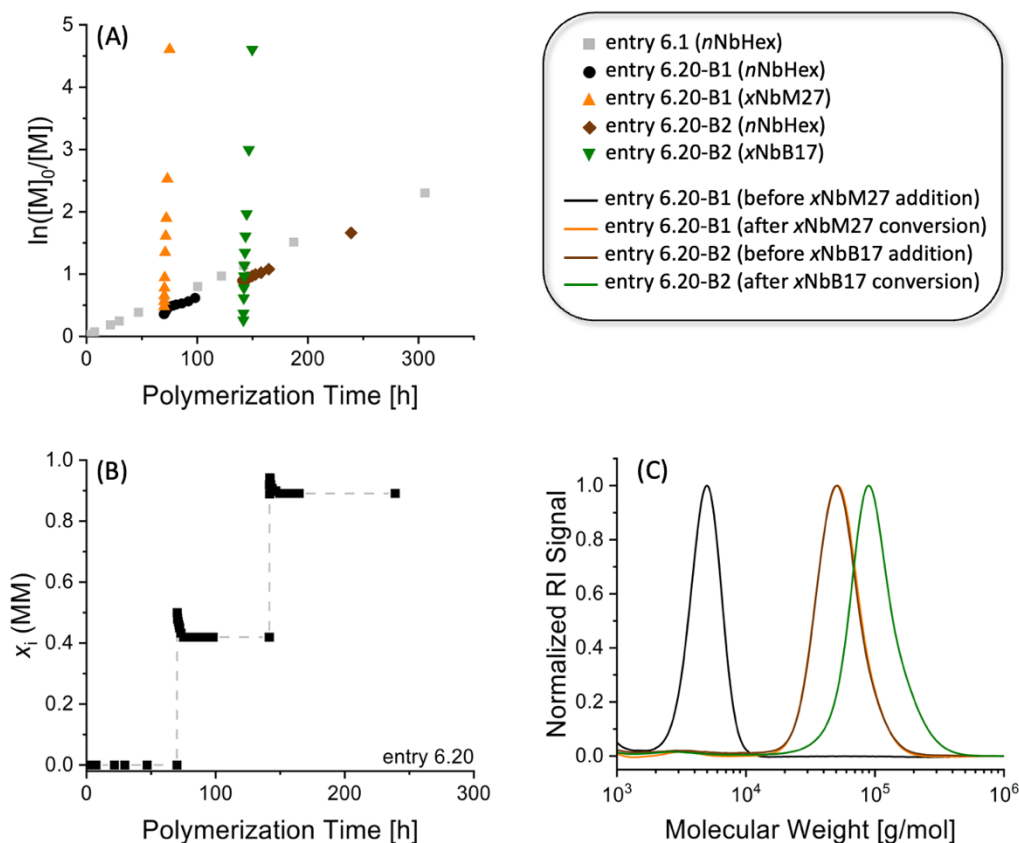


Figure 6.9. (A) Kinetic plots of entry 6.1 (Table 6.1), entry 6.20-B1 and entry 6.20-B2 (Table 6.6), (B) molar fraction (x_i) of the macromonomers (MM) in entry 6.20 as a function of polymerization time, based on ^1H NMR spectroscopy data (Figure S6.79), step-like MM incorporation highlighted by the grey dotted line, and (C) SEC traces of entry 6.20 before addition of first and second macroblock and after complete conversion of the first and second macroblock.

The kinetic data of both the mono- and the diblock of entry 6.20 (Table 6.6) suggested rapid macromonomer conversion immediately after the addition, reaching complete conversion after eight hours (Figure 6.9A). The k_{app} of *x*NbM27 during the first copolymerization (entry 6.20-B1, Table 6.6) was found to be 4.5 times higher than that of the fastest *exo* norbornene dicarboximide-based macromonomer *x*Nb6M13 (entry 6.11, Table 6.2). As expected, the k_{app} s of the mono- and the diblock were found to be similar due to the comparable molecular weights of the macromonomers and their 1:1 ratio. Furthermore, the kinetics of the continuous *n*NbHex polymerization remained unaffected by the incorporation of the macromonomers in a consecutive fashion (Figure 6.9A). Due to the rapid incorporation of the *exo* macromonomers into the polymeric backbone, sharp transitions between the macroblocks and the diluents were detected (Figure 6.9B). Here, the grafting density was

determined as 5.20 for the first block and 16.5 for the second block, suggesting distinct block-like structures with minimized gradient substructures. It is noted that the step-like macromonomer incorporation is highlighted by a grey dotted line in the molar fraction graph (**Figure 6.9B**). The SEC traces of entry 6.20 exhibited narrow molecular weight distributions for both macroblocks with a maximum dispersity of 1.21 while reaching a molecular weight of 87,000 g/mol (**Figure 6.9C, Table 6.6**). Similar to entry 6.19 (**Table 6.5**), these observations suggested that the position of the macroblock along the polymeric chain had no unfavorable effect on the polymerization process. Hence, the ROMP process using the *exo* norbornene ester-based macromonomers was found to be well-controlled, generating a sequence-controlled diblock graft copolymer in a straightforward fashion.

In order to verify the successful incorporation of distinct macroblocks and to obtain a diblock-like graft copolymer with an unequal macromonomer ratio, entry 6.21 (**Table 6.6**) was performed applying a 1:3 ratio for **xNbM27** and **xNbB17** and thus obtaining an ABB-type graft copolymer (**Figure 6.10**).

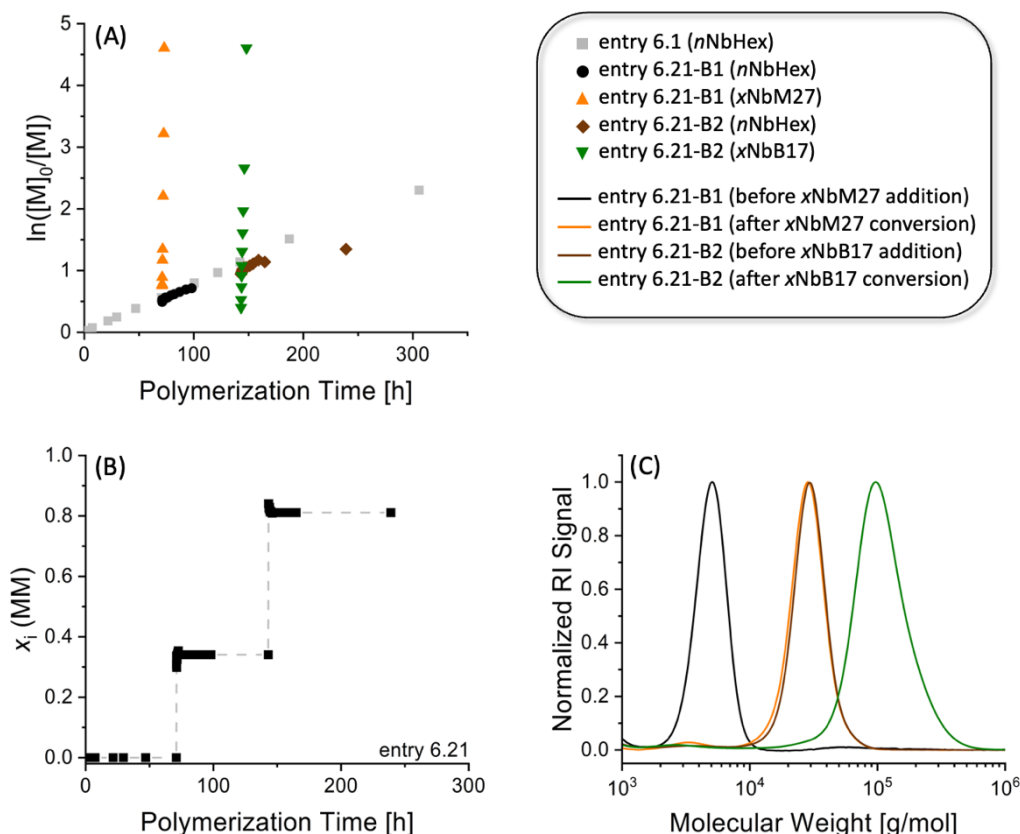


Figure 6.10. (A) Kinetic plots of entry 6.1 (Table 6.1), entry 6.21-B1 and entry 6.21-B2 (Table 6.6), (B) molar fraction (x_i) of the macromonomers (MM) in entry 6.21 as a function of polymerization time, based on ^1H NMR spectroscopy data (Figure S6.82), step-like MM incorporation highlighted by the grey dotted line, and (C) SEC traces of entry 6.21 before addition of first and second macroblock and after complete conversion of the first and second macroblock.

Similar to entry 6.20 (Table 6.6), both macromonomers were rapidly consumed, exhibiting complete conversion after two hours for the monoblock and five hours for the diblock. The determined k_{app} s were comparable to that of entry 6.20 (Figure 6.10A, Table 6.6). As expected, the rapid incorporation of the macromonomers resulted in two distinct macroblocks, visualized by a step-like evolution in the molar fraction of the macromonomers within the graft copolymer (Figure 6.10B). The relationship between the grafting density of the macroblocks and the *exo:endo* ratio was found to be consistent with recent observations discussed in chapter 6.3.1. As such, the second macroblock (entry 6.21-B2, Table 6.6) exhibited a grafting density of 18.4, representing the highest value obtained using this ROMP procedure. The SEC traces of the mono- and the diblock of entry 6.21 (Table 6.6) exhibited narrow molecular weight distributions with a maximum molecular weight of 94,200 g/mol and a dispersity of 1.26. Since the molecular weight distribution of entry 6.21-B2 was found

to be slightly broader compared to entry 6.20-B2 (Table 6.6), steric hindrance of the resulting copolymer was assumed to remain a critical factor regarding the controlled synthesis of high molecular weight graft copolymers. Nonetheless, no distinct high or low molecular weight shoulder was detected after two macromonomer additions and reaching molecular weights of 94,200 g/mol and 156,000 g/mol, determined by SEC and ^1H NMR spectroscopy, respectively.

Finally, a triblock graft copolymer was synthesized by the consecutive addition of **xNbM27** and **xNbB17** applying a comonomer ratio of 2:1:2 (entry 6.22, Table 6.6) and thus obtaining an ABA-type architecture (Figure 6.11).

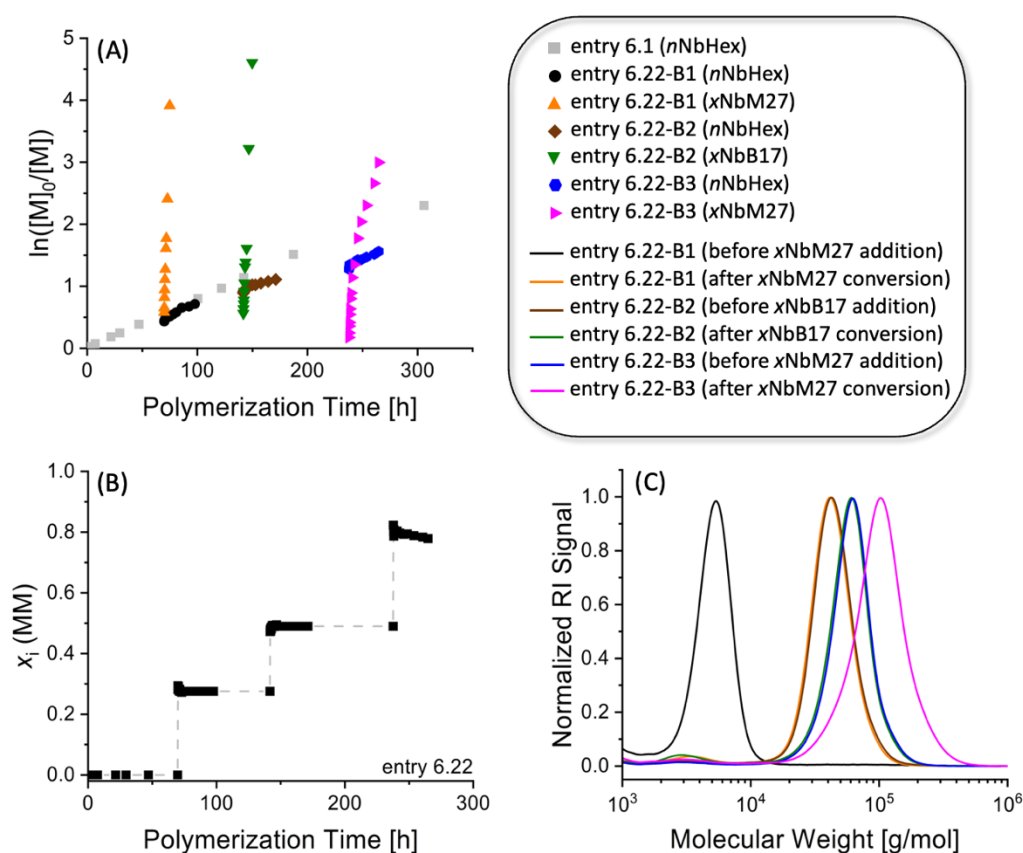


Figure 6.11. (A) Kinetic plots of entry 6.1 (Table 6.1), entry 6.22-B1, entry 6.22-B2 and entry 6.22-B3 (Table 6.6), (B) molar fraction (x_i) of the macromonomers (MM) in entry 6.22 as a function of polymerization time, based on ^1H NMR spectroscopy data (Figure S6.85), step-like MM incorporation highlighted by the grey dotted line, and (C) SEC traces of entry 6.22 before addition of first, second and third macroblock and after complete conversion of the first, second and third macroblock.

The copolymerization kinetics of the first two macroblocks were similar to the entries 6.20 and 6.21, whereby quantitative conversion was reached after five hours for the first block and after eight hours for the second block (**Figure 6.11A**). As expected, the copolymerization kinetics of the third macroblock (entry 6.22-B3, **Table 6.6**) showed pseudo first order kinetic behavior at low macromonomer conversions, whereas the polymerization rate at high conversions decreased with increasing molecular weight of the graft copolymer. This observation was found to be similar compared to the copolymerization kinetics of the *exo* norbornene dicarboximide–based macromonomers (**Figure 6.7**). It was assumed that the preorientation of the graft copolymer in solution was unfavorable toward the accessibility of the propagating chain end for the remaining macromonomer, hampering a controlled ROMP process at high molecular weights. Nonetheless, 95% macromonomer conversion was detected after 27 hours. The structure of entry 6.22 (**Table 6.6**) was found to be block-like with three distinct macroblocks, comprising a minimal gradient substructure (**Figure 6.11B**). Furthermore, the determined grafting densities of the first and the second macroblock were consistent with entries 6.20 and 6.21 (**Table 6.6**), whereas the third macroblock exhibited a lower value as expected. This observation was explained by the decreasing polymerization rate at high molecular weights of the resulting graft copolymer, leading to a longer reaction time and thus to a higher conversion of the *n*NbHex during the copolymerization process. The SEC traces of entry 6.22 exhibited narrow molecular weight distributions, whereby the triblock was found to exhibit a broader distribution compared to the mono- and the diblock (**Figure 6.11C, Table 6.6**). Nonetheless, an ABA-type graft copolymer was successfully synthesized applying three consecutive macromonomer additions, exhibiting a molecular weight of 87,200 g/mol and a dispersity of 1.26.

As a result, the exchange of the polymerizable *exo* norbornene moiety of the macromonomers from a dicarboximide to an ester functionality allowed the synthesis of high molecular weight graft copolymers in a relatively controlled fashion. Although the copolymerization kinetics were slightly skewed, higher apparent propagation rates were found for the *exo* norbornene ester–based macromonomers, leading to sharp transitions between the macroblocks and the diluents and thus generating highly grafted macroblocks. The gradient substructure was still present, albeit strongly reduced compared to the graft copolymers derived from the *exo* norbornene dicarboximide–based macromonomers.

Using this method graft copolymers with controlled macromonomer sequences were obtained, including diblock- and triblock-like architectures.

6.4 Conclusion

In this chapter, it was shown that sequence-controlled graft copolymers were successfully synthesized *via* the G1-mediated ROMP applying a delayed macromonomer addition strategy. An *endo* monomer was polymerized to achieve a relatively slow ROMP acting as a continuous polymerization. After reaching a predetermined conversion, an *exo* norbornene-based macromonomer was added to the ROMP mixture, leading to the fast incorporation of the latter. Initially, different *exo* norbornene dicarboximide-based macromonomers, previously synthesized in **chapter 5.3.1**, were used to evaluate the effect of the macromonomer structure on the copolymerization process. It was found that the macromonomer structure influenced the macromonomer consumption during the copolymerization and thus influenced the architecture of the resulting graft copolymers. Hence, graft copolymers with a block-like structure and molecular weights up to 50,000 g/mol were obtained in a relatively controlled fashion. Furthermore, a sequence-controlled diblock graft copolymer was synthesized by two consecutive macromonomer additions, leading to the formation of two distinct macroblocks along the polymeric backbone. Additionally, the structural effect of the polymerizable norbornene moiety was evaluated regarding the ROMP using the delayed macromonomer addition strategy. Here, *exo* norbornene carboxylic acid was used a precursor for the synthesis of a new norbornene-functional ATRP initiator, followed by the successful ATRP of MMA and BnMA. The herein obtained *exo* norbornene ester-based macromonomers were found to exhibit rapid consumption using an analog ROMP procedure, leading to the formation of densely grafted macroblocks. Hereby, sequence-controlled multiblock graft copolymers (AB-, ABB- and ABA-type) were synthesized with molecular weights up to 100,000 g/mol, exhibiting narrow molecular weight distributions and a high degree of polymerization control.

Future work will focus on the examination of the obtained graft copolymers regarding potential self-assembly in thin films *via* AFM and SAXS. Furthermore, the influences of the gradient substructure and the variation of the copolymer composition on the self-assembly are considered as an encouraging basis for future research.

7 Conclusion and outlook

In this thesis, different approaches to synthesize functional polymers *via* the ROMP of norbornene derivatives were demonstrated, including monomer modification using the P-3CR, iterative ROMP of macromonomers, branched bifunctional macromonomers and delayed macromonomer addition. All the approaches were motivated by the ability of the ROMP process to generate sequence-controlled functional copolymers in a “living” fashion and thus influence the macro- and microscopic properties of the resulting material.

In **chapter 4**, the synthesis of bifunctional norbornene-based monomers using the P-3CR capable of undergoing a controlled ROMP process, was explored. Due to the high versatility of the P-3CR, aliphatic, aromatic, and sterically hindered side groups were successfully connected to the polymerizable norbornene moieties in a straightforward fashion, thus allowing the synthesis of highly functional polymers *via* the G1-mediated ROMP. Although the influence of the attached side groups on the ROMP kinetics was found to be relatively small, all synthesized *exo* and *endo* monomers followed pseudo first order kinetic behavior leading to low dispersity polymers. Furthermore, the combination of monomers led to a variety of copolymers, including statistical copolymers and copolymers exhibiting diblock- and triblock-like structures. This further demonstrated the potential of the herein presented approach in the synthesis of sequence-controlled copolymers. The T_g s of the obtained polymers were found to be influenced by the attached side groups, covering a wide temperature range, whereas the T_d s were found to be independent of the respective monomer structure. Future work on this topic will focus on the mimicking of proteins or enzymes by copolymerizing P-3CR-derived monomers and macromonomers in a sequence-controlled fashion, in order to fulfill functions in cellular environments or catalyze the conversion of biomolecules.⁴⁵⁰

In **chapter 5**, the optimization of the ROMP of norbornene-based macromonomers and the formation of sequence-controlled graft copolymers using an iterative approach was described. The used macromonomers were successfully obtained *via* ATRP and their thermal properties were analyzed to confirm the immiscibility of the PMMA- and the PBnMA-based macromonomers on account of the presence of distinctive thermal transitions that indicate phase separation in the homopolymer blend. Such as, the corresponding copolymers were

hypothesized to self-assemble in bulk. Although the G1-mediated ROMP was hindered from the sterically demanding macromonomers, low molecular weight graft polymers were obtained in a controlled fashion. However, pseudo first order kinetics were determined using the G3 catalyst, leading to low dispersity graft polymers. The synthesis of sequence-controlled graft copolymers *via* an iterative approach was not possible, potentially due to the poisoning of the catalyst during the chain-extension process. Here, the use of low reaction temperatures and dry solvents was found to be beneficial, whereby glovebox conditions are necessary to obtain high chain-extension efficiency.⁴⁷² Furthermore, bifunctional macromonomers were successfully synthesized by combining P-3CR, ATRP and CuAAC. Although the method suffered from coupling side reactions, purification *via* fractionated precipitation was found to be effective to remove byproducts. Subsequent ROMP led to low dispersity Janus graft copolymers comprising two potentially immiscible polymer chains. A future consideration of this project is to examine the self-assembly of the obtained graft copolymers in thin films using AFM and SAXS and further examine the influence of polymer dispersity on the generated self-assembled structures.

In **chapter 6**, the different kinetic behavior of *exo* and *endo* norbornenes in G1-mediated ROMP was used to synthesize sequence-controlled graft copolymers. Here, distinct macroblocks exhibiting local gradient substructures due to the copolymerizability of the norbornene isomers were successfully introduced into a growing PNB backbone by delayed macromonomer addition. Although the ROMP kinetics was found to not follow first order kinetics during the copolymerization process, the obtained graft copolymers were characterized by relatively narrow and monomodal molecular weight distributions and a high degree of polymerization control for copolymers with molecular weights up to 50,000 g/mol. Notably, the achievable molecular weights were increased up to 100,000 g/mol by simple change of the norbornene precursor. Furthermore, the structure of the polymerizable norbornene unit was found to influence the gradient substructure of the resulting block-like graft copolymers. As a result, graft copolymers exhibiting diblock- and triblock-like structures were obtained in a controlled and straightforward fashion, avoiding the use of dry solvents and glovebox conditions. Future work will focus on the examination of the obtained graft copolymers regarding potential self-assembly in thin films *via* AFM and SAXS. Furthermore, the influences of the gradient substructure and the variation of the copolymer composition on the self-assembly are considered as an encouraging basis for future research.

8 Experimental Section

8.1 Materials

1-Adamantyl isocyanide (95%), 1-pyrenecarboxaldehyde (99%), 4,4'-dinonyl-2,2'-dipyridyl (97%), 6-amino-1-hexanol (97%), 11-aminoundecanoic acid (97%), aluminum oxide (neutral & basic), anhydrous dichloromethane ($\geq 99.8\%$, contains 40-150 ppm amylene), anhydrous tetrahydrofuran ($\geq 99.9\%$, inhibitor-free), cerium(IV)-sulfate (99%), copper(I) chloride (99.999% trace metals basis), copper(I) bromide (99.999% trace metals basis), dichloro(benzylidene)-bis(tricyclohexylphosphine)ruthenium(II) (97%), dichloro[1,3-bis(2,4,6-trimethylphenyl)-2-imidazolidinylidene](benzylidene).(tricyclohexylphosphine)ruthenium(II), dithranol ($\geq 98.5\%$, puriss. p.a.), DMT-functionalized silica gel ($\geq 99\%$), ethyl α -bromoisobutyrate (98%), *exo*-5-norbornene carboxylic acid (97%), glycine (99%), hexylamine (99%), Lithium aluminum hydride (1 M in dry THF), magnesium sulfate (dry), 1-pentyl isocyanide (97%), methyl methacrylate (99%, stabilized), *N,N'*-dicyclohexylcarbodiimide ($\geq 99\%$), ninhydrin (ACS reagent), phosphomolybdic acid hydrate (99%), phosphorus pentoxide ($\geq 98.5\%$), *p*-toluenesulfonyl chloride ($\geq 98\%$, reagent grade), potassium-2-isocyanoacetate (85%), sodium (I) iodide ($\geq 99.99\%$), SpheriCal™ 10 Point, *trans*-2-[3-(4-*tert*-butylphenyl)-2-methyl-2-propenylidene] malononitrile ($\geq 99\%$), sodium trifluoroacetate (98%), silica gel (technical grade, pore size 60 Å. 230-400 mesh particle size, tetrabutylammonium fluoride (1 M in dry THF), *N,N,N',N'*-tetramethylethylenediamine (99%), TLC silica gel F₂₅₄ and 40-63 μm particle size), triethylamine ($\geq 99.5\%$) and vanillin (99%, ReagentPlus®) were purchased from **Sigma-Aldrich**. 2-Bromo-2-methylpropionic acid (98%), 4-(dimethylamino)pyridine (99%), α -bromoisobutyryl bromide (98%), benzyl methacrylate (98%, stabilized), Celite® 545, *endo*-norbornene dicarboxylic anhydride ($>99\%$), ethanolamine (99%), ethyl vinyl ether (99%, stabilized), glacial acetic acid ($\geq 99.7\%$), *N,N,N',N',N'*-pentamethyldiethylenetriamine (98%), pyridine ($\geq 99.5\%$), sodium azide (99%), sodium chloride ($>99\%$) and styrene (99%, stabilized) were obtained from **Thermo Scientific**. *Exo*-norbornene dicarboxylic anhydride (96%) and propionaldehyde (97%) were purchased from **abcr**. Copper(II) sulfate and sodium carbonate ($>99\%$) were obtained from **VWR**. Sodium bicarbonate was obtained from **Solvay**. Sodium hydroxide was obtained

from **Bernd Kraft**. 11-Formamidoundecanoic acid and 4-TMS-ethynyl-benzaldehyde were generous gifts provided by K. Waibel and D. Hahn, respectively. All chemicals were used as received, unless otherwise stated. Before applying an ATRP, the monomer was flushed through a plug of basic aluminum oxide to remove present inhibitor. Cu(I)Cl and Cu(I)Br were purified by stirring for 1 h over glacial acetic acid, followed by filtration and a washing step with ethanol and diethyl ether. The dried copper salts were stored under argon atmosphere over P₂O₅ in a desiccator. CD₂Cl₂ (99.8%), CDCl₃ (98%), C₆D₆ (99.5%) and C₄D₈O (99.5%) were purchased from **Eurisotop**. Additional solvents like ethyl acetate and cyclohexane were used in HPLC grade, unless otherwise stated. In some cases, the solvent was additionally degassed by three freeze pump thaw cycles. Argon (99.999%) was purchased from **Air Liquide**.

8.2 Analytical instruments and methods

Differential scanning calorimetry (DSC):

DSC experiments were performed using a DSC 3 (Mettler Toledo) and a TA Q-200 (TA Instruments) using 40 or 100 μ L aluminum crucibles under nitrogen atmosphere. Measurements were performed by applying three consecutive heating cycles with a heating rate of 20 $^{\circ}$ C/min. Each measurement was performed with 5 – 20 mg sample. T_g values were determined from the onset of the second heating cycle.

Infrared spectroscopy (IR):

Infrared spectra (IR) were recorded on an Alpha-p instrument (Bruker) applying ATR-technology (ATR = attenuated total reflection) in a frequency range from 3,998 to 374 cm^{-1} . The band intensities were characterized in relation to the most intense signal as follows: vs = very strong, s = strong, m = medium, w = weak, vw = very weak. In addition, broad signals were expressed by the term: br = broad.

Electrospray ionization-mass spectrometry (ESI-MS):

ESI-MS experiments were recorded on a Q-Exactive (Orbitrap) mass spectrometer (Thermo Fisher Scientific) equipped with a HESI II probe. Calibration was carried out in the m/z range 74 – 1,822 using premixed calibration solutions (Thermo Fisher Scientific). The spectra were

interpreted by peaks of protonated molecules $[M+H]^+$. All peaks are indicated with their mass-to-charge ratio (m/z).

Matrix-assisted laser desorption/ionization time-of-flight mass spectrometry (MALDI-TOF MS):

MALDI-TOF spectra were recorded on an Axima Confidence system (Shimadzu) equipped with a 50 Hz variable repetition rate nitrogen laser. *Trans*-2-[3-(4-*tert*-butylphenyl)-2-methyl-2-propenylidene]malononitrile (DCTB) and dithranol were used as the matrix and NaTFA as the ionizing agent. All components were dissolved in THF and mixed in a ratio of 30:2:1 (matrix : ionizing agent : analyte) and measured in positive reflectron mode. Calibration was carried out in the m/z range of 1,500 – 15,000 using a dendrimer-based calibration kit (SpheriCal™ 10 Point).

Nuclear magnetic resonance (NMR) spectroscopy:

^1H NMR spectra were recorded using a Bruker Ascend™ 400 equipped with a Bruker AVANCE NEO console and a Bruker Ascend™ 500 equipped with a Bruker AVANCE III HD console with 16 scans for small molecules and 32 scans for polymers at ambient temperature. Data is reported in parts-per-million (ppm) relative to CDCl_3 at 7.26 ppm, CD_2Cl_2 at 5.32 ppm or C_6D_6 at 7.16 ppm. ^{13}C NMR spectra were recorded using a Bruker Ascend™ 400 equipped with a Bruker AVANCE NEO console and a Bruker Ascend™ 500 equipped with a Bruker AVANCE III HD console with 1024 scans for small molecules and 2048 scans for polymers at ambient temperature. Data is reported in ppm relative to CDCl_3 at 77.16 ppm, CD_2Cl_2 at 53.84 ppm or C_6D_6 at 128.06 ppm. ^{31}P spectra were recorded using a Bruker Ascend™ 500 equipped with a Bruker AVANCE III HD console with 512 scans at ambient temperature. Data is reported in ppm relative to H_3PO_4 at 0 ppm. Describing the multiplicity of the obtained signals, following shortcuts were used: s = singlet, d = doublet, t = triplet, q = quartet, p = quintet, sex = sextet, m = multiplet, bs = broad signal. Coupling constants were abbreviated as J and determined in hertz (Hz).

Size exclusion chromatography (SEC):

SEC measurements were performed on a Shimadzu SEC system equipped with a Shimadzu isocratic pump (LC-20AD), a Shimadzu refractive index detector (30 °C) (RID-20A), a Shimadzu

autosampler (SIL-20A) and a Shimadzu column oven (30 °C). The column system comprised a SDV 5 µm, 8×50 mm precolumn, a SDV 5 µm, 1,000 Å, 8×300 mm column and a SDV 5 µm, 100,000 Å, 8×300 mm column supplied by PSS, Germany. A mixture of THF stabilized with 250 ppm butylated hydroxytoluene (≥99.9%) and 2 vol% triethylamine (≥99.5%) supplied by Sigma Aldrich was used at a flow rate of 1.00 mL/min. Calibration was carried out by injection of ten narrow PMMA standards ranging from 1,102 to 981,000 kDa.

Thermogravimetric analysis (TGA):

TGA measurements were performed on a TGA 5500 (TA Instruments). The sample (1.25 – 4.09 mg) were placed in a platinum HT pan and heated from ambient temperature to 800 °C, applying a heating rate of 10 °C/min. TGA measurements were performed by S. Frech.

Thin layer chromatography (TLC):

TLC experiments were performed on silica-gel-coated aluminum foil (silica gel 60 F₂₅₄, Sigma-Aldrich). Compounds were visualized by irradiation with a UV lamp, by staining with Seebach solution (mixture of phosphomolybdic acid hydrate, cerium (IV) sulfate, sulfuric acid and water), a solution of vanillin in sulfuric acid or a solution of ninhydrin in ethanol followed by heating with a heat gun.

Cryostat:

Reactions at -15 °C were performed using a Julabo FT901 cryostat and isopropanol as cooling agent.

8.3 Synthesis procedures and analytical data

8.3.1 Materials synthesized in chapter 4

Note: **Chapter 8.3.1** refers to the publication “Ring-Opening Metathesis Polymerization of Norbornene-Based Monomers Obtained *via* the Passerini Three Component Reaction”. The following data is taken from the corresponding SI, yet slightly adjusted to fit the optics of this thesis. Figures are reprinted with permission.⁵¹⁸

General synthesis of carboxylic acid-functional norbornenes (*xNb1*, *xNb10*, *nNb1*, and *nNb10*): 1.00 eq. *cis*-5-norbornene-*exo*-2,3-dicarboxylic anhydride or 1.00 eq. *cis*-5-norbornene-*endo*-2,3-dicarboxylic anhydride (0.2 mol/L), 1.00 eq. of the corresponding amino acid and 0.20 eq. triethylamine were dissolved in toluene. The *exo*-isomer syntheses were performed at 130 °C for 24 hours using a Dean-Stark apparatus to remove forming water, whereas the *endo*-isomer syntheses were performed at 90 °C for 48 hours to avoid conversion to the thermodynamically more stable *exo*-isomer. Then, the solvent was removed under reduced pressure. The crude product was dissolved in DCM and washed with aqueous hydrochloric acid (0.1 mol/L) twice and then with brine. The organic phase was dried over magnesium sulfate and the solvent was removed under reduced pressure. The products were obtained as white solids in yields ranging from 44% to 91%.

***xNb1*:**

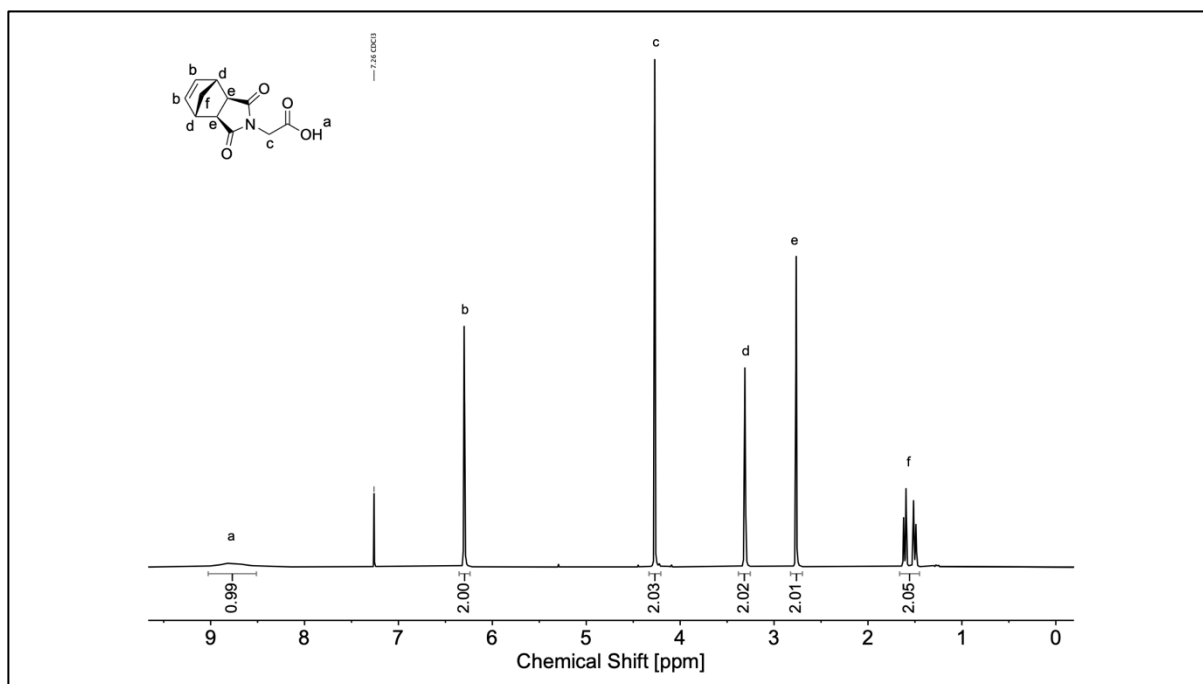


Figure S4.1. ¹H NMR spectrum of *xNb1* in CDCl₃.

¹H NMR: (400 MHz, CDCl₃, δ): 8.77 (bs, 1H; COOH, ^a), 6.36 - 6.24 (m, 2H; CH=CH, ^b), 4.27 (s, 2H; N-CH₂, ^c), 3.37 - 3.26 (m, 2H; =CH-CH, ^d), 2.77 (d, *J* = 1.4 Hz, 2H; =CH-CH-CH, ^e), 1.67 - 1.44 (m, 2H; CH₂ bridge, ^f).

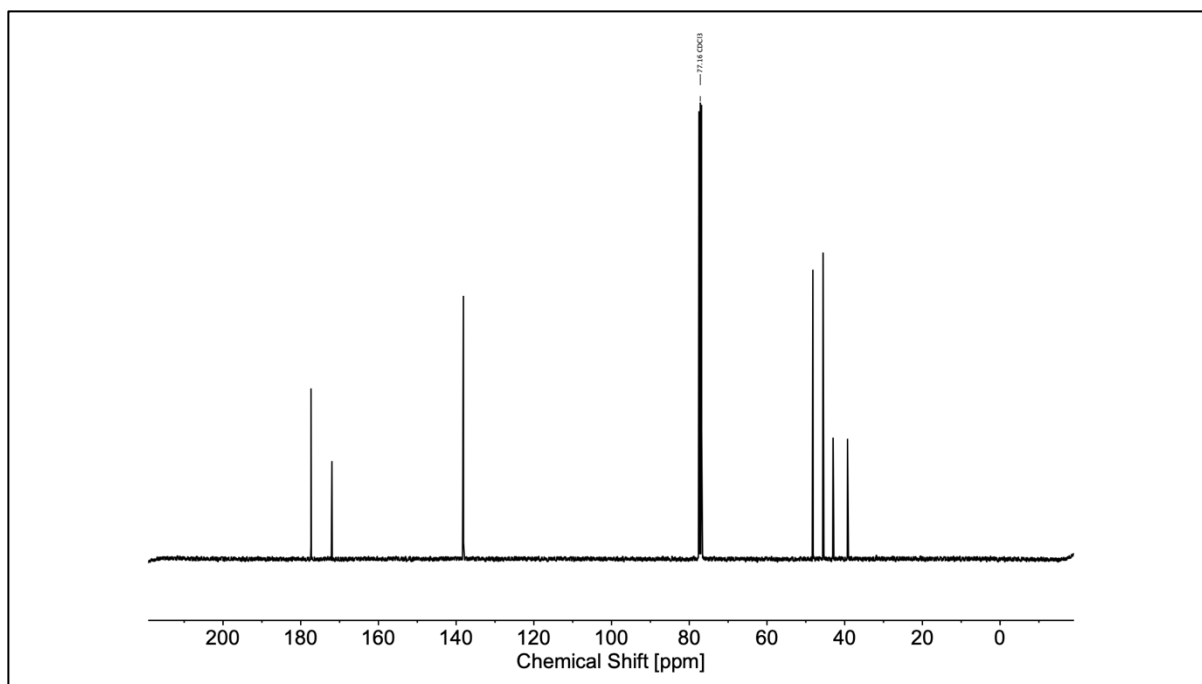
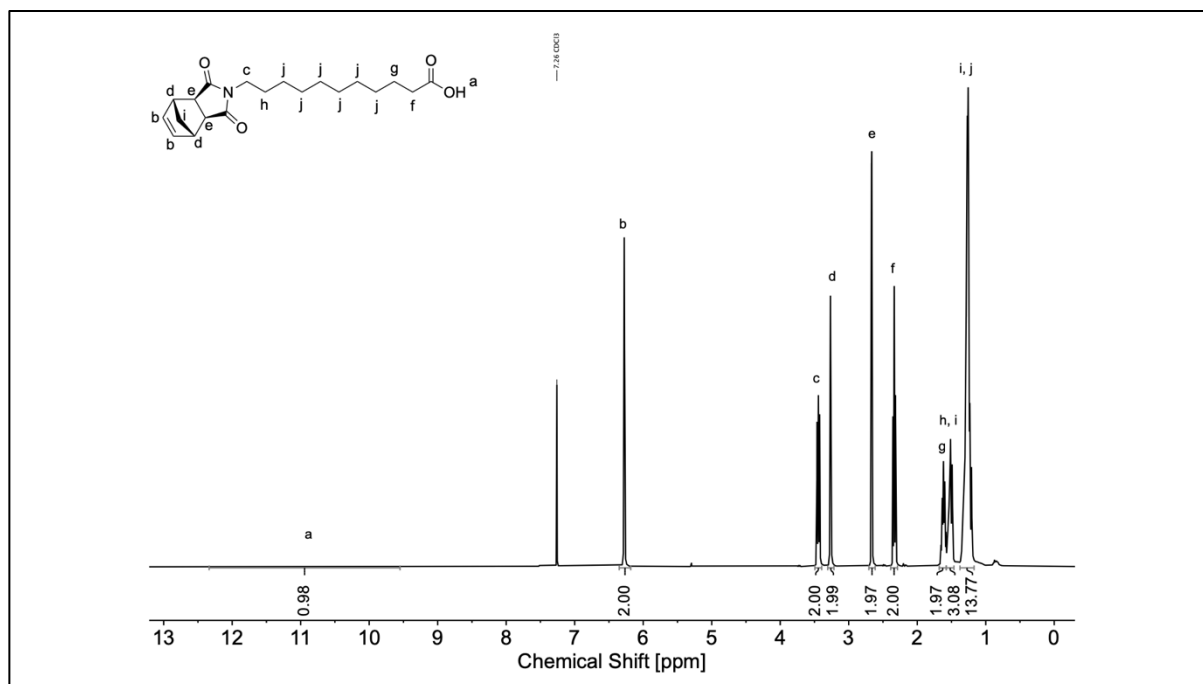


Figure S4.2. ^{13}C NMR spectrum of **xNb1** in CDCl_3 .

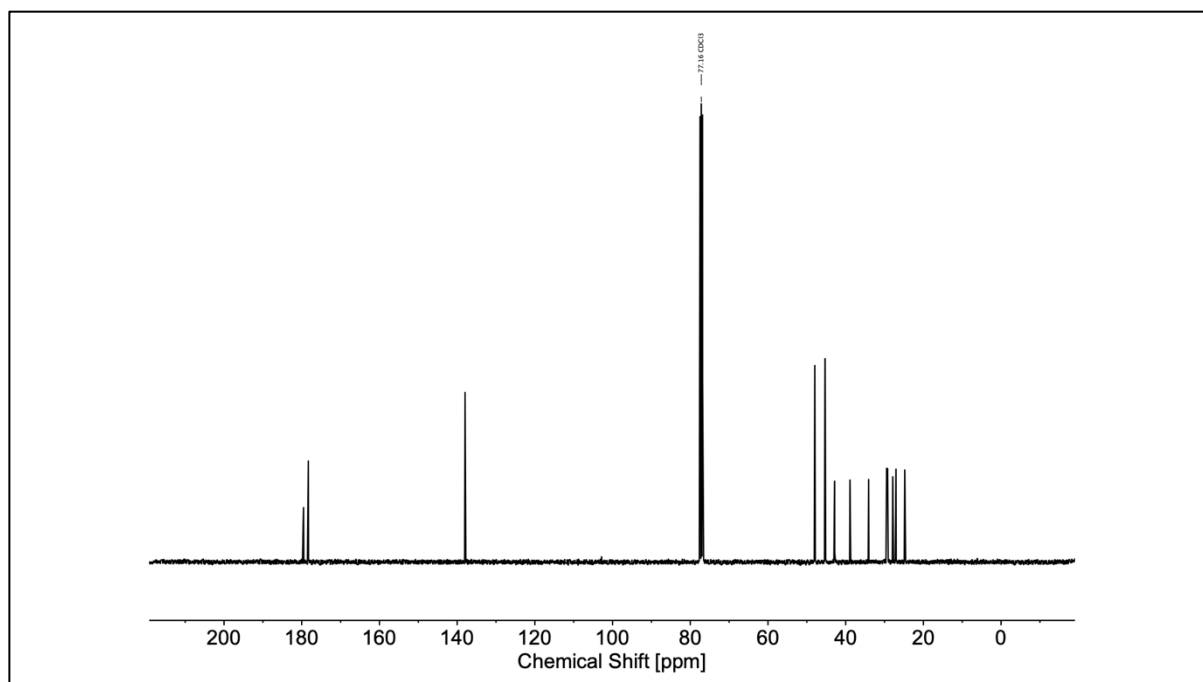
^{13}C NMR: (100 MHz, CDCl_3 , δ): 177.4, 172.0, 138.1, 48.2, 45.6, 43.0, 39.3.

IR (ATR platinum diamond): $\nu / \text{cm}^{-1} = 3075$ (vw), 3044 (vw), 2995 (w), 2985 (w), 2966 (w), 2945 (w), 2915 (w), 2902 (w), 2894 (w), 2820 (w), 2723 (w), 2610 (vw), 2536 (vw), 1763 (w), 1736 (s), 1705 (w), 1660 (vs), 1576 (w), 1473 (vw), 1423 (vs), 1397 (m), 1323 (s), 1288 (w), 1271 (w), 1230 (w), 1203 (vs), 1170 (vs), 1146 (s), 1117 (w), 1092 (w), 1076 (w), 1022 (w), 1006 (w), 938 (s), 909 (m), 899 (m), 884 (s), 815 (w), 784 (vs), 724 (w), 695 (vs), 634 (s), 609 (s), 555 (w), 525 (w), 508 (w), 465 (s), 430 (w).

HRMS (ESI-MS) m/z : $[\text{M}+\text{H}]^+$ calc. for $\text{C}_{11}\text{H}_{11}\text{NO}_4$, 222.0761, found: 222.0758.

xNb10:**Figure S4.3.** ^1H NMR spectrum of **xNb10** in CDCl_3 .

^1H NMR: (400 MHz, CDCl_3 , δ): 10.8 (bs, 1H, COOH, ^a), 6.35 - 6.18 (m, 2H, CH=CH, ^b), 3.44 (t, $J = 7.5$ Hz, 2H, N-CH₂, ^c), 3.31 - 3.22 (m, 2H, =CH-CH, ^d), 2.67 (d, $J = 1.3$ Hz, 2H, =CH-CH-CH, ^e), 2.33 (t, $J = 7.5$ Hz, 2H, CH₂-COOH, ^f), 1.62 (p, $J = 7.4$ Hz, 2H, CH₂-CH₂-COOH, ^g), 1.57 - 1.50 (m, 2H, N-CH₂-CH₂, ^h), 1.52 - 1.18 (m, 2H, CH₂ bridge, ⁱ), 1.37 - 1.17 (m, 12H, CH₂, ^j).

**Figure S4.4.** ^{13}C NMR spectrum of **xNb10** in CDCl_3 .

^{13}C NMR: (100 MHz, CDCl_3 , δ): 179.5, 178.3, 138.0, 47.9, 45.3, 42.9, 38.9, 34.1, 29.4, 29.3, 29.2, 29.1, 27.9, 27.0, 24.8.

IR (ATR platinum diamond): $\nu / \text{cm}^{-1} = 3036$ (vw), 2993 (w), 2976 (vw), 2925 (m), 2880 (w), 2851 (w), 1767 (w), 1691 (vs), 1467 (w), 1430 (w), 1399 (m), 1370 (m), 1353 (m), 1331 (w), 1308 (w), 1298 (w), 1286 (w), 1275 (w), 1246 (m), 1220 (m), 1189 (m), 1146 (s), 1109 (vw), 1070 (vw), 1039 (vw), 1008 (w), 944 (m), 895 (w), 887 (w), 837 (vw), 817 (w), 798 (m), 778 (w), 720 (s), 681 (w), 644 (m), 615 (w), 535 (w), 461 (w), 438 (w).

HRMS (ESI-MS) m/z : $[\text{M}+\text{H}]^+$ calc. for $\text{C}_{20}\text{H}_{29}\text{NO}_4$, 348.2169, found: 348.2170.

nNb1:

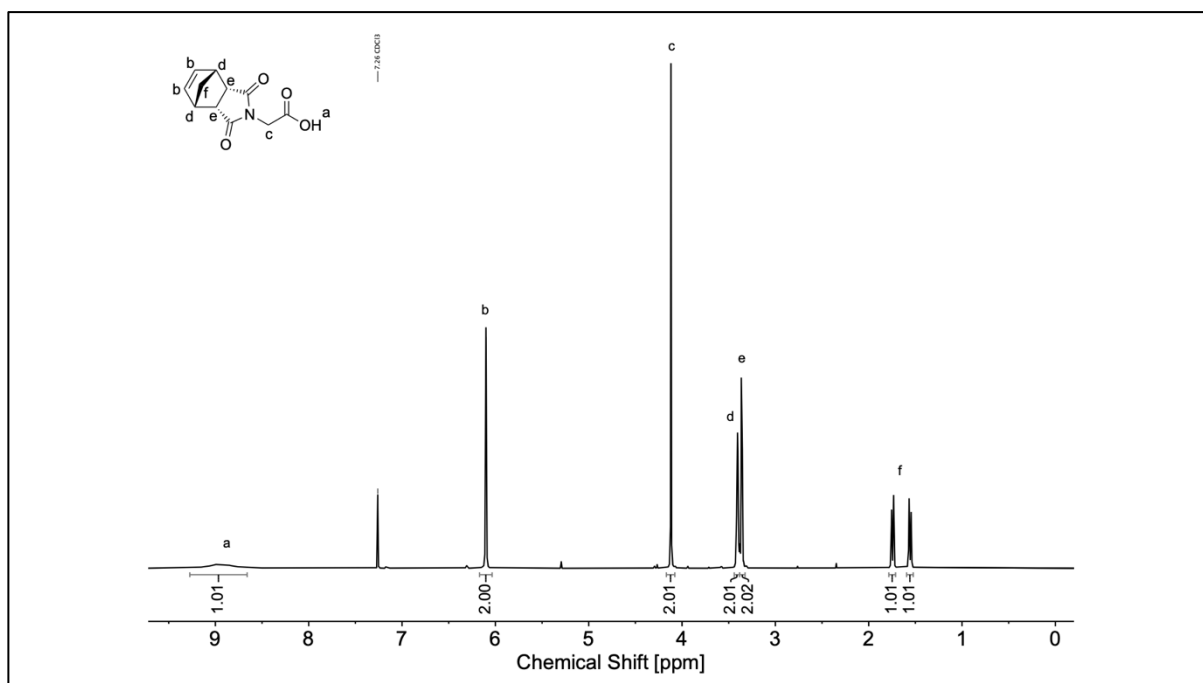


Figure S4.5. ^1H NMR spectrum of *nNb1* in CDCl_3 .

^1H NMR: (400 MHz, CDCl_3 , δ): 8.88 (bs, 1H, COOH, ^a), 6.10 - 5.98 (m, 2H, CH=CH, ^b), 4.05 (s, 2H, N-CH₂, ^c), 3.38 - 3.32 (m, 2H, =CH-CH, ^d), 3.32 - 3.26 (m, 2H, =CH-CH-CH, ^e), 1.73 - 1.47 (m, 2H, CH₂ bridge, ^f).

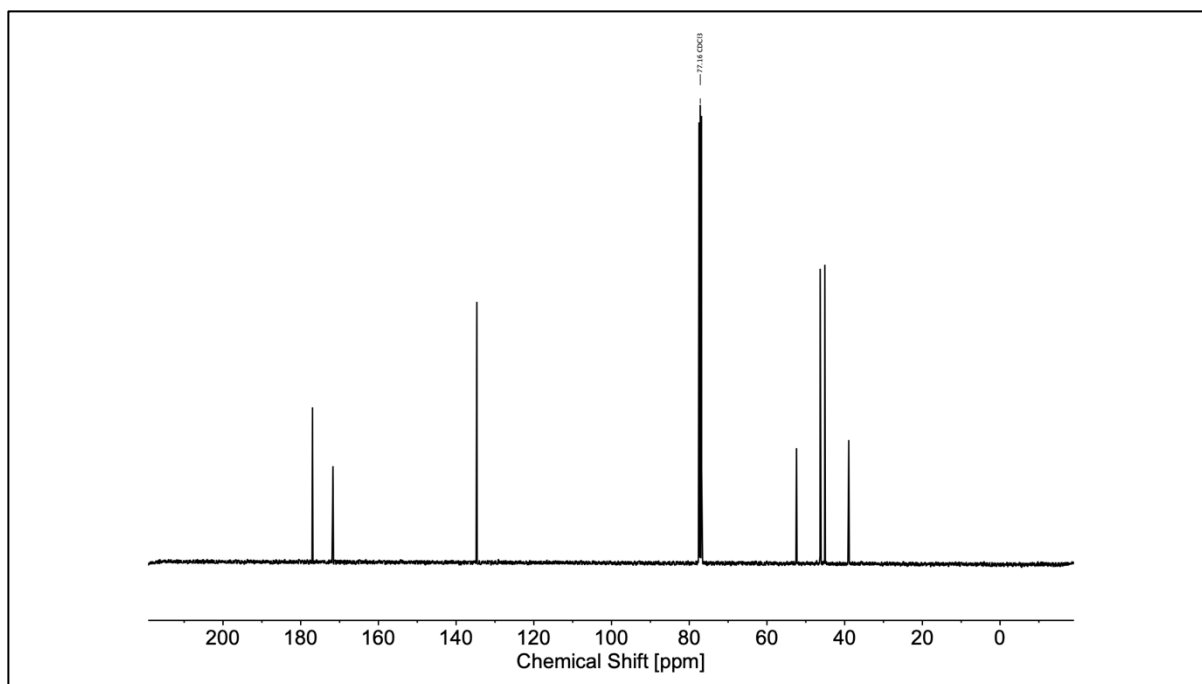


Figure S4.6. ^{13}C NMR spectrum of ***nNb1*** in CDCl_3 .

^{13}C NMR: (100 MHz, CDCl_3 , δ): 177.0, 171.7, 134.7, 52.4, 46.3, 45.1, 38.9.

IR (ATR platinum diamond): ν / cm^{-1} = 3059 (w), 3009 (w), 2991 (w), 2966 (w), 2945 (w), 2931 (w), 2869 (w), 2836 (w), 2822 (w), 2806 (w), 2785 (w), 2715 (w), 1769 (w), 1740 (s), 1701 (vs), 1652 (vs), 1569 (w), 1430 (m), 1415 (s), 1393 (s), 1327 (vs), 1294 (w), 1261 (m), 1234 (w), 1195 (s), 1172 (vs), 1131 (s), 1082 (m), 1053 (w), 973 (w), 948 (m), 930 (m), 919 (s), 907 (m), 884 (s), 841 (s), 815 (m), 806 (w), 798 (w), 786 (w), 747 (m), 734 (vs), 716 (vs), 648 (m), 617 (vs), 607 (vs), 572 (w), 545 (w), 510 (w), 496 (m), 457 (w), 415 (w).

HRMS (ESI-MS) m/z : $[\text{M}+\text{H}]^+$ calc. for $\text{C}_{11}\text{H}_{11}\text{NO}_4$, 222.0761, found: 222.0758.

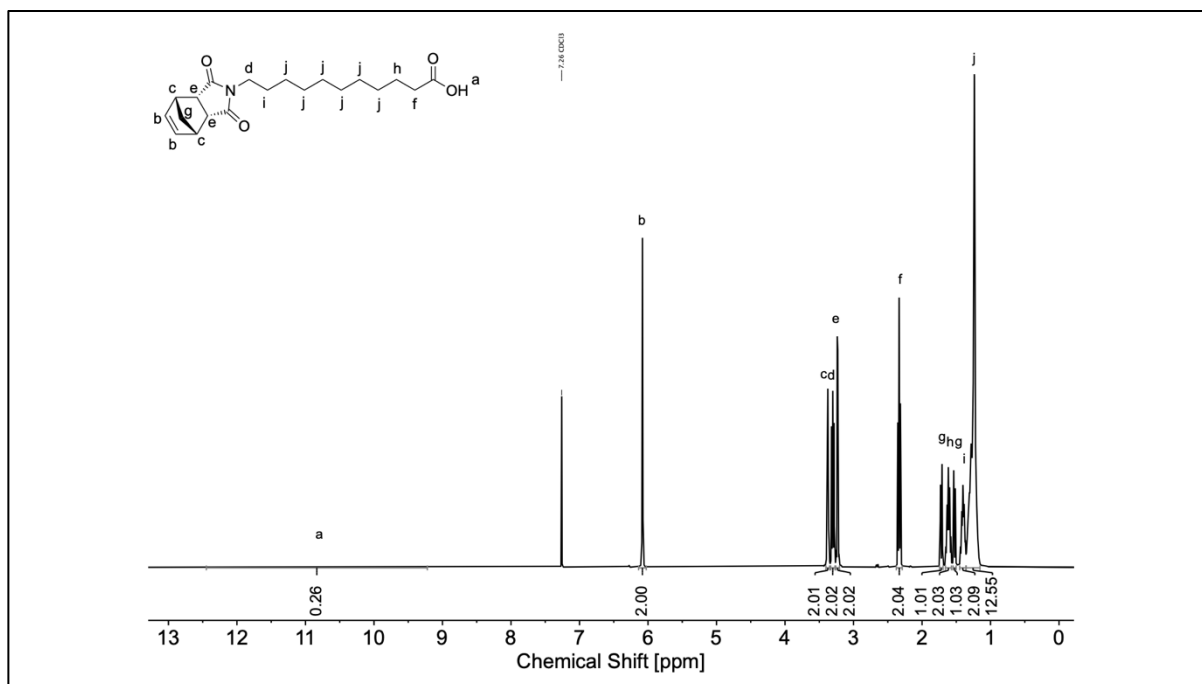
nNb10:

Figure S4.7. ¹H NMR spectrum of *nNb10* in CDCl₃.

¹H NMR: (400 MHz, CDCl₃, δ): 10.8 (bs, 1H, COOH, ^a), 6.12 - 6.03 (m, 2H, CH=CH, ^b), 3.40 - 3.35 (m, 2H, =CH-CH, ^c), 3.30 (t, *J* = 7.4 Hz, 2H, N-CH₂, ^d), 3.26 - 3.20 (m, 2H, =CH-CH-CH, ^e), 2.33 (t, *J* = 7.5 Hz, 2H, CH₂-COOH, ^f), 1.75 - 1.50 (m, 2H, CH₂ bridge, ^g), 1.62 (p, *J* = 7.4 Hz, 2H, CH₂-CH₂-COOH, ^h), 1.45 - 1.36 (m, 2H, N-CH₂-CH₂, ⁱ), 1.35 - 1.15 (m, 12H, CH₂, ^j).

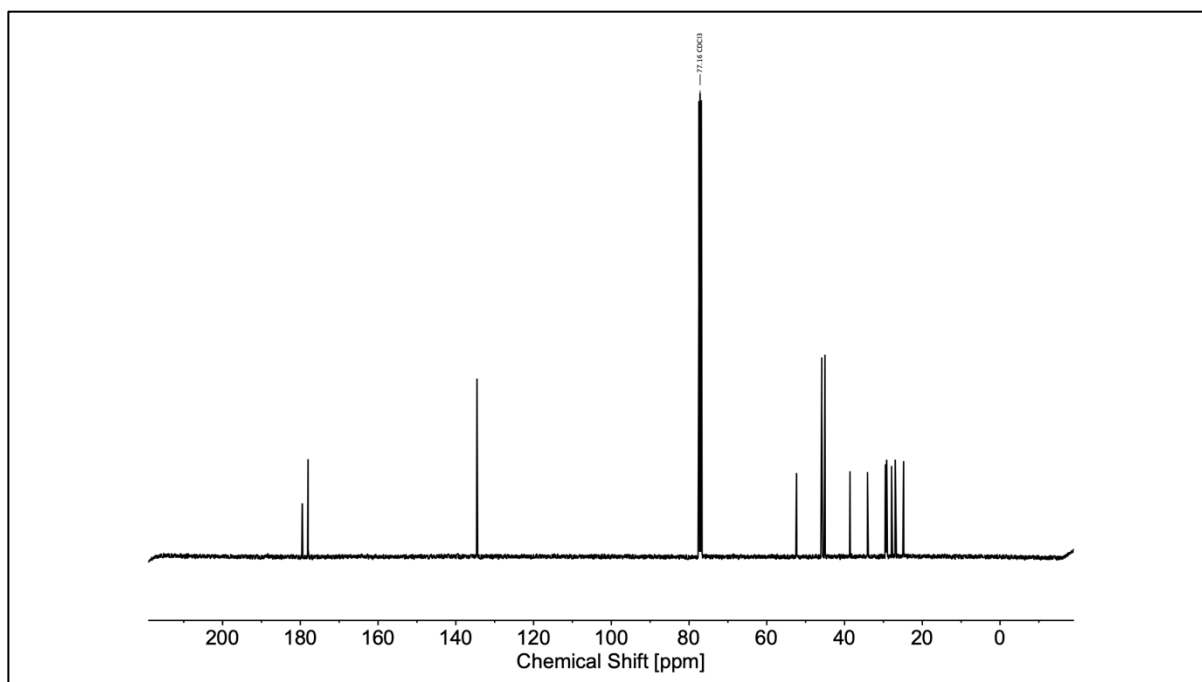


Figure S4.8. ¹³C NMR spectrum of *nNb10* in CDCl₃.

^{13}C NMR: (100 MHz, CDCl_3 , δ): 179.5, 178.0, 134.5, 52.4, 45.9, 45.0, 38.6, 34.1, 29.5, 29.4, 29.3, 29.2, 29.1, 27.9, 27.0, 24.8.

IR (ATR platinum diamond): ν / cm^{-1} = 3063 (vw), 2989 (w), 2927 (m), 2855 (w), 1767 (w), 1732 (m), 1695 (vs), 1454 (w), 1436 (w), 1399 (s), 1368 (m), 1337 (s), 1290 (w), 1261 (w), 1226 (m), 1170 (m), 1144 (s), 1127 (m), 1094 (w), 1049 (w), 1016 (w), 971 (w), 946 (w), 907 (w), 872 (w), 843 (m), 802 (w), 786 (w), 745 (m), 720 (s), 664 (w), 648 (w), 615 (s), 572 (w), 549 (w), 531 (w), 516 (w), 502 (w), 481 (w), 471 (w), 442 (w), 434 (w), 415 (w).

HRMS (ESI-MS) m/z : $[\text{M}+\text{H}]^+$ calc. for $\text{C}_{20}\text{H}_{29}\text{NO}_4$, 348.2169, found: 348.2162.

General synthesis of bifunctional monomers:

1.00 eq. of the corresponding acid-functional norbornene (1 mol/L), 1.50 eq. aldehyde component and 1.50 eq. isocyanide component were dissolved in DCM and stirred for 48 hours at ambient temperature. The crude product was purified *via* column chromatography using a cyclohexane/ethyl acetate mixture as solvent. The products were obtained as white (**xNb1PePr**, **nNb1PePr**) or yellow (**xNb1AdPy**, **xNb10AdPy**, **nNb1AdPy**, **nNb10AdPy**) solids or as colorless oils (**xNb10PePr**, **nNb10PePr**) in yields ranging from 55% to 94%.

xNb1PePr:

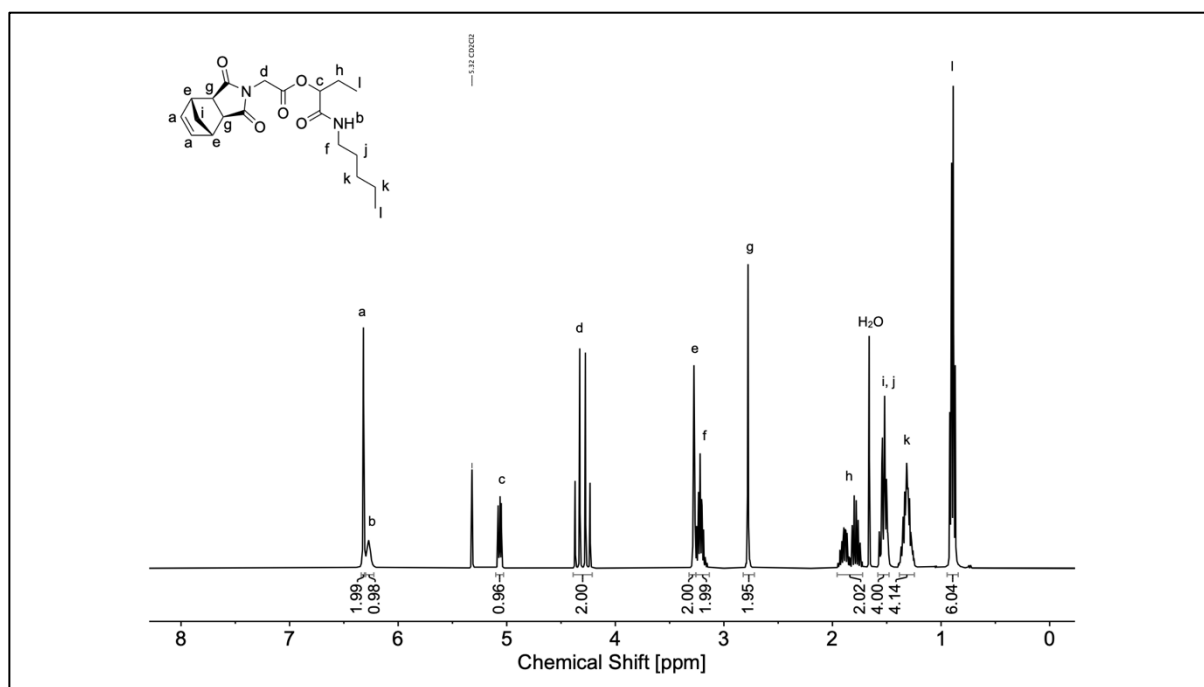


Figure S4.9. ^1H NMR spectrum of **xNb1PePr** in CD_2Cl_2 .

^1H NMR (400 MHz, CD_2Cl_2 , δ): 6.34 - 6.30 (m, 2H, $\text{CH}=\text{CH}$, ^a), 6.28 (bs, 1H, CONH , ^b), 5.06 (dd, $J = 7.3$ Hz, 4.4 Hz, 1H, COO-CH , ^c), 4.31 (dd, $J = 17.0$ Hz, 15.1 Hz, 2H, N-CH_2 , ^d), 3.28 (p, $J = 1.8$ Hz, 2H, $=\text{CH-CH}$, ^e), 3.28 - 3.13 (m, 2H, CONH-CH_2 , ^f), 2.78 (d, $J = 1.4$ Hz, 2H, $=\text{CH-CH-CH}$, ^g), 1.89 - 1.72 (m, 2H, $\text{CH-CH}_2\text{-CH}_3$, ^h), 1.58 - 1.47 (m, 2H, CH_2 bridge, ⁱ), 1.55 - 1.47 (m, 2H, $\text{CONH-CH}_2\text{-CH}_2$, ^j), 1.39 - 1.24 (m, 4H, CH_2 , ^k), 0.94 - 0.84 (m, 6H, CH_3 , ^l).

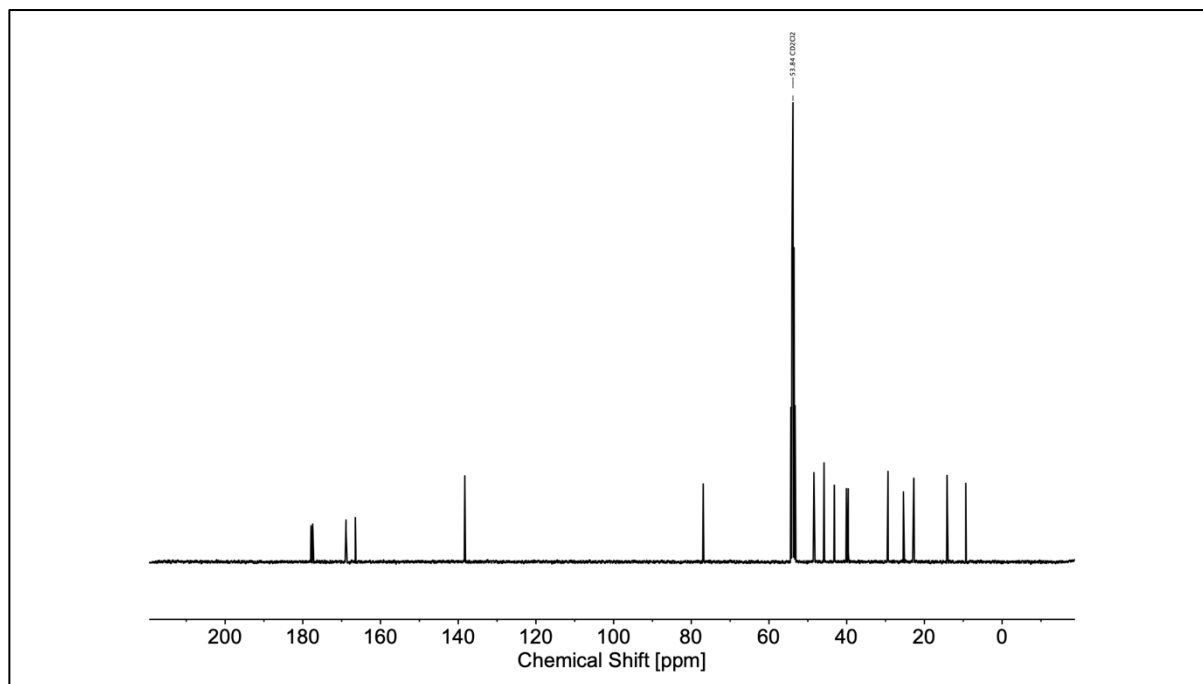


Figure S4.10. ^{13}C NMR spectrum of **xNb1PePr** in CD_2Cl_2 .

^{13}C NMR (100 MHz, CD_2Cl_2 , δ): 179.0, 177.6, 169.0, 166.6, 77.1, 48.6, 48.6, 46.0, 43.4, 40.2, 39.8, 29.6, 29.5, 25.6, 22.9, 14.3, 9.5.

IR (ATR platinum diamond): $\nu / \text{cm}^{-1} = 3275$ (w), 3104 (vw), 2991 (vw), 2962 (w), 2933 (w), 2894 (vw), 2876 (vw), 2859 (w), 1777 (w), 1752 (s), 1699 (vs), 1656 (vs), 1569 (m), 1460 (w), 1440 (w), 1413 (s), 1378 (s), 1325 (s), 1286 (w), 1271 (w), 1214 (vs), 1172 (vs), 1148 (m), 1140 (m), 1109 (w), 1094 (w), 1078 (w), 1068 (w), 1051 (w), 1022 (vw), 1002 (vw), 975 (w), 938 (m), 901 (m), 889 (w), 815 (w), 800 (vw), 782 (m), 740 (w), 726 (m), 716 (m), 689 (w), 640 (m), 621 (w), 568 (w), 508 (vw), 426 (w).

HRMS (ESI-MS) m/z : $[\text{M}+\text{H}]^+$ calc. for $\text{C}_{20}\text{H}_{28}\text{N}_2\text{O}_5$, 377.2071, found: 377.2064.

$R_f = 0.20$ (cyclohexane/ethyl acetate, 2:1).

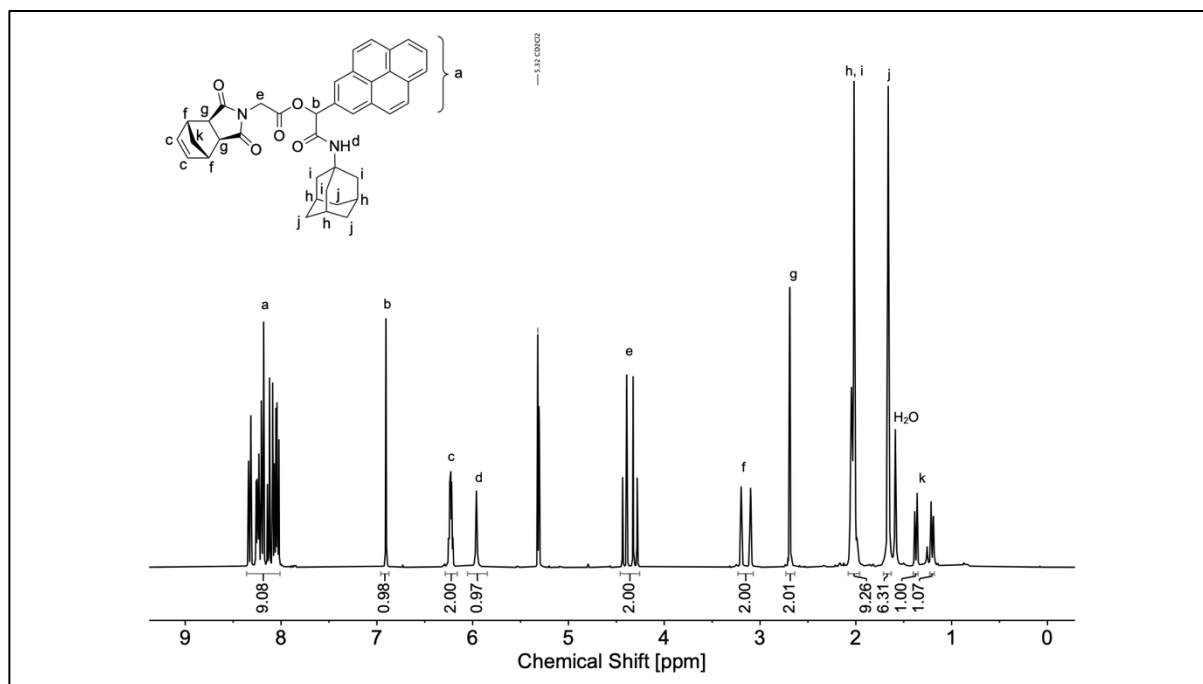
xNb1AdPy:

Figure S4.11. ^1H NMR spectrum of **xNb1AdPy** in CD_2Cl_2 .

^1H NMR (400 MHz, CD_2Cl_2 , δ): 8.35 – 8.02 (m, 9H, H_{Ar} , ^a), 6.91 (s, 1H, COO-CH , ^b), 6.31 - 6.18 (m, 2H, CH=CH , ^c), 5.97 (s, 1H, CONH , ^d), 4.37 (dd, $J = 26.1$ Hz, 17.2 Hz, 2H, N-CH_2 , ^e), 3.21 - 3.10 (m, 2H, $=\text{CH-CH}$, ^f), 2.74 - 2.65 (m, 2H, $=\text{CH-CH-CH}$, ^g), 2.09 - 2.03 (m, 3H, $\text{CH}_2\text{-CH}$, ^h), 2.05 - 1.97 (m, 6H, CONH-C-CH_2 , ⁱ), 1.76 - 1.64 (m, 6H, CH-CH_2 , ^j), 1.41 - 1.19 (m, 2H, CH_2 bridge, ^k).

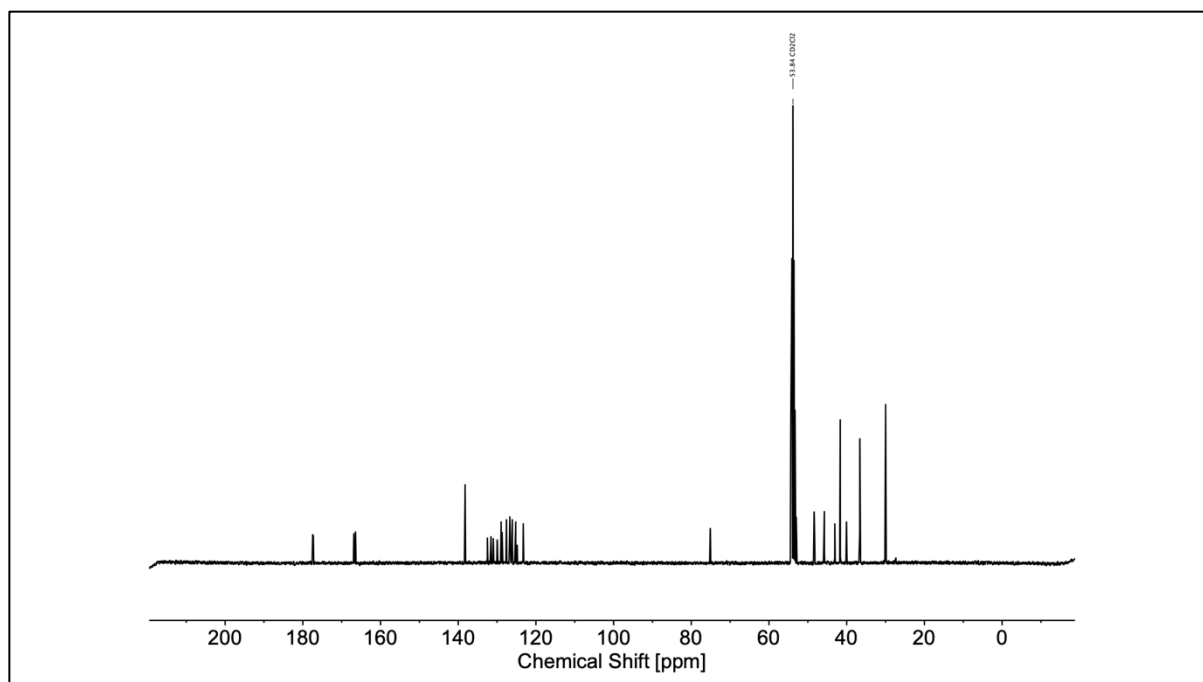


Figure S4.12. ^{13}C NMR spectrum of **xNb1AdPy** in CD_2Cl_2 .

^{13}C NMR (100 MHz, CD_2Cl_2 , δ): 177.6, 177.6, 167.0, 166.6, 138.4, 132.7, 131.7, 131.1, 130.1, 129.1, 128.9, 128.9, 127.7, 126.9, 126.8, 126.4, 126.2, 125.5, 125.3, 125.0, 123.4, 75.3, 53.1, 48.6, 48.5, 46.0, 45.9, 43.2, 41.8, 40.2, 36.8, 30.2.

IR (ATR platinum diamond): ν / cm^{-1} = 3361 (vw), 2904 (w), 2849 (w), 1755 (m), 1703 (vs), 1602 (w), 1518 (m), 1454 (w), 1409 (m), 1393 (w), 1360 (w), 1345 (w), 1318 (m), 1284 (w), 1269 (w), 1214 (m), 1170 (vs), 1125 (w), 1103 (w), 1092 (w), 1057 (w), 1014 (w), 993 (w), 981 (w), 961 (w), 936 (m), 897 (w), 845 (s), 817 (w), 782 (m), 759 (w), 714 (s), 693 (w), 683 (w), 636 (w), 613 (w), 572 (w), 564 (w), 555 (w), 545 (w), 529 (w), 516 (w), 487 (w), 467 (w), 446 (w), 438 (w), 424 (m).

HRMS (ESI-MS) m/z : $[\text{M}+\text{H}]^+$ calc. for $\text{C}_{39}\text{H}_{36}\text{N}_2\text{O}_5$, 613.2697, found: 613.2689.

R_f = 0.30 (cyclohexane/ethyl acetate, 3:1).

xNb10PePr (synthesized by A. Seliwjorstow under my supervision):

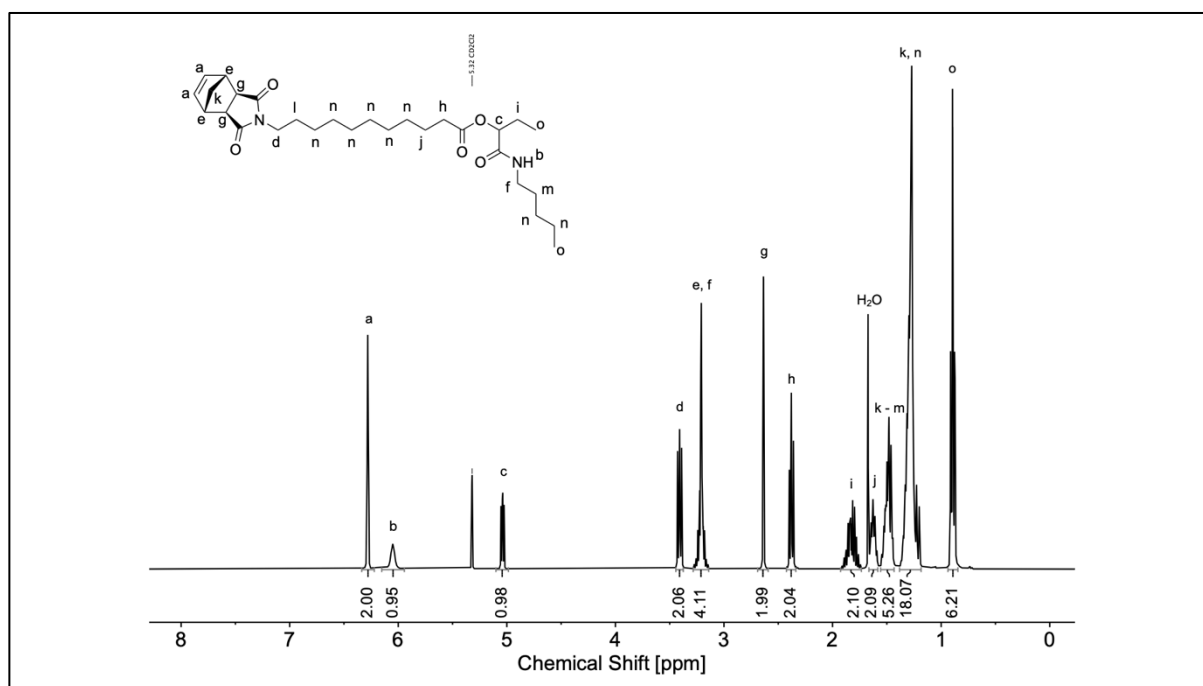


Figure S4.13. ^1H NMR spectrum of **xNb10PePr** in CD_2Cl_2 .

^1H NMR (400 MHz, CD_2Cl_2 , δ): 6.32 - 6.24 (m, 2H, $\text{CH}=\text{CH}$, ^a), 6.10 (bs, 1H, CONH , ^b), 5.04 (dd, J = 6.7 Hz, 4.8 Hz, 1H, $\text{COO}-\text{CH}$, ^c), 3.41 (t, J = 7.5 Hz, 2H, $\text{N}-\text{CH}_2$, ^d), 3.28 - 3.14 (m, 2H, $=\text{CH}-\text{CH}$, ^e), 3.28 - 3.14 (m, 2H, $\text{CONH}-\text{CH}_2$, ^f), 2.64 (d, J = 1.4 Hz, 2H, $=\text{CH}-\text{CH}-\text{CH}$, ^g), 3.48 (t, J = 7.5 Hz, 2H, CH_2-COO , ^h), 1.92 - 1.74 (m, 2H, $\text{CH}-\text{CH}_2-\text{CH}_3$, ⁱ), 1.66 - 1.58 (m, 2H, $\text{CH}_2-\text{CH}_2-\text{COO}$, ^j), 1.49 - 1.17 (m, 2H, CH_2 bridge, ^k), 1.55 - 1.47 (m, 2H, $\text{N}-\text{CH}_2-\text{CH}_2$, ^l), 1.55 - 1.47 (m, 2H, $\text{CONH}-\text{CH}_2-\text{CH}_2$, ^m), 1.39 - 1.23 (m, 16H, CH_2 , ⁿ), 0.94 - 0.83 (m, 6H, CH_3 , ^o).

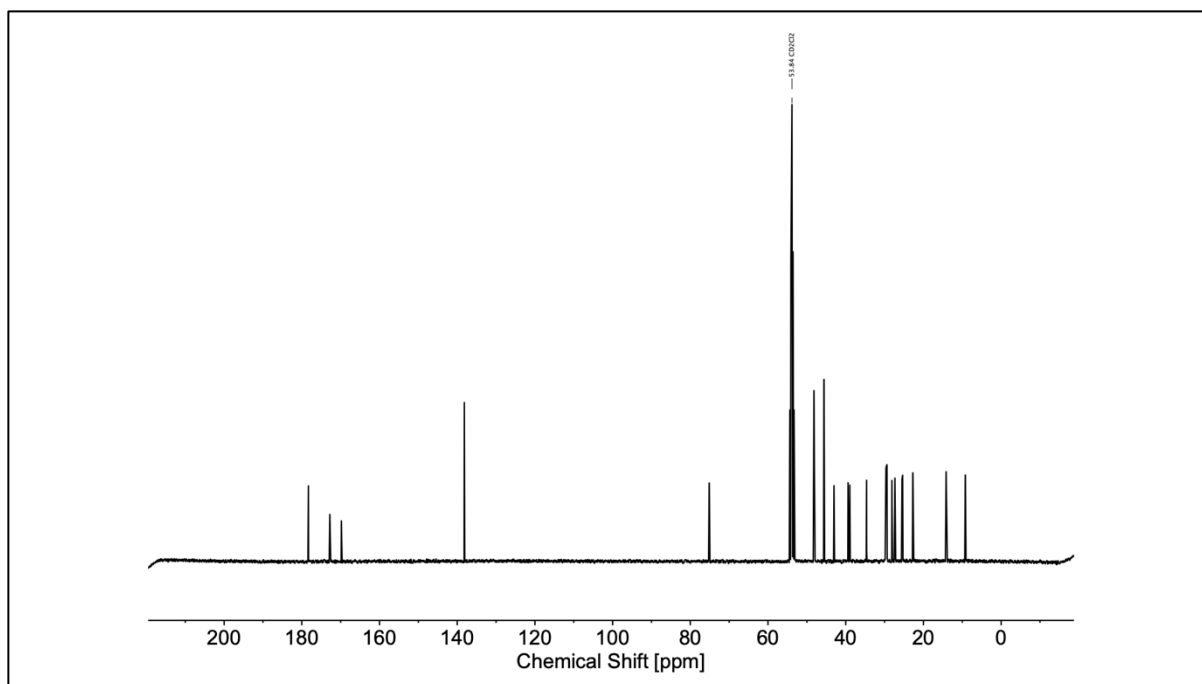


Figure S4.14. ^{13}C NMR spectrum of **xNb10PePr** in CD_2Cl_2 .

^{13}C NMR (100 MHz, CD_2Cl_2 , δ): 178.5, 172.9, 170.0, 75.3, 48.3, 45.8, 43.2, 39.6, 39.1, 34.8, 29.9, 29.9, 29.8, 29.8, 29.7, 29.6, 29.5, 29.3, 27.5, 25.7, 25.5, 22.9, 14.3, 9.4.

IR (ATR platinum diamond): ν / cm^{-1} = 2927 (m), 2855 (w), 1769 (w), 1740 (w), 1695 (vs), 1534 (w), 1460 (w), 1436 (w), 1395 (m), 1368 (m), 1345 (m), 1327 (w), 1286 (w), 1234 (w), 1214 (w), 1164 (s), 1144 (s), 1100 (m), 1047 (w), 1016 (w), 1002 (w), 971 (w), 948 (w), 926 (w), 915 (w), 897 (w), 887 (w), 850 (w), 810 (w), 782 (w), 720 (m), 691 (w), 662 (w), 642 (m), 615 (w), 584 (w), 559 (w), 539 (w), 533 (w), 525 (w), 518 (w), 504 (w), 485 (w), 475 (w), 455 (w), 442 (w), 428 (w), 413 (w), 401 (w).

HRMS (ESI-MS) m/z : $[\text{M}+\text{H}]^+$ calc. for $\text{C}_{29}\text{H}_{46}\text{N}_2\text{O}_5$, 503.3479, found: 503.3466.

R_f = 0.30 (cyclohexane/ethyl acetate, 3:1).

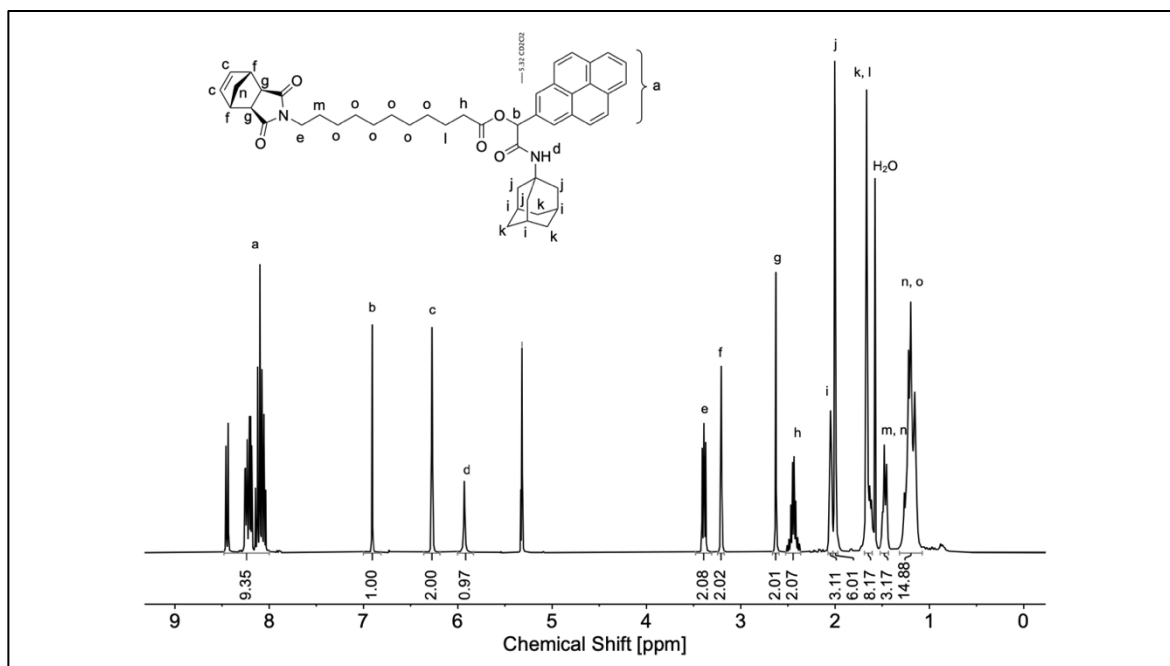
xNb10AdPy:

Figure S4.15. ^1H NMR spectrum of **xNb10AdPy** in CD_2Cl_2 .

^1H NMR (400 MHz, CD_2Cl_2 , δ): 8.45 – 8.03 (m, 9H, H_{Ar} , ^a), 6.91 (s, 1H, COO-CH , ^b), 6.32 - 6.24 (m, 2H, CH=CH , ^c), 5.93 (s, 1H, CONH , ^d), 3.39 (t, $J = 7.5$ Hz, 2H, N-CH_2 , ^e), 3.21 (p, $J = 1.8$ Hz, 2H, $=\text{CH-CH}$, ^f), 2.61 (d, $J = 1.4$ Hz, 2H, $=\text{CH-CH-CH}$, ^g), 2.52 - 2.36 (m, 2H, $\text{CH}_2\text{-COO}$, ^h), 2.08 - 2.02 (m, 3H, $\text{CH}_2\text{-CH}$, ⁱ), 2.02 - 1.97 (m, 6H, CONH-C-CH_2 , ^j), 1.75 - 1.59 (m, 6H, CH-CH_2 , ^k), 1.75 - 1.59 (m, 2H, $\text{CH}_2\text{-CH}_2\text{-COO}$, ^l), 1.53 - 1.43 (m, 2H, $\text{N-CH}_2\text{-CH}_2$, ^m), 1.53 - 1.09 (m, 2H, CH_2 bridge, ⁿ), 1.34 - 1.05 (m, 12H, CH_2 , ^o).

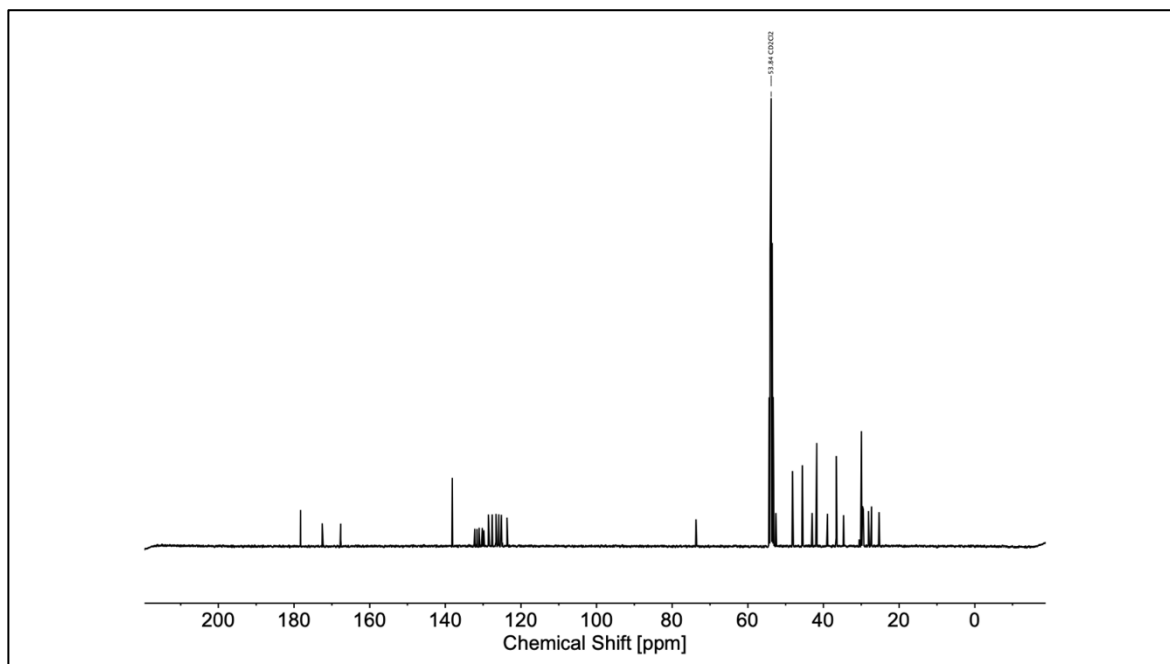


Figure S4.16. ^{13}C NMR spectrum of **xNb10AdPy** in CD_2Cl_2 .

^{13}C NMR (100 MHz, CD_2Cl_2 , δ): 178.4, 172.7, 167.9, 138.0, 132.3, 131.8, 131.2, 130.4, 130.0, 128.8, 128.6, 127.8, 126.8, 126.8, 126.2, 126.0, 125.5, 125.3, 125.1, 123.8, 73.9, 52.8, 48.3, 45.8, 43.2, 42.0, 39.1, 36.8, 34.8, 30.7, 30.1, 29.9, 29.8, 29.7, 29.6, 29.6, 28.3, 27.5, 25.5.

IR (ATR platinum diamond): ν / cm^{-1} = 2906 (m), 2851 (w), 1738 (w), 1693 (vs), 1516 (m), 1454 (w), 1436 (w), 1395 (m), 1360 (m), 1343 (m), 1325 (w), 1310 (w), 1286 (w), 1269 (w), 1232 (w), 1142 (s), 1094 (m), 1057 (w), 1016 (w), 998 (w), 983 (w), 963 (w), 944 (w), 897 (w), 887 (w), 847 (s), 817 (w), 784 (w), 759 (w), 718 (s), 683 (w), 662 (w), 642 (m), 611 (w), 580 (w), 562 (w), 545 (w), 531 (w), 520 (w), 490 (w), 463 (w), 442 (w), 426 (w), 415 (w), 405 (w).

HRMS (ESI-MS) m/z : $[\text{M}+\text{H}]^+$ calc. for $\text{C}_{48}\text{H}_{54}\text{N}_2\text{O}_5$, 739.4105, found: 739.4081.

R_f = 0.46 (cyclohexane/ethyl acetate, 3:1).

***n*Nb1PePr:**

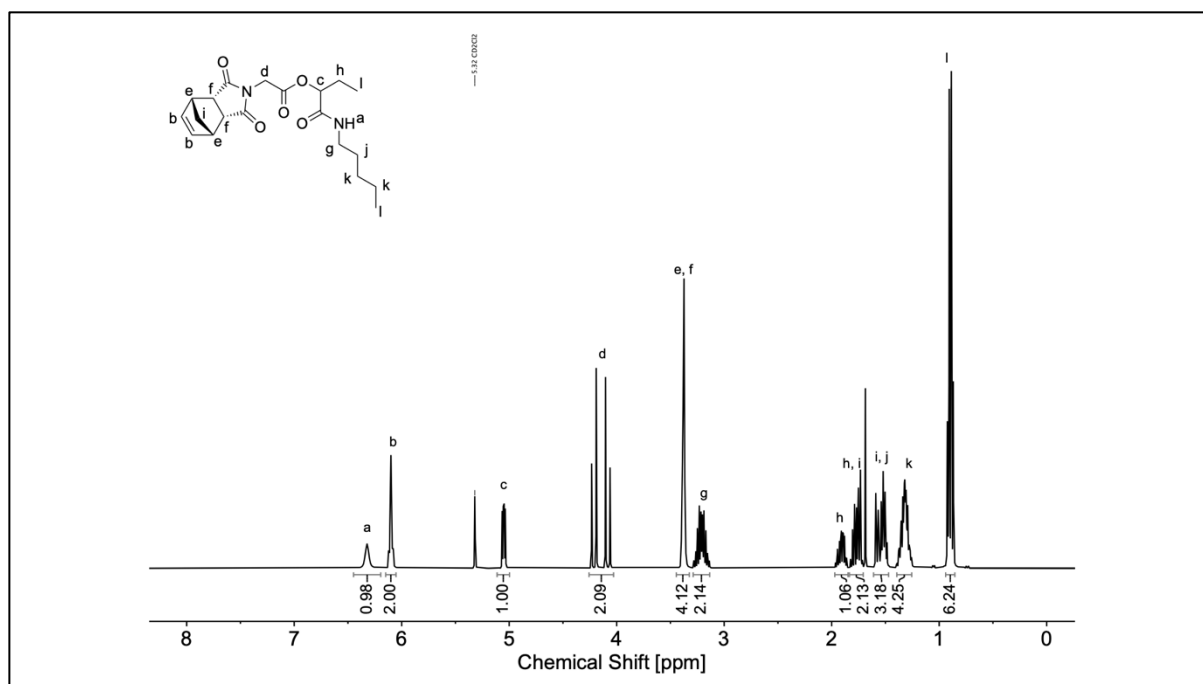


Figure S4.17. ^1H NMR spectrum of *n*Nb1PePr in CD_2Cl_2 .

^1H NMR (400 MHz, CD_2Cl_2 , δ): 6.33 (bs, 1H, CONH, ^a), 6.15 - 6.05 (m, 2H, CH=CH, ^b), 5.05 (dd, $J = 7.6$ Hz, 4.3 Hz, 1H, COO-CH, ^c), 4.15 (dd, $J = 34.7$ Hz, 17.0 Hz, 2H, N-CH₂, ^d), 3.44 - 3.32 (m, 2H, =CH-CH, ^e), 3.44 - 3.32 (m, 2H, =CH-CH-CH, ^f), 3.29 - 3.13 (m, 2H, CONH-CH₂, ^g), 1.97 - 1.71 (m, 2H, CH-CH₂-CH₃, ^h), 1.83 - 1.54 (m, 2H, CH₂ bridge, ⁱ), 1.56 - 1.46 (m, 2H, CONH-CH₂-CH₂, ^j), 1.39 - 1.25 (m, 4H, CH₂, ^k), 0.95 - 0.84 (m, 6H, CH₃, ^l).

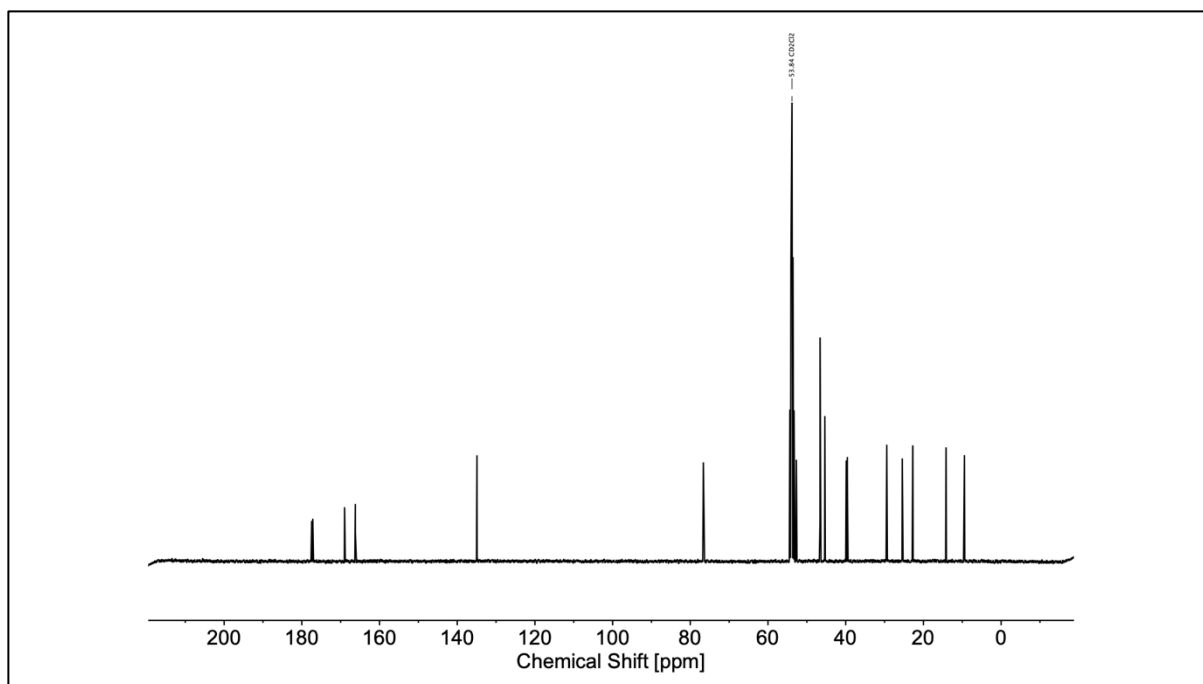


Figure S4.18. ^{13}C NMR spectrum of *nNb1PePr* in CD_2Cl_2 .

^{13}C NMR (100 MHz, CD_2Cl_2 , δ): 177.6, 177.3, 169.2, 166.4, 135.1, 135.1, 76.8, 52.9, 46.8, 45.5, 45.5, 40.0, 39.7, 29.6, 29.5, 25.6, 22.9, 14.3, 9.6.

IR (ATR platinum diamond): $\nu / \text{cm}^{-1} = 3273$ (w), 3100 (vw), 2954 (w), 2931 (w), 2873 (w), 2859 (w), 1759 (m), 1695 (vs), 1656 (vs), 1567 (m), 1458 (w), 1440 (w), 1415 (s), 1382 (m), 1333 (m), 1329 (m), 1306 (w), 1292 (w), 1273 (w), 1255 (w), 1207 (vs), 1174 (vs), 1129 (w), 1113 (m), 1090 (w), 1051 (w), 1012 (vw), 996 (vw), 979 (w), 946 (w), 926 (m), 909 (w), 882 (w), 843 (w), 796 (w), 749 (w), 732 (w), 716 (vs), 683 (w), 652 (w), 615 (m), 574 (w), 559 (vw), 438 (w), 418 (w).

HRMS (ESI-MS) m/z : $[\text{M}+\text{H}]^+$ calc. for $\text{C}_{20}\text{H}_{28}\text{N}_2\text{O}_5$, 377.2071, found: 377.2061.

$R_f = 0.20$ (cyclohexane/ethyl acetate, 3:2).

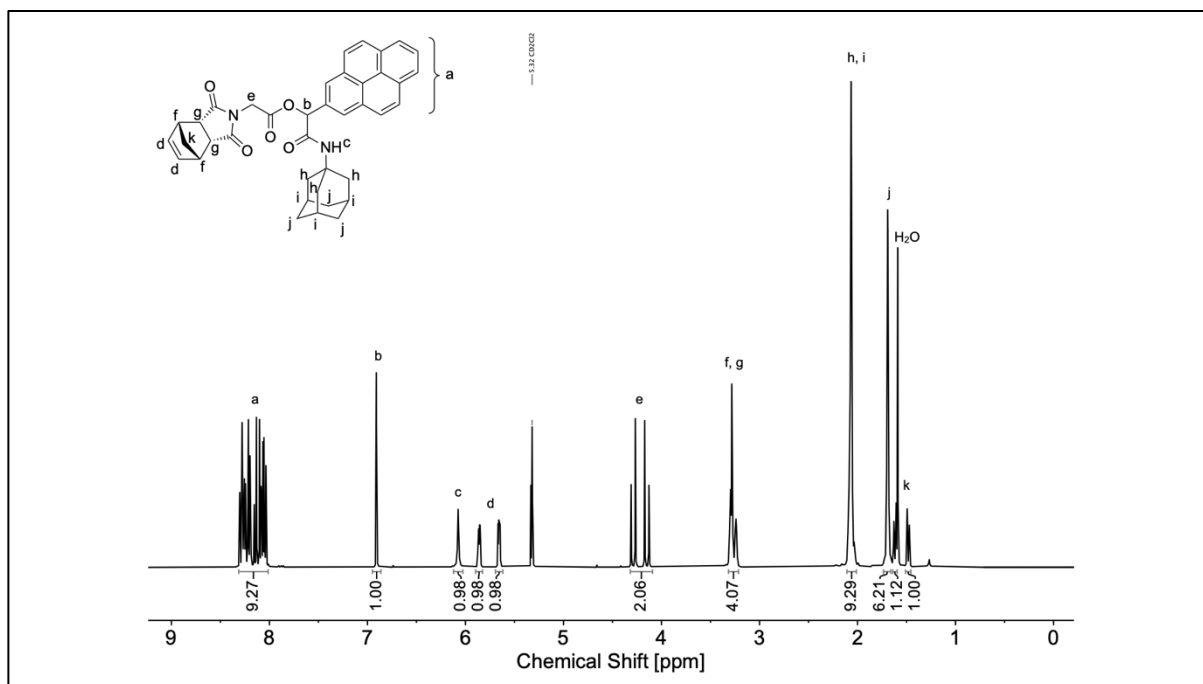
nNb1AdPy:

Figure S4.19. ^1H NMR spectrum of *nNb1AdPy* in CD_2Cl_2 .

^1H NMR (400 MHz, CD_2Cl_2 , δ): 8.31 - 8.03 (m, 9H, H_{Ar} , ^a), 6.91 (s, 1H, COO-CH , ^b), 5.96 (s, 1H, CONH , ^c), 5.86 (dd, $J = 5.7$ Hz, 2.5 Hz, 1H, CH=CH , ^d), 5.66 (dd, $J = 5.7$ Hz, 2.9 Hz, 1H, CH=CH , ^d), 4.22 (dd, $J = 38.2$ Hz, 17.2 Hz, 2H, N-CH_2 , ^e), 3.33 - 3.25 (m, 2H, $=\text{CH-CH}$, ^f), 3.33 - 3.20 (m, 2H, $=\text{CH-CH-CH}$, ^g), 2.12 - 2.00 (m, 6H, CONH-C-CH_2 , ^h), 2.08 - 2.00 (m, 3H, $\text{CH}_2\text{-CH}$, ⁱ), 1.74 - 1.66 (m, 6H, CH-CH_2 , ^j), 1.64 - 1.46 (m, 2H, CH_2 bridge, ^k).

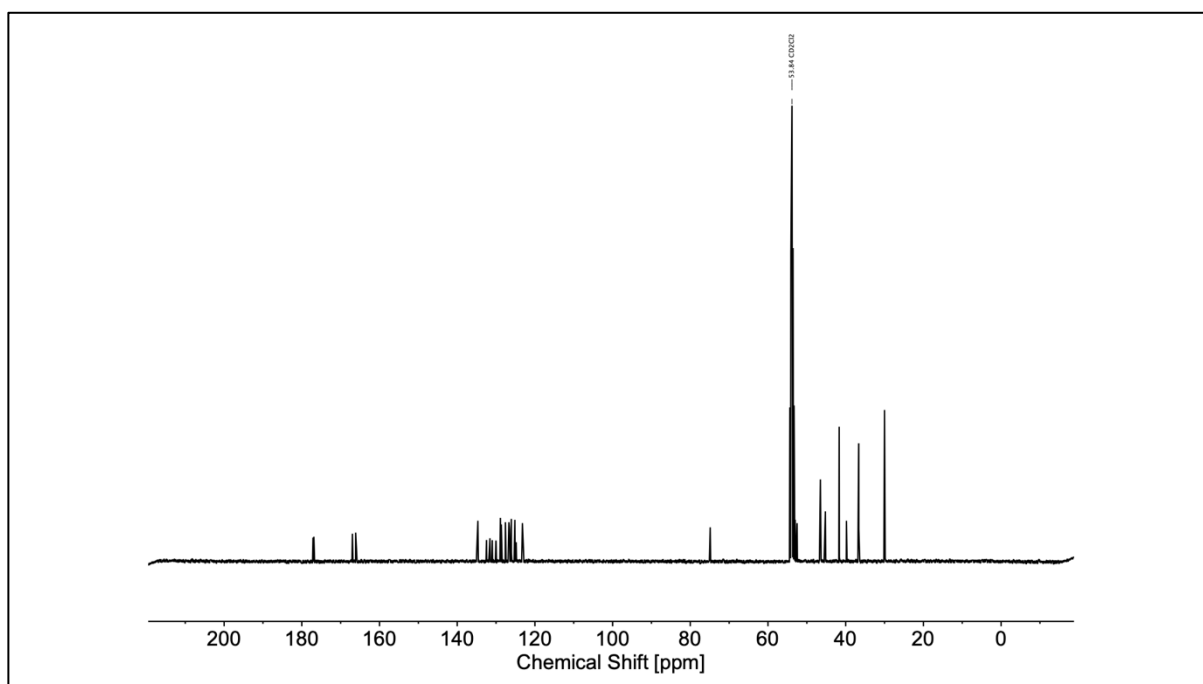


Figure S4.20. ^{13}C NMR spectrum of *nNb1AdPy* in CD_2Cl_2 .

^{13}C NMR (100 MHz, CD_2Cl_2 , δ): 177.3, 177.1, 167.1, 166.3, 135.0, 134.8, 132.6, 131.8, 131.1, 130.2, 129.1, 129.0, 128.8, 127.8, 126.9, 126.7, 126.3, 126.2, 125.4, 125.3, 125.0, 123.4, 75.0, 53.1, 52.7, 46.7, 45.4, 45.4, 41.8, 40.0, 36.8, 30.2.

IR (ATR platinum diamond): ν / cm^{-1} = 3328 (w), 2904 (w), 2849 (w), 1773 (w), 1757 (s), 1701 (vs), 1691 (vs), 1549 (m), 1454 (w), 1415 (s), 1388 (w), 1376 (w), 1360 (w), 1337 (w), 1321 (m), 1292 (w), 1281 (w), 1267 (w), 1244 (w), 1230 (w), 1187 (vs), 1174 (vs), 1129 (w), 1103 (w), 1094 (w), 1053 (w), 1018 (w), 998 (w), 981 (w), 961 (w), 948 (w), 934 (w), 919 (m), 852 (s), 841 (m), 833 (m), 810 (w), 786 (w), 753 (m), 740 (m), 722 (s), 654 (w), 638 (w), 613 (s), 588 (w), 541 (w), 516 (w), 490 (w), 453 (w), 434 (w).

HRMS (ESI-MS) m/z : $[\text{M}+\text{H}]^+$ calc. for $\text{C}_{39}\text{H}_{36}\text{N}_2\text{O}_5$, 613.2697, found: 613.2676.

R_f = 0.35 (cyclohexane/ethyl acetate, 2:1).

nNb10PePr (synthesized by A. Seliwjorstow under my supervision):

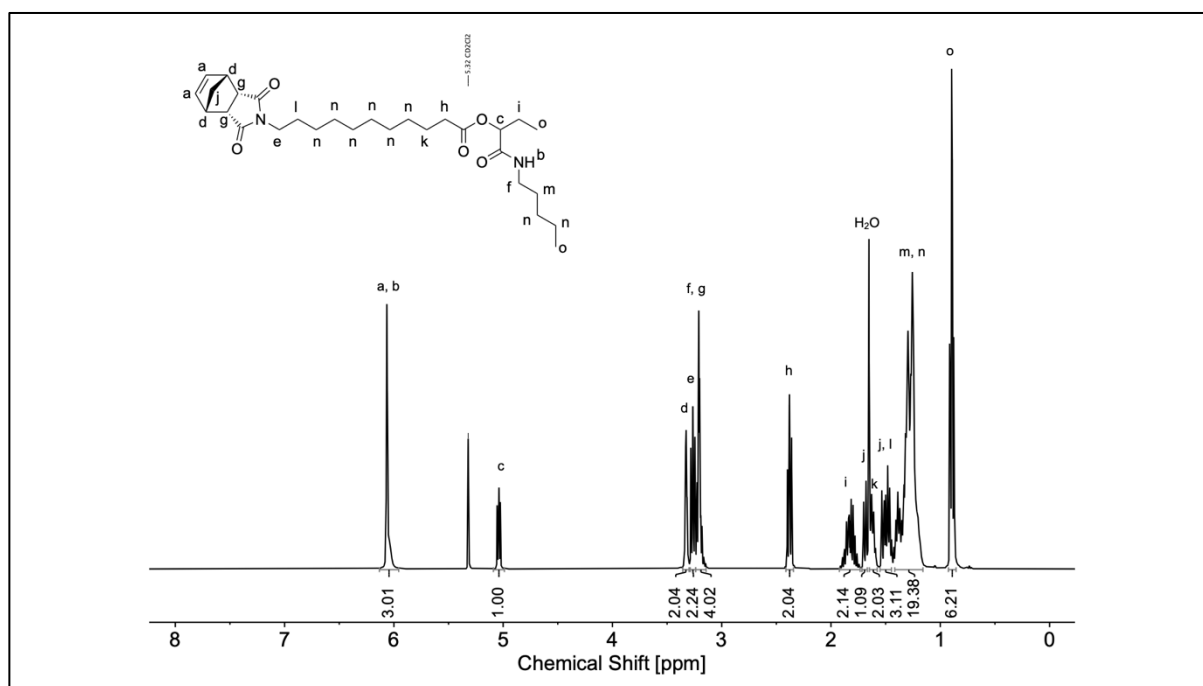


Figure S4.21. ^1H NMR spectrum of *nNb10PePr* in CD_2Cl_2 .

^1H NMR (400 MHz, CD_2Cl_2 , δ): 6.10 - 6.04 (m, 2H, $\text{CH}=\text{CH}$, ^a), 6.08 - 5.95 (m, 1H, CONH, ^b), 5.04 (dd, $J = 6.7$ Hz, 4.9 Hz, 1H, $\text{COO}-\text{CH}$, ^c), 3.36 - 3.30 (m, 2H, $=\text{CH}-\text{CH}$, ^d), 3.26 (m, $J = 7.4$ Hz, 2H, $\text{N}-\text{CH}_2$, ^e), 3.24 - 3.14 (m, 2H, $\text{CONH}-\text{CH}_2$, ^f), 3.22 - 3.20 (m, 2H, $=\text{CH}-\text{CH}-\text{CH}$, ^g), 3.48 (t, $J = 7.6$ Hz, 2H, CH_2-COO , ^h), 1.92 - 1.74 (m, 2H, $\text{CH}-\text{CH}_2-\text{CH}_3$, ⁱ), 1.72 - 1.45 (m, 2H, CH_2 bridge, ^j), 1.65 - 1.58 (m, 2H, $\text{CH}_2-\text{CH}_2-\text{COO}$, ^k), 1.51 - 1.44 (m, 2H, $\text{N}-\text{CH}_2-\text{CH}_2$, ^l), 1.44 - 1.36 (m, 2H, $\text{CONH}-\text{CH}_2-\text{CH}_2$, ^m), 1.36 - 1.16 (m, 16H, CH_2 , ⁿ), 0.93 - 0.86 (m, 6H, CH_3 , ^o).

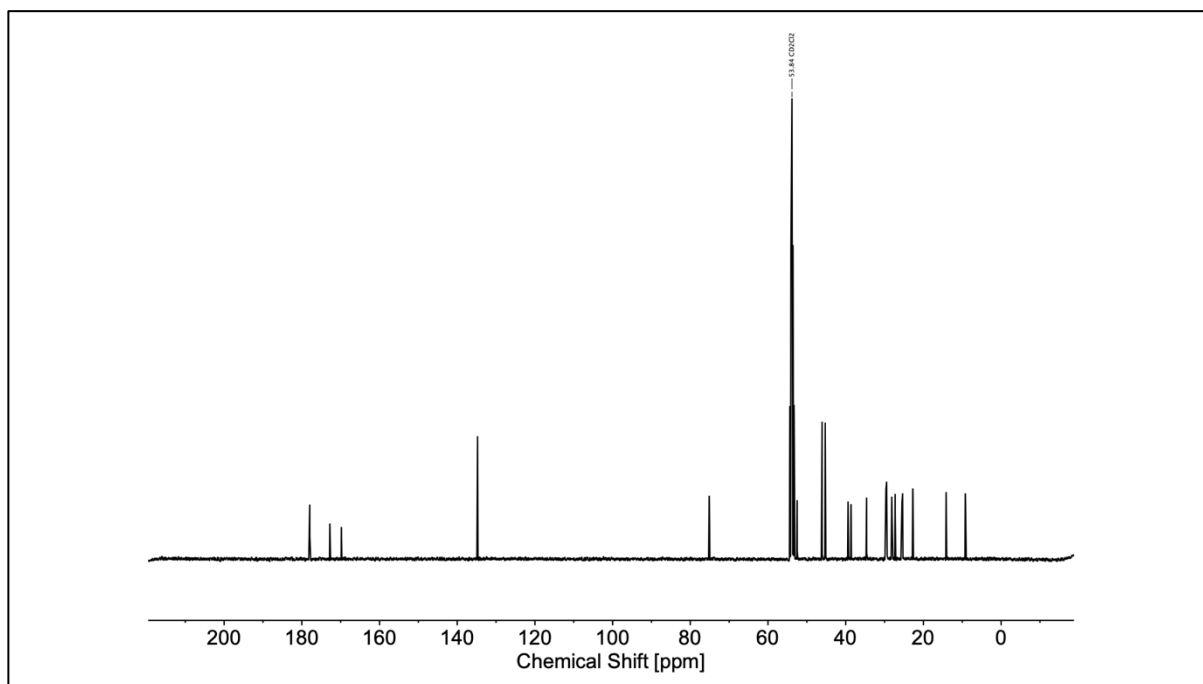


Figure S4.22. ^{13}C NMR spectrum of *nNb10PePr* in CD_2Cl_2 .

^{13}C NMR (100 MHz, CD_2Cl_2 , δ): 178.6, 172.9, 170.0, 75.3, 48.3, 45.8, 43.2, 39.6, 39.1, 34.8, 29.9, 29.9, 29.8, 29.8, 29.7, 29.6, 29.5, 29.3, 27.5, 25.7, 25.5, 22.9, 14.3, 9.4.

IR (ATR platinum diamond): $\nu / \text{cm}^{-1} = 2927$ (m), 2855 (w), 1767 (w), 1740 (m), 1695 (vs), 1534 (m), 1458 (w), 1436 (w), 1397 (m), 1368 (m), 1337 (m), 1290 (w), 1228 (m), 1164 (s), 1144 (s), 1127 (m), 1100 (m), 1049 (w), 1014 (w), 973 (w), 946 (w), 907 (w), 876 (w), 843 (w), 802 (w), 786 (w), 745 (w), 720 (s), 662 (w), 646 (w), 615 (m), 568 (w), 557 (w), 545 (w), 537 (w), 529 (w), 512 (w), 490 (w), 481 (w), 469 (w), 463 (w), 434 (w), 411 (m).

HRMS (ESI-MS) m/z : $[\text{M}+\text{H}]^+$ calc. for $\text{C}_{29}\text{H}_{46}\text{N}_2\text{O}_5$, 503.3479, found: 503.3467.

$R_f = 0.35$ (cyclohexane/ethyl acetate, 2:1).

nNb10AdPy (synthesized by A. Seliwjorstow under my supervision):

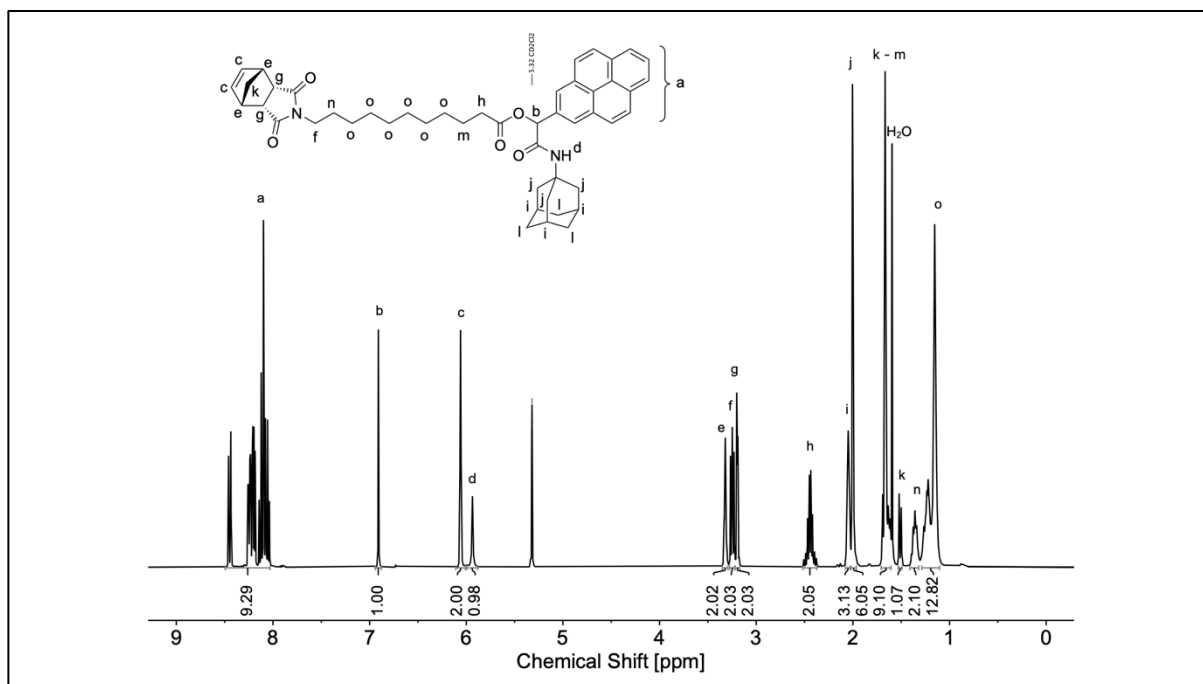


Figure S4.23. ^1H NMR spectrum of *nNb10AdPy* in CD_2Cl_2 .

^1H NMR (400 MHz, CD_2Cl_2 , δ): 8.45 – 8.03 (m, 9H, H_{Ar} , ^a), 6.91 (s, 1H, COO-CH, ^b), 6.11 - 6.01 (m, 2H, CH=CH, ^c), 5.94 (s, 1H, CONH, ^d), 3.21 (p, $J = 1.7$ Hz, 2H, =CH-CH, ^e), 3.25 (t, $J = 7.4$ Hz, 2H, N-CH₂, ^f), 3.22 - 3.17 (m, 2H, =CH-CH-CH, ^g), 2.52 - 2.36 (m, 2H, CH₂-COO, ^h), 2.08 - 2.03 (m, 3H, CH₂-CH, ⁱ), 2.02 - 1.97 (m, 6H, CONH-C-CH₂, ^j), 1.71 - 1.49 (m, 2H, CH₂ bridge, ^k), 1.69 - 1.61 (m, 6H, CH-CH₂, ^l), 1.69 - 1.61 (m, 2H, CH₂-CH₂-COO, ^m), 1.41 - 1.32 (m, 2H, N-CH₂-CH₂, ⁿ), 1.29 - 1.10 (m, 12H, CH₂, ^o).

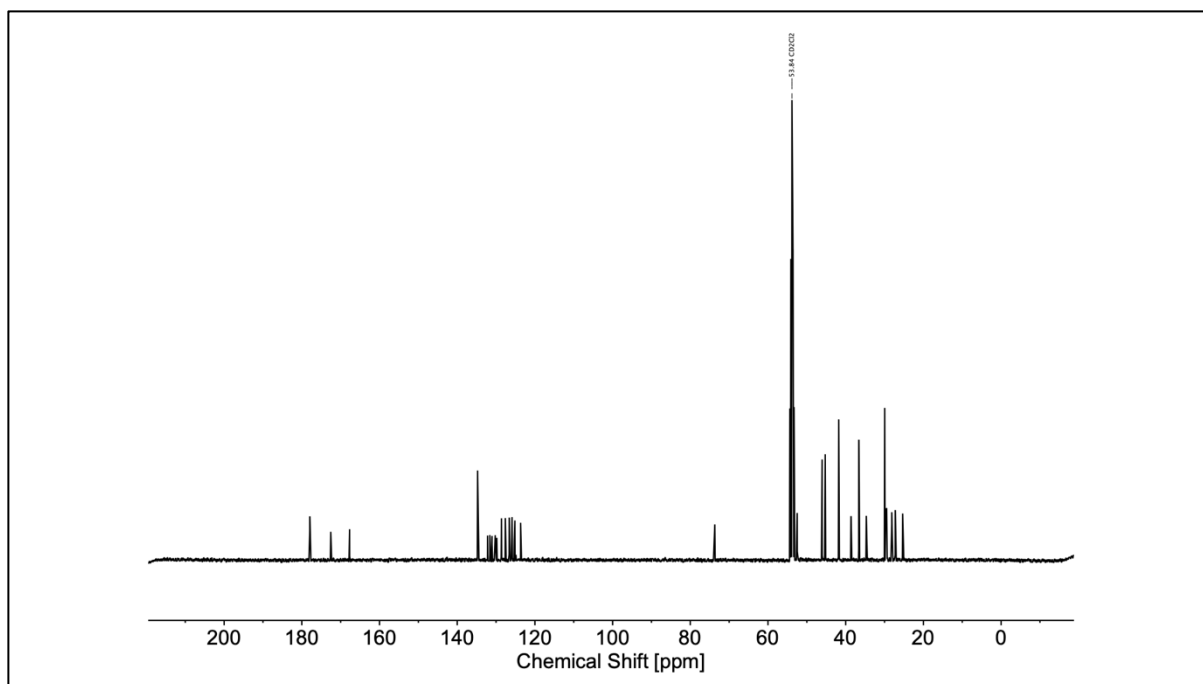


Figure S4.24. ^{13}C NMR spectrum of *nNb10AdPy* in CD_2Cl_2 .

^{13}C NMR (100 MHz, CD_2Cl_2 , δ): 178.1, 172.7, 167.9, 134.9, 132.3, 131.8, 131.2, 130.9, 130.0, 128.8, 128.6, 127.8, 126.9, 126.7, 126.2, 126.0, 125.5, 125.3, 125.1, 123.8, 73.9, 52.8, 52.7, 46.2, 45.4, 42.0, 38.8, 36.8, 34.9, 30.1, 29.9, 29.9, 29.7, 29.6, 29.6, 28.3, 27.4, 25.5.

IR (ATR platinum diamond): ν / cm^{-1} = 2906 (m), 2851 (w), 1736 (w), 1691 (vs), 1514 (m), 1454 (w), 1436 (w), 1397 (m), 1360 (m), 1337 (m), 1310 (w), 1292 (w), 1263 (w), 1228 (m), 1154 (m), 1142 (s), 1127 (m), 1103 (m), 1094 (m), 1053 (w), 1020 (w), 996 (w), 981 (w), 963 (w), 944 (w), 907 (w), 843 (vs), 819 (w), 786 (w), 757 (w), 747 (w), 718 (s), 683 (w), 662 (w), 644 (w), 615 (m), 582 (w), 568 (w), 545 (w), 527 (w), 516 (w), 490 (w), 467 (w), 455 (w), 442 (w), 422 (w), 411 (w).

HRMS (ESI-MS) m/z : $[\text{M}+\text{H}]^+$ calc. for $\text{C}_{48}\text{H}_{54}\text{N}_2\text{O}_5$, 739.4105, found: 739.4084.

R_f = 0.50 (cyclohexane/ethyl acetate, 2:1).

General synthesis of homopolymers (poly(xNb1PePr), poly(xNb1AdPy), poly(xNb10PePr), poly(xNb10AdPy), poly(nNb1PePr), poly(nNb1AdPy), poly(nNb10PePr), and poly(nNb10AdPy)):

An ampoule equipped with a J Young tap was evacuated and purged with argon three times. Subsequently, 50.0 eq. bifunctional monomer (0.1 mol/L) and 1.00 eq. G1 catalyst were each dissolved in degassed DCM and transferred into the ampoule under an argon flow, initiating the polymerization. The polymerization was carried out at ambient temperature under an argon atmosphere and was quenched by adding an excess of ethyl vinyl ether. The polymerization mixture was then flushed through a plug of DMT-functionalized silica to remove residual catalyst. The *endo* derived polymers were additionally purified by precipitating the polymers three times from the tenfold excess of cold ethyl acetate (poly(nNb1PePr), poly(nNb1AdPy), and poly(nNb10AdPy)) or cold methanol (poly(nNb10PePr)) to remove unreacted monomer.

Poly(xNb1PePr):

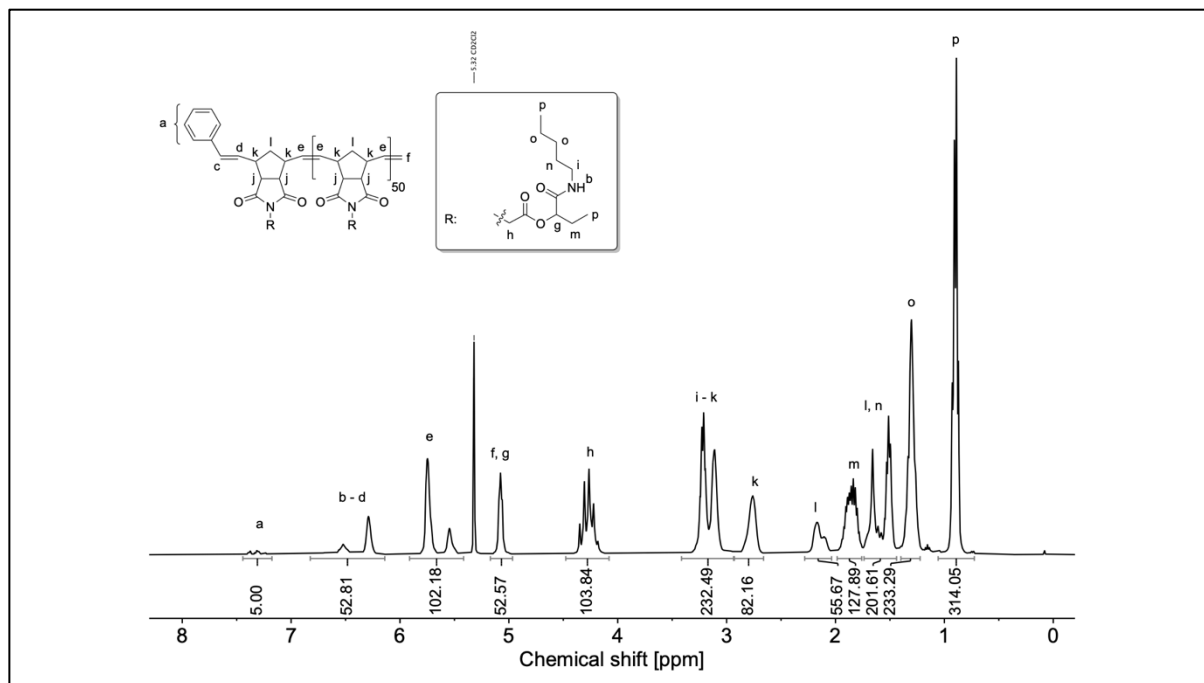


Figure S4.25. ^1H NMR spectrum of poly(xNb1PePr) in CD_2Cl_2 (500 MHz).

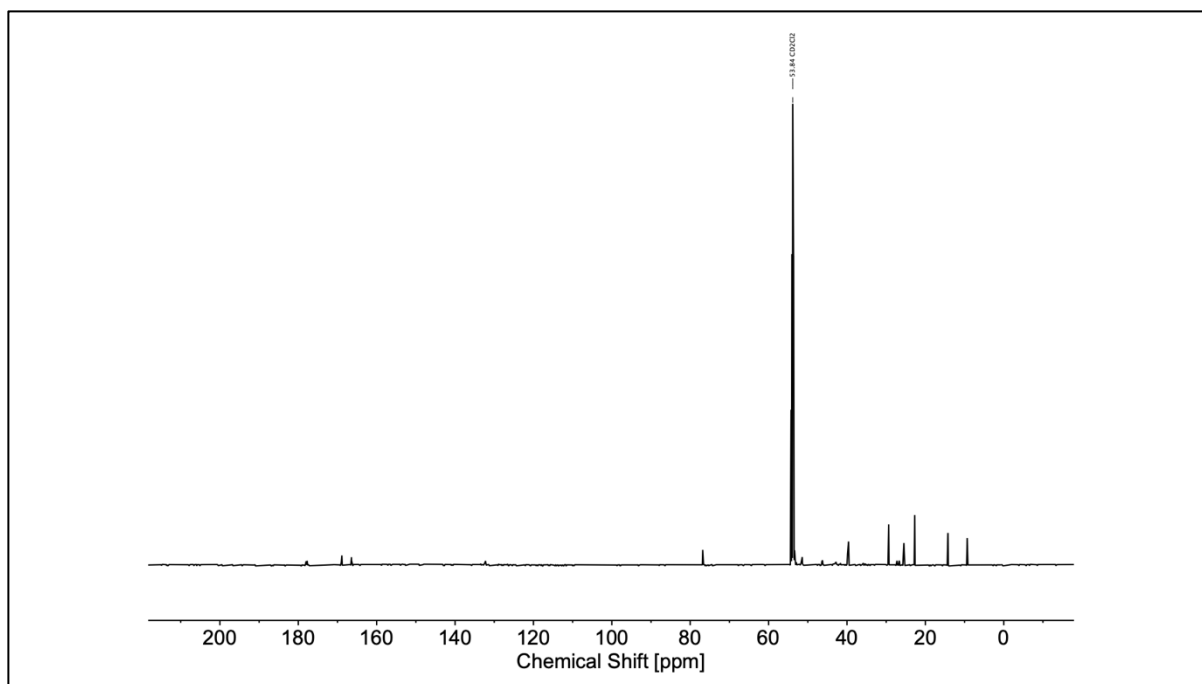


Figure S4.26. ^{13}C NMR spectrum of **poly(xNb1PePr)** in CD_2Cl_2 (126 MHz).

Poly(xNb1AdPy):

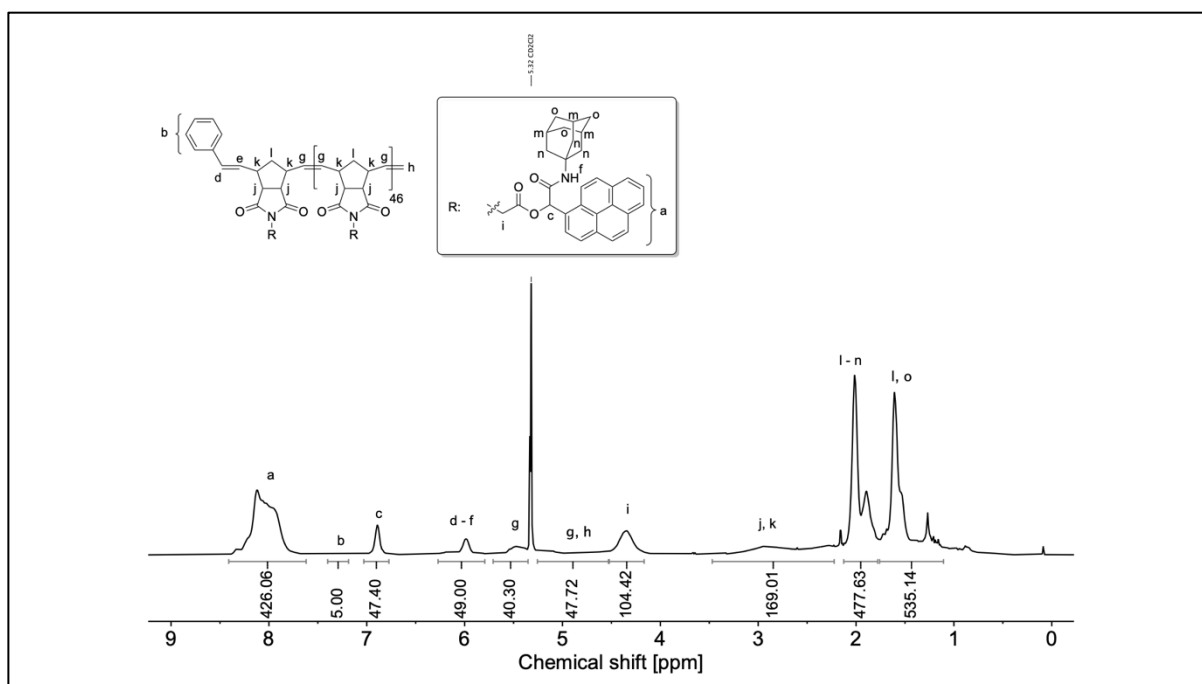


Figure S4.27. ^1H NMR spectrum of **poly(xNb1AdPy)** in CD_2Cl_2 (500 MHz).

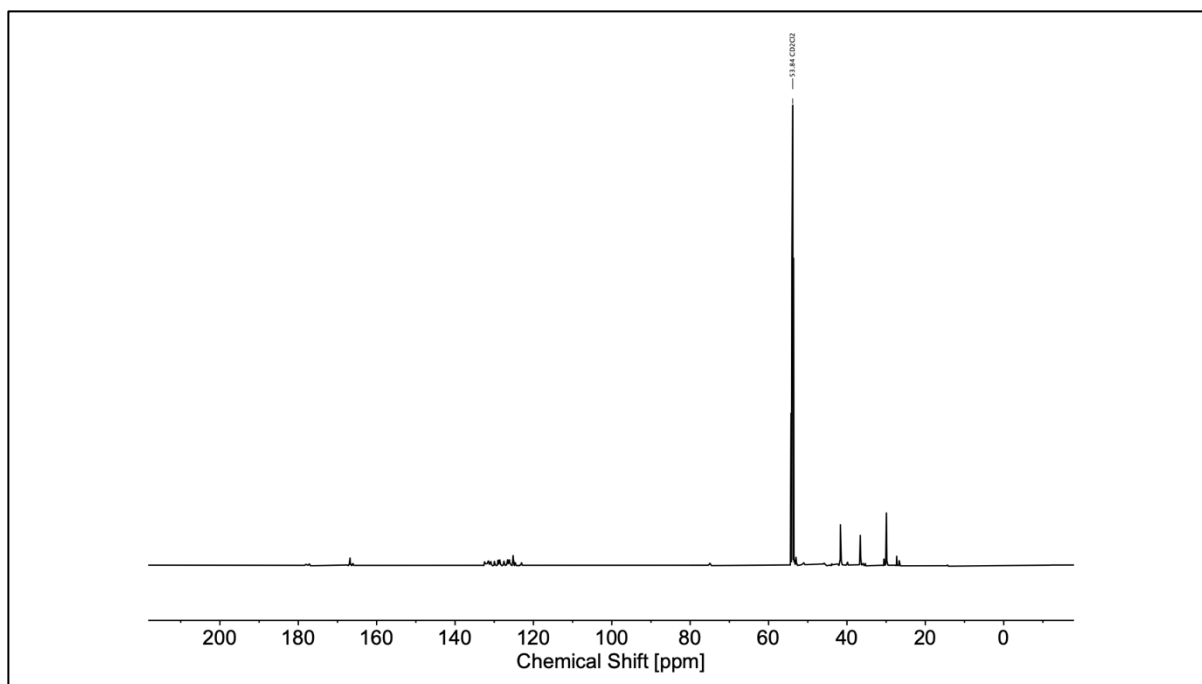


Figure S4.28. ^{13}C NMR spectrum of poly(xNb1AdPy) in CD_2Cl_2 (126 MHz).

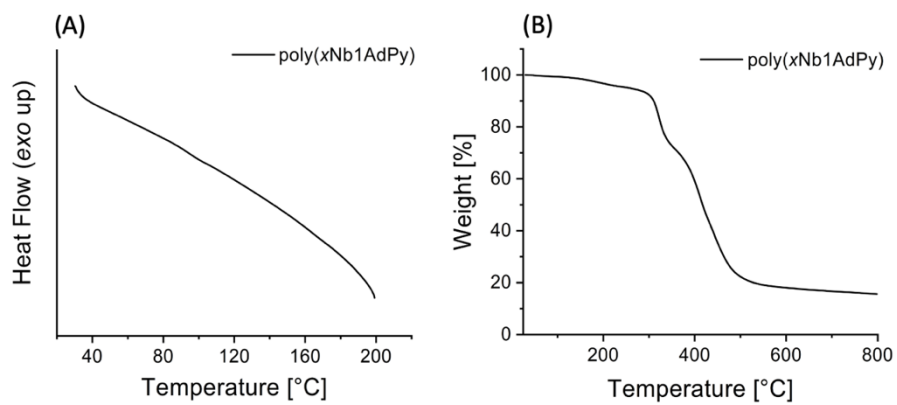
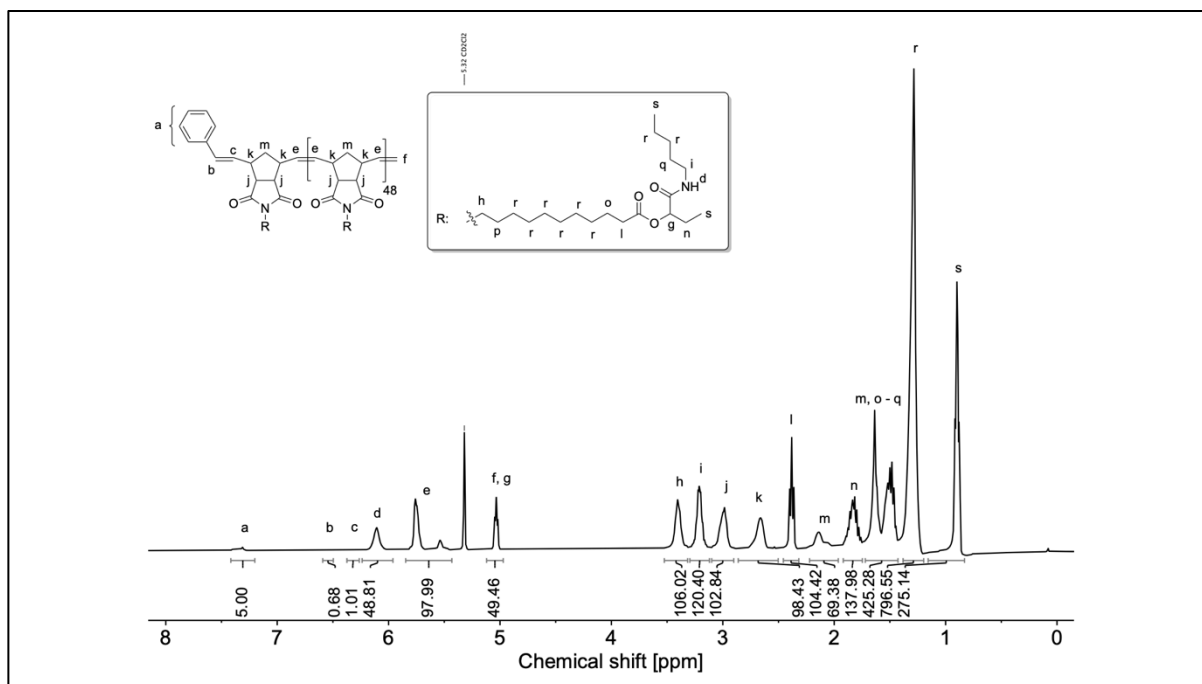
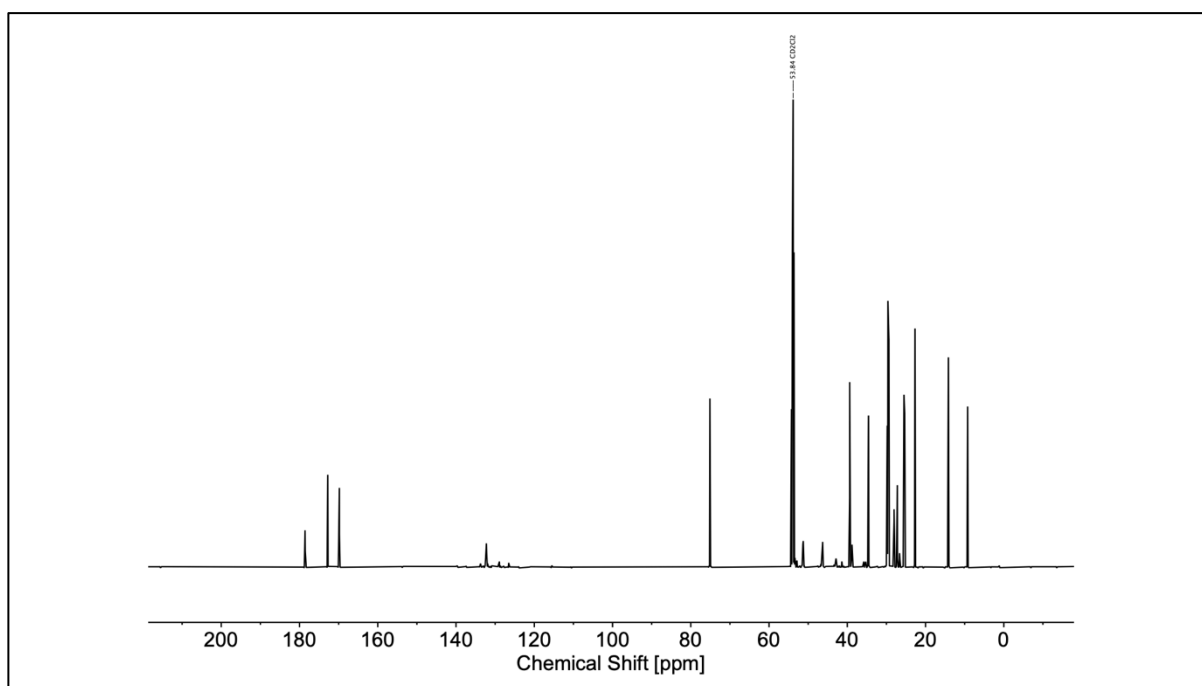


Figure S4.29. (A) DSC and (B) TGA traces of poly(xNb1AdPy).

Poly(xNb10PePr):**Figure S4.30.** ^1H NMR spectrum of poly(xNb10PePr) in CD_2Cl_2 (500 MHz).**Figure S4.31.** ^{13}C NMR spectrum of poly(xNb10PePr) in CD_2Cl_2 (126 MHz).

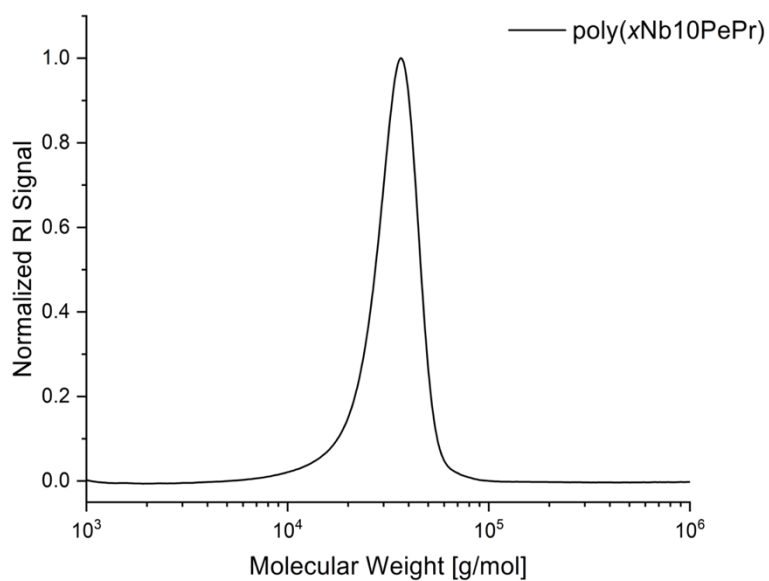


Figure S4.32. SEC trace of poly(xNbPePr).

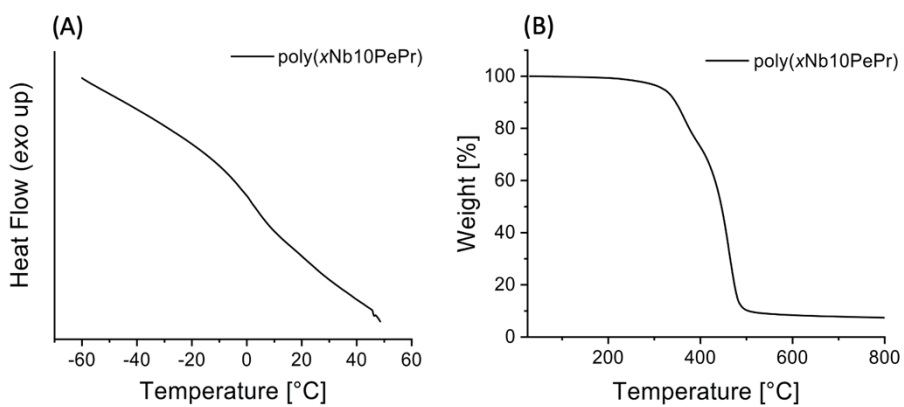
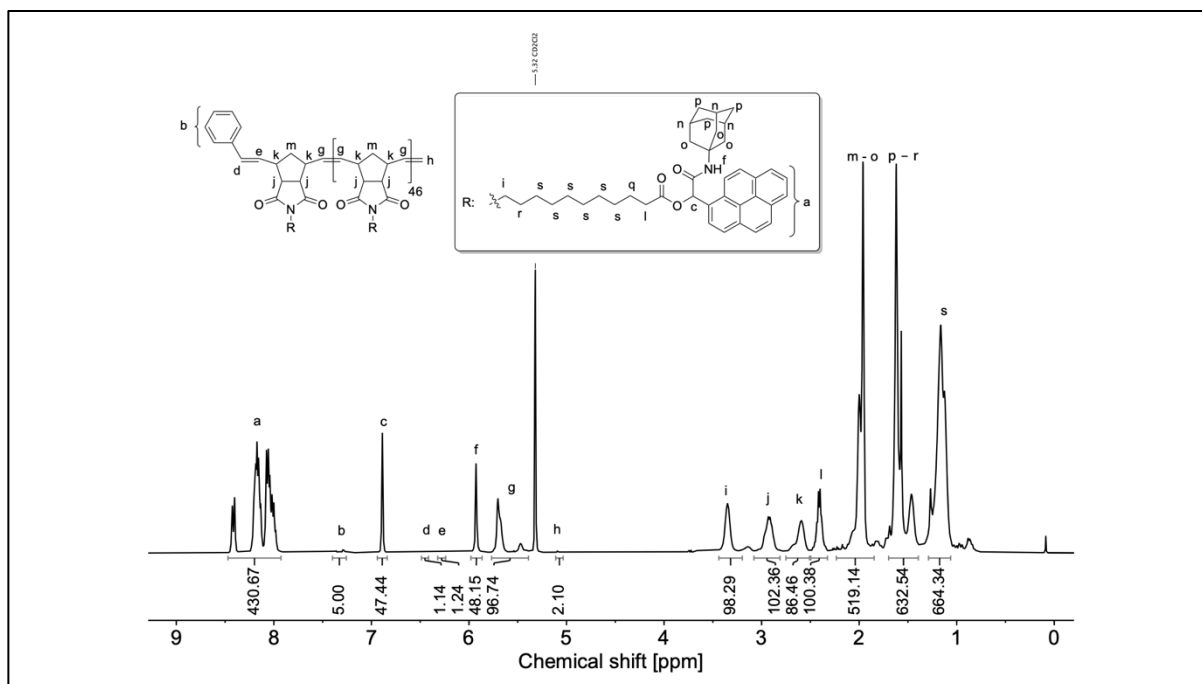
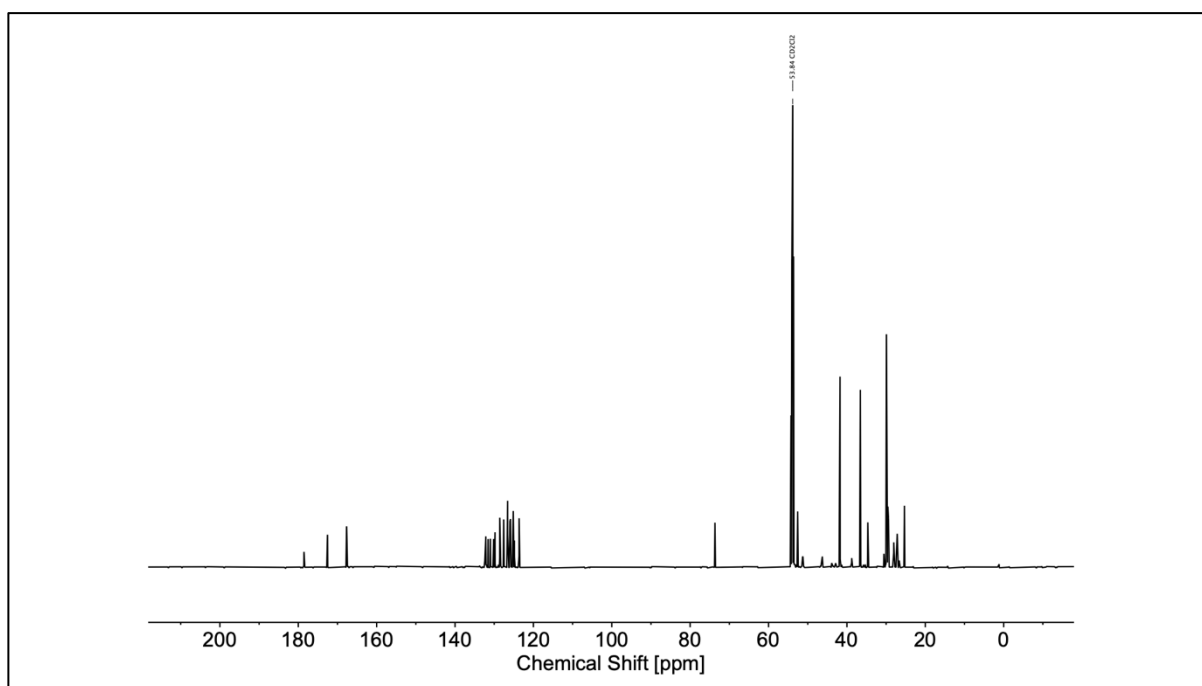


Figure S4.33. (A) DSC and (B) TGA traces of poly(xNb10PePr).

Poly(xNb10AdPy):

Figure S4.34. ^1H NMR spectrum of poly(xNb10AdPy) in CD_2Cl_2 (500 MHz).Figure S4.35. ^{13}C NMR spectrum of poly(xNb10AdPy) in CD_2Cl_2 (126 MHz).

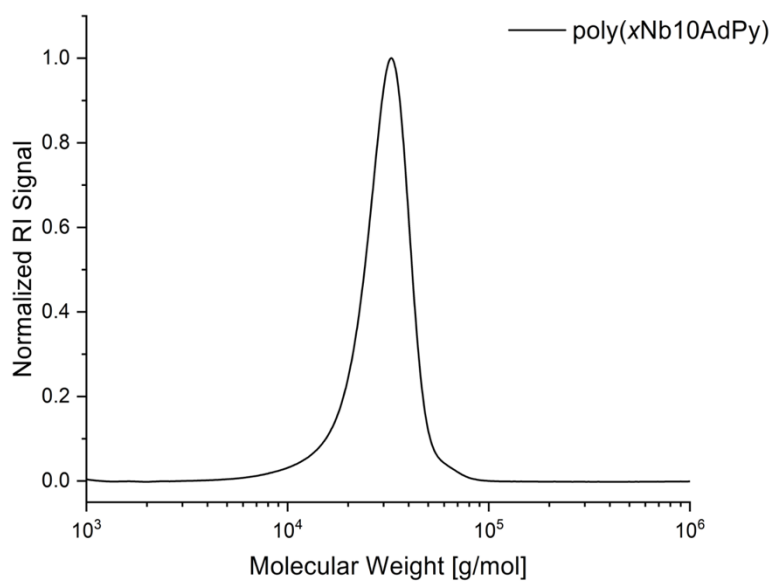


Figure S4.36. SEC trace of poly(xNb10AdPy).

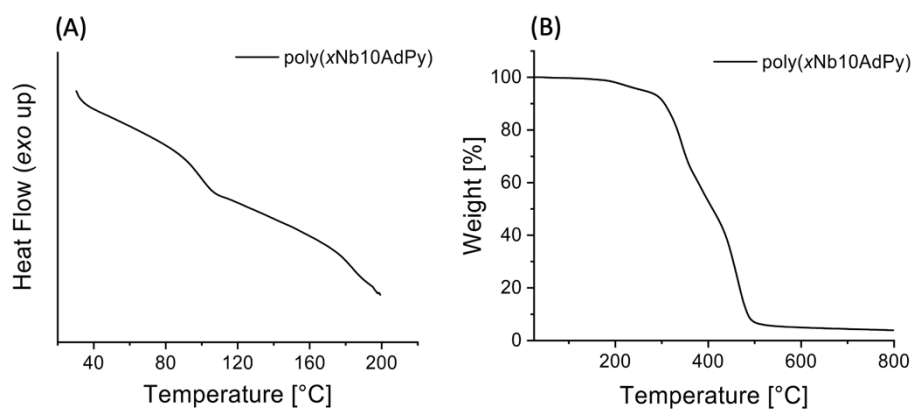


Figure S4.37. (A) DSC and (B) TGA traces of poly(xNb10AdPy).

Cleavage product (Small molecule isolated from exposing **poly(xNb10AdPy)** to potassium 2-isocyanoacetate):

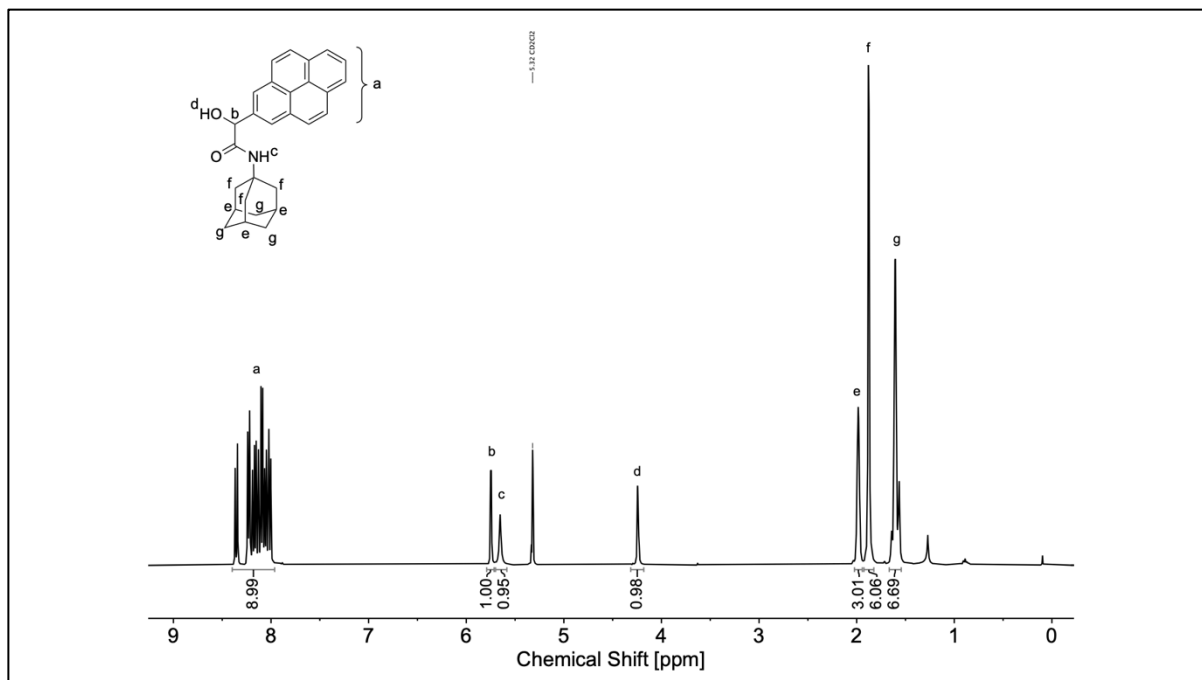


Figure S4.38. ^1H NMR spectrum of the small molecule isolated from exposing **poly(xNb10AdPy)** to potassium 2-isocyanoacetate in CD_2Cl_2 .

^1H NMR (400 MHz, CD_2Cl_2 , δ): 8.35 - 7.97 (m, 9H, H_{Ar} , ^a), 5.75 (d, $J = 2.8$ Hz, 1H, CH-OH , ^b), 5.65 (bs, 1H, CONH , ^c), 4.24 (d, $J = 3.2$ Hz, 1H, OH , ^d), 2.02 - 1.94 (m, 3H, $\text{CH}_2\text{-CH}$, ^e), 1.93 - 1.82 (m, 6H, CONH-C-CH_2 , ^f), 1.66 - 1.55 (m, 6H, CH-CH_2 , ^g).

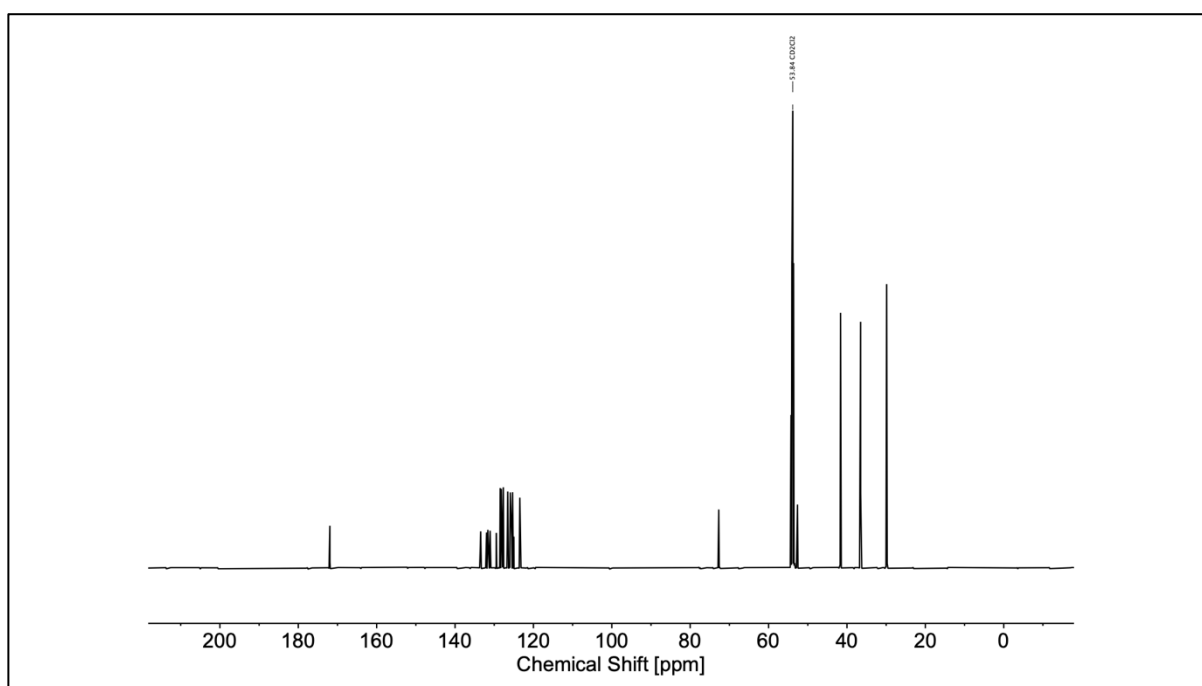


Figure S4.39. ^{13}C NMR spectrum of the small molecule isolated from exposing **poly(xNb10AdPy)** to potassium 2-isocyanoacetate in CD_2Cl_2 .

^{13}C NMR (100 MHz, CD_2Cl_2 , δ): 172.1, 133.6, 132.1, 131.8, 131.2, 129.6, 128.6, 128.4, 127.8, 126.8, 126.7, 126.1, 125.9, 125.7, 125.5, 125.2, 123.6, 72.9, 52.8, 41.8, 36.7, 30.0.

IR (ATR platinum diamond): $\nu / \text{cm}^{-1} = 3361$ (w), 3355 (w), 3334 (w), 3320 (w), 3314 (w), 3305 (w), 3291 (w), 3279 (w), 2902 (s), 2849 (m), 1646 (vs), 1600 (w), 1588 (w), 1520 (vs), 1454 (m), 1438 (w), 1417 (w), 1390 (w), 1360 (m), 1343 (w), 1310 (w), 1296 (m), 1277 (w), 1242 (w), 1230 (w), 1214 (w), 1185 (w), 1162 (w), 1137 (w), 1125 (w), 1103 (w), 1094 (m), 1061 (m), 1041 (m), 837 (vs), 819 (m), 794 (w), 786 (w), 757 (w), 720 (m), 706 (s), 681 (m), 664 (w), 631 (m), 611 (w), 588 (w), 568 (w), 545 (m), 529 (w), 494 (w), 485 (w), 469 (w), 450 (w), 440 (w), 424 (w), 411 (w).

HRMS (ESI-MS) m/z : $[\text{M}+\text{H}]^+$ calc. for $\text{C}_{28}\text{H}_{27}\text{NO}_2$, 410.2115, found: 410.2107.

$R_f = 0.21$ (DCM).

Poly(*n*Nb1PePr):

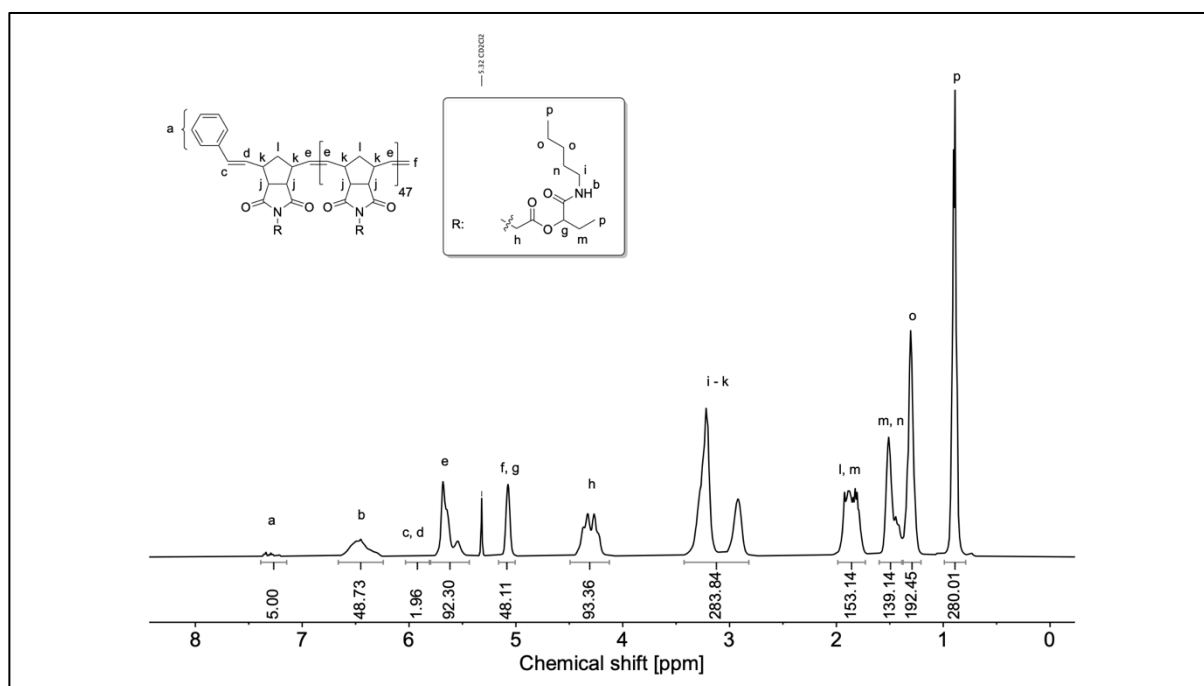


Figure S4.40. ^1H NMR spectrum of poly(*n*Nb1PePr) in CD_2Cl_2 (500 MHz).

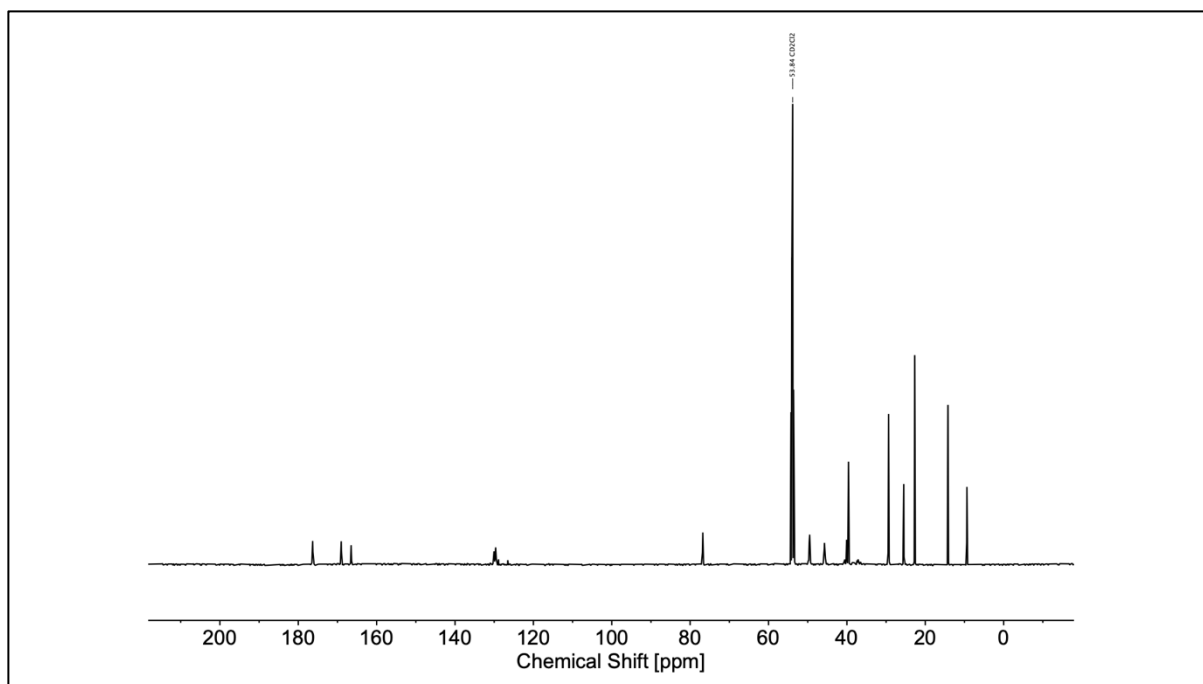


Figure S4.41. ^{13}C NMR spectrum of poly(*n*Nb1PePr) in CD_2Cl_2 (126 MHz).

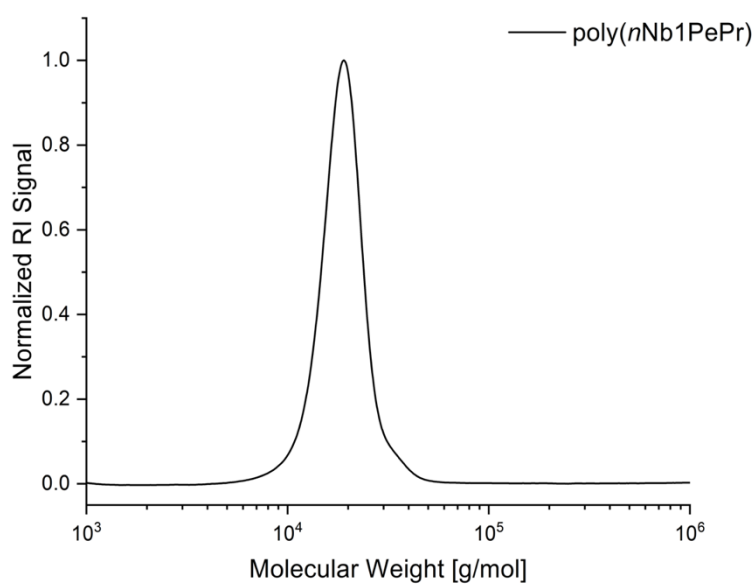


Figure S4.42. SEC trace of poly(*n*Nb1PePr).

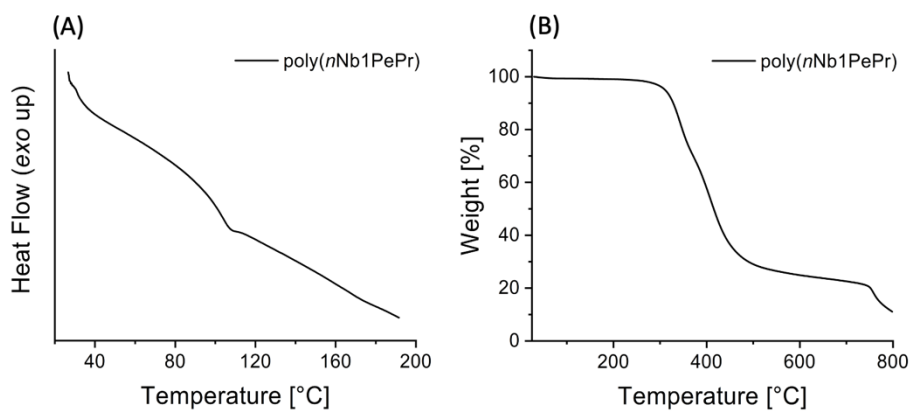


Figure S4.43. (A) DSC and (B) TGA traces of poly(*n*Nb1PePr).

Poly(*n*Nb1AdPy):

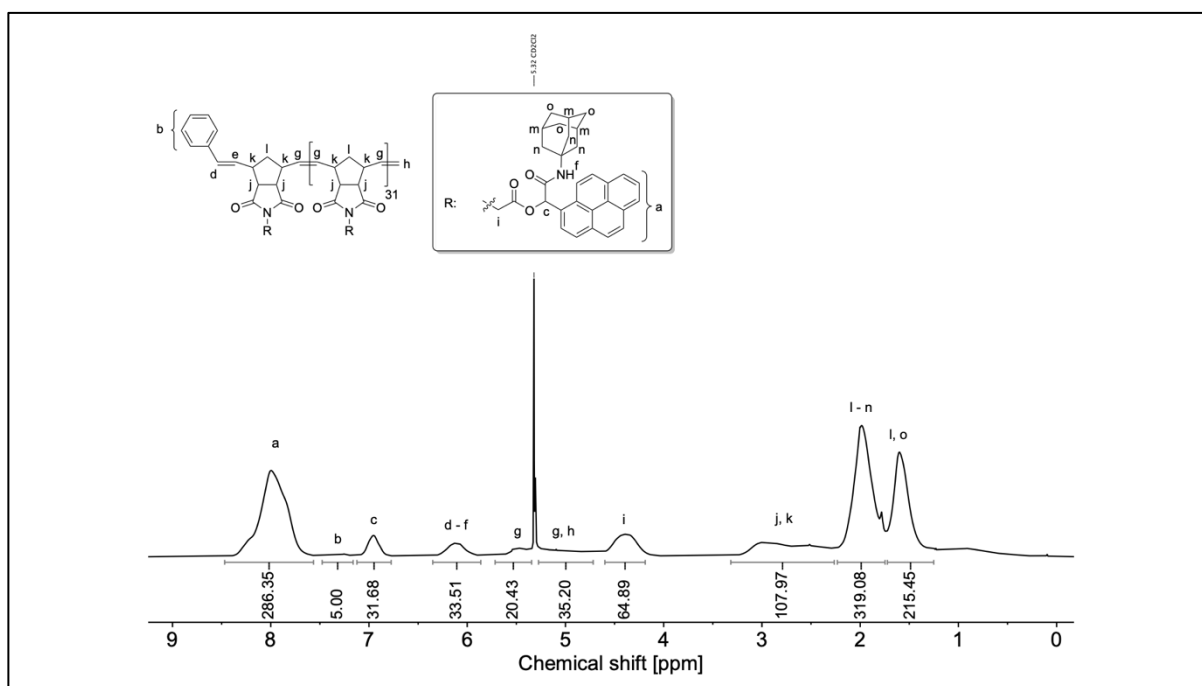


Figure S4.44. ¹H NMR spectrum of poly(*n*Nb1AdPy) in CD₂Cl₂ (500 MHz).

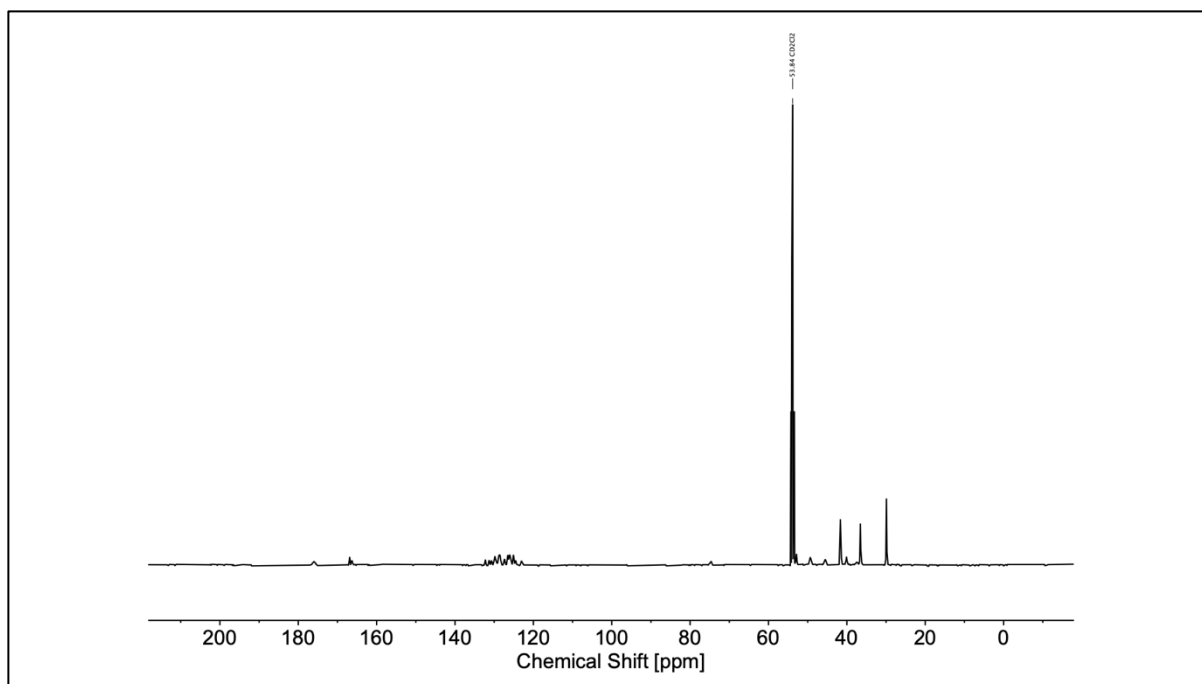


Figure S4.45. ^{13}C NMR spectrum of poly(*n*Nb1AdPy) in CD_2Cl_2 (126 MHz).

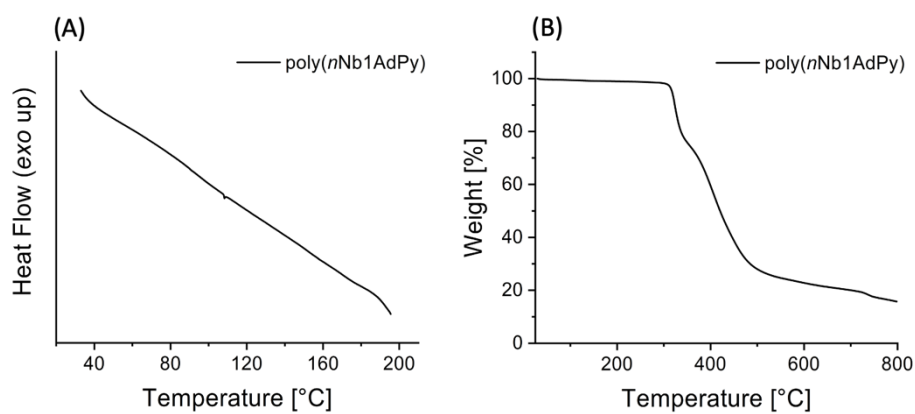
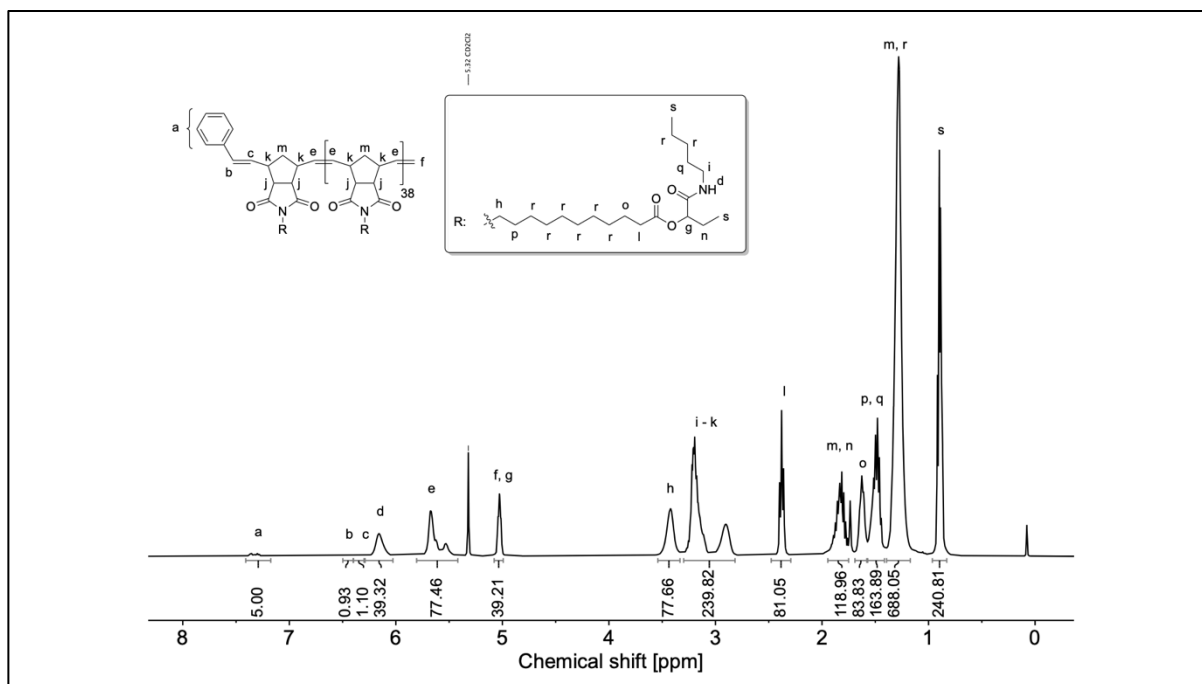
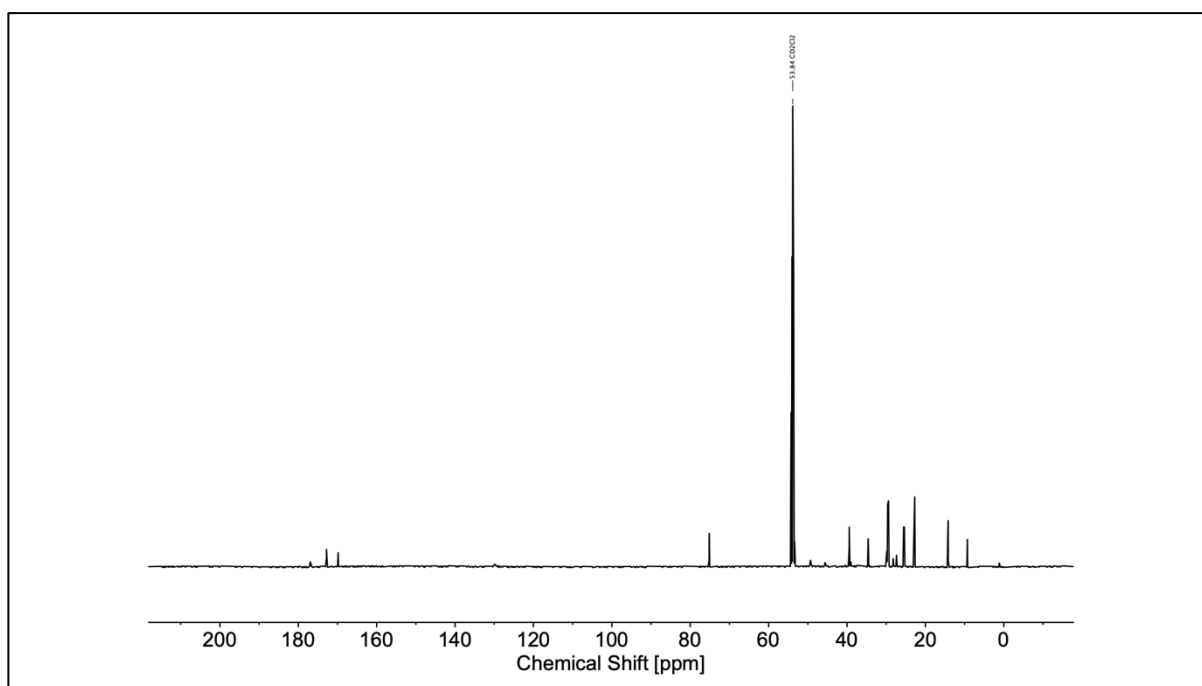


Figure S4.46. (A) DSC and (B) TGA traces of poly(*n*Nb1AdPy).

Poly(*n*Nb10PePr):Figure S4.47. ¹H NMR spectrum of poly(*n*Nb10PePr) in CD₂Cl₂ (500 MHz).Figure S4.48. ¹³C NMR spectrum of poly(*n*Nb10PePr) in CD₂Cl₂ (126 MHz).

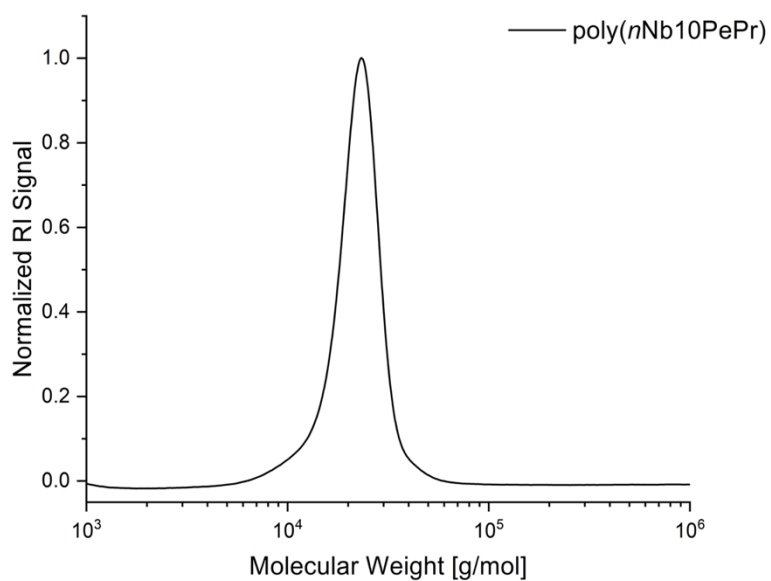


Figure S4.49. SEC trace of poly(*n*Nb10PePr).

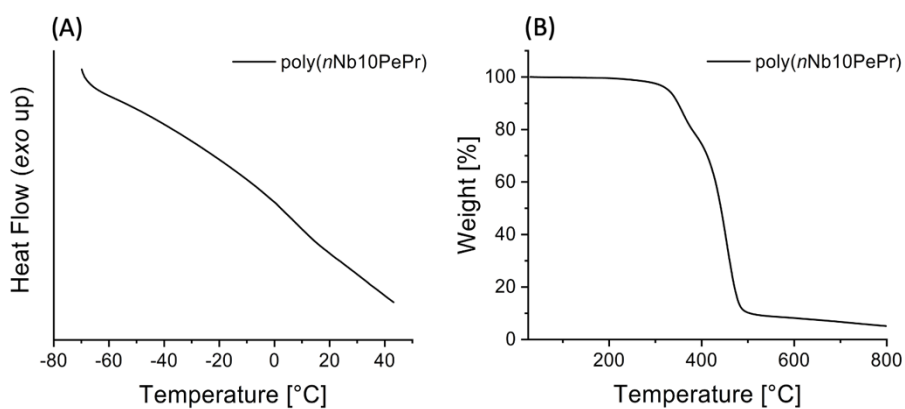
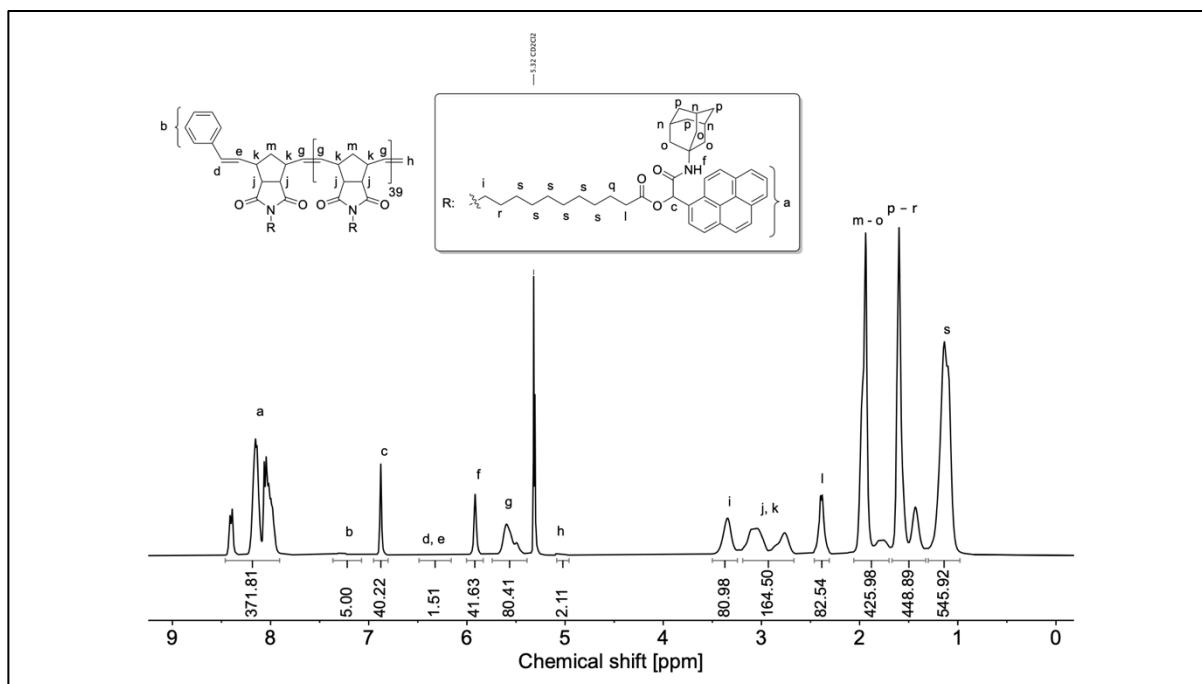
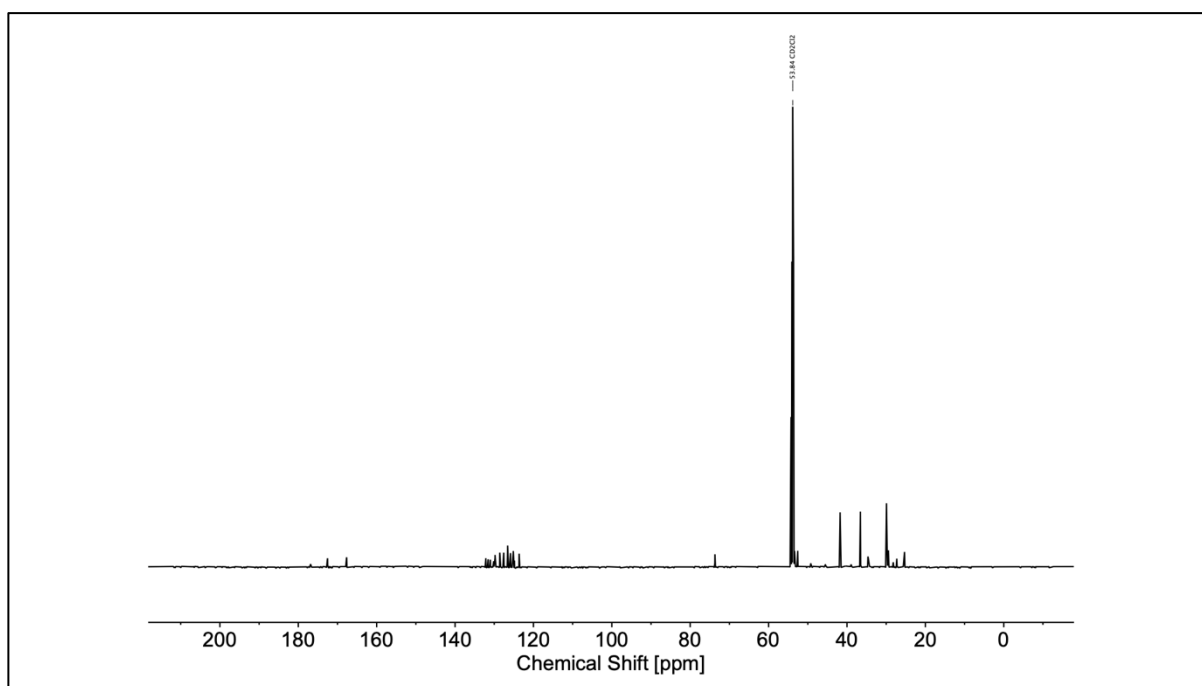


Figure S4.50. (A) DSC and (B) TGA traces of poly(*n*Nb10PePr).

Poly(*n*Nb10AdPy):Figure S4.51. ^1H NMR spectrum of poly(*n*Nb10AdPy) in CD_2Cl_2 (500 MHz).Figure S4.52. ^{13}C NMR spectrum of poly(*n*Nb10AdPy) in CD_2Cl_2 (126 MHz).

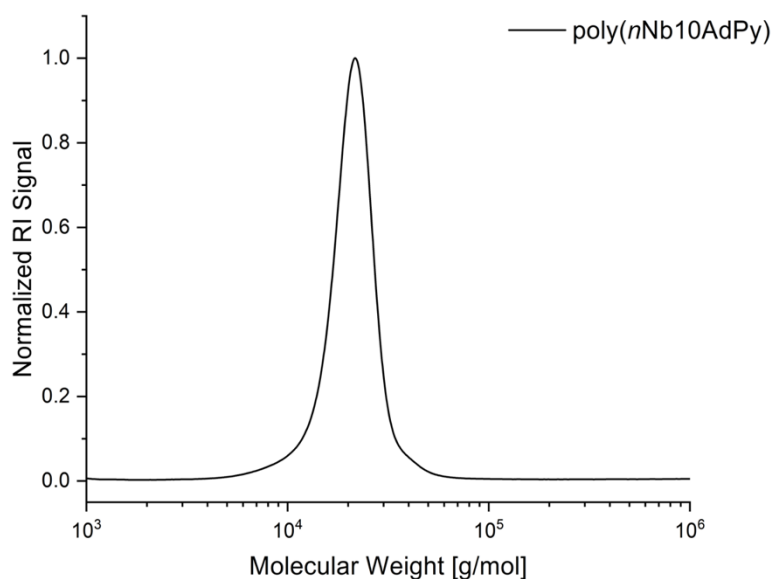


Figure S4.53. SEC trace of **poly(nNb10AdPy)**.

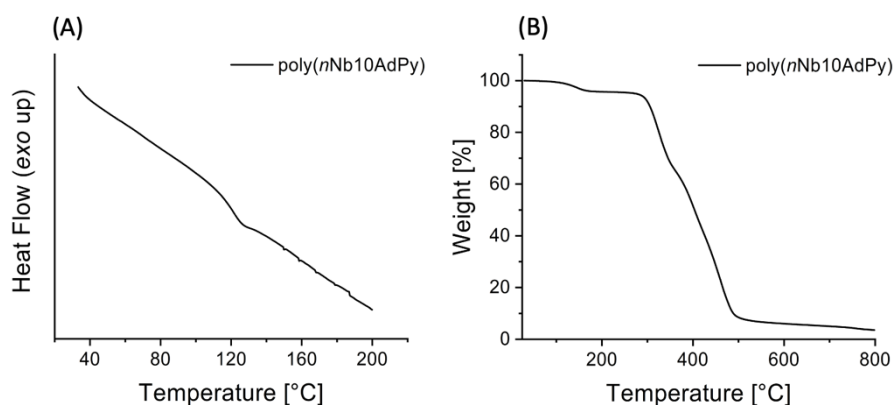


Figure S4.54. (A) DSC and (B) TGA traces of **poly(nNb10AdPy)**.

General synthesis of homopolymers – kinetic measurements (entries 4.1 – 4.9):

An NMR tube equipped with a J Young tap was evacuated and purged with argon three times. Subsequently, 50.0 eq. of the bifunctional monomer (0.10 mol/L) and 1.00 eq. G1 catalyst were each dissolved in degassed DCM-d₂ and transferred to the NMR tube, initiating the polymerization. The polymerization was carried out at ambient temperature under an argon atmosphere and was monitored by on-line ¹H NMR spectroscopy. The polymerization was quenched by adding an excess of ethyl vinyl ether. Entry 4.9 was performed in a similar manner applying a M:I ratio of 200:1 and, whereby the monomer concentration was increased to 0.4 mol/L

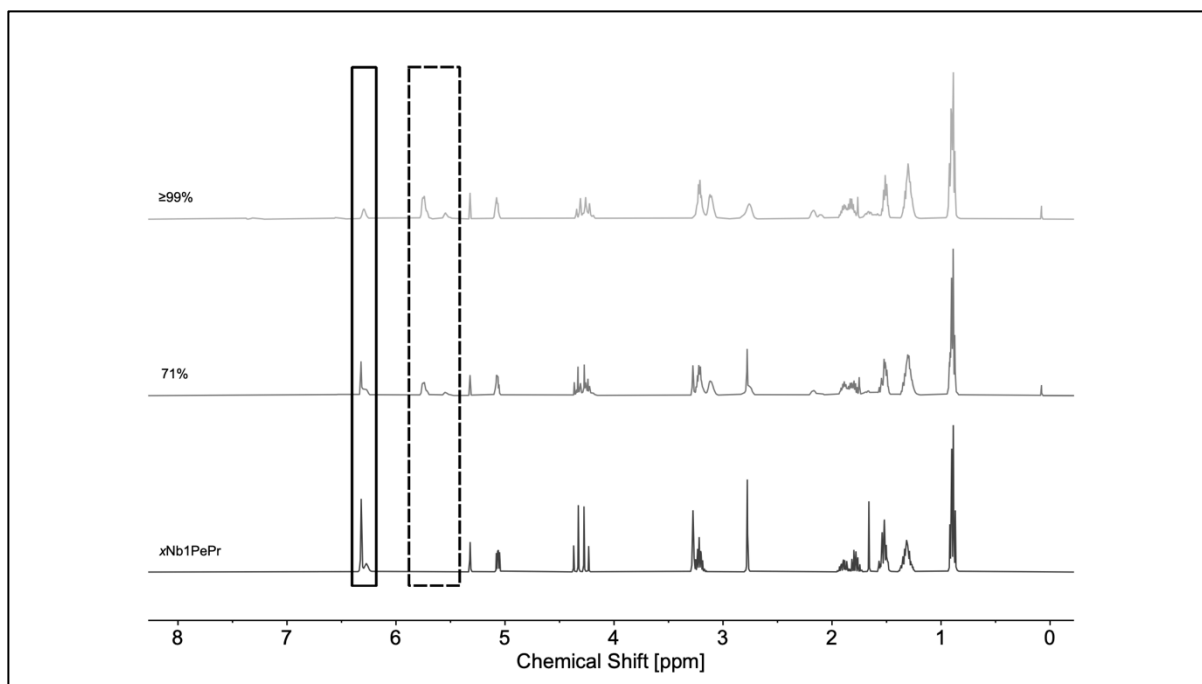


Figure S4.55. Representative stacked ¹H NMR spectra of the ROMP of **xNb1PePr** (entry 4.1) in CD₂Cl₂ (500 MHz) and the ¹H NMR spectrum of the corresponding monomer in CD₂Cl₂ (400 MHz). Boxes: norbornene olefinic moiety (solid); poly(norbornene) olefinic backbone (dashed).

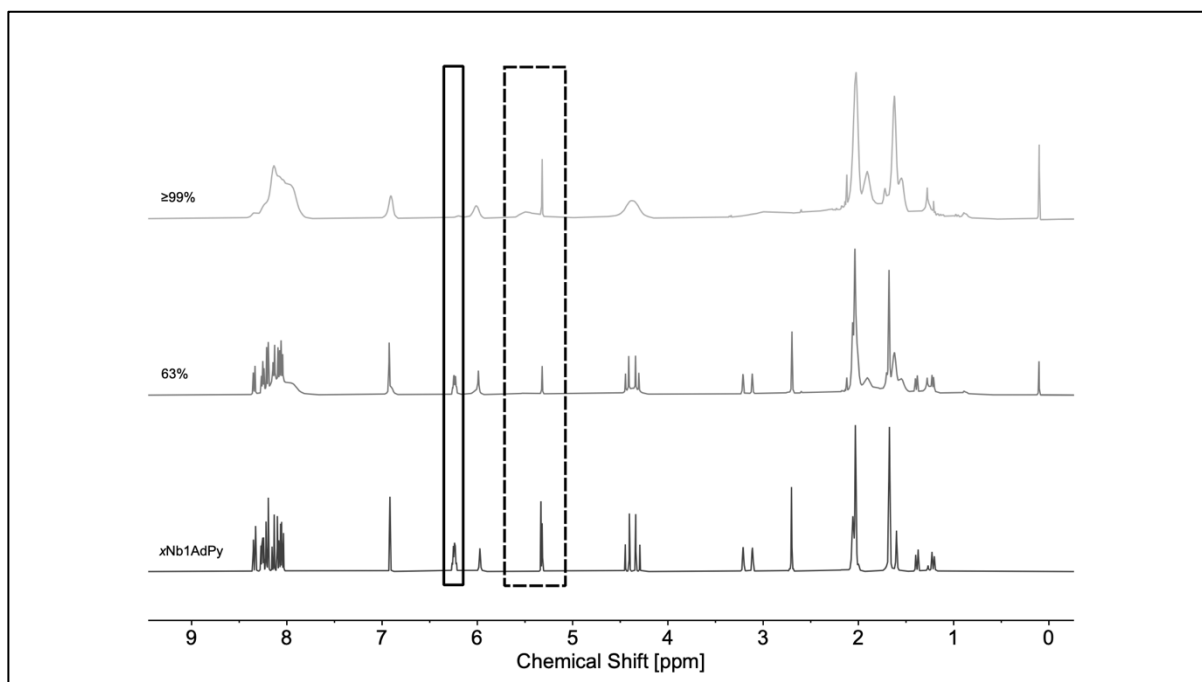


Figure S4.56. Representative stacked ¹H NMR spectra of the ROMP of **xNb1AdPy** (entry 4.2) in CD₂Cl₂ (500 MHz) and the ¹H NMR spectrum of the corresponding monomer in CD₂Cl₂ (400 MHz). Boxes: norbornene olefinic moiety (solid); poly(norbornene) olefinic backbone (dashed).

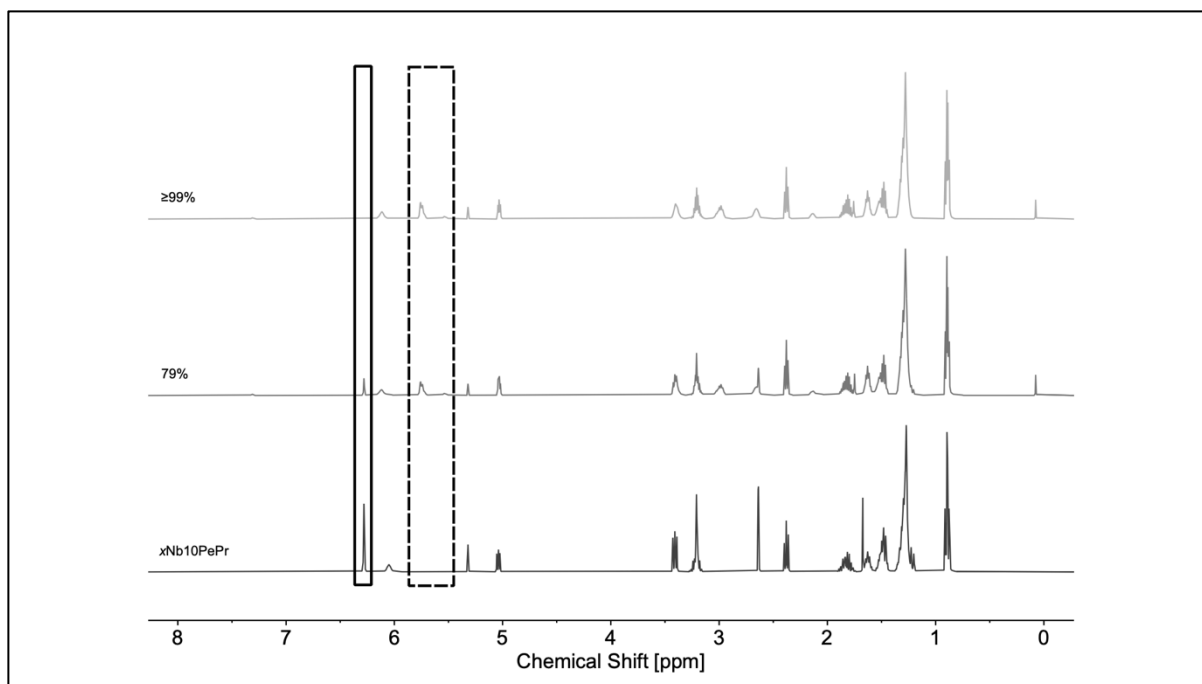


Figure S4.57. Representative stacked ¹H NMR spectra of the ROMP of **xNb10PePr** (entry 4.3) in CD₂Cl₂ (500 MHz) and the ¹H NMR spectrum of the corresponding monomer in CD₂Cl₂ (400 MHz). Boxes: norbornene olefinic moiety (solid); poly(norbornene) olefinic backbone (dashed).

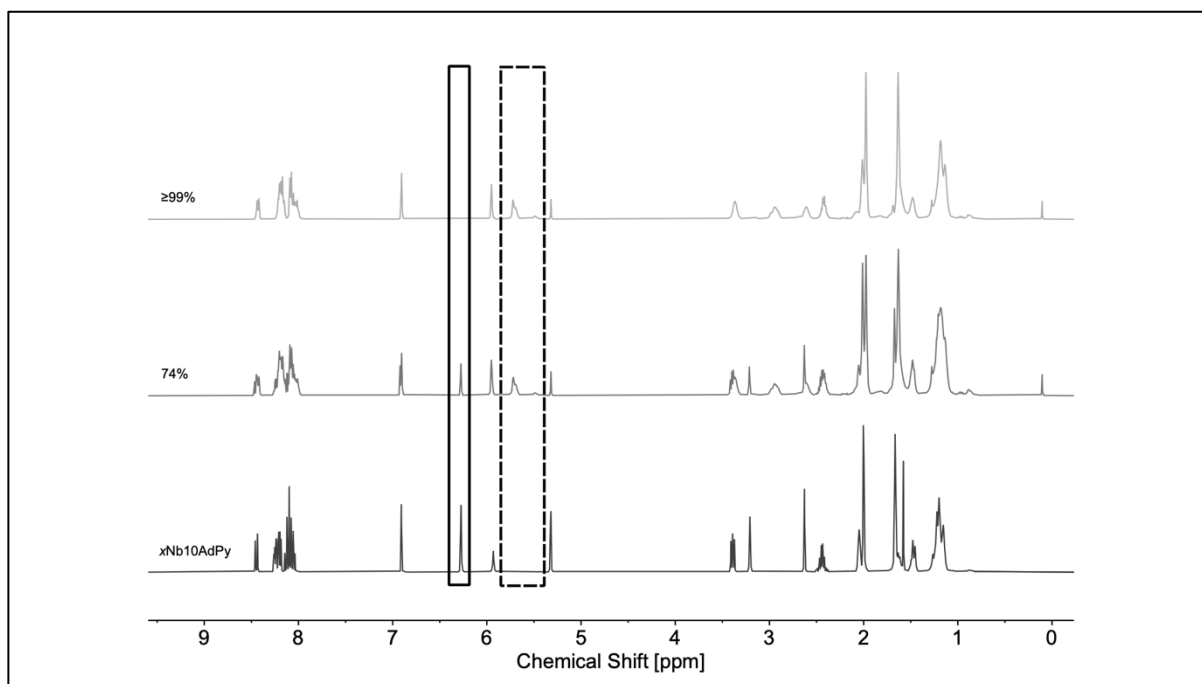


Figure S4.58. Representative stacked ¹H NMR spectra of the ROMP of **xNb10AdPy** (entry 4.4) in CD₂Cl₂ (500 MHz) and the ¹H NMR spectrum of the corresponding monomer in CD₂Cl₂ (400 MHz). Boxes: norbornene olefinic moiety (solid); poly(norbornene) olefinic backbone (dashed).

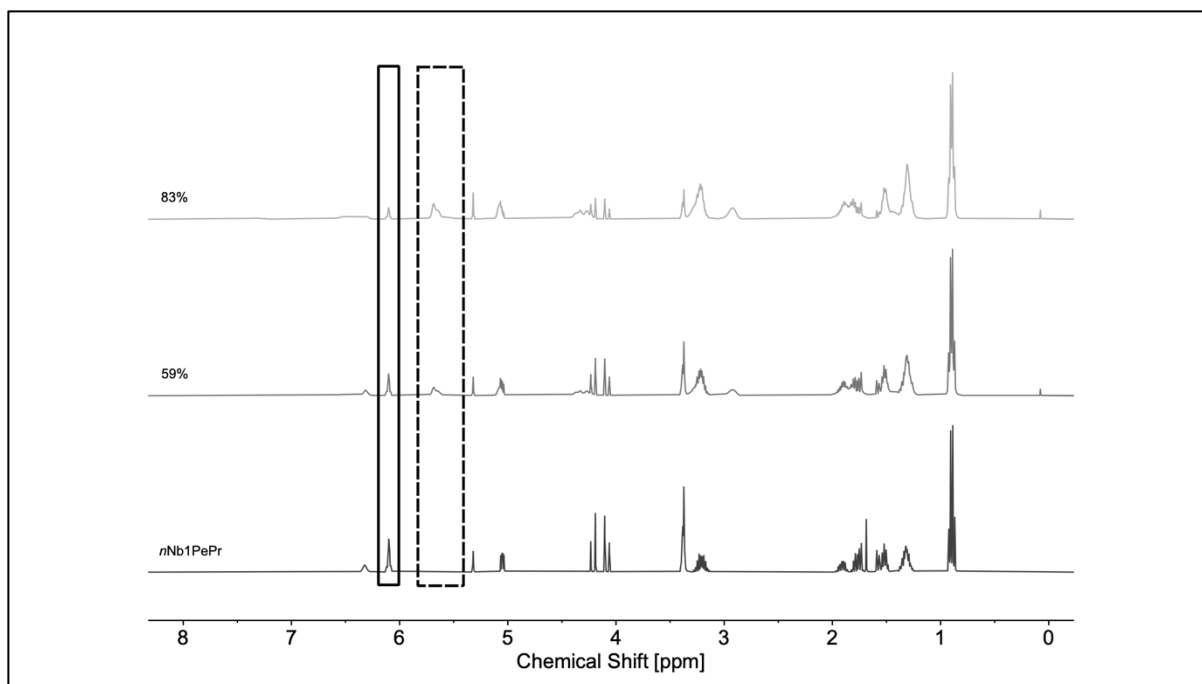


Figure S4.59. Representative stacked ¹H NMR spectra of the ROMP of *nNb1PePr* (entry 4.5) in CD₂Cl₂ (500 MHz) and the ¹H NMR spectrum of the corresponding monomer in CD₂Cl₂ (400 MHz). Boxes: norbornene olefinic moiety (solid); poly(norbornene) olefinic backbone (dashed).

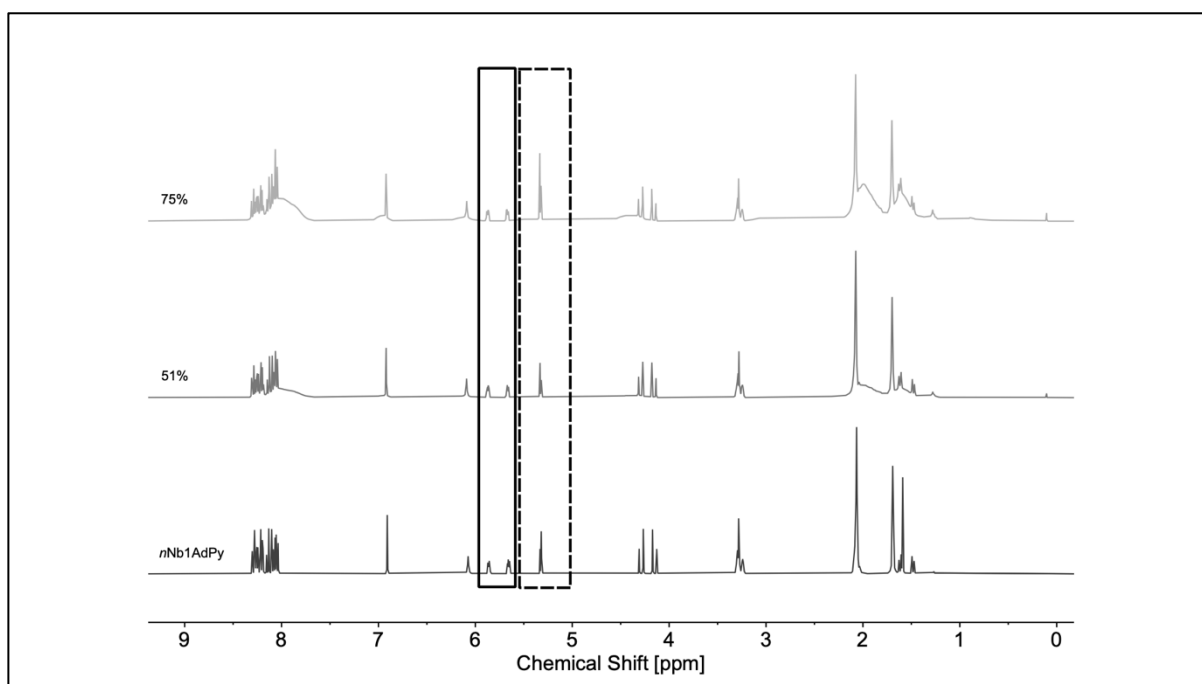


Figure S4.60. Representative stacked ¹H NMR spectra of the ROMP of *nNb1AdPy* (entry 4.6) in CD₂Cl₂ (500 MHz) and the ¹H NMR spectrum of the corresponding monomer in CD₂Cl₂ (400 MHz). Boxes: norbornene olefinic moiety (solid); poly(norbornene) olefinic backbone (dashed).

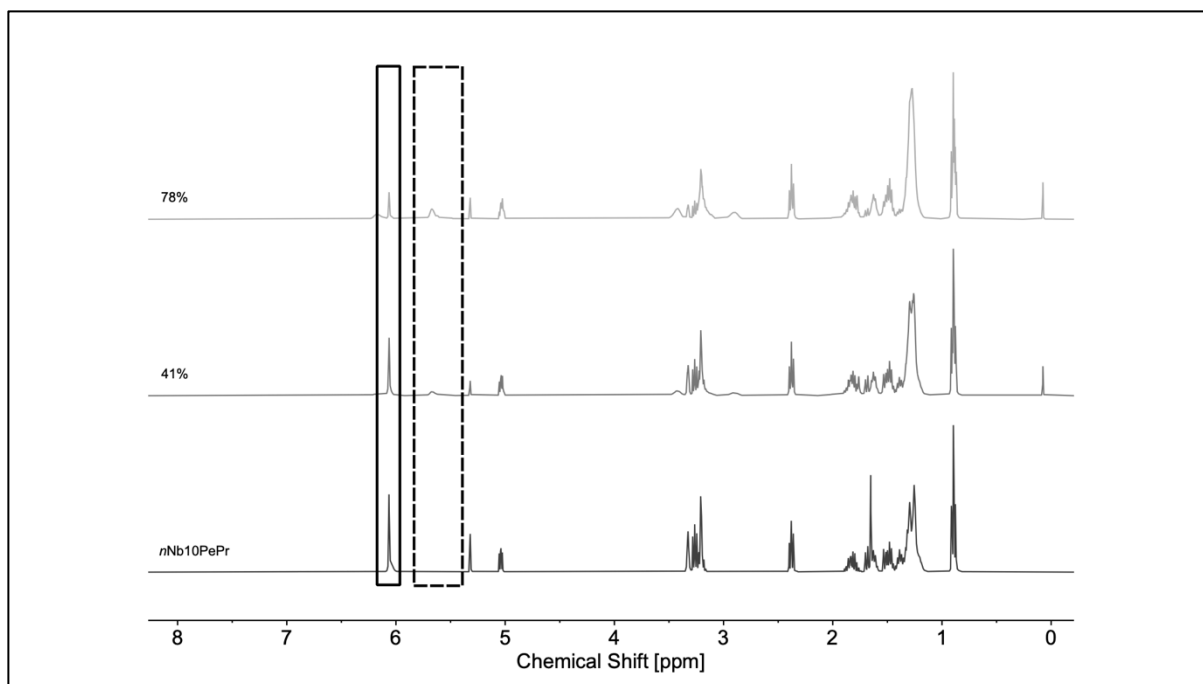


Figure S4.61. Representative stacked ^1H NMR spectra of the ROMP of *n*Nb10PePr (entry 4.7) in CD_2Cl_2 (500 MHz) and the ^1H NMR spectrum of the corresponding monomer in CD_2Cl_2 (400 MHz). Boxes: norbornene olefinic moiety (solid); poly(norbornene) olefinic backbone (dashed).

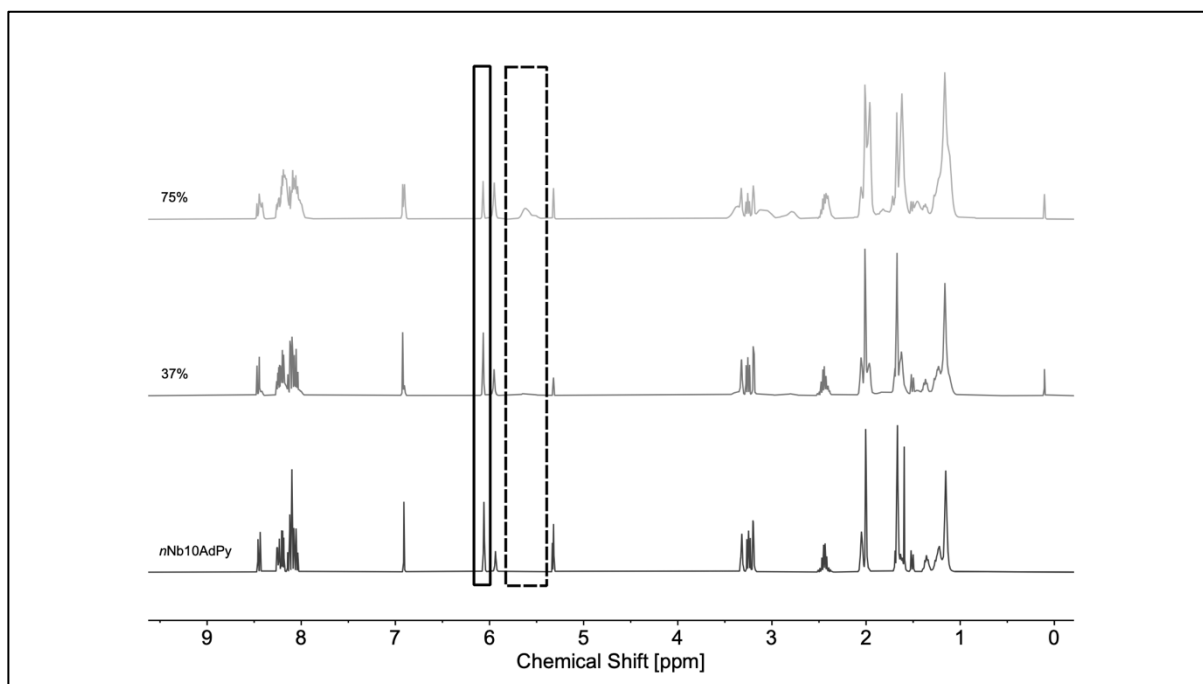


Figure S4.62. Representative stacked ^1H NMR spectra of the ROMP of *n*Nb10AdPy (entry 4.8) in CD_2Cl_2 (500 MHz) and the ^1H NMR spectrum of the corresponding monomer in CD_2Cl_2 (400 MHz). Boxes: norbornene olefinic moiety (solid); poly(norbornene) olefinic backbone (dashed).

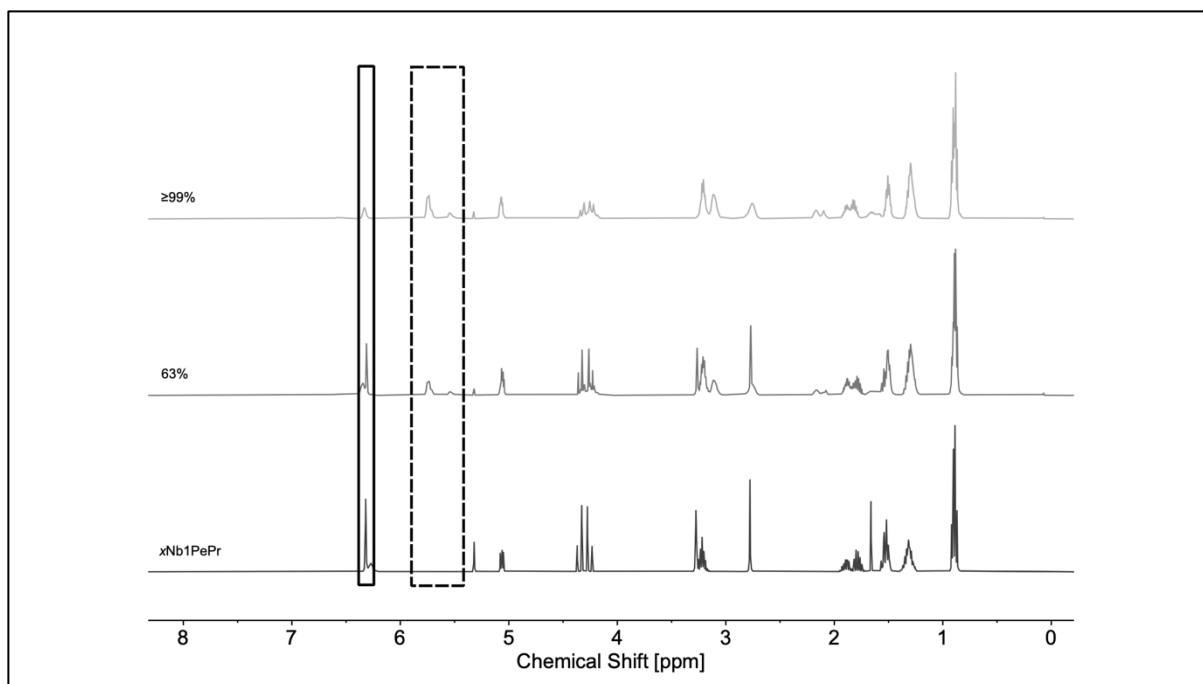


Figure S4.63. Representative stacked ¹H NMR spectra of the ROMP of **xNb1PePr** (entry 4.9) in CD₂Cl₂ (500 MHz) and the ¹H NMR spectrum of the corresponding monomer in CD₂Cl₂ (400 MHz). Boxes: norbornene olefinic moiety (solid); poly(norbornene) olefinic backbone (dashed).

General synthesis of copolymers – kinetic measurements (entries 4.10 – 4.13):

An NMR tube equipped with a J Young tap was evacuated and purged with argon three times. Subsequently, 25.0 eq. of the corresponding bifunctional monomers (0.1 mol/L) and 1.00 eq. G1 catalyst were each dissolved in degassed DCM-d₂ and transferred into the NMR tube, initiating the polymerization. The polymerization was carried out at ambient temperature under an argon atmosphere and was monitored by on-line ¹H NMR spectroscopy. The polymerization was quenched by adding excess of ethyl vinyl ether. Entries 4.11 – 4.13 were purified by removal of the cleaved catalyst *via* a DMT-functionalized silica plug and were additionally precipitated three times from the tenfold excess of cold ethyl acetate to remove unreacted monomer.

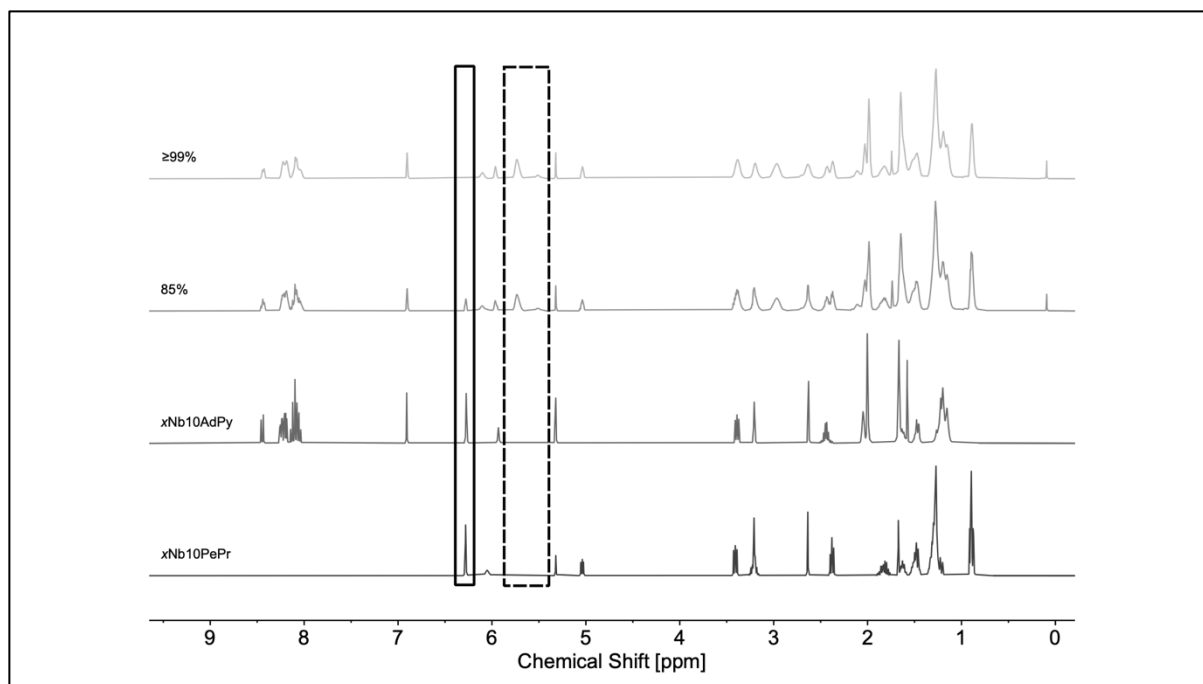


Figure S4.64. Representative stacked ^1H NMR spectra of the copolymerization of **xNb10PePr** and **xNb10AdPy** (entry 4.10) in CD_2Cl_2 (500 MHz) and the ^1H NMR spectra of the corresponding monomers in CD_2Cl_2 (400 MHz). Boxes: norbornene olefinic moieties (solid); poly(norbornene) olefinic backbone (dashed).

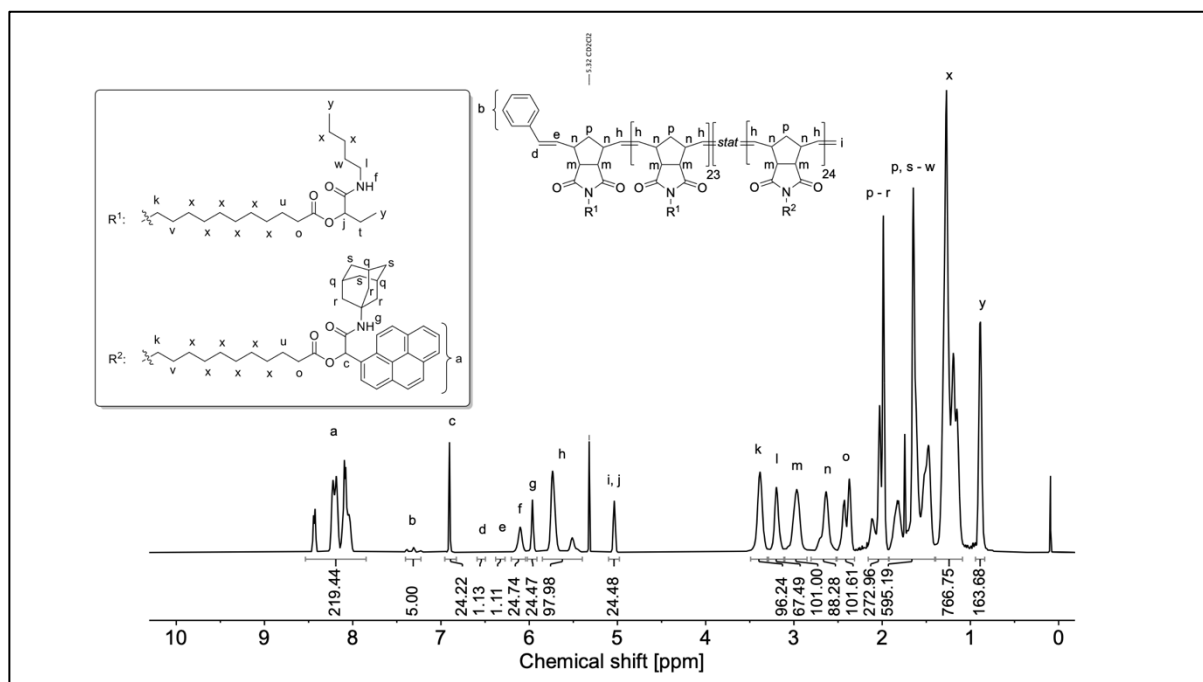


Figure S4.65. ^1H NMR spectrum of **poly(xNb10PePr-stat-xNb10AdPy)** (entry 4.10) in CD_2Cl_2 (500 MHz).

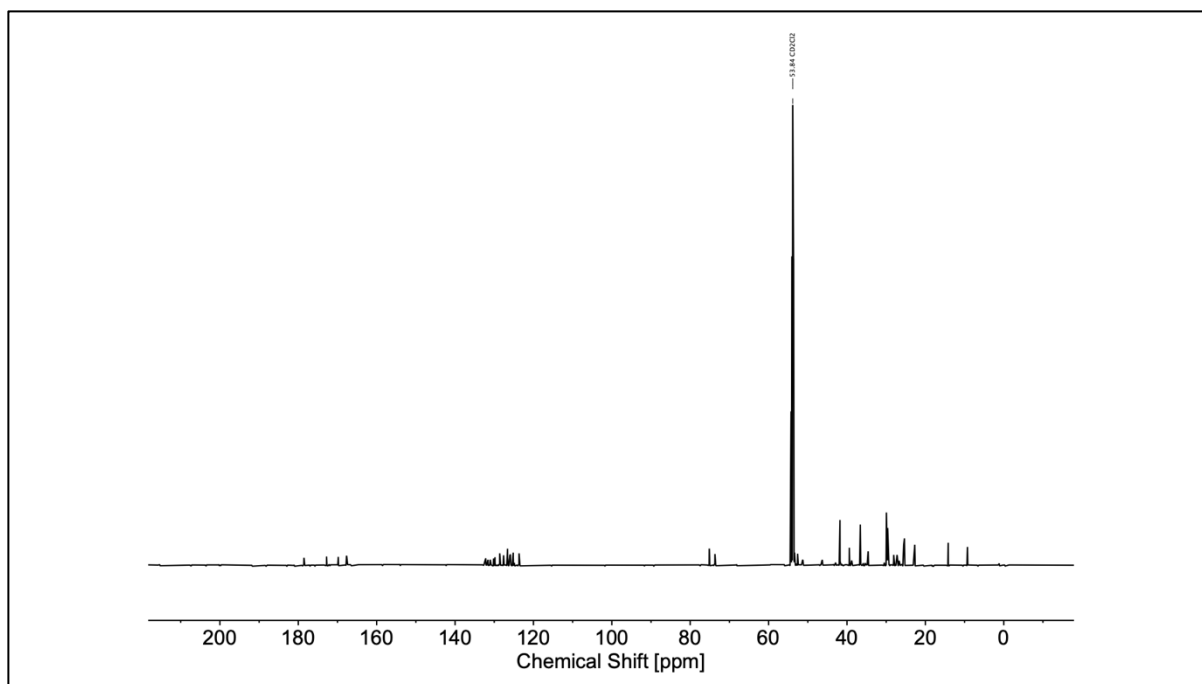


Figure S4.66. ^{13}C NMR spectrum of **poly(xNb10PePr-stat-xNb10AdPy)** (entry 4.10) in CD_2Cl_2 (126 MHz).

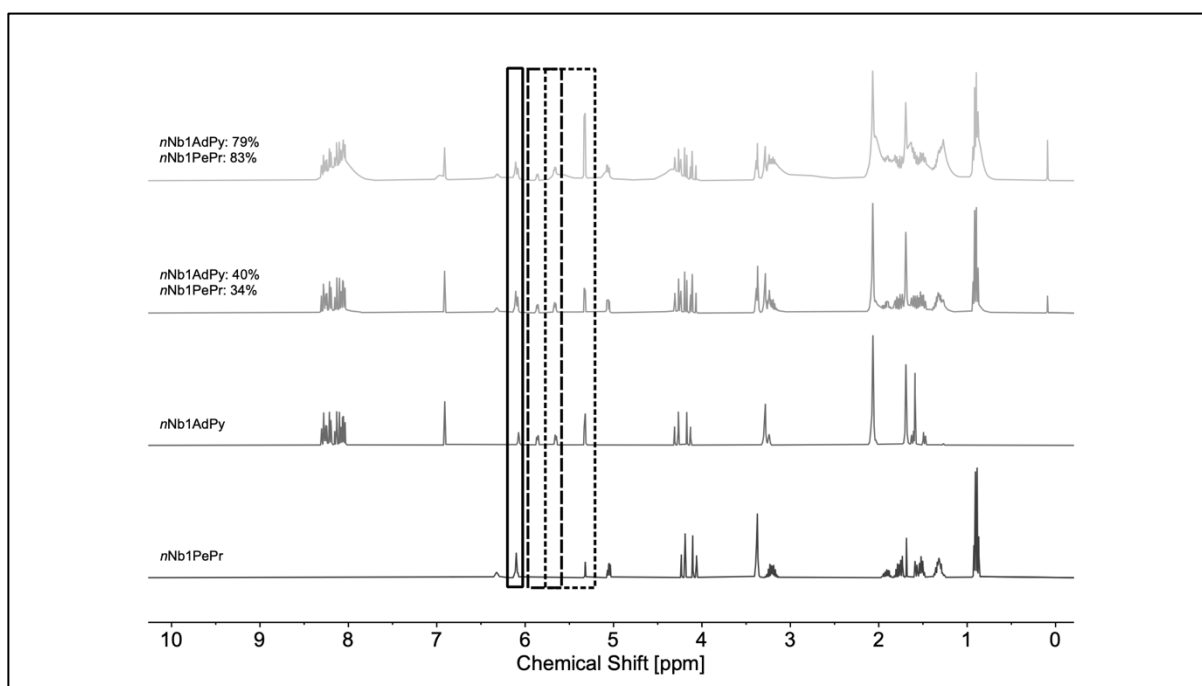


Figure S4.67. Representative stacked ^1H NMR spectra of the copolymerization of ***n*Nb1PePr** and ***n*Nb1AdPy** (entry 4.11) in CD_2Cl_2 (500 MHz) and the ^1H NMR spectra of the corresponding monomers in CD_2Cl_2 (400 MHz). Boxes: ***n*Nb1PePr** olefinic moiety (solid); ***n*Nb1AdPy** olefinic moiety (dashed); poly(norbornene) olefinic backbone (dotted).

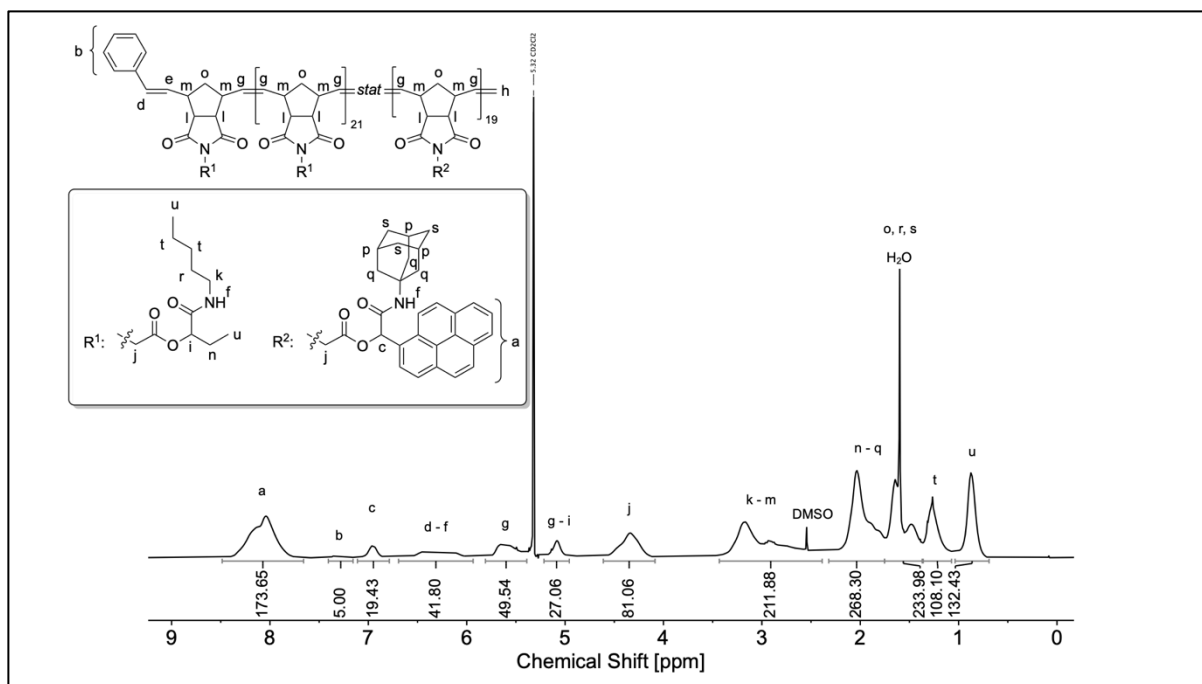


Figure S4.68. ¹H NMR spectrum of entry 4.11 in CD₂Cl₂ (500 MHz). Note: Deuterated solvent was contaminated with traces of DMSO.

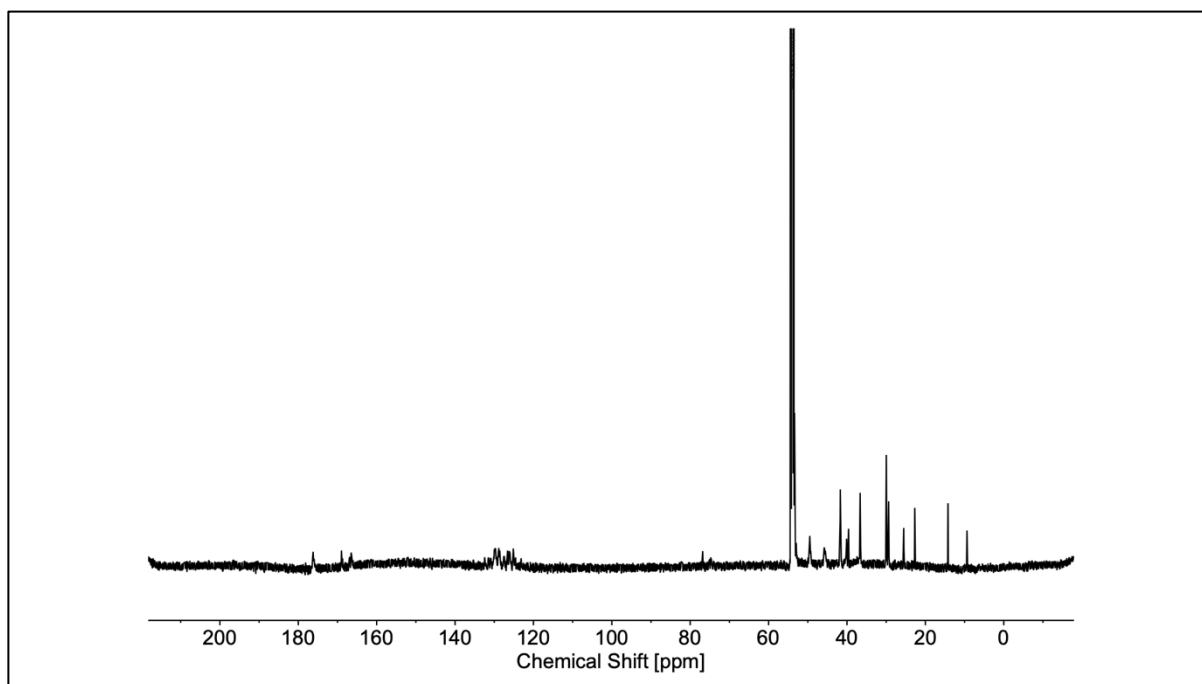


Figure S4.69. ¹³C NMR spectrum of entry 4.11 in CD₂Cl₂ (126 MHz).

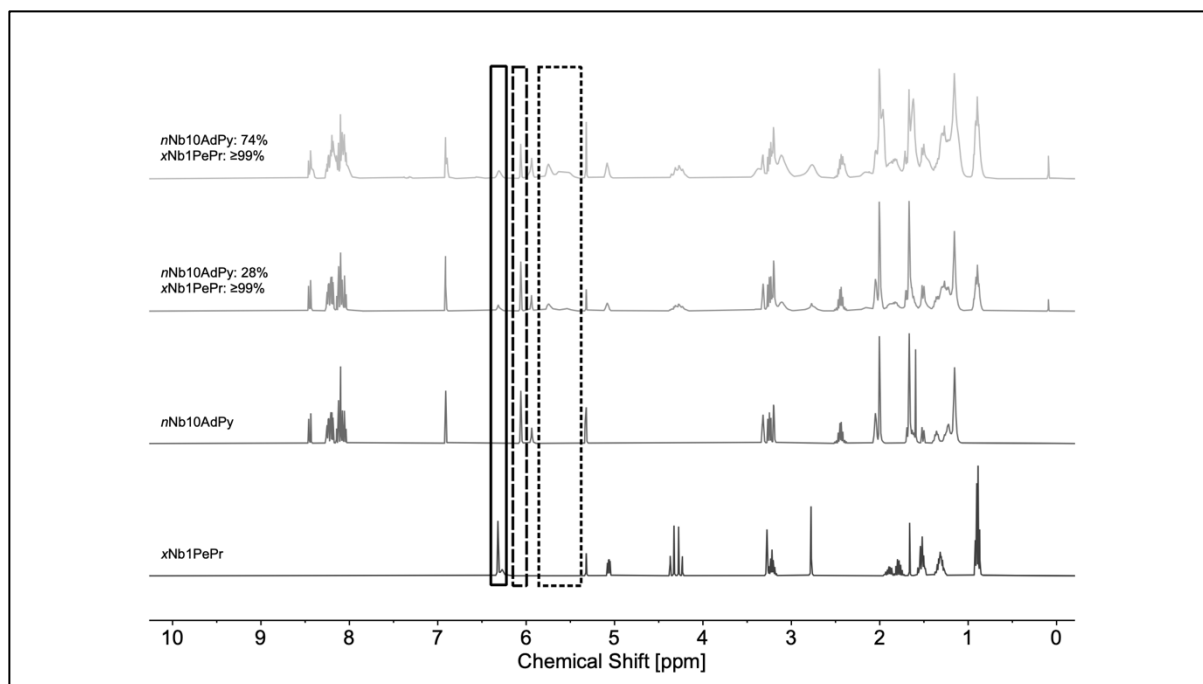


Figure S4.70. Representative stacked ^1H NMR spectra of the copolymerization of $x\text{Nb1PePr}$ and $n\text{Nb10AdPy}$ (entry 4.12) in CD_2Cl_2 (500 MHz) and the ^1H NMR spectra of the corresponding monomers in CD_2Cl_2 (400 MHz). Boxes: $x\text{Nb1PePr}$ olefinic moiety (solid); $n\text{Nb10AdPy}$ olefinic moiety (dashed); poly(norbornene) olefinic backbone (dotted).

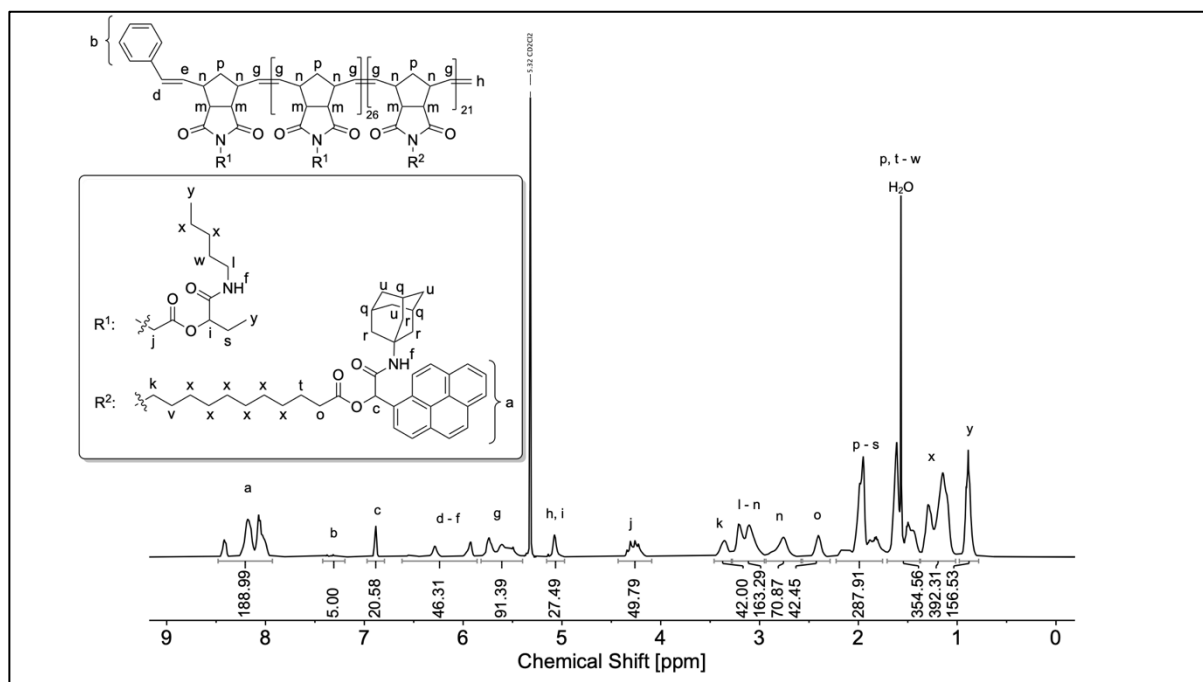


Figure S4.71. ^1H NMR spectrum of entry 4.12 in CD_2Cl_2 (500 MHz).

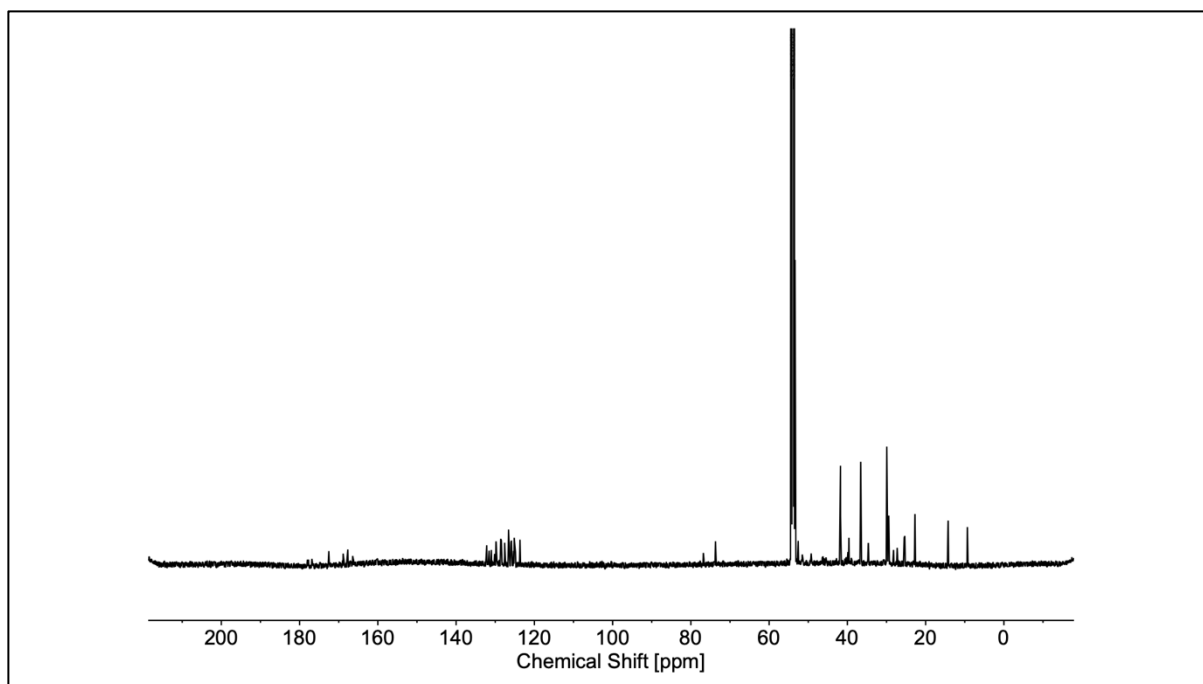


Figure S4.72. ^{13}C NMR spectrum of entry 4.12 in CD_2Cl_2 (126 MHz).

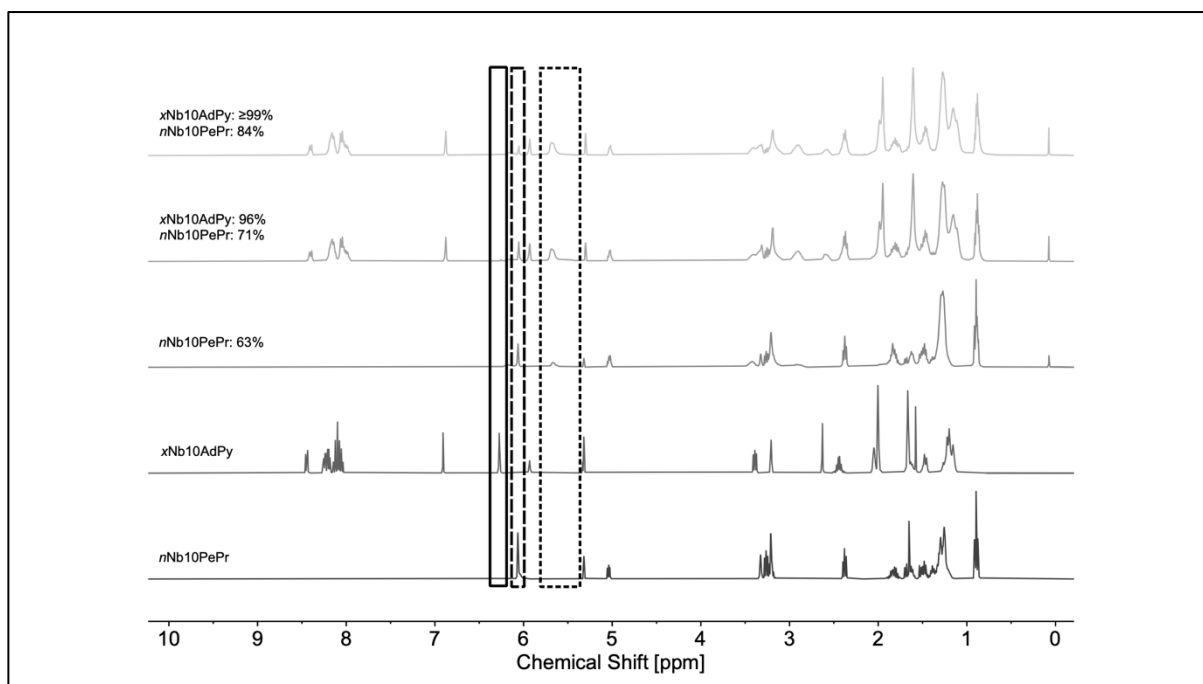


Figure S4.73. Representative stacked ^1H NMR spectra of the copolymerization of **xNb10AdPy** and **nNb10PePr** (entry 4.13) in CD_2Cl_2 (500 MHz) and the ^1H NMR spectra of the corresponding monomers in CD_2Cl_2 (400 MHz). Boxes: **xNb10AdPy** olefinic moiety (solid); **nNb10PePr** olefinic moiety (dashed); poly(norbornene) olefinic backbone (dotted).

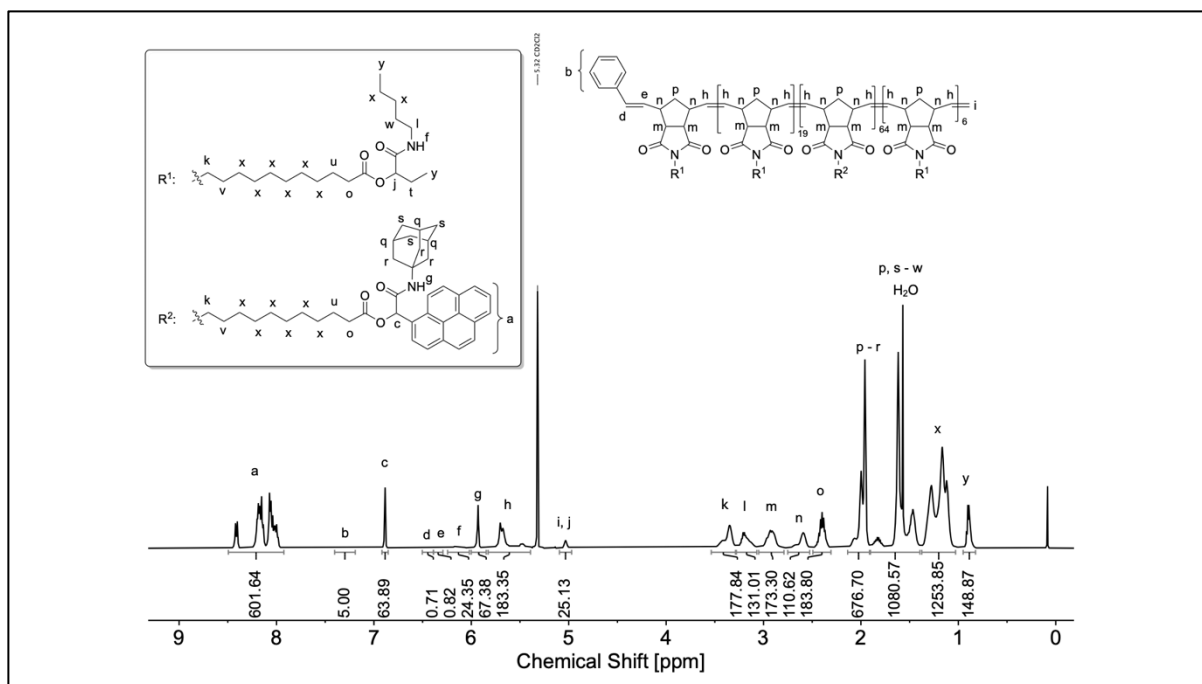


Figure S4.74. ^1H NMR spectrum of entry 4.13 in CD_2Cl_2 (500 MHz).

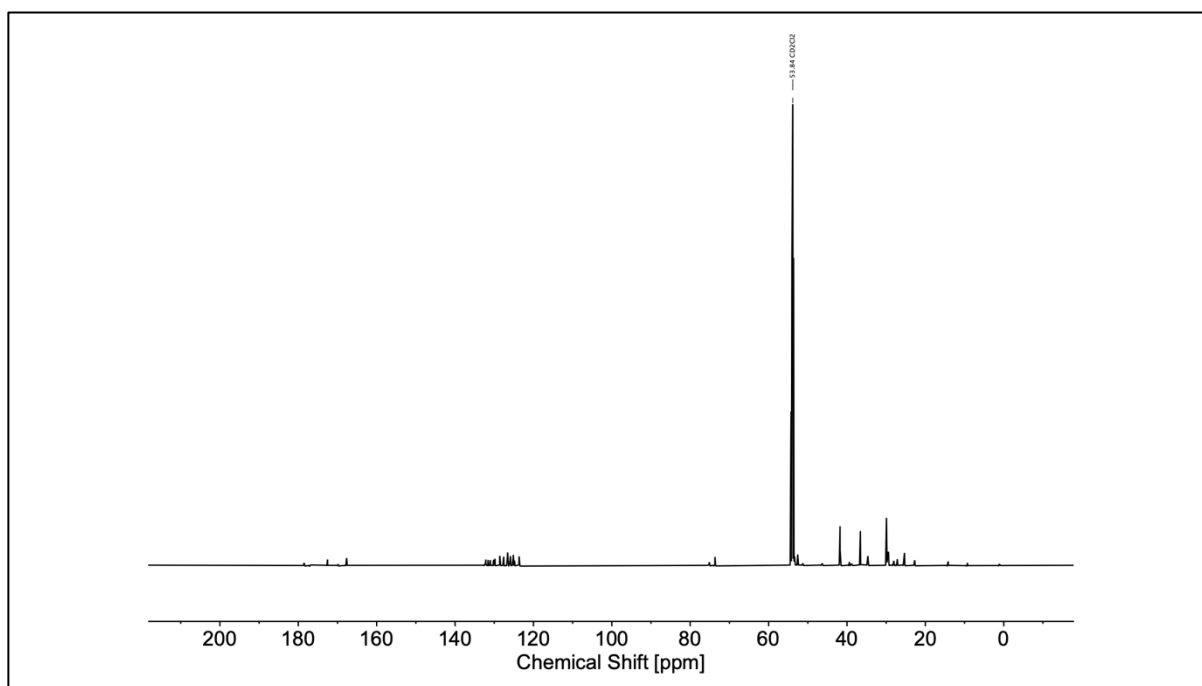


Figure S4.75. ^{13}C NMR spectrum of entry 4.13 in CD_2Cl_2 (126 MHz).

8.3.2 Materials synthesized in chapter 5

It is noted that the stacked ^1H NMR spectra (entries 5.1 – 5.39) represent the crude products after quenching with EVE without further purification. Hence, some spectra may contain signals of remaining EVE, solvent, silicone grease or not polymerized starting material.

Compounds that have been synthesized by M. Jäger and that have been already published (Bachelor thesis under my supervision) are further labelled with a “*” symbol.⁵⁰²

General synthesis of hydroxy-terminated norbornenes (xNb2OH and xNb6OH):

The synthesis procedure was adapted from recent literature.⁴⁷⁴ 1.00 eq. *cis*-5-norbornene-*exo*-2,3-dicarboxylic anhydride (0.21 mol/L), 1.50 eq. of the corresponding amino alcohol and 0.20 eq. triethylamine were dissolved in toluene. The condensation was performed at 130 °C for 16 hours using a Dean-Stark apparatus to remove forming water. Then, the solvent was removed under reduced pressure. The crude product was dissolved in DCM and washed with aqueous hydrochloric acid (0.1 mol/L) twice and then with brine. The organic phase was dried over magnesium sulfate and the solvent was removed under reduced pressure. The products were obtained as a white solid (xNb2OH) in a yield of 85% and as a colorless liquid (xNb6OH) in yield of 98%.

xNb2OH:

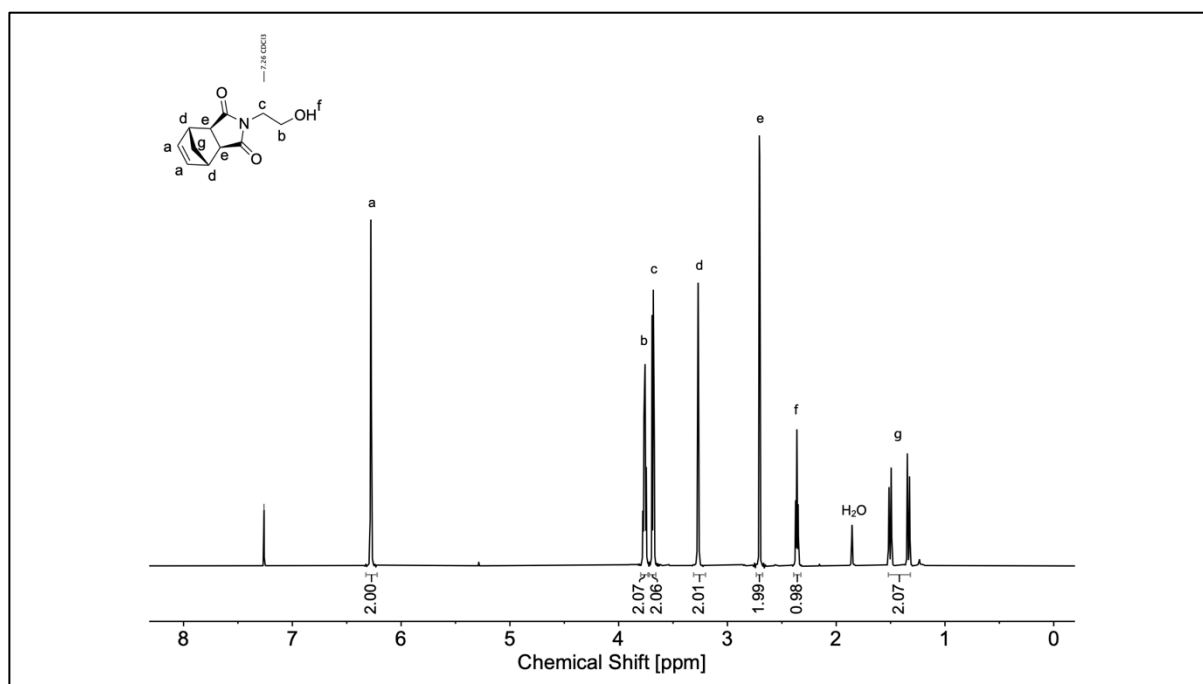


Figure S5.1. ^1H NMR spectrum of xNb2OH.

^1H NMR: (500 MHz, CDCl_3 , δ): 6.28 (t, $J = 2.0$ Hz, 2H; $\text{CH}=\text{CH}$, ^a), 3.78 - 3.73 (m, 2H; $\text{CH}_2\text{-OH}$, ^b), 3.70 - 3.66 (m, 2H; N-CH_2 , ^c), 3.29 - 3.25 (m, 2H; $=\text{CH-CH}$, ^d), 2.71 (d, $J = 1.4$ Hz, 2H; $=\text{CH-CH-CH}$, ^e), 2.36 (t, $J = 5.8$ Hz, 1H; OH , ^f), 1.54 - 1.31 (m, 2H; CH_2 bridge, ^g).

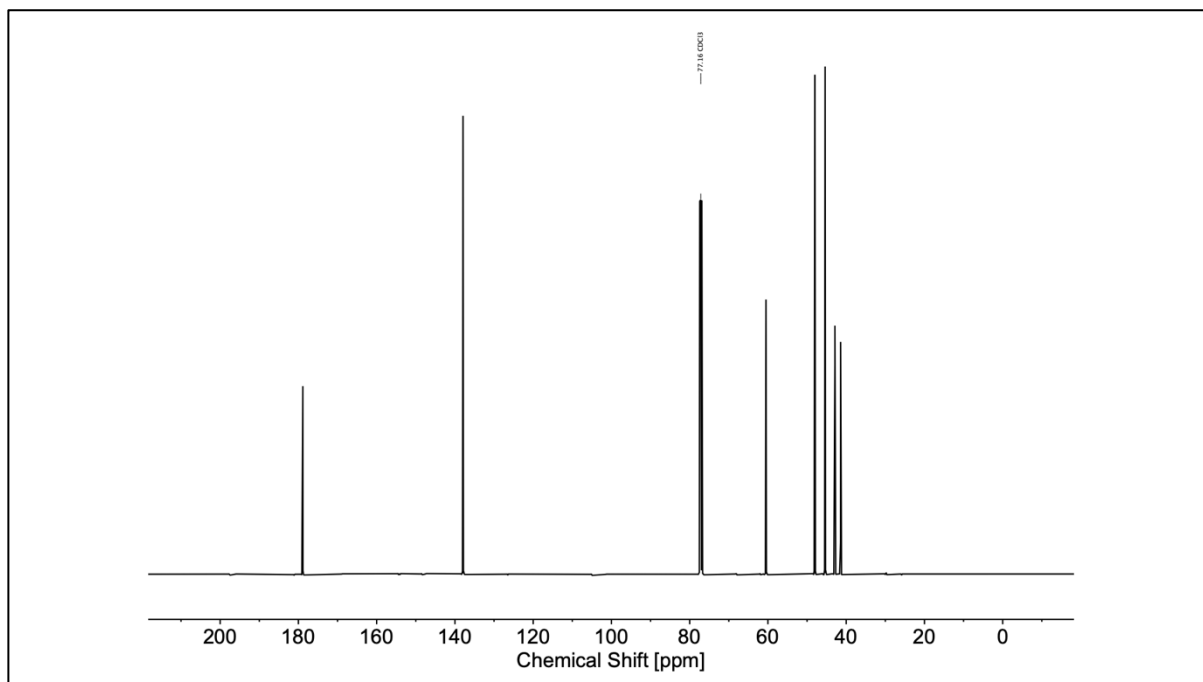


Figure S5.2. ^{13}C NMR spectrum of $x\text{Nb}_2\text{OH}$.

^{13}C NMR: (126 MHz, CDCl_3 , δ): 178.87, 137.94, 60.50, 48.01, 45.39, 42.90, 41.43.

IR (ATR platinum diamond): $\nu / \text{cm}^{-1} = 3509$ (w), 3067 (vw), 2989 (w), 2964 (w), 2948 (w), 2886 (w), 1755 (w), 1678 (vs), 1425 (m), 1401 (s), 1349 (m), 1325 (s), 1298 (w), 1286 (w), 1238 (w), 1168 (s), 1148 (m), 1076 (w), 1063 (s), 989 (s), 934 (w), 903 (w), 880 (w), 854 (s), 771 (s), 732 (s), 646 (s), 603 (w), 514 (w), 483 (w), 479 (w), 471 (w), 455 (w), 428 (w).

HRMS (ESI-MS) m/z : $[\text{M}+\text{H}]^+$ calc. for $\text{C}_{11}\text{H}_{14}\text{NO}_3$, 208.0968, found: 208.0968.

xNb6OH (synthesized by P. Conen under my supervision):

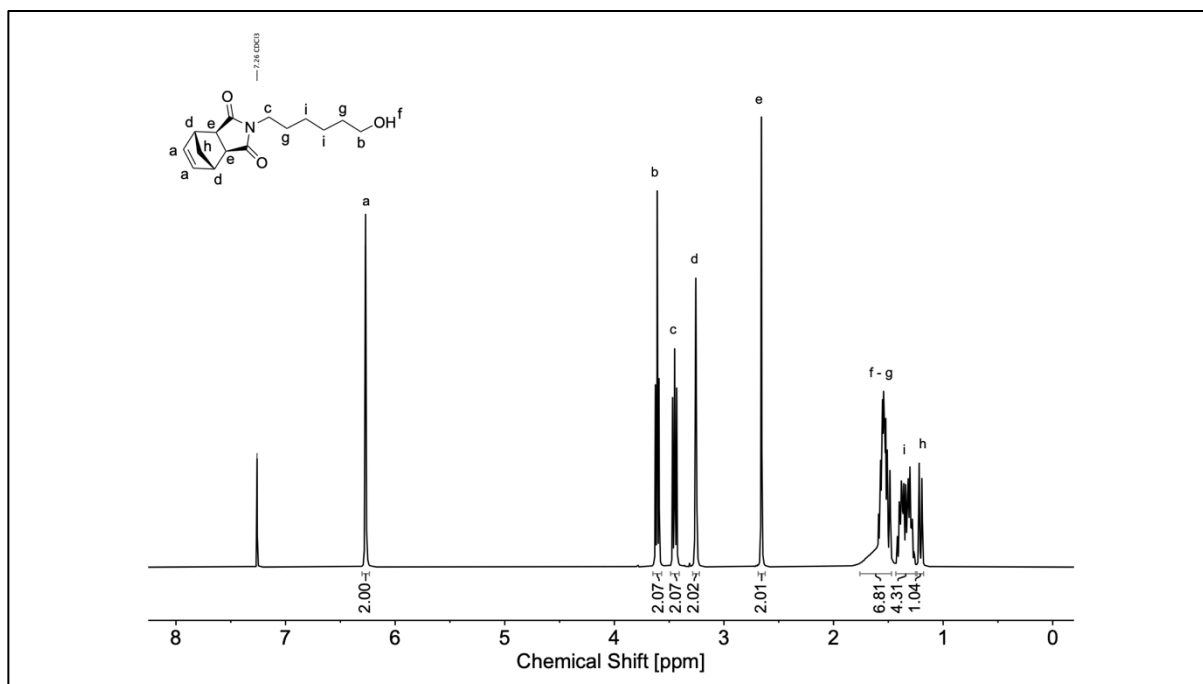


Figure S5.3. ^1H NMR spectrum of **xNb6OH**.

^1H NMR: (400 MHz, CDCl_3 , δ): 6.27 (t, $J = 2.0$ Hz, 2H; $\text{CH}=\text{CH}$, ^a), 3.61 (t, $J = 6.6$ Hz, 2H; $\text{CH}_2\text{-OH}$, ^b), 3.48 - 3.41 (m, 2H; N-CH_2 , ^c), 3.28 - 3.24 (m, 2H; $=\text{CH-CH}$, ^d), 2.66 (d, $J = 1.9$ Hz, 2H; $=\text{CH-CH-CH}$, ^e), 1.75 - 1.55 (bs, 1H; OH, ^f), 1.60 - 1.50 (m, 4H; CH_2 , ^g), 1.53 - 1.17 (m, 2H; CH_2 bridge, ^h), 1.43 - 1.25 (m, 4H; CH_2 , ⁱ).

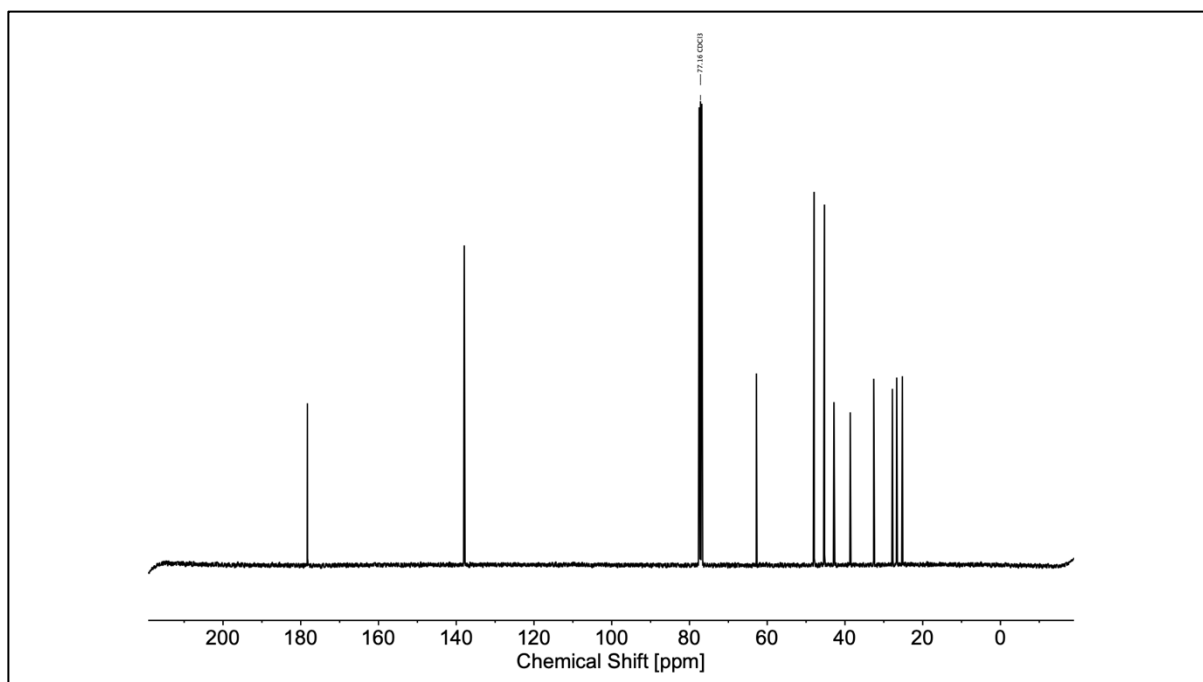


Figure S5.4. ^{13}C NMR spectrum of **xNb6OH**.

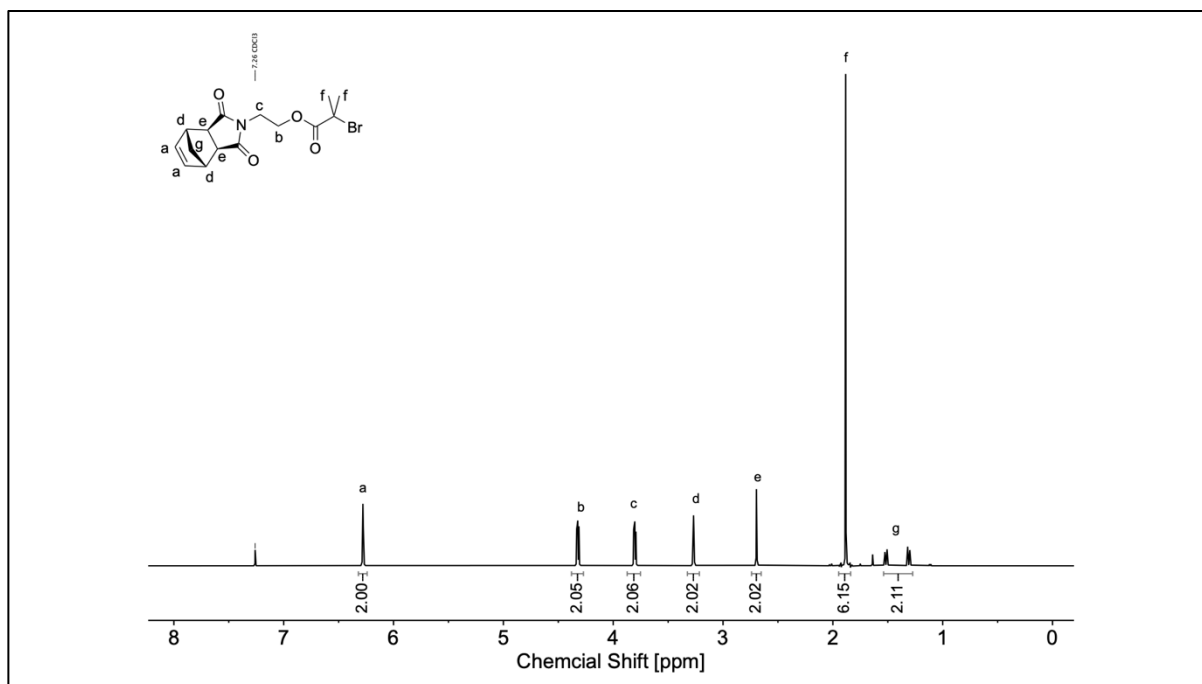
^{13}C NMR: (100 MHz, CDCl_3 , δ): 178.30, 137.94, 62.77, 47.92, 45.27, 42.83, 38.63, 32.59, 27.80, 26.68, 25.23.

IR (ATR platinum diamond): ν / cm^{-1} = 3443 (vw), 2983 (vw), 2935 (w), 2861 (w), 1767 (w), 1683 (vs), 1460 (w), 1436 (w), 1397 (s), 1368 (m), 1343 (m), 1327 (w), 1286 (w), 1269 (w), 1257 (w), 1214 (w), 1195 (w), 1148 (m), 1100 (w), 1072 (w), 1053 (w), 1035 (w), 1018 (w), 1002 (w), 981 (w), 946 (vw), 928 (vw), 887 (w), 858 (w), 812 (w), 780 (m), 720 (m), 691 (w), 662 (w), 642 (s), 617 (w), 584 (w), 553 (w), 520 (w), 504 (w), 477 (w), 465 (w), 455 (w), 428 (w), 407 (w), 401 (w).

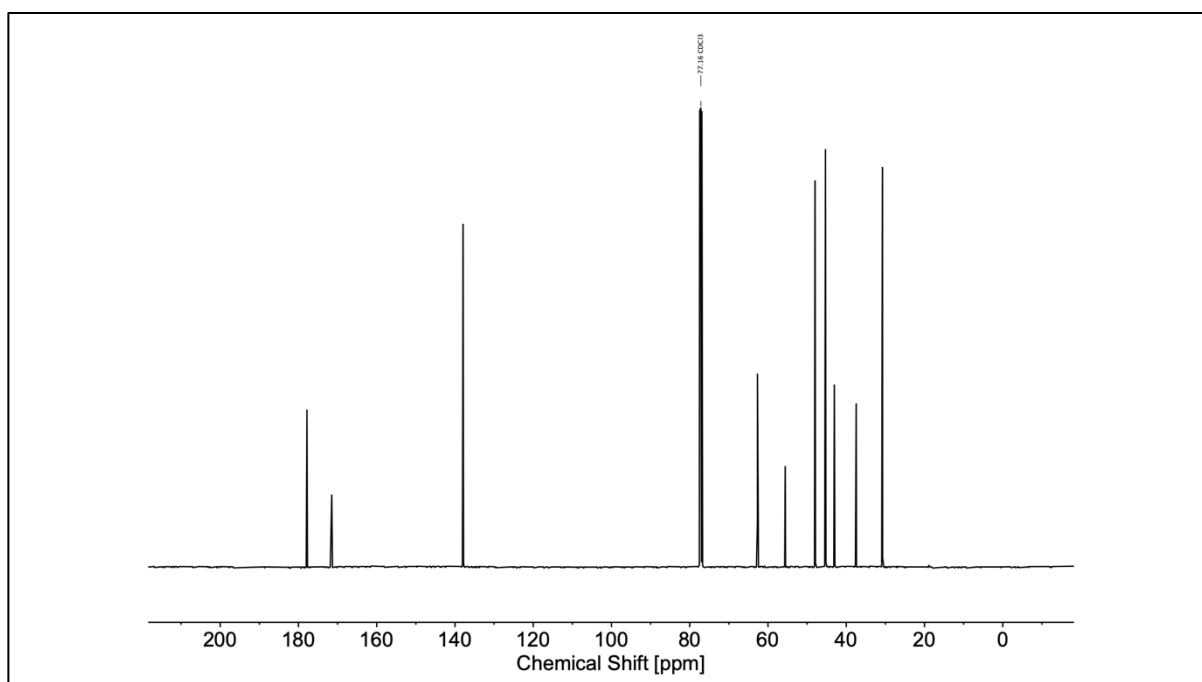
HRMS (ESI-MS) m/z : $[\text{M}+\text{H}]^+$ calc. for $\text{C}_{15}\text{H}_{22}\text{NO}_3$, 264.1594, found: 264.1589.

General synthesis of norbornene-based ATRP initiators (xNb2Br and xNb6Br):

The synthesis procedure was adapted from recent literature.⁴⁷⁴ 1.00 eq. of the corresponding hydroxy-terminated norbornene (0.15 mol/L), 0.40 eq. DMAP and 1.50 eq. triethylamine were dissolved in THF. Subsequently, 1.50 eq. α -bromoisobutyryl bromide were dissolved in THF (0.16 mol/L) and added dropwise to the reaction mixture at 0°C . Afterwards, the mixture was stirred for 16 hours at ambient temperature and the solvent was removed under reduced pressure. The crude product was dissolved in DCM, washed with saturated aqueous NaHCO_3 solution and brine. The organic phase was dried over magnesium sulfate and the solvent was removed under reduced pressure. The crude product was then purified *via* column chromatography using a cyclohexane/ethyl acetate mixture as solvent. The products were obtained as a white solid (xNb2Br) in a yield of 96% and as a colorless liquid (xNb6Br) in a yield of 88%.

xNb2Br:**Figure S5.5.** ^1H NMR spectrum of **xNb2Br**.

^1H NMR: (500 MHz, CDCl_3 , δ): 6.28 (t, $J = 1.9$ Hz, 2H; $\text{CH}=\text{CH}$, ^a), 4.36 - 4.29 (m, 2H; $\text{N}-\text{CH}_2-\text{CH}_2$, ^b), 3.83 - 3.77 (m, 2H; $\text{N}-\text{CH}_2$, ^c), 3.29 - 3.23 (m, 2H; $=\text{CH}-\text{CH}$, ^d), 2.69 (d, $J = 1.4$ Hz, 2H; $=\text{CH}-\text{CH}-\text{CH}$, ^e), 1.88 (s, 6H; CH_3 , ^f), 1.54 - 1.28 (m, 2H; CH_2 bridge, ^g).

**Figure S5.6.** ^{13}C NMR spectrum of **xNb2Br**.

^{13}C NMR: (126 MHz, CDCl_3 , δ): 177.83, 171.49, 137.94, 62.70, 55.59, 47.98, 45.32, 43.03, 37.46, 30.73.

IR (ATR platinum diamond): ν / cm^{-1} = 3003 (w), 2964 (vw), 2886 (vw), 1765 (w), 1734 (s), 1693 (vs), 1467 (w), 1448 (w), 1432 (w), 1417 (w), 1393 (s), 1374 (w), 1360 (w), 1327 (m), 1281 (m), 1267 (m), 1193 (w), 1156 (vs), 1121 (m), 1100 (s), 1010 (w), 985 (m), 950 (w), 942 (w), 928 (w), 903 (w), 880 (w), 850 (w), 825 (w), 775 (s), 759 (w), 732 (w), 720 (m), 691 (w), 654 (s), 648 (s), 599 (w), 475 (w), 426 (w).

HRMS (ESI-MS) m/z : $[\text{M}+\text{H}]^+$ calc. for $\text{C}_{15}\text{H}_{19}\text{BrNO}_4$, 356.0492, found: 356.0486.

xNb6Br (synthesized by P. Conen under my supervision):

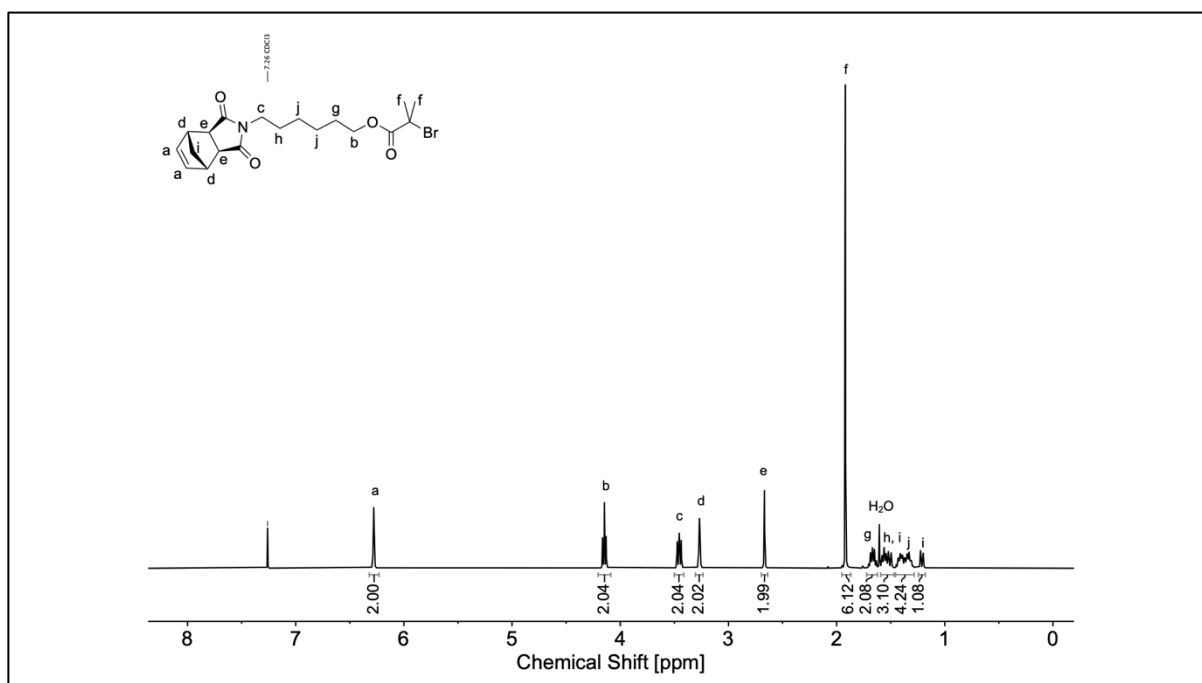


Figure S5.7. ^1H NMR spectrum of **xNb6Br**.

^1H NMR: (400 MHz, CDCl_3 , δ): 6.28 (t, J = 1.9 Hz, 2H; $\text{CH}=\text{CH}$, ^a), 4.15 (t, J = 6.5 Hz, 2H; $\text{CH}_2\text{-O}$, ^b), 4.36 - 4.29 (m, 2H; $\text{N-CH}_2\text{-CH}_2$, ^b), 3.49 - 3.41 (m, 2H; N-CH_2 , ^c), 3.29 - 3.24 (m, 2H; $=\text{CH-CH}$, ^d), 2.67 (d, J = 1.3 Hz, 2H; $=\text{CH-CH-CH}$, ^e), 1.92 (s, 6H; CH_3 , ^f), 1.72 - 1.62 (m, 2H; $\text{CH}_2\text{-CH}_2\text{-O}$, ^g), 1.59 - 1.46 (m, 2H; $\text{N-CH}_2\text{-CH}_2$, ^h), 1.55 - 1.17 (m, 2H; CH_2 bridge, ⁱ), 1.45 - 1.28 (m, 4H; CH_2 , ^j).

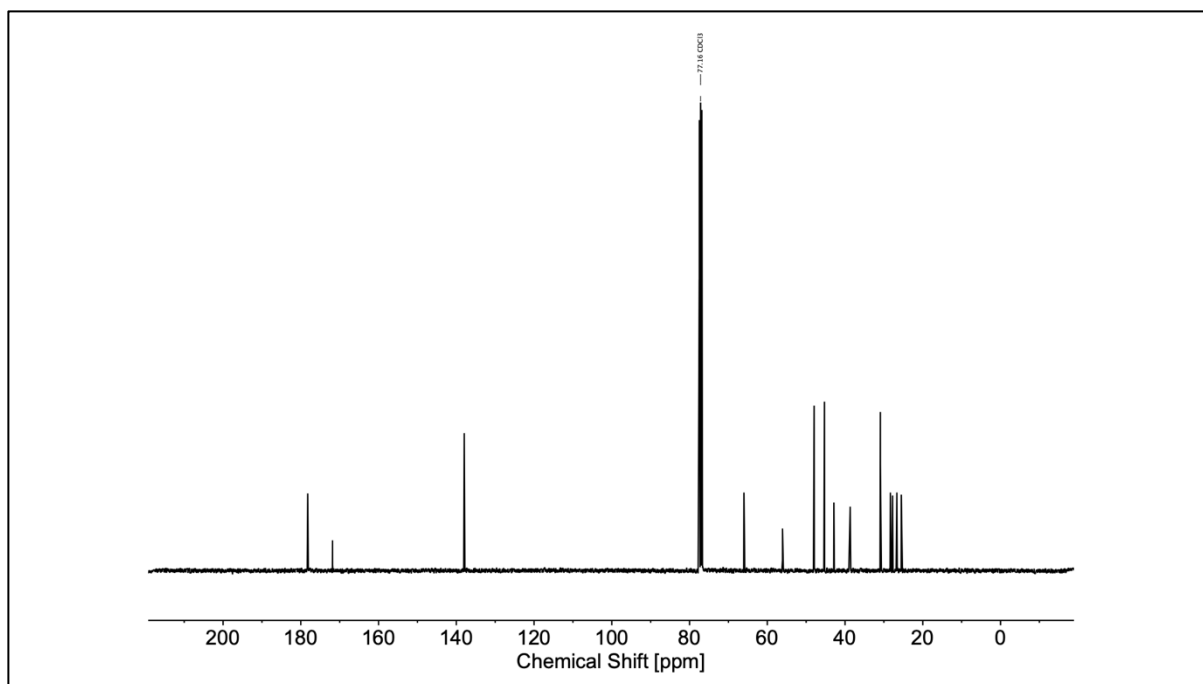


Figure S5.8. ^{13}C NMR spectrum of **xNb6Br**.

^{13}C NMR: (100 MHz, CDCl_3 , δ): 178.23, 171.84, 137.96, 66.00, 56.09, 47.94, 45.29, 42.87, 38.67, 30.91, 28.33, 27.76, 26.67, 25.52.

IR (ATR platinum diamond): $\nu / \text{cm}^{-1} = 2974$ (vw), 2939 (w), 2861 (vw), 1769 (w), 1732 (m), 1693 (vs), 1462 (w), 1436 (w), 1395 (m), 1370 (m), 1345 (w), 1327 (w), 1275 (m), 1238 (w), 1216 (w), 1199 (w), 1160 (vs), 1107 (m), 1014 (w), 975 (w), 946 (vw), 928 (vw), 887 (w), 856 (vw), 835 (vw), 812 (w), 780 (w), 763 (w), 720 (w), 662 (w), 642 (m), 615 (w), 601 (vw), 522 (vw), 475 (w), 455 (vw), 428 (w), 405 (w).

HRMS (ESI-MS) m/z : $[\text{M}+\text{H}]^+$ calc. for $\text{C}_{19}\text{H}_{27}\text{BrNO}_4$, 412.1118, found: 412.1110.

General ATRP procedure using methacrylate monomers (xNb2M12, xNb2M27, xNb6M13, xNb6M17, and xNb2B12):

Two ampoules equipped with J Young taps were evacuated and purged with argon three times. Ampoule 1, equipped with a stirring bar, was charged with 1.00 eq. copper(I) chloride (0.075 mol/L) and 2.00 eq. dNbpy dissolved in toluene. Ampoule 2 was charged with 1.00 eq. of the corresponding norbornene functional ATRP initiator (0.17 mol/L) and 12.0 eq. methacrylate monomer dissolved in toluene. The mixtures were degassed by three consecutive freeze pump thaw cycles under high vacuum. Subsequently, the solution of ampoule 2 was transferred to ampoule 1 by *via* degassed syringe, initiating the polymerization. The polymerization was carried out at 90 °C for 2.5 hours under an argon

atmosphere. After complete monomer conversion, the polymerization was cooled quickly to ambient temperature by immersing the ampoule into liquid nitrogen, exposing to air, and quenching by the addition of THF. The solution was then flushed through a plug of neutral aluminum oxide to remove the copper. Subsequently, the solvent was removed under reduced pressure. The crude product was dissolved in a small amount of THF and precipitated three times from the tenfold amount of cold *n*-hexane. The polymers were filtered, dried under high vacuum, and obtained as white solids.

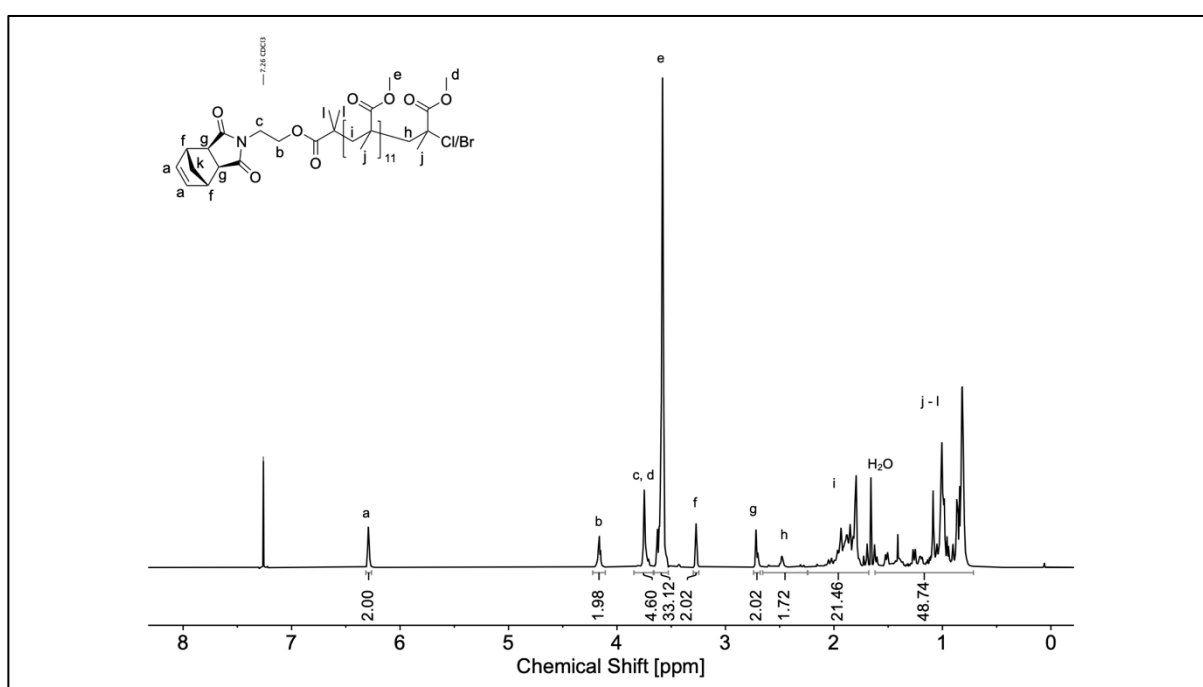
xNb2M12:

Figure S5.9. ¹H NMR spectrum of xNb2M12 in CDCl₃ (500 MHz).

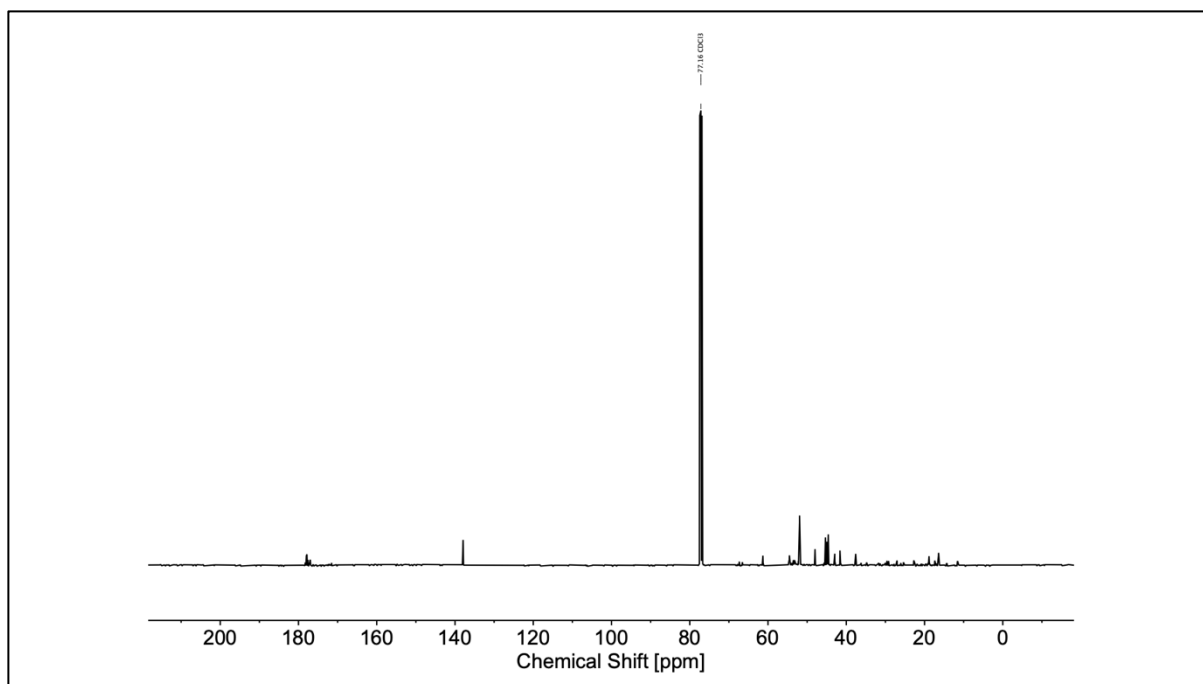


Figure S5.10. ^{13}C NMR spectrum of **xNb2M12** in CDCl_3 (126 MHz).

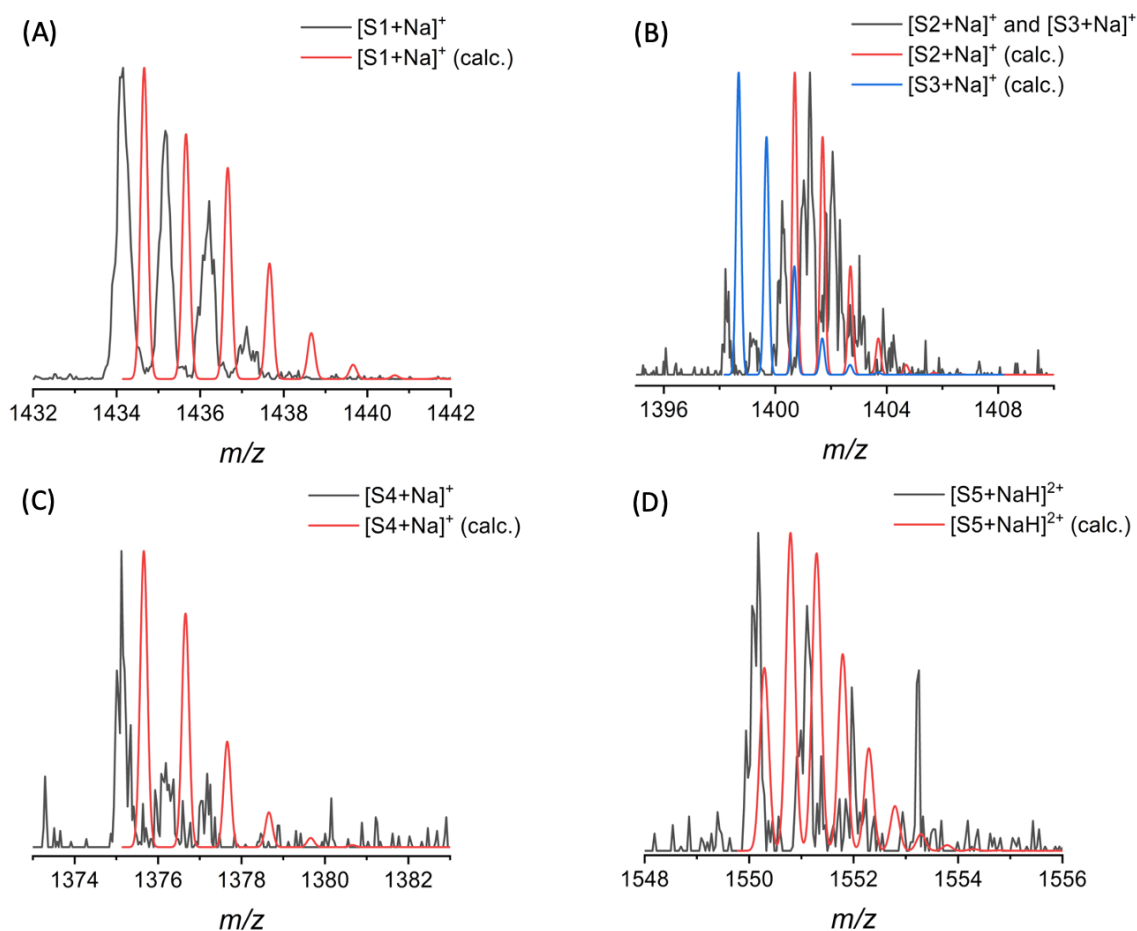
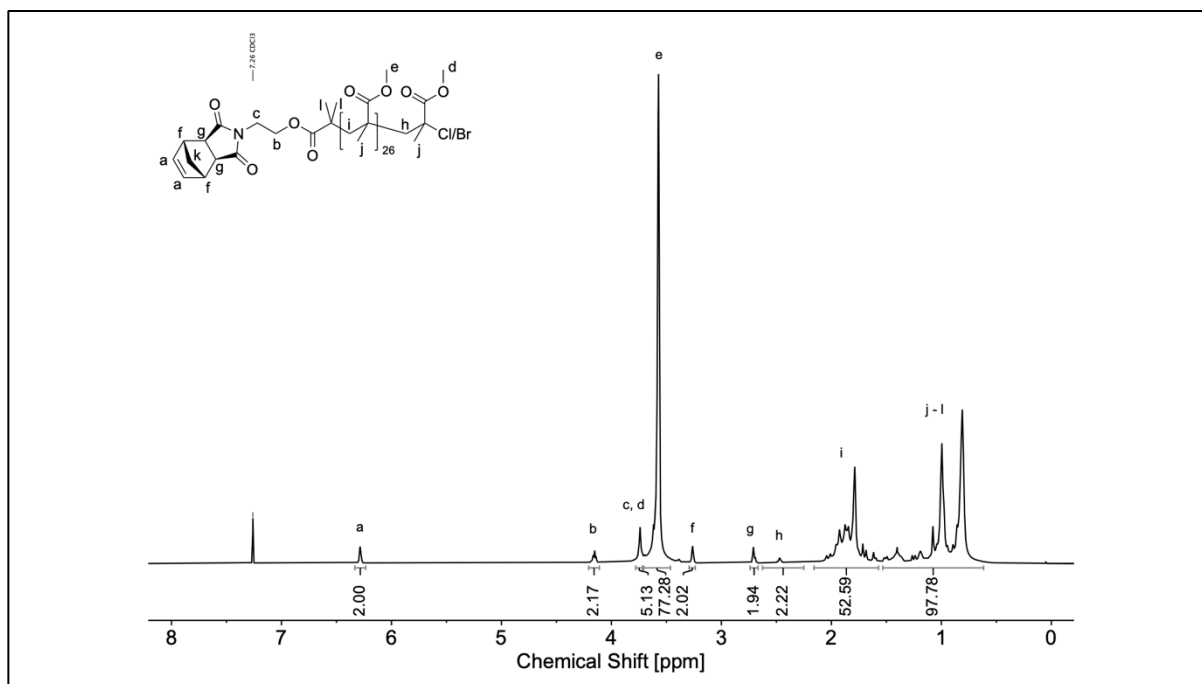
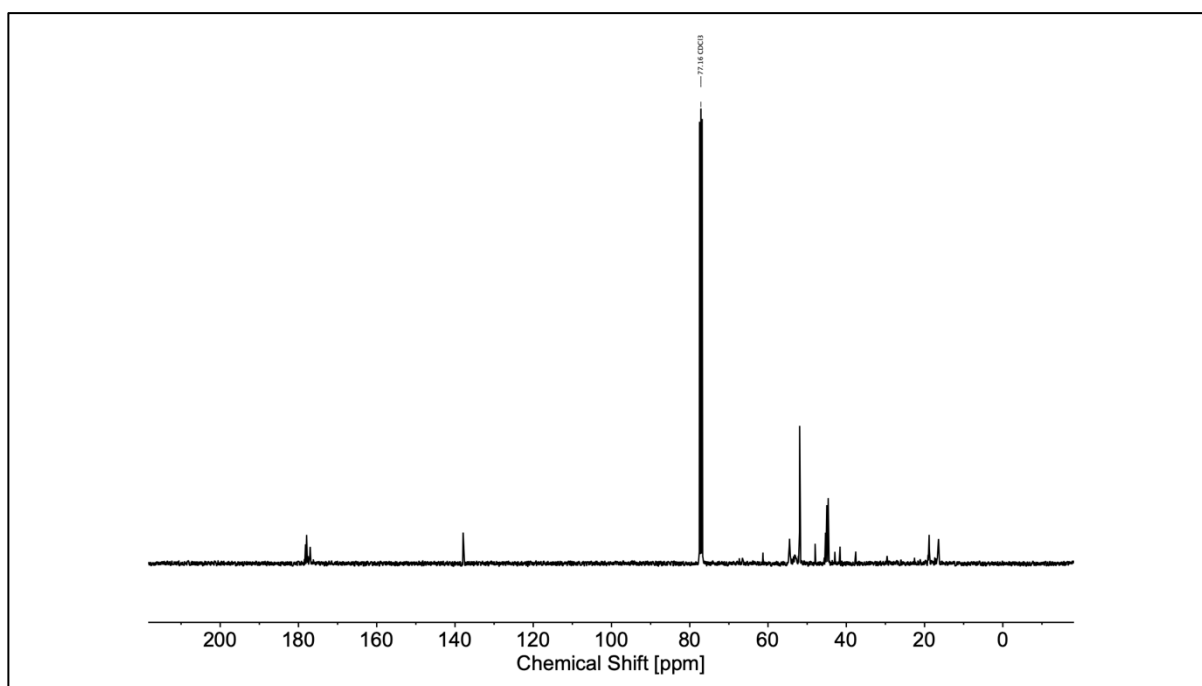


Figure S5.11. Comparison between measured and calculated isotopic patterns of **xNb2M12** determined *via* MALDI-TOF MS (**Figure 5.2**) with (A) the chloride-terminated species (S1), (B) the hydrogen- and the vinylidene-terminated species (S2 and S3), (C) the dinorbornene species (S4), and (D) the double charged vinylidene species (S5).

xNb2M27:**Figure S5.12.** ¹H NMR spectrum of xNb2M27 in CDCl₃ (500 MHz).**Figure S5.13.** ¹³C NMR spectrum of xNb2M27 in CDCl₃ (126 MHz).

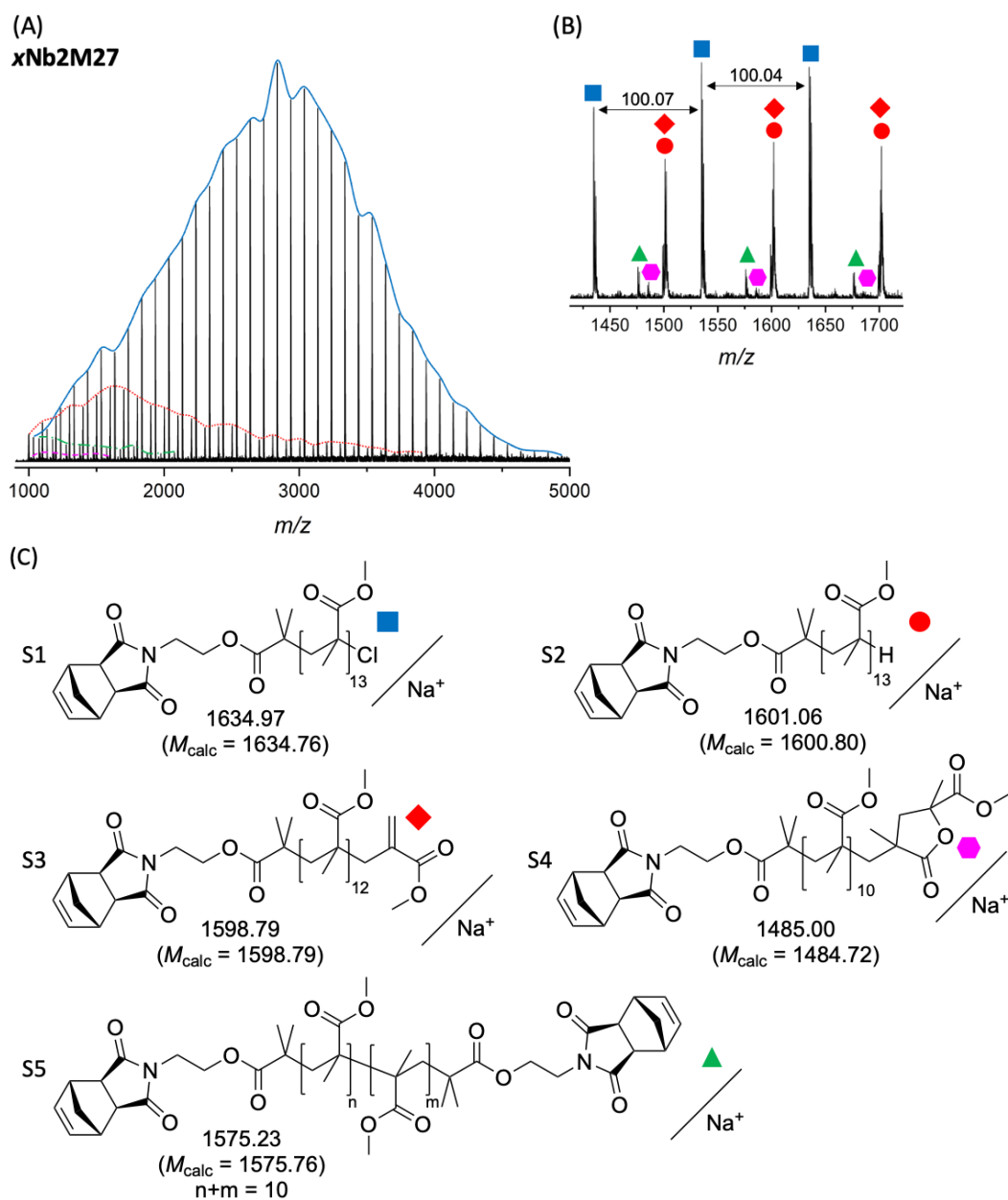


Figure S5.14. (A) MALDI-TOF spectrum (DCTB, NaTFA) of **xNb2M27** with highlighted mass distributions in color to guide the eye, (B) selected region of the spectrum (1410 – 1720 m/z) with peaks color coded as per the identified species, and (C) structures of **xNb2M27** species (S1 – S5) and their calculated and measured monoisotopic masses.

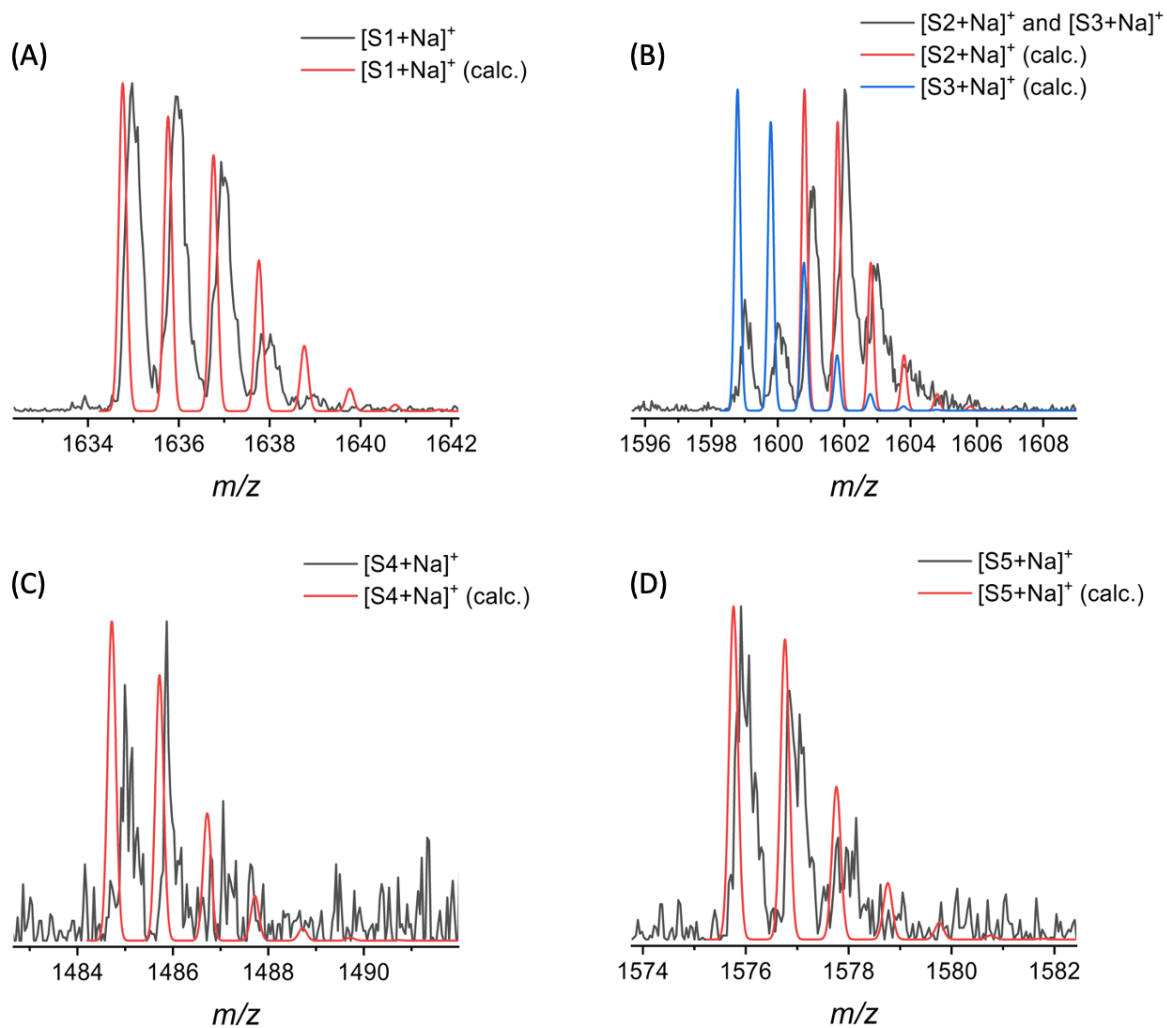
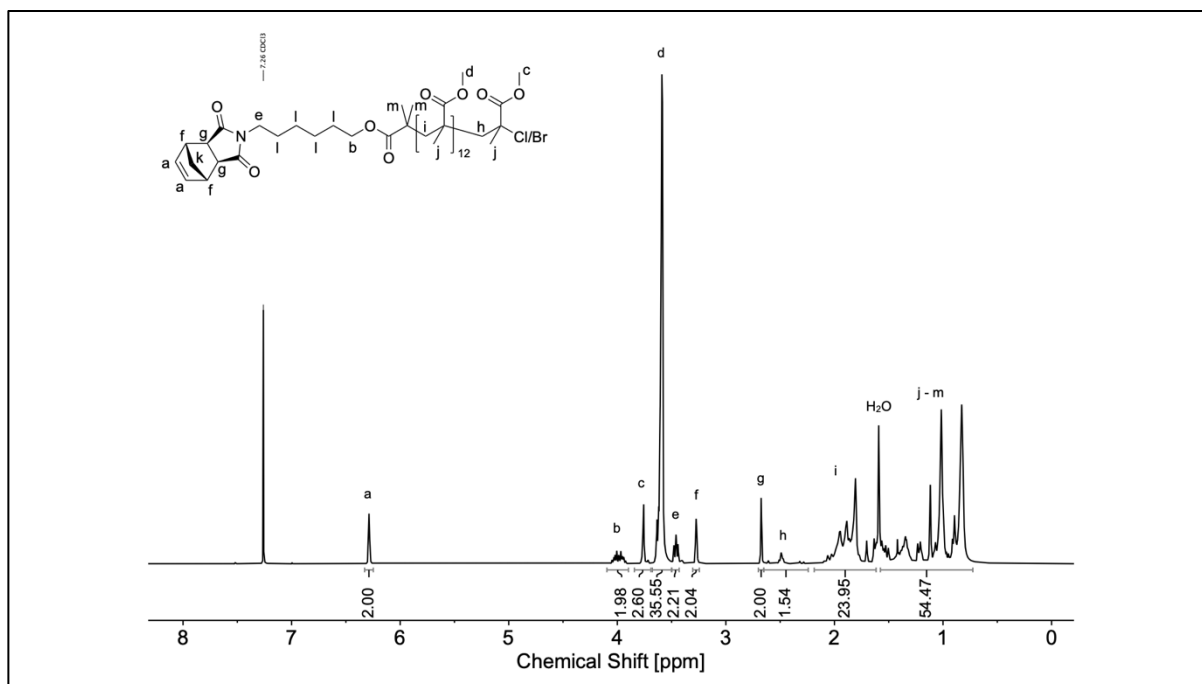
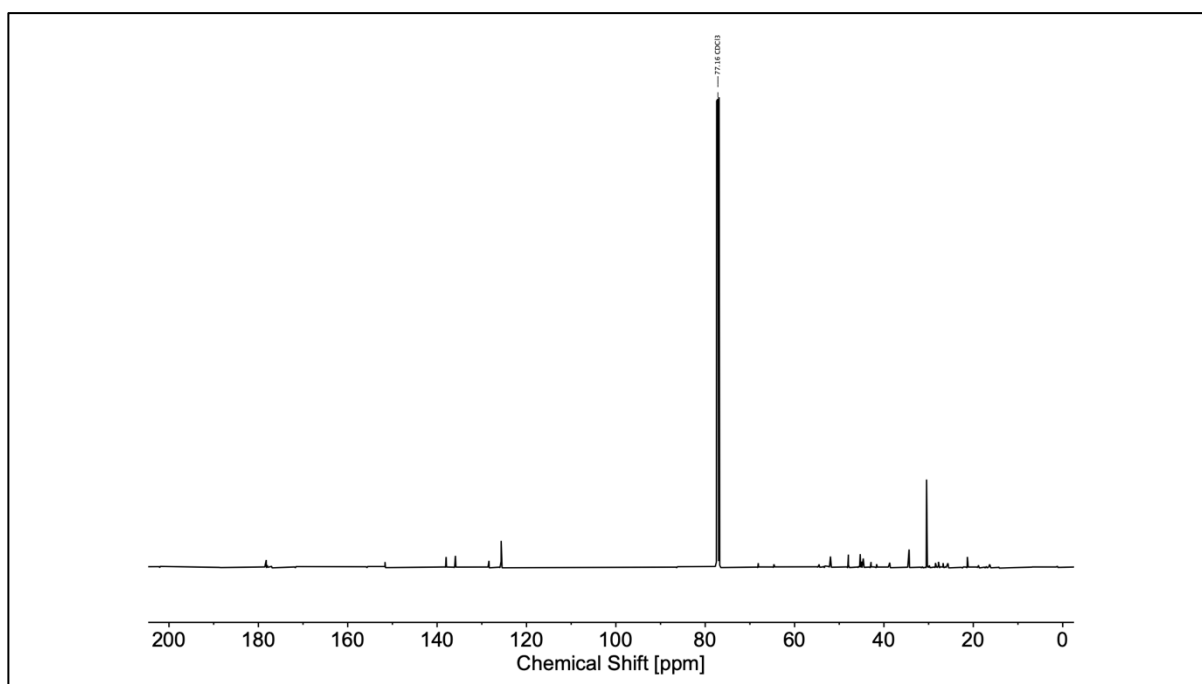


Figure S5.15. Comparison between measured and calculated isotopic patterns of $x\text{Nb}_2\text{M}_{27}$ determined *via* MALDI-TOF MS (Figure S5.14) with (A) the chloride-terminated species (S1), (B) the hydrogen- and the vinylidene-terminated species (S2 and S3), (C) the lactone-terminated species (S4), and (D) the dinorbornene species (S5).

xNb6M13:**Figure S5.16.** ¹H NMR spectrum of **xNb6M13** in CDCl₃ (400 MHz).**Figure S5.17.** ¹³C NMR spectrum of **xNb6M13** in CDCl₃ (126 MHz).

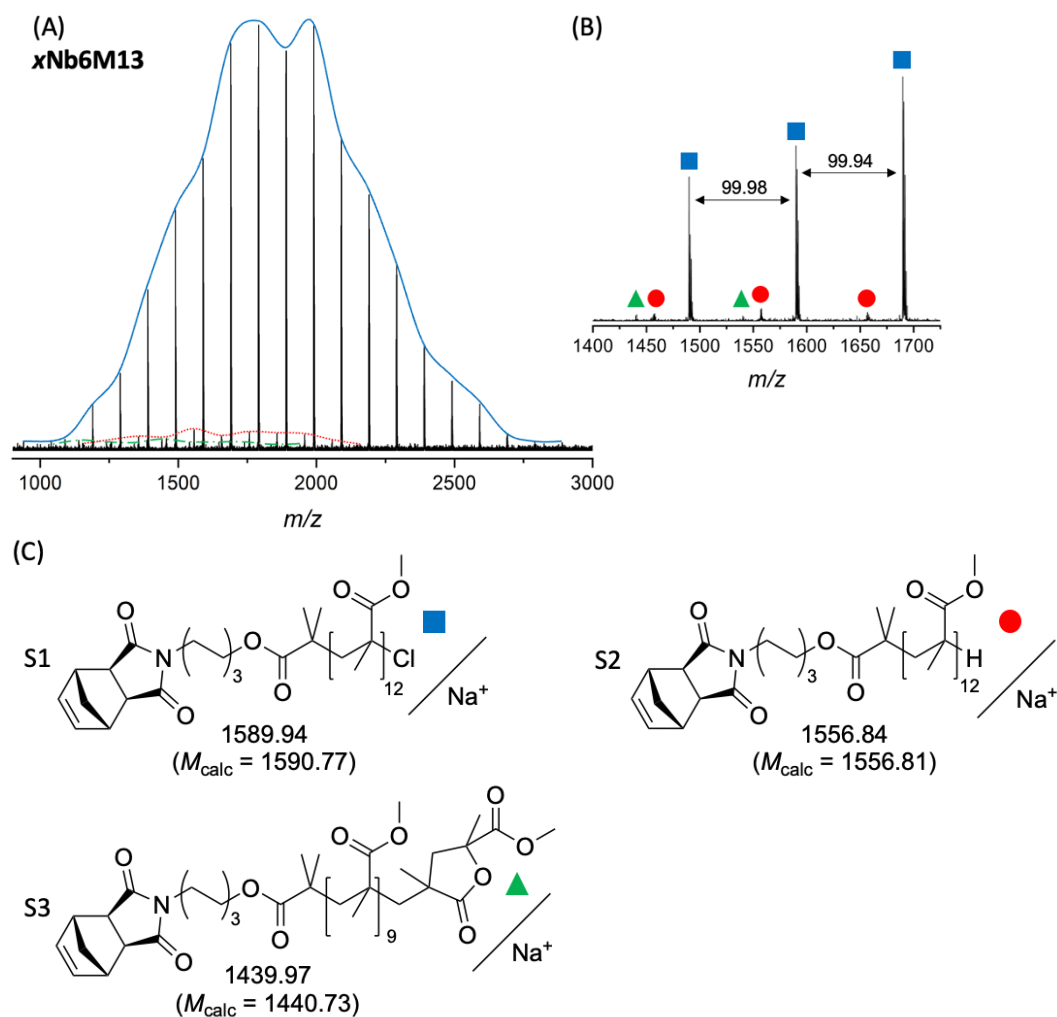


Figure S5.18. (A) MALDI-TOF spectrum (DCTB, NaTFA) of **xNb6M13** with highlighted mass distributions in color to guide the eye, (B) selected region of the spectrum (1400 – 1725 m/z) with peaks color coded as per the identified species, and (C) structures of **xNb6M13** species (S1 – S3) and their calculated and measured monoisotopic masses.

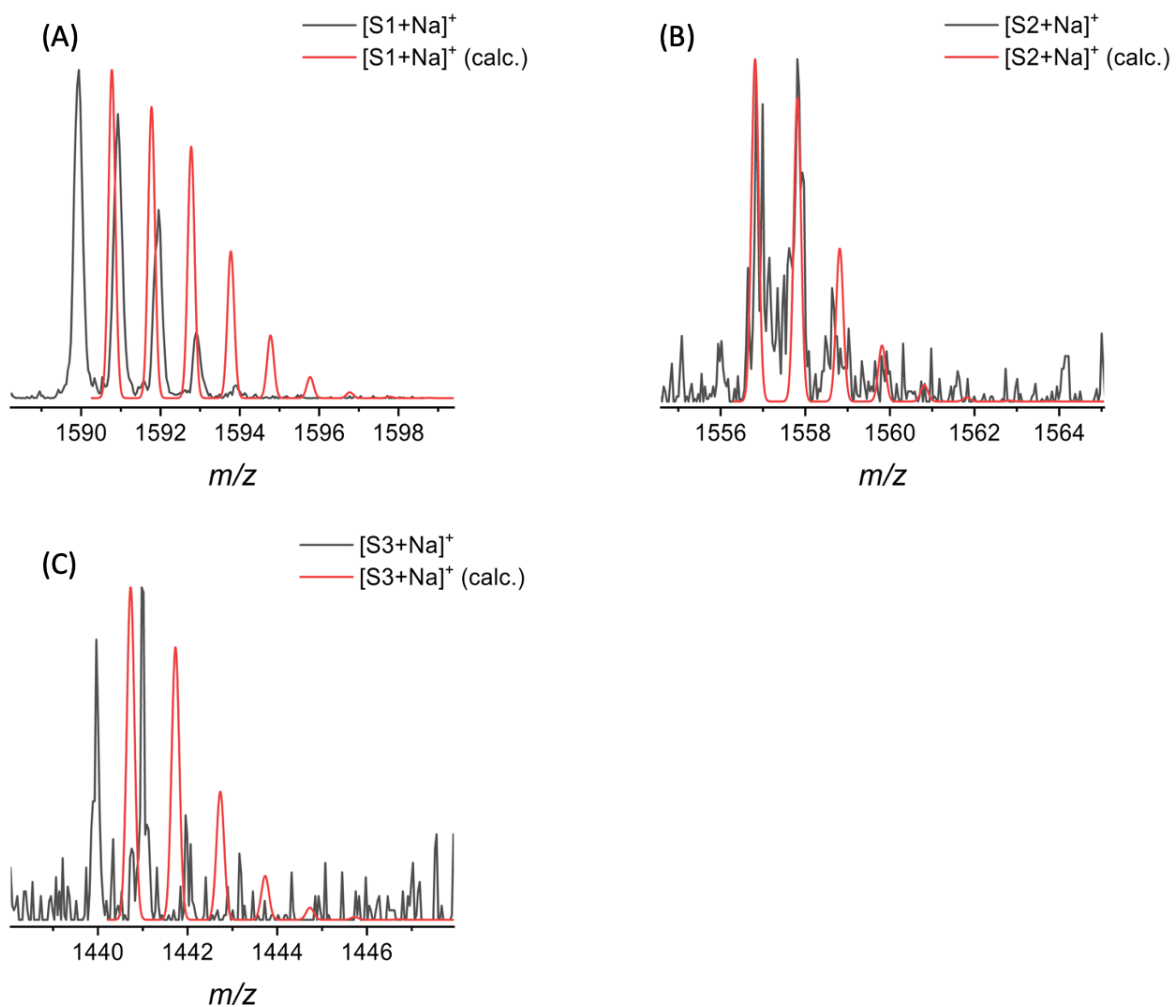


Figure S5.19. Comparison between measured and calculated isotopic patterns of $x\text{Nb}_6\text{M}_{13}$ determined *via* MALDI-TOF MS (**Figure S5.18**) with (A) the chloride-terminated species (S1), (B) the hydrogen-terminated species (S2), and (C) the lactone-terminated species (S3).

xNb6M17 (synthesized by B. Felker under my co-supervision):

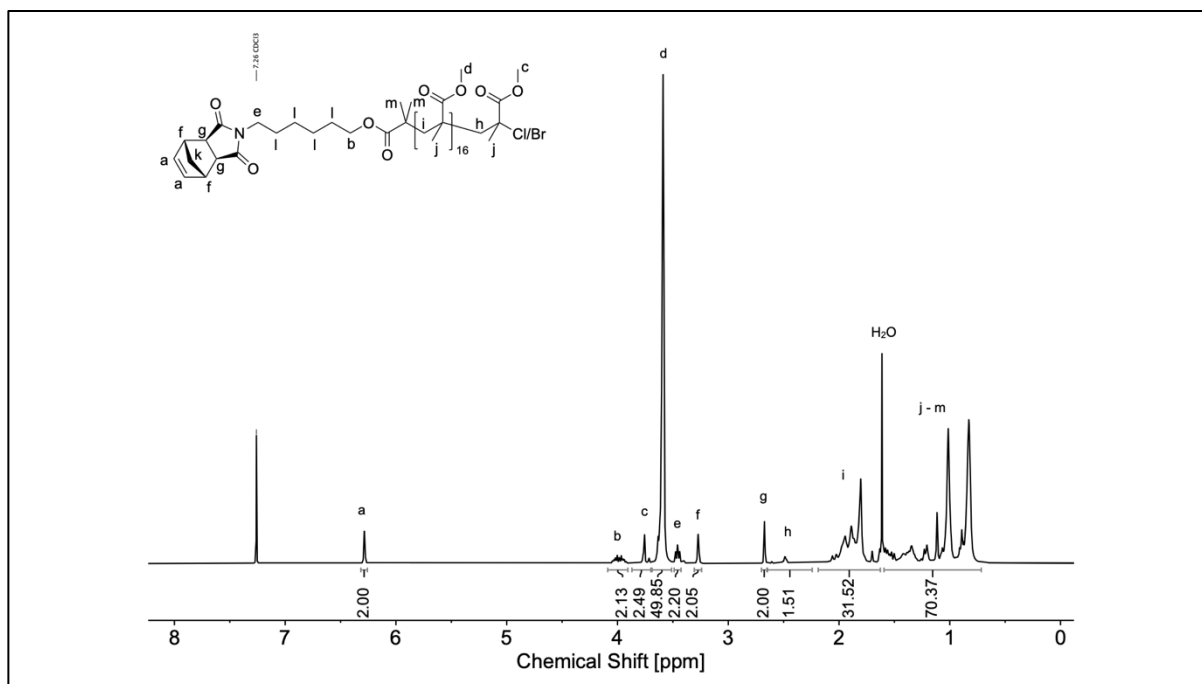


Figure S5.20. ^1H NMR spectrum of **xNb6M17** in CDCl_3 (500 MHz).

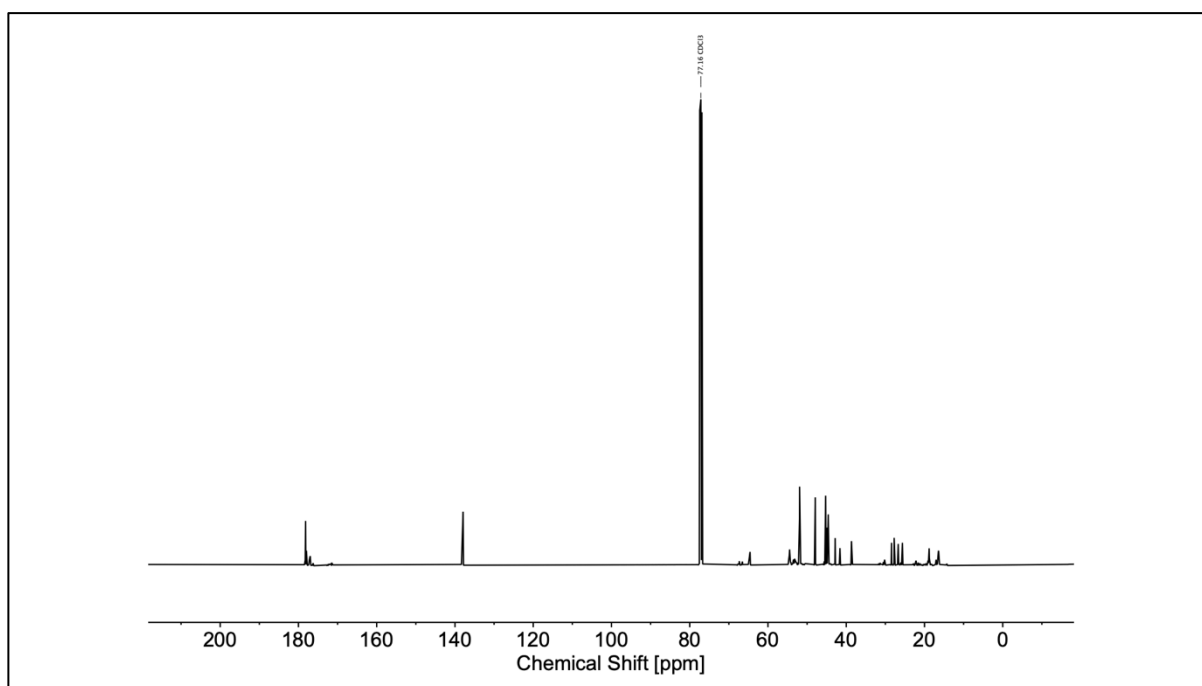


Figure S5.21. ^{13}C NMR spectrum of **xNb6M17** in CDCl_3 (126 MHz).

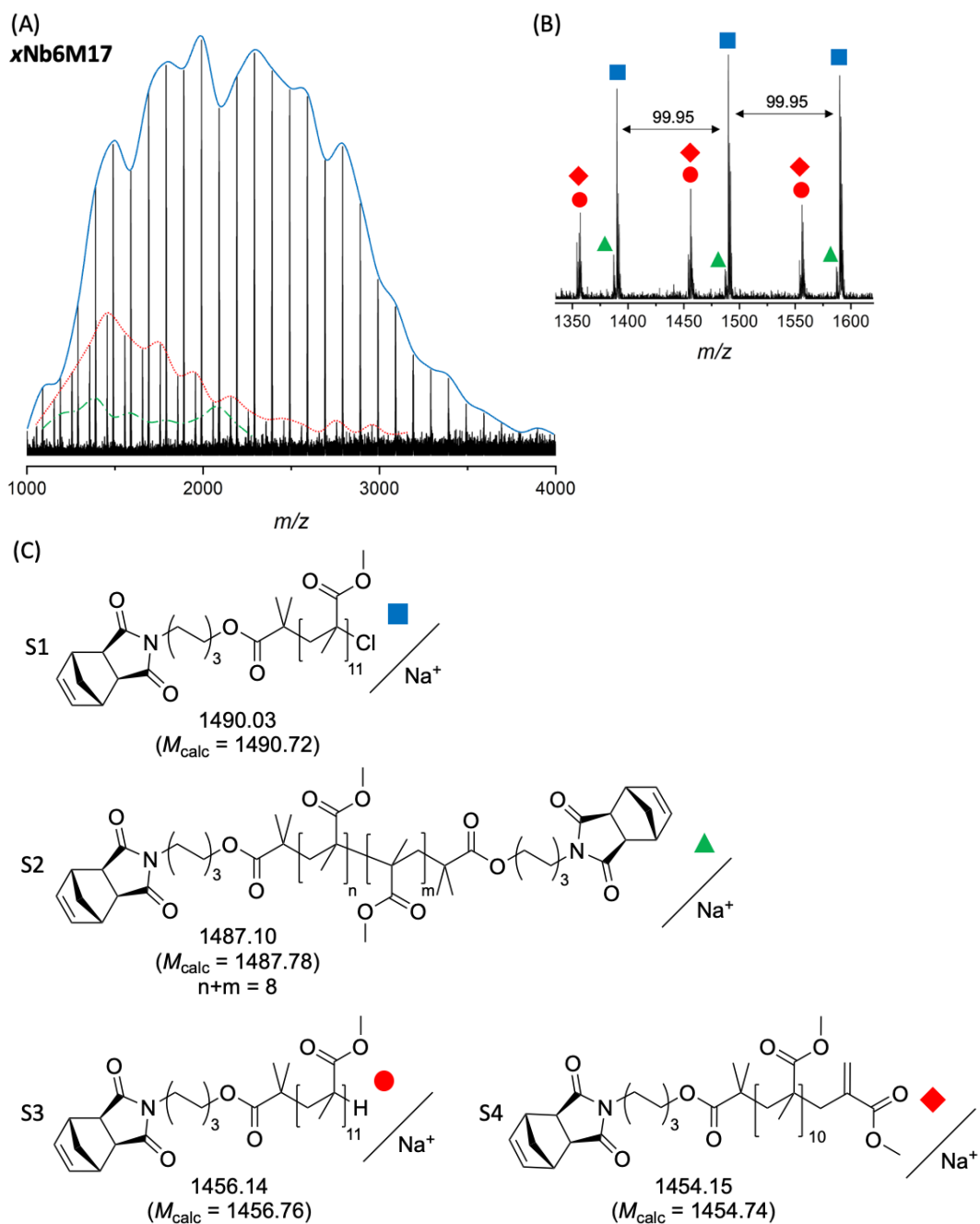


Figure S5.22. (A) MALDI-TOF spectrum (DCTB, NaTFA) of **xNb6M17** with highlighted mass distributions in color to guide the eye, (B) selected region of the spectrum (1330 – 1620 m/z) with peaks color coded as per the identified species, and (C) structures of **xNb6M17** species (S1 – S4) and their calculated and measured monoisotopic masses.

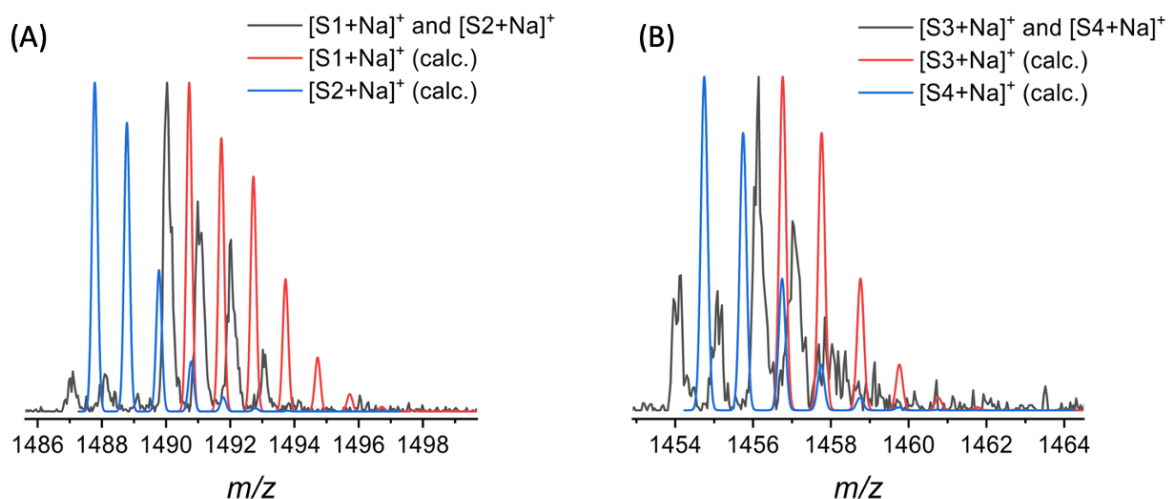


Figure S5.23. Comparison between measured and calculated isotopic patterns of **xNb6M17** determined *via* MALDI-TOF MS (**Figure S5.22**) with (A) the chloride-terminated species (S1), (B) the dinorbornene species (S2), (C) the hydrogen-terminated species (S3), and (C) the vinylidene-terminated species (S4).

xNb2B12:

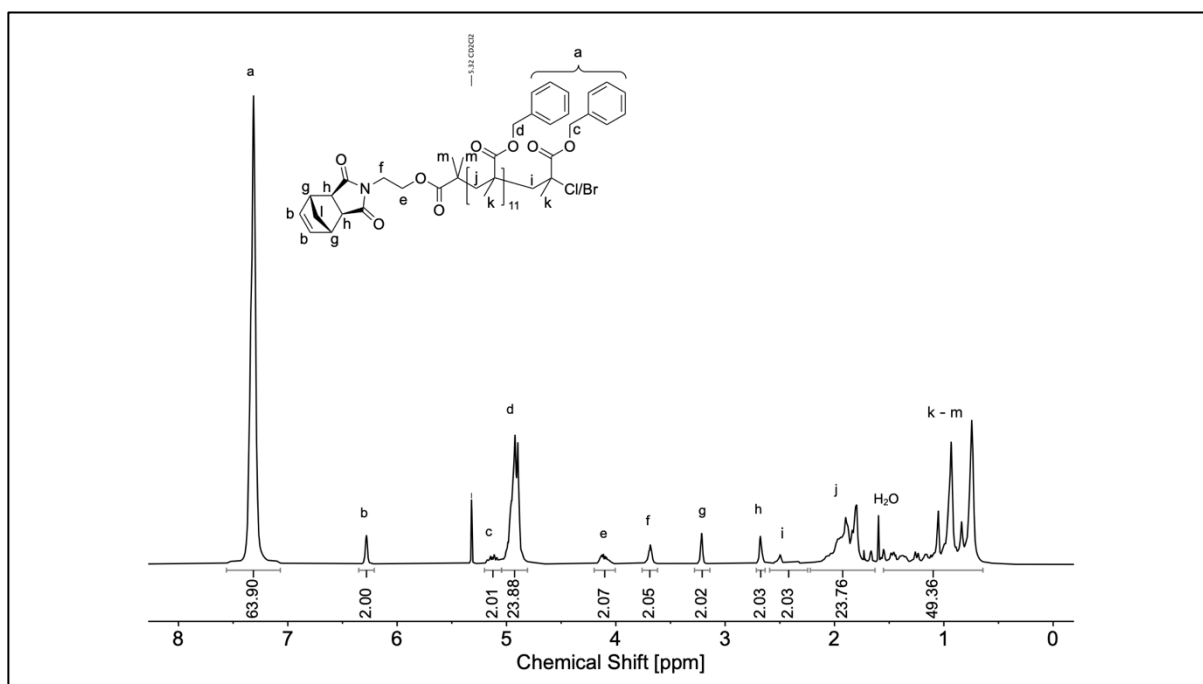


Figure S5.24. ¹H NMR spectrum of **xNb2B12** in CD₂Cl₂ (500 MHz).

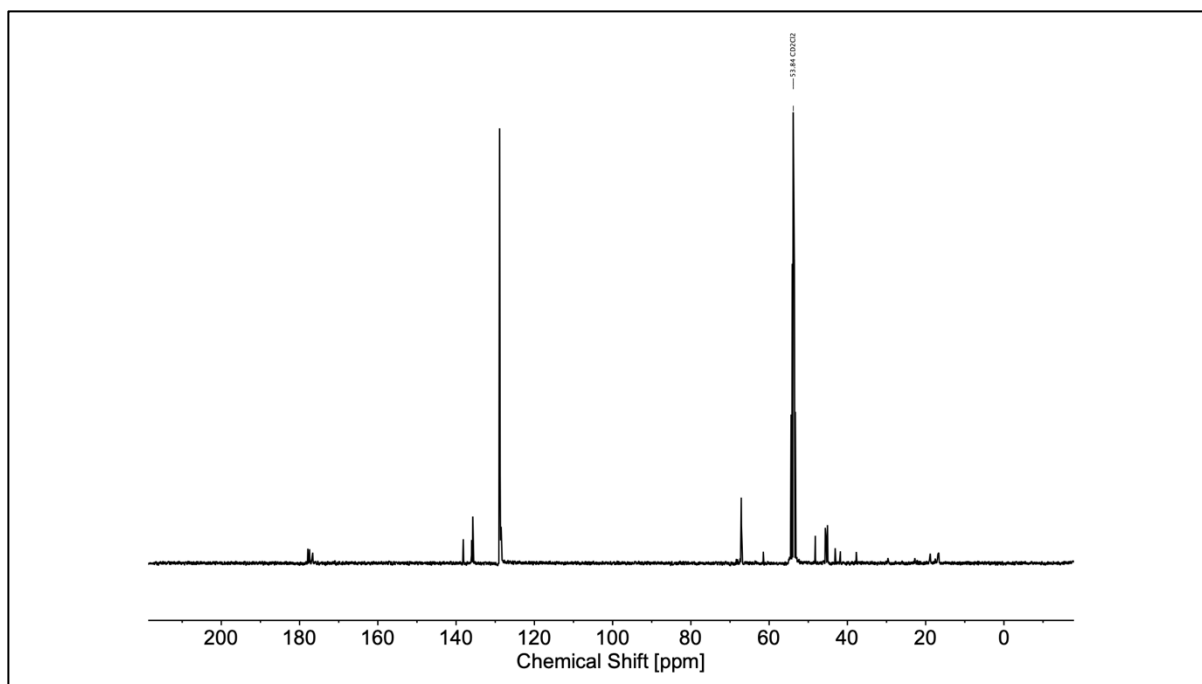


Figure S5.25. ^{13}C NMR spectrum of $x\text{Nb}_2\text{B}_{12}$ in CD_2Cl_2 (126 MHz).

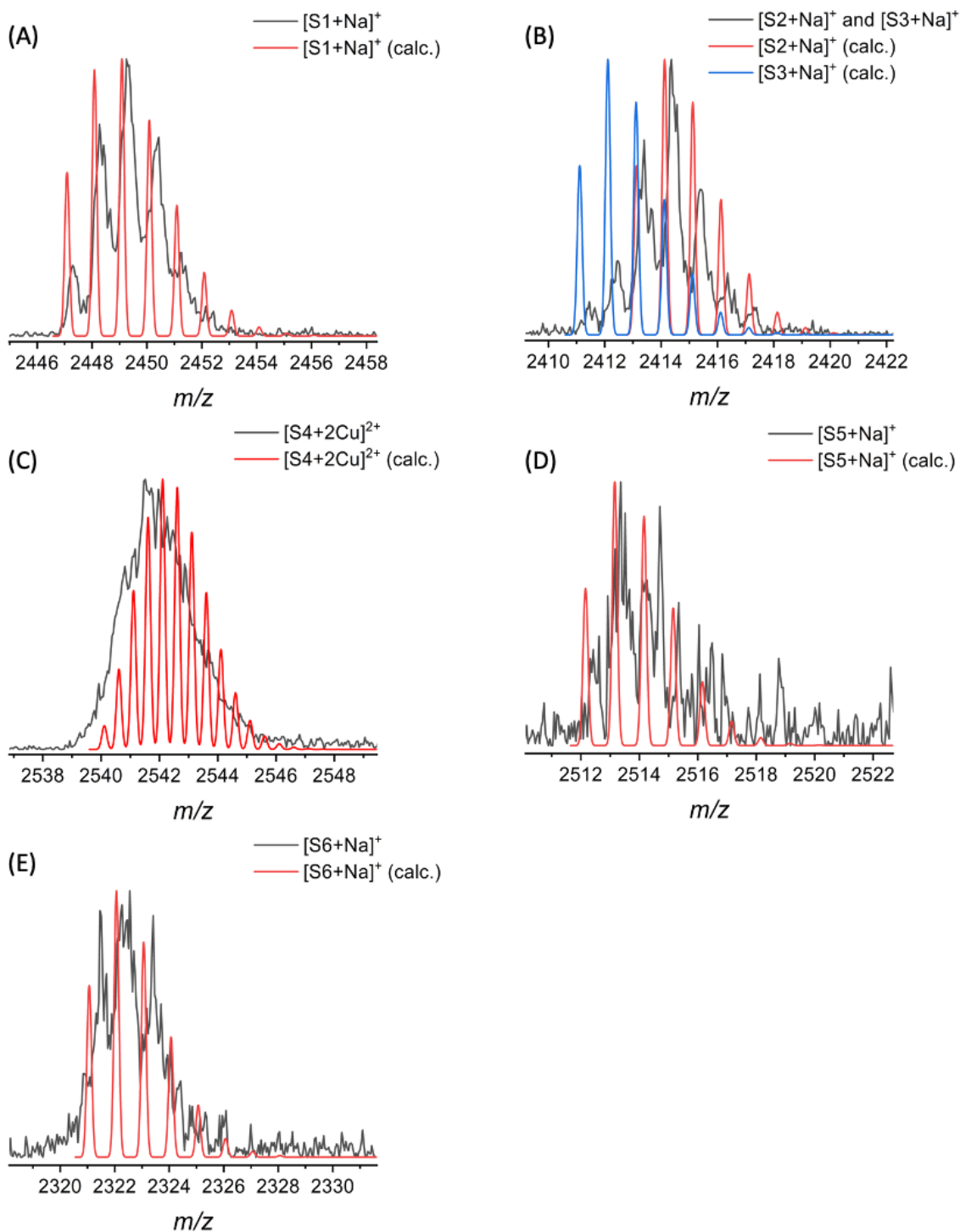


Figure S5.26. Comparison between measured and calculated isotopic patterns of xNb_2B_{12} determined *via* MALDI-TOF MS (**Figure 5.3**) with (A) the chloride-terminated species (S1), (B) the hydrogen- and the vinylidene-terminated species (S2 and S3), (C) the double charged dinorbornene species (S4), (D) the dinorbornene species (S5), and (E) the lactone-terminated species (S6).

General ATRP procedure using styrene as monomer (xNb2S20):

Two ampoules equipped with J Young taps were evacuated and purged with argon three times. Ampoule 1, equipped with a stirring bar, was charged with 1.00 eq. copper(I) bromide. Ampoule 2 was charged with 1.00 eq. **xNb2Br** (0.042 mol/L), 1.00 eq. PMDETA and 120 eq. styrene dissolved in toluene. The mixtures were degassed by three consecutive pump thaw cycles under high vacuum. Subsequently, the solution of ampoule 2 was transferred to ampoule 1 *via* a degassed syringe, initiating the polymerization. The polymerization was carried out at 80 °C for 70 minutes under an argon atmosphere. Afterwards, the reaction was cooled quickly to ambient temperature by immersing the ampoule into liquid nitrogen, exposed to air, and quenched by adding THF. The solution was then flushed through a plug of neutral aluminum oxide to remove the copper. Subsequently, the solvent was removed under reduced pressure. The crude product was dissolved in a small amount of THF and precipitated three times from the tenfold amount of cold methanol. The polymer was filtered, dried under high vacuum, and obtained as a white solid.

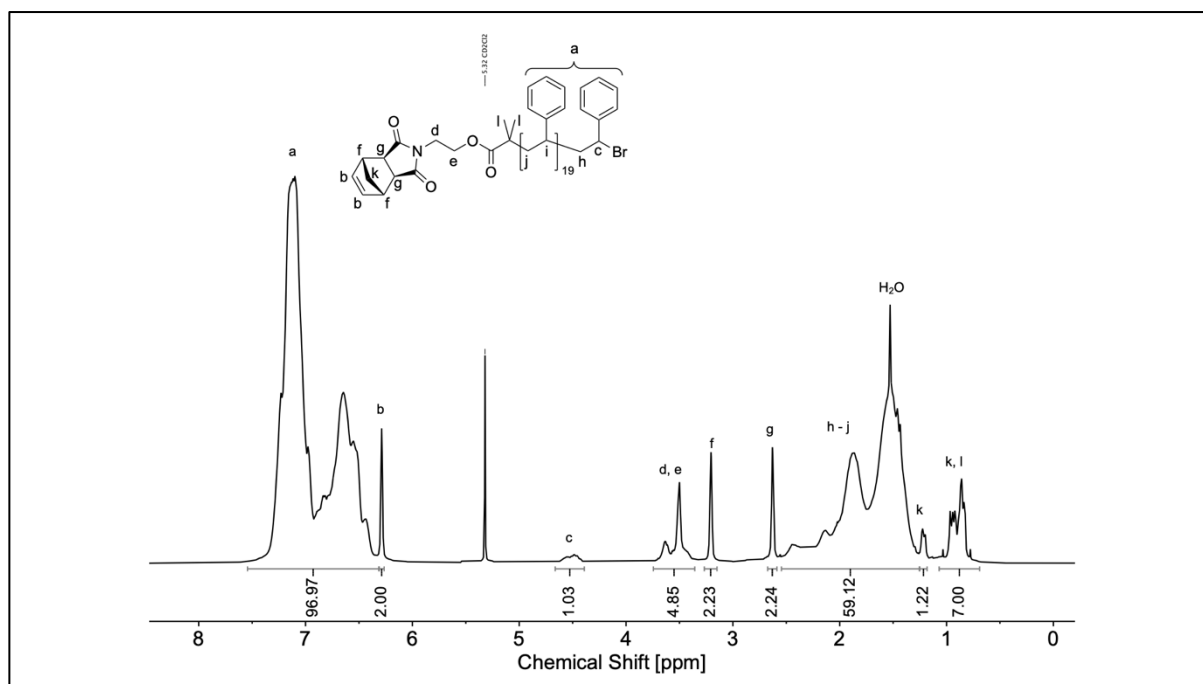


Figure S5.27. ¹H NMR spectrum of **xNb2S20** in CD₂Cl₂ (500 MHz).

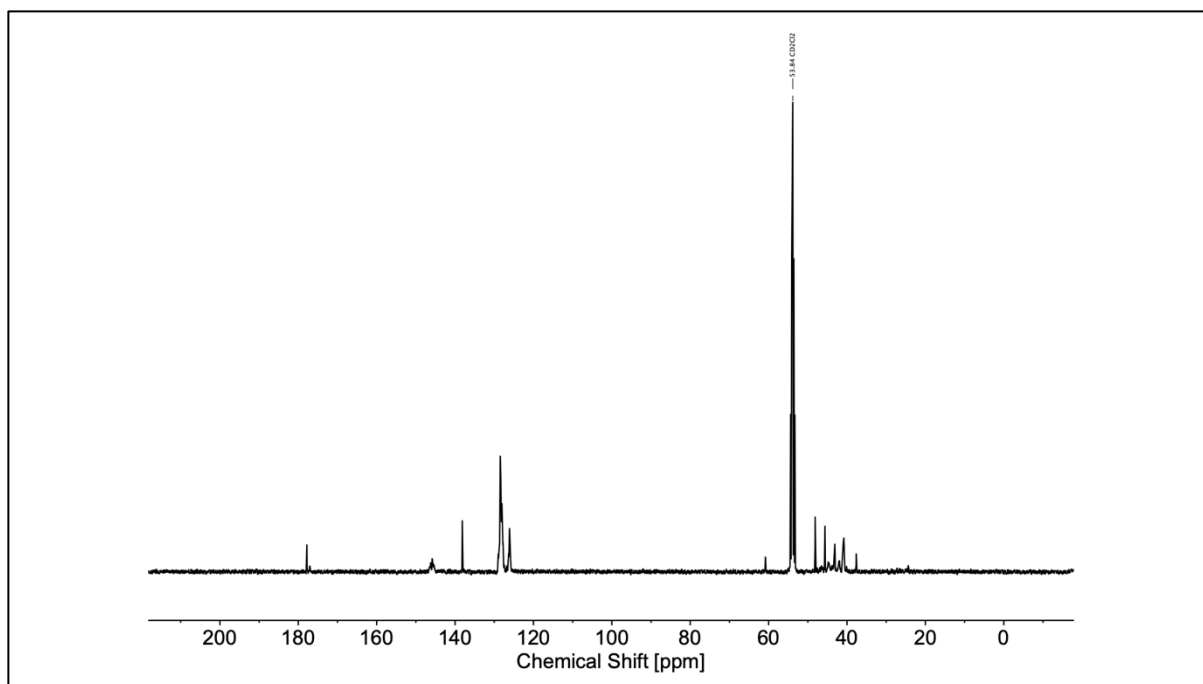


Figure S5.28. ^{13}C NMR spectrum of $x\text{Nb}_2\text{S}_2\text{O}$ in CD_2Cl_2 (126 MHz).

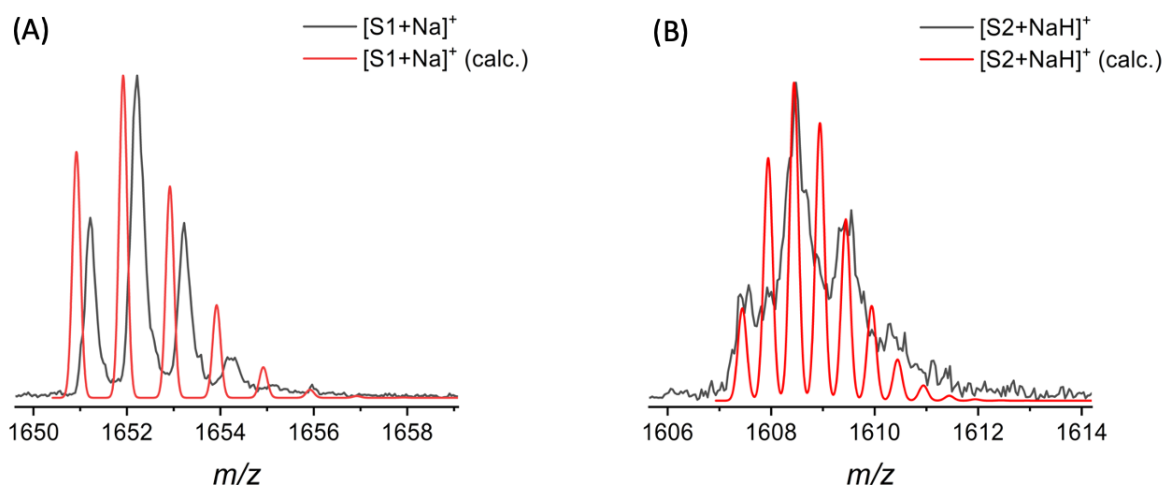


Figure S5.29. Comparison between measured and calculated isotopic patterns of $x\text{Nb}_2\text{S}_2\text{O}$ determined *via* MALDI-TOF MS (**Figure 5.4**) with (A) the olefin-terminated species (S1), and (B) the double charged hydrogen-terminated species (S2).

General ROMP procedure – homopolymerizations using non-degassed solvent (entries 5.1 – 5.16):

A vial equipped with a stirring bar was charged with the desired amount of monomer and G1 catalyst dissolved in the desired solvent. The polymerization was carried out at ambient temperature for 24 hours. Subsequently, the polymerization was quenched by adding an excess of ethyl vinyl ether.

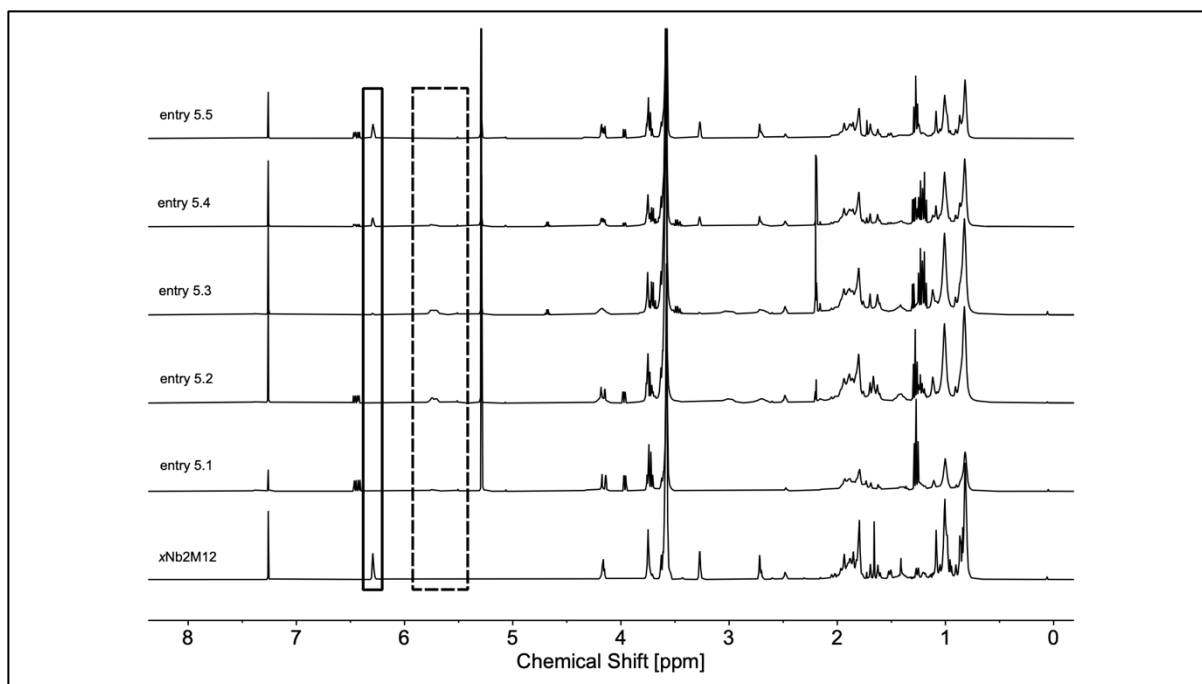


Figure S5.30. Stacked ^1H NMR spectra of entries 5.1 – 5.5 after quenching with EVE in CDCl_3 (400 MHz) and the ^1H NMR spectrum of the corresponding monomer in CDCl_3 (500 MHz). Boxes: norbornene olefinic moiety (solid); poly(norbornene) olefinic backbone (dashed).

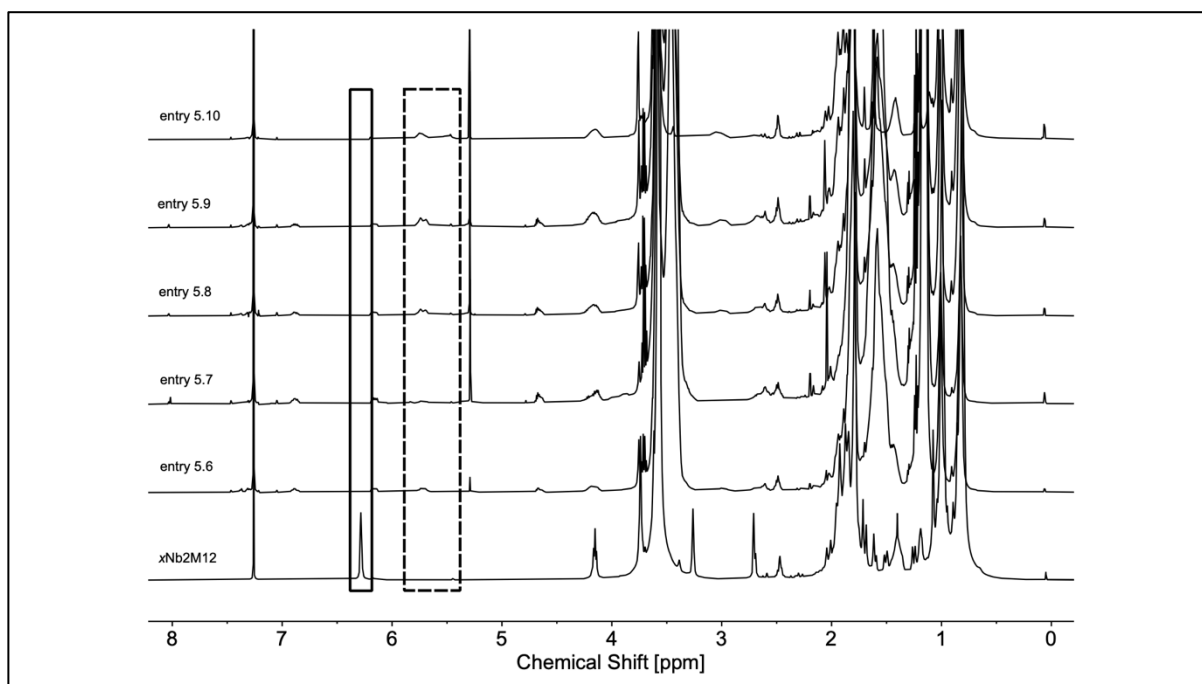


Figure S5.31. Stacked ^1H NMR spectra of entries 5.6 – 5.10 after quenching with EVE and the ^1H NMR spectrum of the corresponding monomer in CDCl_3 (500 MHz). Boxes: norbornene olefinic moiety (solid); poly(norbornene) olefinic backbone (dashed).

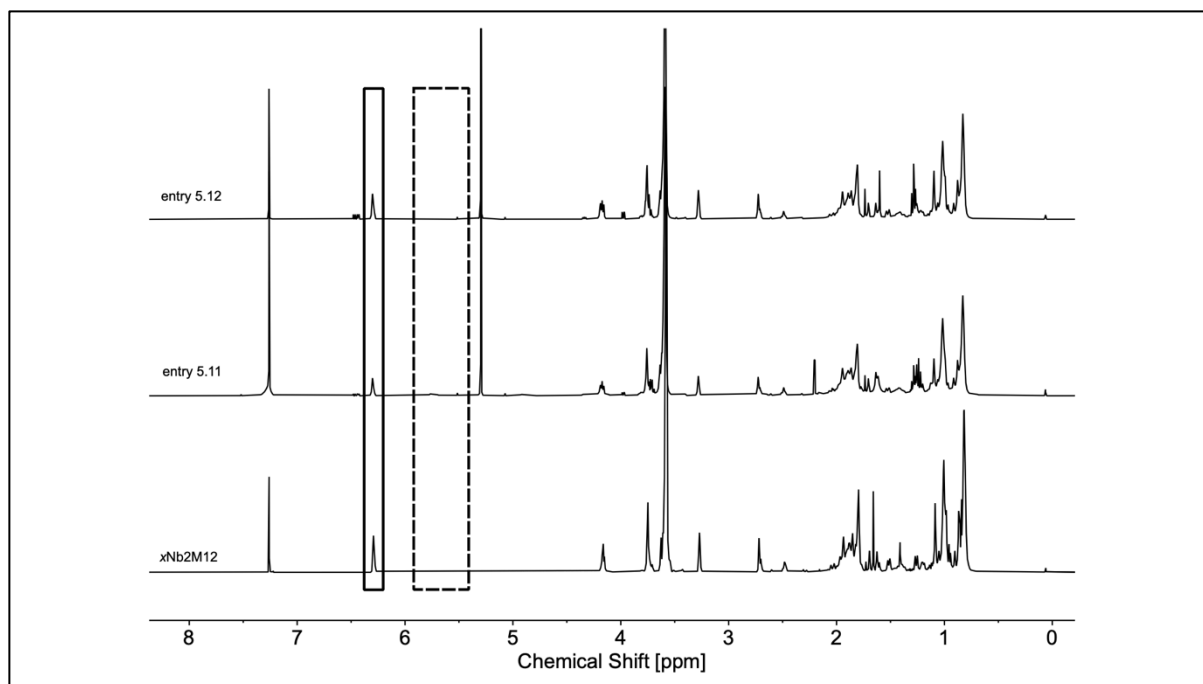


Figure S5.32. Stacked ^1H NMR spectra of entries 5.11 and 5.12 after quenching with EVE in CDCl_3 (400 MHz) and the ^1H NMR spectrum of the corresponding monomer in CDCl_3 (500 MHz). Boxes: norbornene olefinic moiety (solid); poly(norbornene) olefinic backbone (dashed).

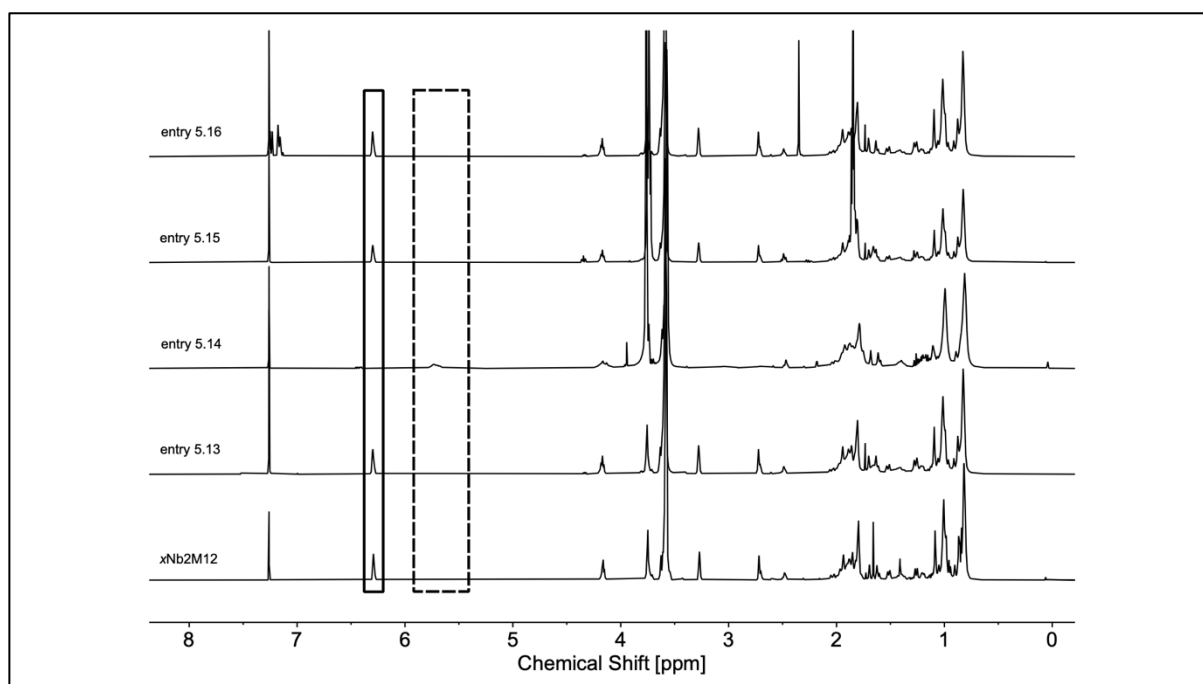


Figure S5.33. Stacked ^1H NMR spectra of entries 5.13 – 5.16 after quenching with EVE in CDCl_3 (400 MHz) and the ^1H NMR spectrum of the corresponding monomer in CDCl_3 (500 MHz). Boxes: norbornene olefinic moiety (solid); poly(norbornene) olefinic backbone (dashed).

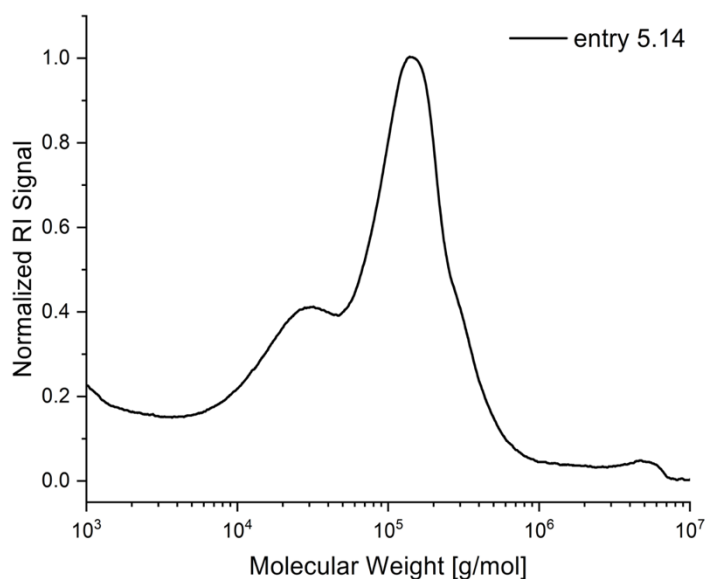


Figure S5.34. SEC trace of entry 5.14.

General ROMP procedure – kinetic measurements (entries 5.17, 5.23 – 5.27):

An NMR tube equipped with a J Young tap was evacuated and purged with argon three times. Subsequently, 25.0 eq. macromonomer (10 mmol/L) and 1.00 eq. Grubbs-type catalyst (0.4 mmol/L) were each dissolved in degassed DCM-d₂ and transferred into the NMR tube, initiating the polymerization. The polymerization was carried out at ambient temperature under an argon atmosphere and monitored by on-line ¹H NMR spectroscopy. After complete conversion, the polymerization was quenched by adding an excess of ethyl vinyl ether.

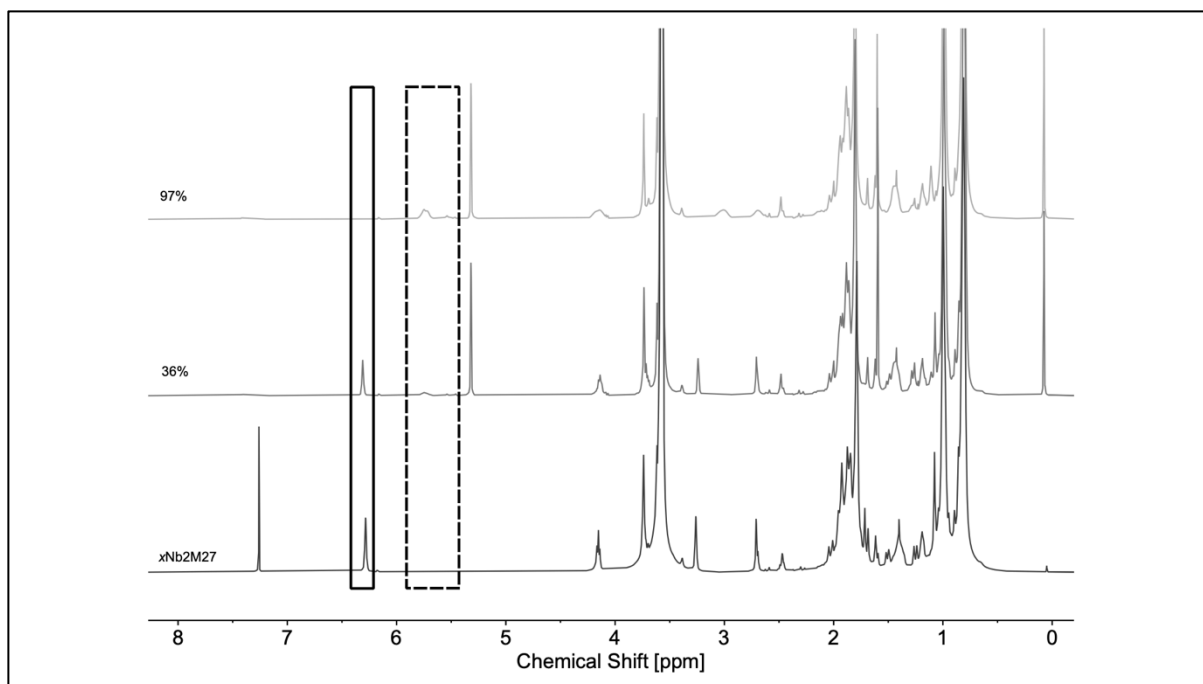


Figure S5.35. Representative stacked ¹H NMR spectra of the ROMP of **xNb2M27** (entry 5.17) in CD₂Cl₂ (500 MHz) and the ¹H NMR spectrum of the corresponding monomer in CDCl₃ (500 MHz). Boxes: norbornene olefinic moiety (solid); poly(norbornene) olefinic backbone (dashed).

General ROMP procedure – homopolymerizations using degassed solvent (entries 5.18 – 5.22):

An ampoule equipped with a J Young tap and a stirring bar was evacuated and purged with argon three times. Subsequently, the desired amount of macromonomer and Grubbs-type catalyst were each dissolved in degassed DCM and transferred into the ampoule under an argon flow, initiating the polymerization. The polymerization was carried out at ambient temperature under an argon atmosphere and was quenched by adding an excess of ethyl vinyl ether.

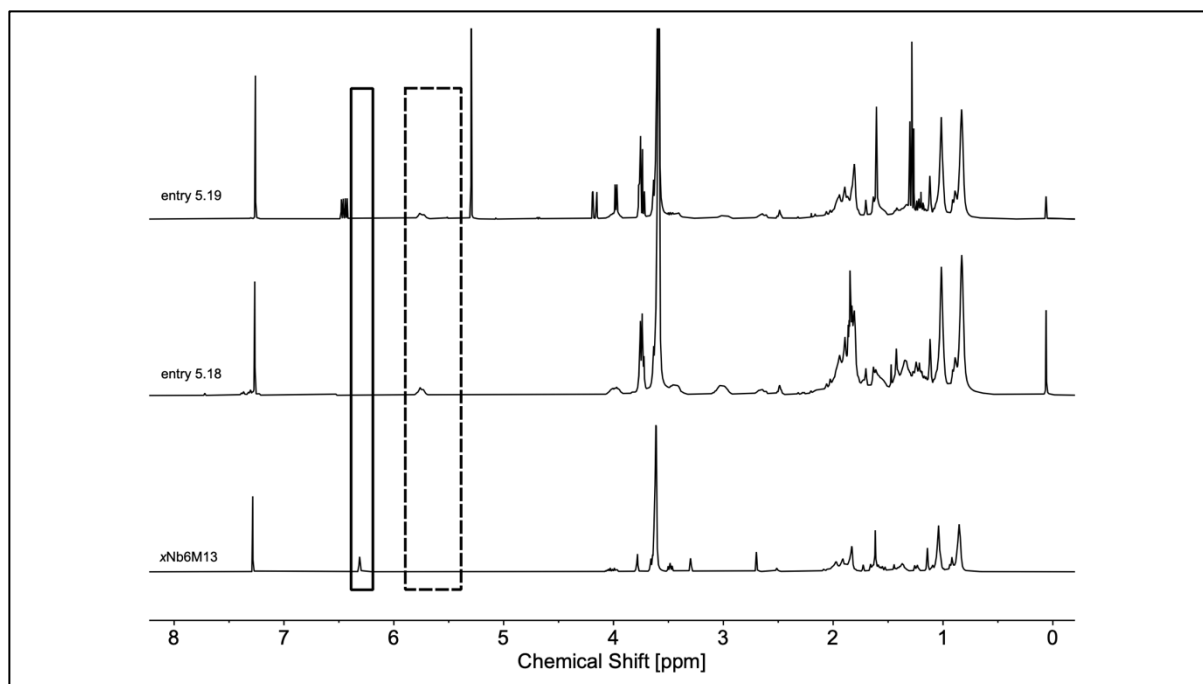


Figure S5.36. Stacked ^1H NMR spectra of entries 5.18 and 5.19 after quenching with EVE in CDCl_3 (400 MHz) and the ^1H NMR spectrum of the corresponding monomer in CDCl_3 (400 MHz). Boxes: norbornene olefinic moiety (solid); poly(norbornene) olefinic backbone (dashed).

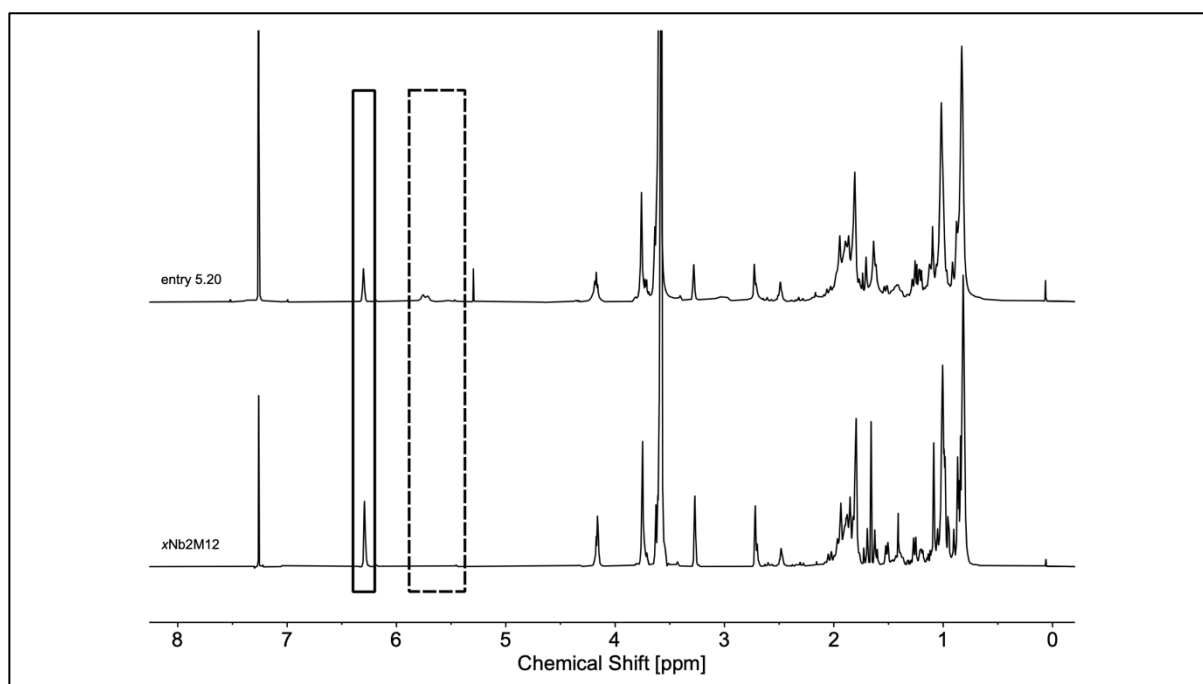


Figure S5.37. Stacked ^1H NMR spectra of entry 5.20 after quenching with EVE in CDCl_3 (400 MHz) and the ^1H NMR spectrum of the corresponding monomer in CDCl_3 (500 MHz). Boxes: norbornene olefinic moiety (solid); poly(norbornene) olefinic backbone (dashed).

G3 catalyst:

The synthesis procedure was adapted from recent literature.³⁷⁶ 1.00 eq. G2 catalyst and 30.0 eq. pyridine were mixed in a vial. The mixture was stirred at ambient temperature for 5 minutes, whereby a color change from dark red to dark green was immediately observed. Afterwards, *n*-pentane (15 mL per gram G2) was layered onto the green mixture and the vial was capped and stored at -15 °C for 24 hours. The crude product was filtered, washed with *n*-pentane three times and dried under high vacuum. The product was obtained as a green solid in a yield of 81% and stored under argon atmosphere at low temperature.

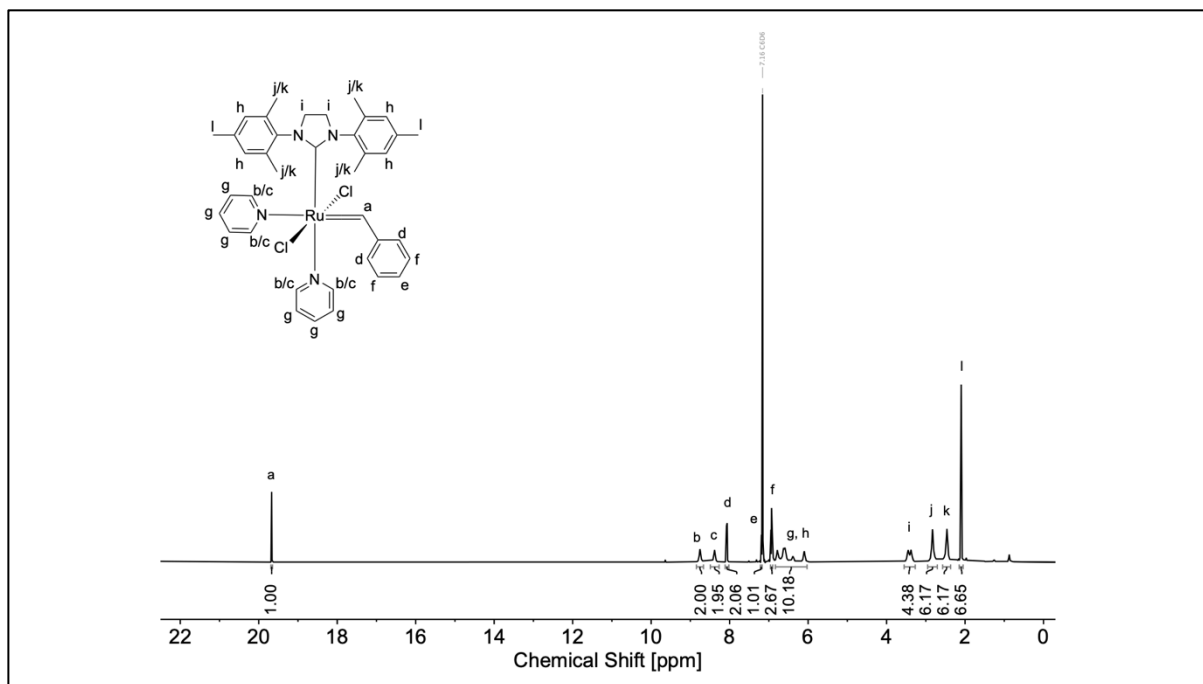


Figure S5.38. ¹H NMR spectrum of the **G3 catalyst**.

¹H NMR: (500 MHz, C₆D₆, δ): 19.67 (s, 1H; CHPh, ^a), 8.76 (bs, 2H; pyridine N-CH, ^b), 8.38 (bs, 2H; pyridine N-CH, ^c), 8.07 (d, *J* = 8.0 Hz, 2H; *ortho* CH, ^d), 7.19 (t, *J* = 7.3 Hz, 1H; *para* CH, ^e), 6.93 (t, *J* = 7.7 Hz, 2H; *meta* CH, ^f), 6.83 - 6.02 (m, 10H; pyridine CH, ^g, Mes CH, ^h), 3.55 - 3.27 (m, 4H; CH₂, ⁱ), 2.83 (bs, 6H; Mes CH₃, ^j), 2.46 (bs, 6H; Mes CH₃, ^k), 2.10 (bs, 6H; Mes *para* CH₃, ^l).

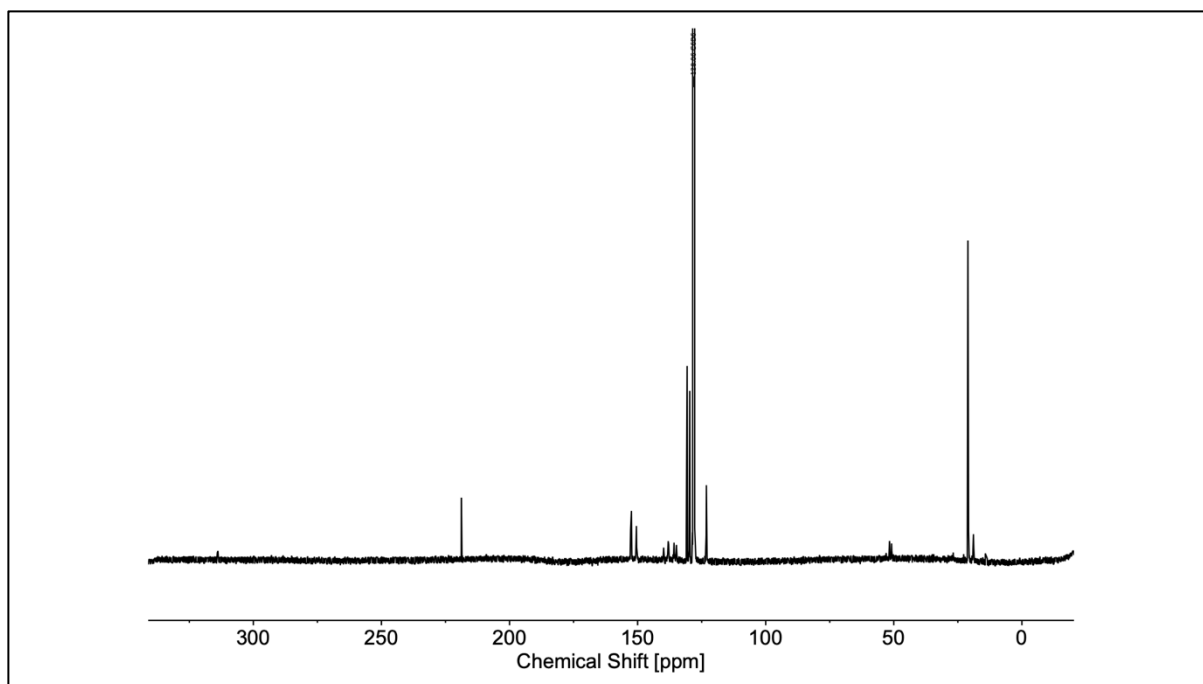


Figure S5.39. ¹³C NMR spectrum of the **G3** catalyst.

¹³C NMR: (126 MHz, C₆D₆, δ): 313.81, 218.80, 152.74, 150.46, 139.82, 138.04, 135.80, 134.85, 130.68, 129.65, 128.35, 128.14, 127.97, 123.16, 51.68, 50.87, 21.07, 20.80, 18.89.

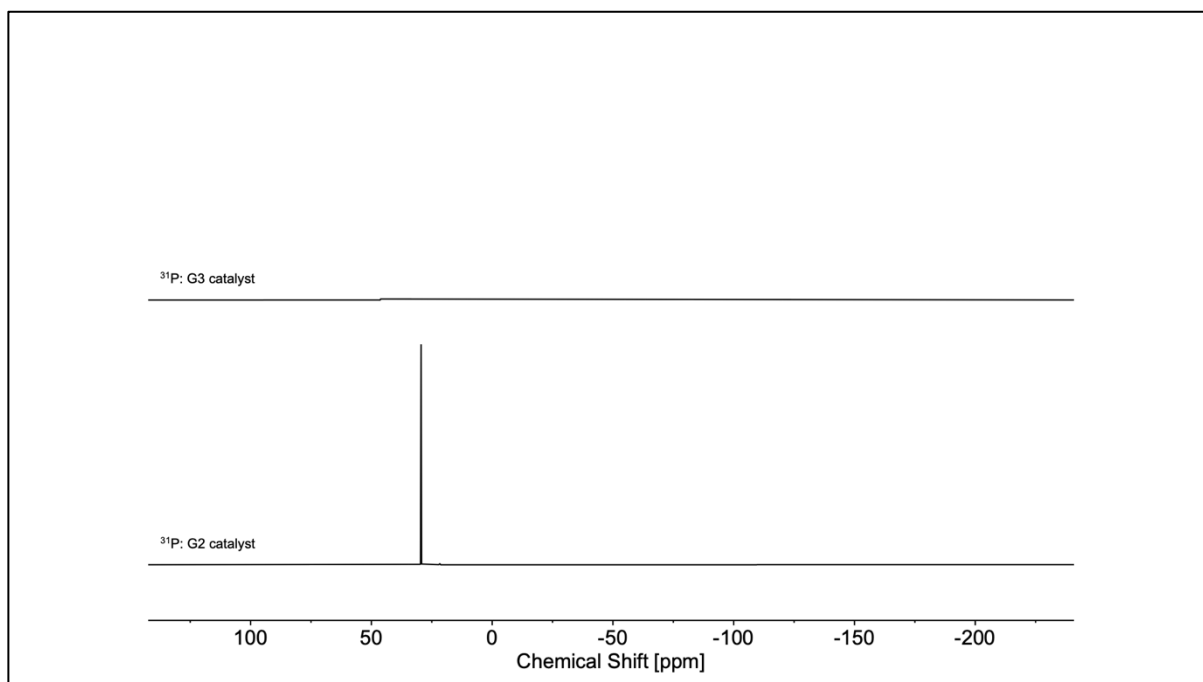


Figure S5.40. Stacked ³¹P NMR spectra of the G2 and the **G3** catalyst.

IR (ATR platinum diamond): ν / cm^{-1} = 3065 (w), 2945 (w), 2913 (w), 1678 (vw), 1629 (w), 1596 (w), 1483 (s), 1446 (s), 1405 (s), 1384 (w), 1263 (vs), 1246 (vs), 1222 (s), 1199 (w), 1177 (w), 1150 (w), 1072 (vs), 1061 (vs), 1053 (vs), 1037 (vs), 1002 (m), 878 (w), 852 (m), 759 (m), 743 (w), 697 (vs), 685 (s), 638 (w), 617 (w), 578 (w), 572 (w), 522 (w), 483 (w), 428 (w).

HRMS (ESI-MS) m/z : [monopyridine species+H]⁺ calc. for C₃₃H₃₈Cl₂N₃Ru, 648.1481, found: 648.1428.

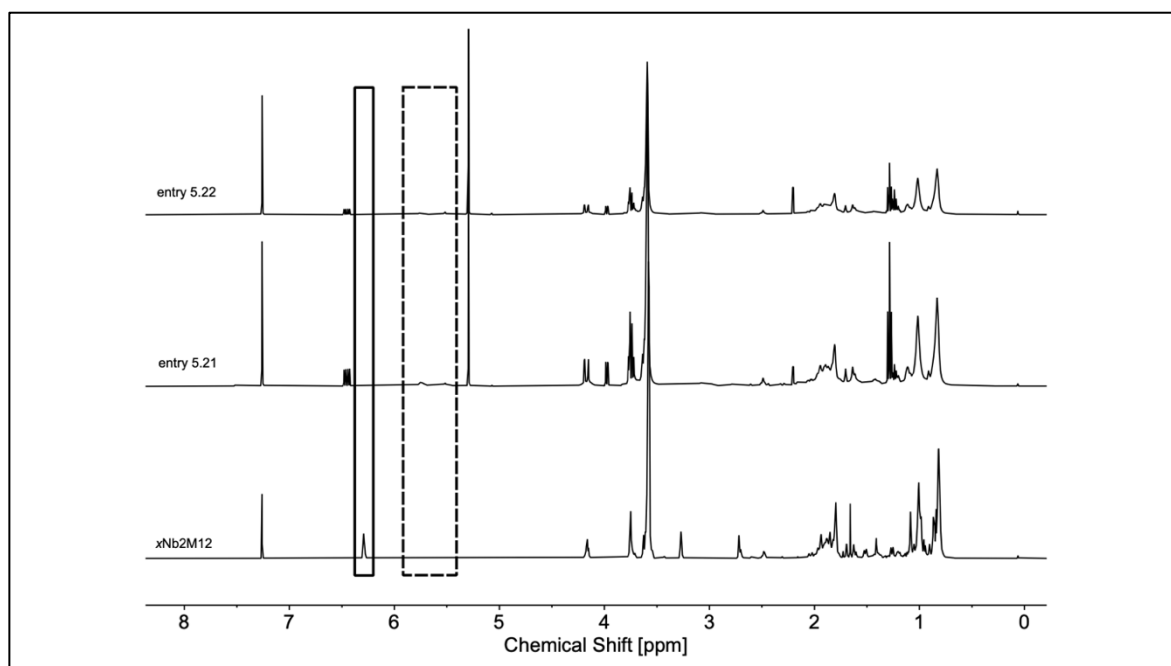


Figure S5.41. Stacked ¹H NMR spectra of entries 5.21 and 5.22 after quenching with EVE in CDCl₃ (400 MHz) and the ¹H NMR spectrum of the corresponding monomer in CDCl₃ (500 MHz). Boxes: norbornene olefinic moiety (solid); poly(norbornene) olefinic backbone (dashed).

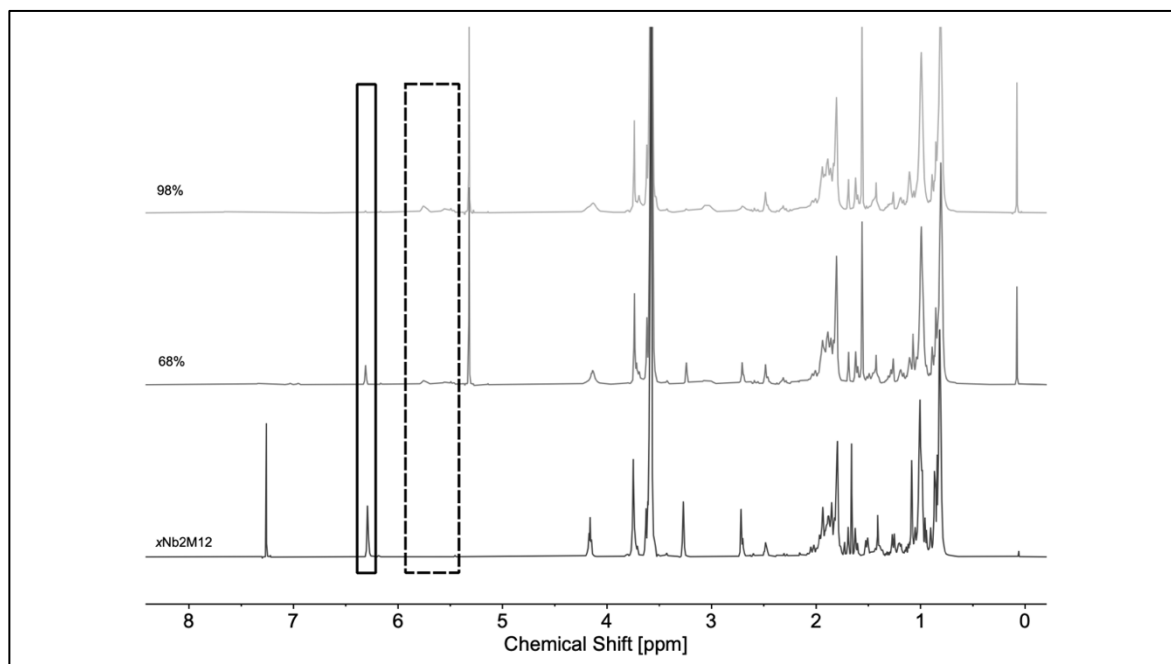


Figure S5.42. Representative stacked ¹H NMR spectra of the ROMP of **xNb2M12** (entry 5.23) in CD₂Cl₂ (500 MHz) and the ¹H NMR spectrum of the corresponding monomer in CDCl₃ (500 MHz). Boxes: norbornene olefinic moiety (solid); poly(norbornene) olefinic backbone (dashed).

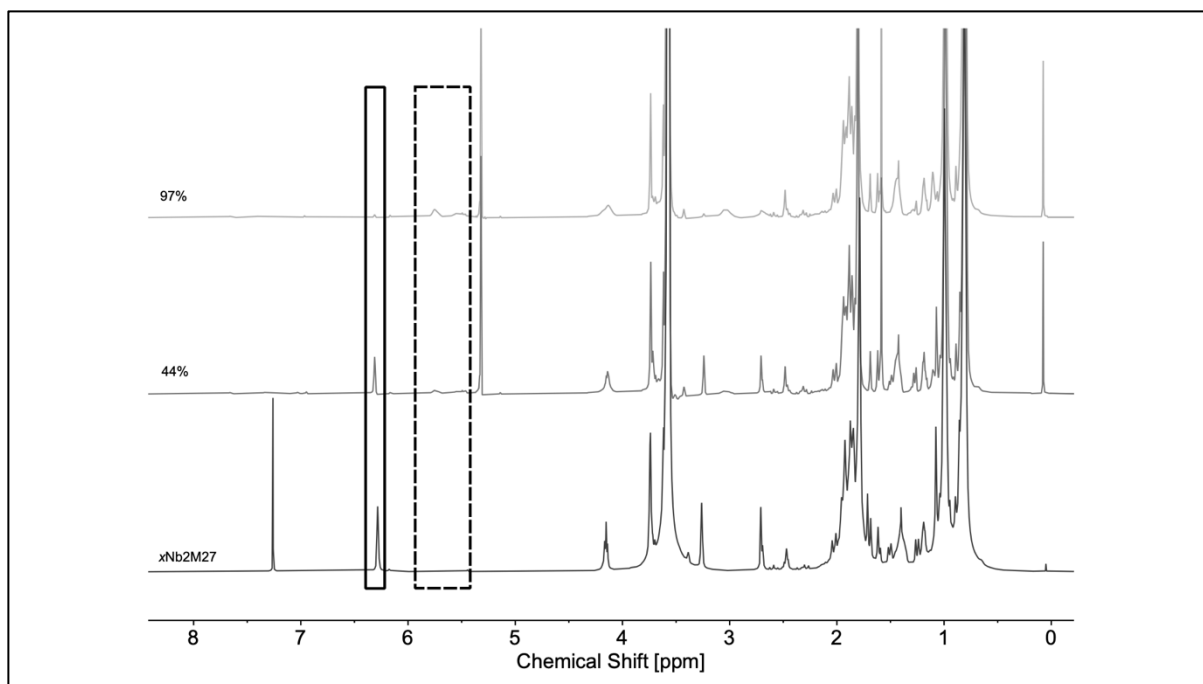


Figure S5.43. Representative stacked ¹H NMR spectra of the ROMP of **xNb2M27** (entry 5.24) in CD₂Cl₂ (500 MHz) and the ¹H NMR spectrum of the corresponding monomer in CDCl₃ (500 MHz). Boxes: norbornene olefinic moiety (solid); poly(norbornene) olefinic backbone (dashed).

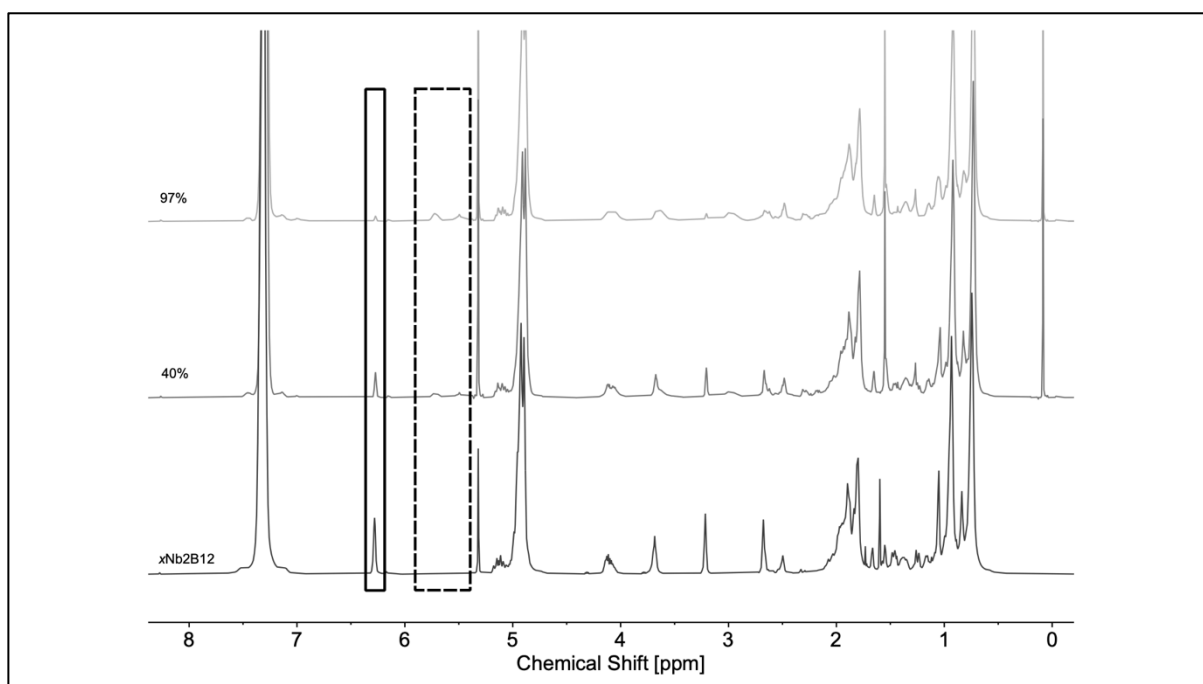


Figure S5.44. Representative stacked ¹H NMR spectra of the ROMP of **xNb2B12** (entry 5.25) and the ¹H NMR spectrum of the corresponding monomer in CD₂Cl₂ (500 MHz). Boxes: norbornene olefinic moiety (solid); poly(norbornene) olefinic backbone (dashed).

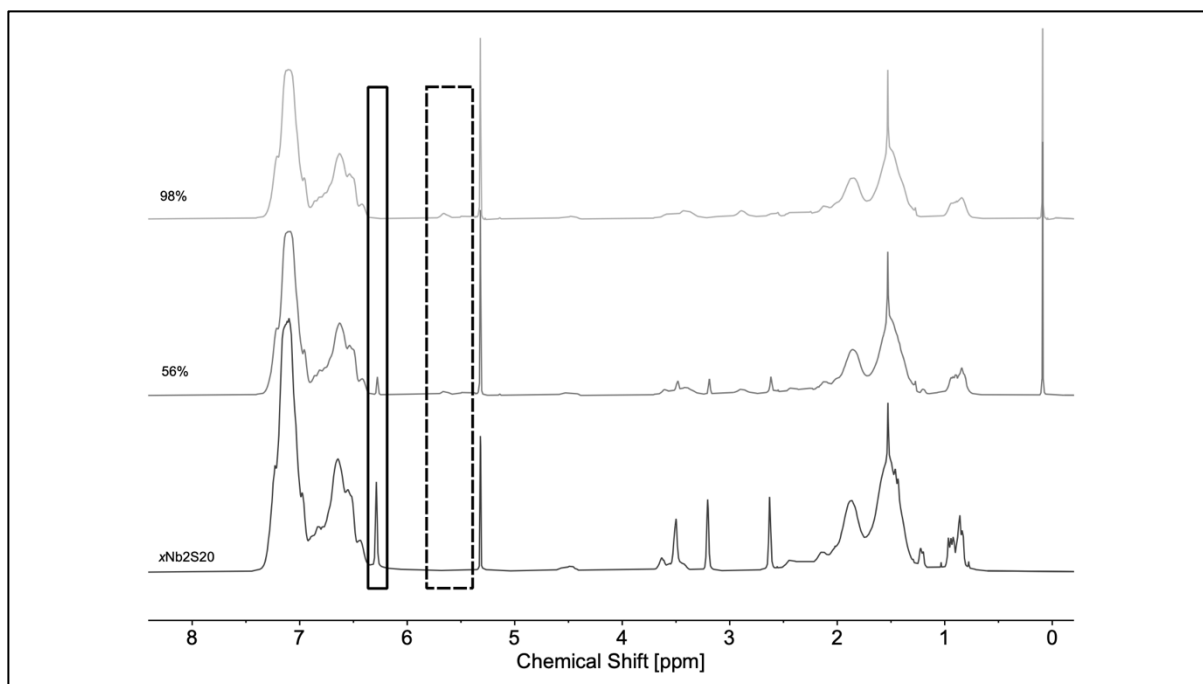


Figure S5.45. Representative stacked ^1H NMR spectra of the ROMP of **xNb2S20** (entry 5.26) and the ^1H NMR spectrum of the corresponding monomer in CD_2Cl_2 (500 MHz). Boxes: norbornene olefinic moiety (solid); poly(norbornene) olefinic backbone (dashed).

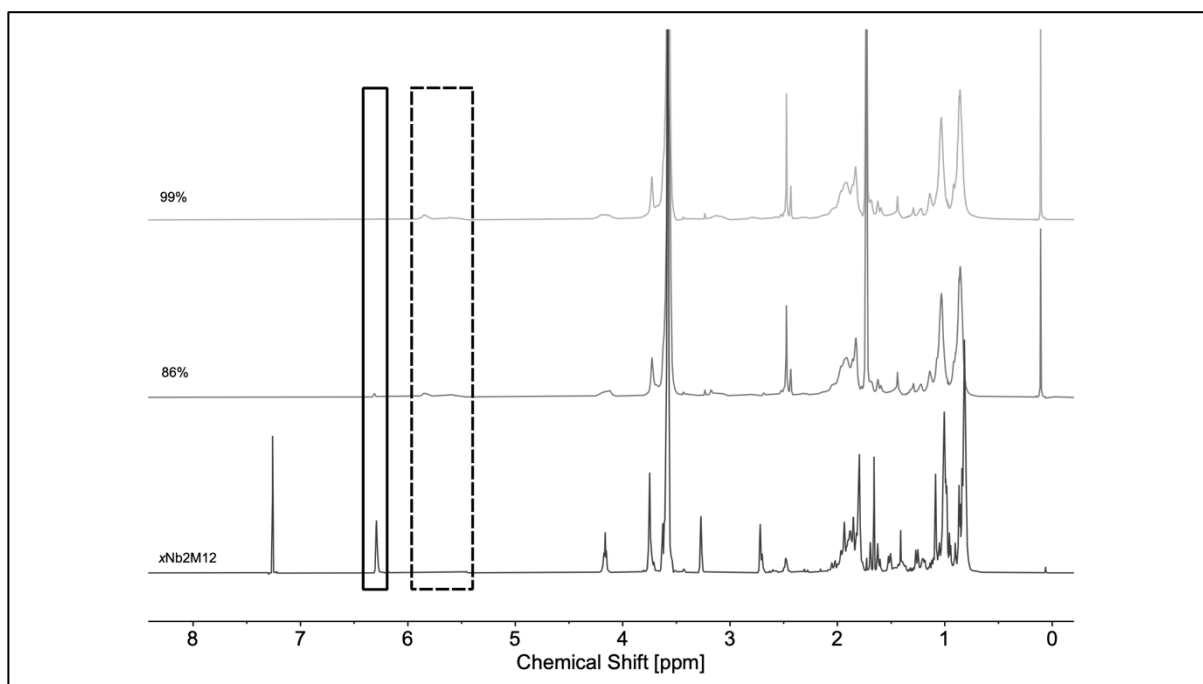


Figure S5.46. Representative stacked ^1H NMR spectra of the ROMP of **xNb2M12** (entry 5.27) in THF-d_8 (500 MHz) and the ^1H NMR spectrum of the corresponding monomer in CDCl_3 (500 MHz). Boxes: norbornene olefinic moiety (solid); poly(norbornene) olefinic backbone (dashed).

xNbHex:

The synthesis procedure was adapted from recent literature.⁹³ 1.00 eq. *cis*-5-norbornene-*exo*-2,3-dicarboxylic anhydride (0.2 mol/L), 1.50 eq. 6-amino-1-hexane and 0.20 eq. triethylamine were dissolved in toluene. The condensation was performed at 130 °C for 16 hours using a Dean-Stark apparatus to remove forming water. Then, the solvent was removed under reduced pressure. The crude products were dissolved in DCM and washed with aqueous hydrochloric acid (0.1 mol/L) twice and then with brine. The organic phase was dried over magnesium sulfate and the solvent was removed under reduced pressure. The product was obtained a colorless viscous liquid in yield of 99%.

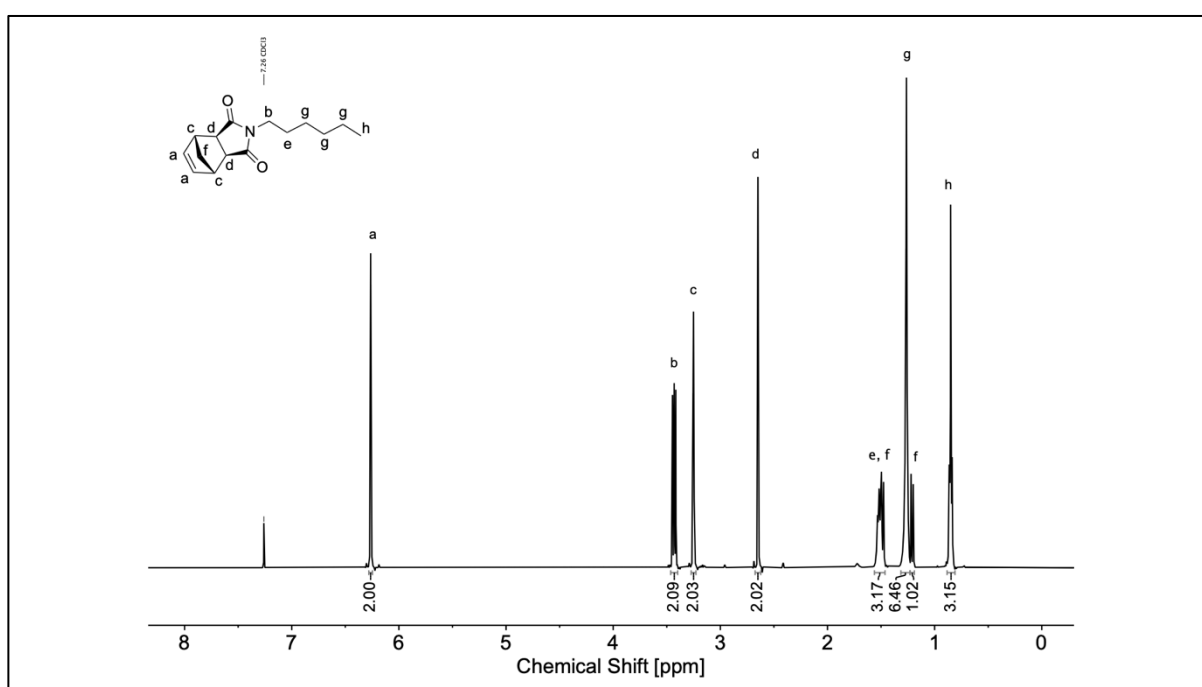


Figure S5.47. ¹H NMR spectrum of **xNbHex**.

¹H NMR: (500 MHz, CDCl₃, δ): 6.26 (t, *J* = 1.9 Hz, 2H; CH=CH, ^a), 3.46 - 3.40 (m, 2H; N-CH₂, ^b), 3.27 - 3.23 (m, 2H; =CH-CH, ^c), 2.65 (d, *J* = 1.4 Hz, 2H; =CH-CH-CH, ^d), 1.56 - 1.48 (m, 2H; N-CH₂-CH₂, ^e), 1.51 - 1.18 (m, 2H; CH₂ bridge, ^f), 1.33 - 1.23 (m, 6H; CH₂, ^g), 0.88 - 0.81 (m, 3H; CH₃, ^h).

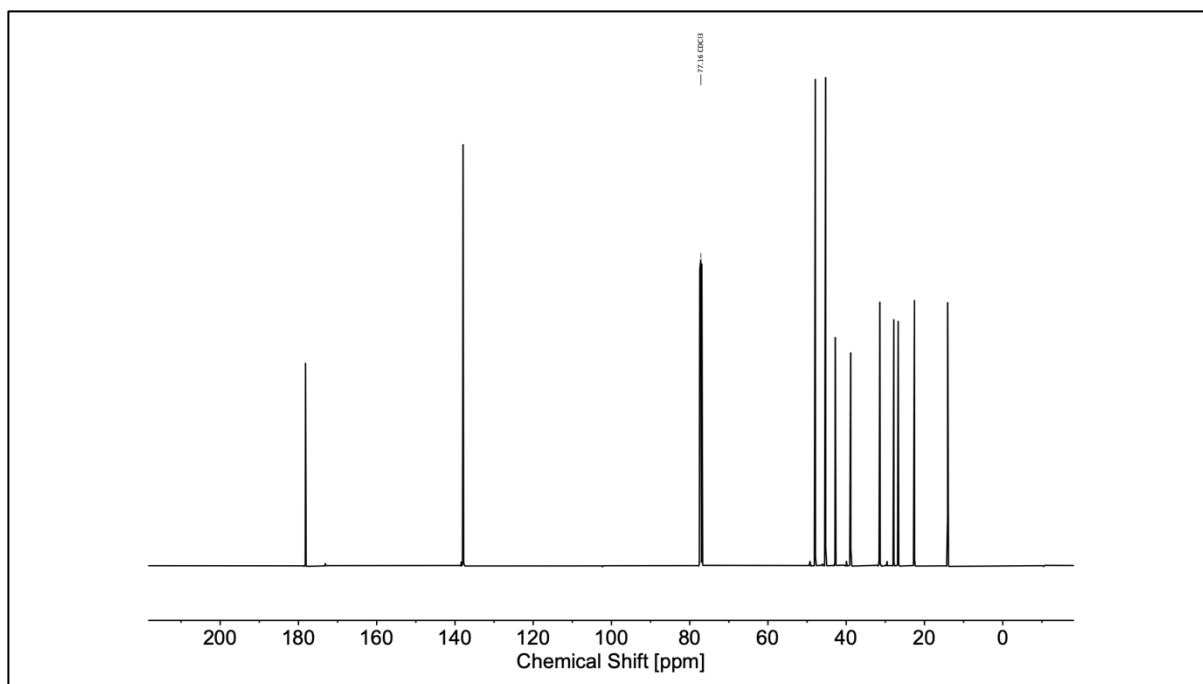


Figure S5.48. ^{13}C NMR spectrum of **xNbHex**.

^{13}C NMR: (126 MHz, CDCl_3 , δ): 178.20, 137.93, 47.90, 45.27, 42.81, 38.86, 31.41, 27.83, 26.72, 22.57, 14.08.

IR (ATR platinum diamond): $\nu / \text{cm}^{-1} = 2954$ (w), 2931 (w), 2871 (w), 2859 (w), 1769 (w), 1693 (vs), 1460 (w), 1436 (w), 1395 (m), 1368 (m), 1343 (m), 1327 (w), 1286 (w), 1232 (w), 1216 (w), 1174 (m), 1140 (m), 1103 (vw), 1033 (vw), 1016 (w), 985 (w), 884 (w), 864 (vw), 812 (w), 800 (w), 778 (w), 755 (vw), 720 (m), 691 (vw), 662 (w), 642 (m), 615 (w), 601 (vw), 453 (vw), 428 (w), 401 (w).

HRMS (ESI-MS) m/z : $[\text{M}+\text{H}]^+$ calc. for $\text{C}_{15}\text{H}_{22}\text{NO}_2$, 248.1645, found: 248.1645.

General iterative ROMP procedure (entries 5.28 – 5.37):

An ampoule equipped with a J Young tap and a stirring bar was evacuated and purged with argon three times. Subsequently, the desired amount of the first monomer and Grubbs-type catalyst were each dissolved in degassed DCM and transferred to the ampoule under an argon flow, initiating the polymerization. After complete conversion of the first monomer, a sample was withdrawn and quenched by adding an excess of ethyl vinyl ether. Then, the second monomer was dissolved in degassed DCM and transferred to the ampoule under an argon flow, initiating the chain-extension. This procedure was repeated depending on the desired number of introduced blocks. The copolymerization was carried out at ambient

temperature under an argon atmosphere and was quenched after reaching the desired number of blocks by adding an excess of ethyl vinyl ether.

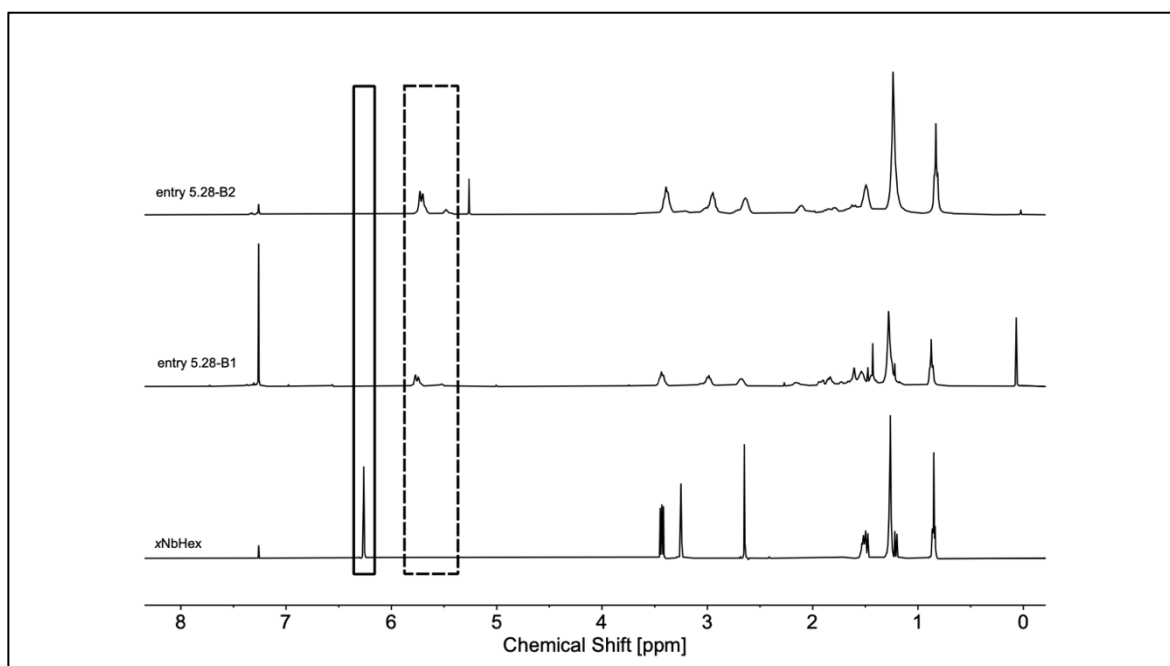


Figure S5.49. Stacked ^1H NMR spectra of the homopolymer and the diblock of entry 5.28 after quenching with EVE in CDCl_3 (400 MHz) and the ^1H NMR spectrum of the corresponding monomer in CDCl_3 (500 MHz). Boxes: norbornene olefinic moiety (solid); poly(norbornene) olefinic backbone (dashed).

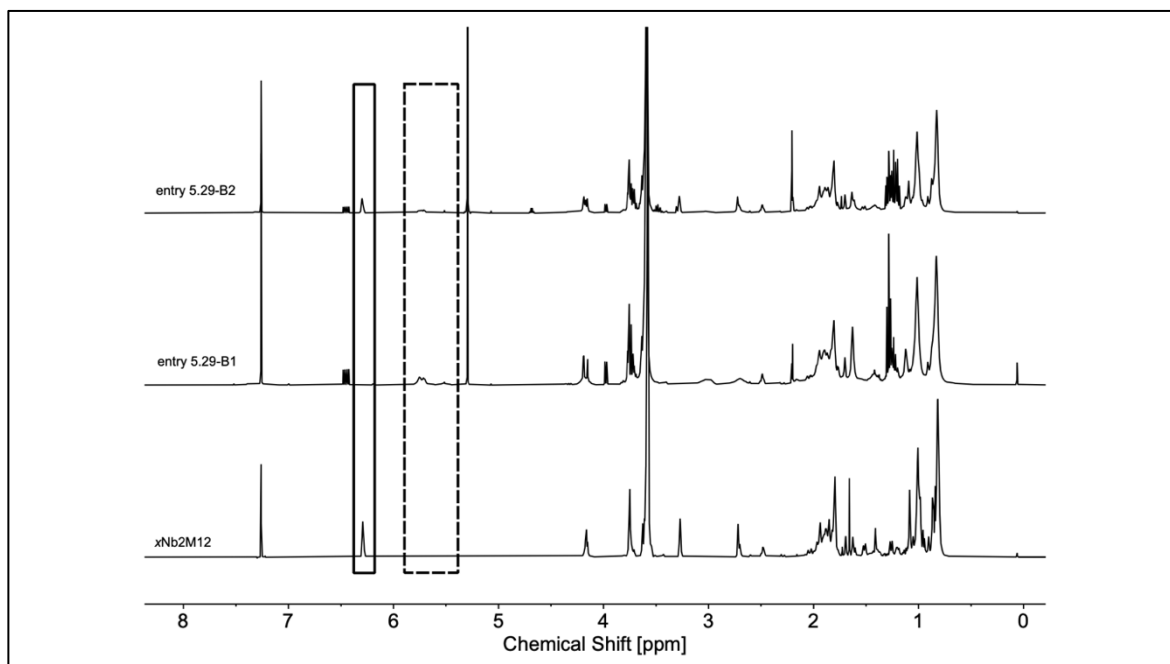


Figure S5.50. Stacked ^1H NMR spectra of the homopolymer and failed re-initiation of entry 5.29 after quenching with EVE in CDCl_3 (400 MHz) and the ^1H NMR spectrum of the corresponding monomer in CDCl_3 (500 MHz). Boxes: norbornene olefinic moiety (solid); poly(norbornene) olefinic backbone (dashed).

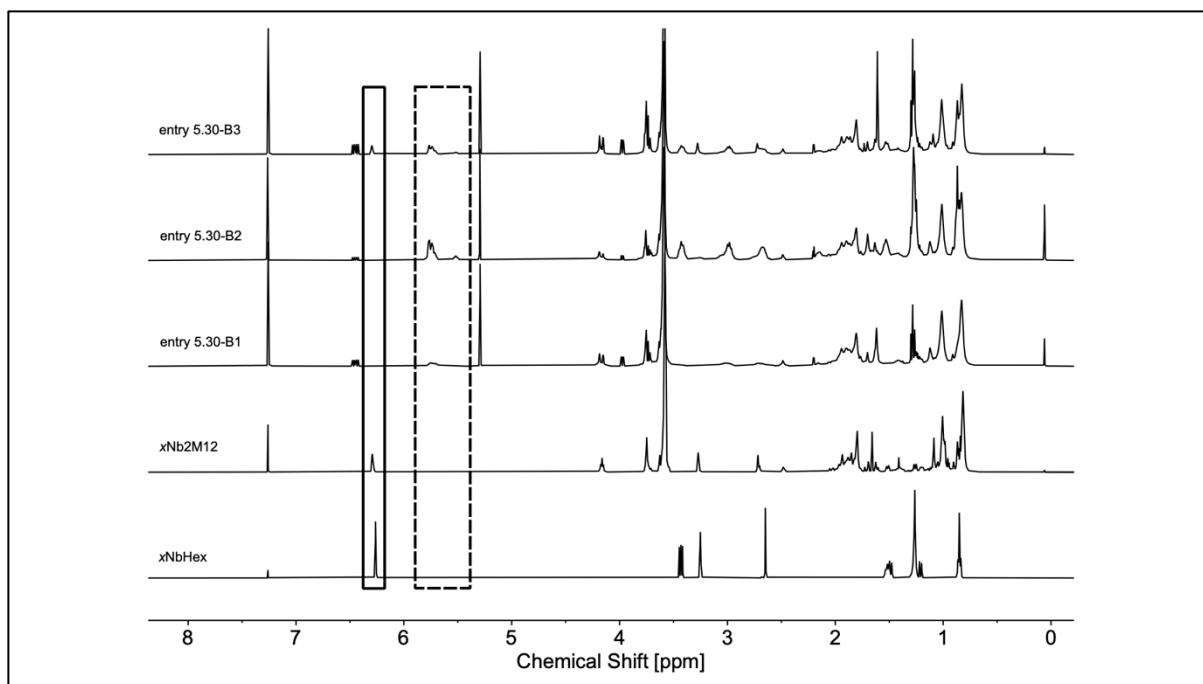


Figure S5.51. Stacked ^1H NMR spectra of the homopolymer and the diblock and failed second re-initiation of entry 5.30 after quenching with EVE in CDCl_3 (400 MHz) and the ^1H NMR spectra of the corresponding monomers in CDCl_3 (500 MHz). Boxes: norbornene olefinic moiety (solid); poly(norbornene) olefinic backbone (dashed).

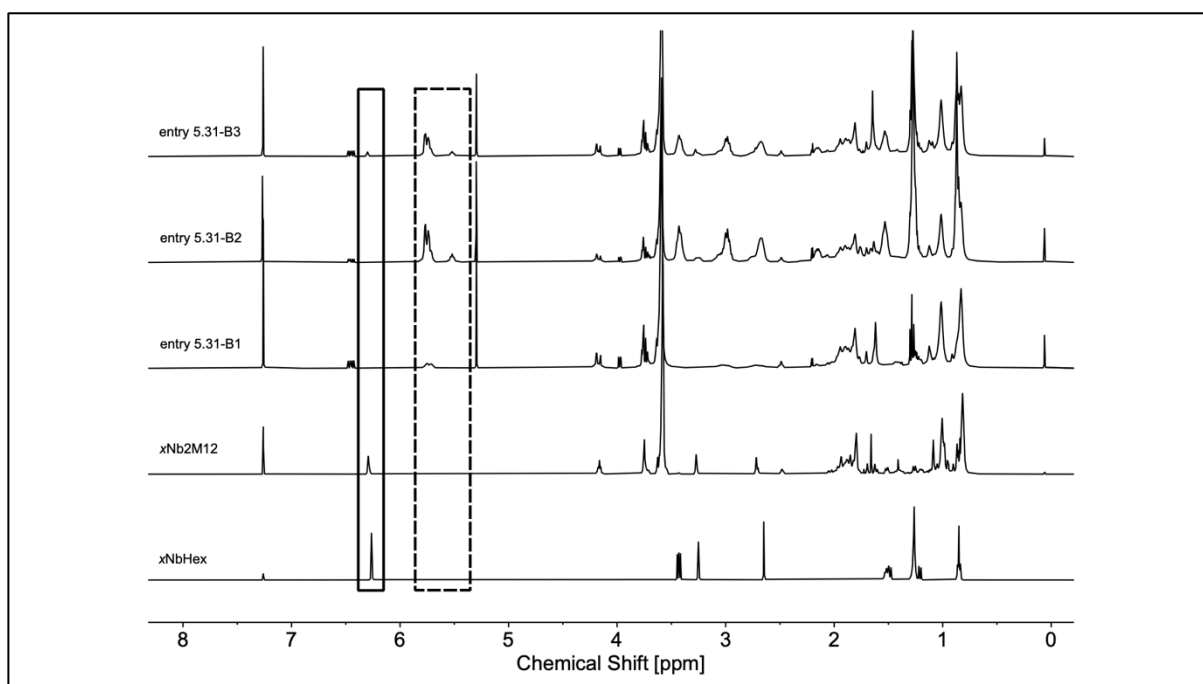


Figure S5.52. Stacked ^1H NMR spectra of the homopolymer and the diblock and failed second re-initiation of entry 5.31 after quenching with EVE in CDCl_3 (400 MHz) and the ^1H NMR spectra of the corresponding monomers in CDCl_3 (500 MHz). Boxes: norbornene olefinic moiety (solid); poly(norbornene) olefinic backbone (dashed).

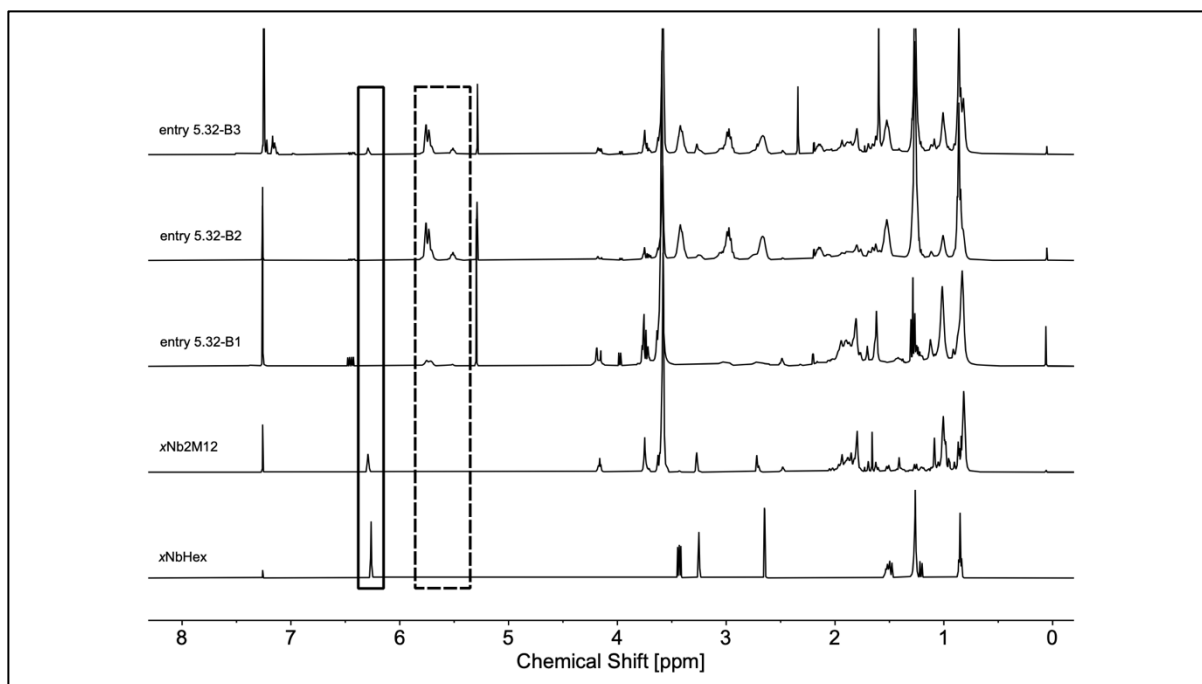


Figure S5.53. Stacked ^1H NMR spectra of the homopolymer and the diblock and failed second re-initiation of entry 5.32 after quenching with EVE in CDCl_3 (400 MHz) and the ^1H NMR spectra of the corresponding monomers in CDCl_3 (500 MHz). Boxes: norbornene olefinic moiety (solid); poly(norbornene) olefinic backbone (dashed).

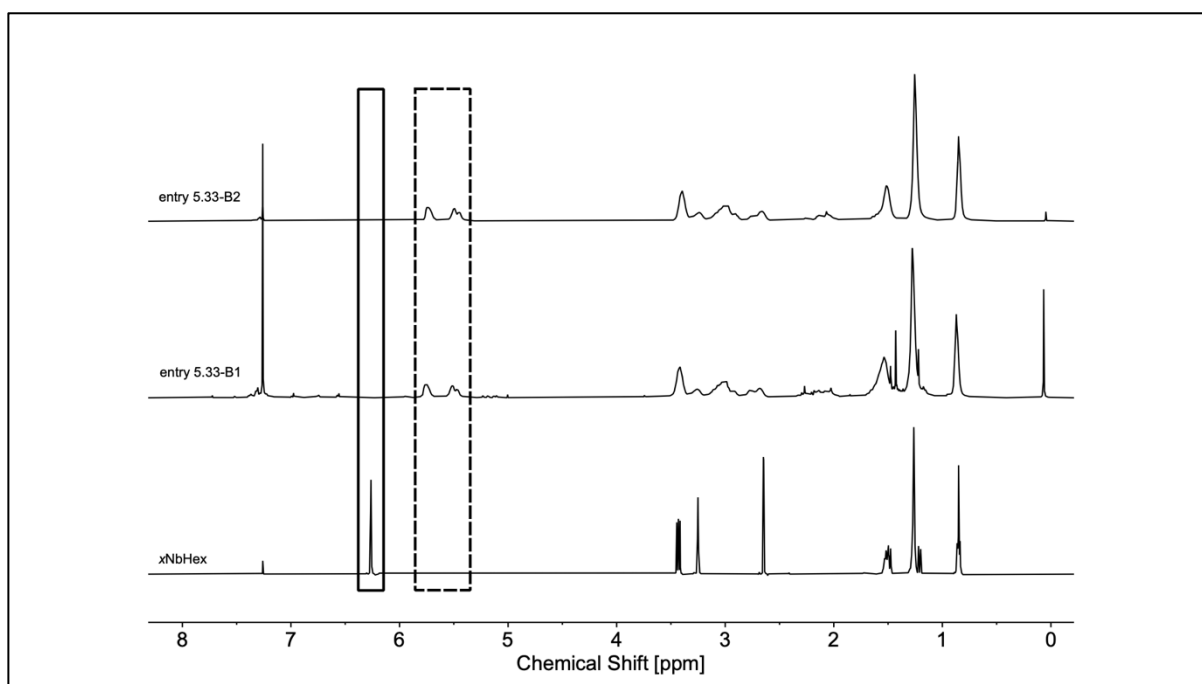


Figure S5.54. Stacked ^1H NMR spectra of the homopolymer and the diblock of entry 5.33 after quenching with EVE in CDCl_3 (400 MHz) and the ^1H NMR spectra of the corresponding monomer in CDCl_3 (500 MHz). Boxes: norbornene olefinic moiety (solid); poly(norbornene) olefinic backbone (dashed).

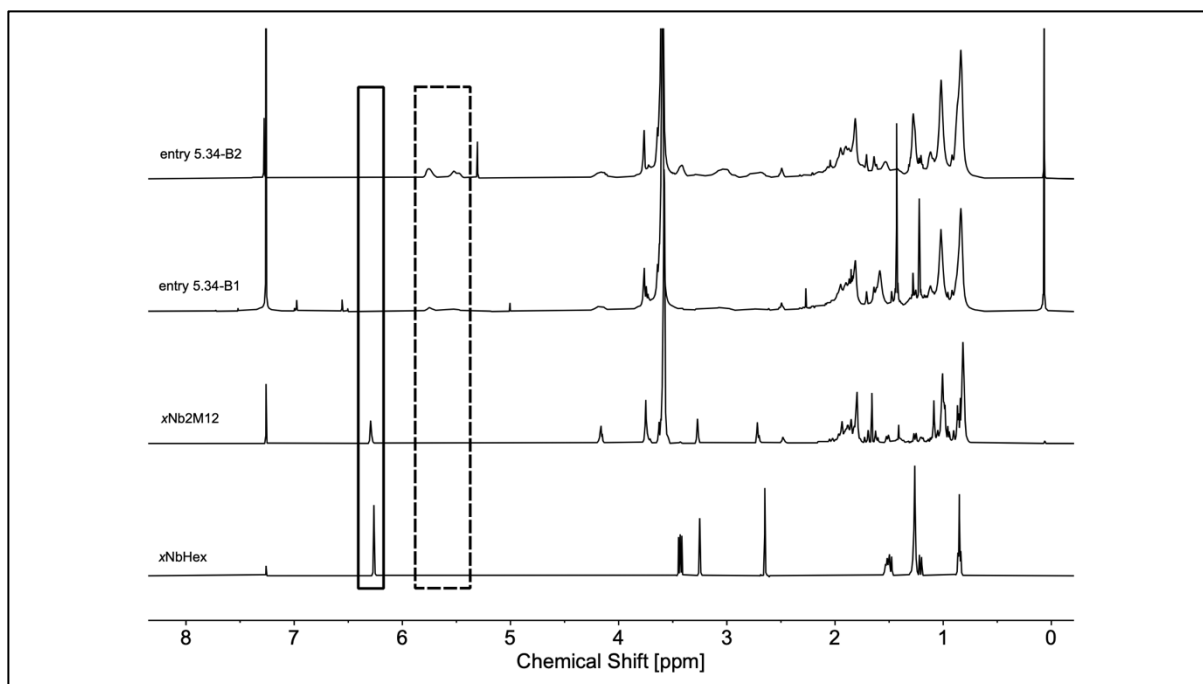


Figure S5.55. Stacked ^1H NMR spectra of the homopolymer and the diblock of entry 5.34 after quenching with EVE in CDCl_3 (400 MHz) and the ^1H NMR spectra of the corresponding monomers in CDCl_3 (500 MHz). Boxes: norbornene olefinic moiety (solid); poly(norbornene) olefinic backbone (dashed).

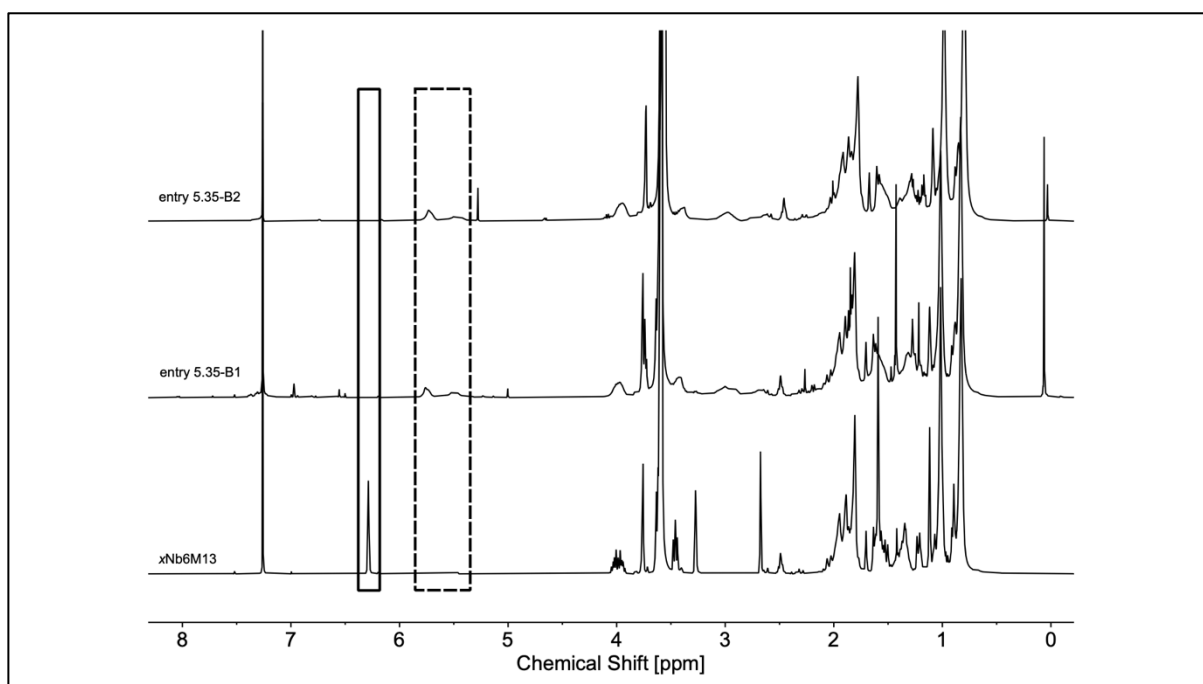


Figure S5.56. Stacked ^1H NMR spectra of the homopolymer and the diblock of entry 5.35 after quenching with EVE and the ^1H NMR spectra of the corresponding monomer in CDCl_3 (400 MHz). Boxes: norbornene olefinic moiety (solid); poly(norbornene) olefinic backbone (dashed).

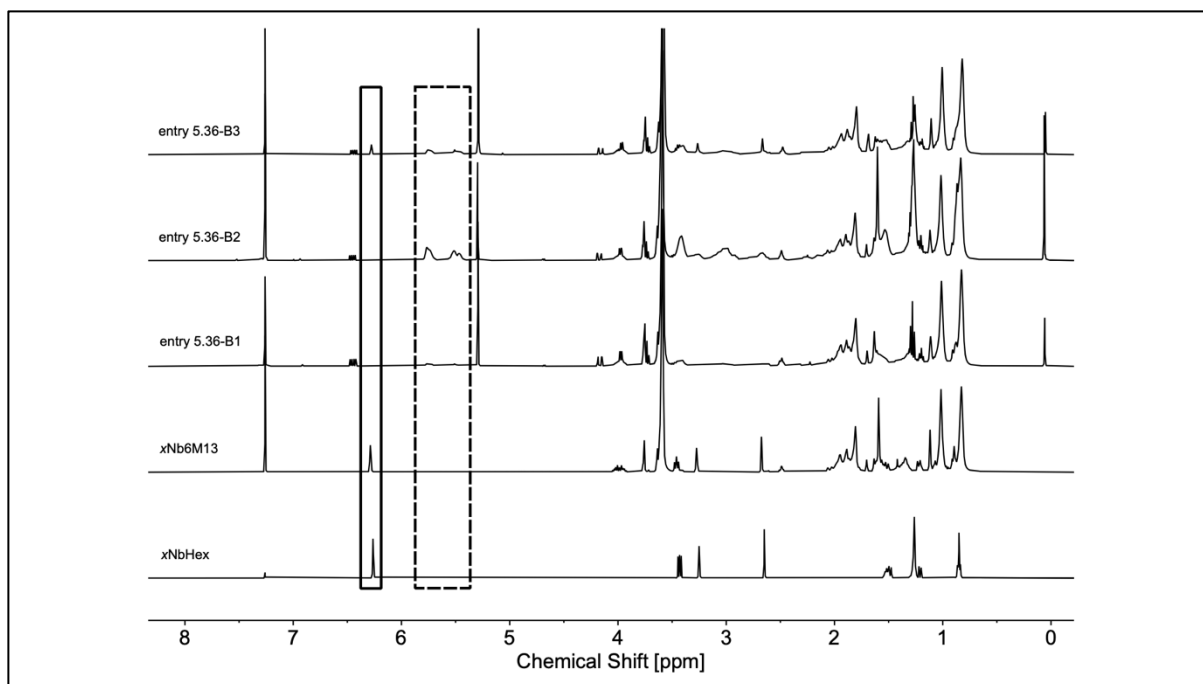


Figure S5.57. Stacked ^1H NMR spectra of the homopolymer, di-, and triblock of entry 5.36 after quenching with EVE in CDCl_3 (400 MHz) and the ^1H NMR spectra of the corresponding monomers in CDCl_3 (xNbHex: 500 MHz; xNb6M13: 400 MHz). Boxes: norbornene olefinic moiety (solid); poly(norbornene) olefinic backbone (dashed).

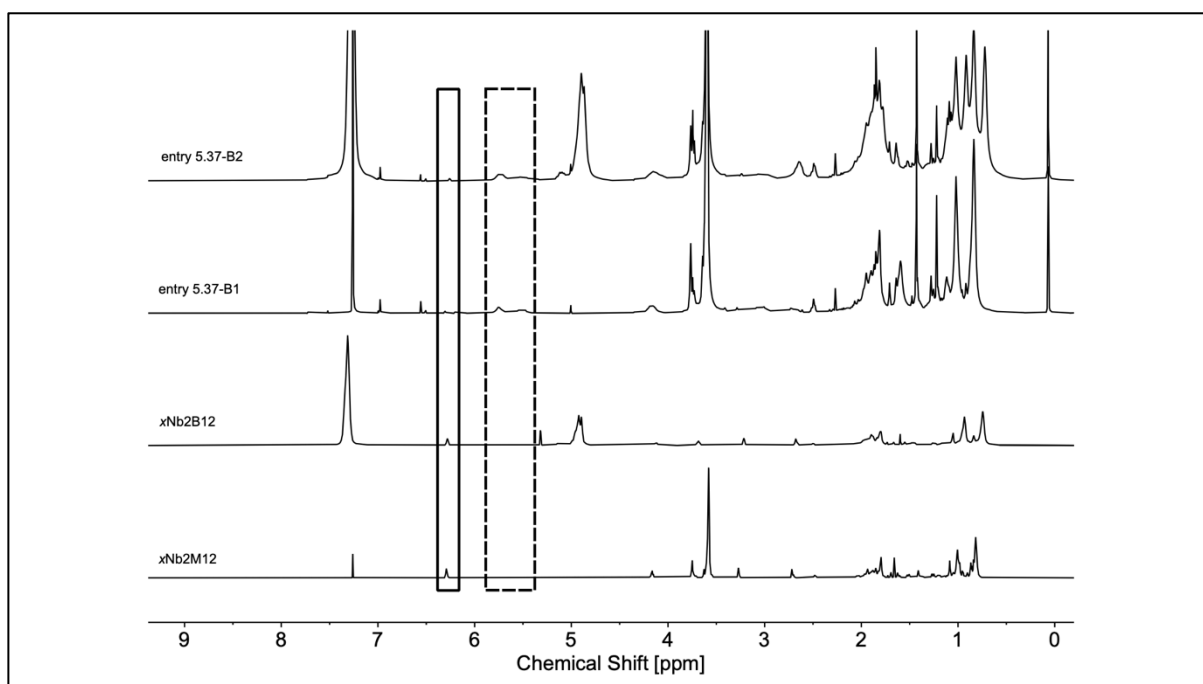


Figure S5.58. Stacked ^1H NMR spectra of the homopolymer and the diblock of entry 5.37 after quenching with EVE in CDCl_3 (400 MHz) and the ^1H NMR spectra of xNb2M12 in CDCl_3 (500 MHz) and xNb2B12 in CD_2Cl_2 (500 MHz). Boxes: norbornene olefinic moiety (solid); poly(norbornene) olefinic backbone (dashed).

General iterative ROMP procedure using dry solvents (entries 5.38 and 5.39):

Gas tight glass syringes and reusable metal needles were used to handle the reagents under argon atmosphere, whereby the metal needles and the used glassware were dried in a vacuum oven at elevated temperature overnight.

Three ampoules equipped with J Young taps and a stirring bar were evacuated and purged with argon three times. Subsequently, the desired amount of the G3 catalyst and the macromonomers was added to the argon-flushed ampoules and dried under high vacuum overnight. The compounds were dissolved in degassed dry DCM and the polymerization was initiated by transferring the solution of the first macromonomer to the ampoule with the catalyst solution under an argon flow. After complete conversion of the first macromonomer, a sample was withdrawn and quenched by adding an excess of ethyl vinyl ether. Then, the second macromonomer was transferred to the ampoule with the polymerization mixture under an argon flow, initiating the chain-extension. Entry 5.38 was performed at ambient temperature, whereas entry 5.39 was performed at $-15\text{ }^{\circ}\text{C}$, using a cryostat. Both polymerizations were carried out under an argon atmosphere and quenched after reaching the desired macromonomer conversion by adding an excess of ethyl vinyl ether.

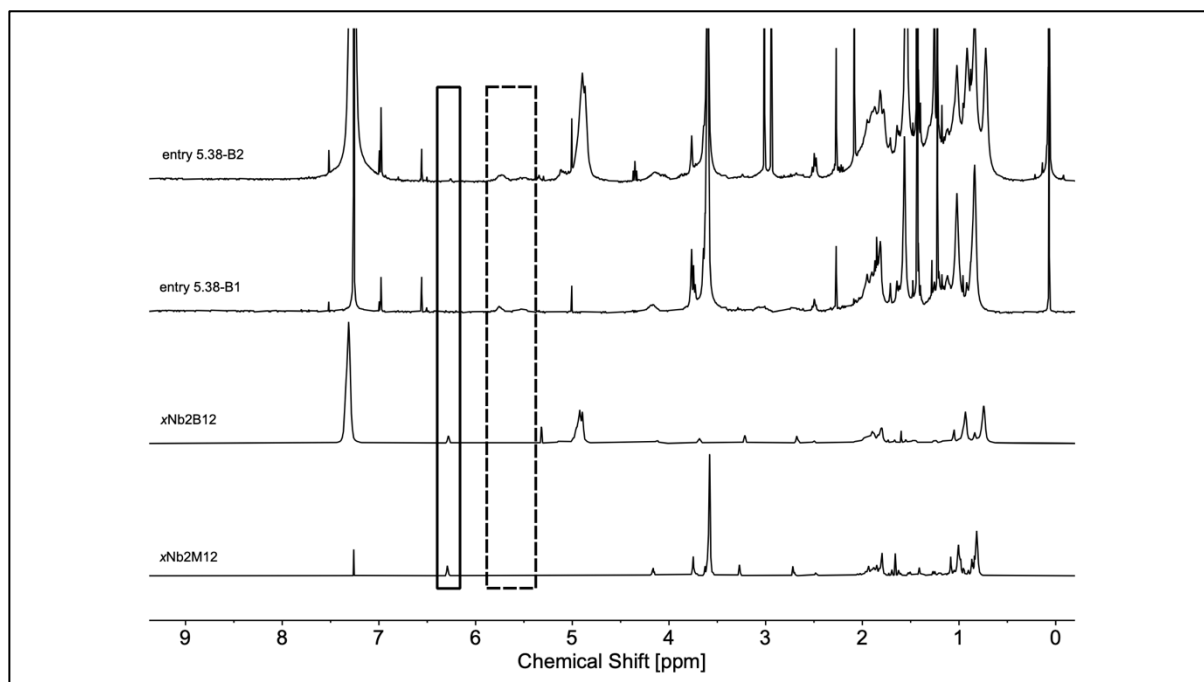


Figure S5.59. Stacked ^1H NMR spectra of the homopolymer and the diblock of entry 5.38 after quenching with EVE in CDCl_3 (400 MHz) and the ^1H NMR spectra of **xNb2M12** in CDCl_3 (500 MHz) and **xNb2B12** in CD_2Cl_2 (500 MHz). Boxes: norbornene olefinic moiety (solid); poly(norbornene) olefinic backbone (dashed).

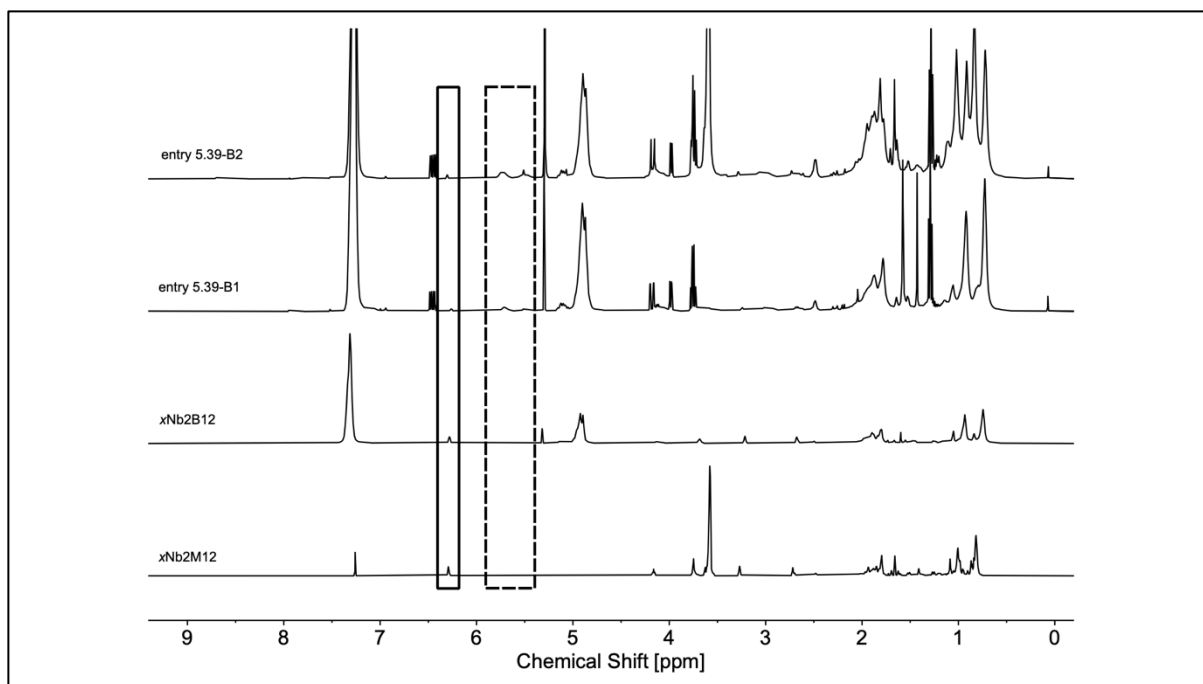


Figure S5.60. Stacked ¹H NMR spectra of the homopolymer and the diblock of entry 5.39 after quenching with EVE in CDCl₃ (400 MHz) and the ¹H NMR spectra of **xNb2M12** in CDCl₃ (500 MHz) and **xNb2B12** in CD₂Cl₂ (500 MHz). Boxes: norbornene olefinic moiety (solid); poly(norbornene) olefinic backbone (dashed).

xNbOH*:

A Schlenk flask was equipped with a stirring bar and evacuated and purged with argon three times. Then, 2.00 eq. LiAlH₄ (1 mol/L in dry THF) were added under argon to the Schlenk flask and placed into an ice bath. Then, 1.00 eq. *exo*-5-norbornene-2-carboxylic acid was dissolved in dry THF (0.5 mol/L) and added slowly. The reaction mixture was refluxed for 25 hours and cooled in an ice bath. Unreacted LiAlH₄ was quenched by adding water, aqueous sodium hydroxide solution (10 wt%) and again water. The flask was allowed to warm to ambient temperature and diluted with diethyl ether. The solid by-products were removed by filtrating through Celite[®], the filtrate was washed with brine and dried over magnesium sulfate. The solvent was removed under reduced pressure to obtain the product as a colorless viscous liquid in a yield of 81%.

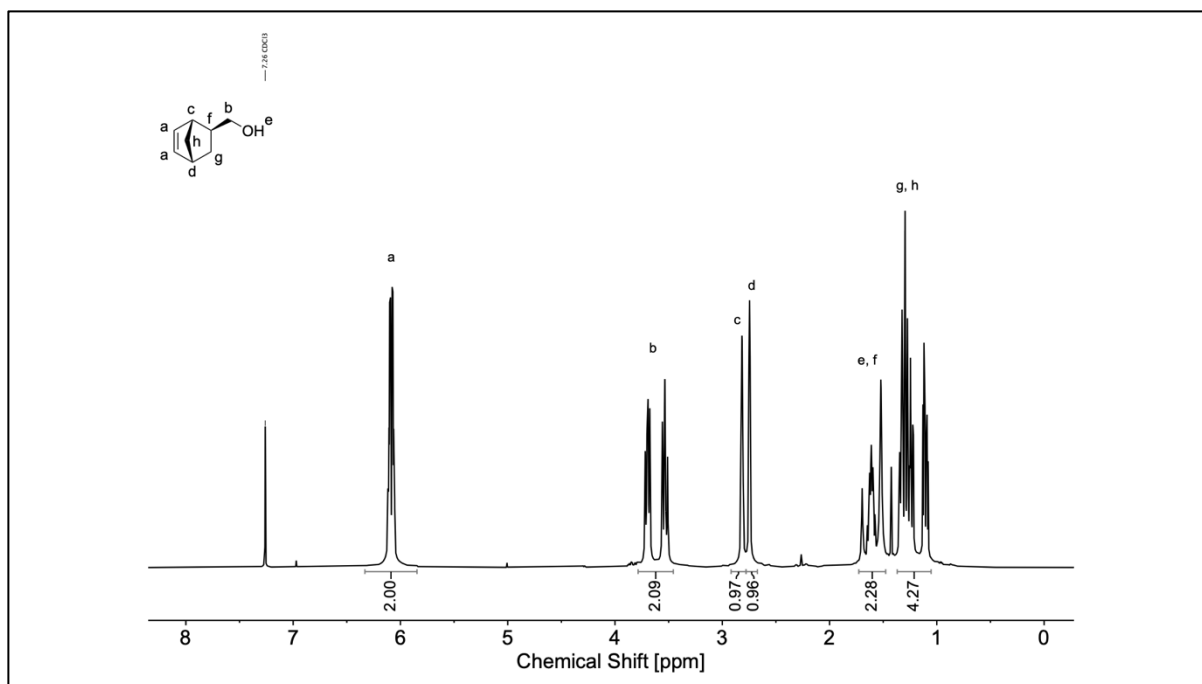


Figure S5.61. ^1H NMR spectrum of $x\text{NbOH}$ in CDCl_3 .

^1H NMR (400 MHz, CDCl_3 , δ): 6.17 - 5.99 (m, 2H; $\text{CH}=\text{CH}$, ^a), 3.77 - 3.45 (m, 2H; $\text{CH}_2\text{-OH}$, ^b), 2.90 - 2.78 (m, 1H; $=\text{CH}-\text{CH}-\text{CH}$, ^c), 2.77 - 2.70 (m, 1H; $=\text{CH}-\text{CH}-\text{CH}_2$, ^d), 1.72 - 1.48 (bs, 1H; OH, ^e), 1.66 - 1.56 (m, 1H; CH, ^f), 1.37 - 1.26 (m, 2H; CH_2 , ^g), 1.26 - 1.07 (m, 2H; CH_2 bridge, ^h).

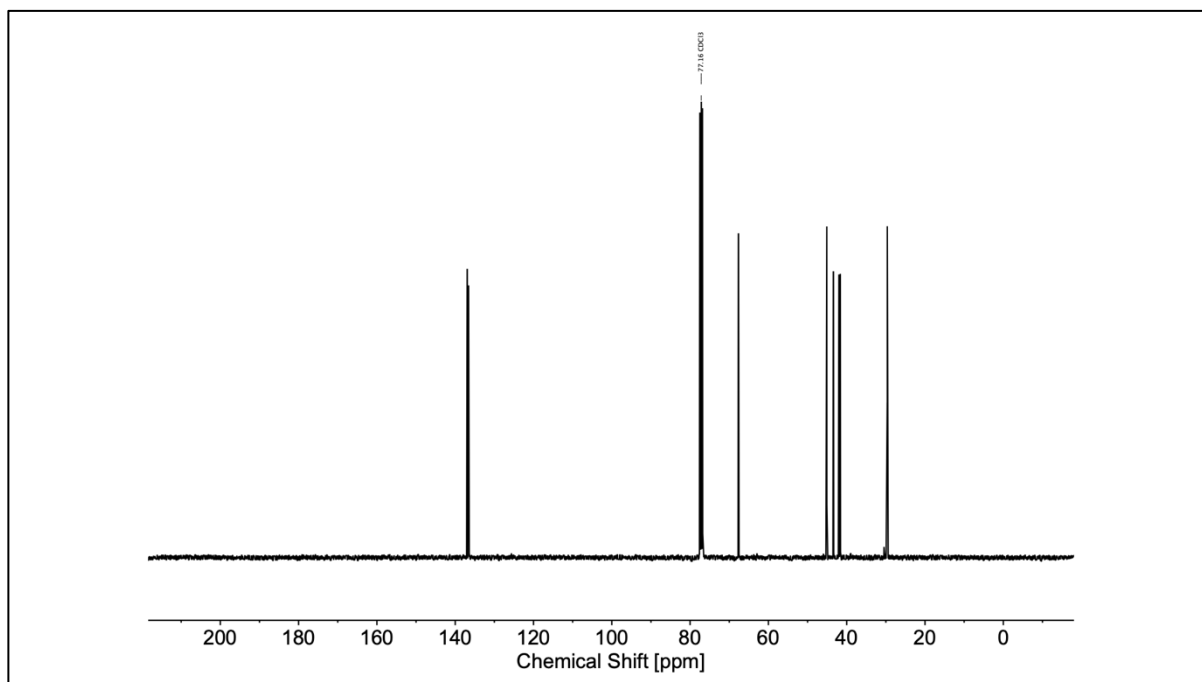


Figure S5.62. ^{13}C NMR spectrum of $x\text{NbOH}$.

^{13}C NMR (100 MHz, CDCl_3 , δ): 136.92, 136.58, 67.65, 45.08, 43.39, 41.99, 41.65, 29.64.

IR (ATR platinum diamond): $\nu / \text{cm}^{-1} = 3332$ (w), 3312 (w), 3141 (vw), 3059 (w), 2958 (m), 2929 (w), 2867 (w), 1469 (vw), 1458 (w), 1446 (w), 1423 (vw), 1415 (vw), 1372 (w), 1333 (w), 1292 (vw), 1279 (vw), 1251 (vw), 1212 (vw), 1084 (m), 1026 (vs), 979 (w), 903 (w), 860 (w), 829 (w), 788 (w), 778 (w), 755 (vw), 703 (vs), 658 (w), 619 (w), 605 (w), 525 (vw), 514 (w), 504 (w), 457 (vw), 438 (vw).

HRMS (ESI-MS) m/z : $[\text{M}+\text{H}]^+$ calc. for $\text{C}_8\text{H}_{13}\text{O}$, 125.0961, found: 125.0963.

xNbHNCHO*:

1.00 eq. ***xNbOH*** (0.4 mol/L), 1.20 eq. 11-formamidoundecanoic acid, 1.20 eq. DCC and 1.20 eq. DMAP were dissolved in DCM. The mixture was stirred for 40 hours at ambient temperature. Subsequently, the reaction mixture was filtered and washed with saturated aqueous CuSO_4 solution, water, and brine. The organic phase was separated, and the solvent was removed under reduced pressure. The crude product was further purified *via* column chromatography using a cyclohexane/ethyl acetate mixture with 2 vol% triethylamine as solvent. The product was obtained as a white waxy solid in a yield of 84%.

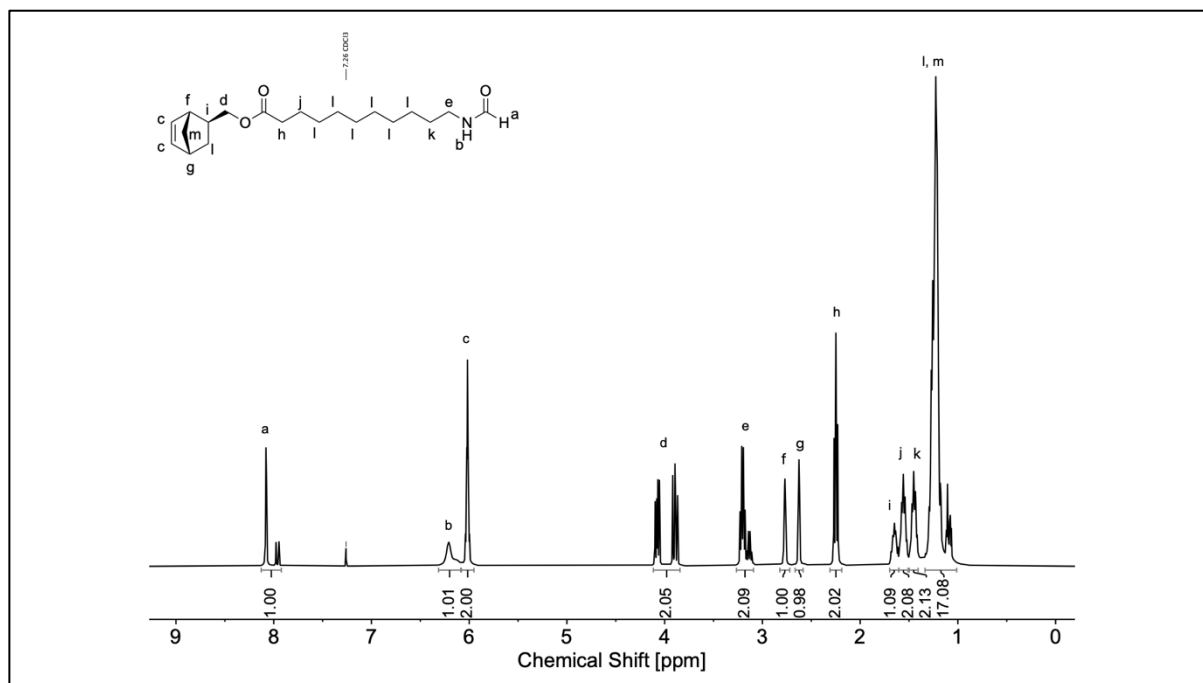


Figure S5.63. ^1H NMR spectrum of ***xNbHNCHO***.

^1H NMR (400 MHz, CDCl_3 , δ): 8.13 - 7.92 (m, 1H; CHO, ^a), 6.31 - 6.09 (bs, 1H; NHCO, ^b), 6.08 - 5.95 (m, 2H; $\text{CH}=\text{CH}$, ^c), 4.13 - 3.83 (m, 2H; $\text{CH}_2\text{-O}$, ^d), 3.27 - 3.09 (m, 2H; $\text{CH}_2\text{-NHCO}$, ^e), 2.82 - 2.71 (m, 1H; $=\text{CH-CH-CH}$, ^f), 2.70 - 2.58 (m, 1H; $=\text{CH-CH-CH}_2$, ^g), 2.25 (t, $J = 7.5$ Hz, 2H; $\text{CH}_2\text{-CO}$, ^h), 1.70 - 1.61 (m, 1H; CH, ⁱ), 1.60 - 1.51 (m, 2H; $\text{CH}_2\text{-CH}_2\text{-CO}$, ^j), 1.50 - 1.41 (m, 2H; $\text{CH}_2\text{-CH}_2\text{-NHCO}$, ^k), 1.34 - 1.14 (m, 14H; CH_2 , ^l), 1.23 - 1.06 (m, 2H; CH_2 bridge, ^m).

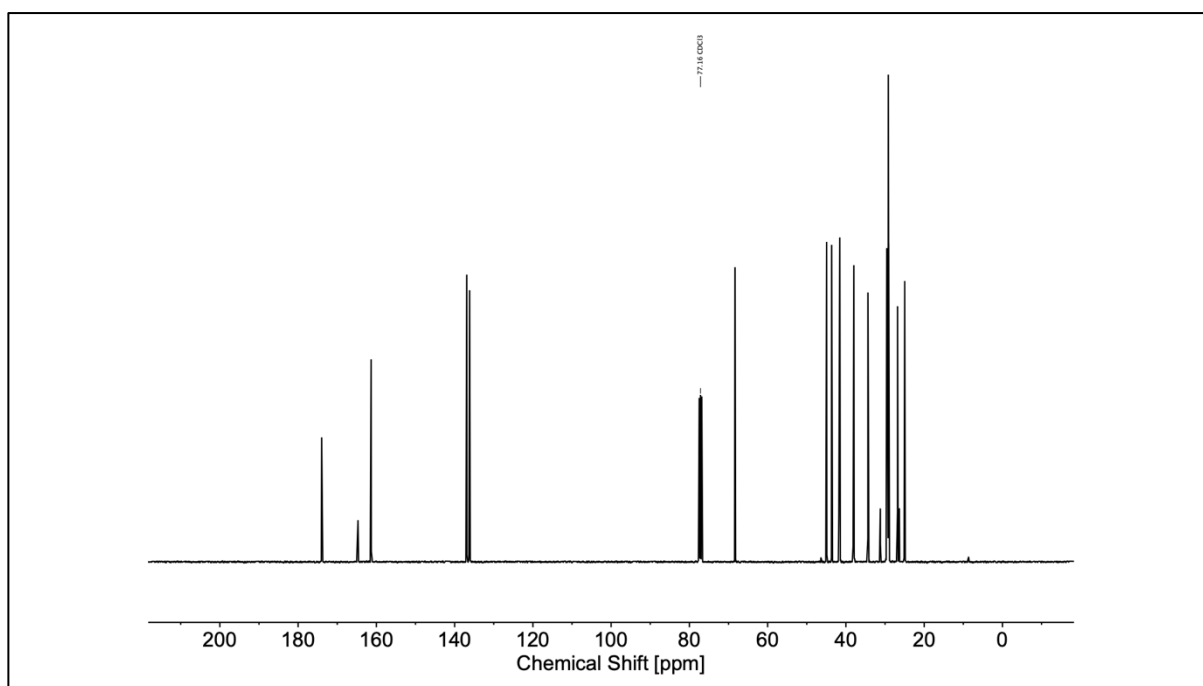


Figure S5.64. ^{13}C NMR spectrum of $x\text{NbHNCHO}$.

^{13}C NMR (100 MHz, CDCl_3 , δ): 173.95, 164.70, 161.33, 136.90, 136.17, 68.34, 44.93, 43.64, 41.81, 41.56, 38.14, 37.97, 34.37, 31.20, 29.55, 29.46, 29.39, 29.30, 29.17, 29.07, 26.81, 26.35, 24.98.

IR (ATR platinum diamond): $\nu / \text{cm}^{-1} = 3295$ (w), 3287 (w), 2925 (vs), 2855 (m), 1734 (vs), 1662 (vs), 1534 (w), 1465 (w), 1448 (w), 1419 (vw), 1384 (m), 1360 (w), 1331 (w), 1284 (w), 1236 (s), 1174 (vs), 1103 (w), 1059 (vw), 1047 (w), 1002 (w), 971 (w), 905 (w), 831 (w), 788 (w), 778 (w), 755 (w), 706 (vs), 658 (w).

HRMS (ESI-MS) m/z : $[\text{M}+\text{H}]^+$ calc. for $\text{C}_{20}\text{H}_{34}\text{NO}_3$, 336.2533, found: 336.2530.

$R_f = 0.20$ (cyclohexane/ethyl acetate, 2:1 with 2 vol% triethylamine).

xNbNC*:

The synthesis procedure was adapted from recent literature.⁵⁰⁶ 1.00 eq. **xNbHNCHO** (1 mol/L) and 3.00 eq. pyridine were dissolved in DCM. Subsequently, 1.50 eq. *p*-TsCl were added under cooling with a water bath. Afterwards, the reaction mixture was stirred for 3 hours at ambient temperature. Remaining *p*-TsCl was quenched by adding aqueous Na₂CO₃ solution (20 wt%) and stirring for 30 minutes. Then, water and DCM were added, and the organic phase was separated. The aqueous phase was extracted three times with DCM, the organic layers were combined and washed three times with water and brine. The organic phase was dried over magnesium sulfate, filtered and the solvent was removed under reduced pressure. The crude product was further purified *via* column chromatography using a cyclohexane/ethyl acetate mixture as solvent. The product was obtained as a brown viscous liquid in a yield of 95%.

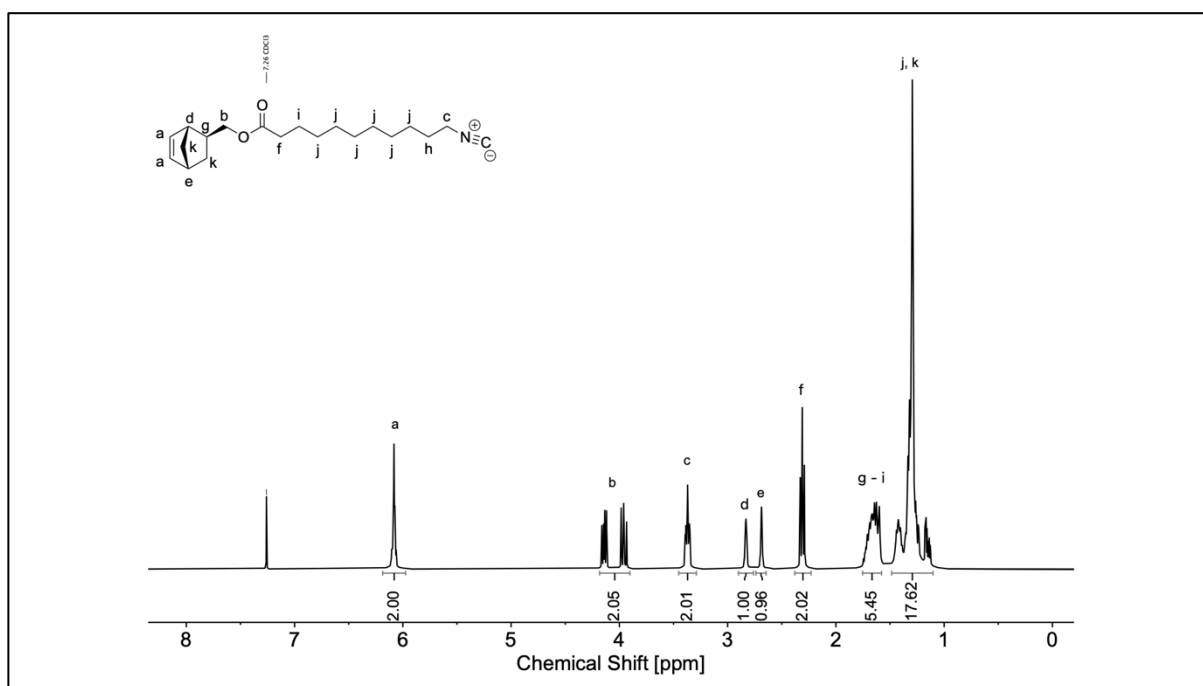


Figure S5.65. ¹H NMR spectrum of **xNbNC**.

¹H NMR (400 MHz, CDCl₃, δ): 6.19 - 5.97 (m, 2H; CH=CH, ^a), 4.18 - 3.91 (m, 2H; CH₂-O, ^b), 3.37 (tt, *J* = 6.6 Hz, 1.9 Hz, 2H; CH₂-NC, ^c), 2.91 - 2.76 (m, 1H; =CH-CH-CH, ^d), 2.75 - 2.62 (m, 1H; =CH-CH-CH₂, ^e), 2.31 (t, *J* = 7.5 Hz, 2H; CH₂-CO, ^f), 1.75 - 1.58 (m, 1H; CH, ^g), 1.75 - 1.58 (m, 2H; CH₂-CH₂-NC, ^h), 1.75 - 1.58 (m, 2H; CH₂-CH₂-CO, ⁱ), 1.48 - 1.22 (m, 14H; CH₂, ^j), 1.29 - 1.10 (m, 2H; CH₂ bridge, ^k).

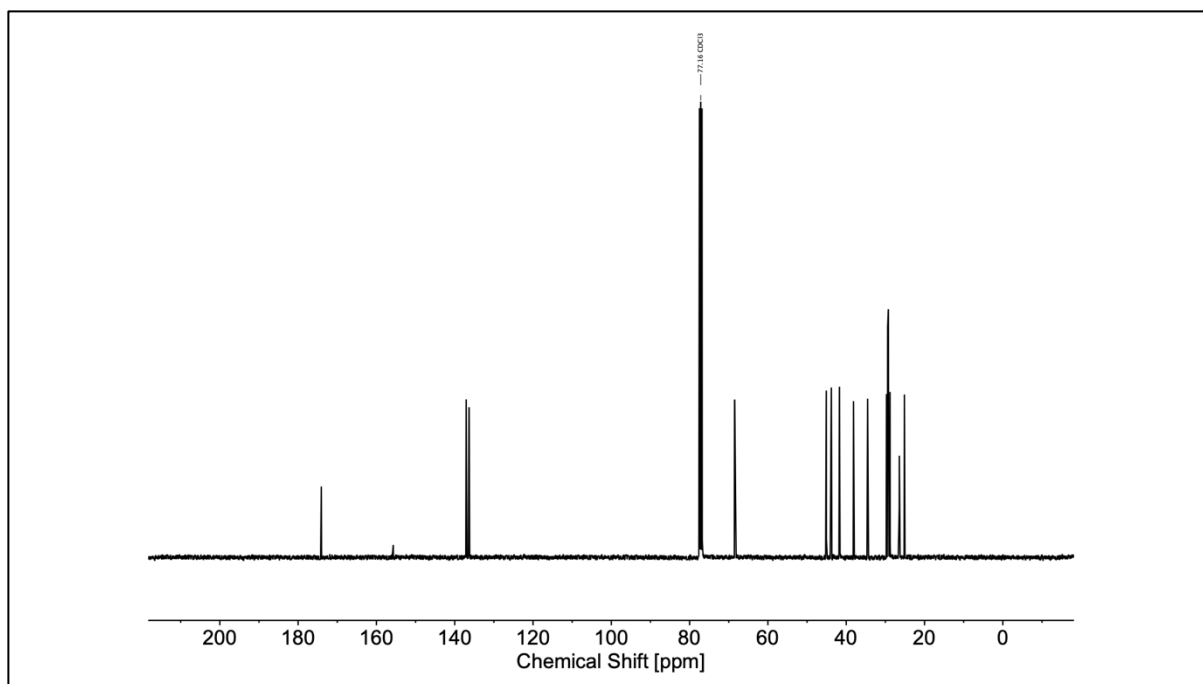


Figure S5.66. ^{13}C NMR spectrum of **xNbNC**.

^{13}C NMR (100 MHz, CDCl_3 , δ): 174.08, 155.82, 155.76, 155.71, 137.07, 136.34, 68.50, 45.09, 43.80, 41.75, 41.72, 41.69, 41.62, 38.13, 34.53, 29.72, 29.42, 29.32, 29.24, 28.80, 26.43, 25.14.

IR (ATR platinum diamond): ν / cm^{-1} = 2927 (s), 2855 (w), 2145 (w), 1732 (vs), 1465 (w), 1456 (w), 1388 (w), 1372 (w), 1358 (w), 1331 (w), 1298 (w), 1238 (s), 1174 (s), 1100 (w), 1047 (m), 1002 (w), 969 (w), 905 (w), 854 (vw), 708 (s).

HRMS (ESI-MS) m/z : $[\text{M}+\text{H}]^+$ calc. for $\text{C}_{20}\text{H}_{32}\text{NO}_2$, 318.2428, found: 318.2427.

R_f = 0.90 (cyclohexane/ethyl acetate, 1:1).

xNbBrTMS*:

1.00 eq. 2-bromo-2-methylpropionic acid (1 mol/L), 1.50 eq. 4-TMS-ethynyl-benzaldehyde and 1.50 eq. **xNbNC** were dissolved in DCM and stirred for 3 days at ambient temperature. Then, the solvent was removed under reduced pressure. The crude product was purified *via* column chromatography using a cyclohexane/ethyl acetate mixture as solvent. The product was obtained as a brown solid in a yield of 53%.

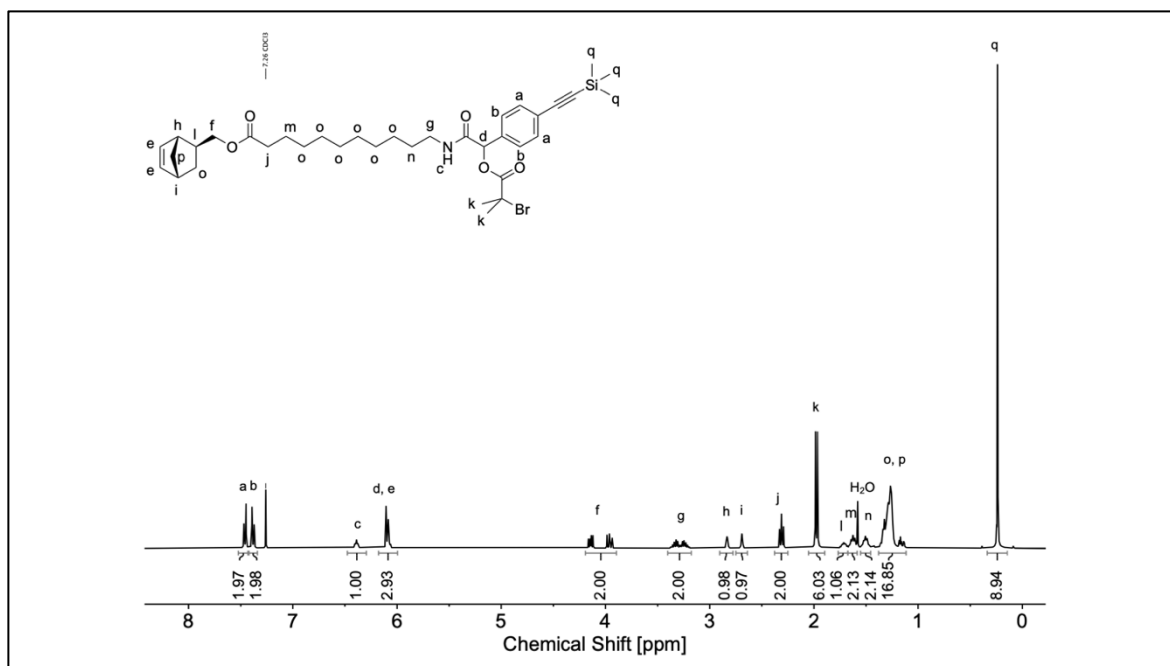


Figure S5.67. ^1H NMR spectrum of $x\text{NbBrTMS}$.

^1H NMR (400 MHz, CDCl_3 , δ): 7.46 (d, $J = 8.5$ Hz, 2H; C-C- CH_{Ar} , ^a), 7.38 (d, $J = 8.1$ Hz, 2H; CH-C- CH_{Ar} , ^b), 6.39 (bs, 1H; CONH, ^c), 6.10 (s, 1H; CH, ^d), 6.09 - 6.05 (m, 2H; CH=CH, ^e), 4.19 - 3.90 (m, 2H; $\text{CH}_2\text{-O}$, ^f), 3.40 - 3.17 (m, 2H; $\text{CH}_2\text{-NHCO}$, ^g), 2.90 - 2.77 (m, 1H; =CH-CH-CH, ^h), 2.75 - 2.64 (m, 1H; =CH-CH- CH_2 , ⁱ), 2.31 (t, $J = 7.5$ Hz, 2H; $\text{CH}_2\text{-CO}$, ^j), 2.04 - 1.95 (m, 6H; C- CH_3 , ^k), 1.77 - 1.68 (m, 1H; =CH-CH-CH, ^l), 1.68 - 1.58 (m, 2H; $\text{CH}_2\text{-CH}_2\text{-CO}$, ^m), 1.55 - 1.45 (m, 2H; $\text{CH}_2\text{-CH}_2\text{-NHCO}$, ⁿ), 1.39 - 1.20 (m, 14H; CH_2 , ^o), 1.30 - 1.09 (m, 2H, CH_2 bridge, ^p), 0.24 (s, 9H; Si- CH_3 , ^q).

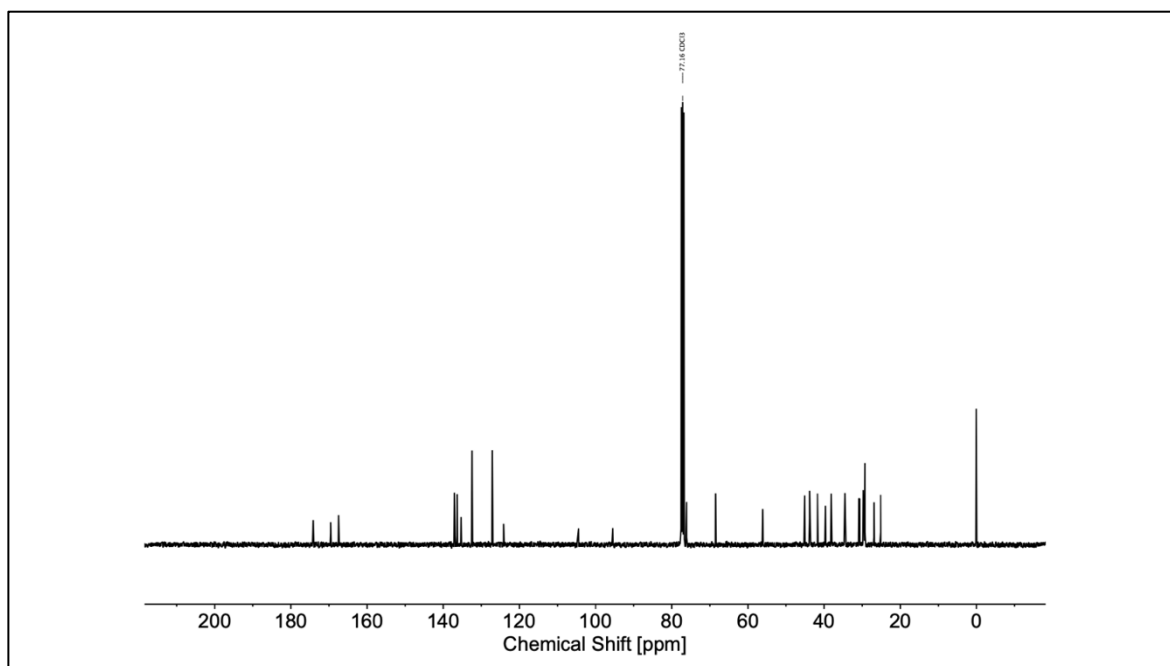


Figure S5.68. ^{13}C NMR spectrum of $x\text{NbBrTMS}$.

^{13}C NMR (100 MHz, CDCl_3 , δ): 174.07, 169.50, 167.43, 137.02, 136.31, 135.26, 132.36, 127.08, 124.08, 104.41, 95.44, 76.09, 68.46, 56.06, 45.05, 43.76, 41.68, 39.59, 38.09, 34.51, 30.82, 30.60, 29.68, 29.52, 29.44, 29.41, 29.31, 29.23, 26.86, 25.12, 0.00.

IR (ATR platinum diamond): ν / cm^{-1} = 3279 (w), 2923 (w), 2853 (w), 2156 (w), 1742 (vs), 1724 (s), 1687 (w), 1656 (vs), 1567 (m), 1499 (w), 1460 (w), 1446 (w), 1436 (w), 1374 (w), 1356 (w), 1337 (w), 1323 (w), 1300 (w), 1265 (s), 1249 (s), 1207 (w), 1189 (w), 1156 (vs), 1105 (s), 1016 (m), 940 (w), 862 (vs), 841 (vs), 810 (w), 763 (m), 732 (w), 712 (s), 642 (w), 634 (w), 551 (w), 537 (w). HRMS (ESI-MS) m/z : $[\text{M}+\text{H}]^+$ calc. for $\text{C}_{36}\text{H}_{53}\text{BrNO}_5\text{Si}$, 686.2871, found: 686.2867.

R_f = 0.20 (cyclohexane/ethyl acetate, 7:1).

$x\text{NbBrH}^*$:

A Schlenk flask equipped with a stirring bar was evacuated and purged with argon three times. The Schlenk flask was charged with 1.00 eq. $x\text{NbBrTMS}$ dissolved in dry THF (0.5 mol/L). The solution was cooled at -78°C using an isopropanol/dry ice bath, then 2.00 eq. TBAF (1 mol/L in dry THF) were added dropwise. The solution was stirred for 3 hours at -78°C . After complete conversion (monitored *via* TLC), remaining TBAF was quenched by adding water. The organic phase was separated, and the aqueous phase was extracted three times with DCM. The combined organic layers were washed with water and brine. The slightly impure product was obtained as an off-white solid in a yield of 89%.

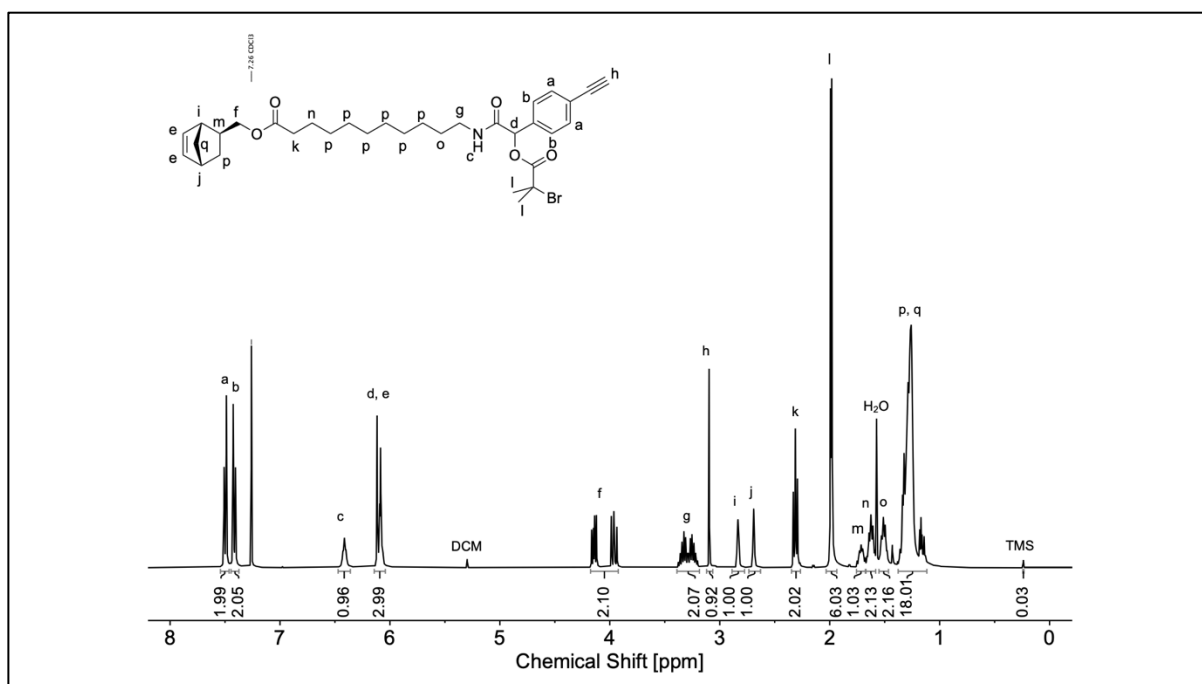


Figure S5.69. ^1H NMR spectrum of $x\text{NbBrH}$.

^1H NMR (400 MHz, CDCl_3 , δ): 7.50 (d, $J = 8.4$ Hz, 2H; C-C- CH_{Ar} , ^a), 7.42 (d, $J = 8.4$ Hz, 2H; CH-C- CH_{Ar} , ^b), 6.41i (bs, 1H; CONH, ^c), 6.12 (s, 1H; CH, ^d), 6.11 - 6.05 (m, 2H; CH=CH, ^e), 4.18 - 3.92 (m, 2H; $\text{CH}_2\text{-O}$, ^f), 3.39 - 3.18 (m, 2H; $\text{CH}_2\text{-NHCO}$, ^g), 3.10 (s, 1H; $\text{C}\equiv\text{CH}$, ^h), 2.89 - 2.77 (m, 1H; =CH-**CH**-CH, ⁱ), 2.74 - 2.63 (m, 1H; =CH-**CH**- CH_2 , ^j), 2.31 (t, $J = 7.6$ Hz, 2H; $\text{CH}_2\text{-CO}$, ^k), 2.03 - 1.94 (m, 6H; C- CH_3 , ^l), 1.76 - 1.68 (m, 1H; =CH-**CH**-**CH**, ^m), 1.67 - 1.58 (m, 2H; $\text{CH}_2\text{-CH}_2\text{-CO}$, ⁿ), 1.55 - 1.46 (m, 2H; $\text{CH}_2\text{-CH}_2\text{-NHCO}$, ^o), 1.38 - 1.19 (m, 14H; CH_2 , ^p), 1.30 - 1.11 (m, 2H, CH_2 bridge, ^q).

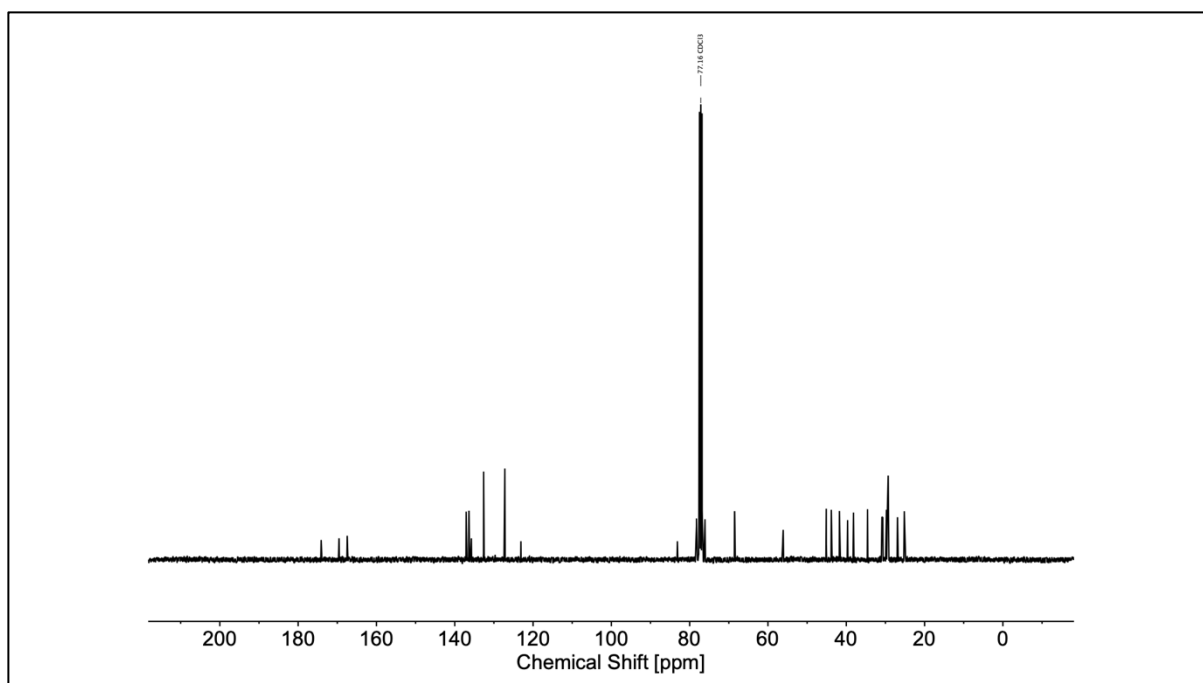


Figure S5.70. ^{13}C NMR spectrum of $x\text{NbBrH}$.

^{13}C NMR (100 MHz, CDCl_3 , δ): 173.98, 169.41, 167.32, 136.94, 136.23, 135.61, 132.47, 127.06, 122.95, 82.99, 78.11, 75.95, 68.38, 55.96, 44.97, 43.68, 41.60, 39.51, 38.01, 34.43, 30.75, 30.52, 29.60, 29.45, 29.35, 29.33, 29.23, 29.15, 26.77, 25.04.

IR (ATR platinum diamond): $\nu / \text{cm}^{-1} = 3293$ (w), 3262 (w), 2962 (w), 2925 (m), 2853 (w), 1728 (vs), 1658 (vs), 1561 (w), 1465 (w), 1448 (w), 1388 (w), 1372 (w), 1329 (w), 1304 (w), 1267 (m), 1244 (m), 1191 (w), 1179 (m), 1156 (vs), 1105 (s), 1010 (w), 905 (w), 827 (w), 706 (m), 650 (w), 636 (w).

HRMS (ESI-MS) m/z : $[\text{M}+\text{H}]^+$ calc. for $\text{C}_{33}\text{H}_{45}\text{BrNO}_5$, 614.2476, found: 614.2466.

$R_f = 0.70$ (cyclohexane/ethyl acetate, 2:1 with 2 vol% triethylamine).

PS-Br*:

The synthesis procedure was adapted from recent literature.⁴⁷² A Schlenk flask equipped with a stirring bar and an ampoule equipped with J Young tap were evacuated and purged with argon three times. The Schlenk flask was charged with 0.10 eq. PMDETA (0.017 mol/L), and 0.50 eq. copper(I) bromide dissolved in anisole. The ampoule was charged with 1.00 eq. ethyl α -bromoisobutyrate (0.4 mol/L) and 100 eq. styrene dissolved in anisole. The mixtures were degassed by three consecutive pump thaw cycles under high vacuum. Subsequently, the solution of the ampoule was transferred to the Schlenk flask *via* a degassed syringe, initiating the polymerization. The polymerization was carried out at 100 °C for 15 hours under an argon atmosphere. Afterwards, the reaction was cooled quickly to ambient temperature by immersing the flask into liquid nitrogen, exposing to air, and quenching by the addition of THF. The solution was then flushed through a plug of neutral aluminum oxide to remove the copper. Subsequently, the solvent was removed under reduced pressure. The crude product was dissolved in a small amount of THF and precipitated three times from the tenfold amount of cold methanol. The polymer was filtered, dried under high vacuum, and obtained as white solid.

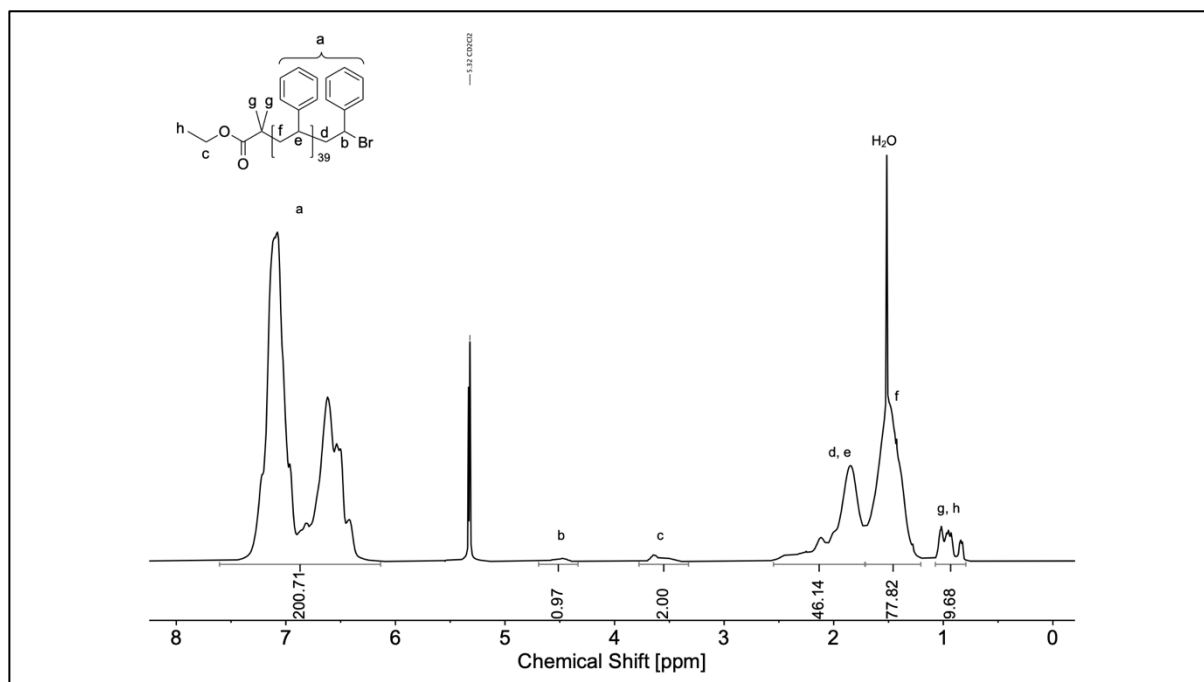


Figure S5.71. ¹H NMR spectrum of PS-Br in CD₂Cl₂ (400 MHz).

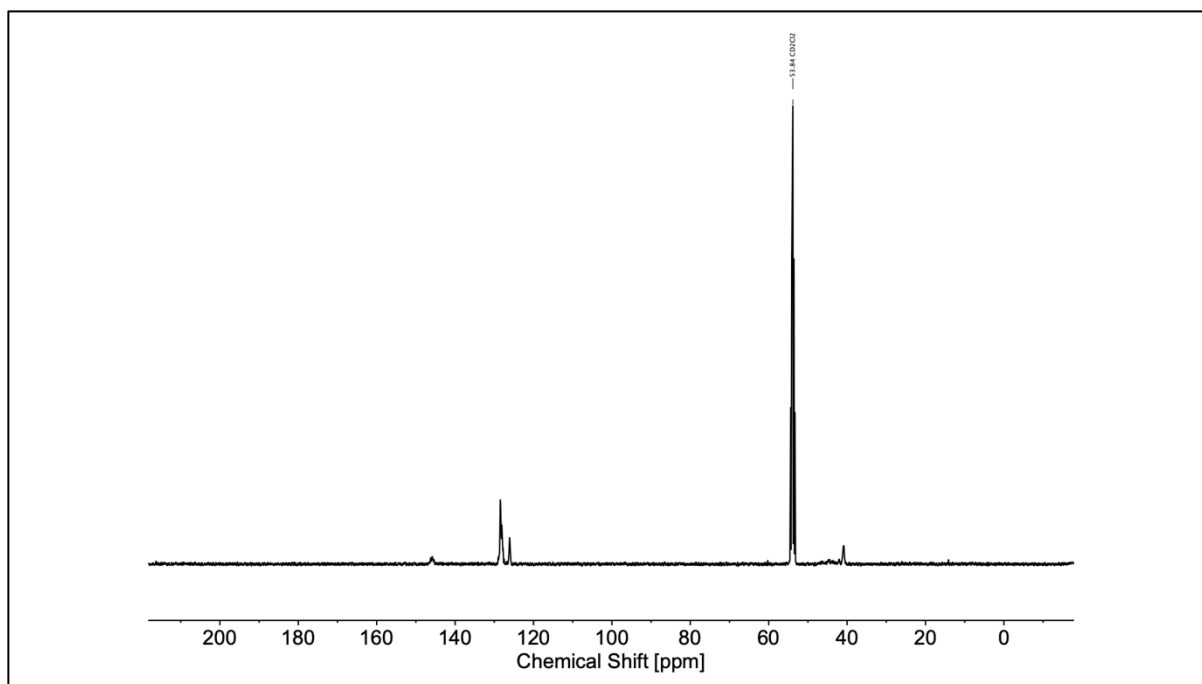


Figure S5.72. ^{13}C NMR spectrum of **PS-Br** in CD_2Cl_2 (100 MHz).

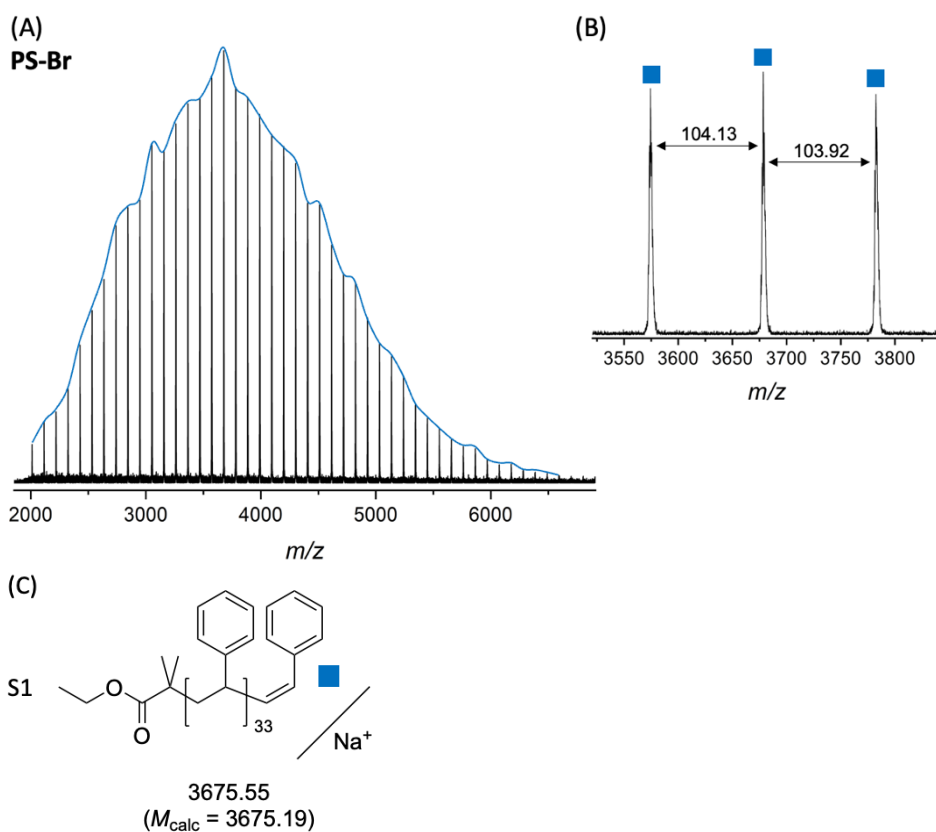


Figure S5.73. (A) MALDI-TOF spectrum (dithranol, NaTFA) of **PS-Br** with highlighted mass distribution in color to guide the eye, (B) selected region of the spectrum (3520 – 3840 m/z) with peak color coded as per the identified species, and (C) structure of **PS-Br** species (S1) and its calculated and measured monoisotopic masses.

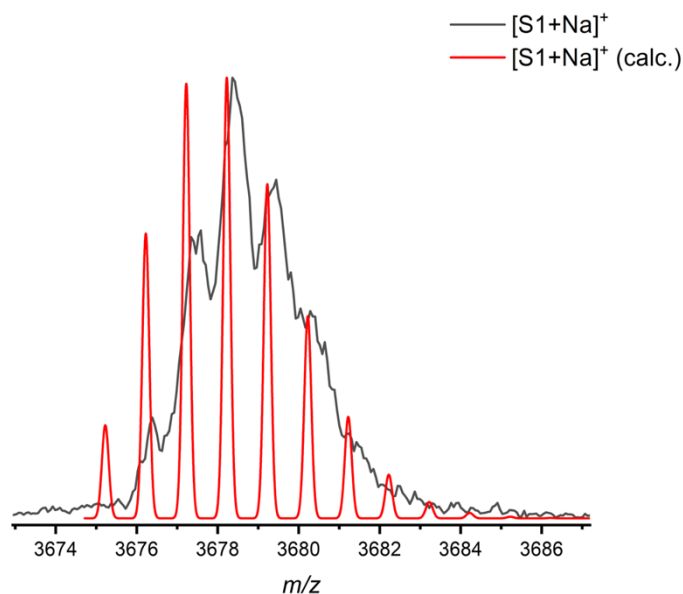


Figure S5.74. Comparison between measured and calculated isotopic patterns of **PS-Br** determined *via* MALDI-TOF MS (**Figure S5.73**) with the olefin-terminated species (S1).

PS-N₃*:

Warning: Within this synthesis procedure a potentially explosive compound (NaN₃) is used. Reading of the MSDS prior use is recommended. Handle with care and avoid contact with acids.

The synthesis procedure was adapted from recent literature.⁴⁷² A Schlenk flask equipped with a rubber septum and a stirring bar was evacuated and purged with argon three times. The flask was charged with 1.50 eq. sodium azide suspended in dry DMF (0.1 mol/L). Then, 1.00 eq. **PS-Br** were dissolved in dry DMF (0.067 mol/L) and added to the azide solution while cooling in a water bath. The reaction was carried out at ambient temperature for 20 hours under an argon atmosphere. The crude product was precipitated three times from the tenfold amount of cold methanol. The polymer was filtered, dried under high vacuum, and obtained as white solid.

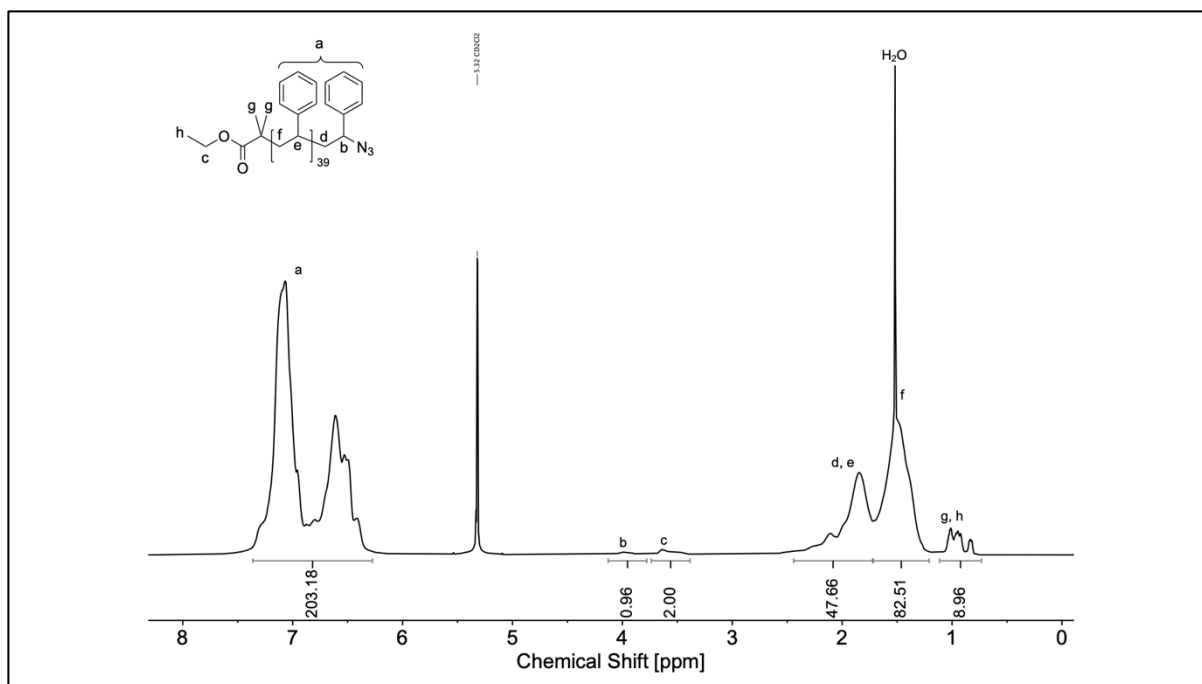


Figure S5.75. ^1H NMR spectrum of **PS-N₃** in CD_2Cl_2 (400 MHz).

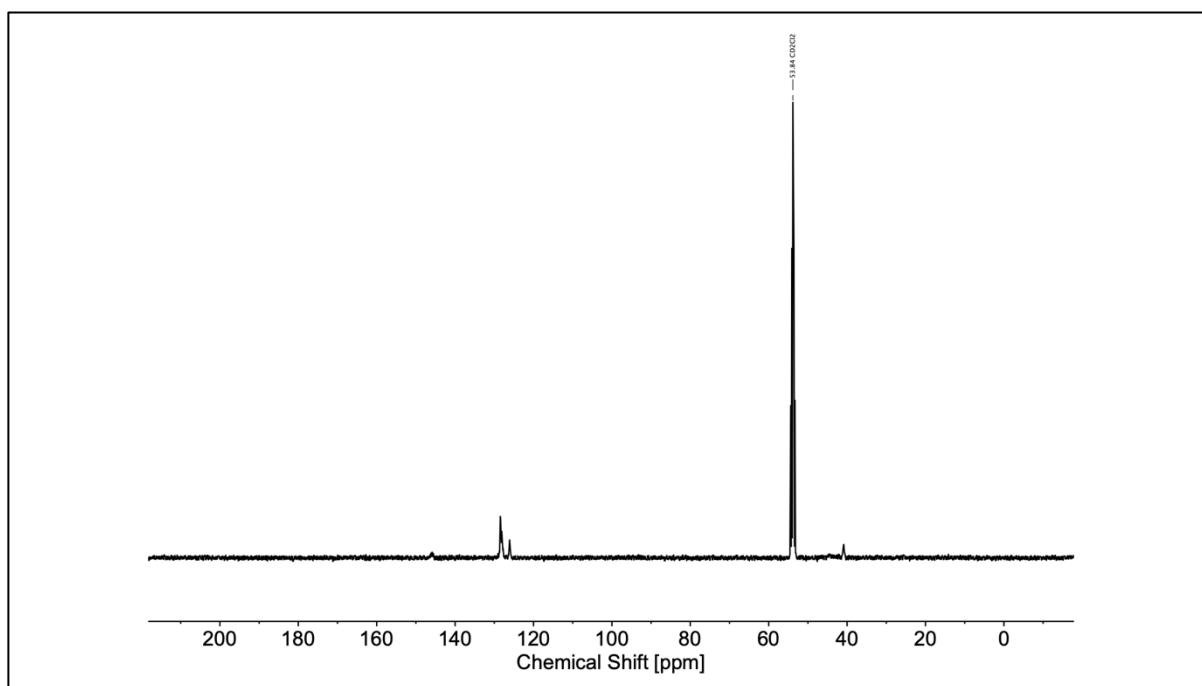


Figure S5.76. ^{13}C NMR spectrum of **PS-N₃** in CD_2Cl_2 (100 MHz).

xNbBr-PS*:

The synthesis procedure was adapted from recent literature.⁴⁷² 1.00 eq. **PS-N₃** and 0.40 eq. Cu(I)Br were added to a pressure tube equipped with a stirring bar. The tube was filled with argon and equipped with an argon balloon. Then, 1.50 eq. **xNbBrH** (0.24 mol/L) and 0.40 eq. PMDETA were dissolved in THF and added to the azide solution *via* a degassed syringe. The

reactions mixture was heated at 50 °C for 16 hours under an argon atmosphere. Afterwards, the reaction was cooled quickly to ambient temperature by immersing the flask into liquid nitrogen, exposing to air, and quenching by the addition of THF. The solution was then flushed through a plug of neutral aluminum oxide to remove the copper. Subsequently, the solvent was removed under reduced pressure. The crude product was dissolved in a small amount of THF and precipitated from the tenfold amount of cold methanol three times. The polymer was filtered, dried under high vacuum, and obtained as white solid.

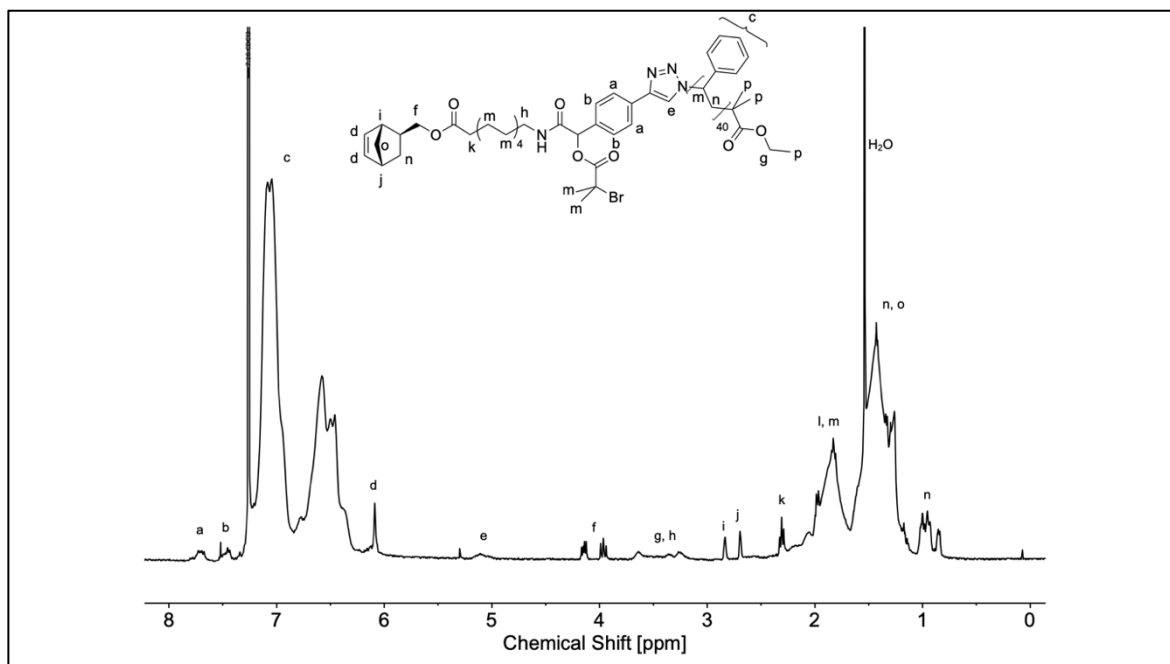


Figure S5.77. ¹H NMR spectrum of the impure xNbBr-PS in CDCl₃ (400 MHz).

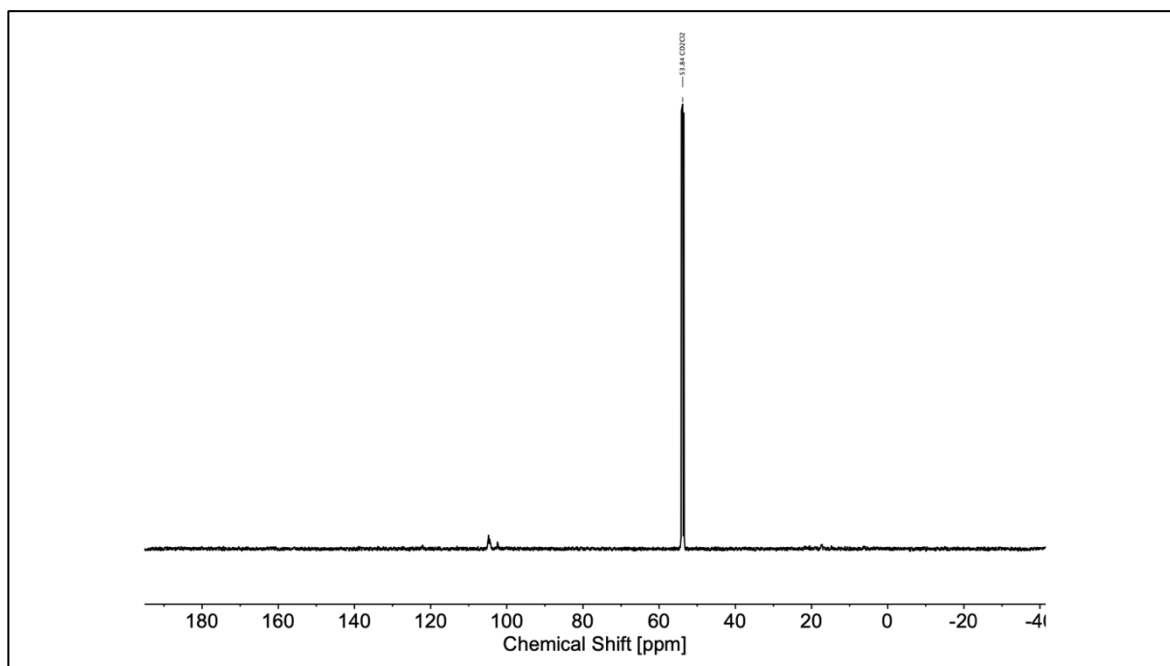


Figure S5.78. ¹³C NMR spectrum of the impure xNbBr-PS in CDCl₃ (100 MHz).

$x\text{Nb-PMMA-PS}^*$:

The synthesis procedure was adapted from recent literature.⁴⁶⁷ A Schlenk flask equipped with a stirring bar and an ampoule equipped with a J Young tap were evacuated and purged with argon (3x). The Schlenk flask was charged with 1.00 eq. copper(I) chloride (0.11 mol/L) and 2.00 eq. TMEDA dissolved in anisole. The ampoule was charged with 1.00 eq. $x\text{NbBr-PS}$ (0.074 mol/L) and 75.0 eq. methyl methacrylate and dissolved in anisole. The mixtures were degassed by three consecutive pump thaw cycles under high vacuum. Subsequently, the solution of the ampoule was transferred to the Schlenk flask *via* a degassed syringe, initiating the polymerization. The polymerization was carried out at 70 °C for 5 hours under an argon atmosphere. Afterwards, the reaction was cooled quickly to ambient temperature by immersing the flask into liquid nitrogen, exposing to air, and quenching by the addition of THF. The solution was then flushed through a plug of neutral aluminum oxide to remove the copper. Subsequently, the solvent was removed under reduced pressure. The crude product was then precipitated three times from the fifteenfold amount of cold cyclohexane. The polymer was filtered, dried under high vacuum, and obtained as white solid.

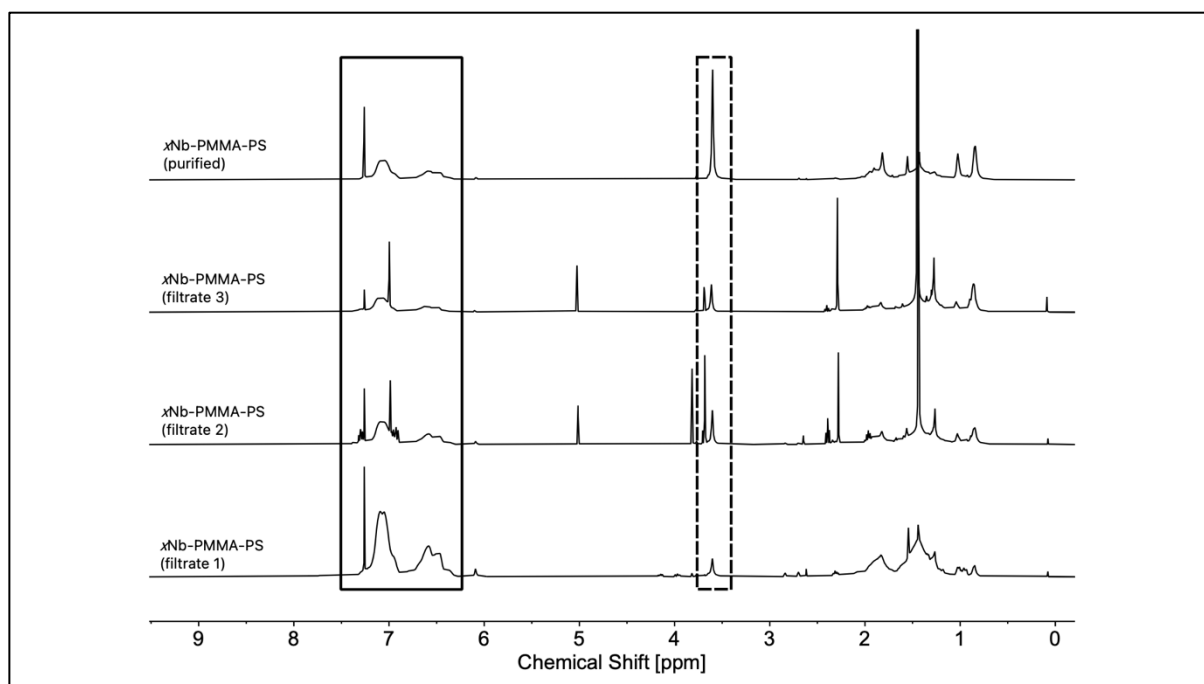


Figure S5.79. Stacked ¹H NMR spectra of the different filtrates obtained during the purification process and the purified bifunctional macromonomer $x\text{Nb-PMMA-PS}$ in CDCl_3 (400 MHz). Boxes: aromatic signals of PS (solid); methoxy signals of PMMA (dashed).

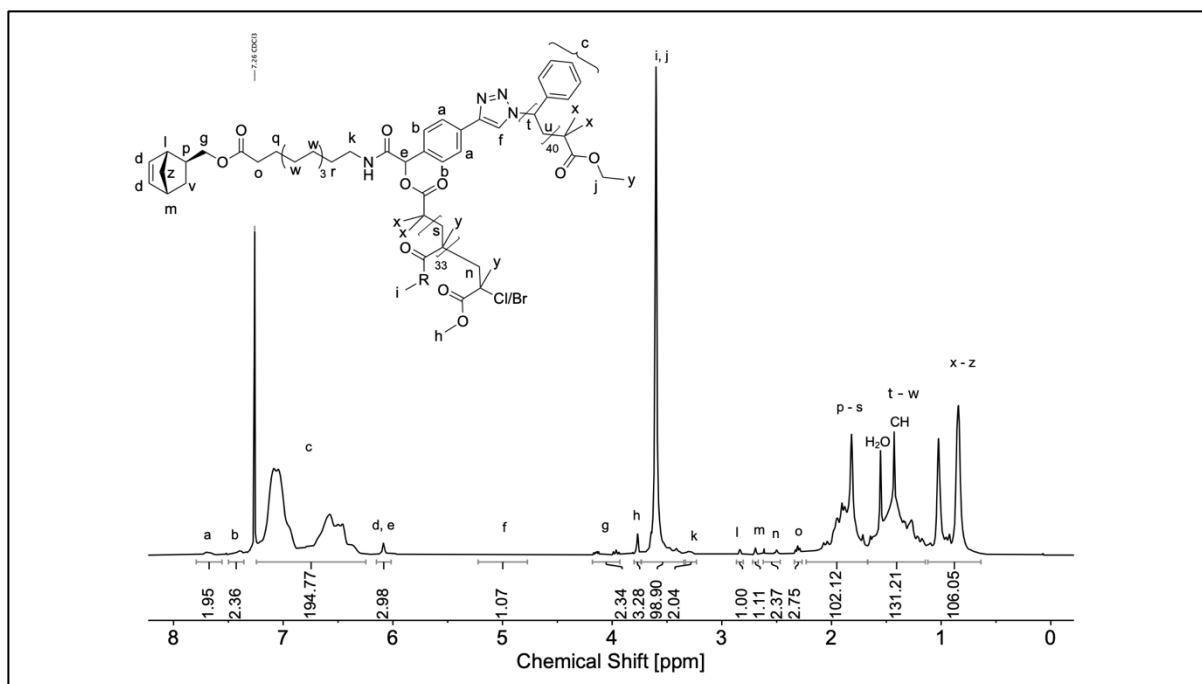


Figure S5.80. ^1H NMR spectrum of $x\text{NbPMMA-PS}$ in CDCl_3 (400 MHz).

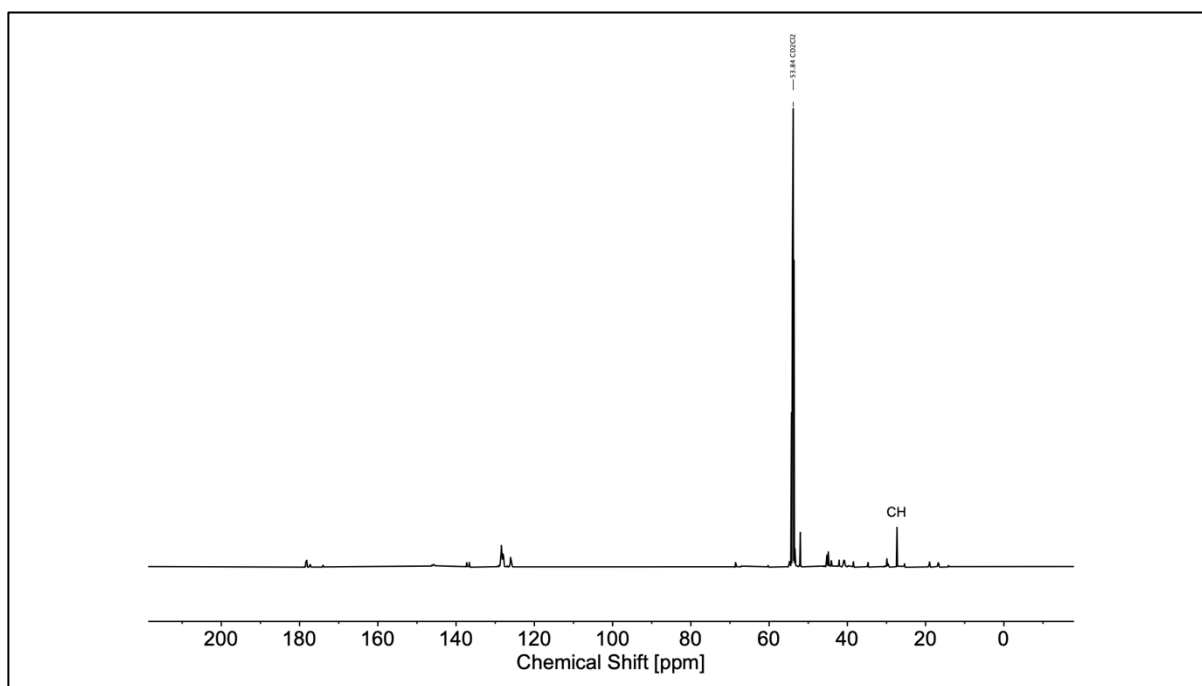


Figure S5.81. ^{13}C NMR spectrum of $x\text{NbPMMA-PS}$ in CDCl_3 (126 MHz).

General synthesis of Janus graft copolymers (Janus10, Janus 20*, and Janus30*):*

An ampoule equipped with a J Young tap was evacuated and purged with argon three times. Subsequently, the desired amount of $x\text{Nb-PMMA-PS}$ and G3 catalyst were each dissolved in degassed DCM and transferred into the ampoule under an argon flow, initiating the polymerization. The polymerization was carried out at ambient temperature for 30 minutes

under an argon atmosphere and was then immediately quenched by adding an excess of ethyl vinyl ether. Afterwards, the polymerization mixture was flushed through a plug of DMT-functionalized silica to remove residual catalyst and was additionally precipitated three times from the tenfold excess of cold *n*-hexane. The polymers were filtered, dried under high vacuum, and obtained as white solids.

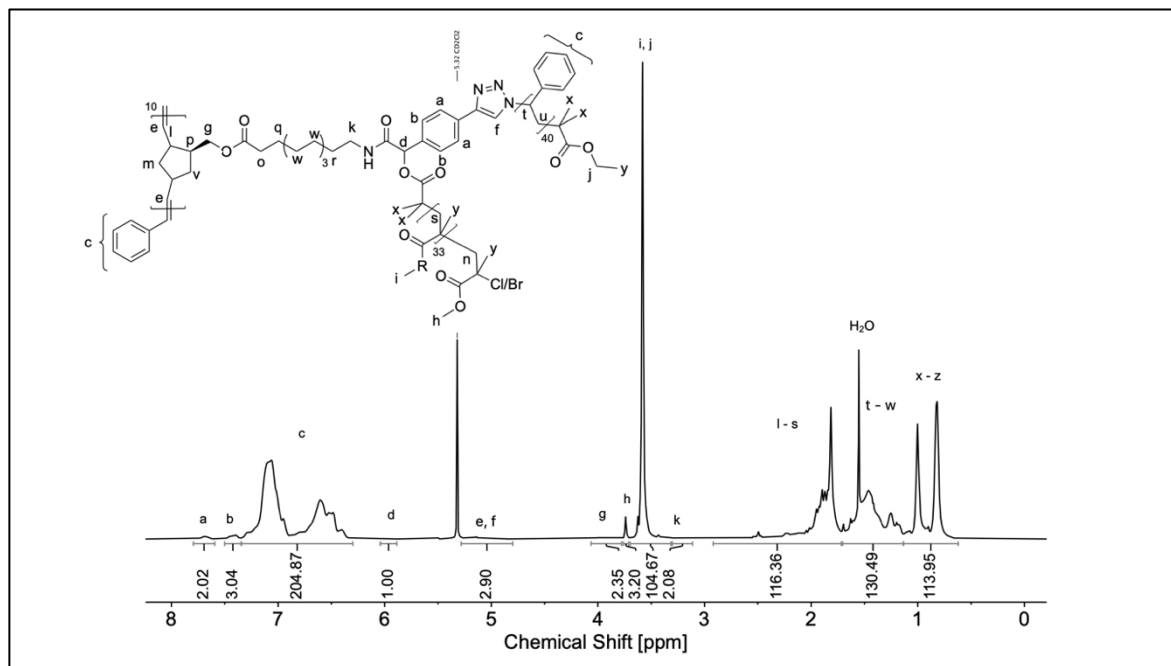


Figure S5.82. Representative ^1H NMR spectrum of a Janus graft copolymers (**Janus10**) in CD_2Cl_2 (500 MHz).

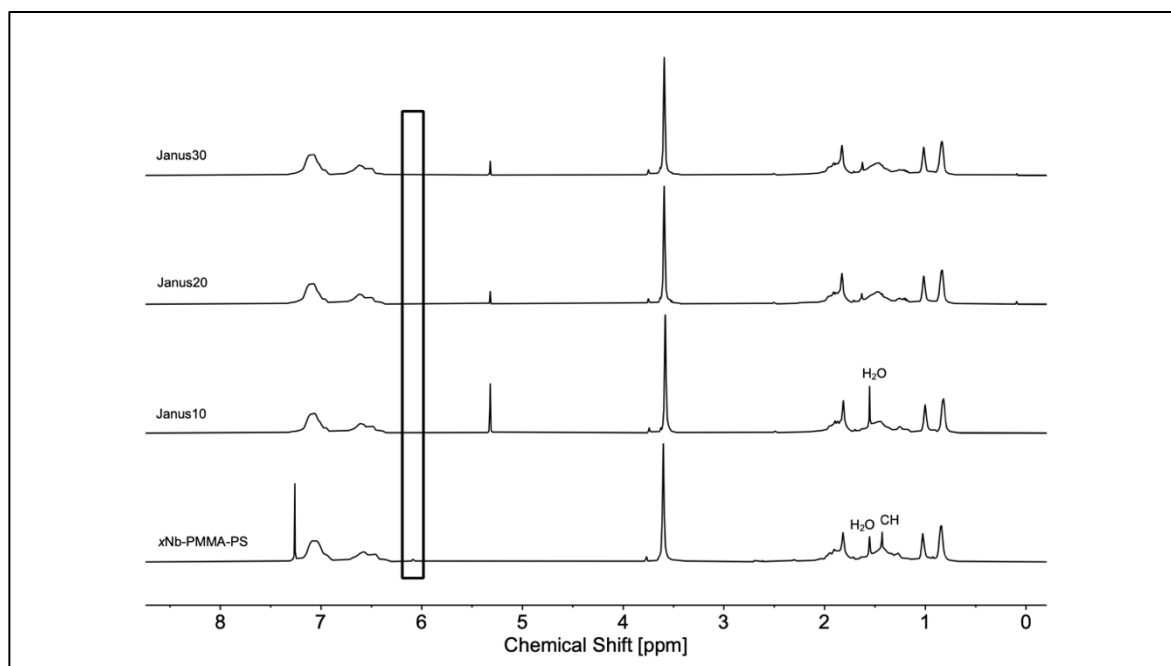


Figure S5.83. Stacked ^1H NMR spectra of the bifunctional macromonomer **xNb-PMMA-PS** in CDCl_3 (400 MHz) and the obtained polymers **Janus10**, **Janus20** and **Janus30** in CD_2Cl_2 (500 MHz). Box: norbornene olefinic moiety.

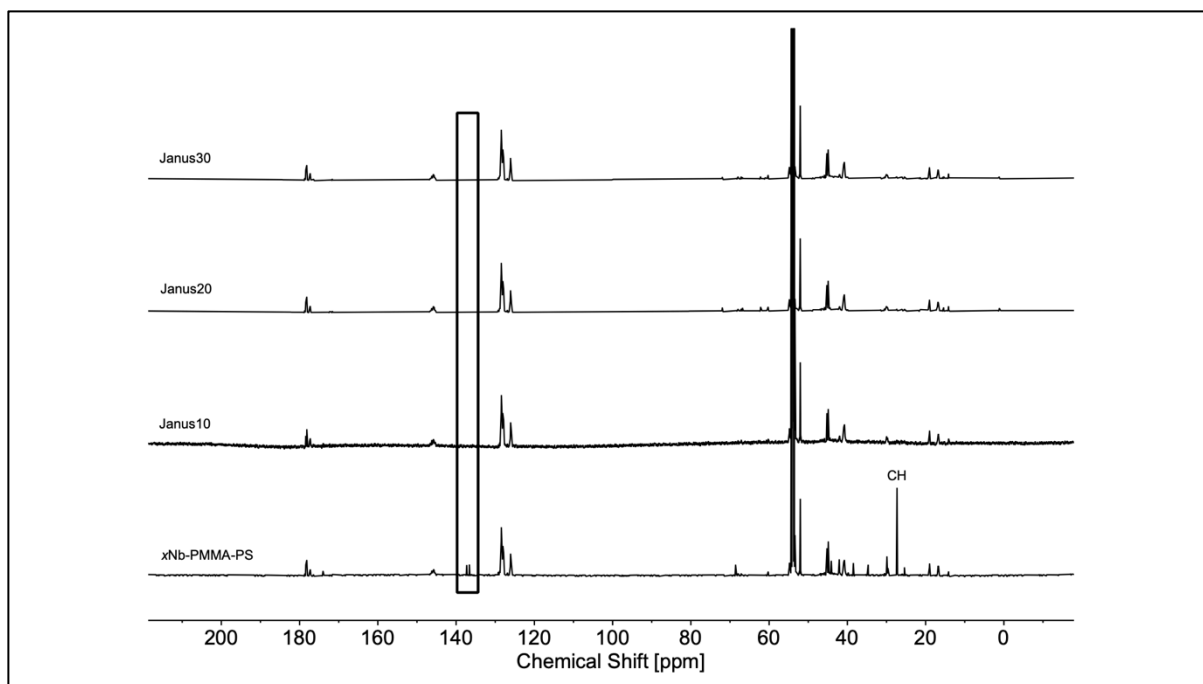


Figure S5.84. Stacked ^{13}C NMR spectra of the bifunctional macromonomer **xNb-PMMA-PS** and the obtained polymers **Janus10**, **Janus20** and **Janus30** in CD_2Cl_2 (500 MHz). Box: norbornene olefinic moiety.

8.3.3 Materials synthesized in chapter 6

It is noted that the stacked ^1H NMR spectra (entries 6.4 – 6.22) represent the crude products after quenching with EVE without further purification. Hence, some spectra may contain signals of remaining EVE, solvent, silicone grease, or not polymerized starting material.

nNbHex:

The synthesis procedure was adapted from recent literature.⁹³ 1.00 eq. *cis*-5-norbornene-*endo*-2,3-dicarboxylic anhydride (0.2 mol/L), 1.50 eq. 6-amino-1-hexane and 0.20 eq. triethylamine were dissolved in toluene. The condensation was performed at 90 °C for 16 hours using a Dean-Stark apparatus to remove forming water. Then, the solvent was removed under reduced pressure. The crude products were dissolved in DCM and washed with aqueous hydrochloric acid (0.1 mol/L) twice and then with brine. The organic phase was dried over magnesium sulfate and the solvent was removed under reduced pressure. The product was obtained a light brown viscous liquid in yield of 82%.

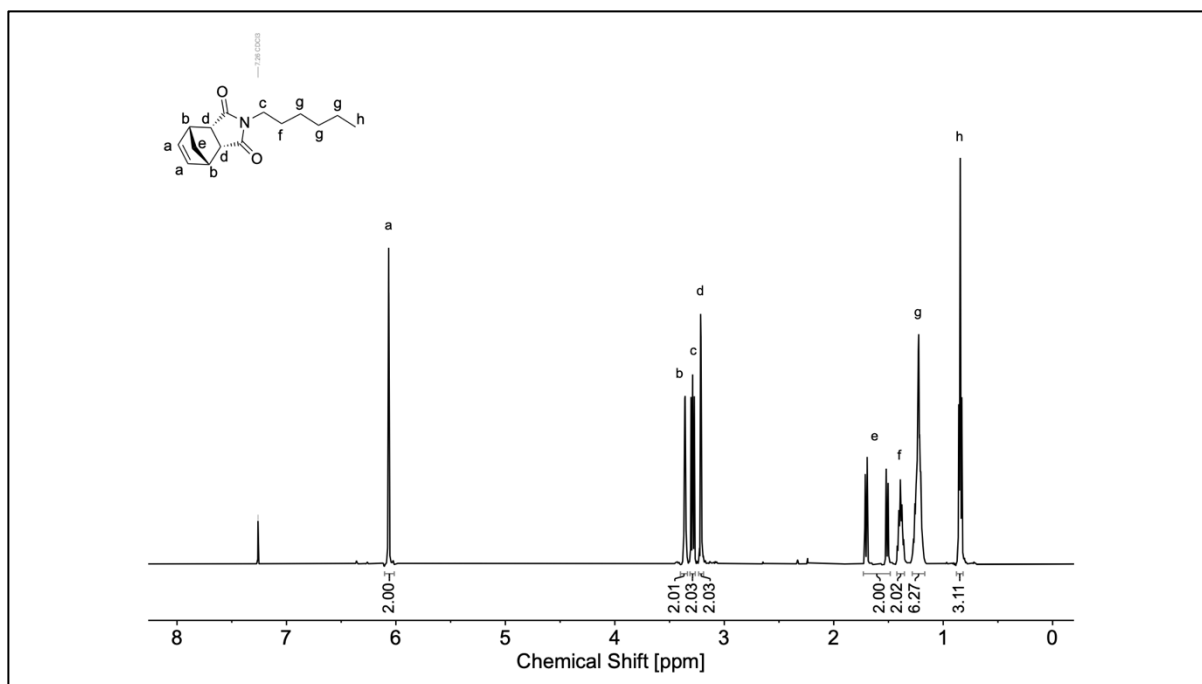


Figure S6.1. ^1H NMR spectrum of *nNbHex*.

^1H NMR: (500 MHz, CDCl_3 , δ): 6.07 (t, $J = 1.9$ Hz, 2H; $\text{CH}=\text{CH}$, ^a), 3.38 - 3.33 (m, 2H; $=\text{CH}-\text{CH}$, ^b), 3.31 - 3.26 (m, 2H; $\text{N}-\text{CH}_2$, ^c), 2.77 (dd, $J = 2.9$ Hz, 1.5 Hz, 2H; $=\text{CH}-\text{CH}-\text{CH}$, ^d), 1.72 - 1.50 (m, 2H; CH_2 bridge, ^e), 1.43 - 1.35 (m, 2H; $\text{N}-\text{CH}_2-\text{CH}_2$, ^f), 1.29 - 1.17 (m, 6H; CH_2 , ^g), 0.84 (t, $J = 6.9$ Hz, 3H; CH_3 , ^h).

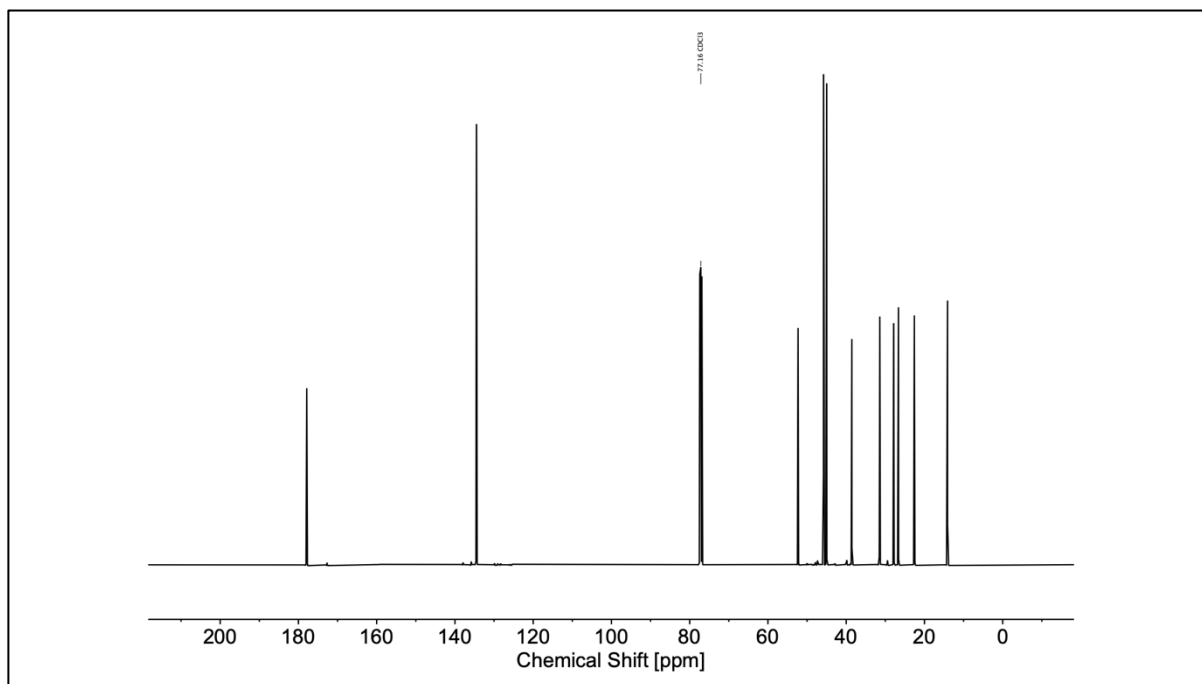


Figure S6.2. ^{13}C NMR spectrum of *nNbHex*.

^{13}C NMR: (126 MHz, CDCl_3 , δ): 177.86, 134.49, 52.31, 45.81, 44.99, 38.56, 31.42, 27.85, 26.64, 22.59, 14.10.

IR (ATR platinum diamond): ν / cm^{-1} = 2933 (w), 2859 (w), 1769 (w), 1691 (vs), 1456 (w), 1436 (w), 1395 (m), 1368 (m), 1353 (m), 1337 (m), 1308 (w), 1292 (w), 1249 (w), 1228 (w), 1172 (m), 1140 (w), 1129 (m), 1092 (vw), 1049 (vw), 987 (w), 975 (w), 917 (vw), 909 (vw), 884 (w), 843 (w), 802 (vw), 786 (vw), 745 (w), 720 (s), 662 (w), 646 (w), 615 (m), 570 (vw), 529 (vw), 502 (vw), 481 (vw), 459 (vw), 436 (w), 413 (w).

HRMS (ESI-MS) m/z : $[\text{M}+\text{H}]^+$ calc. for $\text{C}_{15}\text{H}_{22}\text{NO}_2$, 248.1645, found: 248.1644.

*General ROMP procedure – homopolymerization kinetics of **nNbHex** (entries 6.1 – 6.4):*

An NMR tube equipped with a J Young tap was evacuated and purged with argon three times. Subsequently, the desired amount of **nNbHex** and G1 catalyst (2 mmol/L) were each dissolved in degassed DCM-d_2 and transferred to the NMR tube under an argon flow, initiating the polymerization. The polymerization was carried out at ambient temperature under an argon atmosphere and was monitored by on-line ^1H NMR spectroscopy. After reaching the desired monomer conversion, the polymerization was quenched by adding an excess of ethyl vinyl ether. The crude product was purified by removal of the cleaved catalyst *via* a DMT-functionalized silica plug and was additionally precipitated three times from the tenfold excess of cold *n*-hexane to remove unreacted monomer. The polymers were obtained as brown solids.

Entry 6.4 was performed in an argon-flushed ampoule at ambient temperature under an argon atmosphere. Samples were withdrawn and quenched by adding an excess of ethyl vinyl ether to monitor the monomer conversion and the evolution of the molecular weight distribution. The samples were not further purified.

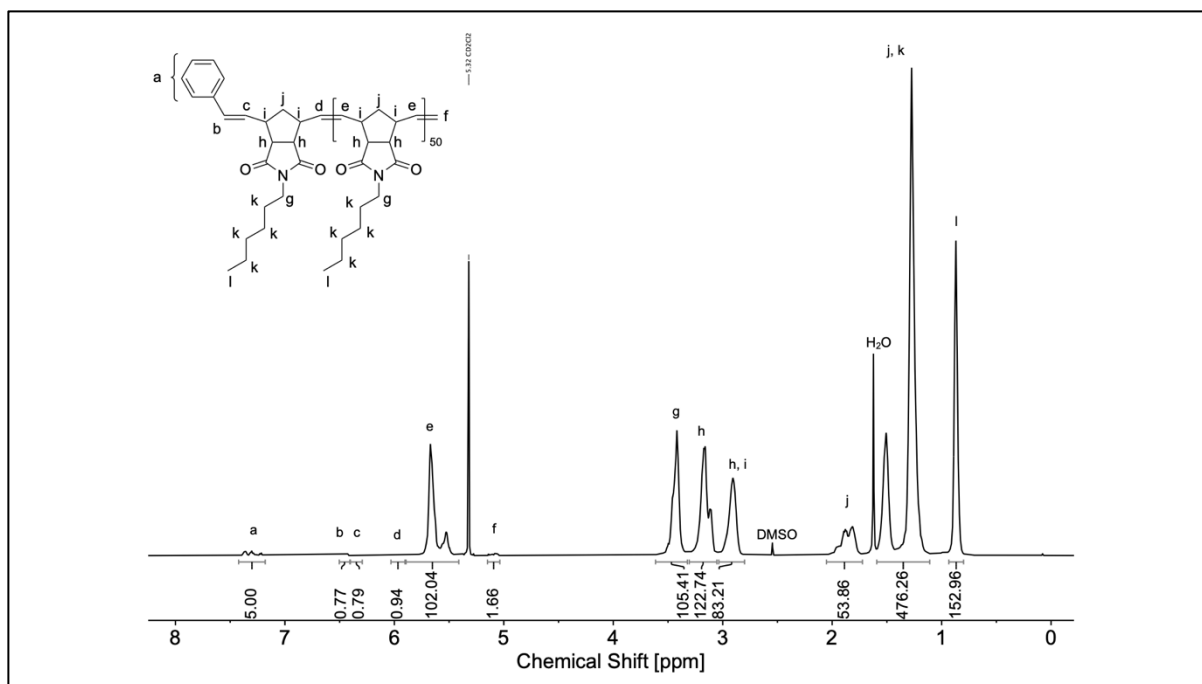


Figure S6.3. ^1H NMR spectrum of entry 6.1 in CD_2Cl_2 (500 MHz). Note: Deuterated solvent was contaminated with traces of DMSO.

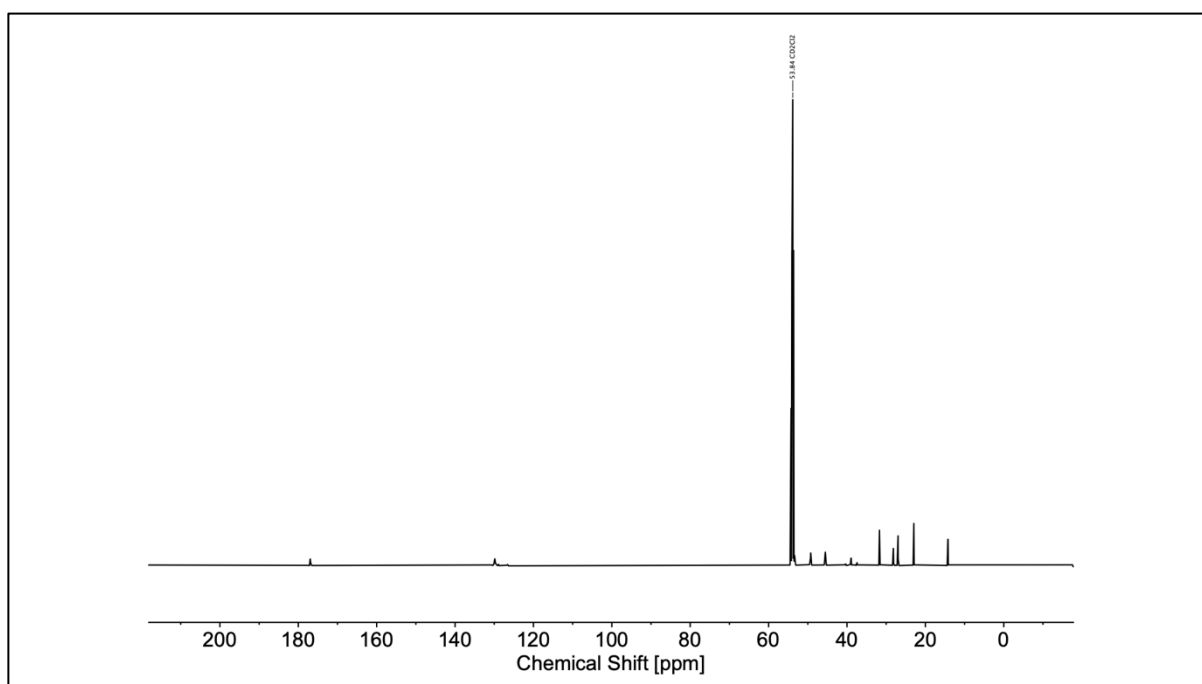


Figure S6.4. ^{13}C NMR spectrum of entry 6.1 in CD_2Cl_2 (126 MHz).

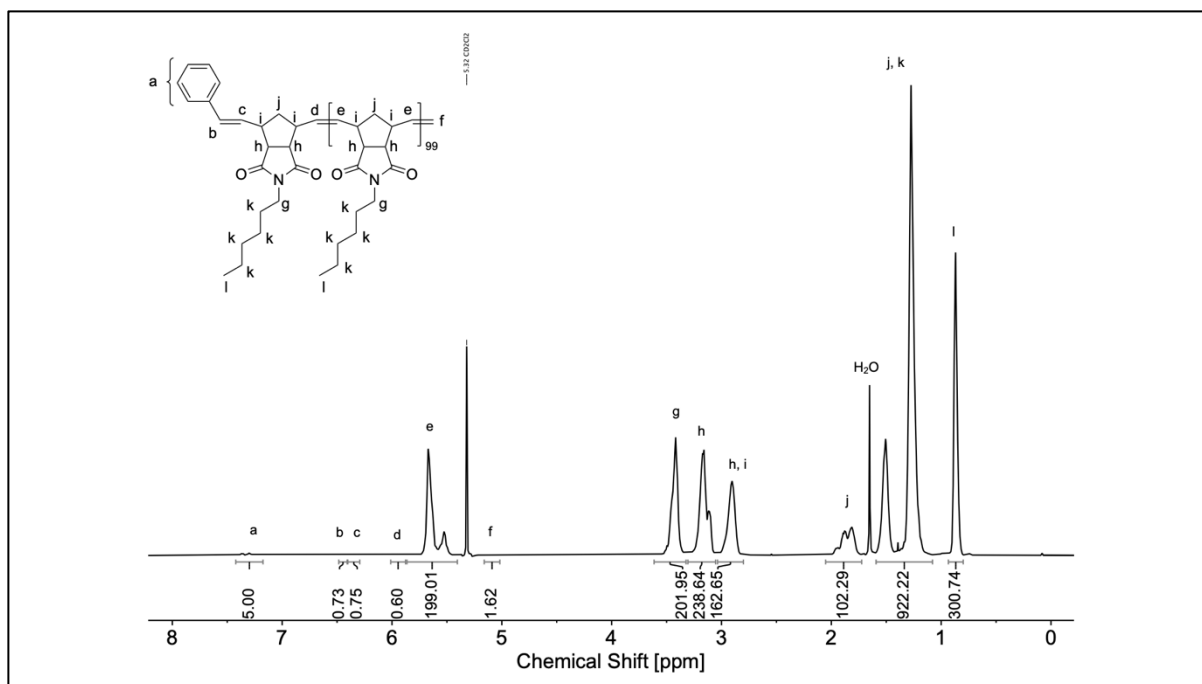


Figure S6.5. ^1H NMR spectrum of entry 6.2 in CD_2Cl_2 (500 MHz).

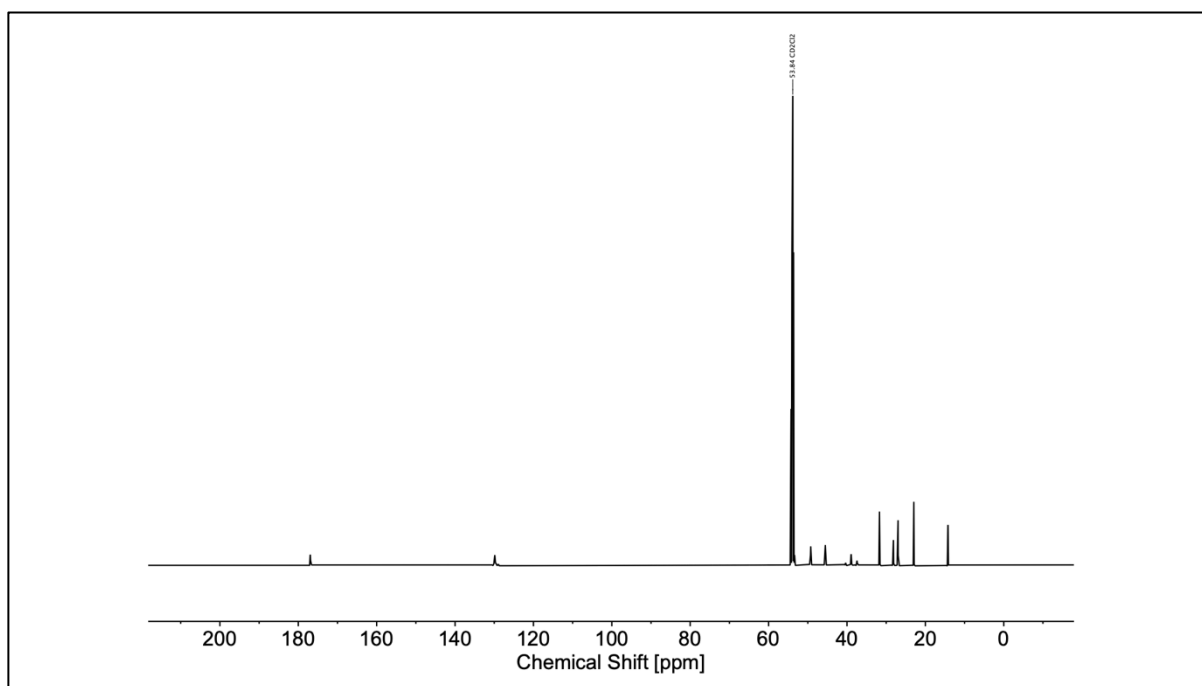


Figure S6.6. ^{13}C NMR spectrum of entry 6.2 in CD_2Cl_2 (126 MHz).

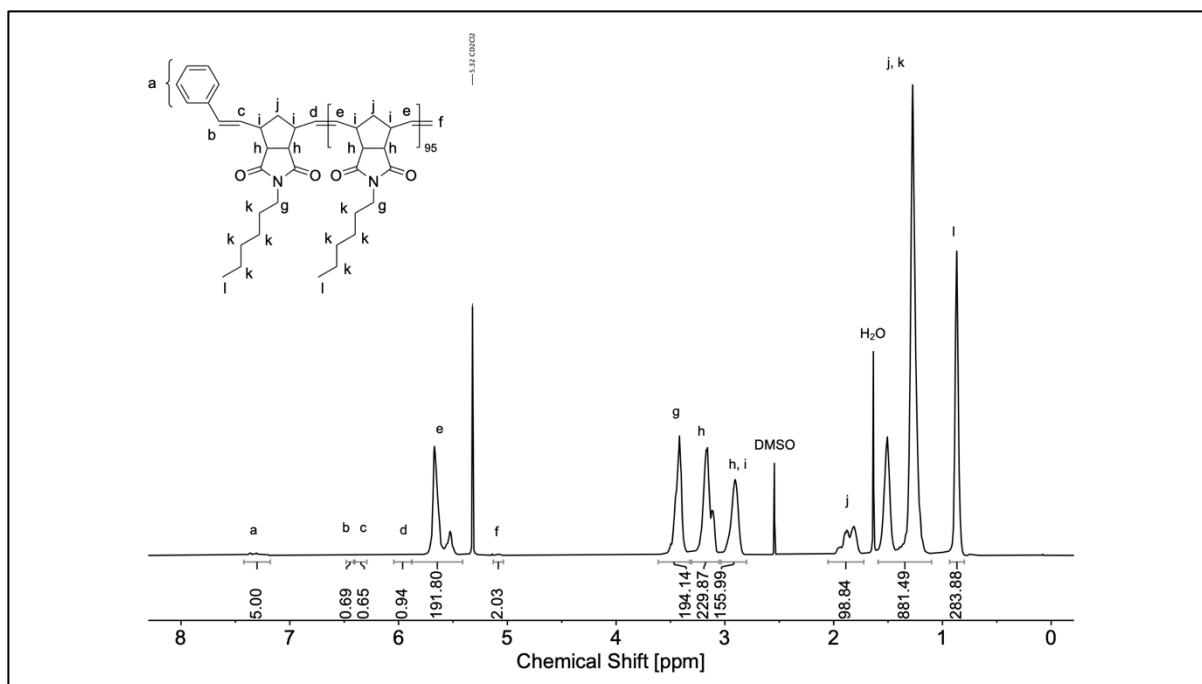


Figure S6.7. ^1H NMR spectrum of entry 6.3 in CD_2Cl_2 (500 MHz). Note: Deuterated solvent was contaminated with traces of DMSO.

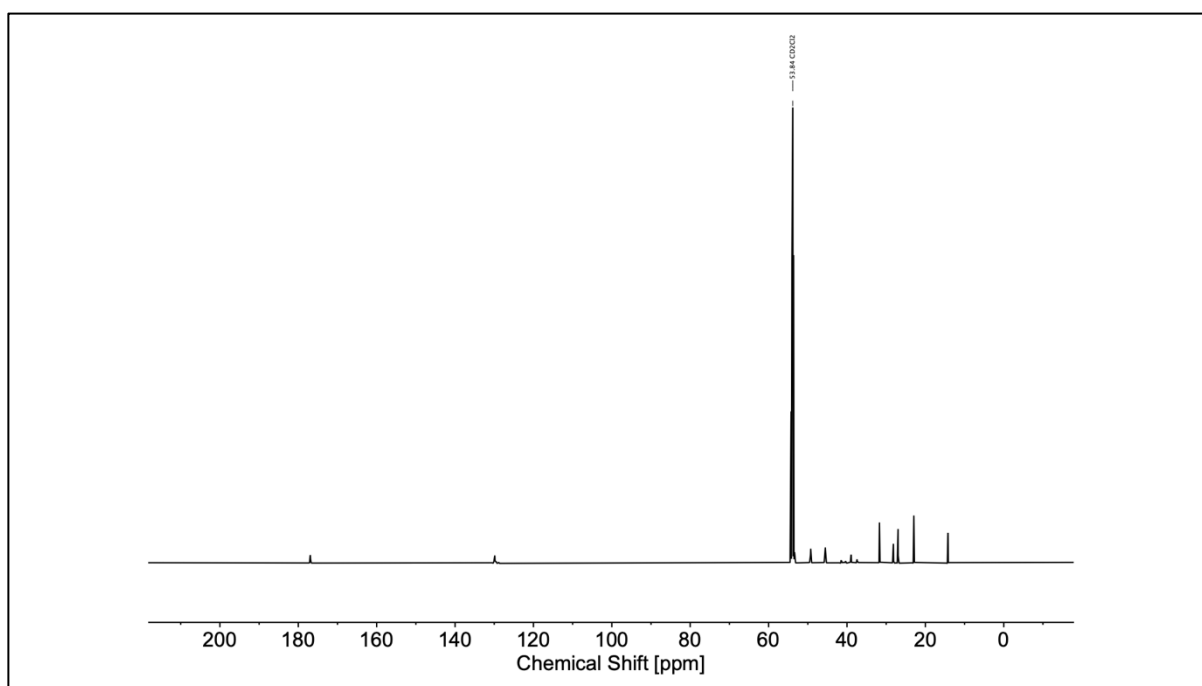


Figure S6.8. ^{13}C NMR spectrum of entry 6.3 in CD_2Cl_2 (126 MHz).

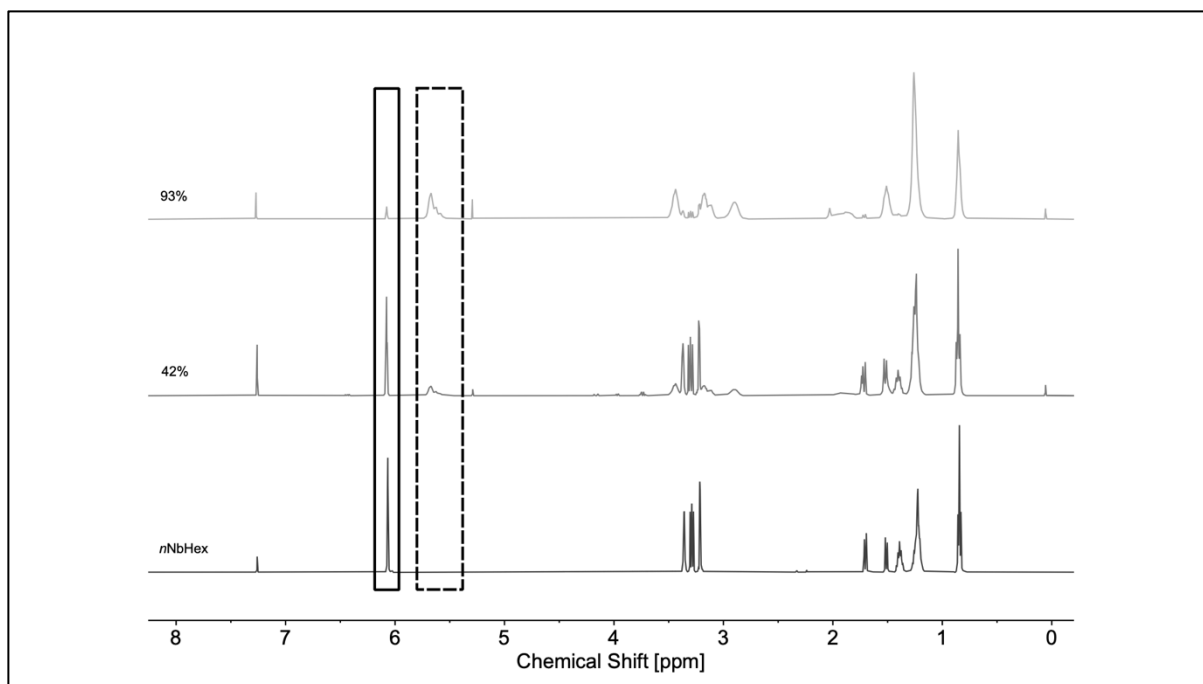


Figure S6.9. Stacked ^1H NMR spectra of entry 6.4 after quenching with EVE in CDCl_3 (400 MHz) and the ^1H NMR spectrum of the corresponding monomer in CDCl_3 (500 MHz). Boxes: norbornene olefinic moiety (solid); poly(norbornene) olefinic backbone (dashed).

General ROMP by delayed addition of macromonomer (entries 6.5 – 6.22):

An ampoule equipped with a J Young tap and a stirring bar was evacuated and purged with argon three times. Subsequently, the desired amount of **nNbHex** and G1 catalyst were each dissolved in degassed DCM and transferred into the ampoule under an argon flow, initiating the polymerization. After reaching a DP of ca. 19, a sample was withdrawn and quenched by adding an excess of ethyl vinyl ether. Then, the desired amount of the first macromonomer was dissolved in degassed DCM and transferred to the ampoule under an argon flow, initiating the copolymerization. A sample was withdrawn and quenched by adding an excess of ethyl vinyl ether after reaching complete macromonomer conversion. This procedure was repeated depending on the desired number of introduced blocks. The polymerization was carried out at ambient temperature under an argon atmosphere and was quenched after reaching the desired number of blocks by adding an excess of ethyl vinyl ether. The crude product was purified by removal of the cleaved catalyst *via* a DMT-functionalized silica plug and was additionally precipitated three times from the tenfold excess of cold *n*-hexane to remove unreacted monomer. The polymers were obtained as off-white solids.

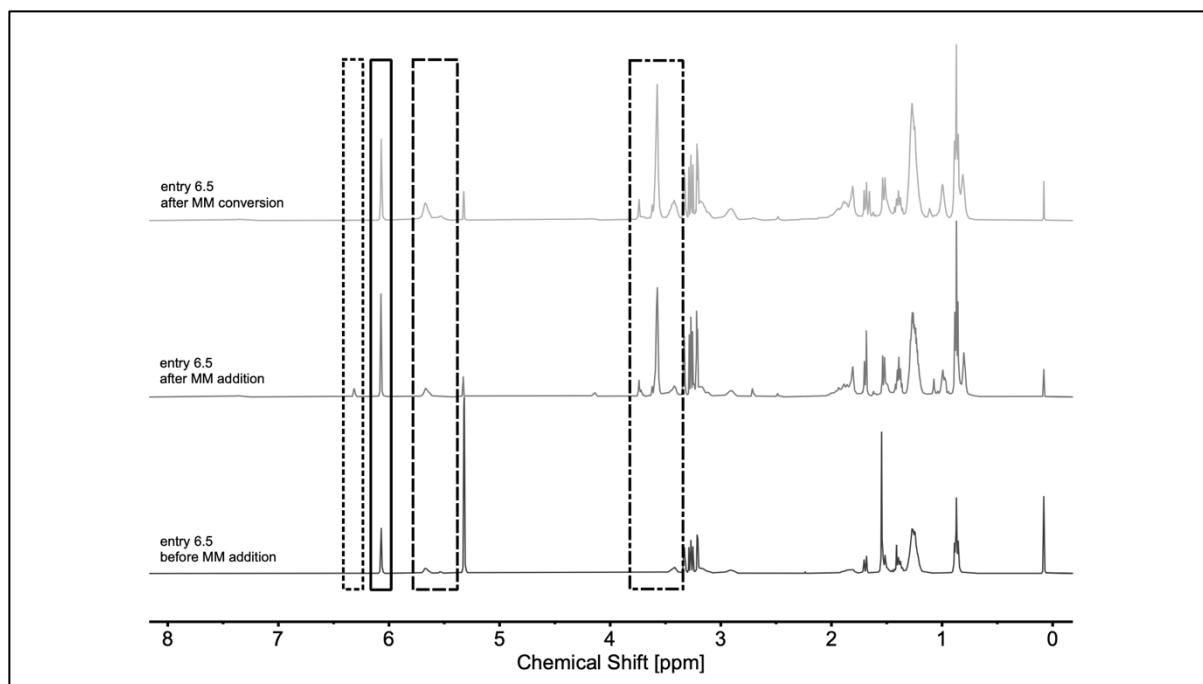


Figure S6.10. Representative stacked ^1H NMR spectra of entry 6.5 before (bottom) and after (middle) the addition of $x\text{Nb}2\text{M}12$, and after its complete conversion (top) in CD_2Cl_2 (500 MHz). Boxes: *endo* norbornene olefin (solid); poly(norbornene) olefin (dashed); *exo* norbornene olefin (dotted); methoxy groups (dash-dotted).

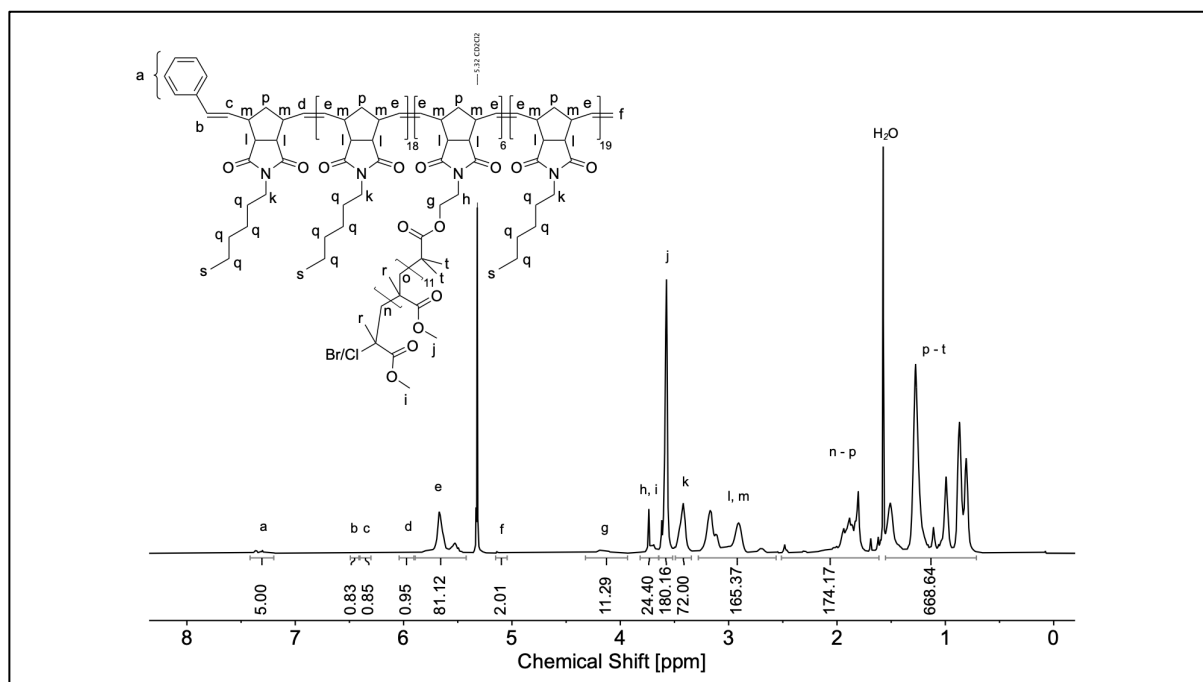


Figure S6.11. ^1H NMR spectrum of entry 6.5 in CD_2Cl_2 (500 MHz).

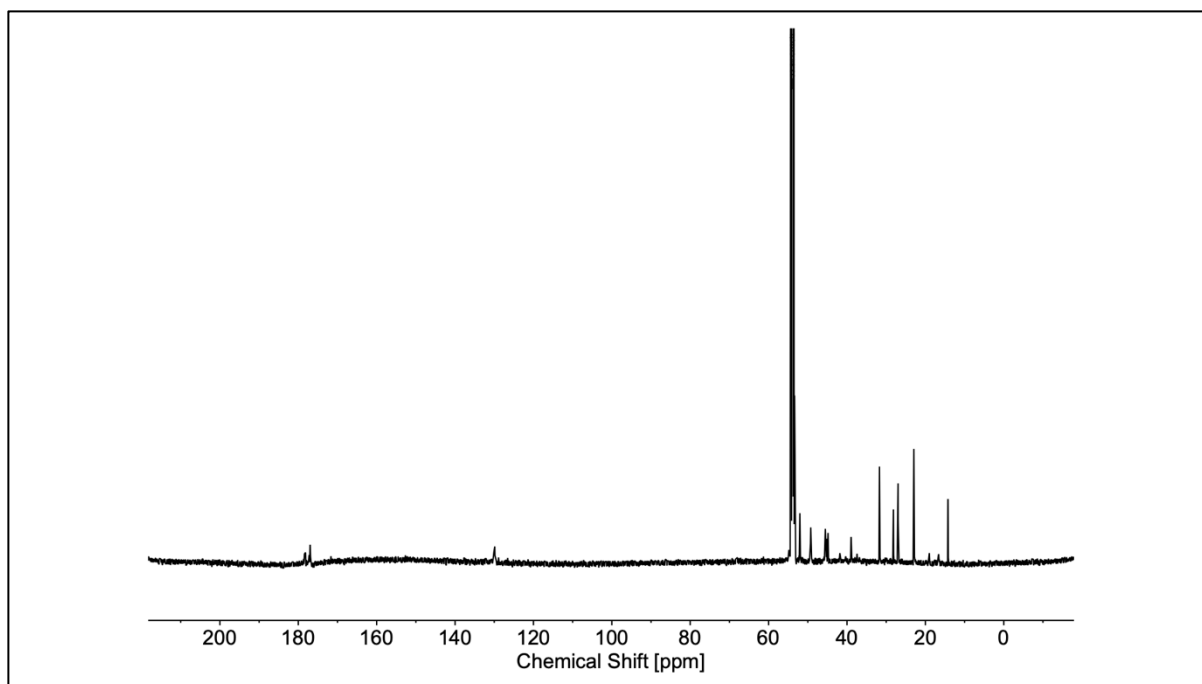


Figure S6.12. ^{13}C NMR spectrum of entry 6.5 in CD_2Cl_2 (126 MHz).

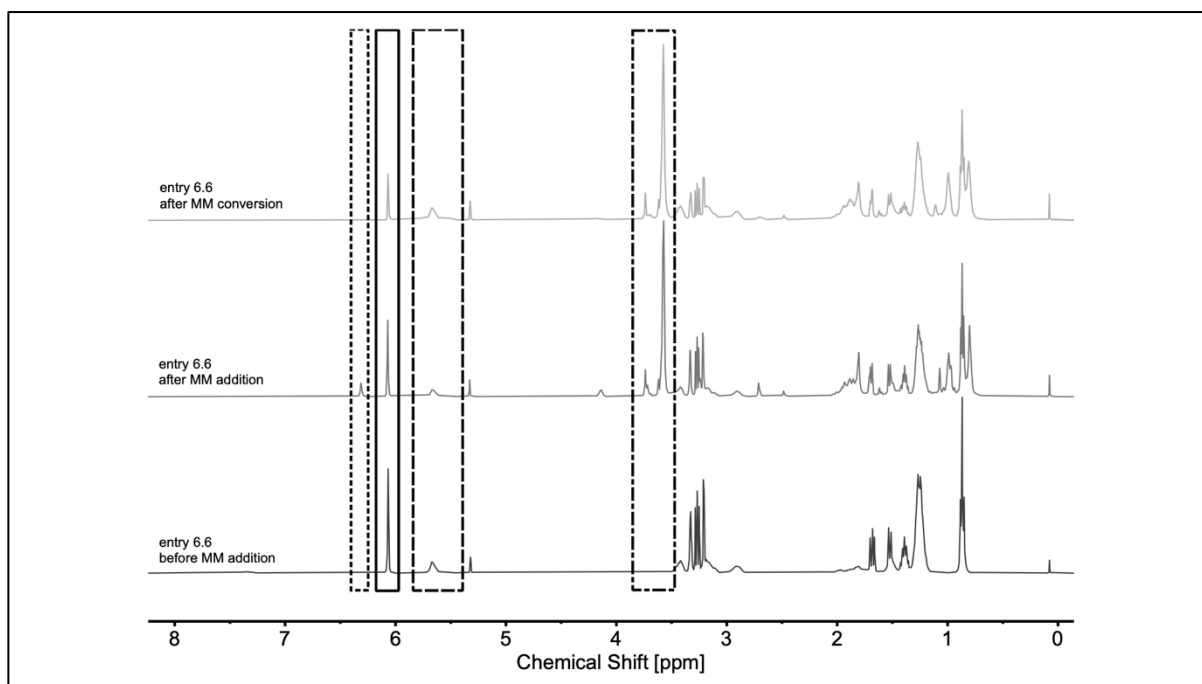


Figure S6.13. Representative stacked ^1H NMR spectra of entry 6.6 before (bottom) and after (middle) the addition of **xNb2M12**, and after its complete conversion (top) in CD_2Cl_2 (500 MHz). Boxes: *endo* norbornene olefin (solid); poly(norbornene) olefin (dashed); *exo* norbornene olefin (dotted); methoxy groups (dash-dotted).

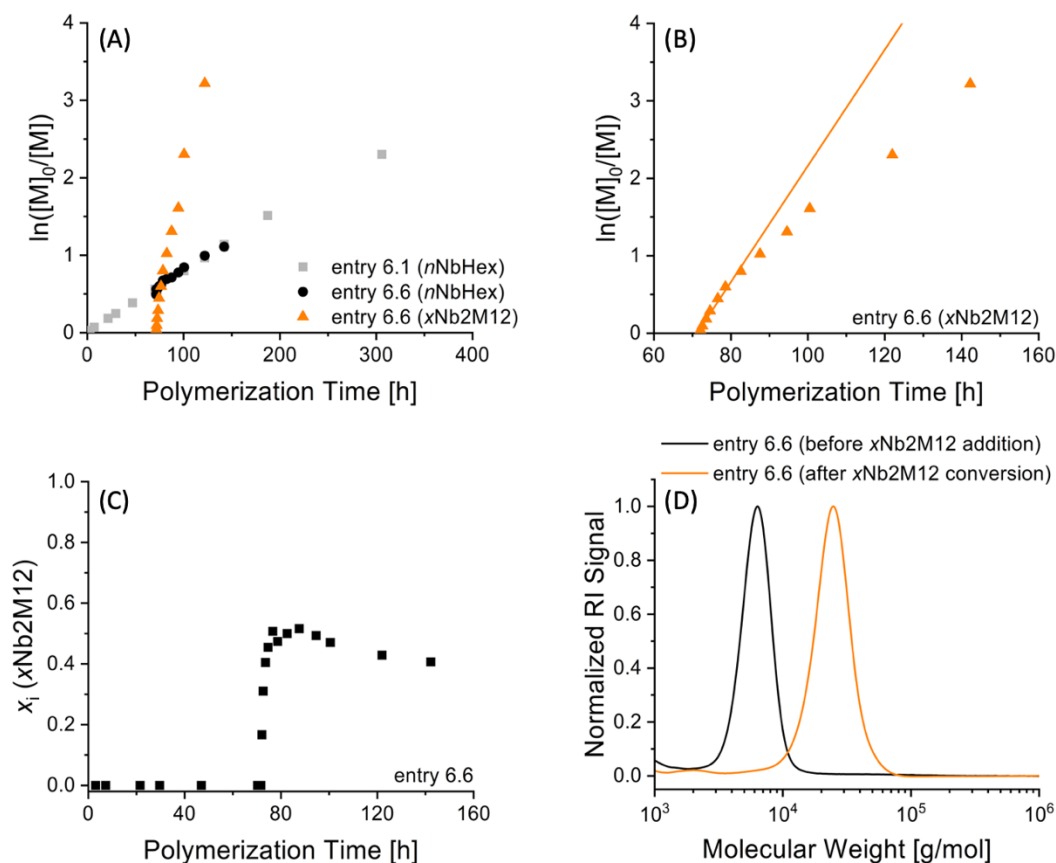


Figure S6.14. (A) Kinetic plots of entries 6.1 (**Table 6.1**) and 6.6 (**Table 6.2**), (B) highlighting **xNb2M12** during copolymerization, (C) molar fraction (x_i) of **xNb2M12** in entry 6.6 as a function of polymerization time, based on ^1H NMR spectroscopy data (**Figure S6.13**), and (D) SEC traces of entry 6.6 before **xNb2M12** addition and after **xNb2M12** conversion. Line represents linear fit.

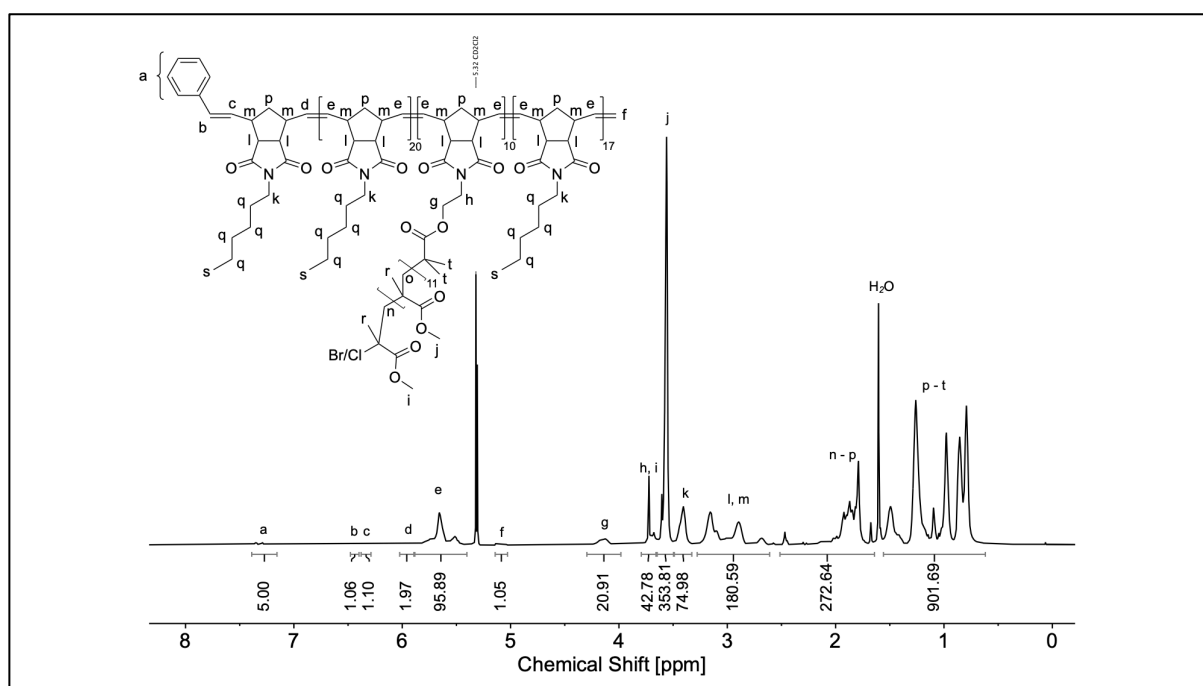


Figure S6.15. ^1H NMR spectrum of entry 6.6 in CD_2Cl_2 (500 MHz).

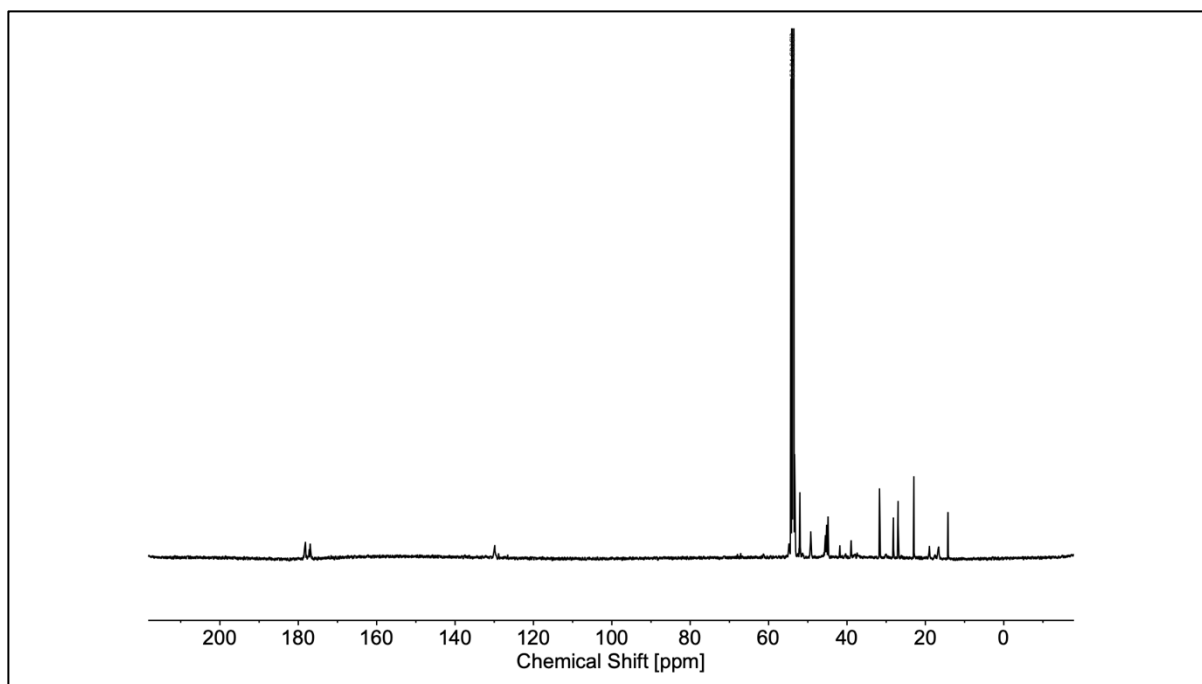


Figure S6.16. ^{13}C NMR spectrum of entry 6.6 in CD_2Cl_2 (126 MHz).

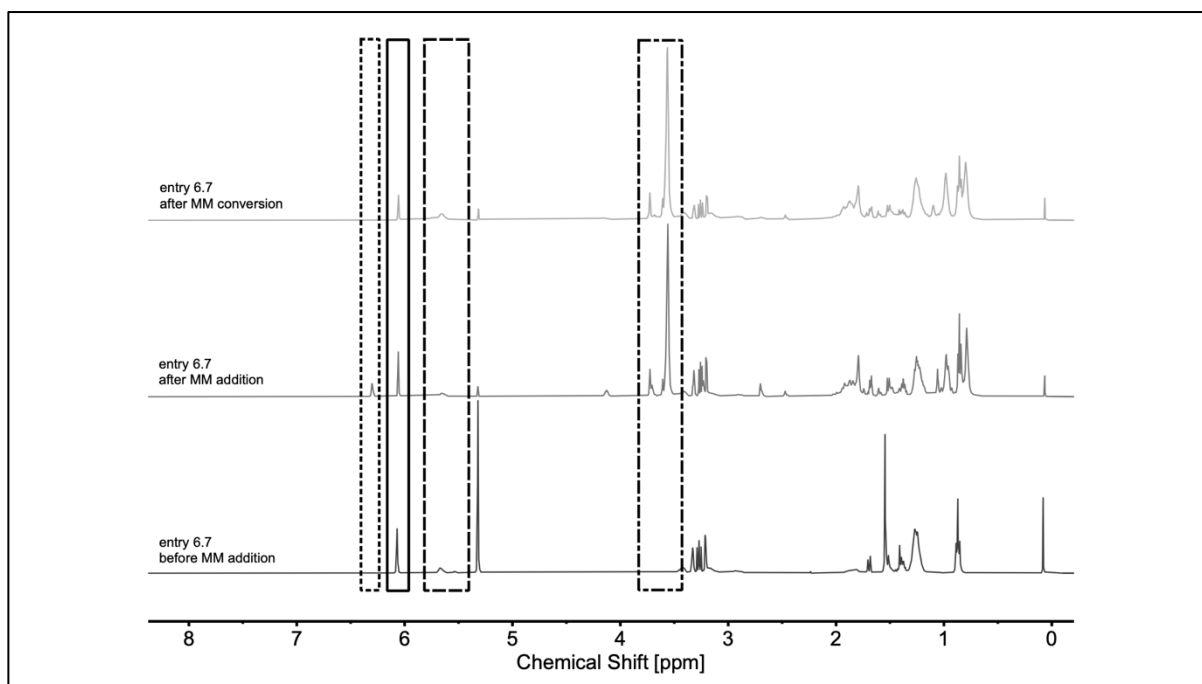


Figure S6.17. Representative stacked ^1H NMR spectra of entry 6.7 before (bottom) and after (middle) the addition of **xNb2M12**, and after its complete conversion (top) in CD_2Cl_2 (500 MHz). Boxes: *endo* norbornene olefin (solid); poly(norbornene) olefin (dashed); *exo* norbornene olefin (dotted); methoxy groups (dash-dotted).

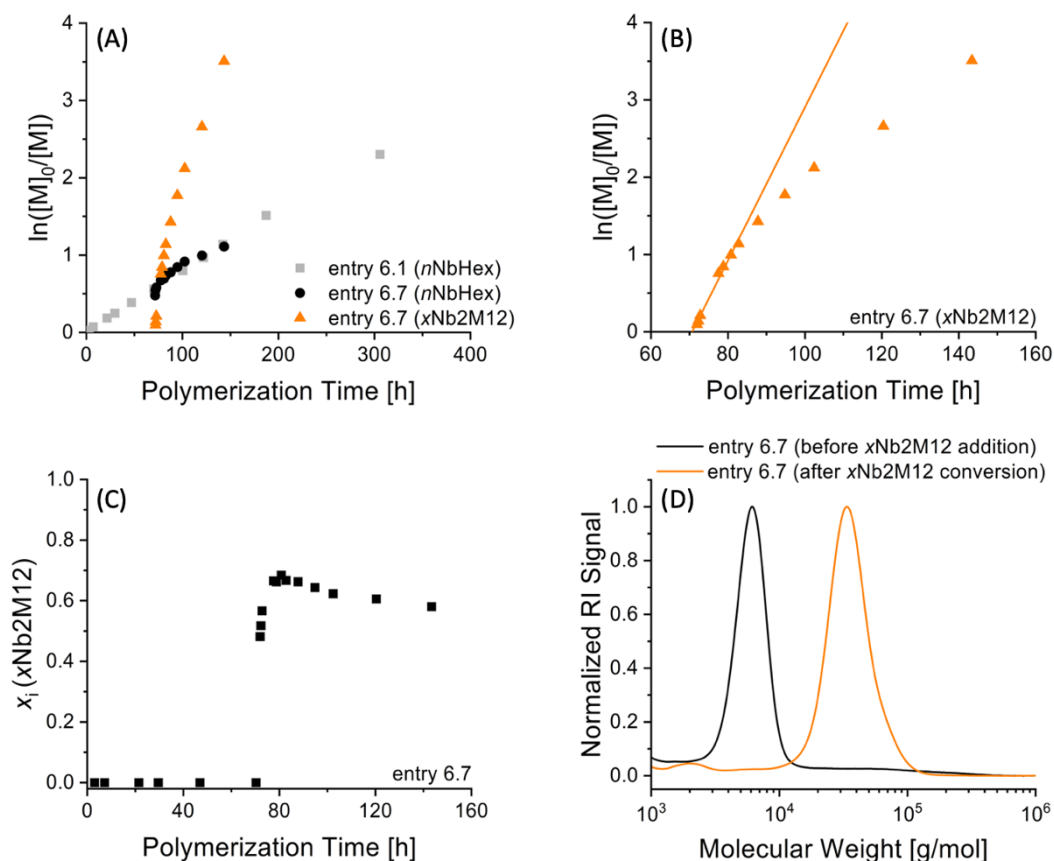


Figure S6.18. (A) Kinetic plots of entries 6.1 (Table 6.1) and 6.7 (Table 6.2), (B) highlighting $x\text{Nb2M12}$ during copolymerization, (C) molar fraction (x_i) of $x\text{Nb2M12}$ in entry 6.7 as a function of polymerization time, based on ^1H NMR spectroscopy data (Figure S6.17), and (D) SEC traces of entry 6.7 before $x\text{Nb2M12}$ addition and after $x\text{Nb2M12}$ conversion. Line represents linear fit.

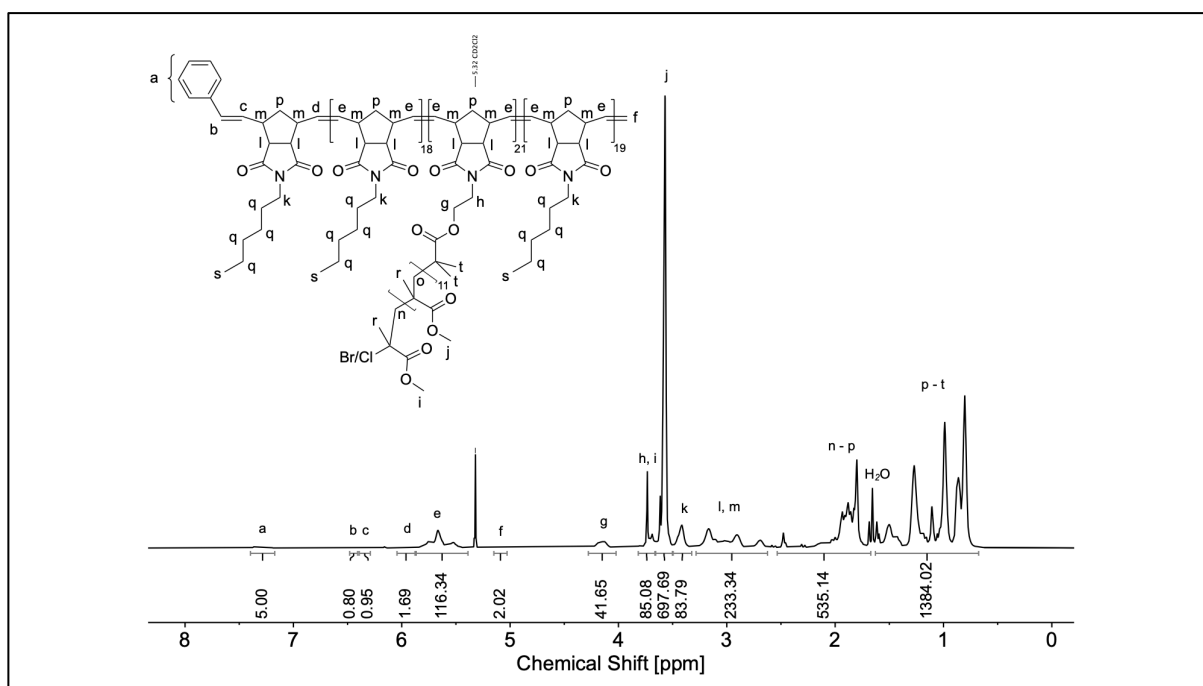


Figure S6.19. ^1H NMR spectrum of entry 6.7 in CD_2Cl_2 (500 MHz).

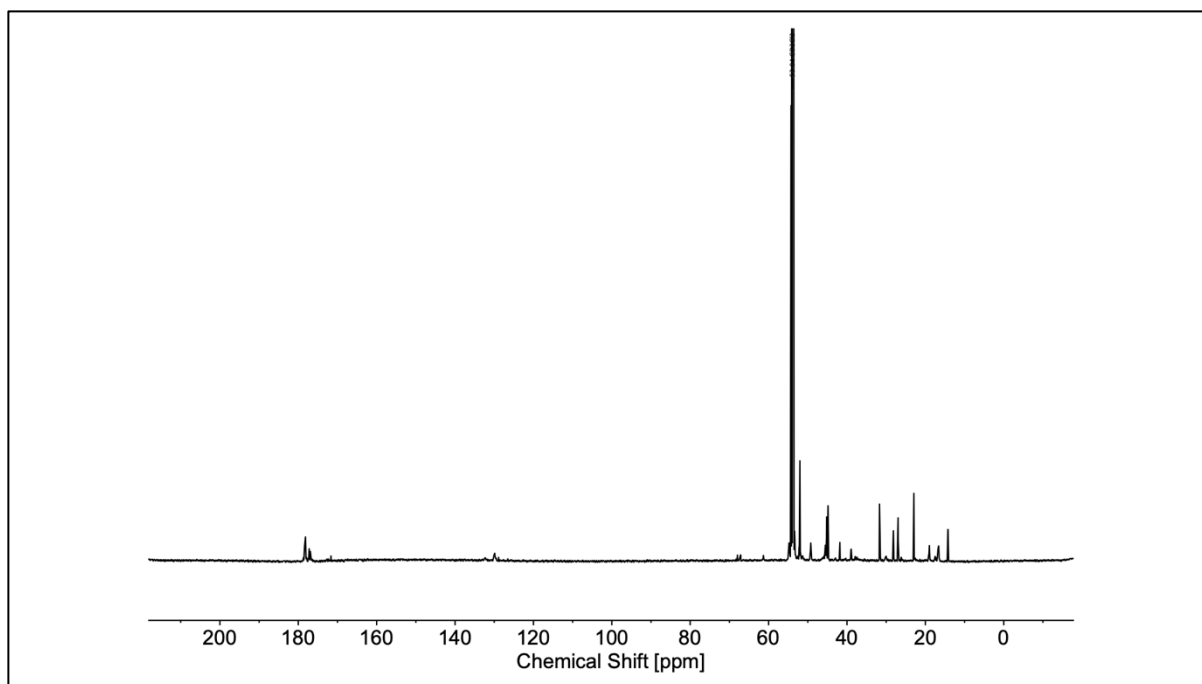


Figure S6.20. ^{13}C NMR spectrum of entry 6.7 in CD_2Cl_2 (126 MHz).

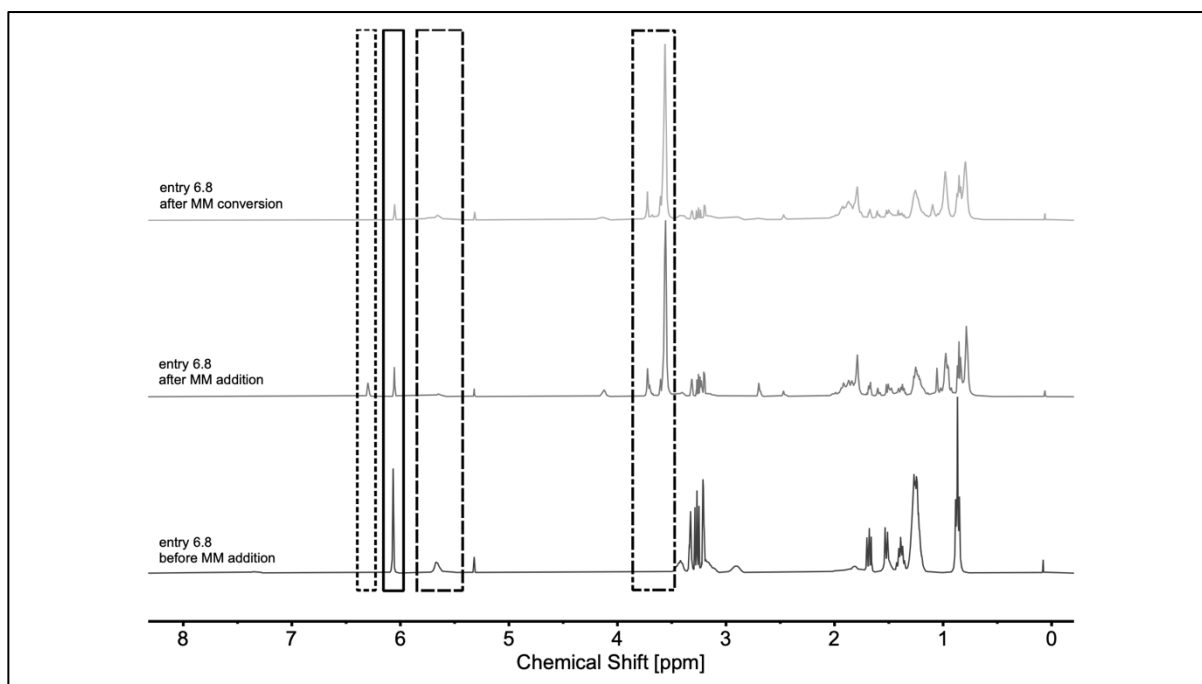


Figure S6.21. Representative stacked ^1H NMR spectra of entry 6.8 before (bottom) and after (middle) the addition of **xNb2M12**, and after its complete conversion (top) in CD_2Cl_2 (500 MHz). Boxes: *endo* norbornene olefin (solid); poly(norbornene) olefin (dashed); *exo* norbornene olefin (dotted); methoxy groups (dash-dotted).

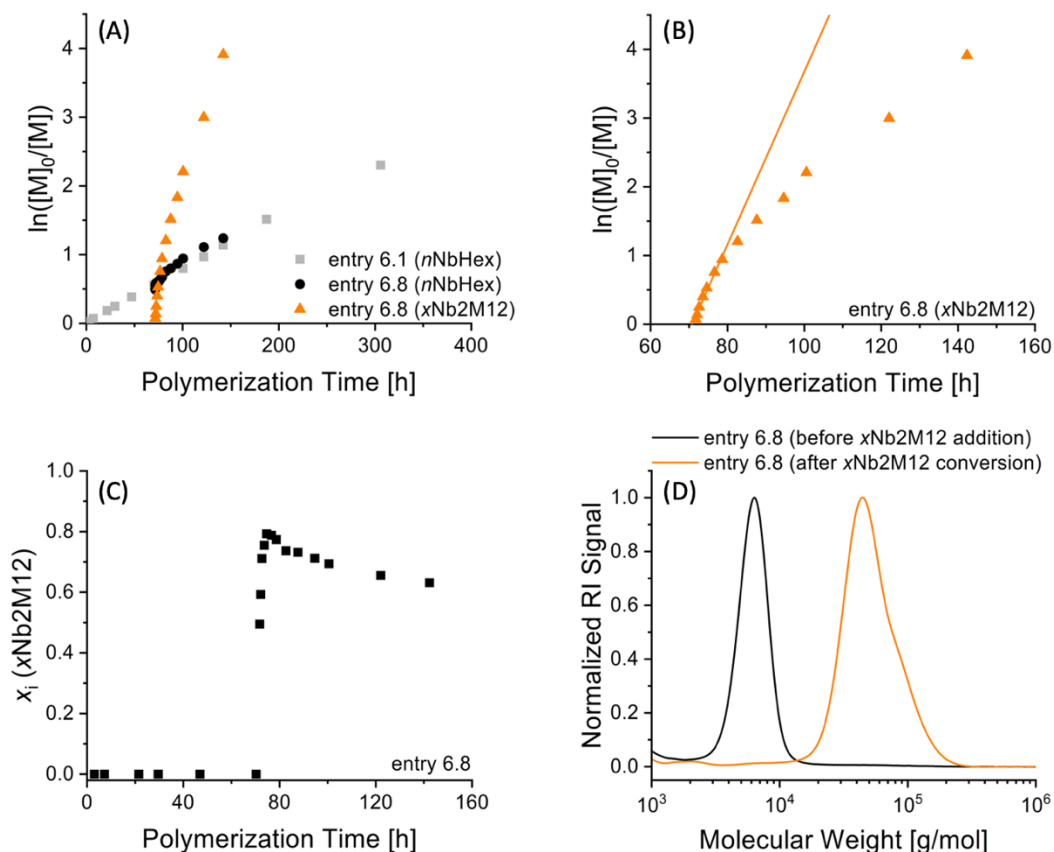


Figure S6.22. (A) Kinetic plots of entries 6.1 (Table 6.1) and 6.8 (Table 6.2), (B) highlighting **xNb2M12** during copolymerization, (C) molar fraction (x_i) of **xNb2M12** in entry 6.8 as a function of polymerization time, based on ^1H NMR spectroscopy data (Figure S6.21), and (D) SEC traces of entry 6.8 before **xNb2M12** addition and after **xNb2M12** conversion. Line represents linear fit.

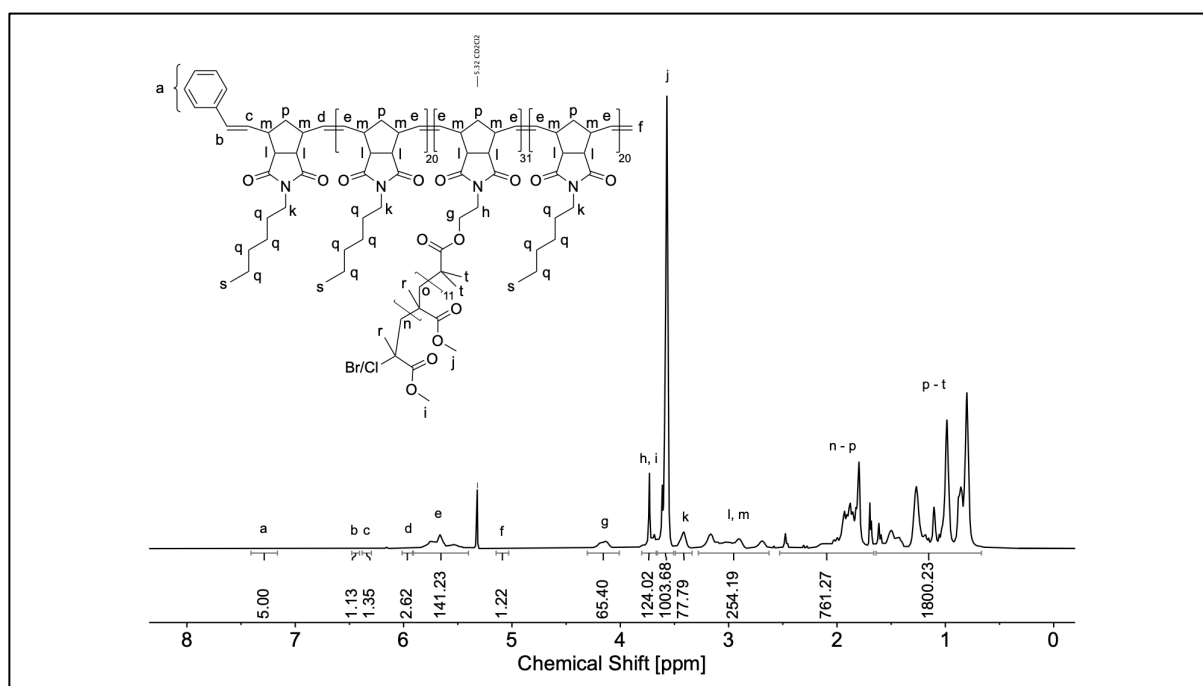


Figure S6.23. ^1H NMR spectrum of entry 6.8 in CD_2Cl_2 (500 MHz).

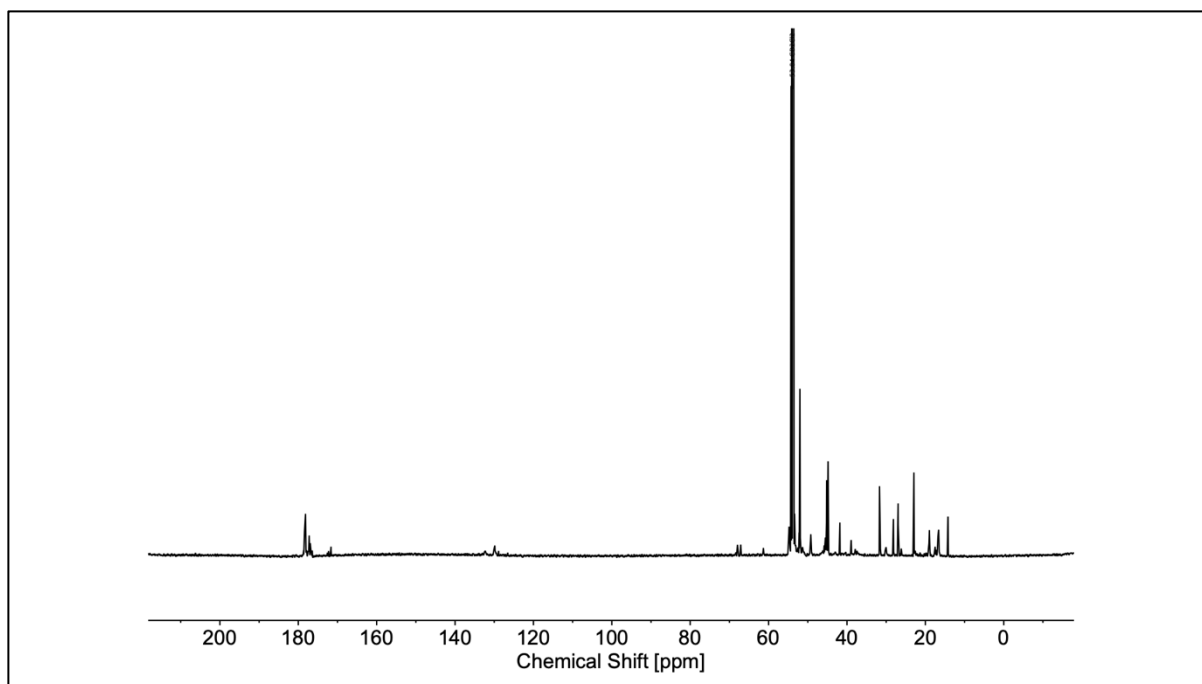


Figure S6.24. ^{13}C NMR spectrum of entry 6.8 in CD_2Cl_2 (126 MHz).

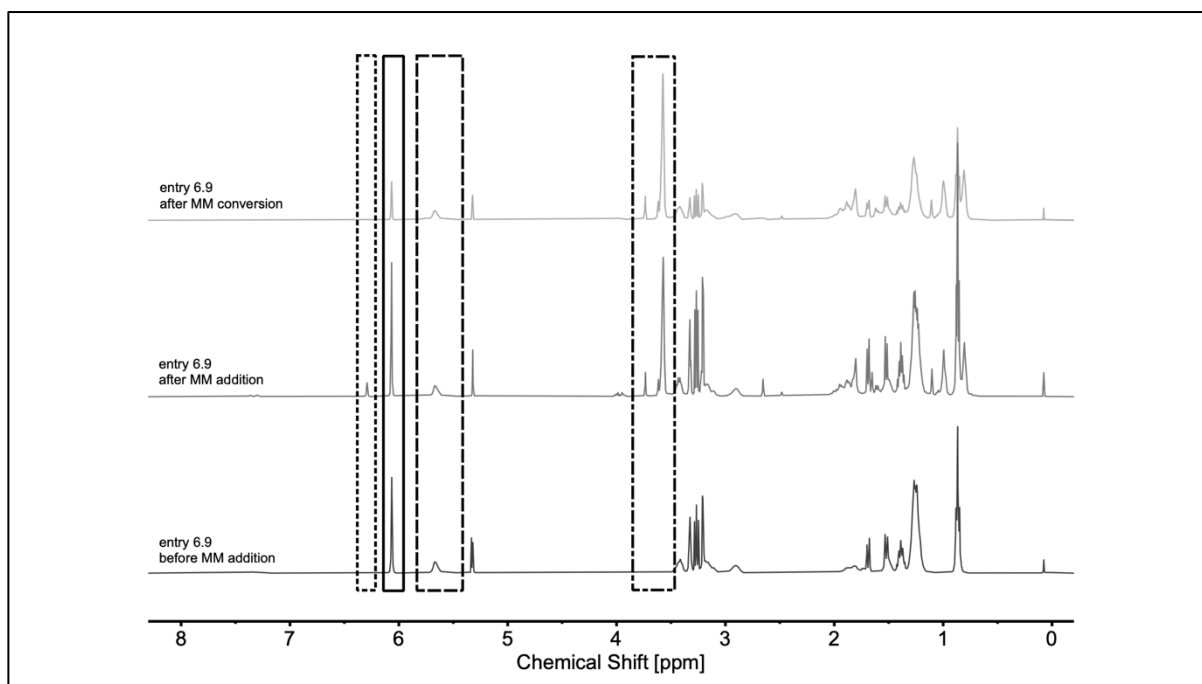


Figure S6.25. Representative stacked ^1H NMR spectra of entry 6.9 before (bottom) and after (middle) the addition of **xNb6M13**, and after its complete conversion (top) in CD_2Cl_2 (500 MHz). Boxes: *endo* norbornene olefin (solid); poly(norbornene) olefin (dashed); *exo* norbornene olefin (dotted); methoxy groups (dash-dotted).

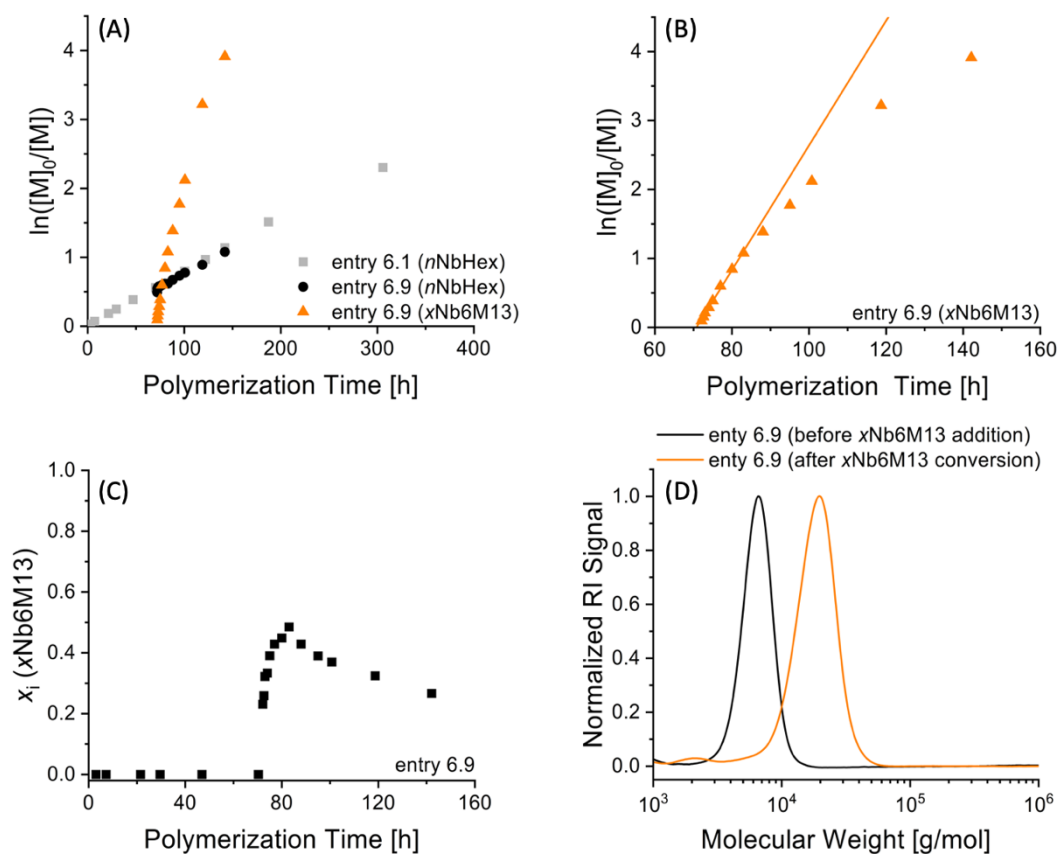


Figure S6.26. (A) Kinetic plots of entries 6.1 (Table 6.1) and 6.9 (Table 6.2), (B) highlighting **xNb6M13** during copolymerization, (C) molar fraction (x_i) of **xNb6M13** in entry 6.9 as a function of polymerization time, based on ^1H NMR spectroscopy data (Figure S6.25), and (D) SEC traces of entry 6.9 before **xNb6M13** addition and after **xNb6M13** conversion. Line represents linear fit.

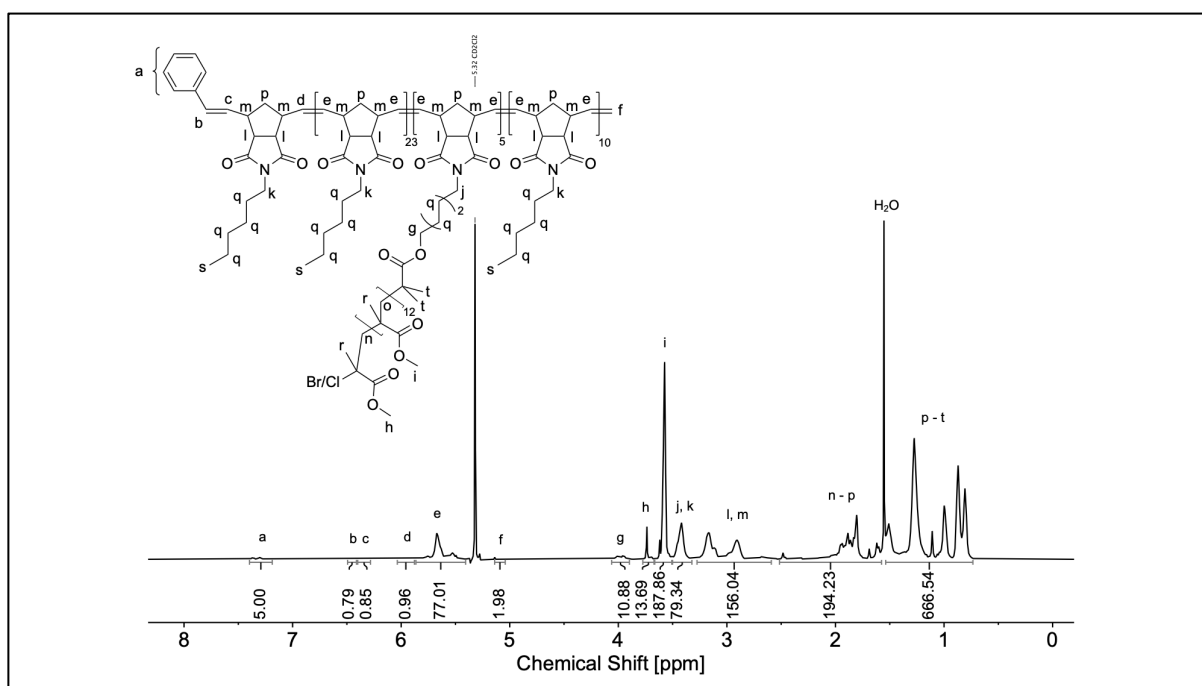


Figure S6.27. ^1H NMR spectrum of entry 6.9 in CD_2Cl_2 (500 MHz).

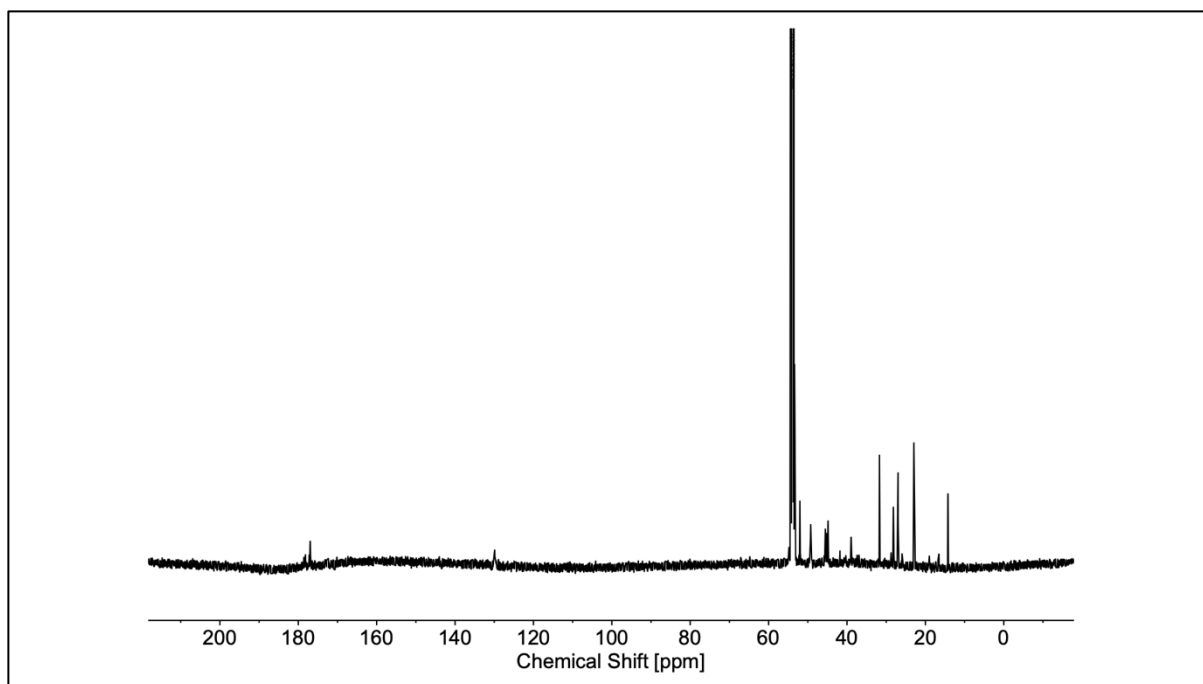


Figure S6.28. ^{13}C NMR spectrum of entry 6.9 in CD_2Cl_2 (126 MHz).

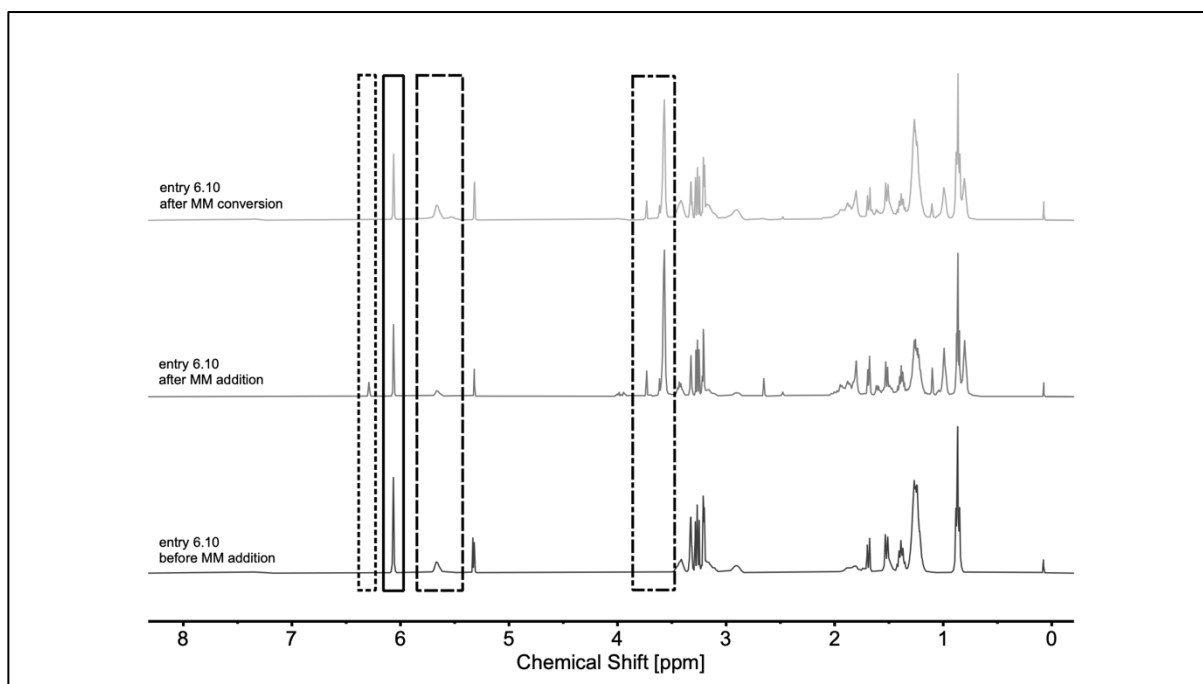


Figure S6.29. Representative stacked ^1H NMR spectra of entry 6.10 before (bottom) and after (middle) the addition of **xNb6M13**, and after its complete conversion (top) in CD_2Cl_2 (500 MHz). Boxes: *endo* norbornene olefin (solid); poly(norbornene) olefin (dashed); *exo* norbornene olefin (dotted); methoxy groups (dash-dotted).

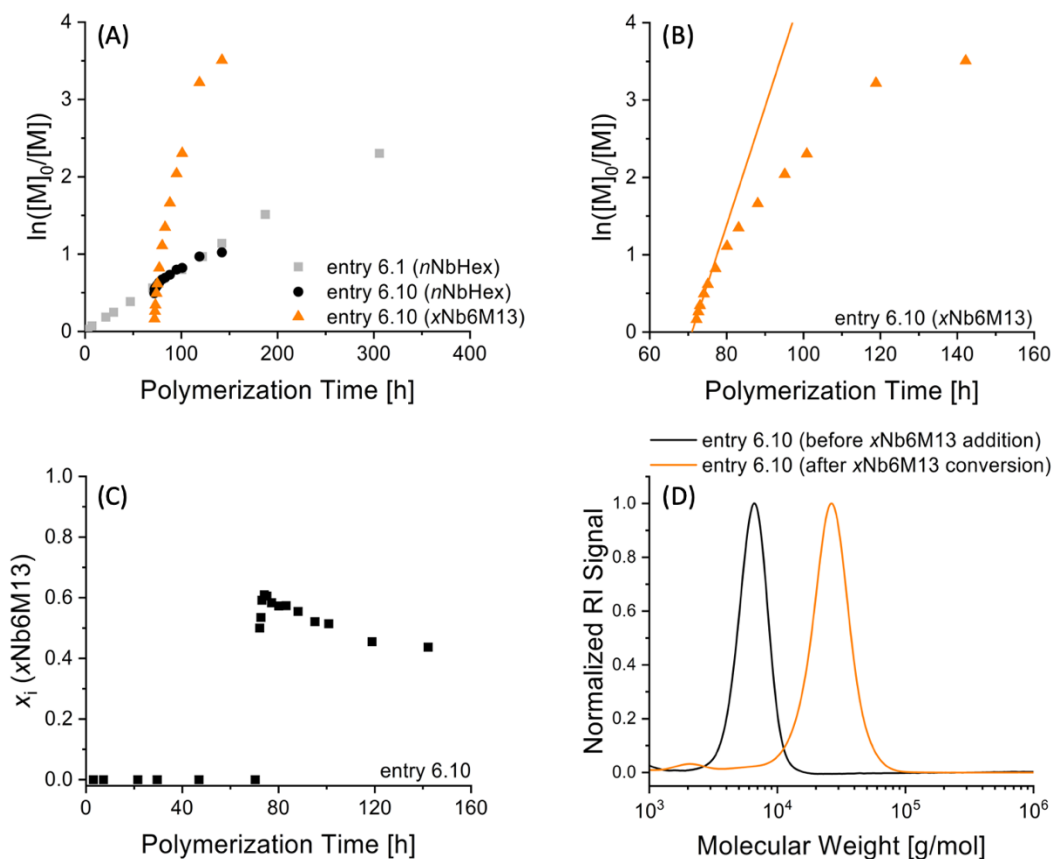


Figure S6.30. (A) Kinetic plots of entries 6.1 (Table 6.1) and 6.10 (Table 6.2), (B) highlighting **xNb6M13** during copolymerization, (C) molar fraction (x_i) of **xNb6M13** in entry 6.10 as a function of polymerization time, based on ^1H NMR spectroscopy data (Figure S6.29), and (D) SEC traces of entry 6.10 before **xNb6M13** addition and after **xNb6M13** conversion. Line represents linear fit.

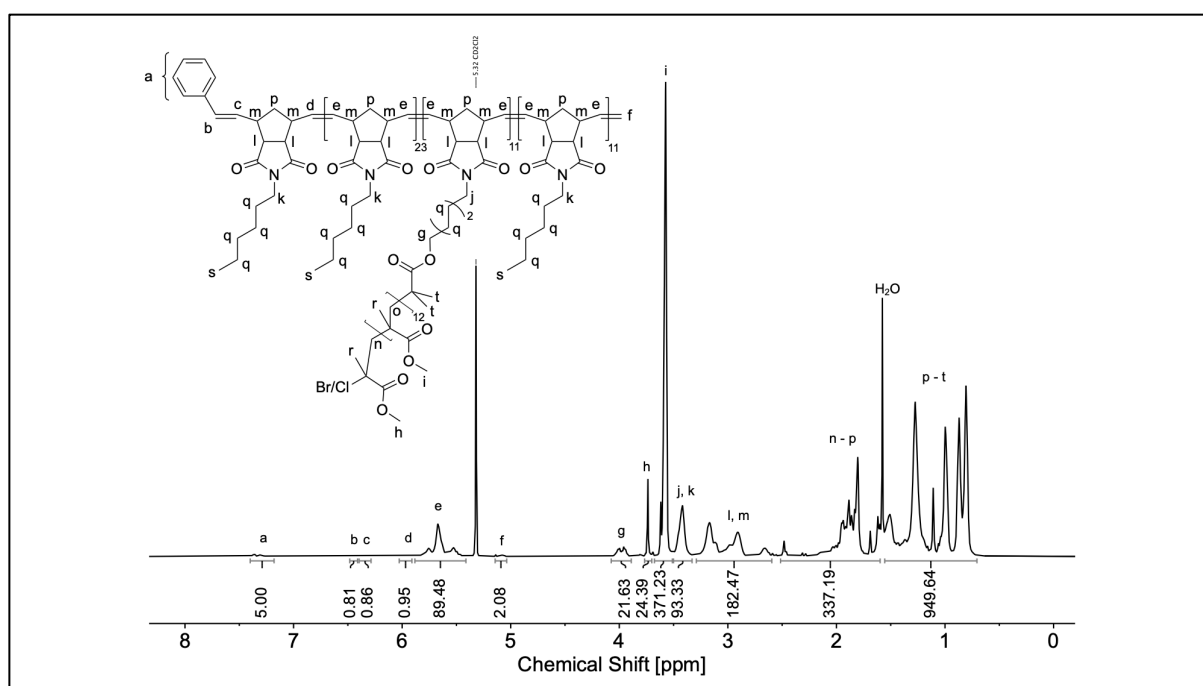


Figure S6.31. ^1H NMR spectrum of entry 6.10 in CD_2Cl_2 (500 MHz).

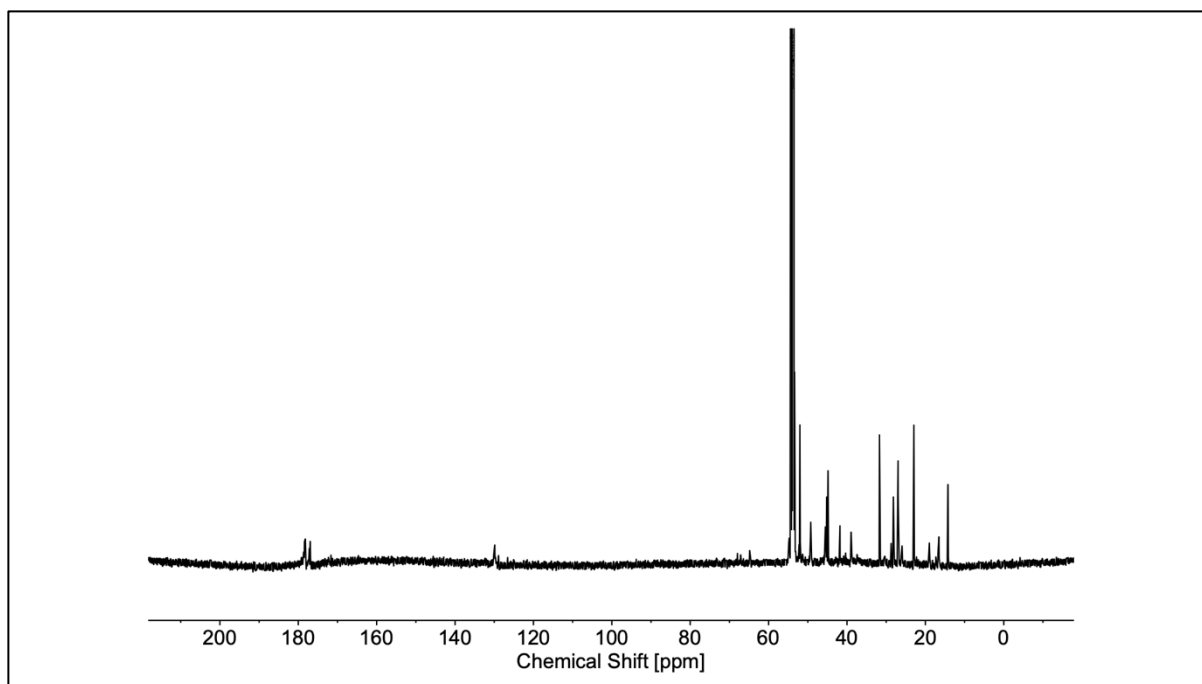


Figure S6.32. ^{13}C NMR spectrum of entry 6.10 in CD_2Cl_2 (126 MHz).

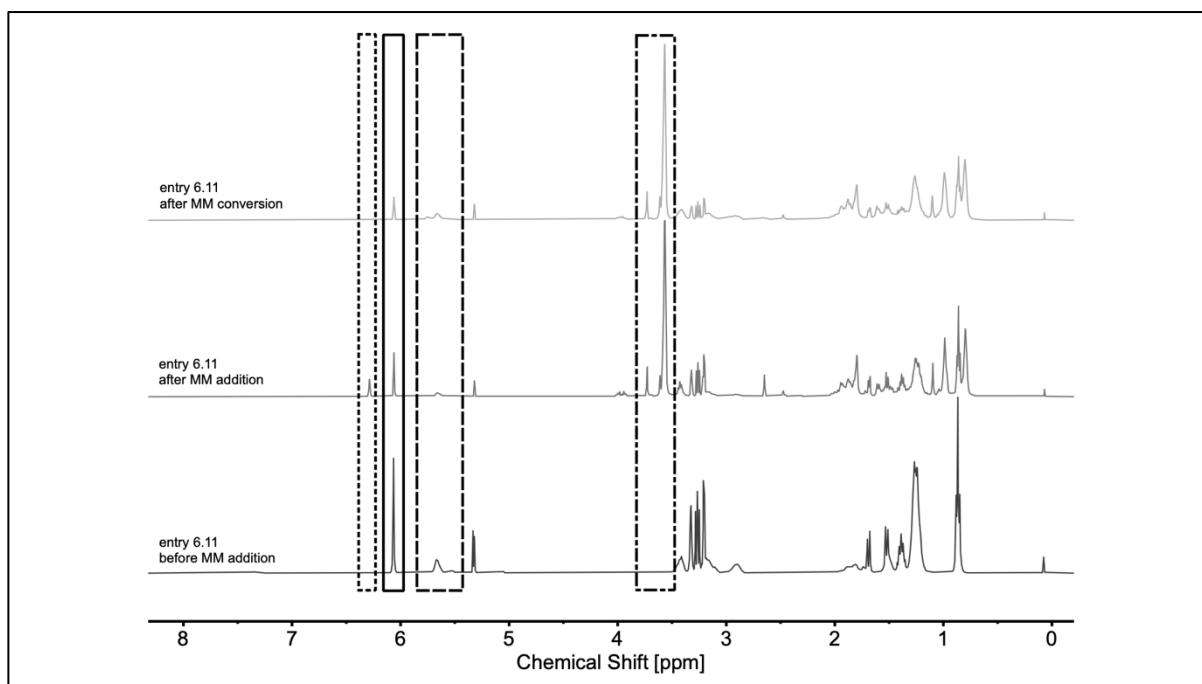


Figure S6.33. Representative stacked ^1H NMR spectra of entry 6.11 before (bottom) and after (middle) the addition of **xNb6M13**, and after its complete conversion (top) in CD_2Cl_2 (500 MHz). Boxes: *endo* norbornene olefin (solid); poly(norbornene) olefin (dashed); *exo* norbornene olefin (dotted); methoxy groups (dash-dotted).

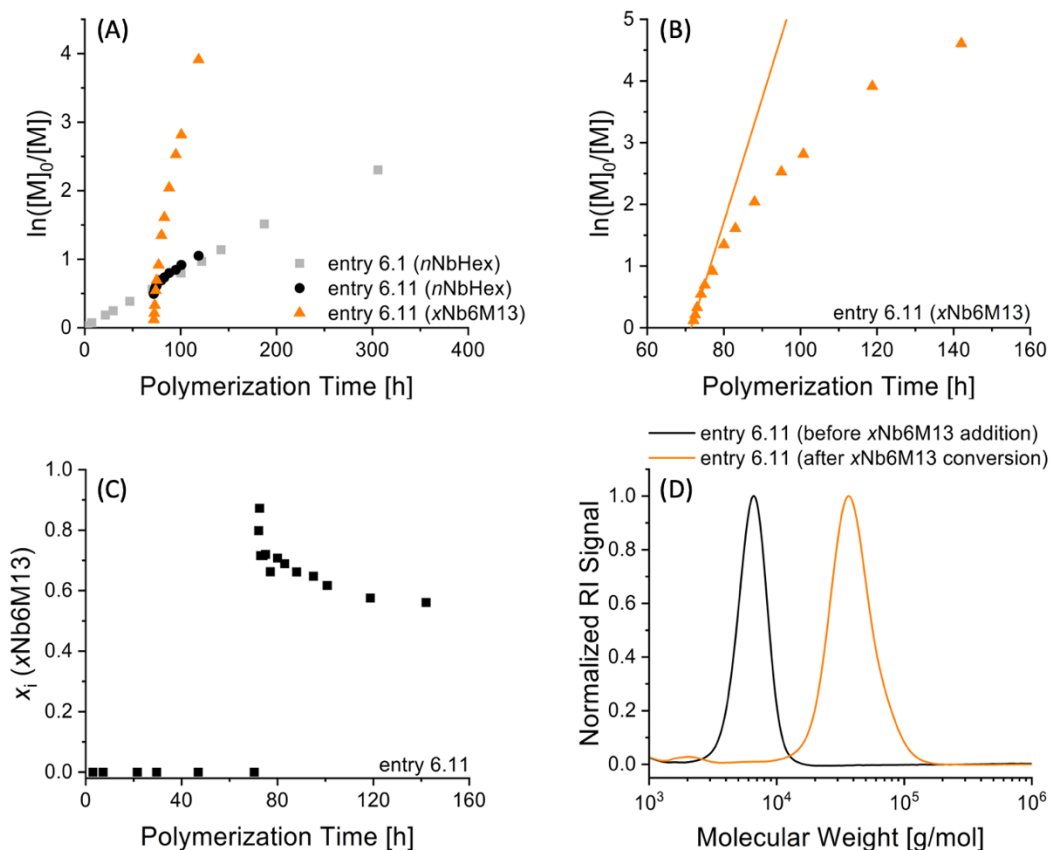


Figure S6.34. (A) Kinetic plots of entries 6.1 (Table 6.1) and 6.11 (Table 6.2), (B) highlighting $x\text{Nb6M13}$ during copolymerization, (C) molar fraction (x_i) of $x\text{Nb6M13}$ in entry 6.11 as a function of polymerization time, based on ^1H NMR spectroscopy data (Figure S6.33), and (D) SEC traces of entry 6.11 before $x\text{Nb6M13}$ addition and after $x\text{Nb6M13}$ conversion. Line represents linear fit.

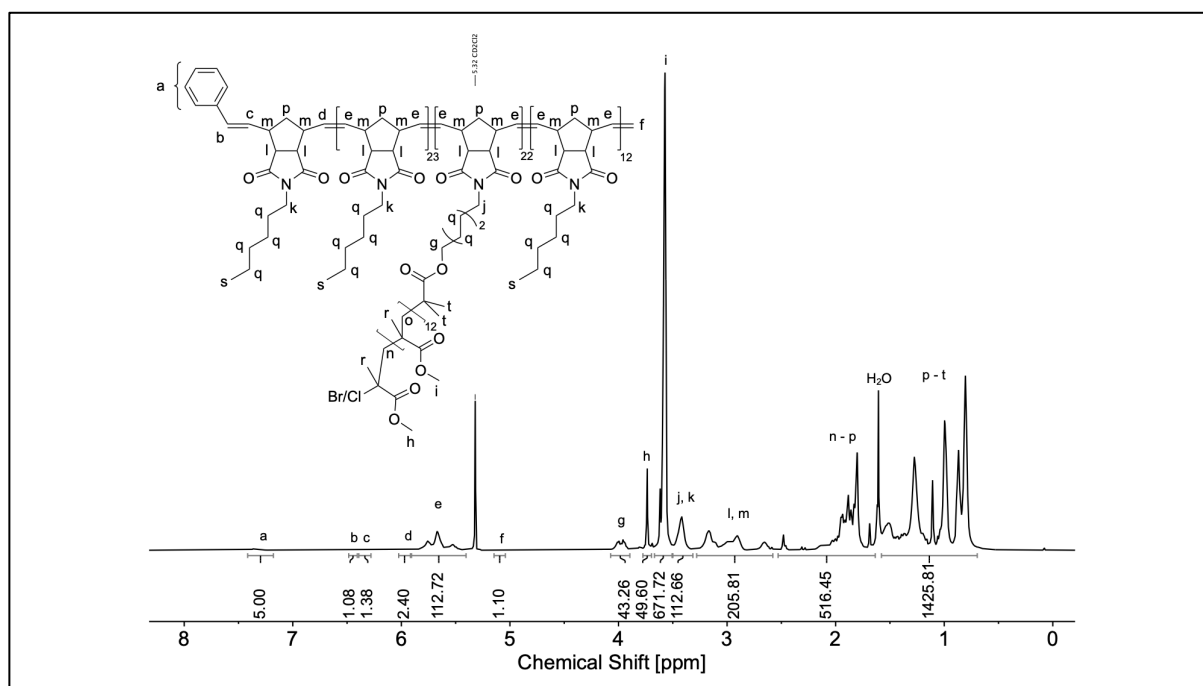


Figure S6.35. ^1H NMR spectrum of entry 6.11 in CD_2Cl_2 (500 MHz).

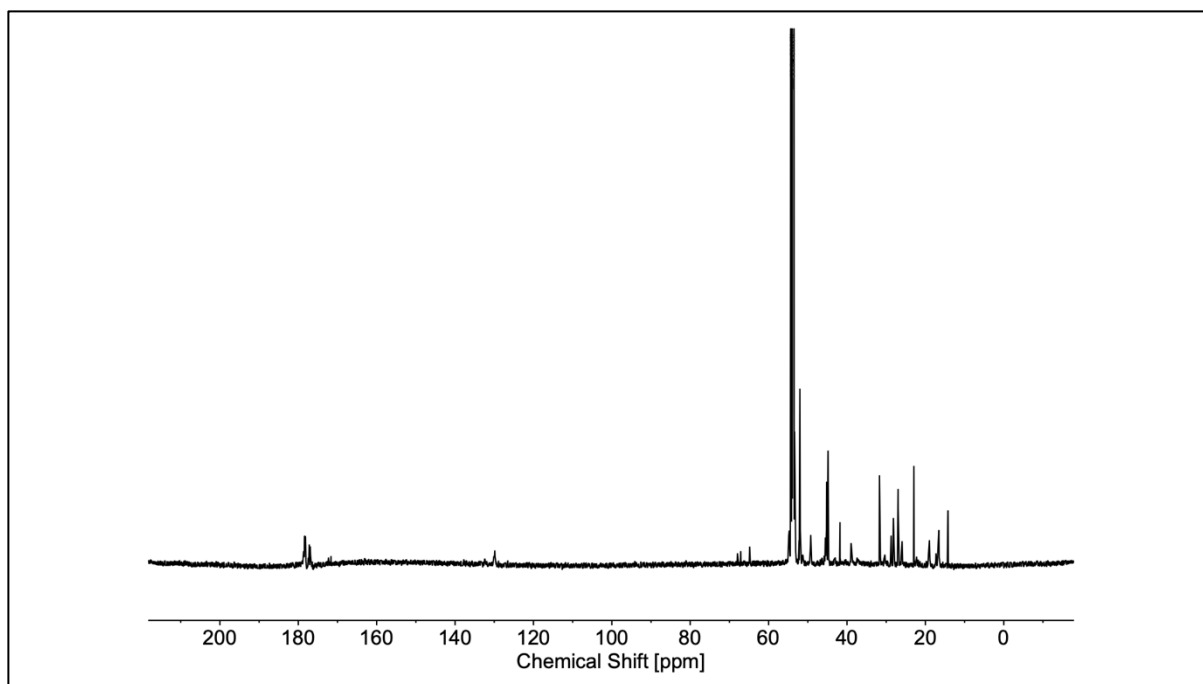


Figure S6.36. ^{13}C NMR spectrum of entry 6.11 in CD_2Cl_2 (126 MHz).

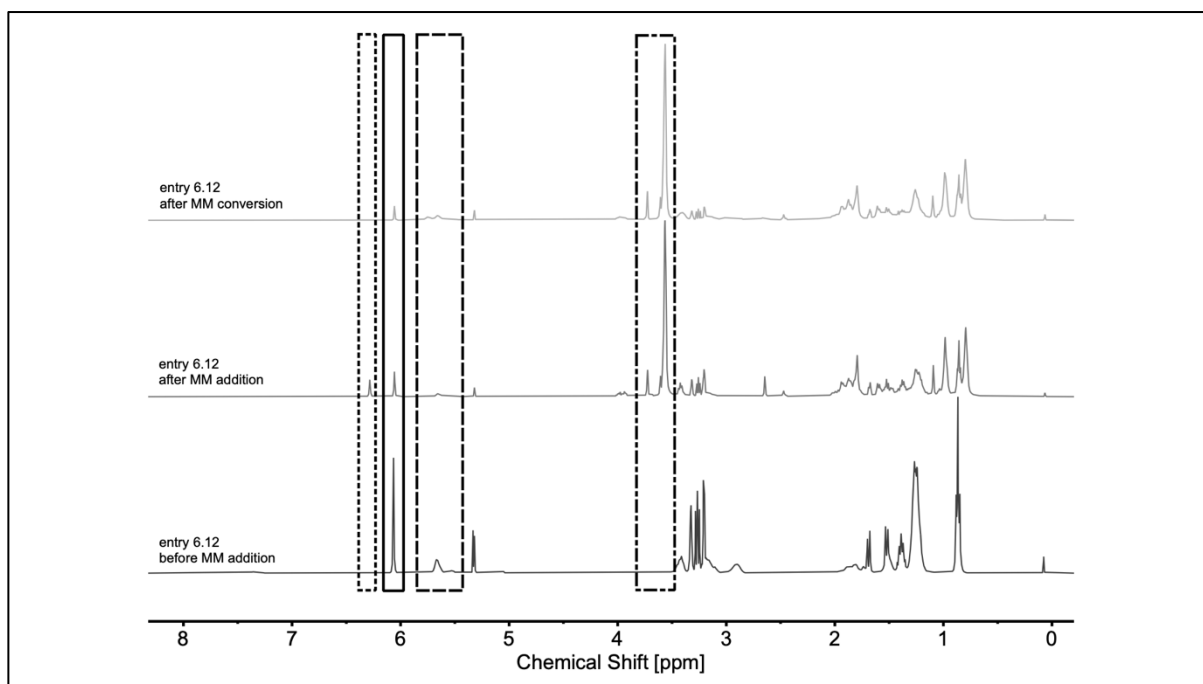


Figure S6.37. Representative stacked ^1H NMR spectra of entry 6.12 before (bottom) and after (middle) the addition of **xNb6M13**, and after its complete conversion (top) in CD_2Cl_2 (500 MHz). Boxes: *endo* norbornene olefin (solid); poly(norbornene) olefin (dashed); *exo* norbornene olefin (dotted); methoxy groups (dash-dotted).

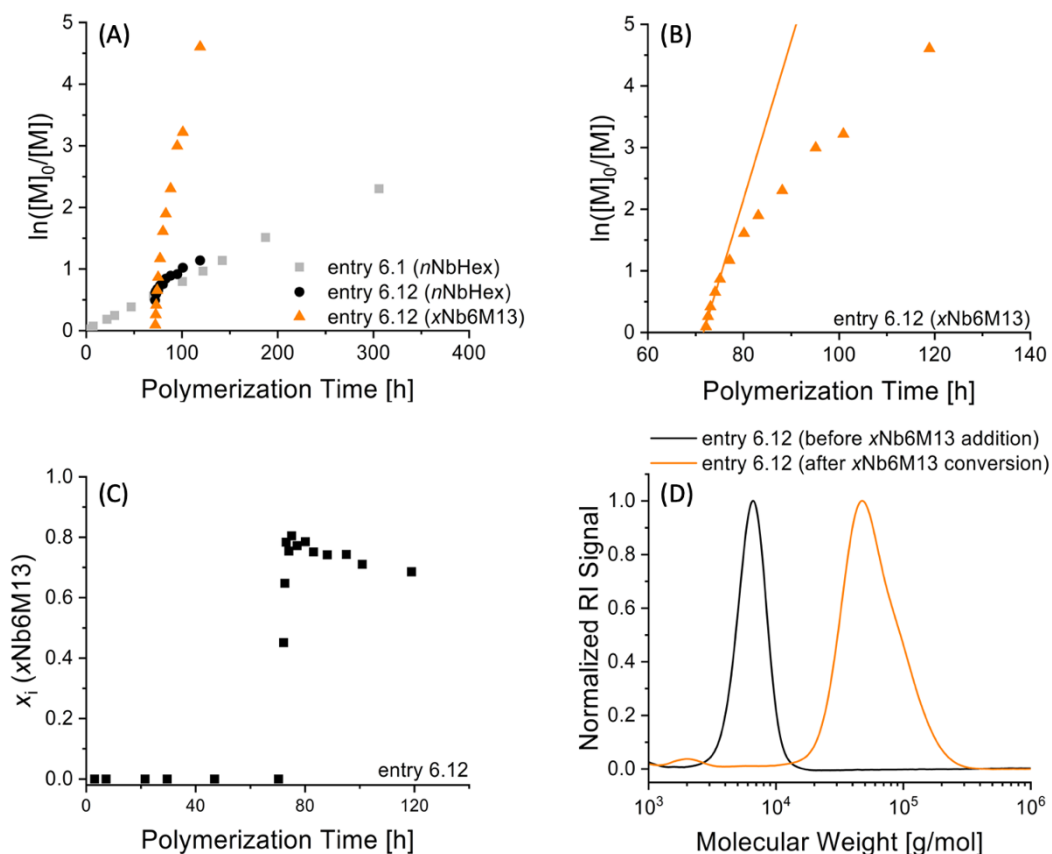


Figure S6.38. (A) Kinetic plots of entries 6.1 (Table 6.1) and 6.12 (Table 6.2), (B) highlighting **xNb6M13** during copolymerization, (C) molar fraction (x_i) of **xNb6M13** in entry 6.12 as a function of polymerization time, based on ^1H NMR spectroscopy data (Figure S6.37), and (D) SEC traces of entry 6.12 before **xNb6M13** addition and after **xNb6M13** conversion. Line represents linear fit.

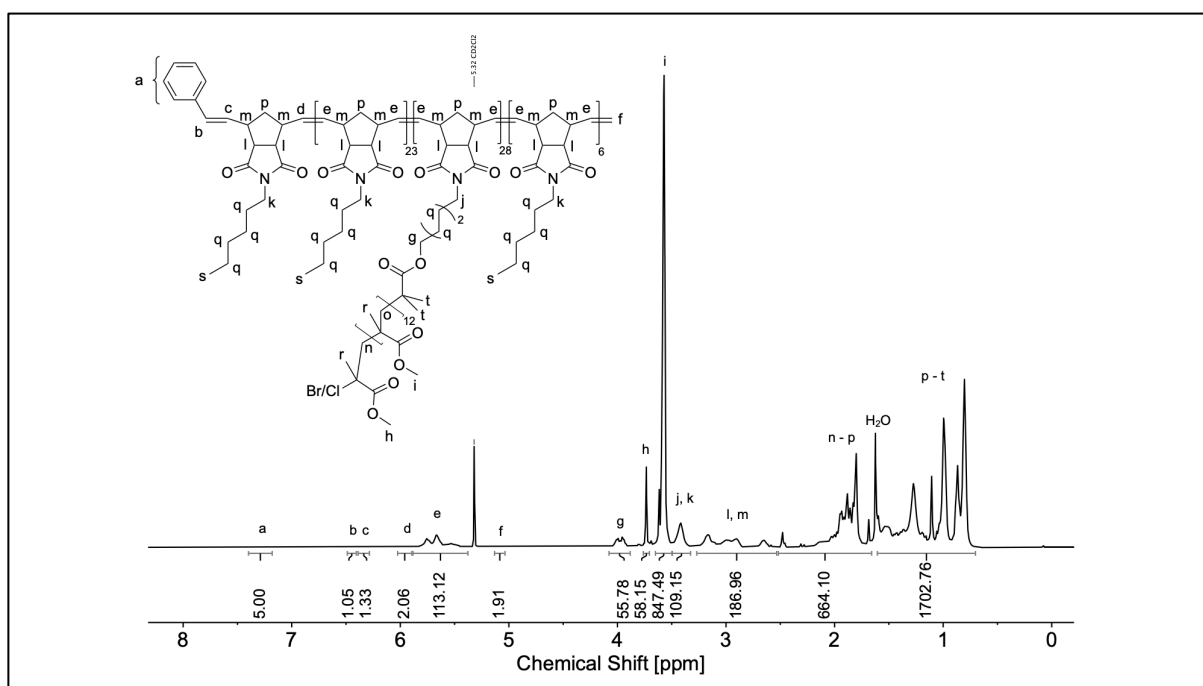


Figure S6.39. ^1H NMR spectrum of entry 6.12 in CD_2Cl_2 (500 MHz).

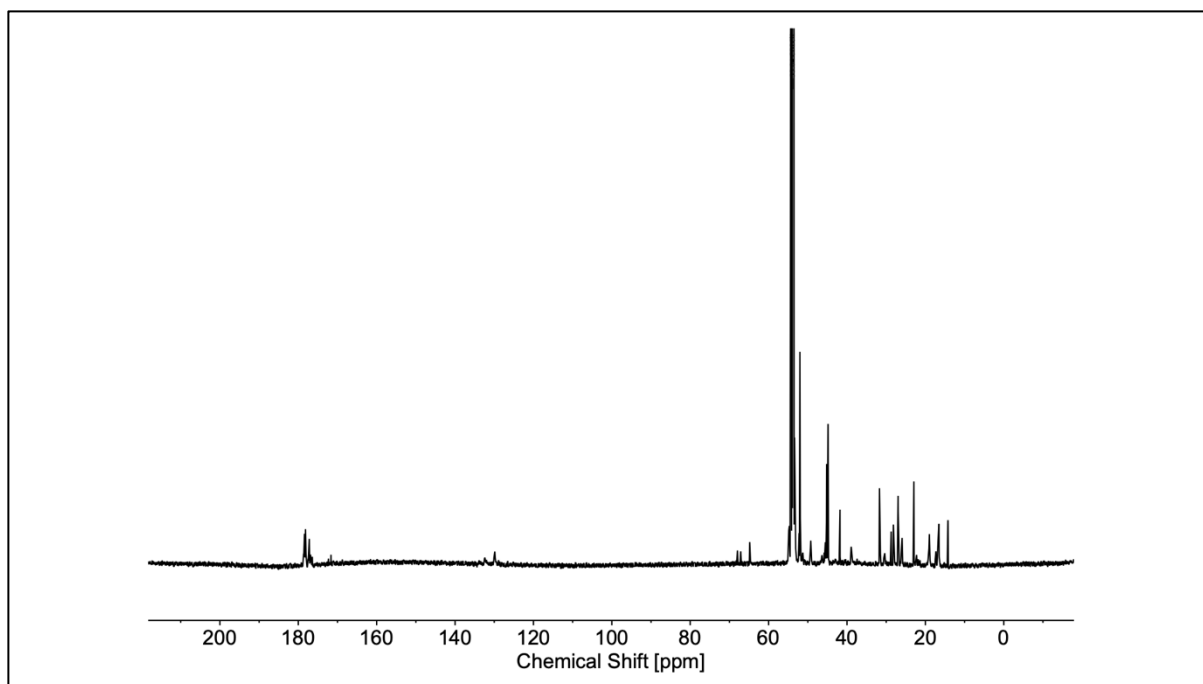


Figure S6.40. ^{13}C NMR spectrum of entry 6.12 in CD_2Cl_2 (126 MHz).

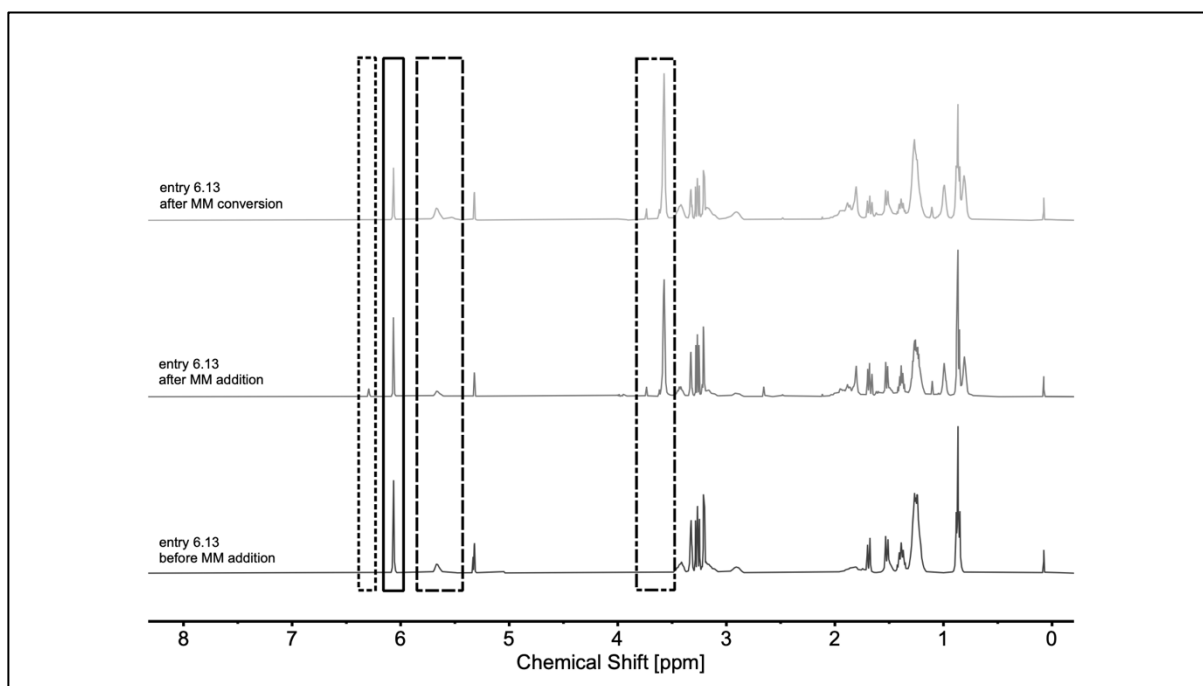


Figure S6.41. Representative stacked ^1H NMR spectra of entry 6.13 before (bottom) and after (middle) the addition of **xNb6M17**, and after its complete conversion (top) in CD_2Cl_2 (500 MHz). Boxes: *endo* norbornene olefin (solid); poly(norbornene) olefin (dashed); *exo* norbornene olefin (dotted); methoxy groups (dash-dotted).

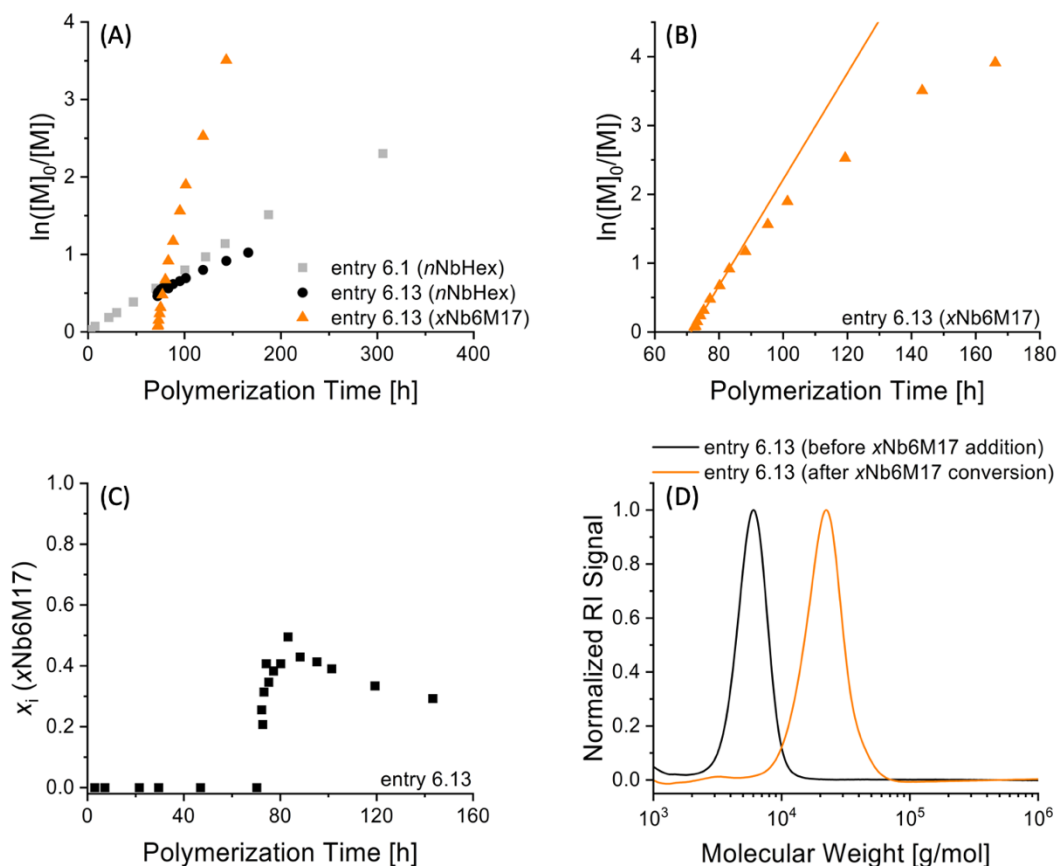


Figure S6.42. (A) Kinetic plots of entries 6.1 (Table 6.1) and 6.13 (Table 6.2), (B) highlighting $x\text{Nb6M17}$ during copolymerization, (C) molar fraction (x_i) of $x\text{Nb6M17}$ in entry 6.13 as a function of polymerization time, based on ^1H NMR spectroscopy data (Figure S6.41), and (D) SEC traces of entry 6.13 before $x\text{Nb6M17}$ addition and after $x\text{Nb6M17}$ conversion. Line represents linear fit.

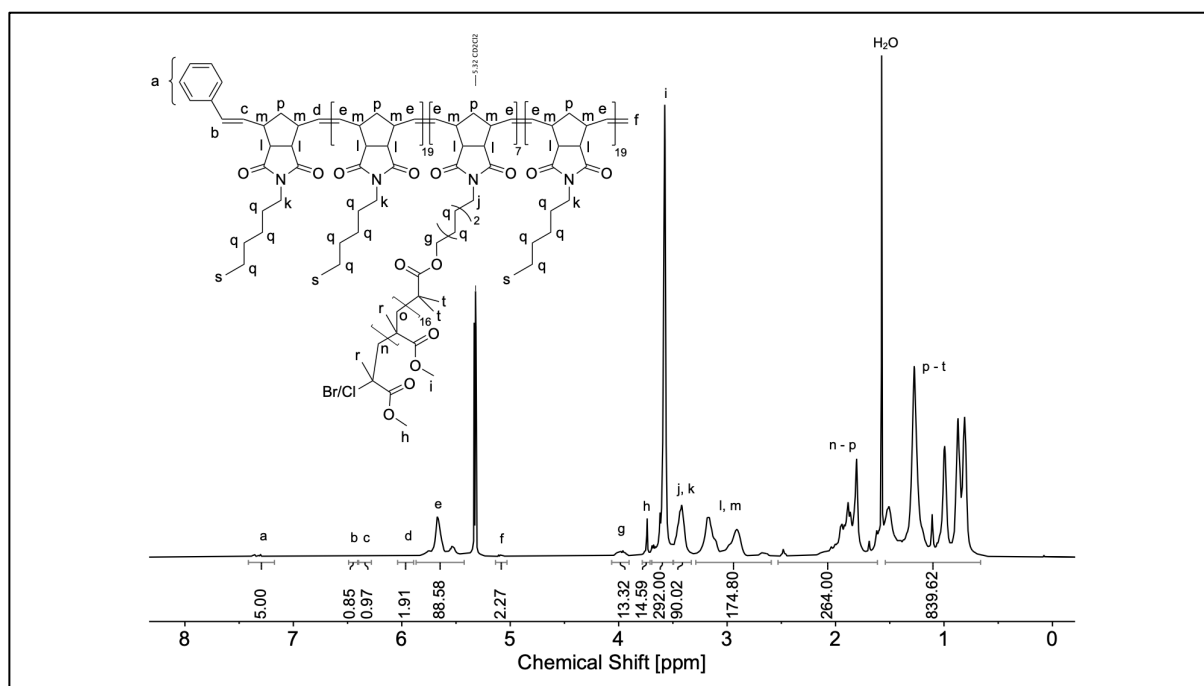


Figure S6.43. ^1H NMR spectrum of entry 6.13 in CD_2Cl_2 (500 MHz).

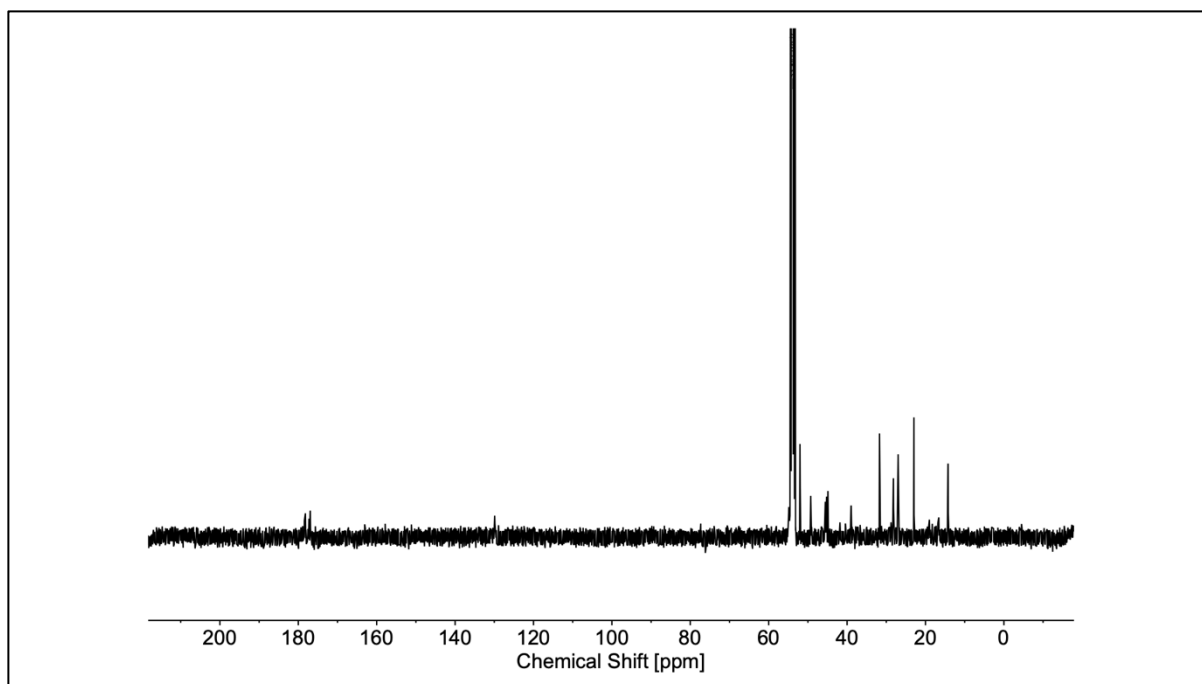


Figure S6.44. ^{13}C NMR spectrum of entry 6.13 in CD_2Cl_2 (126 MHz).

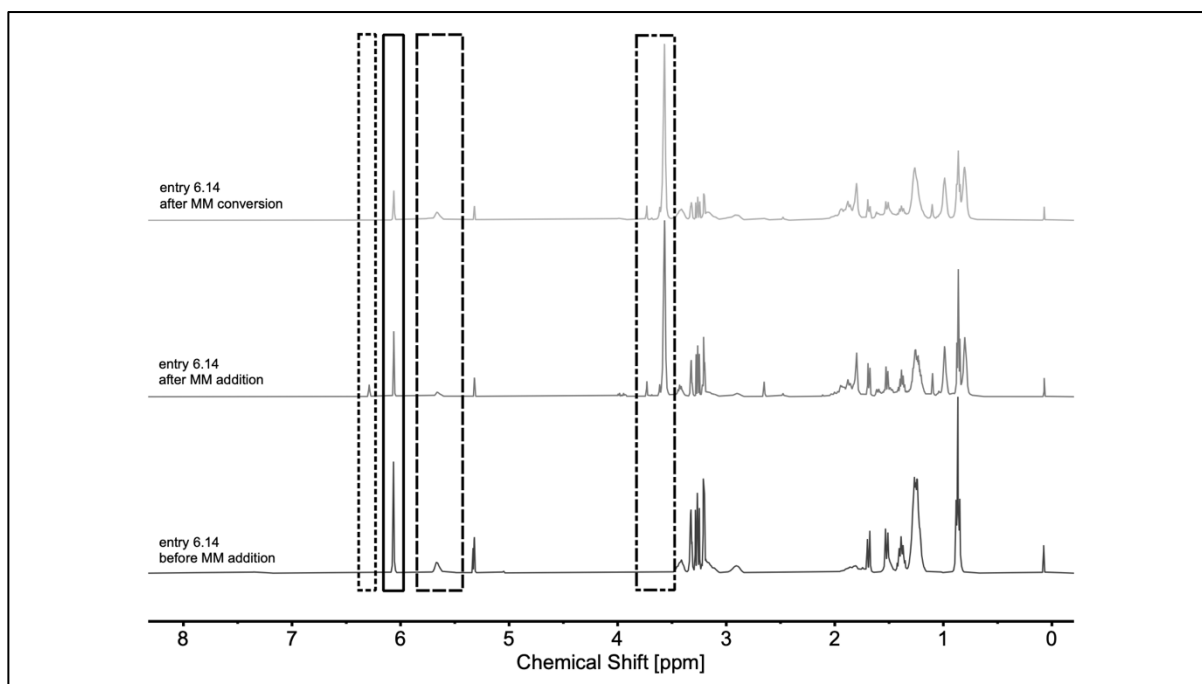


Figure S6.45. Representative stacked ^1H NMR spectra of entry 6.14 before (bottom) and after (middle) the addition of **xNb6M17**, and after its complete conversion (top) in CD_2Cl_2 (500 MHz). Boxes: *endo* norbornene olefin (solid); poly(norbornene) olefin (dashed); *exo* norbornene olefin (dotted); methoxy groups (dash-dotted).

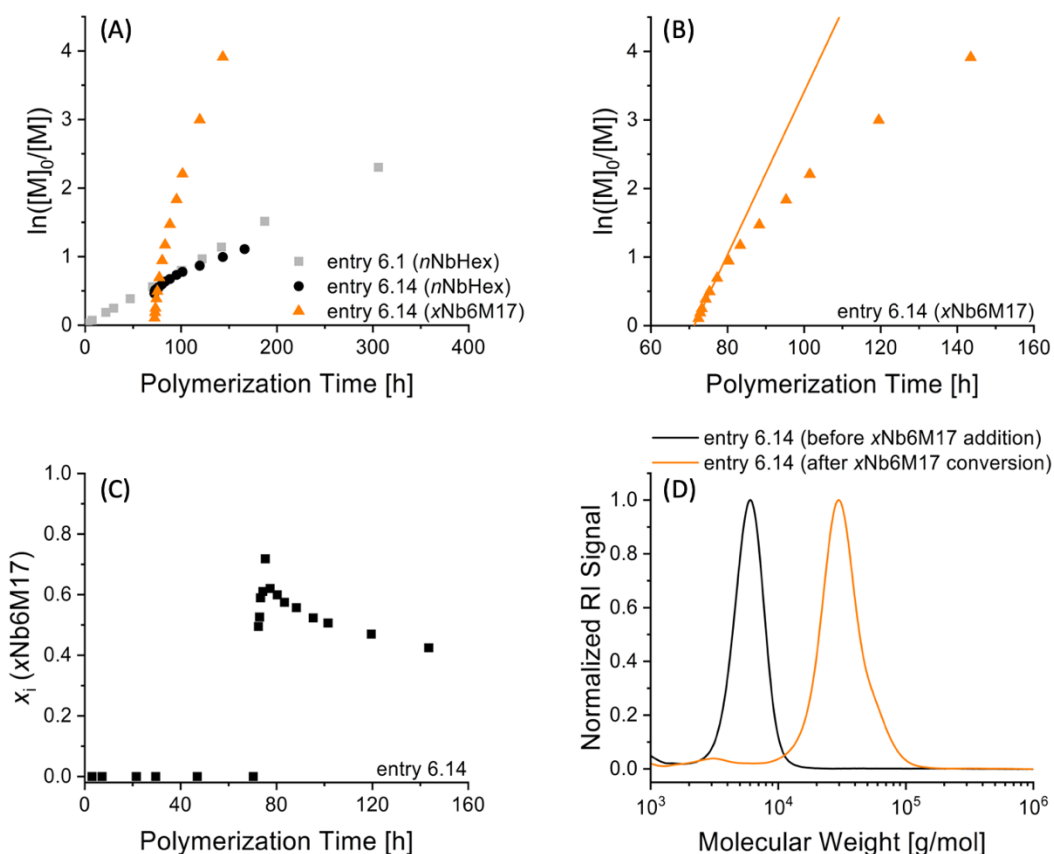


Figure S6.46. (A) Kinetic plots of entries 6.1 (Table 6.1) and 6.14 (Table 6.2), (B) highlighting $x\text{Nb6M17}$ during copolymerization, (C) molar fraction (x_i) of $x\text{Nb6M17}$ in entry 6.14 as a function of polymerization time, based on ^1H NMR spectroscopy data (Figure S6.45), and (D) SEC traces of entry 6.14 before $x\text{Nb6M17}$ addition and after $x\text{Nb6M17}$ conversion. Line represents linear fit.

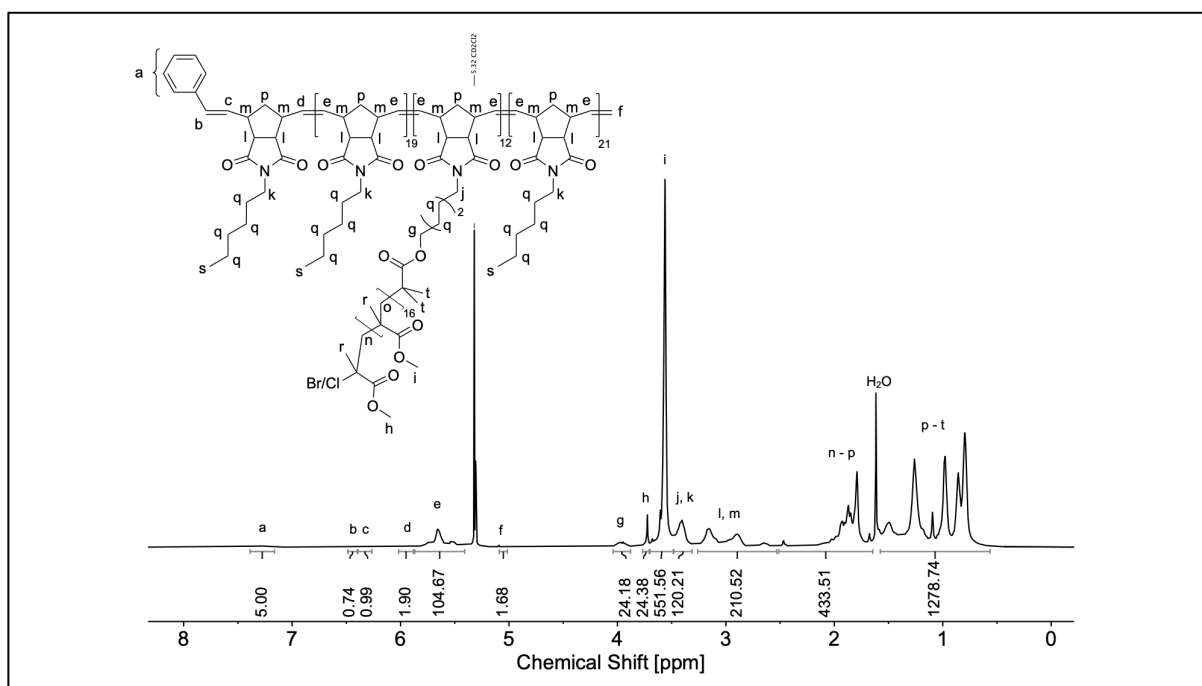


Figure S6.47. ^1H NMR spectrum of entry 6.14 in CD_2Cl_2 (500 MHz).

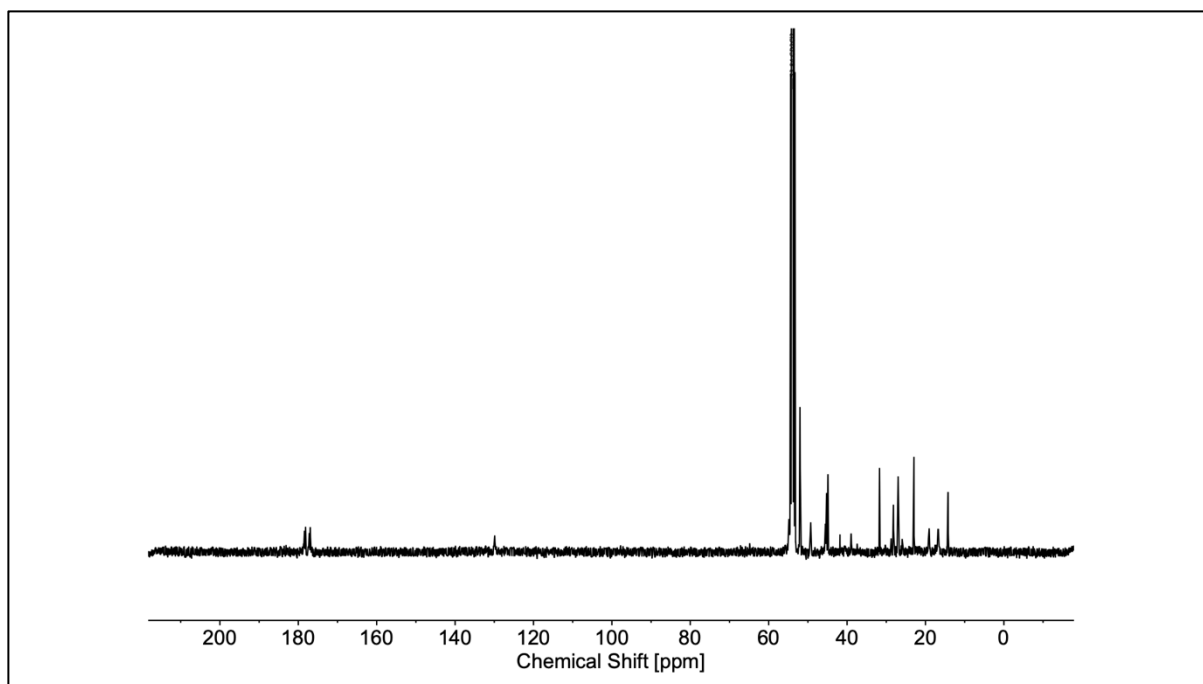


Figure S6.48. ^{13}C NMR spectrum of entry 6.14 in CD_2Cl_2 (126 MHz).

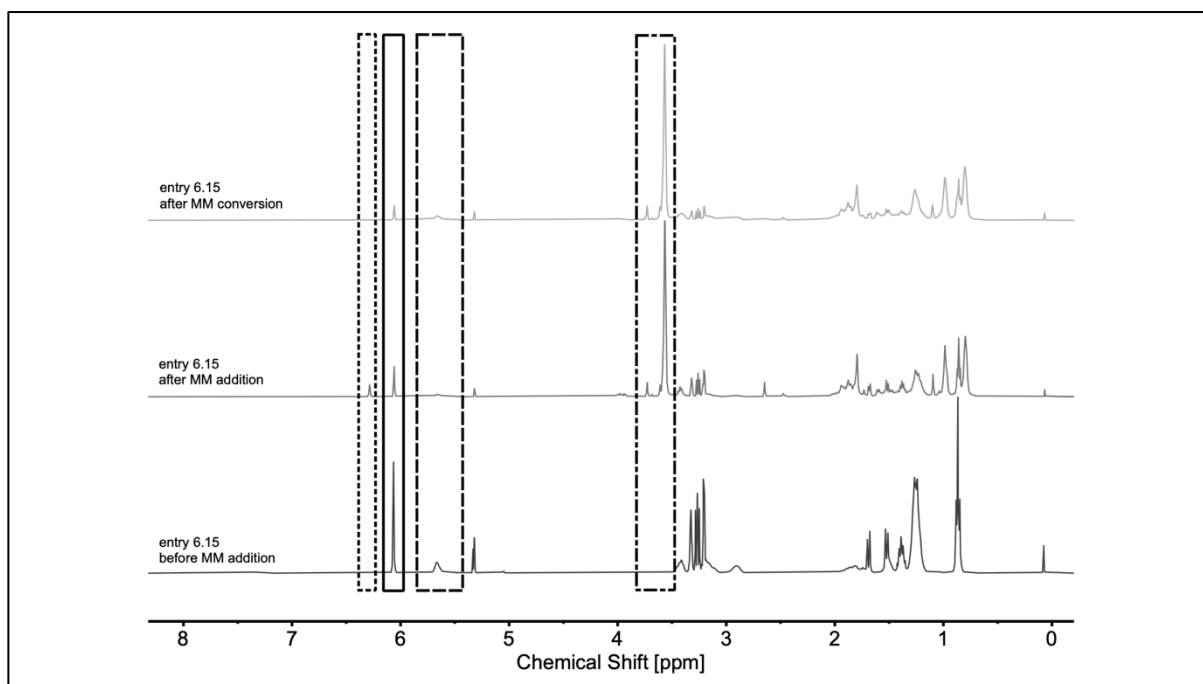


Figure S6.49. Representative stacked ^1H NMR spectra of entry 6.15 before (bottom) and after (middle) the addition of **xNb6M17**, and after its complete conversion (top) in CD_2Cl_2 (500 MHz). Boxes: *endo* norbornene olefin (solid); poly(norbornene) olefin (dashed); *exo* norbornene olefin (dotted); methoxy groups (dash-dotted).

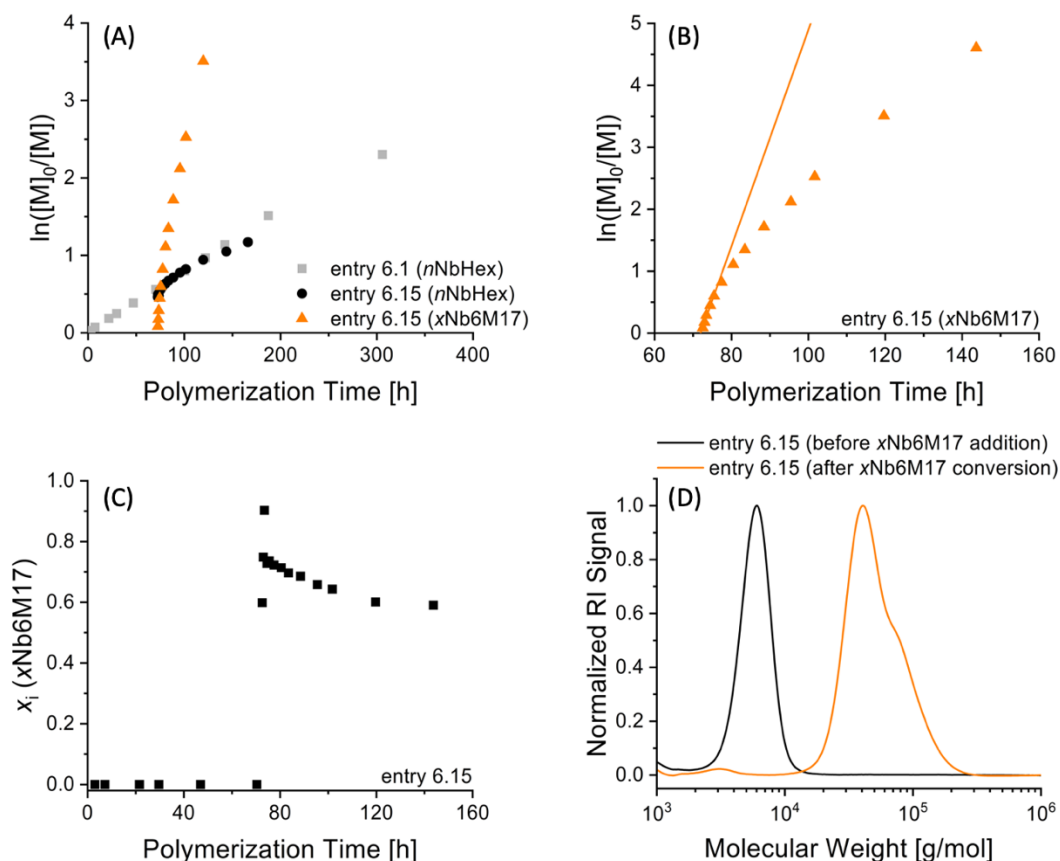


Figure S6.50. (A) Kinetic plots of entries 6.1 (Table 6.1 Scheme 6.1) and 6.15 (Table 6.2), (B) highlighting **xNb6M17** during copolymerization, (C) molar fraction (x_i) of **xNb6M17** in entry 6.15 as a function of polymerization time, based on ^1H NMR spectroscopy data (Figure S6.49), and (D) SEC traces of entry 6.15 before **xNb6M17** addition and after **xNb6M17** conversion. Line represents linear fit.

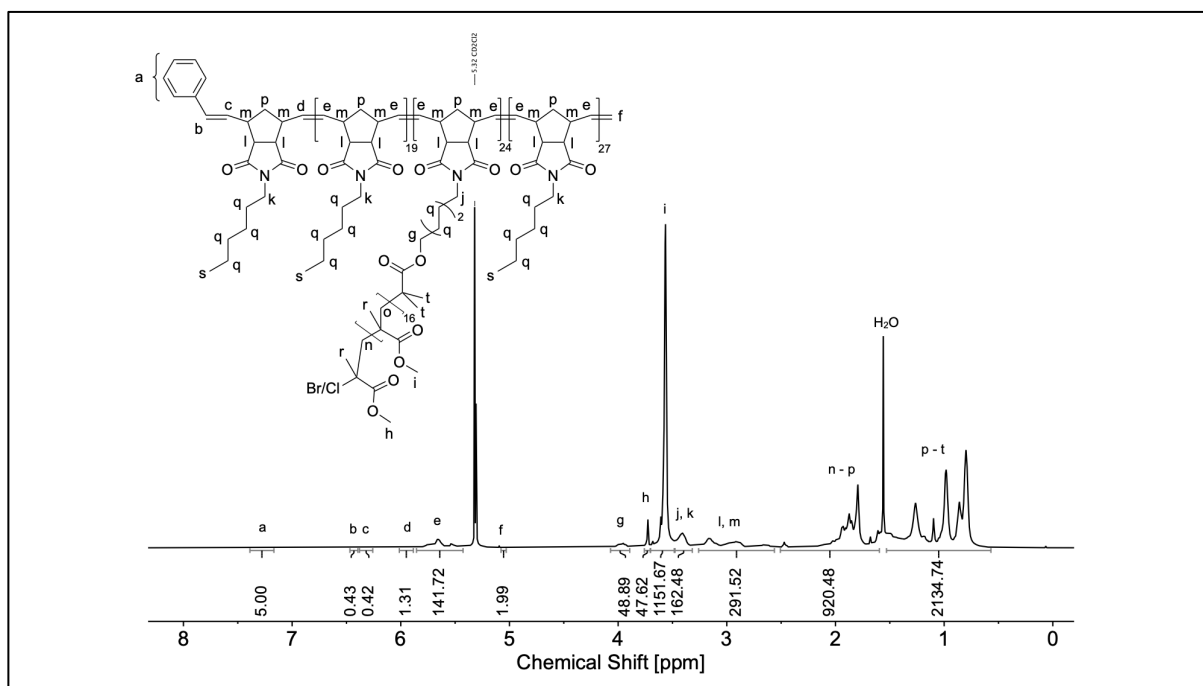


Figure S6.51. ^1H NMR spectrum of entry 6.15 in CD_2Cl_2 (500 MHz).

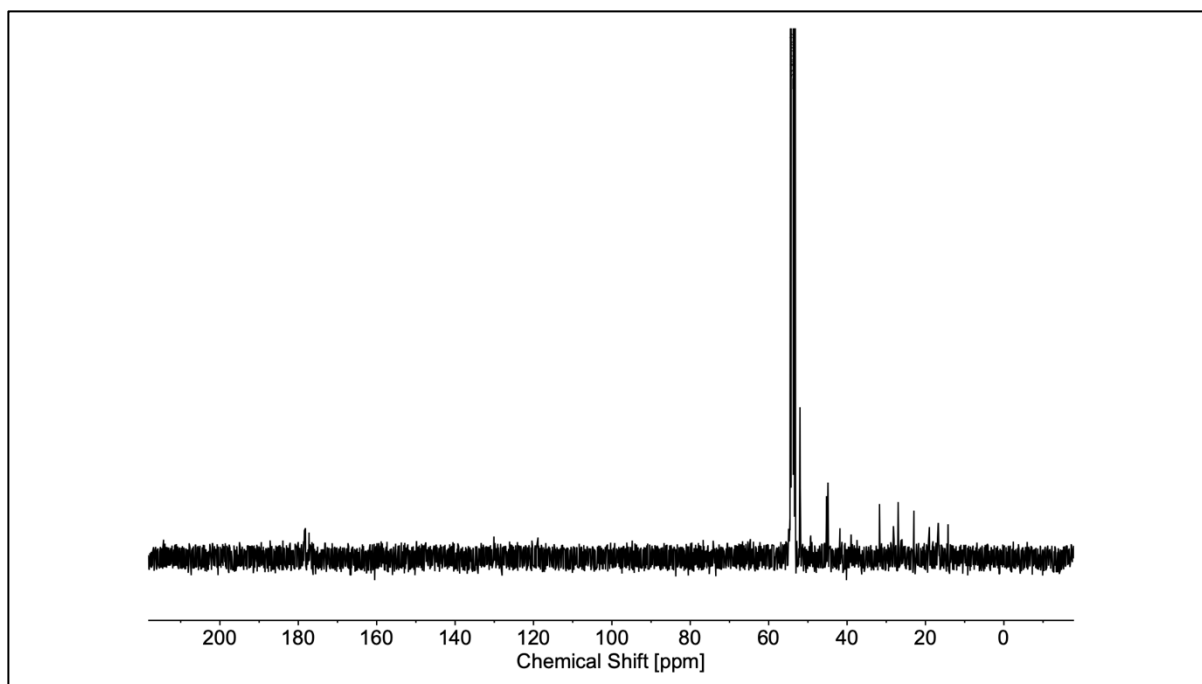


Figure S6.52. ^{13}C NMR spectrum of entry 6.15 in CD_2Cl_2 (126 MHz).

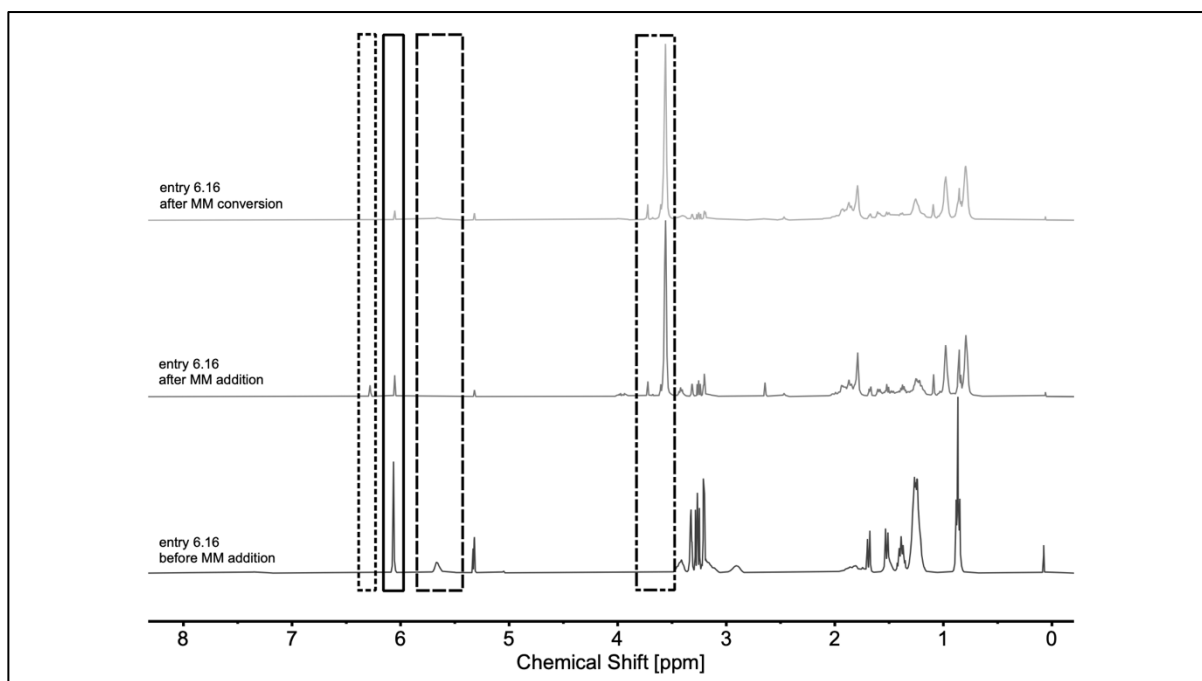


Figure S6.53. Representative stacked ^1H NMR spectra of entry 6.16 before (bottom) and after (middle) the addition of **xNb6M17**, and after its complete conversion (top) in CD_2Cl_2 (500 MHz). Boxes: *endo* norbornene olefin (solid); poly(norbornene) olefin (dashed); *exo* norbornene olefin (dotted); methoxy groups (dash-dotted).

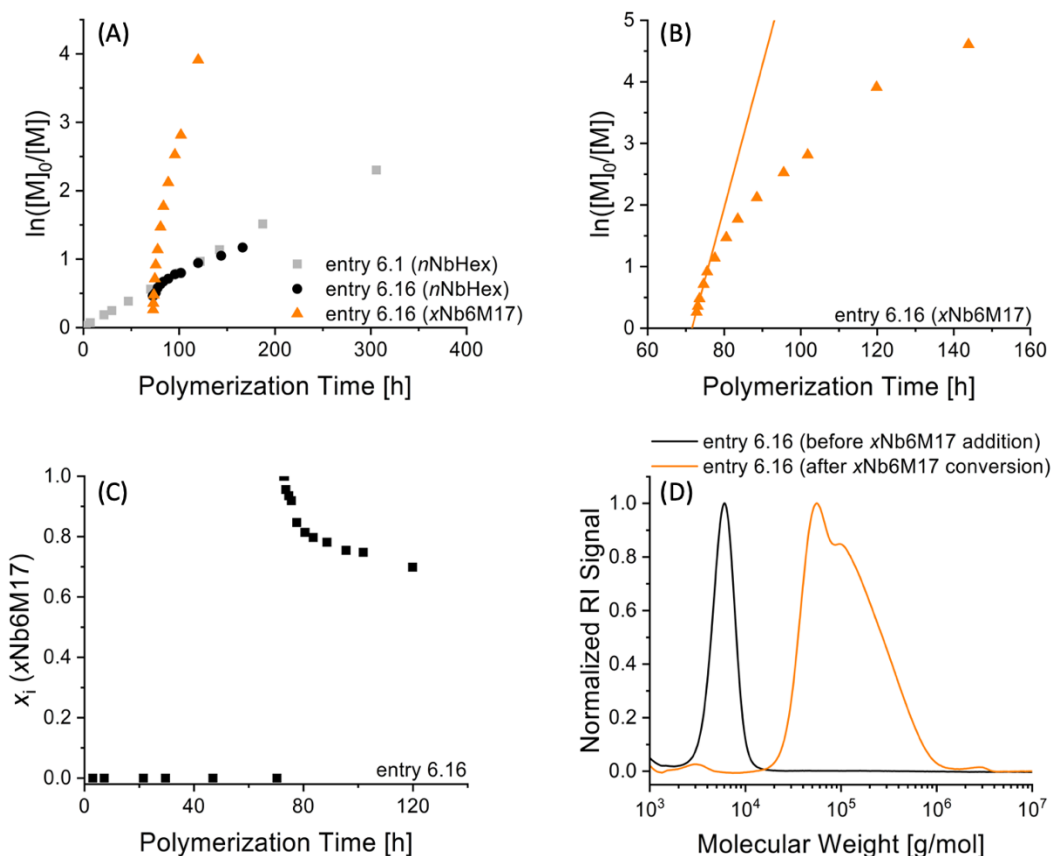


Figure S6.54. (A) Kinetic plots of entries 6.1 (Table 6.1) and 6.16 (Table 6.2), (B) highlighting $x\text{Nb6M17}$ during copolymerization, (C) molar fraction (x_i) of $x\text{Nb6M17}$ in entry 6.16 as a function of polymerization time, based on ^1H NMR spectroscopy data (Figure S6.53), and (D) SEC traces of entry 6.16 before $x\text{Nb6M17}$ addition and after $x\text{Nb6M17}$ conversion. Line represents linear fit.

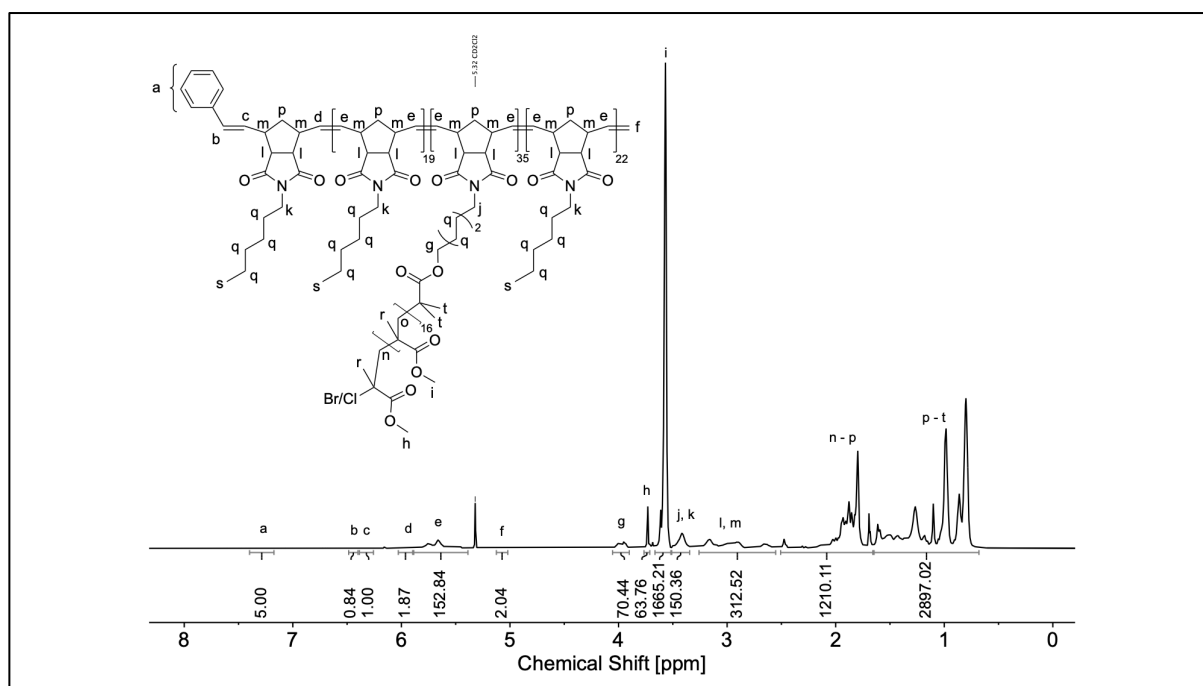


Figure S6.55. ^1H NMR spectrum of entry 6.16 in CD_2Cl_2 (500 MHz).

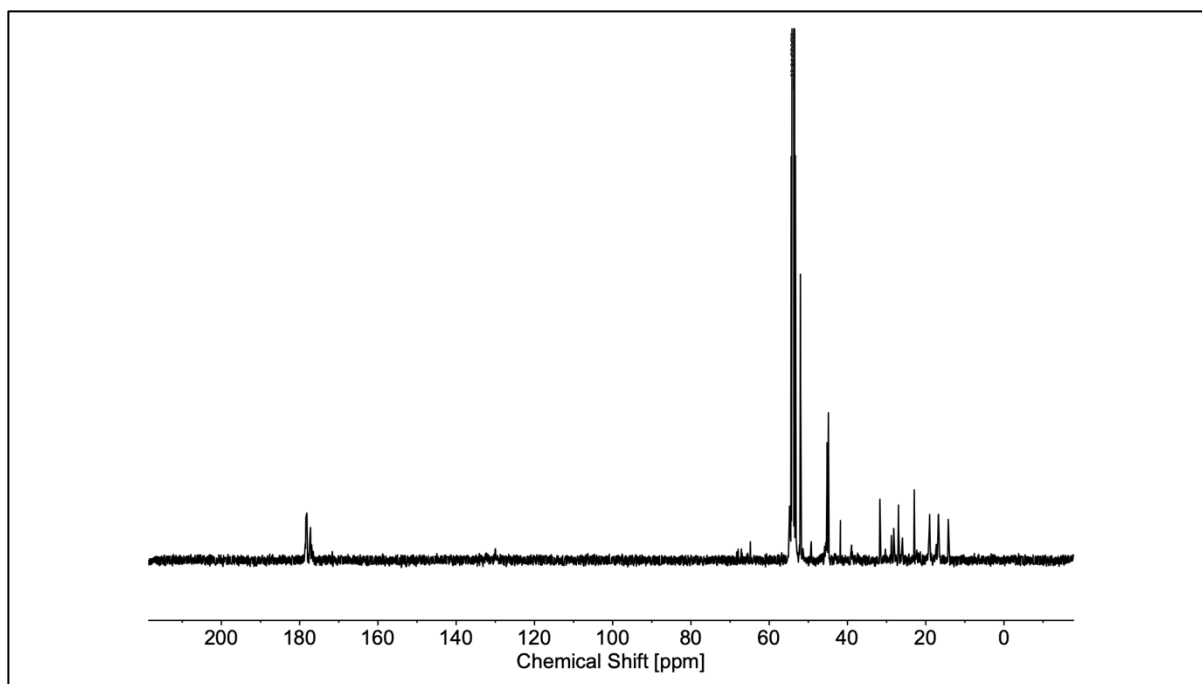


Figure S6.56. ^1H NMR spectrum of entry 6.16 in CD_2Cl_2 (126 MHz).

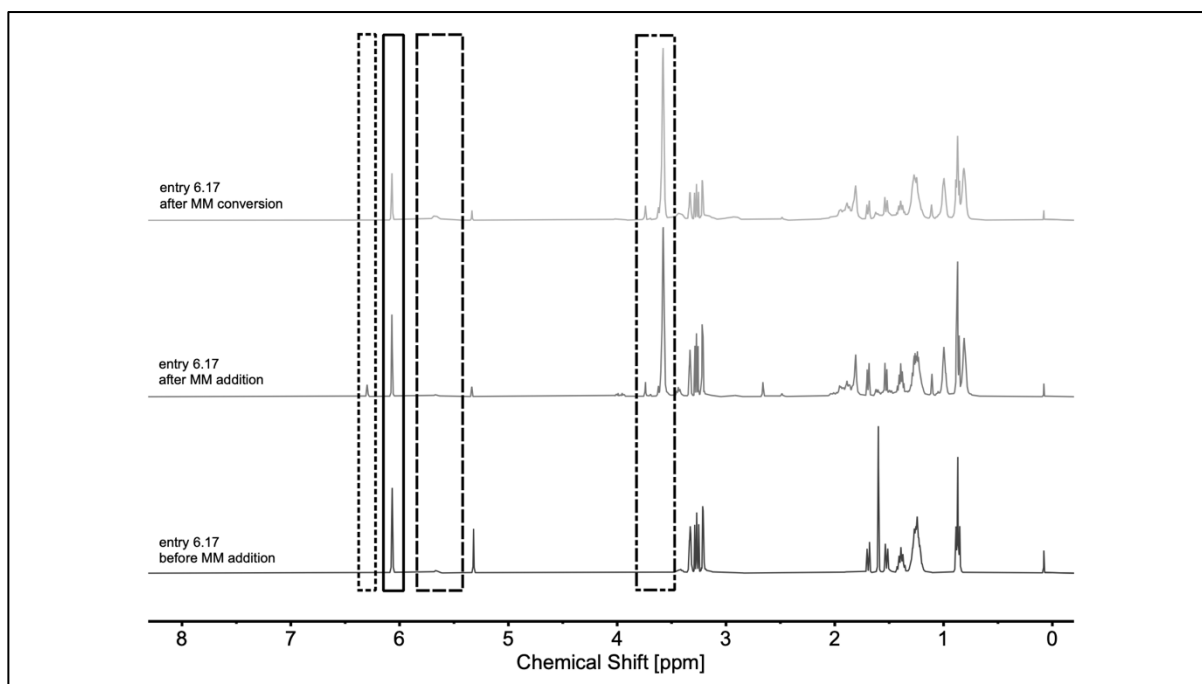


Figure S6.57. Representative stacked ^1H NMR spectra of entry 6.17 before (bottom) and after (middle) the addition of **xNb6M17**, and after its complete conversion (top) in CD_2Cl_2 (500 MHz). Boxes: *endo* norbornene olefin (solid); poly(norbornene) olefin (dashed); *exo* norbornene olefin (dotted); methoxy groups (dash-dotted).

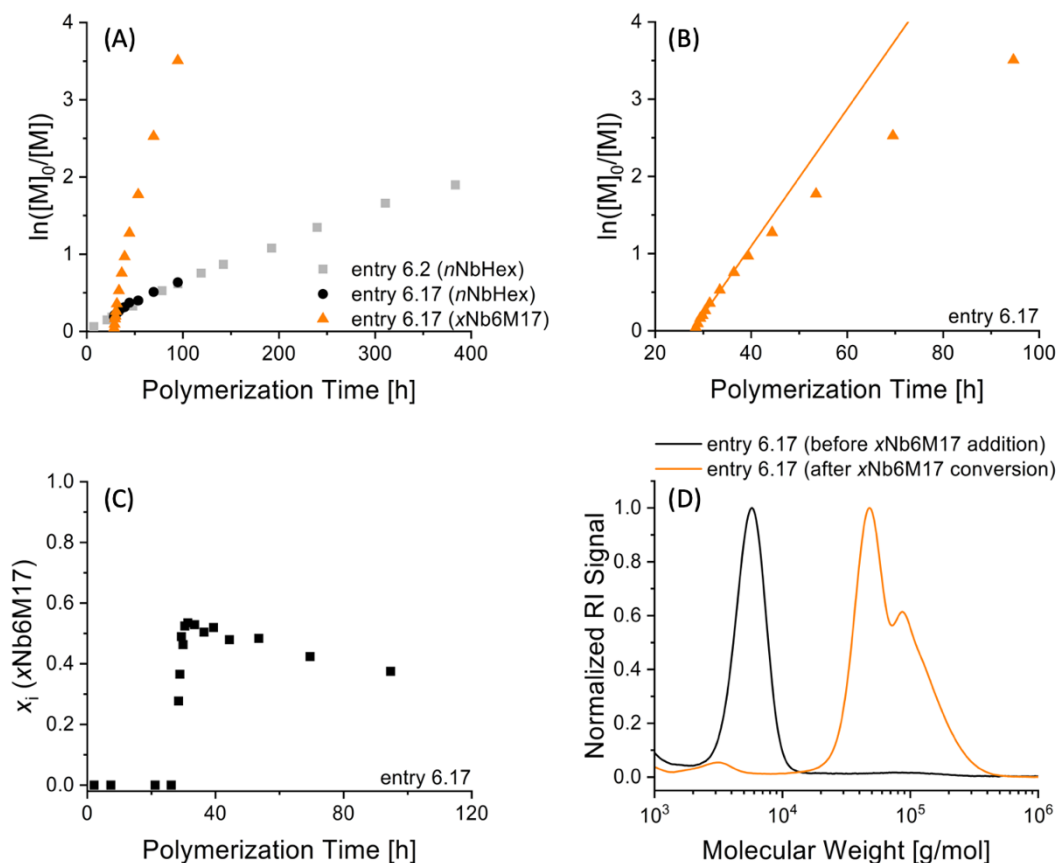


Figure S6.58. (A) Kinetic plots of entries 6.2 (Table 6.1) and 6.17 (Table 6.3), (B) highlighting $x\text{Nb6M17}$ during copolymerization, (C) molar fraction (x_i) of $x\text{Nb6M17}$ in entry 6.17 as a function of polymerization time, based on ^1H NMR spectroscopy data (Figure S6.57), and (D) SEC traces of entry 6.17 before $x\text{Nb6M17}$ addition and after $x\text{Nb6M17}$ conversion. Line represents linear fit.

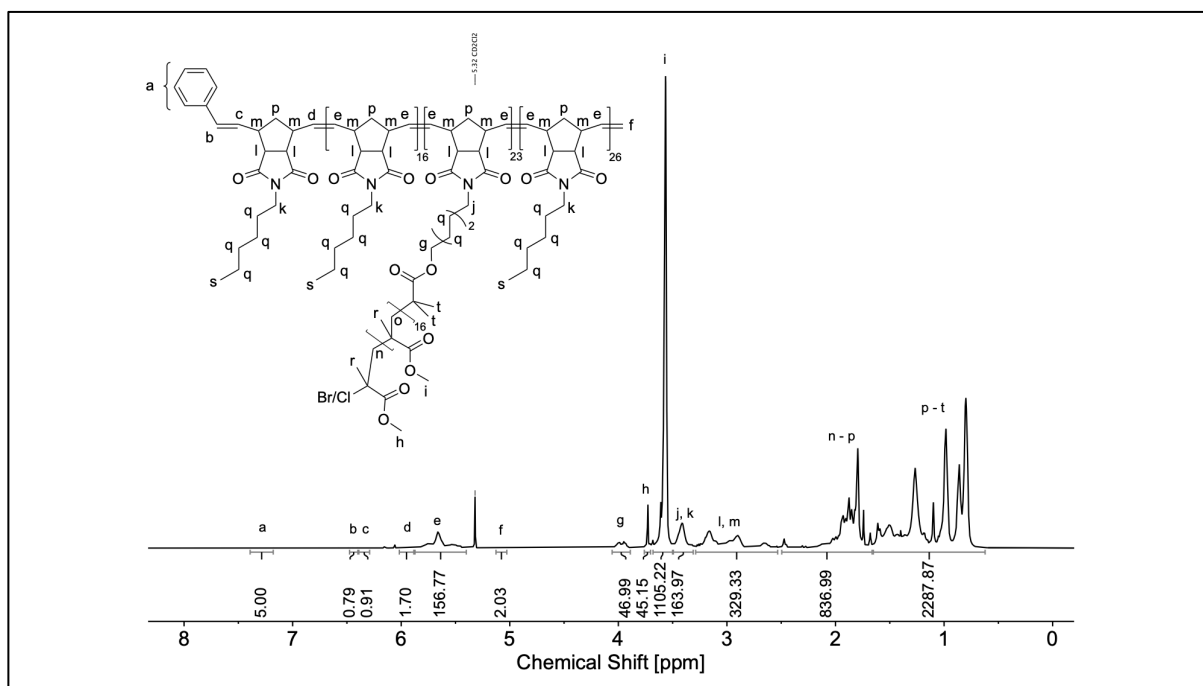


Figure S6.59. ^1H NMR spectrum of entry 6.17 in CD_2Cl_2 (500 MHz).

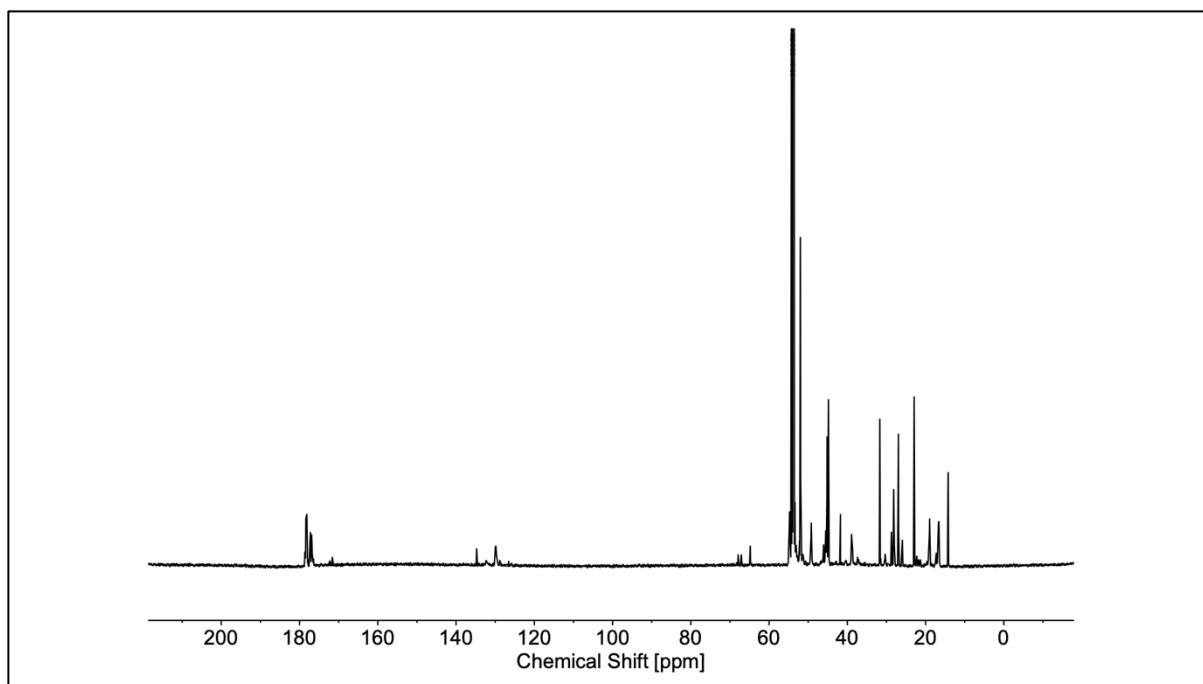


Figure S6.60. ^{13}C NMR spectrum of entry 6.17 in CD_2Cl_2 (126 MHz).

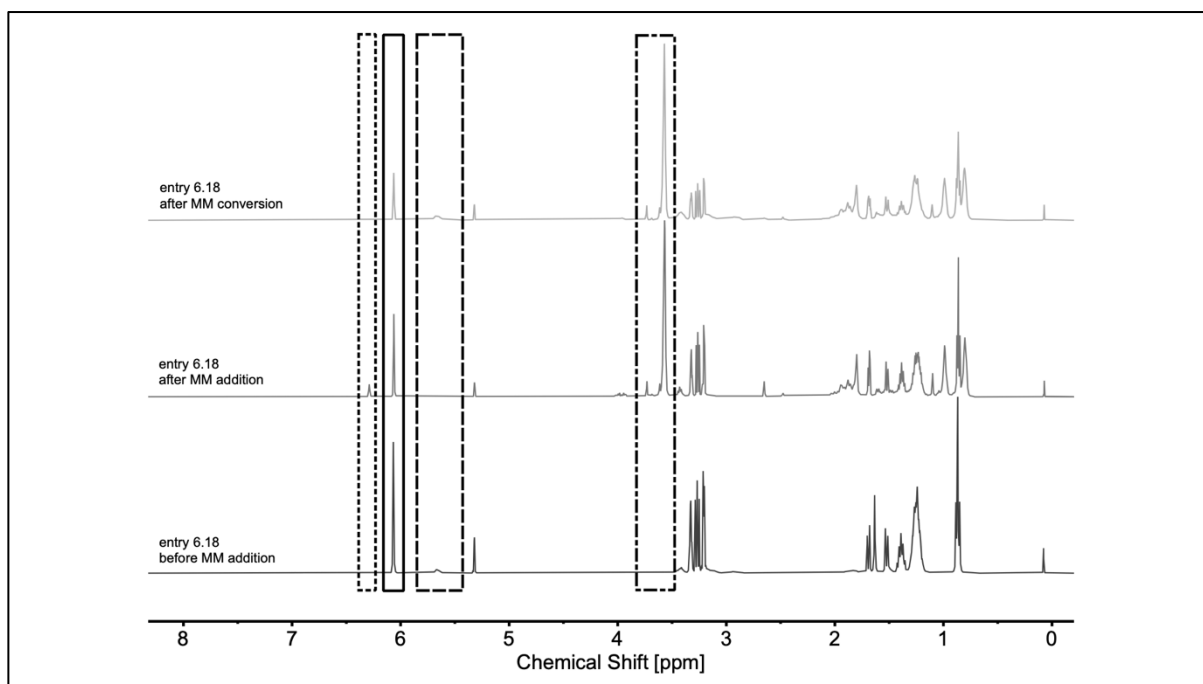


Figure S6.61. Representative stacked ^1H NMR spectra of entry 6.18 before (bottom) and after (middle) the addition of **xNb6M17**, and after its complete conversion (top) in CD_2Cl_2 (500 MHz). Boxes: *endo* norbornene olefin (solid); poly(norbornene) olefin (dashed); *exo* norbornene olefin (dotted); methoxy groups (dash-dotted).

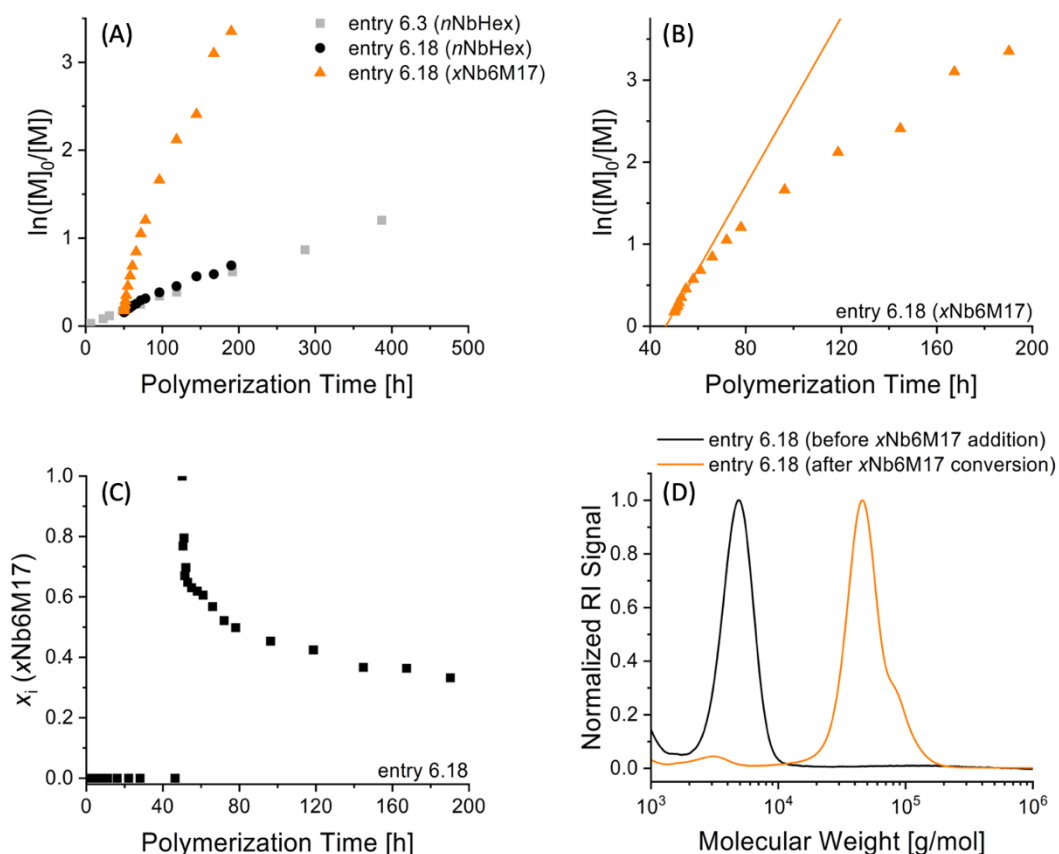


Figure S6.62. (A) Kinetic plots of entries 6.3 (Table 6.1) and 6.18 (Table 6.3), (B) highlighting $x\text{Nb6M17}$ during copolymerization, (C) molar fraction (x_i) of $x\text{Nb6M17}$ in entry 6.18 as a function of polymerization time, based on ^1H NMR spectroscopy data (Figure S6.61), and (D) SEC traces of entry 6.18 before $x\text{Nb6M17}$ addition and after $x\text{Nb6M17}$ conversion. Line represents linear fit.

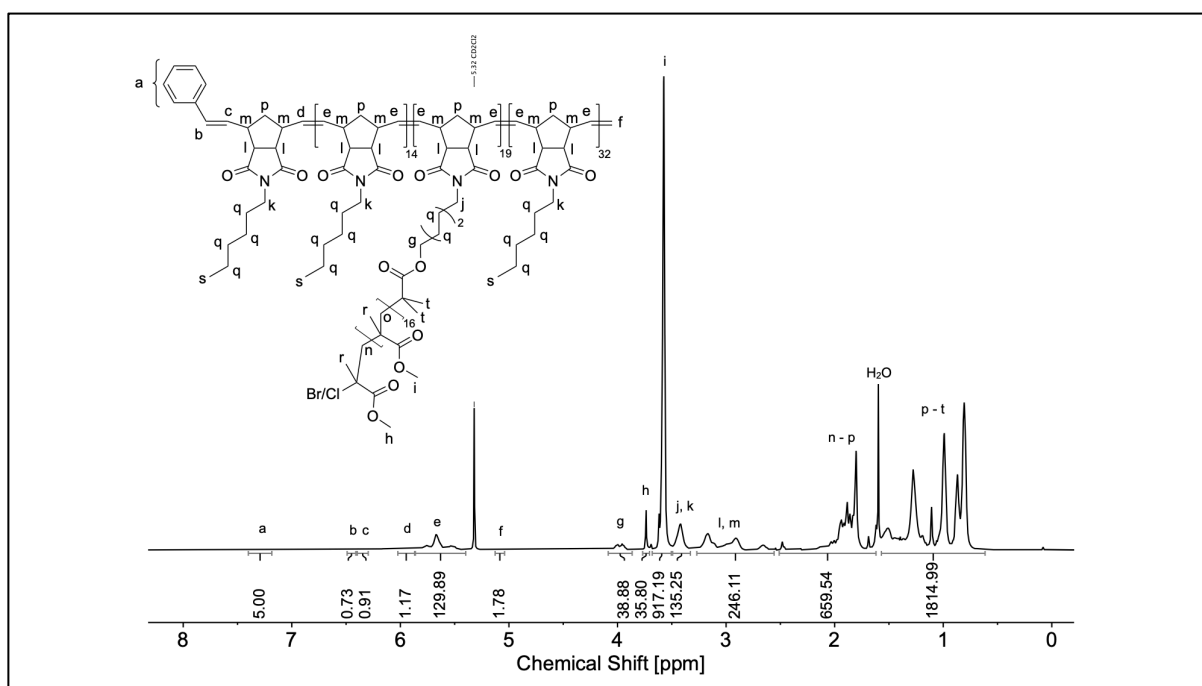


Figure S6.63. ^1H NMR spectrum of entry 6.18 in CD_2Cl_2 (500 MHz).

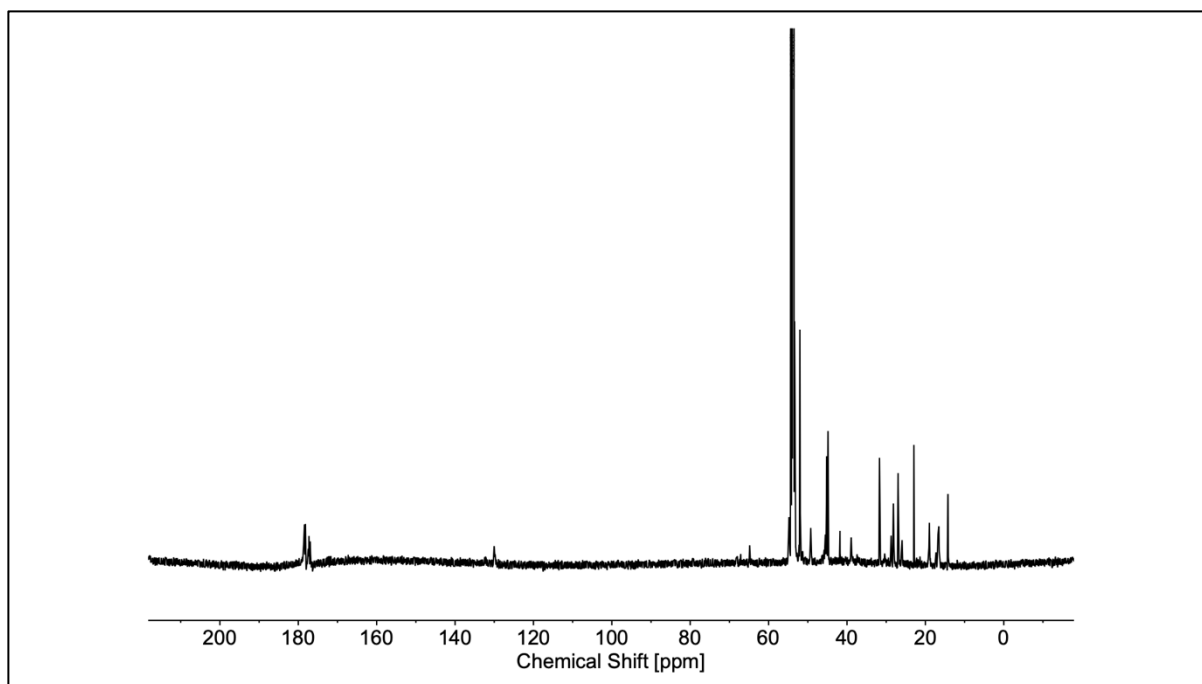


Figure S6.64. ^{13}C NMR spectrum of entry 6.18 in CD_2Cl_2 (126 MHz).

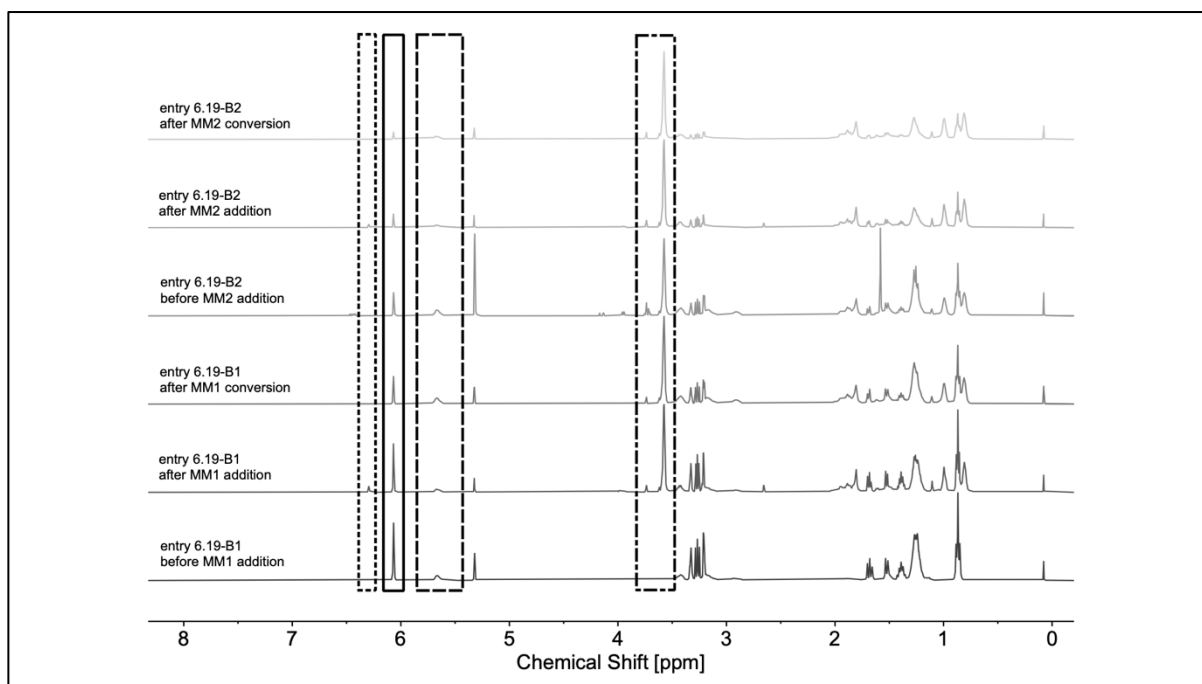


Figure S6.65. Representative stacked ^1H NMR spectra of entry 6.19 (diblock) before and after the additions of $x\text{Nb6M17}$, and after their complete conversions in CD_2Cl_2 (500 MHz). Boxes: *endo* norbornene olefin (solid); poly(norbornene) olefin (dashed); *exo* norbornene olefin (dotted); methoxy groups (dash-dotted).

xNbBr:

The synthesis procedure was adapted from recent literature.⁴⁷⁴ 1.00 eq. of **xNbOH** (0.16 mol/L), 0.40 eq. DMAP and 1.50 eq. triethylamine were dissolved in THF. Subsequently, 1.50 eq. α -bromoisobutyryl bromide were dissolved in THF (0.15 mol/L) and added dropwise to the reaction mixture at 0°C. Afterwards, the mixture was stirred for 16 hours at ambient temperature and the solvent was removed under reduced pressure. The crude product was dissolved in DCM, washed with saturated aqueous NaHCO₃ solution and brine. The organic phase was dried over magnesium sulfate and the solvent was removed under reduced pressure. The crude product was then purified *via* column chromatography using a pentane/ethyl acetate mixture as solvent. The product was obtained as a colorless liquid in a yield of 79%.

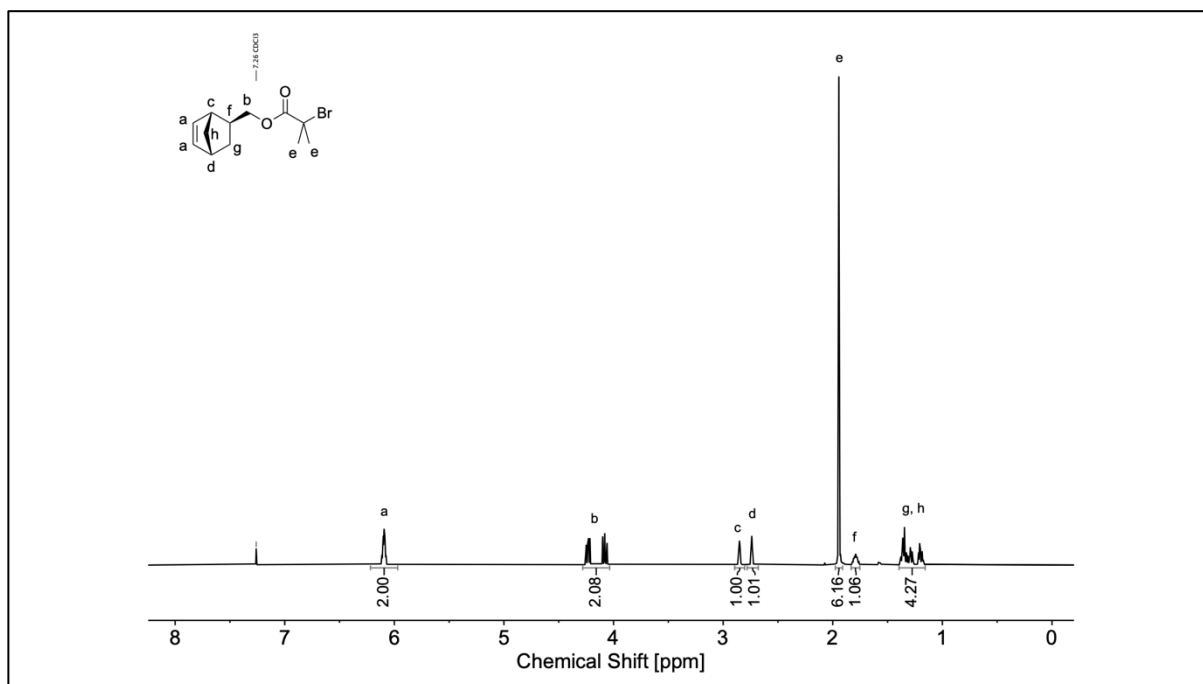


Figure S6.66. ¹H NMR spectrum of **xNbBr**.

¹H NMR: (500 MHz, CDCl₃, δ): 6.13 - 6.06 (m, 2H; CH=CH, ^a), 4.27 - 4.04 (m, 2H; CH₂-OH, ^b), 2.88 - 2.81 (m, 1H; =CH-CH-CH, ^c), 2.77 - 2.71 (m, 1H; =CH-CH-CH₂, ^d), 1.94 (s, 6H; CH₃, ^e), 1.83 - 1.74 (m, 1H; CH, ^f), 1.40 - 1.30 (m, 2H; CH₂, ^g), 1.32 - 1.17 (m, 2H; CH₂ bridge, ^h).

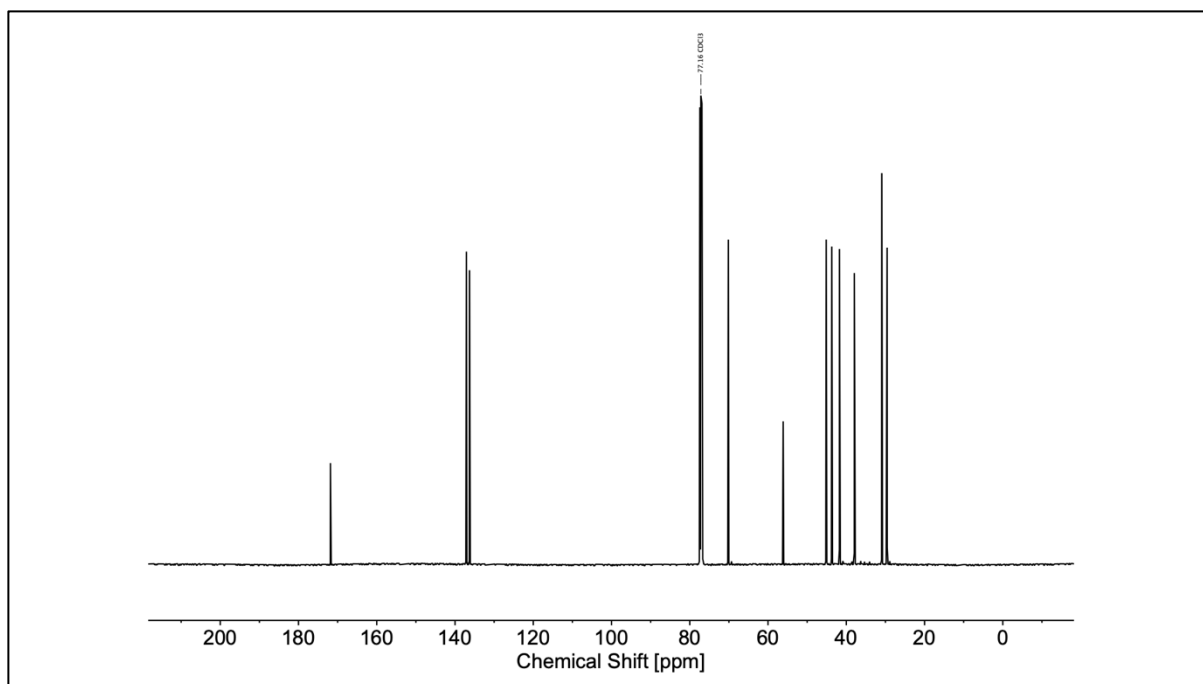


Figure S6.67. ^{13}C NMR spectrum of **xNbBr**.

^{13}C NMR: (126 MHz, CDCl_3 , δ): 171.83, 137.24, 136.30, 70.15, 56.13, 45.13, 43.70, 41.74, 37.95, 30.93, 29.56.

IR (ATR platinum diamond): $\nu / \text{cm}^{-1} = 3065$ (vw), 2966 (w), 2869 (vw), 1732 (vs), 1571 (vw), 1462 (w), 1448 (w), 1388 (w), 1370 (w), 1327 (w), 1273 (vs), 1154 (vs), 1107 (vs), 1047 (vw), 1010 (w), 998 (m), 971 (w), 946 (w), 919 (w), 905 (w), 862 (vw), 850 (w), 831 (vw), 821 (vw), 788 (vw), 778 (vw), 763 (vw), 708 (vs), 660 (w), 644 (w), 514 (vw), 475 (w), 448 (w).

HRMS (ESI-MS) m/z : $[\text{M}+\text{H}]^+$ calc. for $\text{C}_{12}\text{H}_{18}\text{BrO}_3$, 273.0485, found: 273.0481.

General ATRP procedure using methacrylate monomers (xNbM27 and xNbB17):

The synthesis procedure was adapted from recent literature.⁴⁶⁷ A Schlenk flask equipped with a stirring bar and an ampoule equipped with a J Young tap were evacuated and purged with argon (3x). The Schlenk flask was charged with 1.00 eq. copper(I) chloride (0.11 mol/L) and 2.00 eq. TMEDA dissolved in anisole. The ampoule was charged with 1.00 eq. **xNbBr** (0.074 mol/L) and 50.0 eq. methyl methacrylate dissolved in anisole. The mixtures were degassed by three consecutive pump thaw cycles under high vacuum. Subsequently, the solution of the ampoule was transferred to the Schlenk flask *via* a degassed syringe, initiating the polymerization. The polymerization was carried out at 70 °C for 8.75 hours under an argon atmosphere. Afterwards, the reaction was cooled quickly to ambient temperature by

immersing the flask into liquid nitrogen, exposing to air, and quenching by the addition of THF. The solution was then flushed through a plug of neutral aluminum oxide to remove the copper. Subsequently, the solvent was removed under reduced pressure. The crude product was then precipitated three times from the tenfold amount of cold *n*-hexane. The polymers were filtered, dried under high vacuum, and obtained as white solids.

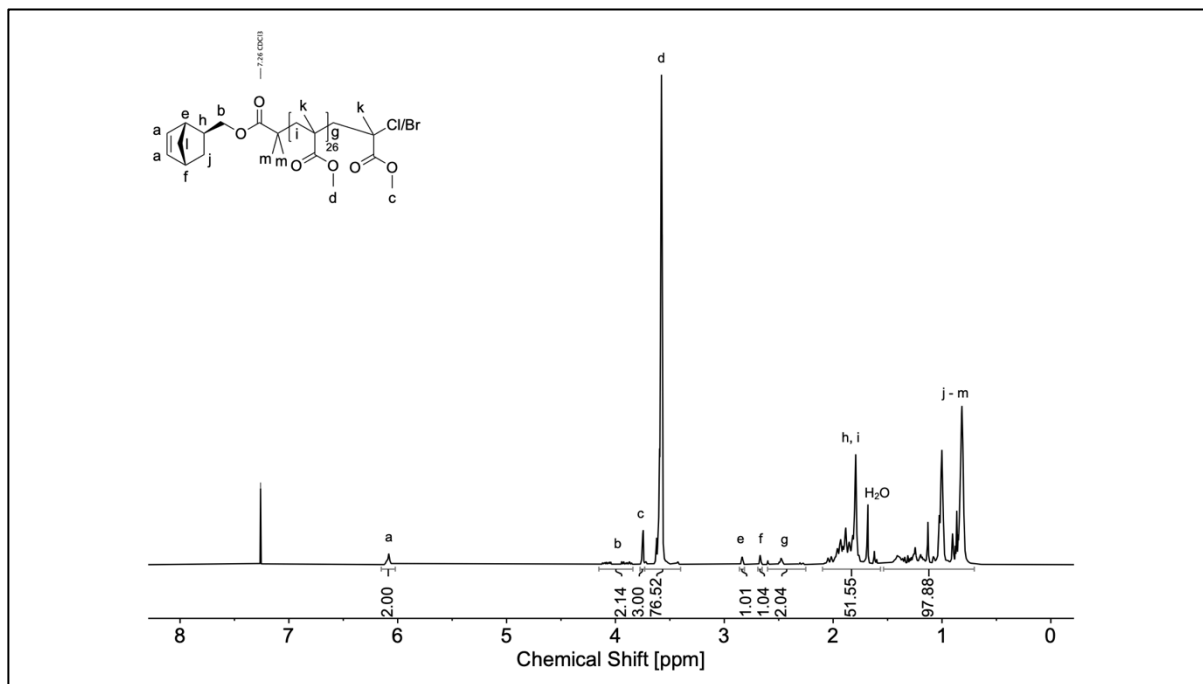


Figure S6.68. ^1H NMR spectrum of **xNbM27** in CDCl_3 (500 MHz).

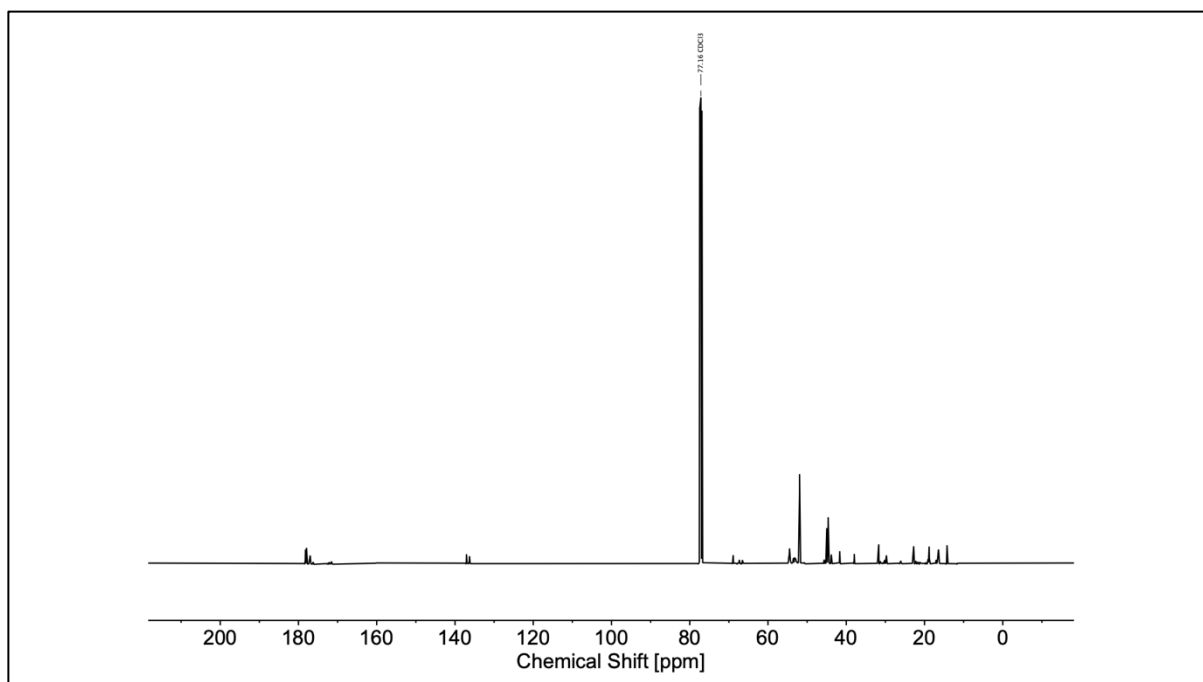


Figure S6.69. ^{13}C NMR spectrum of **xNbM27** in CDCl_3 (126 MHz).

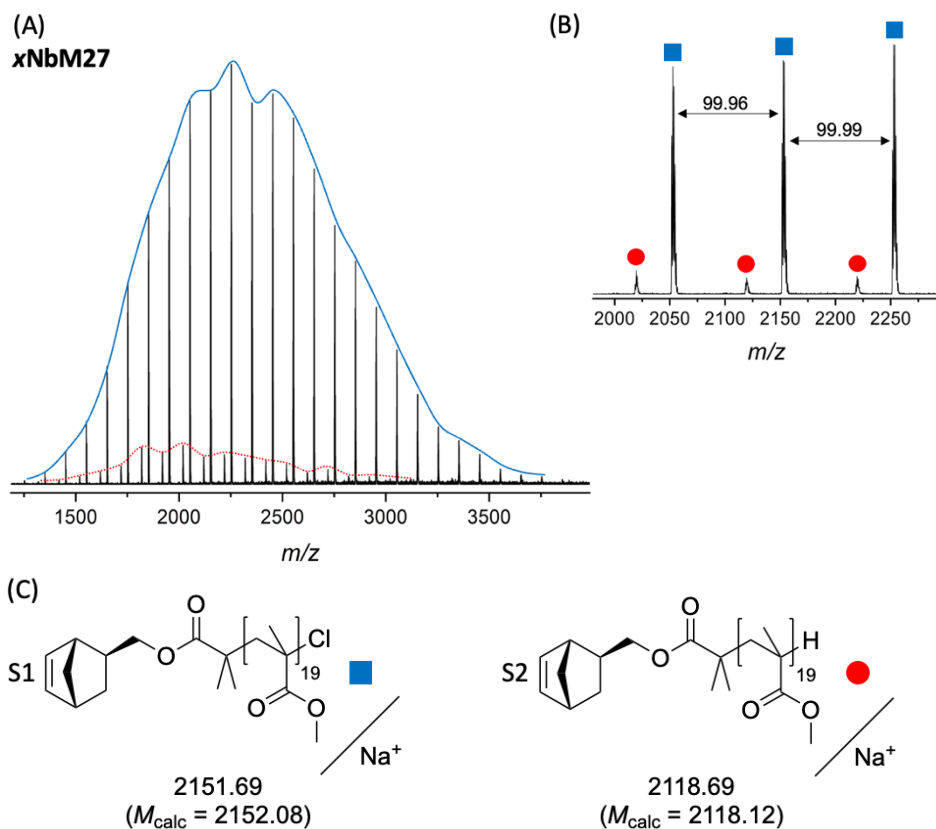


Figure S6.70. (A) MALDI-TOF spectrum (DCTB, NaTFA) of **xNbM27** with highlighted mass distributions in color to guide the eye, (B) selected region of the spectrum (1980 – 2290 m/z) with peaks color coded as per the identified species, and (C) structures of **xNbM27** species (S1 – S2) and their calculated and measured monoisotopic masses.

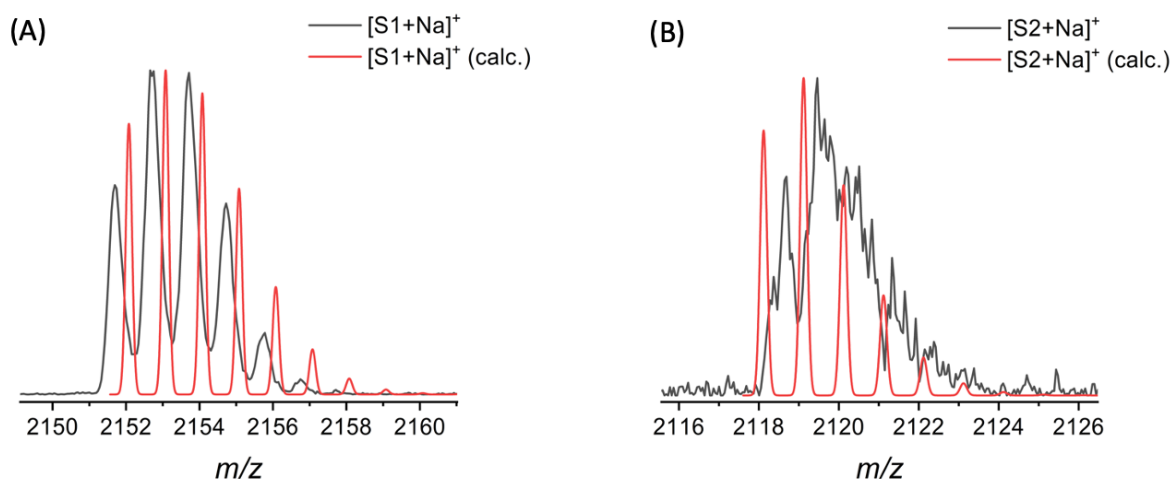


Figure S6.71. Comparison between measured and calculated isotopic patterns of **xNbM27** determined *via* MALDI-TOF MS (**Figure S6.70**) with (A) the chloride-terminated species (S1), and (B) the hydrogen-terminated species (S2).

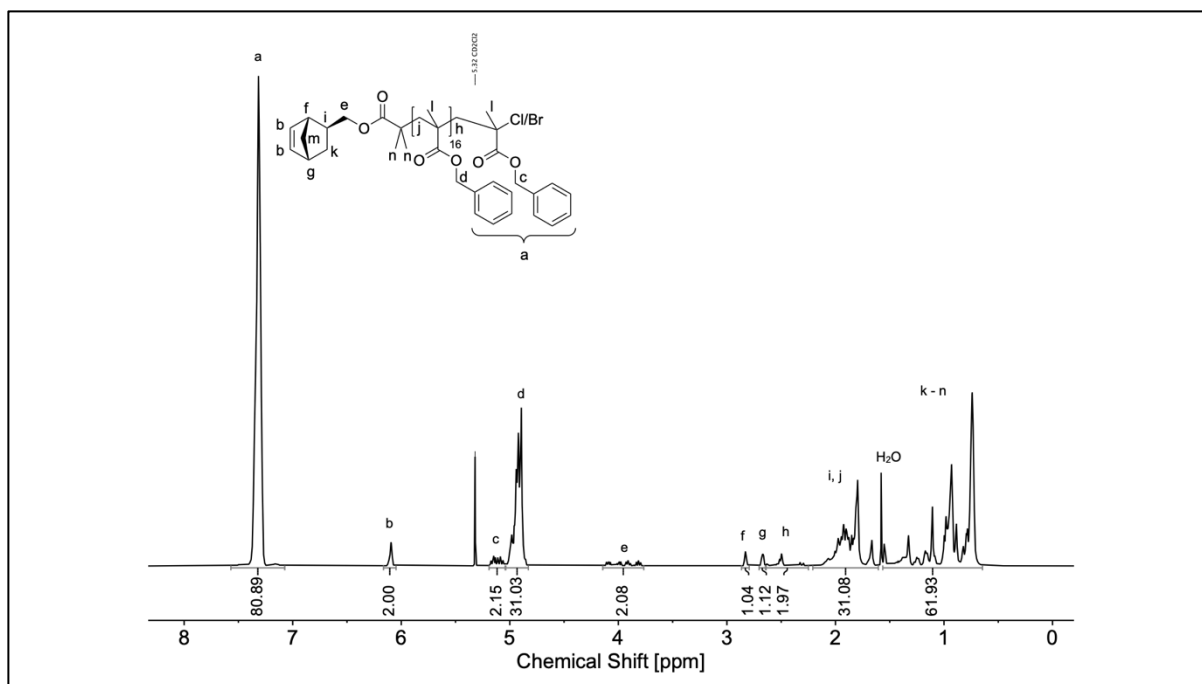


Figure S6.72. ¹H NMR spectrum of **xNbB17** in CD₂Cl₂ (500 MHz).

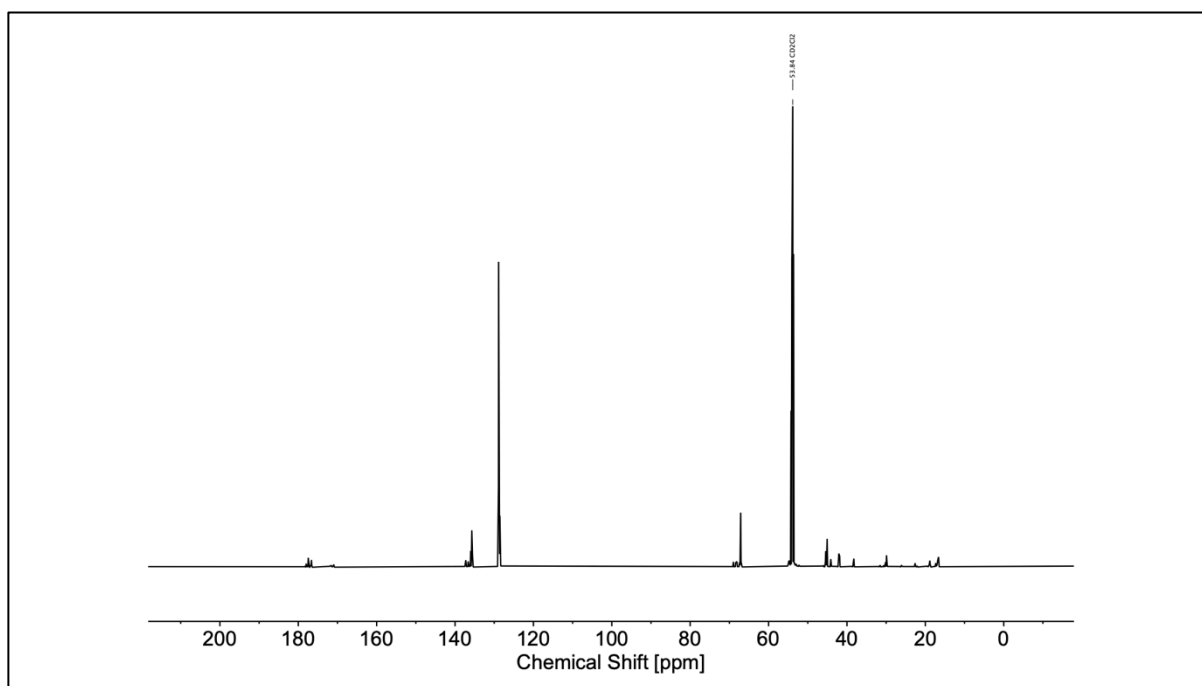


Figure S6.73. ¹³C NMR spectrum of **xNbB17** in CD₂Cl₂ (126 MHz).

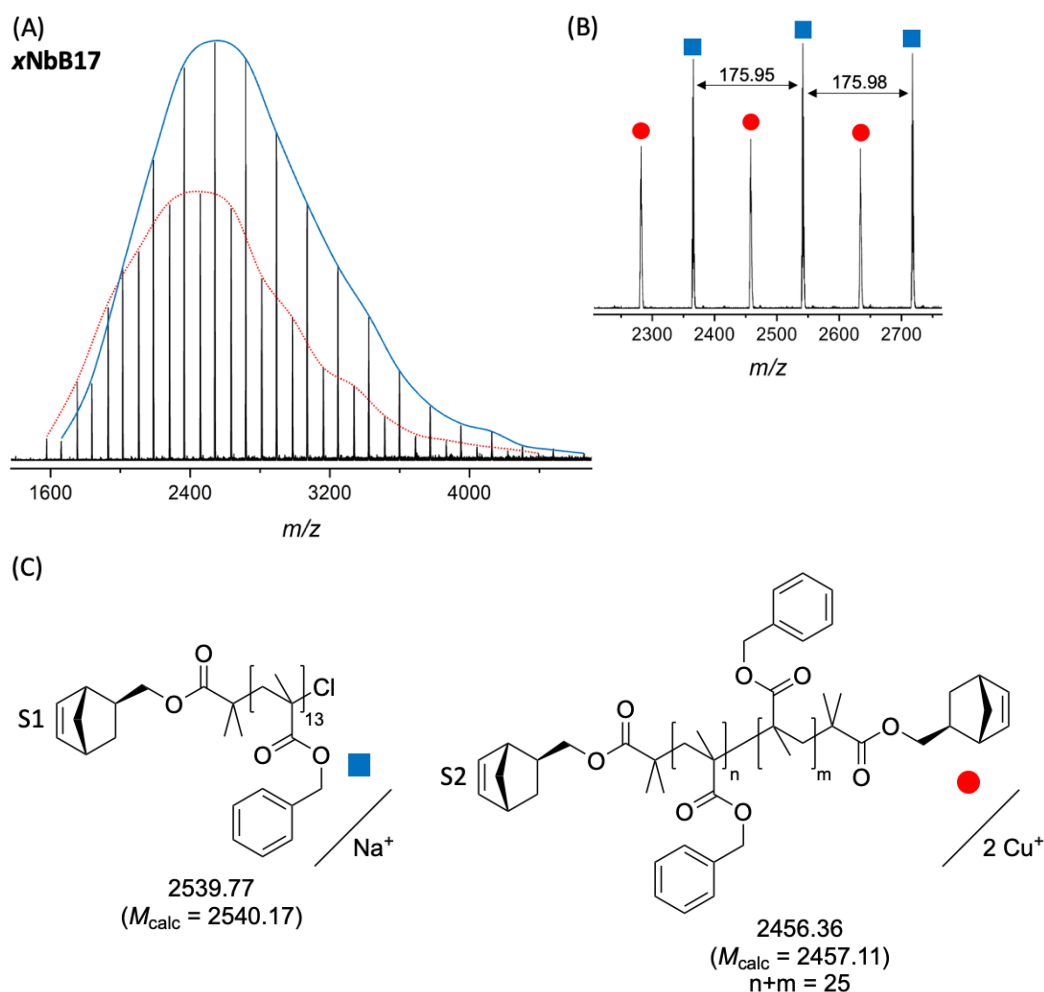


Figure S6.74. (A) MALDI-TOF spectrum (DCTB, NaFA) of **xNbB17** with highlighted mass distributions in color to guide the eye, (B) selected region of the spectrum (2210 – 2760 m/z) with peaks color coded as per the identified species, and (C) structures of **xNbB17** species (S1 – S2) and their calculated and measured monoisotopic masses.

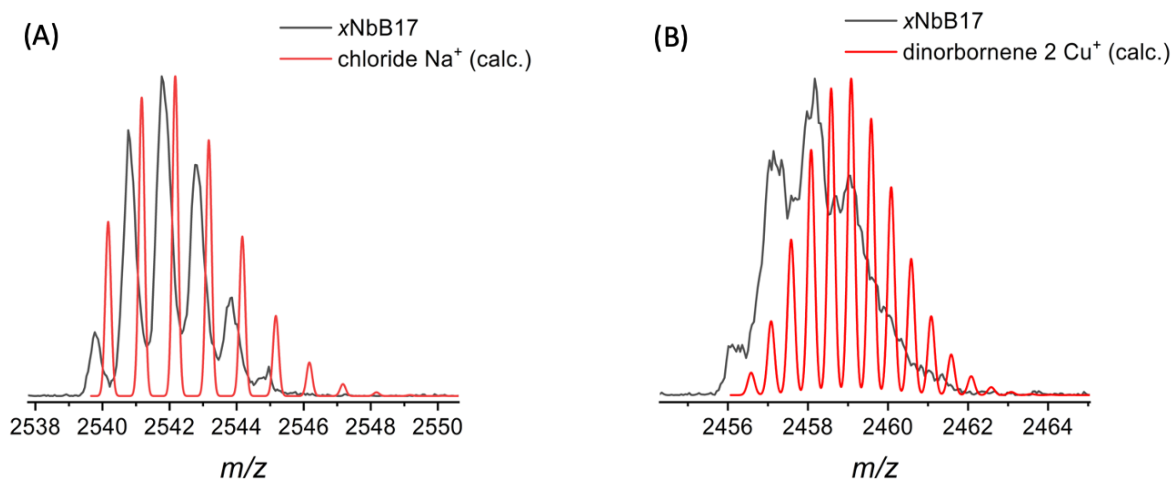


Figure S6.75. Comparison between measured and calculated isotopic patterns of **xNbB17** determined *via* MALDI-TOF MS (Figure S6.74) with (A) the chloride-terminated species (S1), and (B) the double charged dinorbornene species (S2).

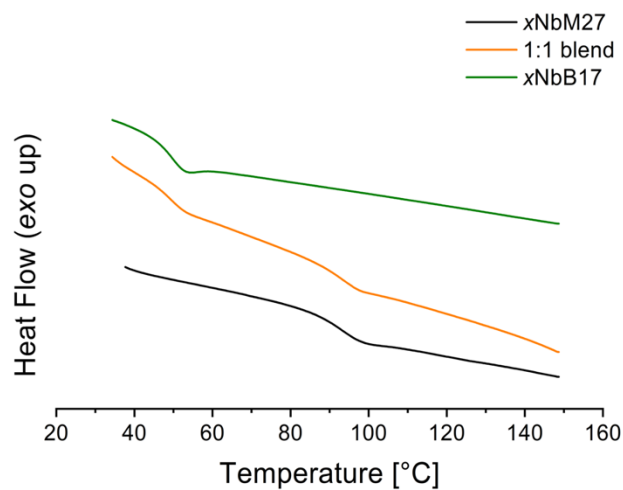


Figure S6.76. DSC traces of (A) **xNbM27**, **xNbB17** and the respective 1:1 polymer blend.

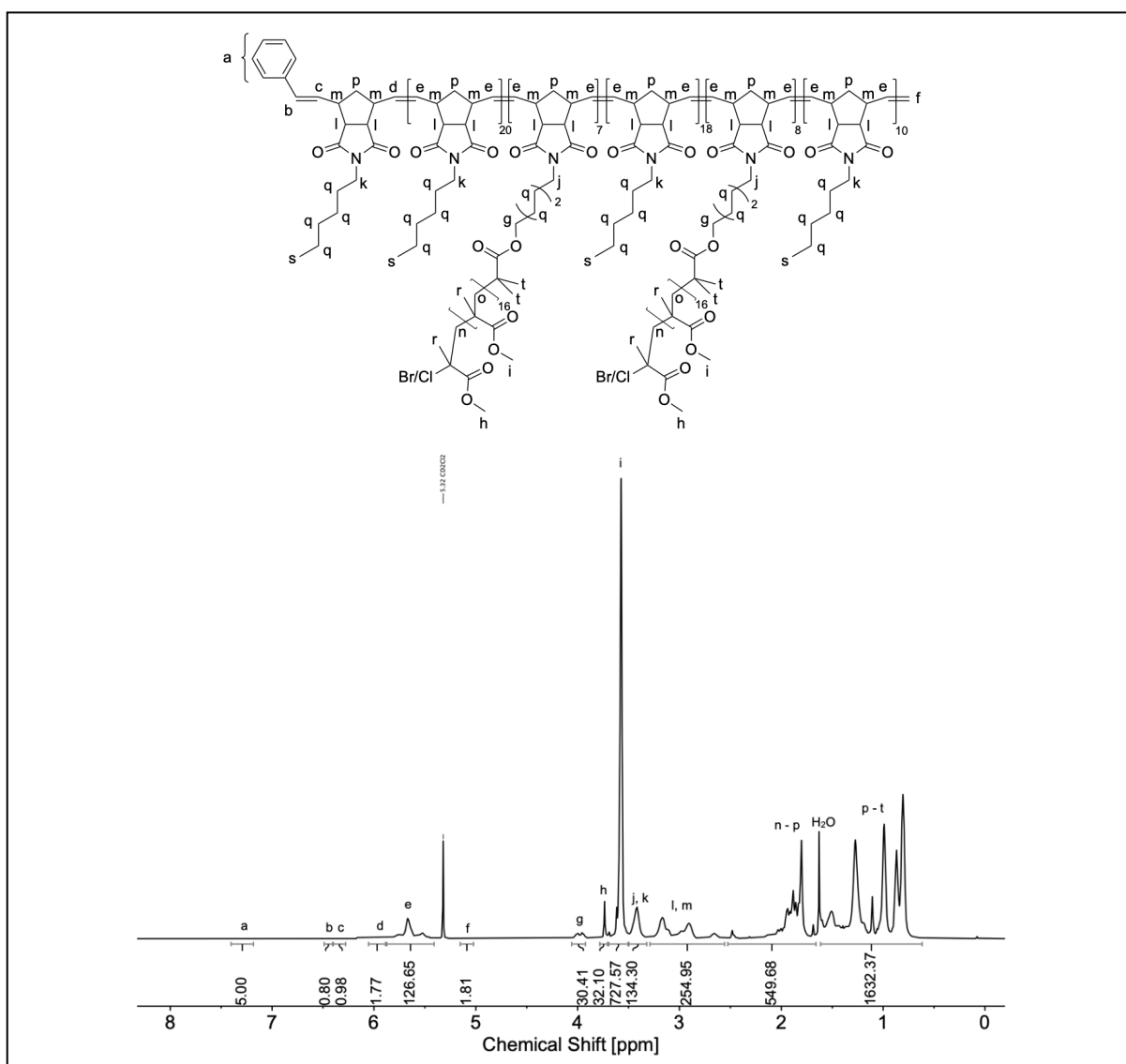


Figure S6.77. ¹H NMR spectrum of entry 6.19 in CD₂Cl₂ (500 MHz) and corresponding chemical structure.

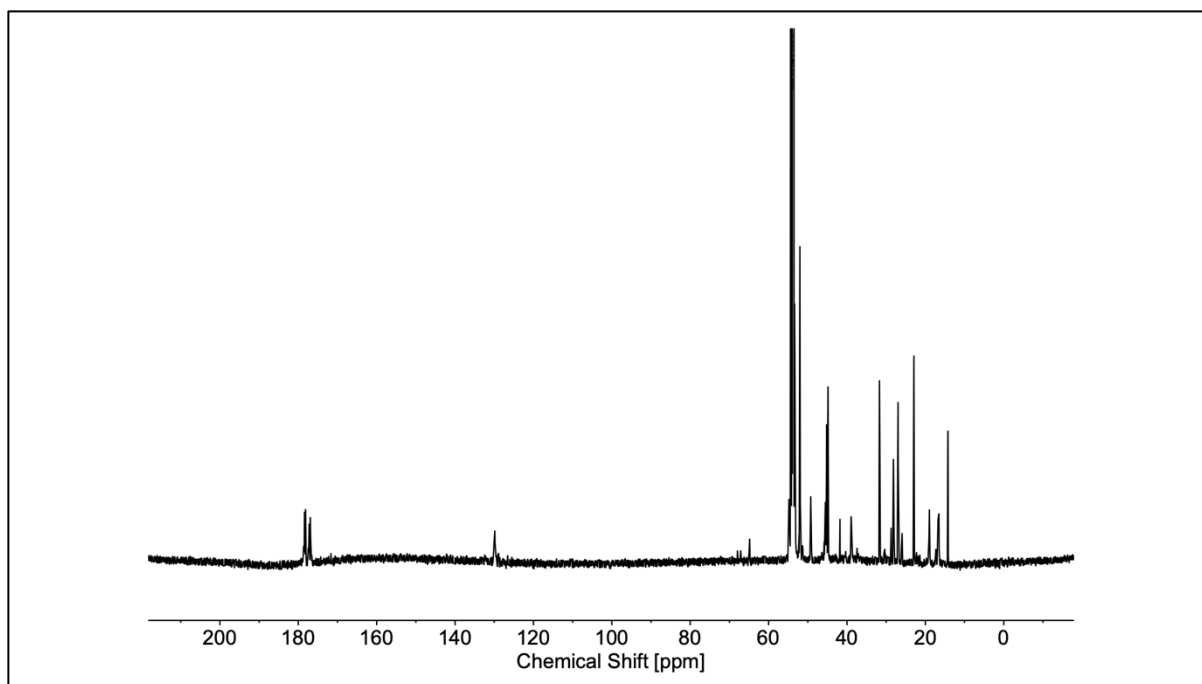


Figure S6.78. ^{13}C NMR spectrum of entry 6.19 in CD_2Cl_2 (126 MHz).

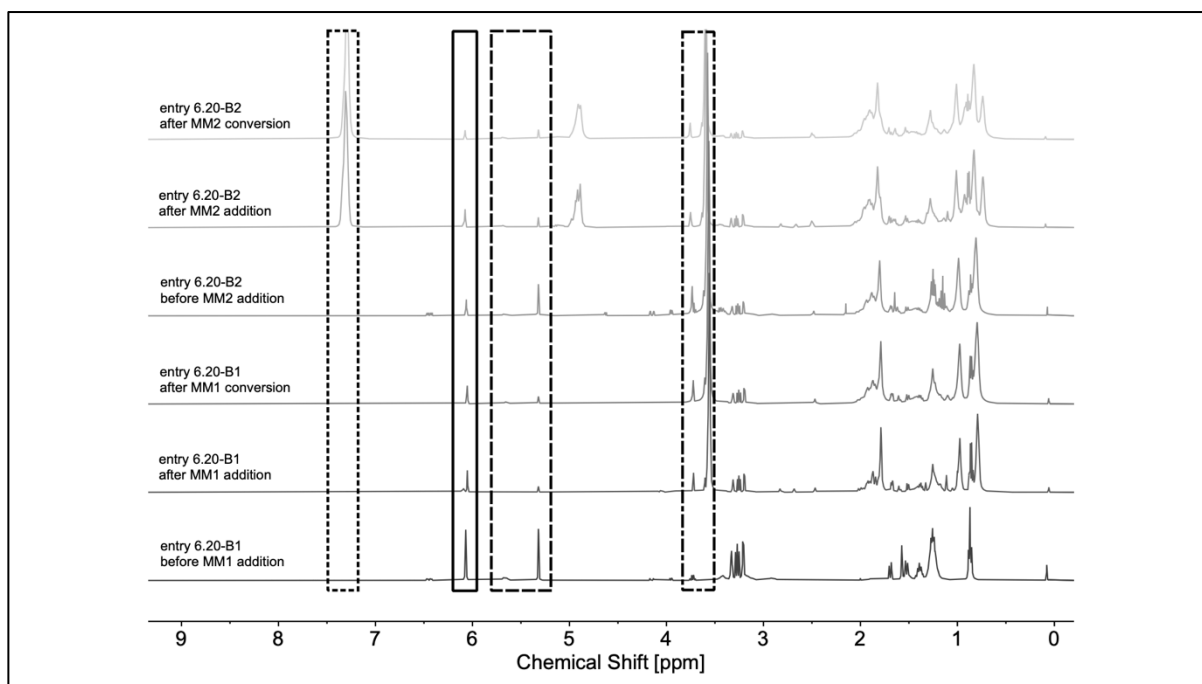


Figure S6.79. Representative stacked ^1H NMR spectra of entry 6.20 (diblock) before and after the additions of $x\text{NbM}27$ and $x\text{NbB}12$, and after their complete conversions in CD_2Cl_2 (500 MHz). Boxes: *exo* and *endo* norbornene olefin (solid); poly(norbornene) olefin (dashed); benzyl groups (dotted); methoxy groups (dash-dotted).

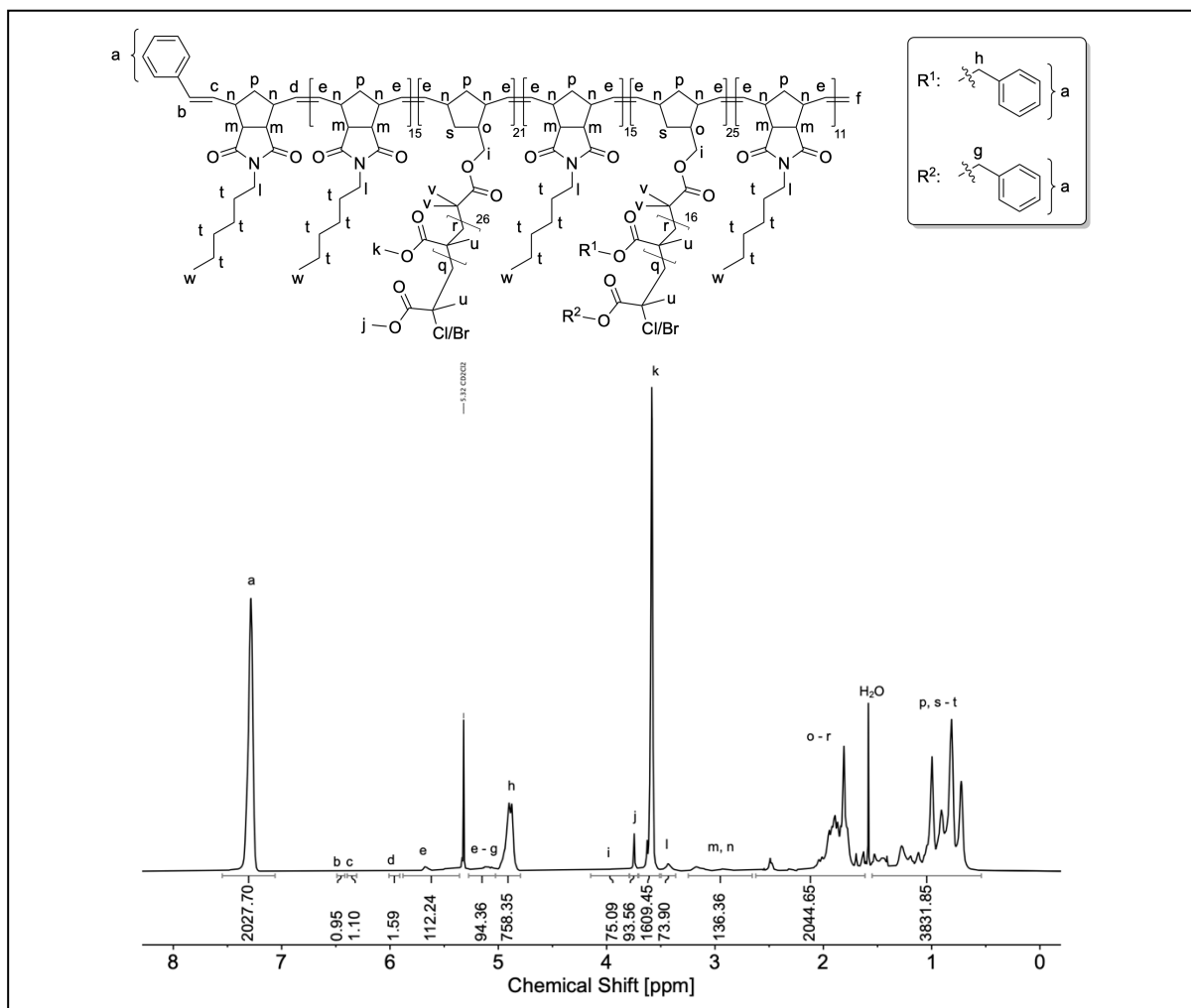


Figure S6.80. ^1H NMR spectrum of entry 6.20 in CD_2Cl_2 (500 MHz) and corresponding chemical structure.

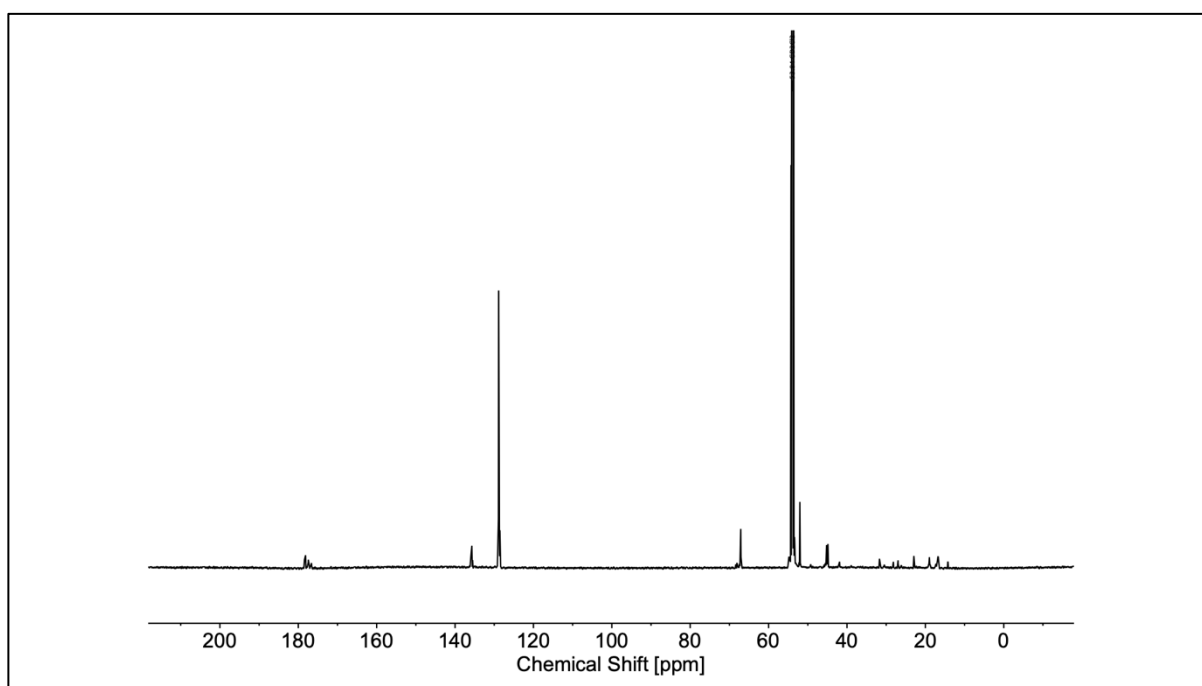


Figure S6.81. ^{13}C NMR spectrum of entry 6.20 in CD_2Cl_2 (126 MHz).

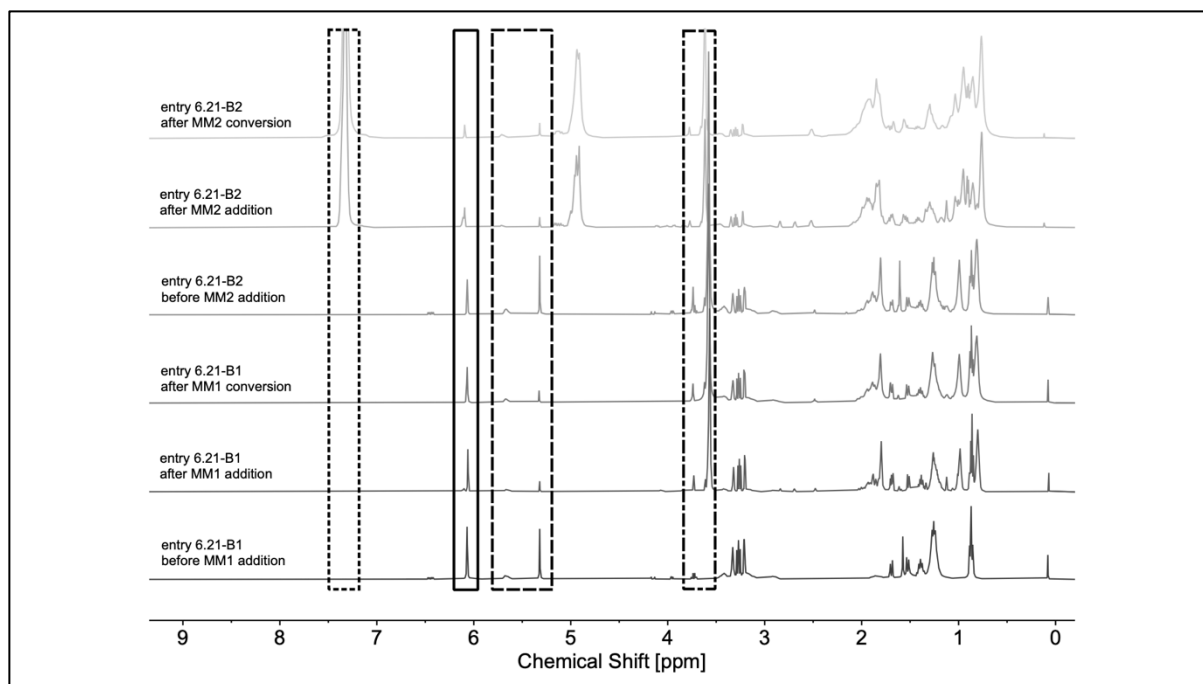


Figure S6.82. Representative stacked ¹H NMR spectra of entry 6.21 (diblock) before and after the additions of **xNbM27** and **xNbB12**, and after their complete conversions in CD₂Cl₂ (500 MHz). Boxes: *exo* and *endo* norbornene olefin (solid); poly(norbornene) olefin (dashed); benzyl groups (dotted); methoxy groups (dash-dotted).

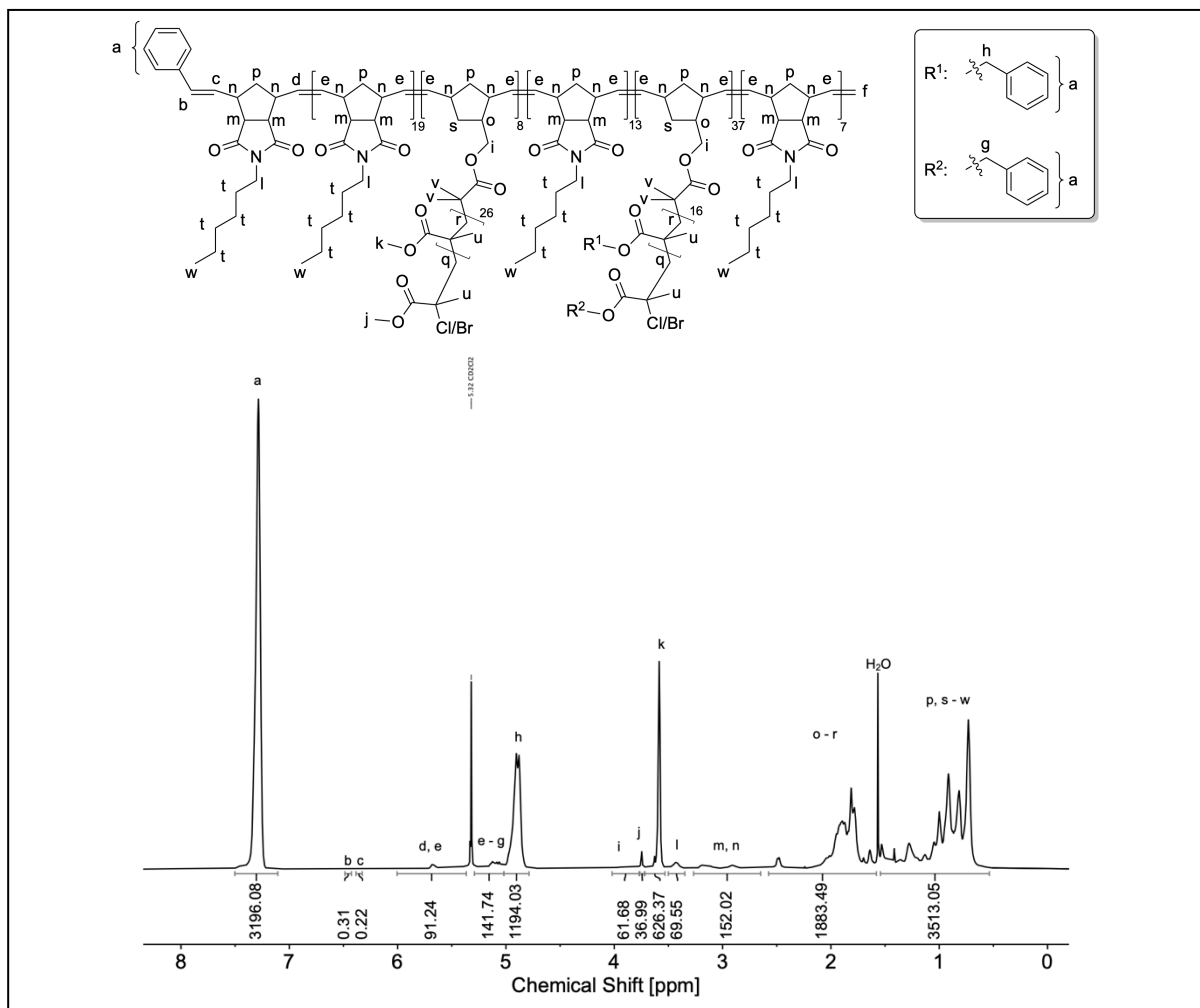


Figure S6.83. ^1H NMR spectrum of entry 6.21 in CD_2Cl_2 (500 MHz) and corresponding chemical structure.

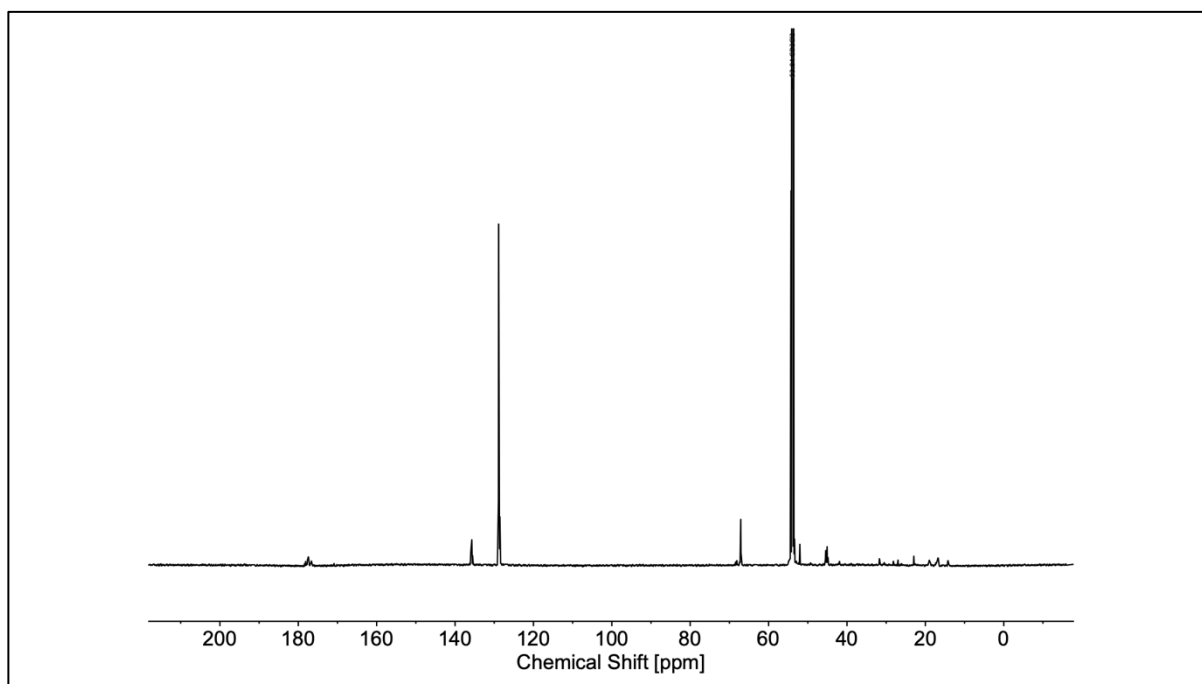


Figure S6.84. ^{13}C NMR spectrum of entry 6.21 in CD_2Cl_2 (126 MHz)

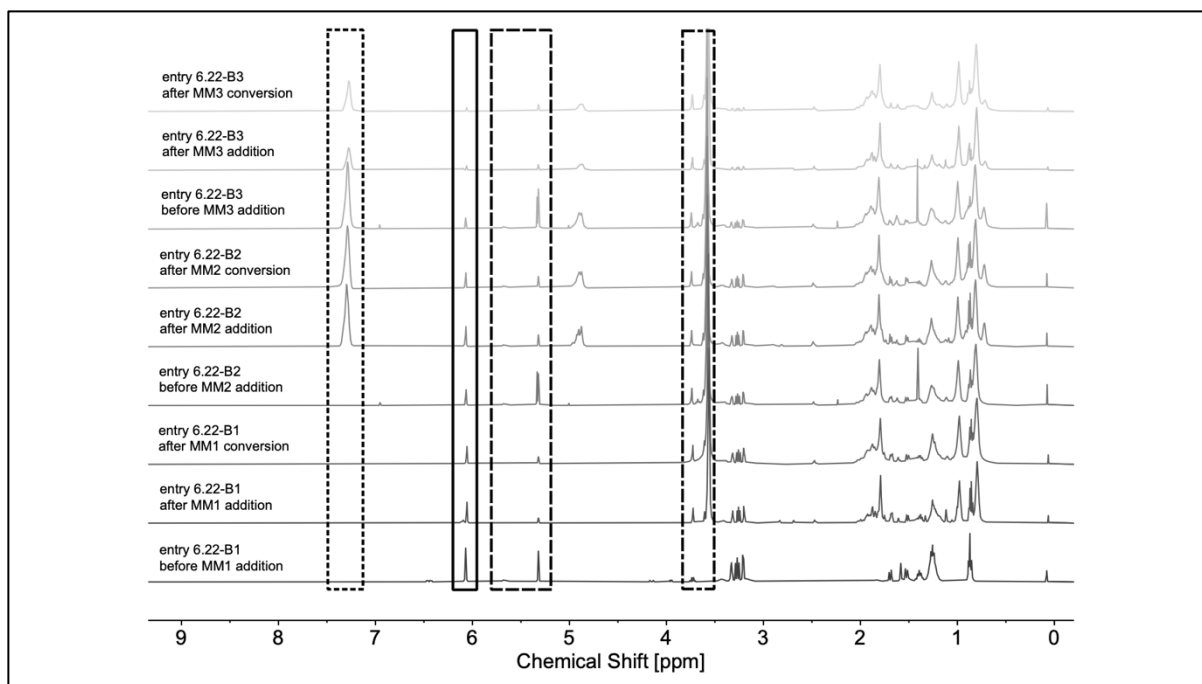


Figure S6.85. Representative stacked ^1H NMR spectra of entry 6.22 (triblock) before and after the additions of $x\text{NbM27}$ (2x) and $x\text{NbB12}$ (1x), and after their complete conversions in CD_2Cl_2 (500 MHz). Boxes: *exo* and *endo* norbornene olefin (solid); poly(norbornene) olefin (dashed); benzyl groups (dotted); methoxy groups (dash-dotted).

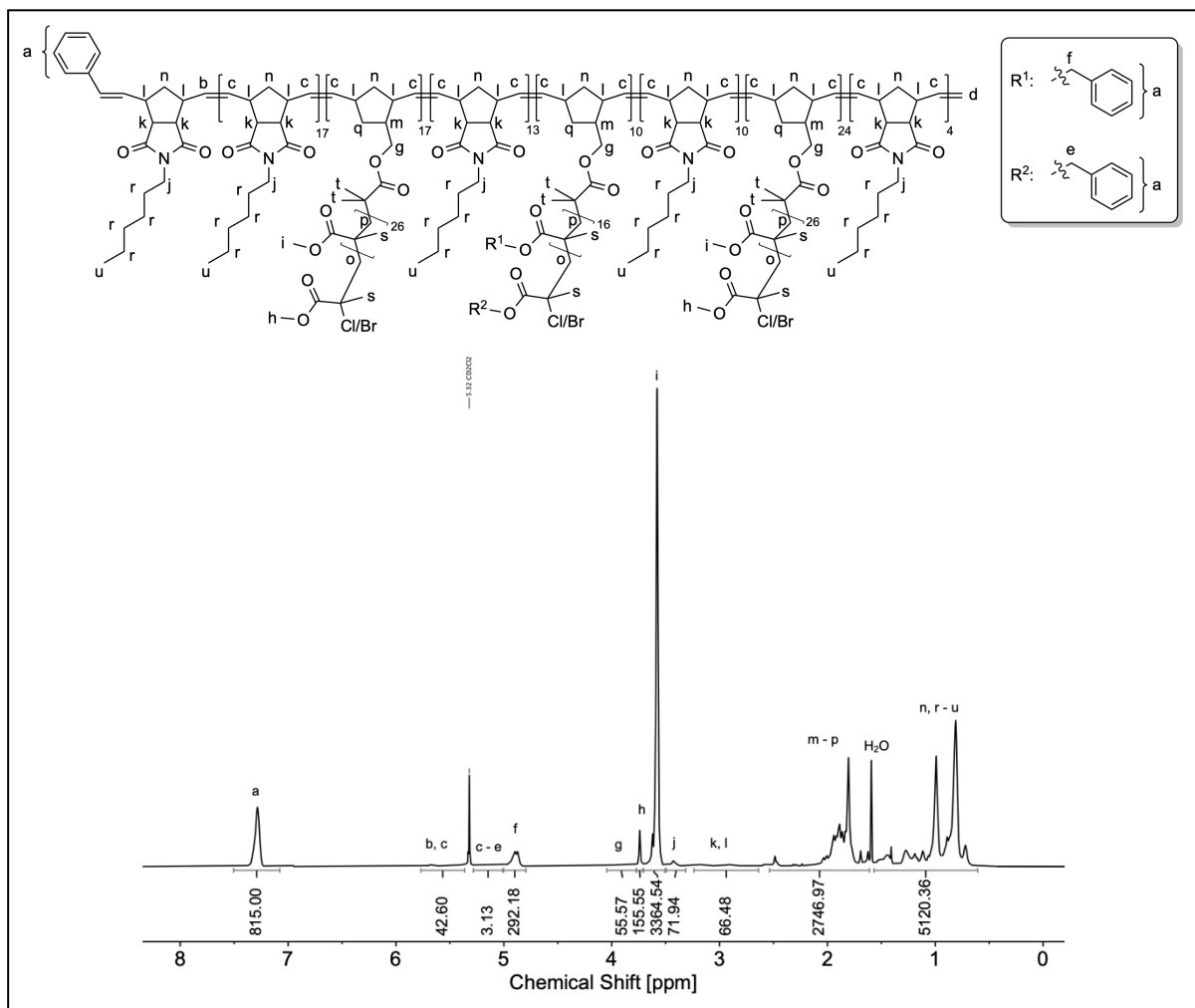


Figure S6.86. ^1H NMR spectrum of entry 6.22 in CD_2Cl_2 (500 MHz) and corresponding chemical structure.

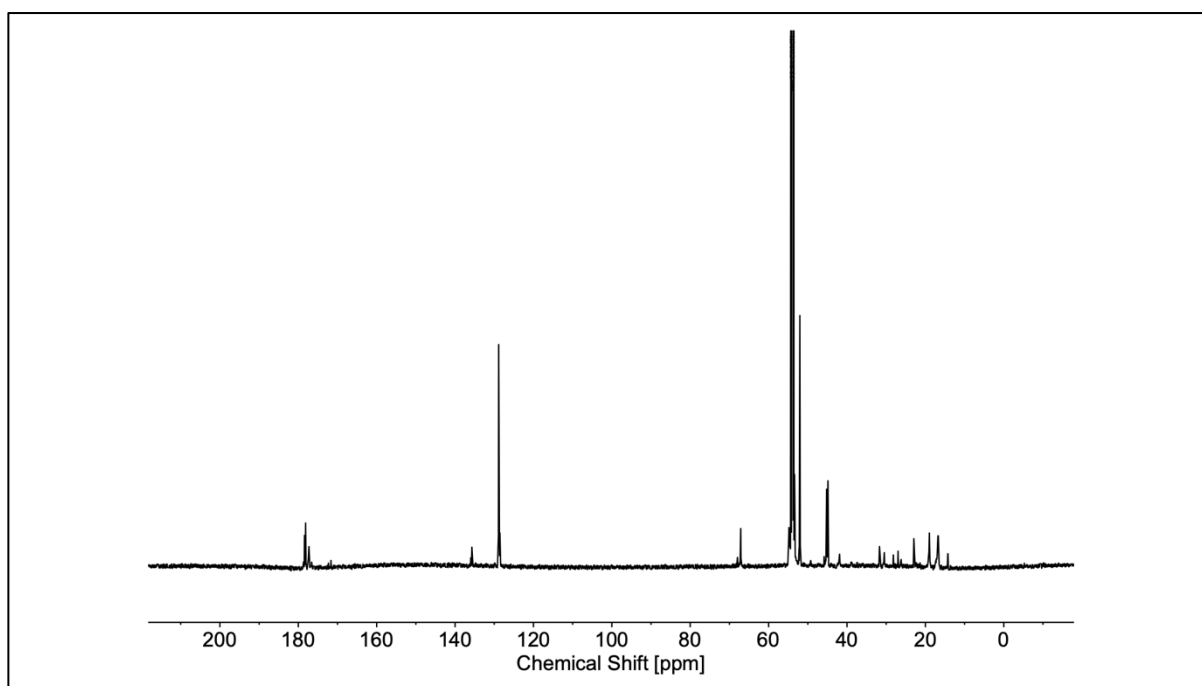


Figure S6.87. ^{13}C NMR spectrum of entry 6.22 in CD_2Cl_2 (126 MHz).

9 Appendix

9.1 List of abbreviations

1,4-DHP	1,4-Dihydropyridine
Ad	Adamantyl
ADMET	Acyclic diene metathesis
AFM	Atomic force microscopy
Ar	Argon
ARGET	Activators regenerated by electron transfer
ATRP	Atom transfer radical polymerization
Bn	Benzyl
BnMA	Benzyl methacrylate
CP	Copolymer
CTA	Chain transfer agent
Cy	Cyclohexyl
d	Days
DCC	<i>N,N'</i> -Dicyclohexylcarbodiimide
DCM	Dichloromethane
DCM-d ₂	Deuterated dichloromethane
DCTB	<i>Trans</i> -2-[3-(4- <i>tert</i> -butylphenyl)-2-methyl-2-propenylidene] malononitrile
DHPM	Dihydropyrimidinone
\bar{D}_M	Molecular weight dispersity
DMAP	4-Dimethylaminopyridine
DMC	Dimethyl carbonate
DMT	Dimercaptotriazine
DNA	Desoxyribonucleic acid
dNbpy	4,4'-Dinonyl-2,2'-dipyridyl
DP	Degree of polymerization
DSC	Differential scanning calorimetry

ED-ROMP	Entropy-driven ring-opening metathesis polymerization
eq.	Equivalents
ESI	Electrospray ionization
EVE	Ethyl vinyl ether
G1	Grubbs first generation catalyst
G2	Grubbs second generation catalyst
G3	Grubbs third generation catalyst
h	Hours
HP	Homopolymer
Hz	Hertz
ICAR	Initiators for continuous activator regeneration
IMCR	Isocyanide-based multicomponent reaction
J	Coupling constant
k_p	Apparent propagation rate constant
L	Ligand
M:I	Monomer-to-initiator ratio
m/z	Mass-to-charge ratio
$M_{0,i}$	Molecular weight of repeat unit i
MALDI	Matrix-assisted laser desorption/ionization
MCO	Macrocyclic oligomers
MCR	Multicomponent reaction
MF-ROMP	Metal-free ring-opening metathesis polymerization
min	Minutes
MM	Macromonomer
MMA	Methyl methacrylate
M_n	Number-average molecular weight
MS	Mass spectrometry
M_w	mass-average molecular weight
NHC	N -heterocyclic carbene
n_i	Number of repeat units i
NIPU	Non-isocyanate polyurethane
NMP	Nitroxide-mediated radical polymerization

NMR	Nuclear magnetic resonance
<i>n</i> Nb	<i>endo</i> norbornene
P-3CR	Passerini three-component reaction
PBnMA	Poly(benzyl methacrylate)
Pe	Pentyl
PEG	Poly(ethylene glycol)
Ph	Phenyl
PMDETA	<i>N,N,N',N'',N'''</i> -Pentamethyl diethylenetriamine
PMMA	Poly(methyl methacrylate)
PNB	Poly(norbornene)
ppm	Parts-per-million
Pr	Propyl
PS	Poly(styrene)
<i>p</i> -TsCl	<i>p</i> -Toluenesulfonyl chloride
PU	Polyurethane
Py	Pyrenyl
r.t.	room temperature
RAFT	Reversible addition-fragmentation chain-transfer
RDRP	Reversible-deactivation radical polymerization
R_h	Hydrodynamic radius
RNA	Ribonucleic acid
ROMP	Ring-opening metathesis polymerization
ROMPISA	Ring-opening metathesis polymerization-induced self-assembly
ROP	Ring-opening polymerization
SARA	Supplemental activator and reducing agent
SAXS	Small-angle X-ray scattering
SEC	Size exclusion chromatography
St	Styrene
stat	Statistical
T	Temperature
$t_{1/2}$	Monomer half-live
TBACl	Tetrabutylammonium chloride

T_d	Decomposition Temperature
TFA	Trifluoroacetate
T_g	Glass transition temperature
TGA	Thermogravimetric analysis
THF	Tetrahydrofuran
TLC	Thin-layer chromatography
TOF	Time-of-flight
U-4CR	Ugi four-component reaction
w_i	Weight fraction of i
x_i	Molar fraction of i
xNb	<i>exo</i> norbornene
σ	Grafting density

9.2 List of publications

- Waibel, K. A.; Barther, D.; Malliaridou, T.; Moatsou, D.; Meier, M. A. R., *Eur. J. Org. Chem.* **2021**, *2021*, 4508-4516.
- Barther, D.; Moatsou, D., *Macromol. Rapid Commun.* **2021**, *42*, 2100027.
- Stefan Oelmann, S.; Travanut, A.; Barther, D.; Romero, M.; Howdle, S. M.; Alexander, C.; Meier, M. A. R., *Biomacromolecules* **2019**, *20*, 90-101.
- Arens, L.; Barther, D.; Landsgesell, J.; Holm, C.; Wilhelm, M., *Soft Matter* **2019**, *15*, 9949-9964.

10 List of figures, schemes, and tables

10.1 List of figures

Figure 2.1. Number of search results per year associated with the term “sequence-controlled polymers” (2000 - 2021) available <i>via</i> Google Scholar (date of excess: 06.03.2022).	3
Figure 2.2. Schematic representation of the terms “sequence-controlled polymers” and “sequence-defined polymers”. Reprinted with permission (https://onlinelibrary.wiley.com/doi/full/10.1002/marc.201700582). ⁷⁰	4
Figure 2.3. Representative examples for the kinetic approach in the synthesis of sequence-controlled polymers, using atom transfer radical polymerization (ATRP, top) and ring-opening metathesis polymerization (ROMP, bottom). ^{87,88}	5
Figure 2.4. Graphical representation of the Carothers equation for (A) linear AB-systems and (B) linear AA/BB-systems. ²³⁸	19
Figure 2.5. ATRP activation rate constants (k_{act}) for different bidentate (red), tridentate (black), and tetradentate (blue) ligands with ethyl α -bromoisobutyrate in the presence of copper(I) bromide in acetonitrile at 35 °C. Reprinted with permission (https://pubs.acs.org/doi/full/10.1021/ma0609634). ³²⁶ Copyright 2006 American Chemical Society.....	25
Figure 2.6. ATRP activation rate constants (k_{act}) for different tertiary (red), secondary (blue), and primary (black) alkyl initiators with Cu^I -X/PMDETA (X = Cl or Br) in acetonitrile at 35 °C. Reprinted with permission (https://pubs.acs.org/doi/full/10.1021/ma062897b). ³²⁸ Copyright 2007 American Chemical Society.....	26
Figure 2.7. The G1-mediated ROMP of kinetically different norbornene-based monomers, generating copolymers with relatively controlled monomer sequences. Reprinted with permission (https://pubs.rsc.org/en/content/articlelanding/2014/sc/c4sc00752b). ⁹³	33
Figure 2.8. G3-mediated synthesis of symmetric and unsymmetric bottlebrush polymers using a sequential addition of macromonomers strategy. Reprinted with permission (https://pubs.acs.org/doi/full/10.1021/acsmacrolett.7b00724). ⁴¹¹ Further permissions related to the material excerpted must be directed to the ACS.	34

- Figure 4.1.** Stacked ^1H NMR spectra (section: 6.85 – 4.85 ppm) of the representative ROMP of *exo* monomer **xNb1PePr** (bottom) and the obtained polymer **poly(xNb1PePr)** (top), highlighting the vanishing of the olefinic norbornene signal at 6.32 ppm and the appearing of a broad signal assigned to the protons at the polymeric backbone at 5.8 – 5.4 ppm, with the respective functional groups (left). The tertiary carbon proton of the Passerini unit served as a reference. Measured in DCM-d_2 45
- Figure 4.2.** Stacked ^1H NMR spectra (section: 6.85 – 4.85 ppm) of the representative ROMP of *endo* monomer **nNb1PePr** (bottom) and the obtained polymer **poly(nNb1PePr)** (top), highlighting the vanishing of the olefinic norbornene signal at 6.1 ppm and the appearing of a broad signal assigned to the protons at the polymeric backbone at 5.8 – 5.4 ppm, with the respective functional groups (left). The tertiary carbon proton of the Passerini unit served as a reference. Measured in deuterated DCM-d_2 46
- Figure 4.3.** Representative SEC traces of (A) **poly(xNb1PePr)** and (B) **poly(xNb1AdPy)** and its *endo*-derived analogue **poly(nNb1AdPy)**. 47
- Figure 4.4.** Representative thermal analysis of **poly(xNb1PePr)**, (A) DSC trace (green dotted line represents the T_g) and (B) TGA trace (red dotted line represents the T_d)..... 49
- Figure 4.5.** Stacked DSC traces of the homopolymers **poly(xNb10PePr)** and **poly(xNb10AdPy)**, and the statistical copolymer **poly(xNb10PePr-*stat*-xNb10AdPy)**. 50
- Figure 4.6.** Kinetic plots of the (A) homopolymerizations of the *exo* monomers **xNb1PePr**, **xNb10PePr**, **xNb1AdPy** and **xNb10AdPy**, and (B) homopolymerizations of the *endo* monomers **nNb1PePr**, **nNb10PePr**, **nNb1AdPy** and **nNb10AdPy**, based on ^1H NMR spectroscopy data (**Figures S4.55 – S4.62, Table 4.3**). Lines represent linear fits..... 53
- Figure 4.7.** (A) SEC trace of the homopolymer obtained from entry 4.9 (**Table 4.3**) and (B) corresponding kinetic plot, based on ^1H NMR spectroscopy data (**Figure S4.63**). Line represents linear fit..... 53
- Figure 4.8.** (A) Kinetic plots of the copolymerization (entry 4.10, **Table 4.3**) of **xNb10PePr** and **xNb10AdPy** and homopolymerizations (HP) of the respective monomers, and the (B) copolymerization (entry 4.11, **Table 4.3**) of **nNb1PePr** and **nNb1AdPy** and homopolymerizations of the respective monomers, based on ^1H NMR spectroscopy data (**Figures S4.64 and S4.67**). Lines represent linear fits..... 54
- Figure 4.9.** (A) Kinetic plot of the copolymerization (entry 4.12, **Table 4.3**) of **xNb1PePr** and **nNb10AdPy** and homopolymerizations (HP) of the respective monomers, and (B) molar

fraction (x_i) of xNb1PePr in the respective copolymer as a function of polymerization time, based on ^1H NMR spectroscopy data (Figure S4.70). Lines represent linear fits.....	55
Figure 4.10. (A) Kinetic plots of the polymerization of nNb10AdPy before addition of xNb10PePr , (B) copolymerization (entry 4.13, Table 4.3) of nNb10AdPy and xNb10PePr , (C) copolymerization kinetics of xNb10PePr , and (D) molar fraction (x_i) of xNb10PePr in the respective copolymer as a function of polymerization time, based on ^1H NMR spectroscopy data (Figure S4.73). Line represents linear fit.....	57
Figure 4.11. SEC traces of (A) <i>exo/exo</i> -derived copolymer of entry 4.10, (B) <i>endo/endo</i> -derived copolymer of entry 4.11, (C) <i>exo/endo</i> -derived diblock-like copolymer of entry 4.12, and (D) <i>endo/exo</i> -derived triblock-like copolymer of entry 4.13 (Table 4.3)......	58
Figure 5.1. SEC traces of (A) the PMMA-based macromonomers comprising an ethyl linker, (B) the PMMA-based macromonomers comprising a hexyl linker, (C) the P BnMA -based macromonomer, and (D) the PS-based macromonomer.....	66
Figure 5.2. (A) MALDI-TOF spectrum (DCTB, NaTFA) of xNb2M12 with highlighted mass distributions in color to guide the eye, (B) selected region of the spectrum (1455 – 1745 m/z) with peaks color coded as per the identified species, and (C) structures of xNb2M12 species (S1 – S5) and their calculated and measured monoisotopic masses.	67
Figure 5.3. (A) MALDI-TOF spectrum (DCTB, NaTFA) of xNb2B12 with highlighted mass distributions in color to guide the eye, (B) selected region of the spectrum (2110 – 2660 m/z) with peaks color coded as per the identified species, and (C) structures of xNb2B12 species (S1 – S6) and their calculated and measured monoisotopic masses.	70
Figure 5.4. (A) MALDI-TOF spectrum (dithranol, NaTFA) of xNb2S20 with highlighted mass distributions in color to guide the eye, (B) selected region of the spectrum (1475 – 1775 m/z) with peaks color coded as per the identified species, and (C) structures of xNb2S20 species (S1 – S2) and their calculated and measured monoisotopic masses.	72
Figure 5.5. DSC traces of (A) xNb2M12 , xNb2B12 , and the respective 1:1 blend, and of (B) xNb2M12 , xNb2S20 , and the respective 1:1 blend.	73
Figure 5.6. SEC traces and plots of the molecular weight and dispersity versus targeted DP, determined by SEC, in the G1-mediated ROMP of (A,B) xNb2M12 and (C,D) xNb2M27 , respectively.	77

Figure 5.7. SEC traces of (A) entry 5.11 and the used macromonomer, and (B) entry 5.12 and the used macromonomer (Tables 5.2 and 5.3).....	79
Figure 5.8. (A) Kinetic plot of the ROMP of xNb2M27 , based on ^1H NMR spectroscopy data (Figure S5.35), and (B) SEC trace of the obtained graft polymer after overnight reaction....	83
Figure 5.9. (A) Schematic ROMP of xNb6M13 under argon atmosphere, (B) corresponding SEC traces and (C) SEC trace entry 5.20 (Table 5.6).....	85
Figure 5.10. SEC traces of the graft polymers obtained by the G3-mediated ROMP of xNb2M12 , applying catalyst concentrations of (A) 2 mmol/L (entry 5.21, Table 5.7) and (B) 1 mmol/L (entry 5.22, Table 5.7).	88
Figure 5.11. (A) Kinetic plot of the polymerization of xNb2M12 , based on ^1H NMR spectroscopy data (Figure S5.42), and (B) SEC traces of xNb2M12 and the obtained graft polymer after 30 minutes of reaction time (entry 5.23, Table 5.8). (C) Kinetic plot of the polymerization of xNb2M27 , based on ^1H NMR spectroscopy data (Figure S5.43), and (D) SEC traces of xNb2M27 and the obtained graft polymer after 72 minutes of reaction time (entry 5.24, Table 5.8). Lines represent linear fits.	90
Figure 5.12. (A) Kinetic plot of the polymerization of xNb2B12 , based on ^1H NMR spectroscopy data (Figure S5.44), and (B) SEC traces of xNb2B12 and the obtained graft polymer after 45 minutes of reaction time (entry 5.25, Table 5.8). (C) Kinetic plot of the polymerization of xNb2S20 , based on ^1H NMR spectroscopy data (Figure S5.45), and (D) SEC traces of xNb2S20 and the obtained graft polymer after 49 minutes of reaction time (entry 5.26, Table 5.8). Lines represent linear fits.....	92
Figure 5.13. (A) Kinetic plot of the polymerization of xNb2M12 in deuterated THF, based on ^1H NMR spectroscopy data (Figure S5.46), and (B) SEC traces of xNb2M12 and comparison between the obtained graft polymers using degassed deuterated DCM (entry 5.23, Table 5.8) and degassed deuterated THF (entry 5.27, Table 5.8) as solvent, both after 30 minutes of reaction time. Line represents linear fit.....	94
Figure 5.14. SEC traces of (A) homopolymer and diblock of entry 5.28, and (B) homopolymer and diblock of entry 5.29 (Table 5.9).	97
Figure 5.15. Schematic representation of a triblock graft copolymer synthesized by the iterative ROMP procedure, comprising two macroblocks (black and green) and a spacer block (orange).....	99

Figure 5.16. SEC traces of the homopolymer and the respective diblocks of entries 5.30 – 5.32 (Table 5.10).....	100
Figure 5.17. SEC traces of the graft copolymers from (A) entry 5.30, (B) entry 5.31, and (C) entry 5.32 (Table 5.10).....	102
Figure 5.18. SEC traces of the homopolymers and the (A) diblock graft copolymers from entry 5.33, (B) entry 5.34, and (C) entry 5.35, and (D) of the triblock graft copolymer from entry 5.36 (Table 5.11).....	104
Figure 5.19. (A) SEC traces of the obtained homopolymer after 34 minutes of reaction time and the diblock after 65 minutes of reaction time and (B) kinetic plot of the copolymerization of xNb2B12 , based on ^1H NMR spectroscopy data (Figure S5.58, Table 5.12). Line represents linear fit.....	107
Figure 5.20. SEC traces of the homopolymers and the diblocks from (A) entry 5.38, compared with the diblock of entry 5.37, and (B) entry 5.39 (Table 5.13).....	110
Figure 5.21. Schematic representation of the synthesis of Janus copolymers <i>via</i> the functionalization of a bifunctional precursor, using copper-catalyzed alkyne-azide cycloaddition (CuAAC) and ATRP, and subsequent ROMP.....	113
Figure 5.22. Stacked ^1H NMR spectra (section: 3.7 – 0 ppm) of xNbBrTMS (bottom) and xNbBrH (top), highlighting the vanishing of the TMS signal at 0.25 ppm (orange box) and the appearing of the proton at the terminal alkyne at 3.1 ppm (green box).....	116
Figure 5.23. SEC traces of PS before (PS-Br) and after (PS-N₃) azidation.	118
Figure 5.24. Stacked ^1H NMR spectra (section: 4.9 – 3.9 ppm) of PS-Br (bottom) and PS-N₃ (top), highlighting the shift of the proton next to the bromide toward high-field after azidation (4.5 ppm → 4.0 ppm), with the respective end groups (left). Methylene groups of the initiator units at 3.6 ppm served as a reference.	119
Figure 5.25. Stacked ^1H NMR spectra (section: 5.25 – 2.95 ppm) of xNbBrH (bottom) and xNbBr-PS (top), highlighting the vanishing of the terminal alkyne signal at 3.1 ppm and the appearing of a signal assigned to the proton next to the triazole at 5.1 ppm, with the respective functional groups (left). Methylene groups (CH ₂ -CO) of the norbornene units at ca. 4.1 ppm served as a reference.	121
Figure 5.26. SEC traces of the polymeric starting material PS-N₃ and the ATRP macroinitiator xNbBr-PS , obtained <i>via</i> CuAAC.	122

Figure 5.27. SEC traces of the macroinitiator xNbBr-PS and the bifunctional macromonomer xNb-PMMA-PS , obtained <i>via</i> ATRP of MMA.....	124
Figure 5.28. DSC trace of bifunctional macromonomer xNb-PMMA-PS	125
Figure 5.29. SEC traces of the bifunctional macromonomer xNb-PMMA-PS and of the obtained Janus copolymers Janus10 , Janus20 and Janus30 (Table 5.14).	127
Figure 6.1. (A) Kinetic plot of the homopolymerizations of nNbHex , based on ¹ H NMR spectroscopy data, and (B) SEC traces of the obtained polymers (entries 6.1 – 6.3, Table 6.1). Lines represent linear fits.....	133
Figure 6.2. (A) Kinetic plot of the homopolymerizations of nNbHex , based on ¹ H NMR spectroscopy data (Figure S6.9), (B) SEC traces of the withdrawn samples during ROMP (entry 6.4), and (C) plot of the monomer conversion versus molecular weight and dispersity, determined by SEC. Line represents linear fit.....	134
Figure 6.3. (A) Homopolymerization of nNbHex using the G1 catalyst and subsequent addition of macromonomer resulting in a block-like graft copolymer. (B) Schematic synthesis of graft copolymers by the delayed addition of macromonomer.....	136
Figure 6.4. Representative (A) kinetic plots of entries 6.1 (Table 6.1) and 6.5 (Table 6.2), (B) highlighting xNb2M12 during copolymerization, (C) molar fraction (x_i) of xNb2M12 in entry 6.5 as a function of polymerization time, based on ¹ H NMR spectroscopy data (Figure S6.10), and (D) SEC traces of entry 6.5 before xNb2M12 addition and after xNb2M12 conversion. Line represents linear fit.....	138
Figure 6.5. (A) Relationship between apparent copolymerization rate (k_{app}) of the macromonomer, its structure and amount, (B) evolution of macroblock grafting density (σ) with increasing macromonomer amount and (C) relationship between dispersity (D_M) of the resulting graft copolymer and its molecular weight.	140
Figure 6.6. SEC traces of polymethacrylate-based macromonomers, comprising polymerizable <i>exo</i> norbornene moieties (Table 6.4).....	146
Figure 6.7. (A) Kinetic plots of entry 6.1 (Table 6.1), entry 6.19-B1 and entry 6.19-B2 (Table 6.5), (B) molar fraction (x_i) of xNb6M17 in entry 6.19 as a function of polymerization time, based on ¹ H NMR spectroscopy data (Figure S6.65), and (C) SEC traces of entry 6.19 before addition of first and second macroblock and after complete conversion of the first and second macroblock.....	150

Figure 6.8. Schematic representation of different polymer architectures using ROMP with delayed addition of macromonomers, indicating the gradient substructures by progressive dilution of the macroblocks. Here, A and B only represent the different macromonomers.

..... 151

Figure 6.9. (A) Kinetic plots of entry 6.1 (**Table 6.1**), entry 6.20-B1 and entry 6.20-B2 (**Table 6.6**), (B) molar fraction (x_i) of the macromonomers (MM) in entry 6.20 as a function of polymerization time, based on ^1H NMR spectroscopy data (**Figure S6.79**), step-like MM incorporation highlighted by the grey dotted line, and (C) SEC traces of entry 6.20 before addition of first and second macroblock and after complete conversion of the first and second macroblock..... 153

Figure 6.10. (A) Kinetic plots of entry 6.1 (**Table 6.1**), entry 6.21-B1 and entry 6.21-B2 (**Table 6.6**), (B) molar fraction (x_i) of the macromonomers (MM) in entry 6.21 as a function of polymerization time, based on ^1H NMR spectroscopy data (**Figure S6.82**), step-like MM incorporation highlighted by the grey dotted line, and (C) SEC traces of entry 6.21 before addition of first and second macroblock and after complete conversion of the first and second macroblock..... 155

Figure 6.11. (A) Kinetic plots of entry 6.1 (**Table 6.1**), entry 6.22-B1, entry 6.22-B2 and entry 6.22-B3 (**Table 6.6**), (B) molar fraction (x_i) of the macromonomers (MM) in entry 6.22 as a function of polymerization time, based on ^1H NMR spectroscopy data (**Figure S6.85**), step-like MM incorporation highlighted by the grey dotted line, and (C) SEC traces of entry 6.22 before addition of first, second and third macroblock and after complete conversion of the first, second and third macroblock. 156

10.2 List of supporting figures

Figure S4.1. ^1H NMR spectrum of **xNb1** in CDCl_3 165

Figure S4.2. ^{13}C NMR spectrum of **xNb1** in CDCl_3 166

Figure S4.3. ^1H NMR spectrum of **xNb10** in CDCl_3 167

Figure S4.4. ^{13}C NMR spectrum of **xNb10** in CDCl_3 167

Figure S4.5. ^1H NMR spectrum of **nNb1** in CDCl_3 168

Figure S4.6. ^{13}C NMR spectrum of **nNb1** in CDCl_3 169

Figure S4.7. ^1H NMR spectrum of <i>n</i>Nb10 in CDCl_3	170
Figure S4.8. ^{13}C NMR spectrum of <i>n</i>Nb10 in CDCl_3	170
Figure S4.9. ^1H NMR spectrum of <i>x</i>Nb1PePr in CD_2Cl_2	171
Figure S4.10. ^{13}C NMR spectrum of <i>x</i>Nb1PePr in CD_2Cl_2	172
Figure S4.11. ^1H NMR spectrum of <i>x</i>Nb1AdPy in CD_2Cl_2	173
Figure S4.12. ^{13}C NMR spectrum of <i>x</i>Nb1AdPy in CD_2Cl_2	173
Figure S4.13. ^1H NMR spectrum of <i>x</i>Nb10PePr in CD_2Cl_2	174
Figure S4.14. ^{13}C NMR spectrum of <i>x</i>Nb10PePr in CD_2Cl_2	175
Figure S4.15. ^1H NMR spectrum of <i>x</i>Nb10AdPy in CD_2Cl_2	176
Figure S4.16. ^{13}C NMR spectrum of <i>x</i>Nb10AdPy in CD_2Cl_2	176
Figure S4.17. ^1H NMR spectrum of <i>n</i>Nb1PePr in CD_2Cl_2	177
Figure S4.18. ^{13}C NMR spectrum of <i>n</i>Nb1PePr in CD_2Cl_2	178
Figure S4.19. ^1H NMR spectrum of <i>n</i>Nb1AdPy in CD_2Cl_2	179
Figure S4.20. ^{13}C NMR spectrum of <i>n</i>Nb1AdPy in CD_2Cl_2	179
Figure S4.21. ^1H NMR spectrum of <i>n</i>Nb10PePr in CD_2Cl_2	180
Figure S4.22. ^{13}C NMR spectrum of <i>n</i>Nb10PePr in CD_2Cl_2	181
Figure S4.23. ^1H NMR spectrum of <i>n</i>Nb10AdPy in CD_2Cl_2	182
Figure S4.24. ^{13}C NMR spectrum of <i>n</i>Nb10AdPy in CD_2Cl_2	183
Figure S4.25. ^1H NMR spectrum of poly(<i>x</i>Nb1PePr) in CD_2Cl_2 (500 MHz).....	184
Figure S4.26. ^{13}C NMR spectrum of poly(<i>x</i>Nb1PePr) in CD_2Cl_2 (126 MHz).	185
Figure S4.27. ^1H NMR spectrum of poly(<i>x</i>Nb1AdPy) in CD_2Cl_2 (500 MHz).	185
Figure S4.28. ^{13}C NMR spectrum of poly(<i>x</i>Nb1AdPy) in CD_2Cl_2 (126 MHz).	186
Figure S4.29. (A) DSC and (B) TGA traces of poly(<i>x</i>Nb1AdPy)	186
Figure S4.30. ^1H NMR spectrum of poly(<i>x</i>Nb10PePr) in CD_2Cl_2 (500 MHz).....	187
Figure S4.31. ^{13}C NMR spectrum of poly(<i>x</i>Nb10PePr) in CD_2Cl_2 (126 MHz).	187
Figure S4.32. SEC trace of poly(<i>x</i>NbPePr)	188
Figure S4.33. (A) DSC and (B) TGA traces of poly(<i>x</i>Nb10PePr)	188
Figure S4.34. ^1H NMR spectrum of poly(<i>x</i>Nb10AdPy) in CD_2Cl_2 (500 MHz).	189
Figure S4.35. ^{13}C NMR spectrum of poly(<i>x</i>Nb10AdPy) in CD_2Cl_2 (126 MHz).	189
Figure S4.36. SEC trace of poly(<i>x</i>Nb10AdPy)	190
Figure S4.37. (A) DSC and (B) TGA traces of poly(<i>x</i>Nb10AdPy)	190

Figure S4.38. ^1H NMR spectrum of the small molecule isolated from exposing poly(xNb10AdPy) to potassium 2-isocyanoacetate in CD_2Cl_2	191
Figure S4.39. ^{13}C NMR spectrum of the small molecule isolated from exposing poly(xNb10AdPy) to potassium 2-isocyanoacetate in CD_2Cl_2	191
Figure S4.40. ^1H NMR spectrum of poly(nNb1PePr) in CD_2Cl_2 (500 MHz).....	192
Figure S4.41. ^{13}C NMR spectrum of poly(nNb1PePr) in CD_2Cl_2 (126 MHz).....	193
Figure S4.42. SEC trace of poly(nNb1PePr)	193
Figure S4.43. (A) DSC and (B) TGA traces of poly(nNb1PePr)	194
Figure S4.44. ^1H NMR spectrum of poly(nNb1AdPy) in CD_2Cl_2 (500 MHz).....	194
Figure S4.45. ^{13}C NMR spectrum of poly(nNb1AdPy) in CD_2Cl_2 (126 MHz).	195
Figure S4.46. (A) DSC and (B) TGA traces of poly(nNb1AdPy)	195
Figure S4.47. ^1H NMR spectrum of poly(nNb10PePr) in CD_2Cl_2 (500 MHz).....	196
Figure S4.48. ^{13}C NMR spectrum of poly(nNb10PePr) in CD_2Cl_2 (126 MHz).....	196
Figure S4.49. SEC trace of poly(nNb10PePr)	197
Figure S4.50. (A) DSC and (B) TGA traces of poly(nNb10PePr)	197
Figure S4.51. ^1H NMR spectrum of poly(nNb10AdPy) in CD_2Cl_2 (500 MHz).....	198
Figure S4.52. ^{13}C NMR spectrum of poly(nNb10AdPy) in CD_2Cl_2 (126 MHz).....	198
Figure S4.53. SEC trace of poly(nNb10AdPy)	199
Figure S4.54. (A) DSC and (B) TGA traces of poly(nNb10AdPy)	199
Figure S4.55. Representative stacked ^1H NMR spectra of the ROMP of xNb1PePr (entry 4.1) in CD_2Cl_2 (500 MHz) and the ^1H NMR spectrum of the corresponding monomer in CD_2Cl_2 (400 MHz). Boxes: norbornene olefinic moiety (solid); poly(norbornene) olefinic backbone (dashed).	200
Figure S4.56. Representative stacked ^1H NMR spectra of the ROMP of xNb1AdPy (entry 4.2) in CD_2Cl_2 (500 MHz) and the ^1H NMR spectrum of the corresponding monomer in CD_2Cl_2 (400 MHz). Boxes: norbornene olefinic moiety (solid); poly(norbornene) olefinic backbone (dashed).	200
Figure S4.57. Representative stacked ^1H NMR spectra of the ROMP of xNb10PePr (entry 4.3) in CD_2Cl_2 (500 MHz) and the ^1H NMR spectrum of the corresponding monomer in CD_2Cl_2 (400 MHz). Boxes: norbornene olefinic moiety (solid); poly(norbornene) olefinic backbone (dashed).	201

Figure S4.58. Representative stacked ^1H NMR spectra of the ROMP of xNb10AdPy (entry 4.4) in CD_2Cl_2 (500 MHz) and the ^1H NMR spectrum of the corresponding monomer in CD_2Cl_2 (400 MHz). Boxes: norbornene olefinic moiety (solid); poly(norbornene) olefinic backbone (dashed).	201
Figure S4.59. Representative stacked ^1H NMR spectra of the ROMP of nNb1PePr (entry 4.5) in CD_2Cl_2 (500 MHz) and the ^1H NMR spectrum of the corresponding monomer in CD_2Cl_2 (400 MHz). Boxes: norbornene olefinic moiety (solid); poly(norbornene) olefinic backbone (dashed).	202
Figure S4.60. Representative stacked ^1H NMR spectra of the ROMP of nNb1AdPy (entry 4.6) in CD_2Cl_2 (500 MHz) and the ^1H NMR spectrum of the corresponding monomer in CD_2Cl_2 (400 MHz). Boxes: norbornene olefinic moiety (solid); poly(norbornene) olefinic backbone (dashed).	202
Figure S4.61. Representative stacked ^1H NMR spectra of the ROMP of nNb10PePr (entry 4.7) in CD_2Cl_2 (500 MHz) and the ^1H NMR spectrum of the corresponding monomer in CD_2Cl_2 (400 MHz). Boxes: norbornene olefinic moiety (solid); poly(norbornene) olefinic backbone (dashed).	203
Figure S4.62. Representative stacked ^1H NMR spectra of the ROMP of nNb10AdPy (entry 4.8) in CD_2Cl_2 (500 MHz) and the ^1H NMR spectrum of the corresponding monomer in CD_2Cl_2 (400 MHz). Boxes: norbornene olefinic moiety (solid); poly(norbornene) olefinic backbone (dashed).	203
Figure S4.63. Representative stacked ^1H NMR spectra of the ROMP of xNb1PePr (entry 4.9) in CD_2Cl_2 (500 MHz) and the ^1H NMR spectrum of the corresponding monomer in CD_2Cl_2 (400 MHz). Boxes: norbornene olefinic moiety (solid); poly(norbornene) olefinic backbone (dashed).	204
Figure S4.64. Representative stacked ^1H NMR spectra of the copolymerization of xNb10PePr and xNb10AdPy (entry 4.10) in CD_2Cl_2 (500 MHz) and the ^1H NMR spectra of the corresponding monomers in CD_2Cl_2 (400 MHz). Boxes: norbornene olefinic moieties (solid); poly(norbornene) olefinic backbone (dashed).	205
Figure S4.65. ^1H NMR spectrum of poly(xNb10PePr-stat-xNb10AdPy) (entry 4.10) in CD_2Cl_2 (500 MHz).	205
Figure S4.66. ^{13}C NMR spectrum of poly(xNb10PePr-stat-xNb10AdPy) (entry 4.10) in CD_2Cl_2 (126 MHz).	206

Figure S4.67. Representative stacked ^1H NMR spectra of the copolymerization of <i>nNb1PePr</i> and <i>nNb1AdPy</i> (entry 4.11) in CD_2Cl_2 (500 MHz) and the ^1H NMR spectra of the corresponding monomers in CD_2Cl_2 (400 MHz). Boxes: <i>nNb1PePr</i> olefinic moiety (solid); <i>nNb1AdPy</i> olefinic moiety (dashed); poly(norbornene) olefinic backbone (dotted).	206
Figure S4.68. ^1H NMR spectrum of entry 4.11 in CD_2Cl_2 (500 MHz). Note: Deuterated solvent was contaminated with traces of DMSO.....	207
Figure S4.69. ^{13}C NMR spectrum of entry 4.11 in CD_2Cl_2 (126 MHz).	207
Figure S4.70. Representative stacked ^1H NMR spectra of the copolymerization of <i>xNb1PePr</i> and <i>nNb10AdPy</i> (entry 4.12) in CD_2Cl_2 (500 MHz) and the ^1H NMR spectra of the corresponding monomers in CD_2Cl_2 (400 MHz). Boxes: <i>xNb1PePr</i> olefinic moiety (solid); <i>nNb10AdPy</i> olefinic moiety (dashed); poly(norbornene) olefinic backbone (dotted).	208
Figure S4.71. ^1H NMR spectrum of entry 4.12 in CD_2Cl_2 (500 MHz).	208
Figure S4.72. ^{13}C NMR spectrum of entry 4.12 in CD_2Cl_2 (126 MHz).	209
Figure S4.73. Representative stacked ^1H NMR spectra of the copolymerization of <i>xNb10AdPy</i> and <i>nNb10PePr</i> (entry 4.13) in CD_2Cl_2 (500 MHz) and the ^1H NMR spectra of the corresponding monomers in CD_2Cl_2 (400 MHz). Boxes: <i>xNb10AdPy</i> olefinic moiety (solid); <i>nNb10PePr</i> olefinic moiety (dashed); poly(norbornene) olefinic backbone (dotted).	209
Figure S4.74. ^1H NMR spectrum of entry 4.13 in CD_2Cl_2 (500 MHz).	210
Figure S4.75. ^{13}C NMR spectrum of entry 4.13 in CD_2Cl_2 (126 MHz).	210
Figure S5.1. ^1H NMR spectrum of <i>xNb2OH</i>	211
Figure S5.2. ^{13}C NMR spectrum of <i>xNb2OH</i>	212
Figure S5.3. ^1H NMR spectrum of <i>xNb6OH</i>	213
Figure S5.4. ^{13}C NMR spectrum of <i>xNb6OH</i>	213
Figure S5.5. ^1H NMR spectrum of <i>xNb2Br</i>	215
Figure S5.6. ^{13}C NMR spectrum of <i>xNb2Br</i>	215
Figure S5.7. ^1H NMR spectrum of <i>xNb6Br</i>	216
Figure S5.8. ^{13}C NMR spectrum of <i>xNb6Br</i>	217
Figure S5.9. ^1H NMR spectrum of <i>xNb2M12</i> in CDCl_3 (500 MHz).	218
Figure S5.10. ^{13}C NMR spectrum of <i>xNb2M12</i> in CDCl_3 (126 MHz).	219
Figure S5.11. Comparison between measured and calculated isotopic patterns of <i>xNb2M12</i> determined <i>via</i> MALDI-TOF MS (Figure 5.2) with (A) the chloride-terminated species (S1), (B)	

the hydrogen- and the vinylidene-terminated species (S2 and S3), (C) the dinorbornene species (S4), and (D) the double charged vinylidene species (S5)..... 219

Figure S5.12. ^1H NMR spectrum of **xNb2M27** in CDCl_3 (500 MHz). 220

Figure S5.13. ^{13}C NMR spectrum of **xNb2M27** in CDCl_3 (126 MHz). 220

Figure S5.14. (A) MALDI-TOF spectrum (DCTB, NaTFA) of **xNb2M27** with highlighted mass distributions in color to guide the eye, (B) selected region of the spectrum (1410 – 1720 m/z) with peaks color coded as per the identified species, and (C) structures of **xNb2M27** species (S1 – S5) and their calculated and measured monoisotopic masses. 221

Figure S5.15. Comparison between measured and calculated isotopic patterns of **xNb2M27** determined *via* MALDI-TOF MS (**Figure S5.14**) with (A) the chloride-terminated species (S1), (B) the hydrogen- and the vinylidene-terminated species (S2 and S3), (C) the lactone-terminated species (S4), and (D) the dinorbornene species (S5)..... 222

Figure S5.16. ^1H NMR spectrum of **xNb6M13** in CDCl_3 (400 MHz). 223

Figure S5.17. ^{13}C NMR spectrum of **xNb6M13** in CDCl_3 (126 MHz). 223

Figure S5.18. (A) MALDI-TOF spectrum (DCTB, NaTFA) of **xNb6M13** with highlighted mass distributions in color to guide the eye, (B) selected region of the spectrum (1400 – 1725 m/z) with peaks color coded as per the identified species, and (C) structures of **xNb6M13** species (S1 – S3) and their calculated and measured monoisotopic masses. 224

Figure S5.19. Comparison between measured and calculated isotopic patterns of **xNb6M13** determined *via* MALDI-TOF MS (**Figure S5.18**) with (A) the chloride-terminated species (S1), (B) the hydrogen-terminated species (S2), and (C) the lactone-terminated species (S3).... 225

Figure S5.20. ^1H NMR spectrum of **xNb6M17** in CDCl_3 (500 MHz). 226

Figure S5.21. ^{13}C NMR spectrum of **xNb6M17** in CDCl_3 (126 MHz). 226

Figure S5.22. (A) MALDI-TOF spectrum (DCTB, NaTFA) of **xNb6M17** with highlighted mass distributions in color to guide the eye, (B) selected region of the spectrum (1330 – 1620 m/z) with peaks color coded as per the identified species, and (C) structures of **xNb6M17** species (S1 – S4) and their calculated and measured monoisotopic masses. 227

Figure S5.23. Comparison between measured and calculated isotopic patterns of **xNb6M17** determined *via* MALDI-TOF MS (**Figure S5.22**) with (A) the chloride-terminated species (S1), (B) the dinorbornene species (S2), (C) the hydrogen-terminated species (S3), and (C) the vinylidene-terminated species (S4)..... 228

Figure S5.24. ^1H NMR spectrum of **xNb2B12** in CD_2Cl_2 (500 MHz). 228

Figure S5.25. ^{13}C NMR spectrum of xNb2B12 in CD_2Cl_2 (126 MHz).....	229
Figure S5.26. Comparison between measured and calculated isotopic patterns of xNb2B12 determined <i>via</i> MALDI-TOF MS (Figure 5.3) with (A) the chloride-terminated species (S1), (B) the hydrogen- and the vinylidene-terminated species (S2 and S3), (C) the double charged dinorbornene species (S4), (D) the dinorbornene species (S5), and (E) the lactone-terminated species (S6).....	230
Figure S5.27. ^1H NMR spectrum of xNb2S20 in CD_2Cl_2 (500 MHz).	231
Figure S5.28. ^{13}C NMR spectrum of xNb2S20 in CD_2Cl_2 (126 MHz).	232
Figure S5.29. Comparison between measured and calculated isotopic patterns of xNb2S20 determined <i>via</i> MALDI-TOF MS (Figure 5.4) with (A) the olefin-terminated species (S1), and (B) the double charged hydrogen-terminated species (S2).	232
Figure S5.30. Stacked ^1H NMR spectra of entries 5.1 – 5.5 after quenching with EVE in CDCl_3 (400 MHz) and the ^1H NMR spectrum of the corresponding monomer in CDCl_3 (500 MHz). Boxes: norbornene olefinic moiety (solid); poly(norbornene) olefinic backbone (dashed).	233
Figure S5.31. Stacked ^1H NMR spectra of entries 5.6 – 5.10 after quenching with EVE and the ^1H NMR spectrum of the corresponding monomer in CDCl_3 (500 MHz). Boxes: norbornene olefinic moiety (solid); poly(norbornene) olefinic backbone (dashed).	233
Figure S5.32. Stacked ^1H NMR spectra of entries 5.11 and 5.12 after quenching with EVE in CDCl_3 (400 MHz) and the ^1H NMR spectrum of the corresponding monomer in CDCl_3 (500 MHz). Boxes: norbornene olefinic moiety (solid); poly(norbornene) olefinic backbone (dashed).	234
Figure S5.33. Stacked ^1H NMR spectra of entries 5.13 – 5.16 after quenching with EVE in CDCl_3 (400 MHz) and the ^1H NMR spectrum of the corresponding monomer in CDCl_3 (500 MHz). Boxes: norbornene olefinic moiety (solid); poly(norbornene) olefinic backbone (dashed).	234
Figure S5.34. SEC trace of entry 5.14.....	235
Figure S5.35. Representative stacked ^1H NMR spectra of the ROMP of xNb2M27 (entry 5.17) in CD_2Cl_2 (500 MHz) and the ^1H NMR spectrum of the corresponding monomer in CDCl_3 (500 MHz). Boxes: norbornene olefinic moiety (solid); poly(norbornene) olefinic backbone (dashed).	236
Figure S5.36. Stacked ^1H NMR spectra of entries 5.18 and 5.19 after quenching with EVE in CDCl_3 (400 MHz) and the ^1H NMR spectrum of the corresponding monomer in CDCl_3	

(400 MHz). Boxes: norbornene olefinic moiety (solid); poly(norbornene) olefinic backbone (dashed).	237
Figure S5.37. Stacked ^1H NMR spectra of entry 5.20 after quenching with EVE in CDCl_3 (400 MHz) and the ^1H NMR spectrum of the corresponding monomer in CDCl_3 (500 MHz). Boxes: norbornene olefinic moiety (solid); poly(norbornene) olefinic backbone (dashed). 237	
Figure S5.38. ^1H NMR spectrum of the G3 catalyst	238
Figure S5.39. ^{13}C NMR spectrum of the G3 catalyst	239
Figure S5.40. Stacked ^{31}P NMR spectra of the G2 and the G3 catalyst	239
Figure S5.41. Stacked ^1H NMR spectra of entries 5.21 and 5.22 after quenching with EVE in CDCl_3 (400 MHz) and the ^1H NMR spectrum of the corresponding monomer in CDCl_3 (500 MHz). Boxes: norbornene olefinic moiety (solid); poly(norbornene) olefinic backbone (dashed).	240
Figure S5.42. Representative stacked ^1H NMR spectra of the ROMP of xNb2M12 (entry 5.23) in CD_2Cl_2 (500 MHz) and the ^1H NMR spectrum of the corresponding monomer in CDCl_3 (500 MHz). Boxes: norbornene olefinic moiety (solid); poly(norbornene) olefinic backbone (dashed).	240
Figure S5.43. Representative stacked ^1H NMR spectra of the ROMP of xNb2M27 (entry 5.24) in CD_2Cl_2 (500 MHz) and the ^1H NMR spectrum of the corresponding monomer in CDCl_3 (500 MHz). Boxes: norbornene olefinic moiety (solid); poly(norbornene) olefinic backbone (dashed).	241
Figure S5.44. Representative stacked ^1H NMR spectra of the ROMP of xNb2B12 (entry 5.25) and the ^1H NMR spectrum of the corresponding monomer in CD_2Cl_2 (500 MHz). Boxes: norbornene olefinic moiety (solid); poly(norbornene) olefinic backbone (dashed).	241
Figure S5.45. Representative stacked ^1H NMR spectra of the ROMP of xNb2S20 (entry 5.26) and the ^1H NMR spectrum of the corresponding monomer in CD_2Cl_2 (500 MHz). Boxes: norbornene olefinic moiety (solid); poly(norbornene) olefinic backbone (dashed).	242
Figure S5.46. Representative stacked ^1H NMR spectra of the ROMP of xNb2M12 (entry 5.27) in THF-d_8 (500 MHz) and the ^1H NMR spectrum of the corresponding monomer in CDCl_3 (500 MHz). Boxes: norbornene olefinic moiety (solid); poly(norbornene) olefinic backbone (dashed).	242
Figure S5.47. ^1H NMR spectrum of xNbHex	243
Figure S5.48. ^{13}C NMR spectrum of xNbHex	244

- Figure S5.49.** Stacked ^1H NMR spectra of the homopolymer and the diblock of entry 5.28 after quenching with EVE in CDCl_3 (400 MHz) and the ^1H NMR spectrum of the corresponding monomer in CDCl_3 (500 MHz). Boxes: norbornene olefinic moiety (solid); poly(norbornene) olefinic backbone (dashed). 245
- Figure S5.50.** Stacked ^1H NMR spectra of the homopolymer and failed re-initiation of entry 5.29 after quenching with EVE in CDCl_3 (400 MHz) and the ^1H NMR spectrum of the corresponding monomer in CDCl_3 (500 MHz). Boxes: norbornene olefinic moiety (solid); poly(norbornene) olefinic backbone (dashed). 245
- Figure S5.51.** Stacked ^1H NMR spectra of the homopolymer and the diblock and failed second re-initiation of entry 5.30 after quenching with EVE in CDCl_3 (400 MHz) and the ^1H NMR spectra of the corresponding monomers in CDCl_3 (500 MHz). Boxes: norbornene olefinic moiety (solid); poly(norbornene) olefinic backbone (dashed). 246
- Figure S5.52.** Stacked ^1H NMR spectra of the homopolymer and the diblock and failed second re-initiation of entry 5.31 after quenching with EVE in CDCl_3 (400 MHz) and the ^1H NMR spectra of the corresponding monomers in CDCl_3 (500 MHz). Boxes: norbornene olefinic moiety (solid); poly(norbornene) olefinic backbone (dashed). 246
- Figure S5.53.** Stacked ^1H NMR spectra of the homopolymer and the diblock and failed second re-initiation of entry 5.32 after quenching with EVE in CDCl_3 (400 MHz) and the ^1H NMR spectra of the corresponding monomers in CDCl_3 (500 MHz). Boxes: norbornene olefinic moiety (solid); poly(norbornene) olefinic backbone (dashed). 247
- Figure S5.54.** Stacked ^1H NMR spectra of the homopolymer and the diblock of entry 5.33 after quenching with EVE in CDCl_3 (400 MHz) and the ^1H NMR spectra of the corresponding monomer in CDCl_3 (500 MHz). Boxes: norbornene olefinic moiety (solid); poly(norbornene) olefinic backbone (dashed). 247
- Figure S5.55.** Stacked ^1H NMR spectra of the homopolymer and the diblock of entry 5.34 after quenching with EVE in CDCl_3 (400 MHz) and the ^1H NMR spectra of the corresponding monomers in CDCl_3 (500 MHz). Boxes: norbornene olefinic moiety (solid); poly(norbornene) olefinic backbone (dashed). 248
- Figure S5.56.** Stacked ^1H NMR spectra of the homopolymer and the diblock of entry 5.35 after quenching with EVE and the ^1H NMR spectra of the corresponding monomer in CDCl_3 (400 MHz). Boxes: norbornene olefinic moiety (solid); poly(norbornene) olefinic backbone (dashed). 248

Figure S5.57. Stacked ^1H NMR spectra of the homopolymer, di-, and triblock of entry 5.36 after quenching with EVE in CDCl_3 (400 MHz) and the ^1H NMR spectra of the corresponding monomers in CDCl_3 (xNbHex : 500 MHz; xNb6M13 : 400 MHz). Boxes: norbornene olefinic moiety (solid); poly(norbornene) olefinic backbone (dashed).....	249
Figure S5.58. Stacked ^1H NMR spectra of the homopolymer and the diblock of entry 5.37 after quenching with EVE in CDCl_3 (400 MHz) and the ^1H NMR spectra of xNb2M12 in CDCl_3 (500 MHz) and xNb2B12 in CD_2Cl_2 (500 MHz). Boxes: norbornene olefinic moiety (solid); poly(norbornene) olefinic backbone (dashed).....	249
Figure S5.59. Stacked ^1H NMR spectra of the homopolymer and the diblock of entry 5.38 after quenching with EVE in CDCl_3 (400 MHz) and the ^1H NMR spectra of xNb2M12 in CDCl_3 (500 MHz) and xNb2B12 in CD_2Cl_2 (500 MHz). Boxes: norbornene olefinic moiety (solid); poly(norbornene) olefinic backbone (dashed).....	250
Figure S5.60. Stacked ^1H NMR spectra of the homopolymer and the diblock of entry 5.39 after quenching with EVE in CDCl_3 (400 MHz) and the ^1H NMR spectra of xNb2M12 in CDCl_3 (500 MHz) and xNb2B12 in CD_2Cl_2 (500 MHz). Boxes: norbornene olefinic moiety (solid); poly(norbornene) olefinic backbone (dashed).....	251
Figure S5.61. ^1H NMR spectrum of xNbOH in CDCl_3	252
Figure S5.62. ^{13}C NMR spectrum of xNbOH	252
Figure S5.63. ^1H NMR spectrum of xNbHNCHO	253
Figure S5.64. ^{13}C NMR spectrum of xNbHNCHO	254
Figure S5.65. ^1H NMR spectrum of xNbNC	255
Figure S5.66. ^{13}C NMR spectrum of xNbNC	256
Figure S5.67. ^1H NMR spectrum of xNbBrTMS	257
Figure S5.68. ^{13}C NMR spectrum of xNbBrTMS	257
Figure S5.69. ^1H NMR spectrum of xNbBrH	258
Figure S5.70. ^{13}C NMR spectrum of xNbBrH	259
Figure S5.71. ^1H NMR spectrum of PS-Br in CD_2Cl_2 (400 MHz).....	260
Figure S5.72. ^{13}C NMR spectrum of PS-Br in CD_2Cl_2 (100 MHz).....	261
Figure S5.73. (A) MALDI-TOF spectrum (dithranol, NaTFA) of PS-Br with highlighted mass distribution in color to guide the eye, (B) selected region of the spectrum (3520 – 3840 m/z) with peak color coded as per the identified species, and (C) structure of PS-Br species (S1) and its calculated and measured monoisotopic masses.....	261

Figure S5.74. Comparison between measured and calculated isotopic patterns of PS-Br determined <i>via</i> MALDI-TOF MS (Figure S5.73) with the olefin-terminated species (S1).....	262
Figure S5.75. ^1H NMR spectrum of PS-N₃ in CD_2Cl_2 (400 MHz).....	263
Figure S5.76. ^{13}C NMR spectrum of PS-N₃ in CD_2Cl_2 (100 MHz).....	263
Figure S5.77. ^1H NMR spectrum of the impure xNbBr-PS in CDCl_3 (400 MHz).....	264
Figure S5.78. ^{13}C NMR spectrum of the impure xNbBr-PS in CDCl_3 (100 MHz).....	264
Figure S5.79. Stacked ^1H NMR spectra of the different filtrates obtained during the purification process and the purified bifunctional macromonomer xNb-PMMA-PS in CDCl_3 (400 MHz). Boxes: aromatic signals of PS (solid); methoxy signals of PMMA (dashed).....	265
Figure S5.80. ^1H NMR spectrum of xNbPMMA-PS in CDCl_3 (400 MHz).....	266
Figure S5.81. ^{13}C NMR spectrum of xNbPMMA-PS in CDCl_3 (126 MHz).	266
Figure S5.82. Representative ^1H NMR spectrum of a Janus graft copolymers (Janus10) in CD_2Cl_2 (500 MHz).	267
Figure S5.83. Stacked ^1H NMR spectra of the bifunctional macromonomer xNb-PMMA-PS in CDCl_3 (400 MHz) and the obtained polymers Janus10 , Janus20 and Janus30 in CD_2Cl_2 (500 MHz). Box: norbornene olefinic moiety.....	267
Figure S5.84. Stacked ^{13}C NMR spectra of the bifunctional macromonomer xNb-PMMA-PS and the obtained polymers Janus10 , Janus20 and Janus30 in CD_2Cl_2 (500 MHz). Box: norbornene olefinic moiety.	268
Figure S6.1. ^1H NMR spectrum of nNbHex	269
Figure S6.2. ^{13}C NMR spectrum of nNbHex	269
Figure S6.3. ^1H NMR spectrum of entry 6.1 in CD_2Cl_2 (500 MHz). Note: Deuterated solvent was contaminated with traces of DMSO.....	271
Figure S6.4. ^{13}C NMR spectrum of entry 6.1 in CD_2Cl_2 (126 MHz).	271
Figure S6.5. ^1H NMR spectrum of entry 6.2 in CD_2Cl_2 (500 MHz).	272
Figure S6.6. ^{13}C NMR spectrum of entry 6.2 in CD_2Cl_2 (126 MHz).	272
Figure S6.7. ^1H NMR spectrum of entry 6.3 in CD_2Cl_2 (500 MHz). Note: Deuterated solvent was contaminated with traces of DMSO.....	273
Figure S6.8. ^{13}C NMR spectrum of entry 6.3 in CD_2Cl_2 (126 MHz).	273

Figure S6.9. Stacked ^1H NMR spectra of entry 6.4 after quenching with EVE in CDCl_3 (400 MHz) and the ^1H NMR spectrum of the corresponding monomer in CDCl_3 (500 MHz). Boxes: norbornene olefinic moiety (solid); poly(norbornene) olefinic backbone (dashed).	274
Figure S6.10. Representative stacked ^1H NMR spectra of entry 6.5 before (bottom) and after (middle) the addition of xNb2M12 , and after its complete conversion (top) in CD_2Cl_2 (500 MHz). Boxes: <i>endo</i> norbornene olefin (solid); poly(norbornene) olefin (dashed); <i>exo</i> norbornene olefin (dotted); methoxy groups (dash-dotted).	275
Figure S6.11. ^1H NMR spectrum of entry 6.5 in CD_2Cl_2 (500 MHz).	275
Figure S6.12. ^{13}C NMR spectrum of entry 6.5 in CD_2Cl_2 (126 MHz).	276
Figure S6.13. Representative stacked ^1H NMR spectra of entry 6.6 before (bottom) and after (middle) the addition of xNb2M12 , and after its complete conversion (top) in CD_2Cl_2 (500 MHz). Boxes: <i>endo</i> norbornene olefin (solid); poly(norbornene) olefin (dashed); <i>exo</i> norbornene olefin (dotted); methoxy groups (dash-dotted).	276
Figure S6.14. (A) Kinetic plots of entries 6.1 (Table 6.1) and 6.6 (Table 6.2), (B) highlighting xNb2M12 during copolymerization, (C) molar fraction (x_i) of xNb2M12 in entry 6.6 as a function of polymerization time, based on ^1H NMR spectroscopy data (Figure S6.13), and (D) SEC traces of entry 6.6 before xNb2M12 addition and after xNb2M12 conversion. Line represents linear fit.	277
Figure S6.15. ^1H NMR spectrum of entry 6.6 in CD_2Cl_2 (500 MHz).	277
Figure S6.16. ^{13}C NMR spectrum of entry 6.6 in CD_2Cl_2 (126 MHz).	278
Figure S6.17. Representative stacked ^1H NMR spectra of entry 6.7 before (bottom) and after (middle) the addition of xNb2M12 , and after its complete conversion (top) in CD_2Cl_2 (500 MHz). Boxes: <i>endo</i> norbornene olefin (solid); poly(norbornene) olefin (dashed); <i>exo</i> norbornene olefin (dotted); methoxy groups (dash-dotted).	278
Figure S6.18. (A) Kinetic plots of entries 6.1 (Table 6.1) and 6.7 (Table 6.2), (B) highlighting xNb2M12 during copolymerization, (C) molar fraction (x_i) of xNb2M12 in entry 6.7 as a function of polymerization time, based on ^1H NMR spectroscopy data (Figure S6.17), and (D) SEC traces of entry 6.7 before xNb2M12 addition and after xNb2M12 conversion. Line represents linear fit.	279
Figure S6.19. ^1H NMR spectrum of entry 6.7 in CD_2Cl_2 (500 MHz).	279
Figure S6.20. ^{13}C NMR spectrum of entry 6.7 in CD_2Cl_2 (126 MHz).	280

Figure S6.21. Representative stacked ^1H NMR spectra of entry 6.8 before (bottom) and after (middle) the addition of xNb2M12 , and after its complete conversion (top) in CD_2Cl_2 (500 MHz). Boxes: <i>endo</i> norbornene olefin (solid); poly(norbornene) olefin (dashed); <i>exo</i> norbornene olefin (dotted); methoxy groups (dash-dotted).	280
Figure S6.22. (A) Kinetic plots of entries 6.1 (Table 6.1) and 6.8 (Table 6.2), (B) highlighting xNb2M12 during copolymerization, (C) molar fraction (x_i) of xNb2M12 in entry 6.8 as a function of polymerization time, based on ^1H NMR spectroscopy data (Figure S6.21), and (D) SEC traces of entry 6.8 before xNb2M12 addition and after xNb2M12 conversion. Line represents linear fit.....	281
Figure S6.23. ^1H NMR spectrum of entry 6.8 in CD_2Cl_2 (500 MHz).	281
Figure S6.24. ^{13}C NMR spectrum of entry 6.8 in CD_2Cl_2 (126 MHz).	282
Figure S6.25. Representative stacked ^1H NMR spectra of entry 6.9 before (bottom) and after (middle) the addition of xNb6M13 , and after its complete conversion (top) in CD_2Cl_2 (500 MHz). Boxes: <i>endo</i> norbornene olefin (solid); poly(norbornene) olefin (dashed); <i>exo</i> norbornene olefin (dotted); methoxy groups (dash-dotted).	282
Figure S6.26. (A) Kinetic plots of entries 6.1 (Table 6.1) and 6.9 (Table 6.2), (B) highlighting xNb6M13 during copolymerization, (C) molar fraction (x_i) of xNb6M13 in entry 6.9 as a function of polymerization time, based on ^1H NMR spectroscopy data (Figure S6.25), and (D) SEC traces of entry 6.9 before xNb6M13 addition and after xNb6M13 conversion. Line represents linear fit.....	283
Figure S6.27. ^1H NMR spectrum of entry 6.9 in CD_2Cl_2 (500 MHz).	283
Figure S6.28. ^{13}C NMR spectrum of entry 6.9 in CD_2Cl_2 (126 MHz).	284
Figure S6.29. Representative stacked ^1H NMR spectra of entry 6.10 before (bottom) and after (middle) the addition of xNb6M13 , and after its complete conversion (top) in CD_2Cl_2 (500 MHz). Boxes: <i>endo</i> norbornene olefin (solid); poly(norbornene) olefin (dashed); <i>exo</i> norbornene olefin (dotted); methoxy groups (dash-dotted).	284
Figure S6.30. (A) Kinetic plots of entries 6.1 (Table 6.1) and 6.10 (Table 6.2), (B) highlighting xNb6M13 during copolymerization, (C) molar fraction (x_i) of xNb6M13 in entry 6.10 as a function of polymerization time, based on ^1H NMR spectroscopy data (Figure S6.29), and (D) SEC traces of entry 6.10 before xNb6M13 addition and after xNb6M13 conversion. Line represents linear fit.....	285
Figure S6.31. ^1H NMR spectrum of entry 6.10 in CD_2Cl_2 (500 MHz).	285

Figure S6.32. ^{13}C NMR spectrum of entry 6.10 in CD_2Cl_2 (126 MHz).	286
Figure S6.33. Representative stacked ^1H NMR spectra of entry 6.11 before (bottom) and after (middle) the addition of xNb6M13 , and after its complete conversion (top) in CD_2Cl_2 (500 MHz). Boxes: <i>endo</i> norbornene olefin (solid); poly(norbornene) olefin (dashed); <i>exo</i> norbornene olefin (dotted); methoxy groups (dash-dotted).	286
Figure S6.34. (A) Kinetic plots of entries 6.1 (Table 6.1) and 6.11 (Table 6.2), (B) highlighting xNb6M13 during copolymerization, (C) molar fraction (x_i) of xNb6M13 in entry 6.11 as a function of polymerization time, based on ^1H NMR spectroscopy data (Figure S6.33), and (D) SEC traces of entry 6.11 before xNb6M13 addition and after xNb6M13 conversion. Line represents linear fit.....	287
Figure S6.35. ^1H NMR spectrum of entry 6.11 in CD_2Cl_2 (500 MHz).	287
Figure S6.36. ^{13}C NMR spectrum of entry 6.11 in CD_2Cl_2 (126 MHz).	288
Figure S6.37. Representative stacked ^1H NMR spectra of entry 6.12 before (bottom) and after (middle) the addition of xNb6M13 , and after its complete conversion (top) in CD_2Cl_2 (500 MHz). Boxes: <i>endo</i> norbornene olefin (solid); poly(norbornene) olefin (dashed); <i>exo</i> norbornene olefin (dotted); methoxy groups (dash-dotted).	288
Figure S6.38. (A) Kinetic plots of entries 6.1 (Table 6.1) and 6.12 (Table 6.2), (B) highlighting xNb6M13 during copolymerization, (C) molar fraction (x_i) of xNb6M13 in entry 6.12 as a function of polymerization time, based on ^1H NMR spectroscopy data (Figure S6.37), and (D) SEC traces of entry 6.12 before xNb6M13 addition and after xNb6M13 conversion. Line represents linear fit.....	289
Figure S6.39. ^1H NMR spectrum of entry 6.12 in CD_2Cl_2 (500 MHz).	289
Figure S6.40. ^{13}C NMR spectrum of entry 6.12 in CD_2Cl_2 (126 MHz).	290
Figure S6.41. Representative stacked ^1H NMR spectra of entry 6.13 before (bottom) and after (middle) the addition of xNb6M17 , and after its complete conversion (top) in CD_2Cl_2 (500 MHz). Boxes: <i>endo</i> norbornene olefin (solid); poly(norbornene) olefin (dashed); <i>exo</i> norbornene olefin (dotted); methoxy groups (dash-dotted).	290
Figure S6.42. (A) Kinetic plots of entries 6.1 (Table 6.1) and 6.13 (Table 6.2), (B) highlighting xNb6M17 during copolymerization, (C) molar fraction (x_i) of xNb6M17 in entry 6.13 as a function of polymerization time, based on ^1H NMR spectroscopy data (Figure S6.41), and (D) SEC traces of entry 6.13 before xNb6M17 addition and after xNb6M17 conversion. Line represents linear fit.....	291

Figure S6.43. ^1H NMR spectrum of entry 6.13 in CD_2Cl_2 (500 MHz).	291
Figure S6.44. ^{13}C NMR spectrum of entry 6.13 in CD_2Cl_2 (126 MHz).	292
Figure S6.45. Representative stacked ^1H NMR spectra of entry 6.14 before (bottom) and after (middle) the addition of xNb6M17 , and after its complete conversion (top) in CD_2Cl_2 (500 MHz). Boxes: <i>endo</i> norbornene olefin (solid); poly(norbornene) olefin (dashed); <i>exo</i> norbornene olefin (dotted); methoxy groups (dash-dotted).	292
Figure S6.46. (A) Kinetic plots of entries 6.1 (Table 6.1) and 6.14 (Table 6.2), (B) highlighting xNb6M17 during copolymerization, (C) molar fraction (x_i) of xNb6M17 in entry 6.14 as a function of polymerization time, based on ^1H NMR spectroscopy data (Figure S6.45), and (D) SEC traces of entry 6.14 before xNb6M17 addition and after xNb6M17 conversion. Line represents linear fit.....	293
Figure S6.47. ^1H NMR spectrum of entry 6.14 in CD_2Cl_2 (500 MHz).	293
Figure S6.48. ^{13}C NMR spectrum of entry 6.14 in CD_2Cl_2 (126 MHz).	294
Figure S6.49. Representative stacked ^1H NMR spectra of entry 6.15 before (bottom) and after (middle) the addition of xNb6M17 , and after its complete conversion (top) in CD_2Cl_2 (500 MHz). Boxes: <i>endo</i> norbornene olefin (solid); poly(norbornene) olefin (dashed); <i>exo</i> norbornene olefin (dotted); methoxy groups (dash-dotted).	294
Figure S6.50. (A) Kinetic plots of entries 6.1 (Table 6.1) and 6.15 (Table 6.2), (B) highlighting xNb6M17 during copolymerization, (C) molar fraction (x_i) of xNb6M17 in entry 6.15 as a function of polymerization time, based on ^1H NMR spectroscopy data (Figure S6.49), and (D) SEC traces of entry 6.15 before xNb6M17 addition and after xNb6M17 conversion. Line represents linear fit.....	295
Figure S6.51. ^1H NMR spectrum of entry 6.15 in CD_2Cl_2 (500 MHz).	295
Figure S6.52. ^{13}C NMR spectrum of entry 6.15 in CD_2Cl_2 (126 MHz).	296
Figure S6.53. Representative stacked ^1H NMR spectra of entry 6.16 before (bottom) and after (middle) the addition of xNb6M17 , and after its complete conversion (top) in CD_2Cl_2 (500 MHz). Boxes: <i>endo</i> norbornene olefin (solid); poly(norbornene) olefin (dashed); <i>exo</i> norbornene olefin (dotted); methoxy groups (dash-dotted).	296
Figure S6.54. (A) Kinetic plots of entries 6.1 (Table 6.1) and 6.16 (Table 6.2), (B) highlighting xNb6M17 during copolymerization, (C) molar fraction (x_i) of xNb6M17 in entry 6.16 as a function of polymerization time, based on ^1H NMR spectroscopy data (Figure S6.53), and (D)	

SEC traces of entry 6.16 before xNb6M17 addition and after xNb6M17 conversion. Line represents linear fit.....	297
Figure S6.55. ^1H NMR spectrum of entry 6.16 in CD_2Cl_2 (500 MHz).	297
Figure S6.56. ^1H NMR spectrum of entry 6.16 in CD_2Cl_2 (126 MHz).	298
Figure S6.57. Representative stacked ^1H NMR spectra of entry 6.17 before (bottom) and after (middle) the addition of xNb6M17 , and after its complete conversion (top) in CD_2Cl_2 (500 MHz). Boxes: <i>endo</i> norbornene olefin (solid); poly(norbornene) olefin (dashed); <i>exo</i> norbornene olefin (dotted); methoxy groups (dash-dotted).	298
Figure S6.58. (A) Kinetic plots of entries 6.2 (Table 6.1) and 6.17 (Table 6.3), (B) highlighting xNb6M17 during copolymerization, (C) molar fraction (x_i) of xNb6M17 in entry 6.17 as a function of polymerization time, based on ^1H NMR spectroscopy data (Figure S6.57), and (D) SEC traces of entry 6.17 before xNb6M17 addition and after xNb6M17 conversion. Line represents linear fit.....	299
Figure S6.59. ^1H NMR spectrum of entry 6.17 in CD_2Cl_2 (500 MHz).	299
Figure S6.60. ^{13}C NMR spectrum of entry 6.17 in CD_2Cl_2 (126 MHz).	300
Figure S6.61. Representative stacked ^1H NMR spectra of entry 6.18 before (bottom) and after (middle) the addition of xNb6M17 , and after its complete conversion (top) in CD_2Cl_2 (500 MHz). Boxes: <i>endo</i> norbornene olefin (solid); poly(norbornene) olefin (dashed); <i>exo</i> norbornene olefin (dotted); methoxy groups (dash-dotted).	300
Figure S6.62. (A) Kinetic plots of entries 6.3 (Table 6.1) and 6.18 (Table 6.3), (B) highlighting xNb6M17 during copolymerization, (C) molar fraction (x_i) of xNb6M17 in entry 6.18 as a function of polymerization time, based on ^1H NMR spectroscopy data (Figure S6.61), and (D) SEC traces of entry 6.18 before xNb6M17 addition and after xNb6M17 conversion. Line represents linear fit.....	301
Figure S6.63. ^1H NMR spectrum of entry 6.18 in CD_2Cl_2 (500 MHz).	301
Figure S6.64. ^{13}C NMR spectrum of entry 6.18 in CD_2Cl_2 (126 MHz).	302
Figure S6.65. Representative stacked ^1H NMR spectra of entry 6.19 (diblock) before and after the additions of xNb6M17 , and after their complete conversions in CD_2Cl_2 (500 MHz). Boxes: <i>endo</i> norbornene olefin (solid); poly(norbornene) olefin (dashed); <i>exo</i> norbornene olefin (dotted); methoxy groups (dash-dotted).	302
Figure S6.66. ^1H NMR spectrum of xNbBr	303
Figure S6.67. ^{13}C NMR spectrum of xNbBr	304

Figure S6.68. ^1H NMR spectrum of xNbM27 in CDCl_3 (500 MHz).....	305
Figure S6.69. ^{13}C NMR spectrum of xNbM27 in CDCl_3 (126 MHz).....	305
Figure S6.70. (A) MALDI-TOF spectrum (DCTB, NaTFA) of xNbM27 with highlighted mass distributions in color to guide the eye, (B) selected region of the spectrum (1980 – 2290 m/z) with peaks color coded as per the identified species, and (C) structures of xNbM27 species (S1 – S2) and their calculated and measured monoisotopic masses.	306
Figure S6.71. Comparison between measured and calculated isotopic patterns of xNbM27 determined <i>via</i> MALDI-TOF MS (Figure S6.70) with (A) the chloride-terminated species (S1), and (B) the hydrogen-terminated species (S2).	306
Figure S6.72. ^1H NMR spectrum of xNbB17 in CD_2Cl_2 (500 MHz).....	307
Figure S6.73. ^{13}C NMR spectrum of xNbB17 in CD_2Cl_2 (126 MHz).....	307
Figure S6.74. (A) MALDI-TOF spectrum (DCTB, NaTFA) of xNbB17 with highlighted mass distributions in color to guide the eye, (B) selected region of the spectrum (2210 – 2760 m/z) with peaks color coded as per the identified species, and (C) structures of xNbB17 species (S1 – S2) and their calculated and measured monoisotopic masses.	308
Figure S6.75. Comparison between measured and calculated isotopic patterns of xNbB17 determined <i>via</i> MALDI-TOF MS (Figure S6.74) with (A) the chloride-terminated species (S1), and (B) the double charged dinorbornene species (S2).....	308
Figure S6.76. DSC traces of (A) xNbM27 , xNbB17 and the respective 1:1 polymer blend..	309
Figure S6.77. ^1H NMR spectrum of entry 6.19 in CD_2Cl_2 (500 MHz) and corresponding chemical structure.....	309
Figure S6.78. ^{13}C NMR spectrum of entry 6.19 in CD_2Cl_2 (126 MHz).	310
Figure S6.79. Representative stacked ^1H NMR spectra of entry 6.20 (diblock) before and after the additions of xNbM27 and xNbB12 , and after their complete conversions in CD_2Cl_2 (500 MHz). Boxes: <i>exo</i> and <i>endo</i> norbornene olefin (solid); poly(norbornene) olefin (dashed); benzyl groups (dotted); methoxy groups (dash-dotted).....	310
Figure S6.80. ^1H NMR spectrum of entry 6.20 in CD_2Cl_2 (500 MHz) and corresponding chemical structure.....	311
Figure S6.81. ^{13}C NMR spectrum of entry 6.20 in CD_2Cl_2 (126 MHz).	311
Figure S6.82. Representative stacked ^1H NMR spectra of entry 6.21 (diblock) before and after the additions of xNbM27 and xNbB12 , and after their complete conversions in CD_2Cl_2	

(500 MHz). Boxes: *exo* and *endo* norbornene olefin (solid); poly(norbornene) olefin (dashed); benzyl groups (dotted); methoxy groups (dash-dotted)..... 312

Figure S6.83. ¹H NMR spectrum of entry 6.21 in CD₂Cl₂ (500 MHz) and corresponding chemical structure..... 313

Figure S6.84. ¹³C NMR spectrum of entry 6.21 in CD₂Cl₂ (126 MHz) 313

Figure S6.85. Representative stacked ¹H NMR spectra of entry 6.22 (triblock) before and after the additions of **xNbM27** (2x) and **xNbB12** (1x), and after their complete conversions in CD₂Cl₂ (500 MHz). Boxes: *exo* and *endo* norbornene olefin (solid); poly(norbornene) olefin (dashed); benzyl groups (dotted); methoxy groups (dash-dotted)..... 314

Figure S6.86. ¹H NMR spectrum of entry 6.22 in CD₂Cl₂ (500 MHz) and corresponding chemical structure..... 315

Figure S6.87. ¹³C NMR spectrum of entry 6.22 in CD₂Cl₂ (126 MHz). 315

10.3 List of schemes

Scheme 2.1. Representative Hantzsch synthesis of 1,4-dihydropyridines (1,4-DHPs) and subsequent oxidation yielding 1,4-disubstituted pyridines.^{115,116} 6

Scheme 2.2. Synthesis of 3,4-dihydropyrimidine-2(1H)-one from urea, benzaldehyde, and ethyl acetoacetate *via* the Biginelli reaction.^{126,127} 7

Scheme 2.3. Resonance structures of isocyanides: zwitterionic (left) and carbenoid (right).¹³⁷ 8

Scheme 2.4. Representative isocyanide synthesis strategies.^{136,141,142,145} 8

Scheme 2.5. Representative applications of isocyanides in organic syntheses.¹⁴⁷⁻¹⁴⁹ 9

Scheme 2.6. U-4CR and commonly accepted mechanism involving a carboxylic acid, a primary amine, an aldehyde, and an isocyanide.¹⁶⁰⁻¹⁶² 10

Scheme 2.7. Representative U-4CR variations: Ugi-Diels-Alder and Ugi-Smiles.^{164,165} 11

Scheme 2.8. Possible application areas of the U-4CR: medical and polymer chemistry.^{170,171} 11

Scheme 2.9. P-3CR involving a carboxylic acid, an aldehyde, and an isocyanide, and non-ionic reaction mechanism in aprotic solvents postulated by I. Ugi.^{162,177,178} 12

Scheme 2.10. Representative P-3CR variations: replacement of the carboxylic acid by an alcohol to obtain α -alkoxy amides and by hydrazoic acid to obtain 5-(1-hydroxyalkyl)tetrazoles. ^{181,182}	13
Scheme 2.11. Possible application areas of the P-3CR: medical and polymer chemistry and the synthesis of sequence-defined macromolecules. ^{170,187,188}	14
Scheme 2.12. Chemical structure of the azide anion (left), ²⁰¹ representative inorganic azide compounds (middle), ²⁰² and representative azidation of organic compounds by nucleophilic substitution using sodium azide and the resonance structure of the obtained organic azide (right). ²⁰³	15
Scheme 2.13. Different reactions of organic azides. Reprinted with permission (https://chemistry-europe.onlinelibrary.wiley.com/doi/full/10.1002/ejoc.201601390). ²²⁰ .	16
Scheme 2.14. Representative copper(I)-mediated azide-alkyne cycloaddition (CuAAC) yielding 1,3-disubstituted 1,2,3-triazoles, and mononuclear mechanism proposed by Sharpless <i>et al.</i> ²²⁸	17
Scheme 2.15. Representative step-growth polymerizations. ²⁴⁶⁻²⁴⁸	20
Scheme 2.16. Representative chain-growth polymerization techniques. ²⁵⁹⁻²⁶³	21
Scheme 2.17. Reaction mechanism of copper-mediated ATRP with termination <i>via</i> (A) combination, (B) disproportionation, and (C) chain transfer. ³⁰²	23
Scheme 2.18. ROMP mechanism based on the related olefin metathesis mechanism proposed by Chauvin, ^{17,348} with metal alkylidene (1) and metallacyclobutane intermediate (2).	28
Scheme 2. 19. Commonly used Ru-, Mo-, and W-based ROMP catalysts. ³⁶²	30
Scheme 2.20. (A) Relationship between the commonly used Grubbs catalysts and (B) initiation phase using the G1 or the G2 catalyst with kinetic constants k_1 , k_{-1} , k_2 , k_{-2} , k_3 and k_{-3} . ^{17,374} .	31
Scheme 4.1. Synthesis of norbornene-functional carboxylic acids xNb1 , xNb10 , nNb1 and nNb10 <i>via</i> condensation of <i>exo</i> and <i>endo</i> norbornene anhydride with glycine and 11-aminoundecanoic acid.	41
Scheme 4.2. P-3CRs using norbornene-functional carboxylic acids xNb1 , xNb10 , nNb1 , and nNb10 , pentyl- and adamantyl isocyanide, and propyl- and pyrenyl aldehyde, forming the <i>exo</i> norbornene bifunctional monomers xNb1PePr , xNb10PePr , xNb1AdPy , and xNb10AdPy , and their <i>endo</i> counterparts nNb1PePr , nNb10PePr , nNb1AdPy , and nNb10AdPy (Table 4.1).	42

Scheme 4.3. ROMP of the <i>exo</i> norbornenes xNb1PePr , xNb10PePr , xNb1AdPy and xNb10AdPy (left) and the <i>endo</i> norbornenes nNb1PePr , nNb10PePr , nNb1AdPy and nNb10AdPy (right) using the G1 catalyst (Table 4.2).....	44
Scheme 5.1. Synthesis of (A) hydroxylated <i>exo</i> norbornenes xNb2OH and xNb6OH <i>via</i> condensation of <i>exo</i> norbornene anhydride with 2-aminoethanol and 6-aminohexanol, and (B) subsequent esterification using α -bromoisobutyryl bromide, obtaining xNb2Br and xNb6Br	63
Scheme 5.2. Synthesis of <i>exo</i> norbornene–functional macromonomers <i>via</i> ATRP using xNb2Br and xNb6Br as ATRP initiators and benzyl methacrylate (BnMA, top), methyl methacrylate (MMA, middle) and styrene (St, bottom) as monomers.....	64
Scheme 5.3. (A) Grubbs-type catalysts used in the ROMP of macromonomers and (B) schematic ROMP of PMMA-based macromonomers.	75
Scheme 5.4. Oxygen-induced poisoning of the G1 catalyst.....	82
Scheme 5.5. Synthesis of the G3 catalyst by reacting the G2 catalyst with an excess of pyridine.	87
Scheme 5.6. Schematic of the iterative ROMP procedure to obtain sequence-controlled graft copolymers, exhibiting a block-like structure (M: metal, L: ligand, B1: first block, B2: second block).....	96
Scheme 5.7. Synthesis of the <i>exo</i> norbornene monomer xNbHex <i>via</i> condensation of <i>exo</i> norbornene anhydride with 1-aminohexane.	96
Scheme 5.8. Synthesis of (A) xNbOH <i>via</i> reduction of <i>exo</i> norbornene carboxylic acid using LiAlH_4 , (B) Steglich esterification using 11-formamidoundecanoic acid, obtaining xNbHNCHO , and (C) subsequent dehydration reaction using <i>p</i> -TsCl, obtaining the <i>exo</i> norbornene–functional isocyanide xNbNC	114
Scheme 5.9. Synthesis of <i>exo</i> norbornene derivative xNbBrTMS comprising a TMS-protected alkyne and an ATRP initiator unit <i>via</i> P-3CR.....	115
Scheme 5.10. TMS-deprotection using TBAF at low temperature, obtaining the <i>exo</i> norbornene derivative xNbBrH comprising a terminal alkyne and an ATRP initiator unit.	116
Scheme 5.11. Synthesis of (A) PS-Br <i>via</i> Cu(I)-mediated ATRP of styrene, and (B) subsequent azidation using NaN_3 , obtaining PS-N₃	117

Scheme 5.12. Synthesis of xNbBr-PS <i>via</i> CuAAC using PS-N₃ as azide and xNbBrH as alkyne.	120
Scheme 5.13. Synthesis of the bifunctional macromonomer xNb-PMMA-PS <i>via</i> ATRP using xNbBr-PS as macroinitiator and MMA as monomer.....	123
Scheme 5.14. Synthesis of Janus copolymers <i>via</i> the G3-mediated ROMP of xNb-PMMA-PS	126
Scheme 6.1. Synthesis of the <i>endo</i> norbornene monomer nNbHex <i>via</i> condensation reaction of <i>endo</i> norbornene anhydride with 1-aminohexane.....	131
Scheme 6.2. Synthesis of (A) xNbOH <i>via</i> reduction of <i>exo</i> norbornene carboxylic acid using LiAlH ₄ , and (B) subsequent esterification using α -bromoisobutyryl bromide, obtaining xNbBr	144
Scheme 6.3. Synthesis of <i>exo</i> norbornene ester-functional macromonomers <i>via</i> ATRP using xNbBr as ATRP initiator and benzyl methacrylate (BnMA, top) and methyl methacrylate (MMA, bottom) as monomers.	145

10.4 List of tables

Table 4.1. Bifunctional norbornene-based monomers obtained <i>via</i> the P-3CR.	43
Table 4.2. Homopolymers synthesized <i>via</i> the G1-mediated ROMP of bifunctional <i>exo</i> and <i>endo</i> norbornene-based monomers.	47
Table 4.3. Summary of kinetic analyses of the homopolymerizations and the copolymerizations of the bifunctional monomers.....	52
Table 5.1. Synthesized <i>exo</i> norbornene dicarboximide-based macromonomers <i>via</i> ATRP..	65
Table 5.2. ROMPs using PMMA-based macromonomers with different molecular weights.	76
Table 5.3. ROMPs with different catalyst concentrations using xNb2M12 as macromonomer.	79
Table 5.4. ROMPs of xNb2M12 as macromonomer using different solvents.....	80
Table 5.5. ROMP of xNb2M27 using G1 catalyst under Schlenk conditions.....	82

Table 5.6. ROMP of macromonomers using degassed DCM and applying different M:I ratios.	84
Table 5.7. ROMPs of xNb2M12 using the G3 catalyst.	87
Table 5.8. Kinetic measurements of G3-mediated ROMPs using different <i>exo</i> norbornene macromonomers.	89
Table 5.9. Graft polymers synthesized using xNbHex and xNb2M12 as monomers <i>via</i> an iterative ROMP procedure.	97
Table 5.10. Triblock graft copolymers comprising a variable spacer block synthesized applying the iterative ROMP procedure using the G1 catalyst.	99
Table 5.11. Multiblock graft copolymers synthesized applying the iterative ROMP procedure using the G3 catalyst.	103
Table 5.12. Multiblock graft copolymers synthesized applying the iterative ROMP procedure using the G3 catalyst.	106
Table 5.13. The G3-mediated iterative ROMP of PMMA- and PBNMA-based macromonomers using dry solvents and low temperatures.	109
Table 5.14. Summary of synthesized Janus copolymers <i>via</i> the G3-mediated ROMP of xNb-PMMA-PS	126
Table 6.1. Homopolymerizations using nNbHex with different M:I ratios and catalyst concentrations <i>via</i> the G1-mediated ROMP.	132
Table 6.2. Graft copolymers synthesized by ROMP of nNbHex and PMMA-based macromonomers.	137
Table 6.3. Graft copolymers synthesized by ROMP from nNbHex and xNb6M17 , applying different catalyst concentrations and M:I ratios of 100:1.	143
Table 6.4. Synthesized <i>exo</i> norbornene ester-based macromonomers <i>via</i> ATRP.	146
Table 6.5. Diblock graft copolymer synthesized by the G1-mediated ROMP of nNbHex and two consecutive additions of xNb6M17	149
Table 6.6. Multiblock graft copolymers synthesized by the G1-mediated ROMP of nNbHex and delayed macromonomer addition.	152

11 Bibliography

1. Liebig, J.; Playfair, L. P.; Webster, J. W., in *Organic chemistry in its applications to agriculture and physiology*. J. Owen; J. Munroe and company, **1841**.
2. Berthelot, M., in *La révolution chimique; Lavoisier; ouvrage suivi de notices et extraits des registres inédits de laboratoire de Lavoisier*. F. Alcan, **1890**.
3. Hall, L., *J. Am. Chem. Soc.* **1901**, *23*, 438-439.
4. Oxtoby, D. W.; Gillis, H. P.; Butler, L. J., in *Principles of modern chemistry*. Cengage learning, **2015**.
5. Staudinger, H., *Berichte der Dtsch. Chem. Gesellschaft* **1920**, *53*, 1073-1085.
6. Staudinger, H., *Berichte der Dtsch. Chem. Gesellschaft* **1924**, *57*, 1203-1208.
7. Staudinger, H., *Berichte der Dtsch. Chem. Gesellschaft* **1926**, *59*, 3019-3043.
8. Watson, J. D.; Crick, F. H. C., *Nature* **1953**, *171*, 737-738.
9. Donohue, J.; Trueblood, K. N., *J. Mol. Biol.* **1960**, *2*, 363-371.
10. Ambrose, E. J.; Hanby, W. E., *Nature* **1949**, *163*, 483-484.
11. Cohen, P. P.; McGilvery, R., *J. of Biol. Chem.* **1947**, *171*, 121-133.
12. Merrifield, R. B., *J. Am. Chem. Soc.* **1963**, *85*, 2149-2154.
13. Gutekunst, W. R.; Hawker, C. J., *J. Am. Chem. Soc.* **2015**, *137*, 8038-8041.
14. Judzewitsch, P. R.; Nguyen, T. K.; Shanmugam, S.; Wong, E. H.; Boyer, C., *Angew. Chem.* **2018**, *130*, 4649-4654.
15. Rieger, E.; Alkan, A.; Manhart, A.; Wagner, M.; Wurm, F. R., *Macromol. Rapid Commun.* **2016**, *37*, 833-839.
16. Zhang, Z.; Zeng, T.-Y.; Xia, L.; Hong, C.-Y.; Wu, D.-C.; You, Y.-Z., *Nat. Commun.* **2018**, *9*, 2577.
17. Bielawski, C. W.; Grubbs, R. H., *Prog. Polym. Sci.* **2007**, *32*, 1-29.
18. Shieh, P.; Nguyen, H. V. T.; Johnson, J. A., *Nature Chem.* **2019**, *11*, 1124-1132.
19. Choi, W.; Sun, H.; Battistella, C.; Berger, O.; Vratsanos, M. A.; Wang, M. M.; Gianneschi, N. C., *Angew. Chem. Int. Ed.* **2020**, *59*, 19762-19772.
20. P'Poo, S. J.; Schanz, H.-J., *J. Am. Chem. Soc.* **2007**, *129*, 14200-14212.
21. Bang, K. T.; Choi, T. L., *J. Polym. Sci.* **2019**, *58*, 48-51.
22. Benedikter, M. J.; Schowner, R.; Elser, I.; Werner, P.; Herz, K.; Stöhr, L.; Imbrich, D. A.; Nagy, G. M.; Wang, D.; Buchmeiser, M. R., *Macromolecules* **2019**, *52*, 4059-4066.
23. Sun, Z.; Morishita, K.; Nomura, K., *Catalysts* **2018**, *8*.
24. Rule, J. D.; Moore, J. S., *Macromolecules* **2002**, *35*, 7878-7882.
25. Mamedov, E. G.; Klabunovskii, E. I., *Russ. J. Org. Chem.* **2008**, *44*, 1097-1120.
26. Zhang, Z.; Peng, Z.-W.; Hao, M.-F.; Gao, J.-G., *Synlett* **2010**, *2010*, 2895-2898.
27. Dong, Z.-m.; Liu, X.-h.; Tang, X.-l.; Li, Y.-s., *Macromolecules* **2009**, *42*, 4596-4603.
28. Song, B.; Zhang, L.; Yin, H.; Liang, H.; Zhang, J.; Gu, H., *Polym. J.* **2020**, *52*, 1333-1347.
29. Williams, R. J.; Barker, I. A.; O'Reilly, R. K.; Dove, A. P., *ACS Macro Lett.* **2012**, *1*, 1285-1290.
30. Basso, A.; Banfi, L.; Riva, R., *Eur. J. Org. Chem.* **2010**, *2010*, 1831-1841.
31. Robotham, C. V.; Baker, C.; Cuevas, B.; Abboud, K.; Wright, D. L., *Mol. Divers.* **2003**, *6*, 237-44.

32. Sehlinger, A.; Meier, M. A. R., In *Multi-component and sequential reactions in polymer synthesis*, Ed.: Theato, P., Springer, **2015**, 61-86.
33. Solleder, S. C.; Zengel, D.; Wetzels, K. S.; Meier, M. A. R., *Angew. Chem. Int. Ed.* **2016**, *55*, 1204-1207.
34. Holloway, J. O.; Wetzels, K. S.; Martens, S.; Du Prez, F. E.; Meier, M. A. R., *Polym. Chem.* **2019**, *10*, 3859-3867.
35. Kim, S. H.; Tan, J. P. K.; Nederberg, F.; Fukushima, K.; Colson, J.; Yang, C.; Nelson, A.; Yang, Y.-Y.; Hedrick, J. L., *Biomaterials* **2010**, *31*, 8063-8071.
36. Feng, C.; Li, Y.; Yang, D.; Hu, J.; Zhang, X.; Huang, X., *Chem. Soc. Rev.* **2011**, *40*, 1282-1295.
37. Hadjichristidis, N.; Pispas, S.; Pitsikalis, M.; Iatrou, H.; Lohse, D., *Encyclopedia of polymer science and technology* **2002**, 1-38.
38. Pantazis, D.; Chalari, I.; Hadjichristidis, N., *Macromolecules* **2003**, *36*, 3783-3785.
39. Karanam, S.; Goossens; Klumperman, B.; Lemstra, *Macromolecules* **2003**, *36*, 8304-8311.
40. Coessens, V.; Pintauer, T.; Matyjaszewski, K., *Prog. Polym. Sci.* **2001**, *26*, 337-377.
41. Neugebauer, D.; Zhang, Y.; Pakula, T., *J. Polym. Sci. Part A: Polym. Chem.* **2006**, *44*, 1347-1356.
42. Le, A. N.; Liang, R.; Zhong, M., *Chem. Eur. J.* **2019**, *25*, 8177-8189.
43. Higa, M.; Fujino, Y.; Koumoto, T.; Kitani, R.; Egashira, S., *Electrochim. Acta* **2005**, *50*, 3832-3837.
44. Grubbs, R. B.; Hawker, C. J.; Dao, J.; Fréchet, J. M. J., *Angew. Chem. Int. Ed.* **1997**, *36*, 270-272.
45. Pawar, G. M.; Lalancette, R. A.; Bonder, E. M.; Sheridan, J. B.; Jäkle, F., *Macromolecules* **2015**, *48*, 6508-6515.
46. Xie, M.; Kong, Y.; Han, H.; Shi, J.; Ding, L.; Song, C.; Zhang, Y., *React. Funct. Polym.* **2008**, *68*, 1601-1608.
47. Guo, Z. H.; Le, A. N.; Feng, X.; Choo, Y.; Liu, B.; Wang, D.; Wan, Z.; Gu, Y.; Zhao, J.; Li, V.; Osuji, C. O.; Johnson, J. A.; Zhong, M., *Angew. Chem. Int. Ed. Engl.* **2018**, *57*, 8493-8497.
48. Senkum, H.; Gramlich, W. M., *Macromol. Chem. Phys.* **2020**, *221*, 1900476.
49. Yu, Y.-G.; Chae, C.-G.; Kim, M.-J.; Seo, H.-B.; Grubbs, R. H.; Lee, J.-S., *Macromolecules* **2018**, *51*, 447-455.
50. Ahmed, E.; Womble, C. T.; Weck, M., *Macromolecules* **2020**, *53*, 9018-9025.
51. Ji, X.; Zhou, Y.; Li, Q.; Song, H.; Fan, C., *ACS Appl. Mater. Interfaces* **2021**, *13*, 31331-31336.
52. Sun, J.; Fu, Y.; Li, R.; Feng, W., *Chem. Mater.* **2018**, *30*, 1625-1634.
53. Goerlitzer, E. S. A.; Klupp Taylor, R. N.; Vogel, N., *Adv. Mater.* **2018**, *30*, 1706654.
54. Barther, D. A Novel Monomer Strategy to Synthesize Sequence-Defined Oligomers with Variable Polar Repeating Units via the Passerini Three-Component Reaction. Master thesis, KIT, Karlsruhe, **2018**.
55. Merrifield, R. B.; Stewart, J. M.; Jernberg, N., *Anal. Chem.* **1966**, *38*, 1905-1914.
56. Seeburg, P. H.; Shine, J.; Martial, J. A.; Ullrich, A.; Goodman, H. M.; Baxter, J. D., *Trans. Assoc. Am. Physicians* **1977**, *90*, 109-16.
57. Hartmann, L.; Börner, H. G., *Adv. Mater.* **2009**, *21*, 3425-31.
58. Minoda, M.; Sawamoto, M.; Higashimura, T., *Macromolecules* **1990**, *23*, 4890-4895.
59. Börner, H. G.; Schlaad, H., *Soft Matter* **2007**, *3*, 394-408.
60. Fox, H. H.; Lee, J. K.; Park, L. Y.; Schrock, R. R., *Organometallics* **1993**, *12*, 759-768.

61. Kishimoto, Y.; Miyatake, T.; Ikariya, T.; Noyori, R., *Macromolecules* **1996**, *29*, 5054-5055.
62. Hillmyer, M. A.; Laredo, W. R.; Grubbs, R. H., *Macromolecules* **1995**, *28*, 6311-6316.
63. Hong, K.; Uhrig, D.; Mays, J. W., *Curr. Opin. Solid State Mater. Sci.* **1999**, *4*, 531-538.
64. Kishimoto, Y.; Eckerle, P.; Miyatake, T.; Ikariya, T.; Noyori, R., *J. Am. Chem. Soc.* **1994**, *116*, 12131-12132.
65. Lutz, J.-F.; Ouchi, M.; Liu, D. R.; Sawamoto, M., *Science* **2013**, *341*, 1238149.
66. Crick, F. H. C., in *The structure of DNA*. Citeseer, **1957**.
67. Jones, M. E., *Yale J. Biol. Med.* **1953**, *26*, 80-97.
68. Rowan, S. J.; Barner-Kowollik, C.; Klumperman, B.; Gaspard, P.; Grubbs, R. B.; Hillmyer, M. A.; Hutchings, L. R.; Mahanthappa, M. K.; O'Reilly, R. K.; Ouchi, M.; Sawamoto, M.; Lodge, T. P., *ACS Macro Lett.* **2016**, *5*, 1-3.
69. Yokota, K., *Prog. Polym. Sci.* **1999**, *24*, 517-563.
70. Lutz, J.-F., *Macromol. Rapid Commun.* **2017**, *38*, 1700582.
71. Lutz, J.-F., *ACS Macro Lett.* **2014**, *3*, 1020-1023.
72. Lutz, J.-F. o., in *Sequence-controlled polymers : synthesis, self-assembly, and properties*. ACS, **2014**.
73. Stepto, R. F. T., *Pure Appl. Chem.* **2009**, *81*, 351-353.
74. Meier, M. A. R.; Barner-Kowollik, C., *Adv. Mater.* **2019**, *31*, 1806027.
75. Benjamin, P.; Strumph, P.; Kenny, M.; Firshein, W., *Nature* **1982**, *298*, 769-771.
76. Bodanszky, M., in *Principles of peptide synthesis*. Springer, **2012**.
77. Krieg, P. A.; Melton, D. A., In *Methods Enzymol.*, Ed.: Academic Press, **1987**, 397-415.
78. van Hest, J. C. M.; Tirrell, D. A., *Chem. Commun.* **2001**, 1897-1904.
79. Mezo, G., *Amino Acids Pept. Proteins* **2013**, *38*, 203-252.
80. Wang, F.; Zuroske, T.; Watts, J. K., *Nat. Rev. Drug Discov.* **2020**, *19*, 441-442.
81. Wetzelsch, K. S.; Frölich, M.; Solleder, S. C.; Nickisch, R.; Treu, P.; Meier, M. A. R., *Commun. Chem.* **2020**, *3*.
82. Culf, A. S., *Biopolymers* **2019**, *110*, e23285.
83. Zhao, W.; Tropp, J.; Qiao, B.; Pink, M.; Azoulay, J. D.; Flood, A. H., *J. Am. Chem. Soc.* **2020**, *142*, 2579-2591.
84. Nomura, K.; Tsujii, A.; Matsumoto, A., *Macromol. Chem. Phys.* **2017**, *218*, 1700156.
85. Zhang, J.; Matta, M. E.; Hillmyer, M. A., *ACS Macro Lett.* **2012**, *1*, 1383-1387.
86. Berthet, M.-A.; Zarafshani, Z.; Pfeifer, S.; Lutz, J.-F., *Macromolecules* **2010**, *43*, 44-50.
87. Pfeifer, S.; Lutz, J.-F., *J. Am. Chem. Soc.* **2007**, *129*, 9542-9543.
88. Yasir, M.; Liu, P.; Markwart, J. C.; Suraeva, O.; Wurm, F. R.; Smart, J.; Lattuada, M.; Kilbinger, A. F. M., *Angew. Chem. Int. Ed.* **2020**, *59*, 13597-13601.
89. Lutz, J.-F.; Schmidt, B. V. K. J.; Pfeifer, S., *Macromol. Rapid Commun.* **2011**, *32*, 127-135.
90. Satoh, K.; Matsuda, M.; Nagai, K.; Kamigaito, M., *J. Am. Chem. Soc.* **2010**, *132*, 10003-10005.
91. Brooks, P. P.; Natalello, A.; Hall, J. N.; Eccles, E. A. L.; Kimani, S. M.; Bley, K.; Hutchings, L. R., *Macromol. Symp.* **2013**, *323*, 42-50.
92. Hutchings, L. R.; Brooks, P. P.; Parker, D.; Mosely, J. A.; Sevinc, S., *Macromolecules* **2015**, *48*, 610-628.
93. Moatsou, D.; Hansell, C. F.; O'Reilly, R. K., *Chem. Sci.* **2014**, *5*, 2246-2250.
94. Pal, S.; Alizadeh, M.; Kong, P.; Kilbinger, A. F. M., *Chem. Sci.* **2021**, *12*, 6705-6711.

95. Chae, C.-G.; Yu, Y.-G.; Seo, H.-B.; Kim, M.-J.; Kishore, M. Y. L. N.; Lee, J.-S., *Polym. Chem.* **2018**, *9*, 5179-5189.
96. Song, A.; Parker, K. A.; Sampson, N. S., *J. Am. Chem. Soc.* **2009**, *131*, 3444-3445.
97. Boyer, C.; Soeriyadi, A. H.; Zetterlund, P. B.; Whittaker, M. R., *Macromolecules* **2011**, *44*, 8028-8033.
98. Elacqua, E.; Geberth, G. T.; Vanden Bout, D. A.; Weck, M., *Chem. Sci.* **2019**, *10*, 2144-2152.
99. Tong, J.; Shi, Y.; Liu, G.; Huang, T.; Xu, N.; Zhu, Z.; Cai, Y., *Macromol. Rapid Commun.* **2013**, *34*, 1827-1832.
100. Satoh, K.; Ozawa, S.; Mizutani, M.; Nagai, K.; Kamigaito, M., *Nat. Commun.* **2010**, *1*, 6.
101. Stayshich, R. M.; Meyer, T. Y., *J. Am. Chem. Soc.* **2010**, *132*, 10920-10934.
102. Driessen, F.; Du Prez, F. E.; Espeel, P., *ACS Macro Lett.* **2015**, *4*, 616-619.
103. Dolan, J. A.; Wilts, B. D.; Vignolini, S.; Baumberg, J. J.; Steiner, U.; Wilkinson, T. D., *Adv. Opt. Mater.* **2015**, *3*, 12-32.
104. Stefik, M.; Guldin, S.; Vignolini, S.; Wiesner, U.; Steiner, U., *Chem. Soc. Rev.* **2015**, *44*, 5076-5091.
105. Vignolini, S.; Yufa, N. A.; Cunha, P. S.; Guldin, S.; Rushkin, I.; Stefik, M.; Hur, K.; Wiesner, U.; Baumberg, J. J.; Steiner, U., *Adv. Mater.* **2012**, *24*, OP23-OP27.
106. Wang, Z.; Sheng, R.; Luo, T.; Sun, J.; Cao, A., *Polym. Chem.* **2017**, *8*, 472-484.
107. Sun, P.; Wang, G.; Hou, H.; Yuan, P.; Deng, W.; Wang, C.; Lu, X.; Fan, Q.; Huang, W., *Polym. Chem.* **2017**, *8*, 5836-5844.
108. Martyn, B.; Biggs, C. I.; Gibson, M. I., *J. Polym. Sci. Part A: Polym. Chem.* **2019**, *57*, 40-47.
109. Hussain, I.; Capricho, J.; Yawer, M. A., *Adv. Synth. Catal.* **2016**, *358*, 3320-3349.
110. Makosza, M.; Wojciechowski, K., *Chem. Rev.* **2004**, *104*, 2631-2666.
111. Wang, Y. G.; Wang, X. J.; Xie, Y. J.; Zhang, K., *Cellulose* **2018**, *25*, 3703-3731.
112. Hu, Y. J.; Li, L. X.; Han, J. C.; Min, L.; Li, C. C., *Chem. Rev.* **2020**, *120*, 5910-5953.
113. Armstrong, R. W.; Combs, A. P.; Tempest, P. A.; Brown, S. D.; Keating, T. A., *Acc. Chem. Res.* **1996**, *29*, 123-131.
114. Theato, P., in *Multi-Component and Sequential Reactions in Polymer Synthesis*. Springer, **2015**.
115. Hantzsch, A., *Liebigs Ann. Chem.* **1882**, *215*, 1-82.
116. Norcross, B. E.; Clement, G.; Weinstein, M., *J. Chem. Educ.* **1969**, *46*, 694.
117. Xia, J. J.; Wang, G. W., *Synthesis* **2005**, 2379-2383.
118. Kumar, A.; Maurya, R. A., *Synlett* **2008**, 883-885.
119. Triggle, D. J., *Eur. J. Pharmacol.* **1999**, *375*, 311-325.
120. Khot, S.; Auti, P. B.; Khedkar, S. A., *Mini-Rev. Med. Chem.* **2021**, *21*, 135-149.
121. Tusell, J. M.; Barro'n, S.; Serratos, J., *Brain Res.* **1993**, *622*, 99-104.
122. Quinonero, O.; Lemaitre, C.; Jean, M.; Vanthuyne, N.; Roussel, C.; Bonne, D.; Constantieux, T.; Bressy, C.; Bugaut, X.; Rodriguez, J., *Org. Lett.* **2021**, *23*, 3394-3398.
123. Hussain-Khil, N.; Ghorbani-Choghamarani, A.; Mohammadi, M., *Sci. Rep.* **2021**, *11*.
124. Sharma, M. G.; Rajani, D. P.; Patel, H. M., *R. Soc. Open Sci.* **2017**, *4*.
125. Devasthale, P.; Wang, Y.; Wang, W.; Fevig, J.; Feng, J.; Wang, A.; Harrity, T.; Egan, D.; Morgan, N.; Cap, M.; Fura, A.; Klei, H. E.; Kish, K.; Weigelt, C.; Sun, L.; Levesque, P.; Moulin, F.; Li, Y.-X.; Zahler, R.; Kirby, M. S.; Hamann, L. G., *J. Med. Chem.* **2013**, *56*, 7343-7357.

126. Biginelli, P., *Eur. J. Inorg. Chem.* **1891**.
127. Biginelli, P., *Gazz. Chim. Ital.* **1893**.
128. Ryabukhin, S. V.; Plaskon, A. S.; Ostapchuk, E. N.; Volochnyuk, D. M.; Tolmachev, A. A., *Synthesis* **2007**, *2007*, 417-427.
129. Zhu, J.; Bienaymé, H., in *Multicomponent reactions*. John Wiley & Sons, **2006**.
130. Rovnyak, G. C.; Atwal, K. S.; Hedberg, A.; Kimball, S. D.; Moreland, S.; Gougoutas, J. Z.; Oreilly, B. C.; Schwartz, J.; Malley, M. F., *J. Med. Chem.* **1992**, *35*, 3254-3263.
131. Matos, L. H. S.; Masson, F. T.; Simeoni, L. A.; Homem-de-Mello, M., *Eur. J. Med. Chem.* **2018**, *143*, 1779-1789.
132. Zeng, M.; Xue, Y.; Qin, Y.; Peng, F.; Li, Q.; Zeng, M.-H., *Chin. Chem. Lett.* **2022**.
133. Li, Y. S.; Tan, T. H.; Zhao, Y.; Wei, Y.; Wang, D.; Chen, R. J.; Tao, L., *ACS Macro Lett.* **2020**, *9*, 1249-1254.
134. Windbiel, J. T.; Meier, M. A. R., *Polym. Int.* **2021**, *70*, 506-513.
135. Mao, T. F.; Liu, G. Q.; Wu, H. B.; Wei, Y.; Gou, Y. Z.; Wang, J.; Tao, L., *J. Am. Chem. Soc.* **2018**, *140*, 6865-6872.
136. Lieke, W., *Liebigs Ann. Chem.* **1859**, *112*, 316-321.
137. Ugi, I.; Fetzer, U.; Eholzer, U.; Knupfer, H.; Offermann, K., *Angew. Chem. Int. Ed.* **1965**, *4*, 472-484.
138. Onitsuka, K.; Suzuki, S.; Takahashi, S., *Tetrahedron Lett.* **2002**, *43*, 6197-6199.
139. Saegusa, T.; Ito, Y.; Kobayashi, S.; Hirota, K., *Tetrahedron Lett.* **1967**, *8*, 521-524.
140. Appel, R.; Kleinstück, R.; Ziehn, K.-D., *Angew. Chem. Int. Ed.* **1971**, *10*, 132-132.
141. Hoffmann, A. W., *Berichte der Dtsch. Chem. Gesellschaft* **1867**, *144*, 114.
142. Ugi, I.; Meyr, R., *Chem. Ber.* **1960**, *93*, 239-248.
143. Waibel, K. A.; Nickisch, R.; Möhl, N.; Seim, R.; Meier, M. A. R., *Green Chem.* **2020**, *22*, 933-941.
144. Wang, X.; Wang, Q.-G.; Luo, Q.-L., *Synthesis* **2015**, *47*, 49-54.
145. Gassman, P. G.; Guggenheim, T. L., *J. Am. Chem. Soc.* **1982**, *104*, 5849-5850.
146. Yamaguchi, T.; Miyake, Y.; Miyamura, A.; Ishiwata, N.; Tatsuta, K., *J. Antibiot.* **2006**, *59*, 729-734.
147. Yoshihiko, I.; Hiroshi, I.; Kazuo, S.; Takeo, S., *Chem. Lett.* **1984**, *13*, 937-940.
148. Camaggi, C. M.; Leardini, R.; Nanni, D.; Zanardi, G., *Tetrahedron* **1998**, *54*, 5587-5598.
149. Waibel, K. A.; Barther, D.; Malliaridou, T.; Moatsou, D.; Meier, M. A. R., *Eur. J. Org. Chem.* **2021**, *2021*, 4508-4516.
150. Tobisu, M.; Ito, S.; Kitajima, A.; Chatani, N., *Org. Lett.* **2008**, *10*, 5223-5225.
151. Kroke, E.; Willms, S.; Weidenbruch, M.; Saak, W.; Pohl, S.; Marsmann, H., *Tetrahedron Lett.* **1996**, *37*, 3675-3678.
152. Suginome, M.; Fukuda, T.; Nakamura, H.; Ito, Y., *Organometallics* **2000**, *19*, 719-721.
153. Saegusa, T.; Ito, Y.; Kobayashi, S.; Hirota, K.; Yoshioka, H., *Tetrahedron Lett.* **1966**, *7*, 6121-6124.
154. Saegusa, T.; Kobayashi, S.; Hirota, K.; Okumura, Y.; Ito, Y., *Bull. Chem. Soc. Jpn.* **1968**, *41*, 1638-1642.
155. Ito, Y.; Suginome, M.; Matsuura, T.; Murakami, M., *J. Am. Chem. Soc.* **1991**, *113*, 8899-8908.
156. Kuniyasu, H.; Sugoh, K.; Su, M. S.; Kurosawa, H., *J. Am. Chem. Soc.* **1997**, *119*, 4669-4677.
157. Millich, F., *Chem. Rev.* **1972**, *72*, 101-113.
158. Cai, Z.; Ren, Y.; Li, X.; Shi, J.; Tong, B.; Dong, Y., *Acc. Chem. Res.* **2020**, *53*, 2879-2891.

159. Tian, T.; Hu, R.; Tang, B. Z., *J. Am. Chem. Soc.* **2018**, *140*, 6156-6163.
160. Koopmanschap, G.; Ruijter, E.; Orru, R. V. A., *Beilstein J. Org. Chem.* **2014**, *10*, 544-598.
161. Ugi, I., *Angew. Chem. Int. Ed.* **1959**, *71*, 386-386.
162. Ugi, I.; Meyr, R., *Chem. Ber.* **1961**, *94*, 2229-2233.
163. Mumm, O., *Berichte der Dtsch. Chem. Gesellschaft* **1910**, *43*, 886-893.
164. Gordon, C. P.; Young, K. A.; Robertson, M. J.; Hill, T. A.; McCluskey, A., *Tetrahedron* **2011**, *67*, 554-561.
165. Sidhoum, M. A.; El Kaïm, L.; Grimaud, L., *Tetrahedron* **2018**, *74*, 5222-5231.
166. Levy, A. A.; Rains, H. C.; Smiles, S., *J. Chem. Soc.* **1931**, 3264-3269.
167. Liu, L.; Ping Li, C.; Cochran, S.; Ferro, V., *Bioorg. Med. Chem. Lett.* **2004**, *14*, 2221-2226.
168. Ugi, I.; Werner, B.; Domling, A., *Molecules* **2003**, *8*, 53-66.
169. Lowe, G., *Chem. Soc. Rev.* **1995**, *24*, 309-317.
170. Slobbe, P.; Ruijter, E.; Orru, R. V. A., *Med. Chem. Comm.* **2012**, *3*, 1189-1218.
171. Sehlinger, A.; Dannecker, P.-K.; Kreye, O.; Meier, M. A. R., *Macromolecules* **2014**, *47*, 2774-2783.
172. Stiernet, P.; Couturaud, B.; Bertrand, V.; Eppe, G.; De Winter, J.; Debuigne, A., *Polym. Chem.* **2021**, *12*, 2141-2151.
173. Boukis, A. C.; Reiter, K.; Frölich, M.; Hofheinz, D.; Meier, M. A. R., *Nat. Commun.* **2018**, *9*, 1439.
174. Shaabani, S.; Dömling, A., *Angew. Chem. Int. Ed.* **2018**, *57*, 16266-16268.
175. Liang, H.; Ji, D.-S.; Xu, G.-Q.; Luo, Y.-C.; Zheng, H.; Xu, P.-F., *Chem. Sci.* **2022**, *13*, 1088-1094.
176. Nazeri, M. T.; Javanbakht, S.; Nabi, M.; Shaabani, A., *Carbohydr. Polym.* **2022**, *283*, 119144.
177. Passerini, M.; Simone, L., *Gazz. Chim. Ital.* **1921**, *51*, 126.
178. Passerini, M.; Simone, L., *Gazz. Chim. Ital.* **1931**.
179. Baker, R. H.; Stanonis, D., *J. Am. Chem. Soc.* **1951**, *73*, 699-702.
180. Solleder, S. C.; Meier, M. A. R., *Angew. Chem. Int. Ed.* **2014**, *53*, 711-714.
181. Lyu, L.; Xie, H.; Mu, H.; He, Q.; Bian, Z.; Wang, J., *Org. Chem. Front.* **2015**, *2*, 815-818.
182. Yue, T.; Wang, M. X.; Wang, D. X.; Zhu, J. P., *Angew. Chem. Int. Ed.* **2008**, *47*, 9454-9457.
183. Wang, S. X.; Wang, M. X.; Wang, D. X.; Zhu, J. P., *Angew. Chem. Int. Ed.* **2008**, *47*, 388-391.
184. Zhao, M.; Liu, N.; Zhao, R.-H.; Zhang, P.-F.; Li, S.-N.; Yue, Y.; Deng, K.-L., *ACS Appl. Bio Mater.* **2019**, *2*, 1714-1723.
185. Oelmann, S.; Travanut, A.; Barther, D.; Romero, M.; Howdle, S. M.; Alexander, C.; Meier, M. A. R., *Biomacromolecules* **2019**, *20*, 90-101.
186. Khanna, K.; Varshney, S.; Kakkar, A., *Polym. Chem.* **2010**, *1*, 1171-1185.
187. Solleder, S. C. Novel Approaches Towards Sequence-Defined Macromolecules using Isocyanide-Based Multicomponent Reactions. Dissertation, KIT, Karlsruhe, **2016**.
188. Kreye, O.; Tóth, T.; Meier, M. A. R., *J. Am. Chem. Soc.* **2011**, *133*, 1790-1792.
189. Kreye, O.; Kugele, D.; Faust, L.; Meier, M. A. R., *Macromol. Rapid Commun.* **2014**, *35*, 317-322.
190. Waibel, K. A.; Moatsou, D.; Meier, M. A. R., *Macromol. Rapid Commun.* **2021**, *42*, 2000467.

191. Llevot, A.; Boukis, A. C.; Oelmann, S.; Wetzel, K.; Meier, M. A. R., *Top. Curr. Chem.* **2017**, *375*.
192. Sehlinger, A.; de Espinosa, L. M.; Meier, M. A. R., *Macromol. Chem. Phys.* **2013**, *214*, 2821-2828.
193. Tuten, B. T.; De Keer, L.; Wiedbrauk, S.; Van Steenberge, P. H. M.; D'hooge, D. R.; Barner-Kowollik, C., *Angew. Chem. Int. Ed.* **2019**, *58*, 5672-5676.
194. Zhang, J.; Zhang, M.; Du, F.-S.; Li, Z.-C., *Macromolecules* **2016**, *49*, 2592-2600.
195. Kakuchi, R.; Okura, Y., *Polym. J.* **2020**, *52*, 1057-1066.
196. Alkan, B.; Daglar, O.; Luleburgaz, S.; Gungor, B.; Gunay, U. S.; Hizal, G.; Tunca, U.; Durmaz, H., *Polym. Chem.* **2022**, *13*, 258-266.
197. Pettignano, A.; Daunay, A.; Moreau, C.; Cathala, B.; Charlot, A.; Fleury, E., *ACS Sustainable Chem. Eng.* **2019**, *7*, 14685-14696.
198. Tuten, B. T.; Bui, A. H.; Wiedbrauk, S.; Truong, V. X.; Raston, C. L.; Barner-Kowollik, C., *Chem. Commun.* **2021**, *57*, 8328-8331.
199. Onwukamike, K. N.; Grelier, S.; Grau, E.; Cramail, H.; Meier, M. A. R., *RSC Adv.* **2018**, *8*, 31490-31495.
200. Curtius, T.; Burkhardt, A., *J. Prakt. Chem.* **1898**, *58*, 205-233.
201. Brockway, L. O.; Pauling, L., *Proc. Natl. Acad. Sci. U. S. A.* **1933**, *19*, 860-867.
202. Wiberg, E.; Michaud, H., *Angew. Chem.* **1954**, *66*, 334-334.
203. Bräse, S.; Gil, C.; Knepper, K.; Zimmermann, V., *Angew. Chem. Int. Ed.* **2005**, *44*, 5188-5240.
204. Bräse, S.; Mende, M.; Jobelius, H. H.; Scharff, H.-D., in *Hydrazoic Acid and Azides*. Wiley-VCH, **2015**.
205. Evans, B. L.; Yoffe, A. D.; Gray, P., *Chem. Rev.* **1959**, *59*, 515-568.
206. Gray, P., *Quarterly Reviews* **1963**, *17*, 441-473.
207. Chehade, K. A. H.; Spielmann, H. P., *J. Org. Chem.* **2000**, *65*, 4949-4953.
208. Maffei, S.; Rivolta, A. M., *Gazz. Chim. Ital.* **1954**, *84*, 750-752.
209. Kim, Y. H.; Kim, K.; Shim, S. B., *Tetrahedron Lett.* **1986**, *27*, 4749-4752.
210. Guerin, D. J.; Horstmann, T. E.; Miller, S. J., *Org. Lett.* **1999**, *1*, 1107-1109.
211. Baruah, M.; Bols, M., *Synlett* **2002**, *2002*, 1111-1112.
212. Zhao, B.; Burgess, K., *ACS Med. Chem. Lett.* **2018**, *9*, 155-158.
213. Cai, S. X.; Glenn, D. J.; Kanskar, M.; Wybourn, M.; Keana, J. F., *Chem. Mater.* **1994**, *6*, 1822-1829.
214. Tsuchimochi, I.; Kitamura, Y.; Aoyama, H.; Akai, S.; Nakai, K.; Yoshimitsu, T., *Chem. Commun.* **2018**, *54*, 9893-9896.
215. Pothukanuri, S.; Winssinger, N., *Org. Lett.* **2007**, *9*, 2223-2225.
216. Rozhkov, V. V.; Kuvshinov, A. M.; Shevelev, S. A., *Org. Prep. Proced. Int.* **2000**, *32*, 94-96.
217. Müller, P.; Fruit, C., *Chem. Rev.* **2003**, *103*, 2905-2920.
218. Ju, C.; Meng, C.; Ma, J.; Zhang, X.; Ding, S., *Chem. Commun.* **2020**, *56*, 3955-3958.
219. Chandgude, A. L.; Dömling, A., *Eur. J. Org. Chem.* **2016**, *2016*, 2383-2387.
220. Goswami, M.; de Bruin, B., *Eur. J. Org. Chem.* **2017**, *2017*, 1152-1176.
221. Huisgen, R., *Angew. Chem. Int. Ed.* **1963**, *2*, 565-598.
222. Breugst, M.; Reissig, H.-U., *Angew. Chem. Int. Ed.* **2020**, *59*, 12293-12307.
223. Hlasta, D. J.; Ackerman, J. H., *J. Org. Chem.* **1994**, *59*, 6184-6189.
224. Rostovtsev, V. V.; Green, L.; Sharpless, K. B., *Abstr. Pap. Am. Chem. Soc.* **2002**, *224*, U186-U186.

225. Tornøe, C. W.; Christensen, C.; Meldal, M., *J. Org. Chem.* **2002**, *67*, 3057-3064.
226. Hein, J. E.; Fokin, V. V., *Chem. Soc. Rev.* **2010**, *39*, 1302-1315.
227. Topchiy, M. A.; Agheshina, A. A.; Gribanov, P. S.; Masoud, S. M.; Akmalov, T. R.; Nefedov, S. E.; Osipov, S. N.; Nechaev, M. S.; Asachenko, A. F., *Eur. J. Org. Chem.* **2019**, *2019*, 1016-1020.
228. Rostovtsev, V. V.; Green, L. G.; Fokin, V. V.; Sharpless, K. B., *Angew. Chem.* **2002**, *114*, 2708-2711.
229. Cantillo, D.; Ávalos, M.; Babiano, R.; Cintas, P.; Jiménez, J. L.; Palacios, J. C., *Org. Biomol. Chem.* **2011**, *9*, 2952-2958.
230. Özkılıç, Y.; Tüzün, N. Ş., *Organometallics* **2016**, *35*, 2589-2599.
231. Fang, Y.; Bao, K.; Zhang, P.; Sheng, H.; Yun, Y.; Hu, S.-X.; Astruc, D.; Zhu, M., *J. Am. Chem. Soc.* **2021**, *143*, 1768-1772.
232. Ganz, D.; Harijan, D.; Wagenknecht, H.-A., *RSC Chem. Biol.* **2020**, *1*, 86-97.
233. Pranantyo, D.; Xu, L. Q.; Hou, Z.; Kang, E.-T.; Chan-Park, M. B., *Polym. Chem.* **2017**, *8*, 3364-3373.
234. Iannone, M. N.; Stucchi, S.; Turolla, E. A.; Beretta, C.; Ciceri, S.; Chinello, C.; Pagani, L.; Todde, S.; Ferraboschi, P., *J. Labelled Comp. Radiopharm.* **2021**, 1-15.
235. Song, H. B.; Sowan, N.; Baranek, A.; Sinha, J.; Cook, W. D.; Bowman, C. N., *Macromolecules* **2021**, *54*, 747-756.
236. Obhi, N. K.; Jarrett-Wilkins, C. N.; Hicks, G. E. J.; Seferos, D. S., *Macromolecules* **2020**, *53*, 8592-8599.
237. Stille, J. K., *J. Chem. Educ.* **1981**, *58*, 862.
238. Cowie, J. M. G., in *Polymers: chemistry and physics of modern materials*. Blackie; Chapman and Hall, **1991**.
239. Allcock, H. R.; Lampe, F. W.; Mark, J. E., in *Contemporary polymer chemistry*. Pearson/Prentice Hall, **2003**.
240. Carothers, W. H., *J. Chem. Soc. Faraday Trans.* **1936**, *32*, 39-49.
241. Mita, I.; Stepto, R. F. T.; Suter, U. W., *Pure Appl. Chem.* **1994**, *66*, 2483-2486.
242. Tomida, M.; Nakato, T.; Matsunami, S.; Kakuchi, T., *Polymer* **1997**, *38*, 4733-4736.
243. Renard, E.; Sebillé, B.; Barnathan, G.; Deratani, A., *Macromol. Symp.* **1997**, *122*, 229-234.
244. Kim, M.-R.; Kim, H.-S.; Ha, C.-S.; Park, D.-W.; Lee, J.-K., *J. Appl. Polym. Sci.* **2001**, *81*, 2735-2743.
245. Chanda, M.; Roy, S. K., in *Industrial polymers, specialty polymers, and their applications*. CRC press, **2008**.
246. Hardy, D. V. N., *J. Soc. Chem. Ind.* **1948**, *67*, 426-432.
247. Shor, M., *J. Chem. Educ.* **1944**, *21*, 88.
248. Bayer, O., *Angew. Chem.* **1947**, *59*, 257-272.
249. Akindoyo, J. O.; Beg, M. D. H.; Ghazali, S.; Islam, M. R.; Jeyaratnam, N.; Yuvaraj, A. R., *RSC Adv.* **2016**, *6*, 114453-114482.
250. Six, C.; Richter, F., in *Ullmann's Encyclopedia of Industrial Chemistry*. **2013**.
251. Mikoczy, Z.; Welinder, H.; Tinnerberg, H.; Hagmar, L., *Occup. Environ. Med.* **2004**, *61*, 432-437.
252. Sorahan, T.; Pope, D., *Br. J. Ind. Med.* **1993**, *50*, 528-536.
253. Suryawanshi, Y.; Sanap, P.; Wani, V., *Polym. Bull.* **2019**, *76*, 3233-3246.
254. Liu, G.; Wu, G.; Huo, S.; Jin, C.; Kong, Z., *Prog. Org. Coat.* **2017**, *112*, 169-175.

255. Błażek, K.; Beneš, H.; Walterová, Z.; Abbrent, S.; Eceiza, A.; Calvo-Correas, T.; Datta, J., *Polym. Chem.* **2021**, *12*, 1643-1652.
256. Bähr, M.; Bitto, A.; Mülhaupt, R., *Green Chem.* **2012**, *14*, 1447-1454.
257. Young, R. J.; Lovell, P. A., in *Introduction to polymers*. Chapman & Hall, **1991**.
258. Penczek, S.; Moad, G., *Pure Appl. Chem.* **2008**, *80*, 2163-2193.
259. Abreu, C. M. R.; Mendonça, P. V.; Serra, A. C.; Coelho, J. F. J.; Popov, A. V.; Gryn'ova, G.; Coote, M. L.; Guliashvili, T., *Macromolecules* **2012**, *45*, 2200-2208.
260. Burnett, G. M.; Cameron, G. G.; Joiner, S. N., *J. Chem. Soc., Faraday Trans. 1* **1973**, *69*, 322-327.
261. Dechy-Cabaret, O.; Martin-Vaca, B.; Bourissou, D., *Chem. Rev.* **2004**, *104*, 6147-6176.
262. Wahlen, C.; Frey, H., *Macromolecules* **2021**, *54*, 7323-7336.
263. Ziegler, K.; Holzkamp, E.; Breil, H.; Martin, H., *Angew. Chem.* **1955**, *67*, 541-547.
264. Soares, J. B.; McKenna, T.; Cheng, C., *Polym. React. Eng.* **2007**, 29-117.
265. Aoshima, S.; Kanaoka, S., *Chem. Rev.* **2009**, *109*, 5245-5287.
266. Hirao, A.; Goseki, R.; Ishizone, T., *Macromolecules* **2014**, *47*, 1883-1905.
267. Bisht, H. S.; Chatterjee, A. K., *J. Polym. Sci. C* **2001**, *41*, 139-173.
268. Nuyken, O.; Pask, S. D., *Polymers* **2013**, *5*, 361-403.
269. Shipp, D. A., *Polym. Rev.* **2011**, *51*, 99-103.
270. Doi, Y.; Suzuki, S.; Soga, K., *Macromolecules* **1986**, *19*, 2896-2900.
271. Tomita, I.; Kondo, Y.; Takagi, K.; Endo, T., *Macromolecules* **1994**, *27*, 4413-4414.
272. Held, A.; Bauers, F. M.; Mecking, S., *Chem. Commun.* **2000**, 301-302.
273. Chen, E. Y. X., *Chem. Rev.* **2009**, *109*, 5157-5214.
274. Kuran, W., *Prog. Polym. Sci.* **1998**, *23*, 919-992.
275. Claverie, J. P.; Schaper, F., *MRS Bull.* **2013**, *38*, 213-218.
276. Aoshima, S.; Yoshida, T.; Kanazawa, A.; Kanaoka, S., *J. Polym. Sci. Part A: Polym. Chem.* **2007**, *45*, 1801-1813.
277. Matyjaszewski, K., *Makromolekulare Chemie. Macromolecular Symposia* **1992**, *60*, 107-117.
278. Hayashi, K.; Hayashi, K.; Okamura, S., *Polym. J.* **1973**, *4*, 426-436.
279. Sharaby, Z.; Jagur-Grodzinski, J.; Martan, M.; Vofsi, D., *J. Polym. Sci., Part A-1: Polym. Chem.* **1982**, *20*, 901-915.
280. Van Beylen, M.; Bywater, S.; Smets, G.; Szwarc, M.; Worsfold, D. J., in *Developments in anionic polymerization — A critical review*. Springer, **1988**.
281. Bolig, A. D.; Chen, E. Y.-X., *J. Am. Chem. Soc.* **2001**, *123*, 7943-7944.
282. Eßwein, B.; Steidl, N. M.; Möller, M., *Macromol. Rapid Commun.* **1996**, *17*, 143-148.
283. Takeuchi, D.; Nakamura, T.; Aida, T., *Macromolecules* **2000**, *33*, 725-729.
284. Yagi, K.; Miyazaki, T.; Okitsu, H.; Toda, F.; Iwakura, Y., *J. Polym. Sci. Part A: Polym. Chem.* **1972**, *10*, 1149-1156.
285. Arens, L.; Barther, D.; Landsgesell, J.; Holm, C.; Wilhelm, M., *Soft Matter* **2019**, *15*, 9949-9964.
286. Bartlett, P. D.; Altschul, R., *J. Am. Chem. Soc.* **1945**, *67*, 816-822.
287. Hamielec, A. E.; Hodgins, J. W.; Tebbens, K., *AIChE J.* **1967**, *13*, 1087-1091.
288. Roy, J.-C.; Nash, J.; Williams Jr, R.; Hamill, W., *J. Am. Chem. Soc.* **1956**, *78*, 519-521.
289. Davis, T. P.; Kukulj, D.; Haddleton, D. M.; Maloney, D. R., *Trends Polym. Sci.* **1995**, *3*, 365-373.
290. Isobe, Y.; Yamada, K.; Nakano, T.; Okamoto, Y., *J. Polym. Sci. Part A: Polym. Chem.* **2000**, *38*, 4693-4703.

291. Gao, Y.; Zhou, D.; Lyu, J.; A, S.; Xu, Q.; Newland, B.; Matyjaszewski, K.; Tai, H.; Wang, W., *Nat. Rev. Chem.* **2020**, *4*, 194-212.
292. Fang, S.; Wang, G.; Li, P.; Xing, R.; Liu, S.; Qin, Y.; Yu, H.; Chen, X.; Li, K., *Int. J. Biol. Macromol.* **2018**, *115*, 754-761.
293. Nakahara, K.; Iwasa, S.; Satoh, M.; Morioka, Y.; Iriyama, J.; Suguro, M.; Hasegawa, E., *Chem. Phys. Lett.* **2002**, *359*, 351-354.
294. Rusu, G.; Ueda, K.; Rusu, E.; Rusu, M., *Polymer* **2001**, *42*, 5669-5678.
295. Sanda, F.; Endo, T., *J. Polym. Sci. Part A: Polym. Chem.* **2001**, *39*, 265-276.
296. Chutayothin, P.; Ishida, H., *Macromolecules* **2010**, *43*, 4562-4572.
297. Carrillo, A.; Kane, R. S., *J. Polym. Sci. Part A: Polym. Chem.* **2004**, *42*, 3352-3359.
298. Duda, A.; Kowalski, A., in *Thermodynamics and Kinetics of Ring-Opening Polymerization*. **2009**.
299. Corrigan, N.; Jung, K.; Moad, G.; Hawker, C. J.; Matyjaszewski, K.; Boyer, C., *Prog. Polym. Sci.* **2020**, *111*, 101311.
300. Moad, G.; Rizzardo, E.; Thang, S. H., *Chem. Asian J.* **2013**, *8*, 1634-1644.
301. Audran, G.; Bagryanskaya, E. G.; Marque, S. R. A.; Postnikov, P., *Polymers* **2020**, *12*, 1481.
302. Wang, J.-S.; Matyjaszewski, K., *Macromolecules* **1995**, *28*, 7901-7910.
303. Kato, M.; Kamigaito, M.; Sawamoto, M.; Higashimura, T., *Macromolecules* **1995**, *28*, 1721-1723.
304. Matyjaszewski, K., *Macromolecules* **2012**, *45*, 4015-4039.
305. Krys, P.; Matyjaszewski, K., *Eur. Polym. J.* **2017**, *89*, 482-523.
306. Ribelli, T. G.; Augustine, K. F.; Fantin, M.; Krys, P.; Poli, R.; Matyjaszewski, K., *Macromolecules* **2017**, *50*, 7920-7929.
307. Nakamura, Y.; Ogihara, T.; Yamago, S., *ACS Macro Lett.* **2016**, *5*, 248-252.
308. Fujisawa, S.; Kadoma, Y.; Yokoe, I., *Chem. Phys. Lipids* **2004**, *130*, 189-195.
309. Bhanu, V.; Kishore, K., *Chem. Rev.* **1991**, *91*, 99-117.
310. Rabea, A. M.; Zhu, S., *Polymers* **2015**, *7*, 819-835.
311. Sharma, R.; Goyal, A.; Caruthers, J. M.; Won, Y.-Y., *Macromolecules* **2006**, *39*, 4680-4689.
312. Tan, S.; Li, J.; Zhang, Z., *Macromolecules* **2011**, *44*, 7911-7916.
313. Wang, Y.; Soerensen, N.; Zhong, M.; Schroeder, H.; Buback, M.; Matyjaszewski, K., *Macromolecules* **2013**, *46*, 683-691.
314. Chan, N.; Cunningham, M. F.; Hutchinson, R. A., *Macromol. Chem. Phys.* **2008**, *209*, 1797-1805.
315. Hoffmann, A.; Bienemann, O.; Vieira, I. D. S.; Herres-Pawlis, S., *Polymers* **2014**, *6*, 995-1007.
316. Kütahya, C.; Schmitz, C.; Strehmel, V.; Yagci, Y.; Strehmel, B., *Angew. Chem. Int. Ed.* **2018**, *57*, 7898-7902.
317. Zhang, L.; Cheng, Z.; Tang, F.; Li, Q.; Zhu, X., *Macromol. Chem. Phys.* **2008**, *209*, 1705-1713.
318. Maria, S.; Biedroń, T.; Poli, R.; Kubisa, P., *J. Appl. Polym. Sci.* **2007**, *105*, 278-281.
319. Fernández-Zúmel, M. A.; Kiefer, G.; Thommes, K.; Scopelliti, R.; Severin, K., *Eur. J. Inorg. Chem.* **2010**, *2010*, 3596-3601.
320. Braunecker, W. A.; Brown, W. C.; Morelli, B. C.; Tang, W.; Poli, R.; Matyjaszewski, K., *Macromolecules* **2007**, *40*, 8576-8585.

321. Lanzalaco, S.; Fantin, M.; Scialdone, O.; Galia, A.; Isse, A. A.; Gennaro, A.; Matyjaszewski, K., *Macromolecules* **2017**, *50*, 192-202.
322. Golub, G.; Cohen, H.; Paoletti, P.; Bencini, A.; Messori, L.; Bertini, I.; Meyerstein, D., *J. Am. Chem. Soc.* **1995**, *117*, 8353-8361.
323. M. Haddleton, D.; J. Clark, A.; C. Crossman, M.; J. Duncalf, D.; M. Heming, A.; R. Morsley, S.; J. Shooter, A., *Chem. Commun.* **1997**, 1173-1174.
324. Zeng, F.; Shen, Y.; Zhu, S.; Pelton, R., *Macromolecules* **2000**, *33*, 1628-1635.
325. Rorabacher, D. B., *Chem. Rev.* **2004**, *104*, 651-698.
326. Tang, W.; Matyjaszewski, K., *Macromolecules* **2006**, *39*, 4953-4959.
327. Matyjaszewski, K.; Göbelt, B.; Paik, H.-j.; Horwitz, C. P., *Macromolecules* **2001**, *34*, 430-440.
328. Tang, W.; Matyjaszewski, K., *Macromolecules* **2007**, *40*, 1858-1863.
329. Tang, W.; Kwak, Y.; Braunecker, W.; Tsarevsky, N. V.; Coote, M. L.; Matyjaszewski, K., *J. Am. Chem. Soc.* **2008**, *130*, 10702-10713.
330. Ribelli, T. G.; Lorandi, F.; Fantin, M.; Matyjaszewski, K., *Macromol. Rapid Commun.* **2019**, *40*, 1800616.
331. Simakova, A.; Averick, S. E.; Konkolewicz, D.; Matyjaszewski, K., *Macromolecules* **2012**, *45*, 6371-6379.
332. Paterson, S. M.; Brown, D. H.; Chirila, T. V.; Keen, I.; Whittaker, A. K.; Baker, M. V., *J. Polym. Sci. Part A: Polym. Chem.* **2010**, *48*, 4084-4092.
333. Li, X.; Wang, W.-J.; Li, B.-G.; Zhu, S., *Macromol. React. Eng.* **2011**, *5*, 467-478.
334. Jiang, X.; Wu, J.; Zhang, L.; Cheng, Z.; Zhu, X., *Macromol. Rapid Commun.* **2014**, *35*, 1879-1885.
335. Konkolewicz, D.; Magenau, A. J. D.; Averick, S. E.; Simakova, A.; He, H.; Matyjaszewski, K., *Macromolecules* **2012**, *45*, 4461-4468.
336. Wang, G.; Wang, Z.; Lee, B.; Yuan, R.; Lu, Z.; Yan, J.; Pan, X.; Song, Y.; Bockstaller, M. R.; Matyjaszewski, K., *Polymer* **2017**, *129*, 57-67.
337. Abreu, C. M. R.; Fu, L.; Carmali, S.; Serra, A. C.; Matyjaszewski, K.; Coelho, J. F. J., *Polym. Chem.* **2017**, *8*, 375-387.
338. Krysz, P.; Wang, Y.; Matyjaszewski, K.; Harrisson, S., *Macromolecules* **2016**, *49*, 2977-2984.
339. Oliveira, A. S. R.; Mendonça, P. V.; Serra, A. C.; Coelho, J. F. J., *J. Polym. Sci.* **2020**, *58*, 145-153.
340. Konkolewicz, D.; Schröder, K.; Buback, J.; Bernhard, S.; Matyjaszewski, K., *ACS Macro Lett.* **2012**, *1*, 1219-1223.
341. Chmielarz, P.; Fantin, M.; Park, S.; Isse, A. A.; Gennaro, A.; Magenau, A. J. D.; Sobkowiak, A.; Matyjaszewski, K., *Prog. Polym. Sci.* **2017**, *69*, 47-78.
342. Lattke, Y. M.; Corbin, D. A.; Sartor, S. M.; McCarthy, B. G.; Miyake, G. M.; Damrauer, N. H., *J. Phys. Chem. A* **2021**, *125*, 3109-3121.
343. Li, M.; Fu, S., *Carbohydr. Polym.* **2021**, *259*, 117736.
344. Rodrigues, P. R.; Junior, L. M.; de Souza, W. F. C.; Sato, H. H.; Alves, R. M. V.; Vieira, R. P., *Int. J. Biol. Macromol.* **2021**, *193*, 425-432.
345. Cuthbert, J.; Wanasinghe, S. V.; Matyjaszewski, K.; Konkolewicz, D., *Macromolecules* **2021**, *54*, 8331-8340.
346. Messina, M. S.; Messina, K. M. M.; Bhattacharya, A.; Montgomery, H. R.; Maynard, H. D., *Prog. Polym. Sci.* **2020**, *100*, 101186.
347. Anderson, A.; Merckling, N., *US2721189* **1955**.

348. Jean-Louis Hérisson, P.; Chauvin, Y., *Makromol. Chem.* **1971**, *141*, 161-176.
349. Szwarc, M., *Nature* **1956**, *178*, 1168-1169.
350. Flory, P. J., *J. Am. Chem. Soc.* **1940**, *62*, 1561-1565.
351. Matyjaszewski, K., *Macromolecules* **1993**, *26*, 1787-1788.
352. Benson, S. W.; Cruickshank, F.; Golden, D.; Haugen, G. R.; O'neal, H.; Rodgers, A.; Shaw, R.; Walsh, R., *Chem. Rev.* **1969**, *69*, 279-324.
353. Tastard, C. Y.; Hodge, P.; Ben-Haida, A.; Dobinson, M., *React. Funct. Polym.* **2006**, *66*, 93-107.
354. Calderon, N.; Chen, H. Y.; Scott, K. W., *Tetrahedron Lett.* **1967**, *8*, 3327-3329.
355. Michelotti, F. W.; Keaveney, W. P., *J. Polym. Sci., Part A: Gen. Pap.* **1965**, *3*, 895-905.
356. Pampus, G.; Lehnert, G., *Macromol. Chem. Phys.* **1974**, *175*, 2605-2616.
357. Kroll, W.; Doyle, G., *J. Chem. Soc. D* **1971**, 839-839.
358. McConville, D. H.; Wolf, J. R.; Schrock, R. R., *J. Am. Chem. Soc.* **1993**, *115*, 4413-4414.
359. Schrock, R. R.; DePue, R. T.; Feldman, J.; Yap, K. B.; Yang, D. C.; Davis, W. M.; Park, L.; DiMare, M.; Schofield, M., *Organometallics* **1990**, *9*, 2262-2275.
360. Nguyen, S. T.; Johnson, L. K.; Grubbs, R. H.; Ziller, J. W., *J. Am. Chem. Soc.* **1992**, *114*, 3974-3975.
361. Schwab, P.; France, M. B.; Ziller, J. W.; Grubbs, R. H., *Angew. Chem. Int. Ed.* **1995**, *34*, 2039-2041.
362. Martinez, H.; Ren, N.; Matta, M. E.; Hillmyer, M. A., *Polym. Chem.* **2014**, *5*, 3507-3532.
363. Schrock, R.; Feldman, J.; Cannizzo, L.; Grubbs, R., *Macromolecules* **1987**, *20*, 1169-1172.
364. Schrock, R. R.; Murdzek, J. S.; Bazan, G. C.; Robbins, J.; DiMare, M.; O'Regan, M., *J. Am. Chem. Soc.* **1990**, *112*, 3875-3886.
365. Cantrell, G. K.; Geib, S. J.; Meyer, T. Y., *Organometallics* **1999**, *18*, 4250-4252.
366. Bazan, G.; Schrock, R.; Cho, H.-N.; Gibson, V., *Macromolecules* **1991**, *24*, 4495-4502.
367. Bazan, G. C.; Oskam, J. H.; Cho, H. N.; Park, L. Y.; Schrock, R. R., *J. Am. Chem. Soc.* **1991**, *113*, 6899-6907.
368. Nguyen, S. T.; Grubbs, R. H.; Ziller, J. W., *J. Am. Chem. Soc.* **1993**, *115*, 9858-9859.
369. Schwab, P.; Grubbs, R. H.; Ziller, J. W., *J. Am. Chem. Soc.* **1996**, *118*, 100-110.
370. Demonceau, A.; Stumpf, A. W.; Saive, E.; Noels, A. F., *Macromolecules* **1997**, *30*, 3127-3136.
371. Bielawski, C. W.; Grubbs, R. H., *Angew. Chem. Int. Ed.* **2000**, *39*, 2903-2906.
372. Choi, T.-L.; Grubbs, R. H., *Angew. Chem. Int. Ed.* **2003**, *42*, 1743-1746.
373. Scholl, M.; Ding, S.; Lee, C. W.; Grubbs, R. H., *Org. Lett.* **1999**, *1*, 953-956.
374. Sanford, M. S.; Love, J. A.; Grubbs, R. H., *J. Am. Chem. Soc.* **2001**, *123*, 6543-6554.
375. Arduengo, A. J.; Goerlich, J. R.; Marshall, W. J., *J. Am. Chem. Soc.* **1995**, *117*, 11027-11028.
376. Sanford, M. S.; Love, J. A.; Grubbs, R. H., *Organometallics* **2001**, *20*, 5314-5318.
377. Walsh, D. J.; Lau, S. H.; Hyatt, M. G.; Guironnet, D., *J. Am. Chem. Soc.* **2017**, *139*, 13644-13647.
378. Gordon, E. J.; Gestwicki, J. E.; Strong, L. E.; Kiessling, L. L., *Chem. Biol.* **2000**, *7*, 9-16.
379. Louie, J.; Grubbs, R. H., *Organometallics* **2002**, *21*, 2153-2164.
380. Minenkov, Y.; Occhipinti, G.; Jensen, V. R., *Organometallics* **2013**, *32*, 2099-2111.
381. Lexer, C.; Saf, R.; Slugovc, C., *J. Polym. Sci. Part A: Polym. Chem.* **2009**, *47*, 299-305.
382. Hilf, S.; Grubbs, R. H.; Kilbinger, A. F. M., *Macromolecules* **2008**, *41*, 6006-6011.
383. Nagarkar, A. A.; Kilbinger, A. F. M., *Chem. Sci.* **2014**, *5*, 4687-4692.

384. Mahanthappa, M. K.; Bates, F. S.; Hillmyer, M. A., *Macromolecules* **2005**, *38*, 7890-7894.
385. Matson, J. B.; Grubbs, R. H., *Macromolecules* **2010**, *43*, 213-221.
386. Hilf, S.; Kilbinger, A. F. M., *Macromol. Rapid Commun.* **2007**, *28*, 1225-1230.
387. Liu, X.; Liu, F.; Liu, W.; Gu, H., *Polym. Rev.* **2021**, *61*, 1-53.
388. Kim, D.-Y.; Shin, S.; Yoon, W.-J.; Choi, Y.-J.; Hwang, J.-K.; Kim, J.-S.; Lee, C.-R.; Choi, T.-L.; Jeong, K.-U., *Adv. Funct. Mater.* **2017**, *27*, 1606294.
389. Foster, J. C.; Grocott, M. C.; Arkinstall, L. A.; Varlas, S.; Redding, M. J.; Grayson, S. M.; O'Reilly, R. K., *J. Am. Chem. Soc.* **2020**, *142*, 13878-13885.
390. Arkinstall, L. A.; Husband, J. T.; Wilks, T. R.; Foster, J. C.; O'Reilly, R. K., *Chem. Commun.* **2021**, *57*, 5466-5469.
391. Callmann, C. E.; Thompson, M. P.; Gianneschi, N. C., *Acc. Chem. Res.* **2020**, *53*, 400-413.
392. Yang, J.; Horst, M.; Werby, S. H.; Cegelski, L.; Burns, N. Z.; Xia, Y., *J. Am. Chem. Soc.* **2020**, *142*, 14619-14626.
393. Horst, M.; Yang, J.; Meisner, J.; Kouznetsova, T. B.; Martínez, T. J.; Craig, S. L.; Xia, Y., *J. Am. Chem. Soc.* **2021**, *143*, 12328-12334.
394. Miyasako, N.; Matsuoka, S.-i.; Suzuki, M., *Macromol. Rapid Commun.* **2021**, *42*, 2000326.
395. Yarolimek, M. R.; Coia, B. M.; Bookbinder, H. R.; Kennemur, J. G., *Polym. Chem.* **2021**, *12*, 5048-5058.
396. Naguib, M.; Rashed, A.; Keddie, D. J., *J. Mater. Sci.* **2021**, *56*, 8900-8909.
397. Arrington, K. J.; Waugh, J. B.; Radzinski, S. C.; Matson, J. B., *Macromolecules* **2017**, *50*, 4180-4187.
398. Huang, B.; Wei, M.; Vargo, E.; Qian, Y.; Xu, T.; Toste, F. D., *J. Am. Chem. Soc.* **2021**, *143*, 17920-17925.
399. Lutz, J.-F., *Polym. Chem.* **2010**, *1*, 55-62.
400. Onbulak, S.; Hillmyer, M. A., *Polym. Chem.* **2021**, *12*, 1681-1691.
401. Zhang, H.; Zhou, Z.; Chen, X.; Yu, B.; Luo, Z.; Li, X.; Rahman, M. A.; Sha, Y., *Macromolecules* **2021**, *54*, 9174-9184.
402. Koehler, S. J.; Hu, J. Z.; Elacqua, E., *Synlett* **2020**, *31*, 1435-1442.
403. Jha, S.; Dutta, S.; Bowden, N. B., *Macromolecules* **2004**, *37*, 4365-4374.
404. Xia, Y.; Kornfield, J. A.; Grubbs, R. H., *Macromolecules* **2009**, *42*, 3761-3766.
405. Xia, Y.; Olsen, B. D.; Kornfield, J. A.; Grubbs, R. H., *J. Am. Chem. Soc.* **2009**, *131*, 18525-18532.
406. Kim, M.-J.; Yu, Y.-G.; Chae, C.-G.; Seo, H.-B.; Bak, I.-G.; Mallela, Y. L. N. K.; Lee, J.-S., *Macromolecules* **2019**, *52*, 103-112.
407. Neary, W. J.; Fultz, B. A.; Kennemur, J. G., *ACS Macro Lett.* **2018**, *7*, 1080-1086.
408. Gegenhuber, T.; Mullner, M., *Macromol. Chem. Phys.* **2021**, *222*.
409. Nikovia, C.; Sougioltzoupoulou, E.; Rigas, V.; Pitsikalis, M., *Polymers* **2019**, *11*, 1606.
410. Nguyen, H. V. T.; Gallagher, N. M.; Vohidov, F.; Jiang, Y. V.; Kawamoto, K.; Zhang, H.; Park, J. V.; Huang, Z. H.; Ottaviani, M. F.; Rajca, A.; Johnson, J. A., *ACS Macro Lett.* **2018**, *7*, 472-476.
411. Radzinski, S. C.; Foster, J. C.; Scannelli, S. J.; Weaver, J. R.; Arrington, K. J.; Matson, J. B., *ACS Macro Lett.* **2017**, *6*, 1175-1179.
412. Bates, C. M.; Chang, A. B.; Momčilović, N.; Jones, S. C.; Grubbs, R. H., *Macromolecules* **2015**, *48*, 4967-4973.

413. Varlas, S.; Lawrenson, S. B.; Arkinstall, L. A.; O'Reilly, R. K.; Foster, J. C., *Prog. Polym. Sci.* **2020**, *107*, 101278.
414. Liberman-Martin, A. L.; Chu, C. K.; Grubbs, R. H., *Macromol. Rapid Commun.* **2017**, *38*, 1700058.
415. Varlas, S.; Foster, J. C.; O'Reilly, R. K., *Chem. Commun.* **2019**, *55*, 9066-9071.
416. Hagmann, D. F.; Goodey, N. M.; Mathieu, C.; Evans, J.; Aronson, M. F. J.; Gallagher, F.; Krumins, J. A., *Soil Biol. Biochem.* **2015**, *91*, 291-297.
417. Vougioukalakis, G. C., *Chem. Eur. J.* **2012**, *18*, 8868-8880.
418. Riener, M.; Nicewicz, D. A., *Chem. Sci.* **2013**, *4*, 2625-2629.
419. Daub, M. E.; Jung, H.; Lee, B. J.; Won, J.; Baik, M.-H.; Yoon, T. P., *J. Am. Chem. Soc.* **2019**, *141*, 9543-9547.
420. Pascual, L. M.; Dunford, D. G.; Goetz, A. E.; Ogawa, K. A.; Boydston, A. J., *Synlett* **2016**, *27*, 759-762.
421. Maravigna, P.; Montaudo, G., In *Comprehensive Polymer Science and Supplements*, Ed.: Allen, G.; Bevington, J. C., Pergamon, **1989**, 63-90.
422. Xue, Z.; Mayer, M. F., *Soft Matter* **2009**, *5*, 4600-4611.
423. Chen, Z.-R.; Claverie, J. P.; Grubbs, R. H.; Kornfield, J. A., *Macromolecules* **1995**, *28*, 2147-2154.
424. Gautrot, J. E.; Zhu, X. X., *Chem. Commun.* **2008**, 1674-1676.
425. Chatterjee, A. K.; Choi, T.-L.; Sanders, D. P.; Grubbs, R. H., *J. Am. Chem. Soc.* **2003**, *125*, 11360-11370.
426. Xie, M.; Wang, W.; Ding, L.; Liu, J.; Yang, D.; Wei, L.; Zhang, Y., *J. Polym. Sci. Part A: Polym. Chem.* **2010**, *48*, 380-388.
427. Gautrot, J. E.; Zhu, X., *Macromolecules* **2009**, *42*, 7324-7331.
428. Kang, S.; Cetin, M. M.; Jiang, R.; Clevenger, E. S.; Mayer, M. F., *J. Am. Chem. Soc.* **2014**, *136*, 12588-12591.
429. van Zoelen, W.; ten Brinke, G., *Soft Matter* **2009**, *5*, 1568-1582.
430. Ozturk, B. O.; Yakut, E.; Ak, E.; Sehitoglu, S. K., *React. Funct. Polym.* **2017**, *111*, 22-29.
431. Lee, J.; Han, S.; Kim, M.; Kim, B. S., *Macromolecules* **2020**, *53*, 355-366.
432. McCormack, C. L.; Lowe, A. B., *Acc. Chem. Res.* **2004**, *37*, 312-325.
433. Andreu, R.; Reina, I. A.; Ronda, J. C., *J. Polym. Sci. Part A: Polym. Chem.* **2008**, *46*, 3353-3366.
434. Ota, Y.; Ito, S.; Kuroda, J.; Okumura, Y.; Nozaki, K., *J. Am. Chem. Soc.* **2014**, *136*, 11898-11901.
435. Vidal, F.; McQuade, J.; Lalancette, R.; Jakle, F., *J. Am. Chem. Soc.* **2020**, *142*, 14427-14431.
436. Pollino, J. M.; Stubbs, L. P.; Weck, M., *Macromolecules* **2003**, *36*, 2230-2234.
437. Dong, T. T.; Zhang, J. J.; Xu, G. J.; Chai, J. C.; Du, H. P.; Wang, L. L.; Wen, H. J.; Zang, X.; Du, A. B.; Jia, Q. M.; Zhou, X. H.; Cui, G. L., *Energy Environ. Sci.* **2018**, *11*, 1197-1203.
438. Song, C.; Liu, X.; Liu, D.; Ren, C. L.; Yang, W. T.; Deng, J. P., *Macromol. Rapid Commun.* **2013**, *34*, 1426-1445.
439. Travanut, A.; Monteiro, P. F.; Oelmann, S.; Howdle, S. M.; Grabowska, A. M.; Clarke, P. A.; Ritchie, A. A.; Meier, M. A. R.; Alexander, C., *Macromol. Rapid Commun.* **2021**, *42*.
440. Suarez, D.; Sordo, J. A., *Chem. Commun.* **1998**, 385-386.
441. van der Westhuizen, H. J.; Roodt, A.; Meijboom, R., *Polyhedron* **2010**, *29*, 2776-2779.
442. Wu, Z.; Nguyen, S. T.; Grubbs, R. H.; Ziller, J. W., *J. Am. Chem. Soc.* **1995**, *117*, 5503-5511.

443. Galan, B. R.; Kalbarczyk, K. P.; Szczepankiewicz, S.; Keister, J. B.; Diver, S. T., *Org. Lett.* **2007**, *9*, 1203-1206.
444. Dyre, J. C., *Rev. Mod. Phys.* **2006**, *78*, 953-972.
445. Li, C.-T.; Hsiao, S.-H., *J. Polym. Sci. A Polym. Chem.* **1999**, *37*, 1435-1442.
446. Fox, T. G., *Bull. Am. Phys. Soc.* **1956**, *2*, 123.
447. Esteruelas, M. A.; Gonzalez, F.; Herrero, J.; Lucio, P.; Olivan, M.; Ruiz-Labrador, B., *Polym. Bull.* **2007**, *58*, 923-931.
448. Wang, Y. Z.; Deng, X. X.; Li, L.; Li, Z. L.; Du, F. S.; Li, Z. C., *Polym. Chem.* **2013**, *4*, 444-448.
449. Radzinski, S. C.; Foster, J. C.; Chapleski, R. C.; Troya, D.; Matson, J. B., *J. Am. Chem. Soc.* **2017**, *139*, 563-563.
450. Ji, X. Y.; Zhou, Y. F.; Li, Q.; Song, H. Y.; Fan, C. H., *ACS Appl. Mater. Interfaces* **2021**, *13*, 31331-31336.
451. Nam, J.; Kwon, S.; Yu, Y. G.; Seo, H. B.; Lee, J. S.; Lee, W. B.; Kim, Y.; Seo, M., *Macromolecules* **2021**, *54*, 8829-8838.
452. Dong, Y. H.; Yao, C.; Zhu, Y.; Yang, L.; Luo, D.; Yang, D. Y., *Chem. Rev.* **2020**, *120*, 9420-9481.
453. Heinzinger, M.; Elnaggar, A.; Wang, Y.; Dallago, C.; Nechaev, D.; Matthes, F.; Rost, B., *BMC Bioinform.* **2019**, *20*.
454. Lutz, J. F., *Macromol. Rapid Commun.* **2017**, *38*.
455. Arias, S.; Maron, E.; Borner, H. G., *Biomacromolecules* **2021**, *22*, 213-221.
456. Liberman-Martin, A. L.; Chu, C. K.; Grubbs, R. H., *Macromol. Rapid Commun.* **2017**, *38*.
457. Ouchi, M.; Sawamoto, M., *Polym. J.* **2018**, *50*, 83-94.
458. Pearce, A. K.; Foster, J. C.; O'Reilly, R. K., *J. Polym. Sci. Part A: Polym. Chem.* **2019**, *57*, 1621-1634.
459. Choinopoulos, I., *Polymers* **2019**, *11*, 298.
460. Teo, Y. C.; Xia, Y., *Macromolecules* **2015**, *48*, 5656-5662.
461. Li, Z.; Zhang, K.; Ma, J.; Cheng, C.; Wooley, K. L., *J. Polym. Sci. Part A: Polym. Chem.* **2009**, *47*, 5557-5563.
462. Ma, J.; Cheng, C.; Wooley, K. L., *Aust. J. Chem.* **2009**, *62*, 1507-1519.
463. Mecerreyes, D.; Dahan, D.; Lecomte, P.; Dubois, P.; Demonceau, A.; Noels, A. F.; Jérôme, R., *J. Polym. Sci. Part A: Polym. Chem.* **1999**, *37*, 2447-2455.
464. Radzinski, S. C.; Foster, J. C.; Matson, J. B., *Macromol. Rapid Commun.* **2016**, *37*, 616-621.
465. Xie, M.; Dang, J.; Han, H.; Wang, W.; Liu, J.; He, X.; Zhang, Y., *Macromolecules* **2008**, *41*, 9004-9010.
466. Morandi, G.; Piogé, S.; Pascual, S.; Montembault, V.; Legoupy, S.; Fontaine, L., *Mater. Sci. Eng. C* **2009**, *29*, 367-371.
467. Cheng, C.; Khoshdel, E.; Wooley, K. L., *Macromolecules* **2005**, *38*, 9455-9465.
468. Li, Y.; Themistou, E.; Zou, J.; Das, B. P.; Tsiangou, M.; Cheng, C., *ACS Macro Lett.* **2012**, *1*, 52-56.
469. Leroux, F.; Montembault, V.; Pascual, S.; Guerin, W.; Guillaume, S. M.; Fontaine, L., *Polym. Chem.* **2014**, *5*, 3476-3486.
470. Le, D.; Morandi, G.; Legoupy, S.; Pascual, S.; Montembault, V.; Fontaine, L., *Eur. Polym. J.* **2013**, *49*, 972-983.
471. Le, D.; Montembault, V.; Pascual, S.; Legoupy, S.; Fontaine, L., *Macromolecules* **2012**, *45*, 7758-7769.

472. Jiang, L. Y.; Nykypanchuk, D.; Ribbe, A. E.; Rzaev, J., *ACS Macro Lett.* **2018**, *7*, 619-623.
473. Hoy, R. S.; Grest, G. S., *Macromolecules* **2007**, *40*, 8389-8395.
474. Sveinbjornsson, B. R.; Weitekamp, R. A.; Miyake, G. M.; Xia, Y.; Atwater, H. A.; Grubbs, R. H., *Proc. Natl. Acad. Sci. U. S. A.* **2012**, *109*, 14332-14336.
475. Matyjaszewski, K., *Polym. Int.* **2003**, *52*, 1559-1565.
476. Kok, C. M.; Rudin, A., *Macromol. Rapid Commun.* **1981**, *2*, 655-659.
477. Stevens, M. P., in *Polymer chemistry : an introduction*. Oxford University Press, **1999**.
478. Charles, L., *Mass Spectrom. Rev.* **2014**, *33*, 523-543.
479. Sharma, V. K.; Millero, F. J., *Inorg. Chem.* **1988**, *27*, 3256-3259.
480. Wong, C. K. L.; Chan, T. W. D., *Rapid Commun. Mass Spectrom.* **1997**, *11*, 513-519.
481. Zhou, L.; Russell, D. H.; Zhao, M. Q.; Crooks, R. M., *Macromolecules* **2001**, *34*, 3567-3573.
482. Borman, C. D.; Jackson, A. T.; Bunn, A.; Cutter, A. L.; Irvine, D. J., *Polymer* **2000**, *41*, 6015-6020.
483. Demirelli, K.; Coskun, M.; Kaya, E., *J. Polym. Sci. Part A: Polym. Chem.* **2004**, *42*, 5964-5973.
484. Brandrup, J.; Immergut, E. H.; Grulke, E. A.; Abe, A.; Bloch, D. R., in *Polymer handbook*. Wiley New York, **1999**.
485. Olabis, O., in *Polymer-polymer miscibility*. Elsevier, **2012**.
486. Coleman, M. M.; Serman, C. J.; Bhagwagar, D. E.; Painter, P. C., *Polymer* **1990**, *31*, 1187-1203.
487. Albert, J. N. L.; Epps, T. H., *Mater. Today* **2010**, *13*, 24-33.
488. Fox, T. G.; Flory, P. J., *J. Appl. Phys.* **1950**, *21*, 581-591.
489. O'Driscoll, K.; Sanayei, R. A., *Macromolecules* **1991**, *24*, 4479-4480.
490. Shultz, A. R.; Young, A. L., *Macromolecules* **1980**, *13*, 663-668.
491. Robeson, L. M., in *Polymer blends : a comprehensive review*. Hanser, **2007**.
492. Grubbs, R. H., *J. Macromol. Sci. A* **1994**, *A31*, 1829-1833.
493. Neary, W. J.; Kennemur, J. G., *Macromolecules* **2017**, *50*, 4935-4941.
494. Dutertre, F.; Bang, K. T.; Vereroudakis, E.; Loppinet, B.; Yang, S.; Kang, S. Y.; Fytas, G.; Choi, T. L., *Macromolecules* **2019**, *52*, 3342-3350.
495. Dinger, M. B.; Mol, J. C., *Organometallics* **2003**, *22*, 1089-1095.
496. Jawiczuk, M.; Marczyk, A.; Trzaskowski, B., *Catalysts* **2020**, *10*.
497. Love, J. A.; Morgan, J. P.; Trnka, T. M.; Grubbs, R. H., *Angew. Chem. Int. Ed.* **2002**, *41*, 4035-4037.
498. Kim, K. O.; Choi, T. L., *Macromolecules* **2013**, *46*, 5905-5914.
499. Krevelen, D. W. v.; Nijenhuis, K. t., in *Properties of polymers : their correlation with chemical structure : their numerical estimation and prediction from additive group contributions*. Elsevier, **2009**.
500. Shibuya, Y.; Tataru, R.; Jiang, Y.; Shao-Horn, Y.; Johnson, J. A., *J. Polym. Sci. Part A: Polym. Chem.* **2019**, *57*, 448-455.
501. Blanco, C. O.; Sims, J.; Nascimento, D. L.; Goudreau, A. Y.; Steinmann, S. N.; Michel, C.; Fogg, D. E., *ACS Catal.* **2021**, *11*, 893-899.
502. Jäger, M. Synthesis of Y-Shaped Macromonomers Using an α -Acyloxy Amide Linkage with Possible Applications in Ring-Opening Metathesis Polymerization. Bachelor thesis, KIT, Karlsruhe, **2022**.
503. Degennes, P. G., *Angew. Chem. Int. Ed.* **1992**, *31*, 842-845.

504. Zhang, M.; Rugar, P. A.; Feng, C.; Lin, K. X.; Lunn, D. J.; Oliver, A.; Nunns, A.; Whittell, G. R.; Manners, I.; Winnik, M. A., *Macromolecules* **2013**, *46*, 1296-1304.
505. Radzinski, S. C.; Foster, J. C.; Chapleski, R. C., Jr.; Troya, D.; Matson, J. B., *J. Am. Chem. Soc.* **2016**, *138*, 6998-7004.
506. Waibel, K. A.; Nickisch, R.; Mohl, N.; Seim, R.; Meier, M. A. R., *Green Chem.* **2020**, *22*, 933-941.
507. Alizadeh, A.; Oskueyan, Q.; Rostamnia, S., *Synth. Commun.* **2008**, *38*, 4337-4344.
508. Li, Y. J.; Hoskins, J. N.; Sreerama, S. G.; Grayson, S. M., *Macromolecules* **2010**, *43*, 6225-6228.
509. Leophairatana, P.; Samanta, S.; De Silva, C. C.; Koberstein, J. T., *J. Am. Chem. Soc.* **2017**, *139*, 3756-3766.
510. Zhang, B.; Blum, F. D., *Macromolecules* **2003**, *36*, 8522-8527.
511. Zhang, H.; Hong, K.; Mays, J. W., *Macromolecules* **2002**, *35*, 5738-5741.
512. Shen, H.; Leng, X.; Han, L.; Liu, P.; Li, C.; Zhang, S.; Lei, L.; Ma, H.; Li, Y., *Polym. Chem.* **2020**, *11*, 6206-6214.
513. Yang, L.; Ma, H.; Han, L.; Liu, P.; Shen, H.; Li, C.; Li, Y., *Macromolecules* **2018**, *51*, 5891-5903.
514. Engelis, N. G.; Anastasaki, A.; Nurumbetov, G.; Truong, N. P.; Nikolaou, V.; Shegiwal, A.; Whittaker, M. R.; Davis, T. P.; Haddleton, D. M., *Nat. Chem.* **2017**, *9*, 171-178.
515. Pelras, T.; Mahon, C. S.; Mullner, M., *Angew. Chem. Int. Ed.* **2018**, *57*, 6982-6994.
516. Martens, S.; Landuyt, A.; Espeel, P.; Devreese, B.; Dawyndt, P.; Du Prez, F., *Nat. Commun.* **2018**, *9*, 4451.
517. Kammeyer, J. K.; Blum, A. P.; Adamiak, L.; Hahn, M. E.; Gianneschi, N. C., *Polym. Chem.* **2013**, *41*, 3929-3933.
518. Barther, D.; Moatsou, D., *Macromol. Rapid Commun.* **2021**, *42*, 2100027.
519. Gai, Y.; Song, D.-P.; Yavitt, B. M.; Watkins, J. J., *Macromolecules* **2017**, *50*, 1503-1511.
520. Seo, H.-B.; Yu, Y.-G.; Chae, C.-G.; Kim, M.-J.; Lee, J.-S., *Polymer* **2019**, *177*, 241-249.
521. Beevers, R.; White, E., *J. Chem. Soc. Faraday Trans.* **1960**, *56*, 744-752.